



Institiúid Teicneolaíochta Chorcaí
Cork Institute of Technology

Bachelor of Engineering (Honours)

In

Mechanical Engineering

*An Analysis into Wind Induced Loading
Effects on a STS crane and Investigation
into Design Optimisation*

Name: Brian Hand

Industrial Partner: Liebherr Group

Project Supervisor:

Dr. Andrew Cashman

Date:

2nd May 2014

**AN ANALYSIS INTO WIND INDUCED LOADING EFFECTS
ON A STS CRANE AND INVESTIGATION INTO DESIGN
OPTIMISATION**

A Final Year Dissertation Presented

by

BRIAN P.HAND

Submitted to the School of Engineering & Science of the

Cork Institute of Technology

in partial fulfillment

of the requirements for the degree of

Bachelor of Engineering in Mechanical Engineering

May 2014

Department of Mechanical, Biomedical and Manufacturing Engineering

Attestation of Authorship

I hereby declare that this dissertation is the work of Brian P Hand of the Department of Mechanical Engineering at the Cork Institute of Technology during the period from September 2013 to May 2014. I understand that significant plagiarism, as determined by the examiner, may result in the award of zero marks for the entire assignment. Anything taken from or based upon the work of others has its source clearly and explicitly cited.

Signature: _____

Date: _____

Abstract

The rising demand in the maritime transport industry has dictated that container cranes are increasing in size to cope with larger international traffic and containerised volumes. Due to the environmental location of these cranes, they are invariably exposed to the damaging meteorological effects of storms and other adverse weather phenomena. The crane's safety devices such as the tie-downs prevent the crane from overturning and being pushed along the quay during extreme weather. However studies and investigations of wind induced collapses of these cranes have determined that the crane's tie-down system were the primary cause of failure and were found to be lacking in their mechanical response due to failing at a fraction of the design load.

It was therefore proposed to examine the wind loading effects on a container crane with varied environmental operating conditions using state of the art computational fluid dynamics and compare with traditional conservative means. Coupled with this also the crane's current tie-down system design has been analysed and a more optimal solution has been put forward which will allow for better safety, usability and overall mechanical performance.

Extensive computational fluid dynamics analysis has been conducted on a critical section of the crane structure and appropriately complemented by the use of wind tunnel testing. Analysis of mesh size, mesh type, and turbulence model selection have been undertaken to independently characterise the accuracy of this analysis and grid independence obtained. Key results from this analysis and testing have depicted lower values for drag coefficients on these structures in comparison with current utilised methods. Substantial design and testing has been performed on the purposed redesign of the crane's tie-down mechanism that encompasses detailed finite element analysis, photoelastic experimentation and prototype testing.

Acknowledgements

It would not have been possible to complete this project without the help and support of the kind people around me, to only some of whom it is possible to give particular mention here.

Firstly and foremost, I would like to express my sincere gratitude to my project supervisor Dr. Andrew Cashman for his continuous support throughout this project, for his patience, motivation, enthusiasm and immense knowledge. At many stages in the course of this project I benefited from his advice, particularly so when exploring new concepts.

I would like to give praise to Senior Lecturer Sean F O' Leary for his advice on many aspects of this project including photoelasticity testing and also for his dedicated support with entering undergraduate project competitions.

I would also like to acknowledge the lecturers I have met throughout the Mechanical Engineering programme for their high standard of mechanical engineering knowledge.

Special thanks to the mechanical technicians who were always willing to help with various technicalities of the project.

I would particularly like to thank the engineers and designers at Liebherr Group, in particular James Scanlon (chief design engineer) for giving me a very interesting and stimulating project. Also special thanks to Kieran Hanley (stress analysis engineer) for his training of finite element analysis software while I was on work placement, which became invaluable in many aspects of this project.

I would like to thank my classmates and friends of DME4 for their unending support throughout the past four years.

Finally I would like to thank my parents Brendan and Margaret Hand and my brother Ronan for their support, advice and assistance not alone for the duration of this project, but throughout my academic career.

“Give me a place to stand and with a lever long enough I will move the whole world.”

Archimedes

Table of Contents

Attestation of Authorship	I
Acknowledgements	III
Table of Figures	XI
Table of Tables	XVIII
Nomenclature	XIX
Roman Symbols	XIX
Dimensionless Roman Values	XXI
Greek Symbols.....	XXI
Dimensionless Greek Values	XXII
Subscripts.....	XXIII
Abbreviations.....	XXIII
1.0 Introduction	1
1.1 Project Motivation.....	1
1.2 Project Objectives	2
1.2.1 Analysis Objectives	2
1.2.2 Experimental/Validation Objectives.....	2
1.3 Chapter Descriptor	3
2.0 Containerisation-The Concept	4
2.2 Economics of Containerisation	5
2.3 Standardisation	6
2.3.1 The Container.....	6
2.4 The Container Crane	7
2.4.1 Introduction.....	7
2.4.2 Brief History	7
2.4.3 Evolution of the Container Crane	8
3.0 Container Crane Loads	9
3.1 Atmospheric Conditions.....	9
3.2 Wind Speed	10
3.3 Roughness	11
3.4 Wind Induced Failure of Crane Components.....	12
3.4.1 Wind Force Calculation	14
3.5 Wind Effects on Container Crane Structures	15

3.5.1 Dynamic Behaviour	15
3.6 Aerodynamic Instability	16
4.0 Fluid-Structure Interaction.....	17
4.1 Introduction	17
4.2 Drag and Lift forces on a Structure	17
4.2.1 Frictional and Pressure Drag	18
4.3 Characteristics of Fluid Flow past a Structure	18
4.3.1 Fluid Shear Stress	18
4.3.2 Reynolds's Number Effects	19
4.3.3 Boundary Layer	20
4.3.4 Transition from Laminar to Turbulent Flow	23
4.3.5 Turbulent Boundary Layer Flow	24
4.3.6 Boundary Layer Separation	26
4.3.7 Wake Region.....	26
5.0 Computational Fluid Dynamics.....	27
5.1 Computational Approach	29
Computational Fluid Dynamics	30
5.2 Geometry.....	30
5.2.1 3D Model	30
5.2.2 Computational Domain.....	30
5.3 Discretisation.....	31
5.3.1 Mesh Type	31
5.3.2 Mesh Requirements	32
5.3.3 Mesh Quality.....	32
5.3.4 Mesh Method	34
5.3.5 The Mesh	36
5.4 Turbulence Airflow Model.....	41
5.4.1 Applicable CFD Model.....	41
5.5 Numerical Simulation	47
5.6 Grid Sensitivity Analysis	48
5.7 Turbulent Flows	50
5.7.1 Turbulent near wall flow.....	50
5.7.2 Near Wall Treatments.....	51

5.7.3 Y Plus.....	52
5.8 Numerical Results	53
5.9 Graphic Results	56
5.9.1 Velocity Contours	56
5.9.2 Static Pressure Contours	57
5.9.3 Turbulence Intensity Contours.....	58
5.9.4 Results Discussion	59
6.0 Wind Tunnel Modelling	60
6.1 Introduction	60
6.2 Modelling Criteria	61
6.2.1 Background	61
6.2.2 Theories of Scale Model Similitude	61
6.2.3 Scaling Laws	62
6.2.1 Froude’s Number	62
6.2.2 Reynold’s Number	63
6.2.3 Strouhal Similitude	64
6.2.4 Cauchy Number	65
6.3 The Model	66
6.3.1 Physical Model.....	66
6.3.2 Model Manufacture.....	69
6.4 The Wind Tunnel	72
6.4.1 Calibration.....	74
6.5 Force Balance	77
6.5.1 Calibration.....	78
6.5.2 Data Acquisition	81
6.6 Wind Tunnel Test.....	83
6.6.1 Equipment Set-Up.....	83
6.6.2 Test Procedure	85
6.6.3 Flow Visualisation	86
6.7 Hazard Analysis for Wind Tunnel Testing	90
6.8 Wind Tunnel Test Results	91
6.9 Experimental Uncertainty	94
6.9.1 Random Error.....	94

6.9.2 Systematic Error.....	94
6.9.2 Human Error	95
6.10 Use of Wind Tunnel Models and CFD.....	96
6.11 Model CFD Analysis.....	97
6.11.1 Grid Independence	97
6.11.2 CFD Contour Plots.....	99
6.12 Model Results Comparison	100
6.12.1 Results Scaling.....	102
6.13 Full Scale Results	103
6.13.1 Scaling Effects	106
6.14 Benefits of this Approach.....	108
7.0 Design Optimisation	109
7.1 Introduction	109
7.2 Design.....	110
7.2.1 Establishing Functions	111
7.2.2 Setting Requirements	112
7.2.3 Possible Designs	113
7.2.4 Optimal Design	114
7.3 Material Selection	116
7.3.1 Material Selection Process.....	116
7.4 Design Calculations.....	121
7.4.1 Direct Loading	121
7.4.2 Torque-Tightening Method.....	133
7.4.3 Hazard Analysis for Redesign of Tie-down.....	134
7.5 Finite Element Analysis (FEA).....	135
7.5.1 Introduction.....	135
7.5.2 Methodology	135
7.5.3 Mesh.....	136
7.5.4 Torque Applied	137
7.5.5 Direct Tensile load.....	139
7.6 Photoelasticity Testing	142
7.6.1 Circular Polariscope.....	143
7.6.2 Calibration.....	144

7.6.3 The Test Piece.....	146
7.6.4 Test Piece Support Rig.....	147
7.6.5 Test Procedure	148
7.6.6 Photoelasticity FEA	152
7.6.7 Hazard Analysis for Photoelascity Testing.....	154
7.7 Prototype Testing	155
7.7.1 Force Measurement.....	155
7.7.2 Prototype Manufacture.....	157
7.7.3 Prototype Testing.....	163
7.7.3 Results.....	166
7.6.7 Hazard Analysis for Prototype Testing.....	173
8.0 Project Management.....	174
8.1 Introduction	174
8.2 Time Management Techniques	174
8.3 Overview of Work Complete	176
8.3.1 Semester 1	176
8.3.2 Semester 2.....	176
8.4 Project Constraints	177
9.0 Discussion.....	178
9.1 Ethical Considerations.....	179
10.0 Conclusions.....	180
10.1 Recommendations	181
11.0 References.....	182
12.0 Bibliography.....	199
Appendix A.....	A-1
Liebherr STS Crane Technical Description	A-1
STS Crane Legend	A-4
Container Crane Loads.....	A-8
Crane Overall Dimensions	A-9
Putting the Crane Out of Service.....	A-10
Container Crane Components	A-11
Appendix B – Project Management	B-1
Work Breakdown Schedule.....	B-1

Network Diagram.....	B-2
Gantt Charts.....	B-3
Semester 1.....	B-3
Semester 2.....	B-4
Resources.....	B-5
Wind Analysis.....	B-5
Design Optimisation.....	B-5
Limitations/Constraints.....	B-5
Appendix C – Computational Fluid Dynamics.....	C-1
Model & Mesh Setup.....	C-2
<i>SST k-ω model</i> Scaled Residuals.....	C-3
<i>SST k-ω model</i> Computed Results (Full Scale).....	C-4
<i>SST k-ω model</i> Graphic Results (Full Scale Model).....	C-12
Reynold’s Number.....	C-12
Dynamic Pressure.....	C-13
Total Pressure.....	C-14
<i>SST k-ω model</i> Computed Results (Model Scale).....	C-15
<i>SST k-ω model</i> Graphic Results (Scale Model).....	C-19
Velocity.....	C-19
Y Plus.....	C-20
CFD Model Selection Computations.....	C-22
K- ϵ Model.....	C-22
K- ϵ Realisable model.....	C-23
Air Flow Type Approximation.....	C-24
Hand Calculation.....	C-25
Appendix D - Wind Tunnel Testing.....	D-1
Wind Tunnel Calibration.....	D-1
Model.....	D-2
Specification Sheets.....	D-3
Appendix E – Design Optimisation.....	E-1
Crane Wind Load Calculation.....	E-1
Relevant FEM 1.004 Standard Sections for Calculations.....	E-11
Redesign Drawings.....	E-18

Material Specification	E-25
Photoelastic Specifications & Support Rig drawings	E-28
Photoelastic Test Piece CNC Code.....	E-32
Primary Prototype Manufacture Drawings	E-34
Strain Gauge Specification.....	E-38
Hazard Analysis Tables.....	E-39
Appendix F	F-1
Electronic Files.....	F-1
Exhibition Material	F-1
Experimental & Simulation Videos	F-1
ANSYS Files.....	F-1
Excel Files.....	F-1

Table of Figures

Figure 1.1 Liebherr logo (<i>Liebherr-Group-a, 2013</i>)	1
Figure 2.0 Early shipping of goods (<i>WSC,2013</i>)	4
Figure 2.1 McLean’s Sea-Land Service (<i>Container-Handbook, 2013</i>).....	4
Figure 2.2 Increase in containerisation (<i>Financial-Press,2013</i>)	5
Figure 2.3 Container lifted off truck (<i>Liebherr, 2013</i>)	5
Figure 2.4 Container flow chart (<i>Hand, 2013</i>)	6
Figure 2.5 Global container volumes (<i>UN,2005</i>).....	6
Figure 2.6 Liebherr container cranes (<i>Liebherr-Group-a, 2013</i>)	7
Figure 2.7 The first container crane (<i>ASME-b,1983</i>).....	7
Figure 2.8 Size increases (<i>Almeida,2013</i>).....	8
Figure 2.9 Panamax ship (<i>Canal Museum, 2012</i>).....	8
Figure 3.0 Wind formation (<i>Hk-Electric,2011</i>) ³	10
Figure 3.1 Anemometer location (<i>Hand,2013</i>)	10
Figure 3.2 Hurricane-related collapse (<i>Ye,2004</i>)	12
Figure 3.3 Toppled crane after storm (<i>Vertikal,2008</i>)	12
Figure 3.4 Hurricanes intensity increase (<i>NASA,2011</i>).	12
Figure 3.5 Tie-down system (<i>Liebherr-Group, a 2013</i>)	13
Figure 3.6 Brittle-failure (<i>Warnes, 2006</i>)	13
Figure 3.7 Uneven loading (<i>Lee, 2004</i>)	13
Figure 3.8 Error in tie down force (<i>McCarthy & Vazifdar, 2004</i>).....	14
Figure 3.9 Exposure of cranes to wind (<i>Liebherr, 2013</i>).....	15
Figure 3.10 Crane boom is effected by aeroelastic effects (<i>Liebherr, 2013</i>)	16
Figure 3.11 Collar Triangle of Aeroelastic Forces (<i>EPFL, 2011</i>)	16
Figure 3.12 Tacoma Bridge (<i>Scott, 2001</i>).....	16
Figure 4.0 Pressure Drag (<i>Warner,2010</i>).....	18
Figure 4.1 Frictional Drag (<i>Warner,2010</i>).....	18
Figure 4.2 Fluid shear stress (<i>Stack Exchange, 2014</i>)	19
Figure 4.3 High Re number (<i>NTUU,2011</i>)	20
Figure 4.4 Moderate Re number (<i>NTUU,2011</i>).....	20
Figure 4.5 Low Re number (<i>NTUU,2011</i>).....	20
Figure 4.6 Boundary layer over a flat surface (<i>Roymech, 2013</i>)	21
Figure 4.7 Boundary layer analysis on NASA rocket showing boundary layer transition (<i>NASA, 2012</i>)	21
Figure 4.8 Boundary layer thickness and displacement thickness (<i>RIT, 2013</i>).....	22
Figure 4.9 Transition of laminar flow to turbulent flow (<i>MIT, 2002</i>)	23
Figure 4.10 Tollmien-Schlichting waves (<i>Onera, 2006</i>)	23
Figure 4.11 Hairpin eddies (<i>TU/e, 2013</i>).....	23
Figure 4.12 Detailed view of transition phrase (<i>White, 1991</i>).....	24
Figure 4.13 Turbulent Spots (<i>NTUU, 2011</i>)	24
Figure 4.14 Fully developed turbulent flow (<i>Smith et al, 1995</i>).....	24
Figure 4.15 Velocity Fluctuations in turbulent flow (<i>ANSYS, 2012</i>).....	25
Figure 4.16 Kolmogorov’s Cascade Theory of Turbulence	25

Figure 4.17 Boundary Layer Separation and Wake Region (<i>Hand, 2014</i>).....	26
Figure 5.0 The fundamental structure to solving fluid dynamic problems (<i>Hand, 2014</i>)	28
Figure 5.1 Choice of CFD models in ANSYS Fluent (<i>Hand, 2014</i>)	29
Figure 5.2 Overview of computation approaches available (<i>ANSYS, 2011</i>).....	29
Figure 5.3 3D geometry (<i>Hand, 2013</i>).....	30
Figure 5.4 Domain Size	30
Figure 5.5 The different element types a) triangle, b) quadrilateral, c) tetrahedron, d) hexahedron, e) prismatic and f) pyramid (<i>Nielsen, 2011</i>)	31
Figure 5.6 Structured Mesh (<i>Nielsen, 2011</i>)	31
Figure 5.7 Mesh Skewness (<i>Bakker, 2006</i>)	32
Table 5.8 Grid element skewness quality (<i>Bakker, 2006</i>)	33
Figure 5.9 Aspect Ratio determination (<i>UTAS, 2012</i>).....	33
Figure 5.10 Cell Orthogonality (<i>Virginia Tech, 2012</i>)	33
Figure 5.11 Parametric mesh settings (<i>Hand, 2014</i>).....	34
Figure 5.12 Coarse mesh (Left) and Fine mesh (right) (<i>Hand, 2013</i>)	34
Figure 5.13 Model in mesh domain prior grid refinement (<i>Hand, 2014</i>)	34
Figure 5.14 Inflation grid cells (<i>Hand, 2013</i>)	35
Figure 5.15 View showing mesh size difference	36
Figure 5.16 Cross section view (<i>Hand, 2014</i>)	36
Figure 5.17 Cross Section across bottom of model (<i>Hand, 2014</i>).....	36
Figure 5.18 Magnified grid cells (<i>Hand, 2014</i>)	37
Figure 5.19 Grid nodes (<i>Hand, 2014</i>)	37
Figure 5.20 Grid elements (<i>Hand, 2014</i>)	37
Figure 5.21 Average element sizes with standard deviation (<i>Hand, 2014</i>)	38
Figure 5.22 Average aspect ratio (<i>Hand, 2014</i>).....	39
Figure 5.23 Grid Skewness (<i>Hand, 2014</i>)	40
Figure 5.24 Summary of mesh analysis undertaken (<i>Hand, 2014</i>).....	40
Figure 5.25 Available turbulence models in ANSYS Fluent (<i>ANSYS, 2011</i>).....	41
Figure 5.26 Failed convergence of k- ϵ model at 10m/s flow velocity (<i>Hand, 2013</i>).....	42
Figure 5.27 SST model switching (<i>ANSYS, 2011</i>).....	43
Figure 5.28 Successful convergence using the SST model at 10m/s (<i>Hand, 2013</i>)	43
Figure 5.29 SST model solution method (<i>Hand, 2014</i>).....	43
Figure 5.30 Graphic comparison of three models showing turbulence intensity (<i>Hand, 2014</i>)	44
Figure 5.31 Graphical comparison of CFD results (<i>Hand, 2014</i>).....	45
Figure 5.32 Graph showing the percentage difference for each model (<i>Hand, 2014</i>).....	46
Figure 5.33 Solution Flowchart (<i>Hand, 2014</i>).....	47
Figure 5.34 Mass flow rate solution monitor (<i>Hand, 2014</i>)	47
Table 5.35 Grid independence study (<i>Hand, 2014</i>)	48
Figure 5.36 Convergence plot for analysis (<i>Hand, 2014</i>).....	49
Figure 5.37 Percentage difference for three mesh types (<i>Hand, 2014</i>)	49
Figure 5.38 Structure of turbulent flows (<i>ANSYS, 2011</i>)	50
Figure 5.39 The three sub-layers of a flow field of the near wall region in semi-log plot (<i>Zhanga et al, 2010</i>).....	50

Figure 5.40 Near wall treatments (<i>VT ARC, 2013</i>).....	51
Figure 5.41 Y + plot for CFD model (<i>Hand, 2014</i>).....	52
Figure 5.42 Plot of drag and lift forces on boom section.....	53
Figure 5.43 Drag induced from pressure & viscous forces (<i>Hand, 2013</i>).....	54
Figure 5.44 Lift induced from pressure & viscous forces	54
Figure 5.45 Drag and Lift Coefficients (<i>Hand, 2014</i>)	55
Figure 5.46 Plot showing velocity (<i>Hand, 2014</i>).....	55
Figure 5.47 Velocity Contours (m/s) (<i>Hand, 2014</i>).....	56
Figure 5.48 Static pressure contours (Pa) (<i>Hand, 2014</i>).....	57
Figure 5.49 Turbulence Intensity (%) (<i>Hand, 2014</i>)	58
Figure 5.50 Static pressure on section (<i>Hand, 2014</i>).....	59
Figure 5.51 Static Pressure (<i>Hand, 2013</i>).....	59
Figure 5.52 Structure geometry (<i>Hand, 2013</i>).....	59
Figure 5.53 Flow separation (<i>Hand, 2014</i>)	59
Figure 6.0 Proposed wind tunnel methodology (<i>Hand, 2013</i>).....	60
Figure 6.1 Ensure sharp edges (<i>Abrahamsen, 2012</i>).....	64
Figure 6.2 Vortex Shedding (<i>Simerics,Inc, 2012</i>)	64
Figure 6.3 Aeroelastic analysis of a wing (<i>CD-Adapco, 20</i>	65
Figure 6.4 Model showing clearance between wind tunnel walls (<i>Hand, 2014</i>).....	66
Figure 6.5 3D generated scaled model (<i>Hand, 2013</i>)	66
Figure 6.6 Force balance attachment (<i>Hand, 2013</i>).....	67
Figure 6.7 Model attachment design (<i>Hand, 2013</i>)	67
Figure 6.8 Equivalent stress on design (<i>Hand, 2013</i>).....	68
Figure 6.9 Design mesh detail (<i>Hand, 2013</i>).....	68
Figure 6.10 Design boundary conditions (<i>Hand, 2013</i>)	68
Figure 6.11 Equivalent stress vs predicted drag force for design (<i>Hand, 2013</i>)	68
Figure 6.12 Mesh Settings (<i>Hand, 2013</i>).....	69
Figure 6.13 F1 team Red Bull regularly use RP for early results for aerodynamic performance (<i>Ridge, 2013</i>).....	69
Figure 6.14 Rapid Prototyping configuration (<i>SRL, 2004</i>).....	70
Figure 6.15 College RP Machine (<i>Hand, 2013</i>)	71
Figure 6.16 Joints used in model (<i>Hand, 2013</i>).....	71
Figure 6.17 Reynold's Number range for internal flow (<i>MIT, 2002</i>).....	72
Figure 6.18 Reynold's Number vs Flow velocity (<i>Hand, 2013</i>)	73
Figure 6.19 Pitot tube and water manometer (<i>Hand, 2013</i>)	75
Figure 6.20 Velocity distribution inside the wind tunnel (<i>Hand, 2013</i>).....	75
Figure 6.21 Graph of calculated boundary layer thickness and wall shear stress (<i>Hand, 2013</i>).....	77
Figure 6.22 Slender shaft (<i>Hand, 2014</i>).....	77
Figure 6.23 Model connected to force balance (<i>Hand, 2014</i>)	77
Figure 6.24 Parts of force balance (<i>Hand, 2014</i>).....	78
Figure 6.25 Balance calibration set-up (<i>Hand, 2013</i>).....	78
Figure 6.26 Summary of calibration process (<i>Hand, 2014</i>).....	79
Figure 6.27 Balance calibration (<i>Hand, 2014</i>).....	80

Figure 6.28 Percentage difference for each reading (<i>Hand, 2013</i>).....	80
Figure 6.29 Data acquisition system (<i>TecQuipment,, 2000</i>).....	81
Figure 6.30 VDAS System (<i>TecQuipment, 2000</i>)	81
Figure 6.31 Aliased frequency (<i>NI, 2014</i>)	82
Figure 6.32 Dial gauge (<i>Hand, 2014</i>)	82
Figure 6.33 Accurate sampling of frequency (<i>Franz et al, 2011</i>)	82
Figure 6.34 Data Acquisition set-up (<i>Hand, 2014</i>).....	83
Figure 6.34 Model aligned with airflow	83
Figure 6.35 Model positioned in wind tunnel.....	83
Figure 6.36 VDAS enabled with force balance and controlled with a laptop	84
Figure 6.37 Pressure and airflow velocity measurement in wind tunnel	84
Figure 6.38 Wind Tunnel test equipment set-up (<i>Hand,2014</i>)	85
Figure 6.39 Control Panel	85
Figure 6.40 Tufts on model (<i>Hand, 2014</i>)	86
Figure 6.41 Uniform and non-uniform tufts (<i>Hand, 2014</i>).....	87
Figure 6.42 Flow straighter at the inlet of wind tunnel (<i>Hand, 2014</i>).....	88
Figure 6.43 Video Camera (<i>Hand, 2014</i>).....	88
Figure 6.44 Smoke generator used (<i>Hand, 2014</i>).....	88
Figure 6.45 Smoke Visualisation on model.....	89
Figure 6.46 Force vs airflow velocity results (<i>Hand, 2014</i>)	92
Figure 6.47 Average and standard deviation of the results (<i>Hand, 2014</i>)	92
Figure 6.48 Standard deviation of results (<i>Hand, 2014</i>).....	93
Figure 6.49 Aeroelastic effects were observed (<i>Hand, 2014</i>)	93
Figure 6.50 Balance error (<i>Hand, 2014</i>)	94
Figure 6.51 Wind Tunnel exit (<i>Hand, 2014</i>)	95
Figure 6.52 Streamlines at exit of model (<i>Hand, 2014</i>)	96
Figure 6.53 Streamlines from side of model (<i>Hand, 2014</i>)	96
Figure 6.54 Convergence of CFD results for model scale (<i>Hand, 2014</i>)	98
Figure 6.55 Plot CFD predicted drag and lift forces for model (<i>Hand, 2014</i>)	98
Figure 6.56 Static Pressure on Model (Pa) (<i>Hand, 2014</i>)	99
Figure 6.57 Turbulence on model (J/kg) (<i>Hand, 2014</i>)	99
Figure 6.58 Wall shear stress on model (Pa) (<i>Hand, 2014</i>).....	99
Figure 6.59 Plot of drag force on model for three techniques (<i>Hand, 2014</i>).....	100
Figure 6.60 Percentage difference between hand calculation ,CFD and wind tunnel results (<i>Hand, 2014</i>).....	101
Figure 6.61 Standard deviation of results with respect to the hand calculations (<i>Hand, 2014</i>)	101
Figure 6.62 Plot of scaled up model results (<i>Hand, 2014</i>)	103
Figure 6.63 Full scale results (<i>Hand, 2014</i>).....	104
Figure 6.64 Percentage difference between results (<i>Hand, 2014</i>).....	105
Figure 6.65 Standard Deviation for results (<i>Hand, 2014</i>)	105
Figure 6.66 Drag Coefficients (<i>Hand, 2014</i>)	107
Figure 6.67 CFD and wind tunnel results have predicted lower CD values (<i>Hand,2014</i>).....	108
Figure 7.0 Location of tie-down anchors (<i>Hand, 2014</i>)	109

Figure 7.1 Current Tie down system (<i>Hand, 2013</i>)	109
Figure 7.2 Failure of tie-down system (<i>Liftech, 2009</i>)	109
Figure 7.3 Tie down pin locations (<i>Liebherr, 2013</i>).....	109
Figure 7.4 Design 1 (<i>Hand, 2014</i>)	113
Figure 7.5 Design 2 (<i>Hand, 2014</i>)	113
Figure 7.6 Design 3 (<i>Hand, 2013</i>)	114
Figure 7.7 Proposed redesign of tie-down system (<i>Hand, 2014</i>)	115
Figure 7.8 Material σ range limits (<i>CES, 2014</i>).	116
Figure 7.9 Material E performance limits (<i>CES, 2014</i>).	116
Figure 7.10 Material cost ranges (<i>CES, 2014</i>).	116
Figure 7.11 Material cycling fatigue (<i>CES, 2014</i>).	116
Figure 7.12 Yield strength versus Young's Modulus (<i>CES, 2014</i>)	117
Figure 7.13 Fatigue strength versus Yield strength (<i>CES, 2014</i>)	118
Figure 7.14 Corrosion resistance of SAF 2507 (<i>Sandvik, 2014</i>)	119
Figure 7.15 Impact energy for SAF 2507 (<i>Sandvik, 2014</i>).....	119
Figure 7.16 Uplift Force at crane corner base unit (<i>Hand, 2014</i>).....	121
Figure 7.17 Mohr's Circle of Stress (<i>MD Solids, 2012</i>)	124
Figure 7.18 Max in plane shear stress direction (L) Principal stress direction (R) (<i>MD Solids, 2012</i>)	124
Figure 7.19 Von Mises Criterion (<i>MD Solids, 2012</i>).....	125
Figure 7.20 Alternating and mean stresses (<i>Materials Engineer, 2012</i>)	125
Figure 7.21 Attachment area (<i>Hand, 2014</i>)	126
Figure 7.22 Stress Concentration factor for a circular hole in a rectangular plate (<i>Huston & Harold, 2011</i>).....	128
Figure 7.23 Tension Arm weld detail (<i>Hand, 2014</i>).....	129
Figure 7.24 Turnbuckle weld detail (<i>Hand, 2014</i>)	130
Figure 7.25 Torque Wrench attachment (<i>Hand, 2014</i>).....	131
Figure 7.26 Torque applied.....	131
Figure 7.27 Option of two torques.....	132
Figure 7.28 Torque-Preload Chart	132
Figure 7.29 Redesigned tie-down	133
Figure 7.30 Tightening procedure (<i>Liebherr, 2014</i>)	133
Figure 7.31 Turnbuckle centre (<i>Hand, 2014</i>)	133
Figure 7.32 Finite element analysis flowchart (<i>Hand, 2014</i>)	135
Figure 7.33 Modified material properties (<i>ANSYS, 2014</i>)	135
Figure 7.34 Grid independent mesh (<i>Hand, 2014</i>)	136
Figure 7.35 FEA mesh detail (<i>Hand, 2014</i>).....	137
Figure 7.36 Boundary Conditions (<i>Hand, 2014</i>)	137
Figure 7.37 Equivalent Stress (MPa) (<i>Hand, 2014</i>)	138
Figure 7.38 Maximum Shear Stress (MPa) (<i>Hand, 2014</i>).....	138
Figure 7.39 Displacement (mm) (<i>Hand, 2014</i>).....	139
Figure 7.40 Boundary Conditions (<i>Hand, 2014</i>)	139
Figure 7.41 Equivalent Stress (MPa) (<i>Hand, 2014</i>)	140
Figure 7.42 Maximum Shear Stress (MPa) (<i>Hand, 2014</i>).....	140

Figure 7.43 Displacement (mm) (<i>Hand, 2014</i>).....	141
Figure 7.44 Photoelasticity (<i>Wang, 2008</i>)	142
Figure 7.45 Critical sections (<i>Hand, 2014</i>).....	142
Figure 7.46 College circular polariscope equipment (<i>Hand, 2014</i>)	143
Figure 7.47 Cicular Polariscope (<i>Phillips, 2006</i>).....	143
Figure 7.48 Polariscope filters set up (<i>TERCO AB, 1977</i>)	144
Figure 7.49 Calibration test piece (<i>Hand, 2014</i>).....	144
Figure 7.50 Measuring test piece (<i>Hand, 2014</i>)	144
Figure 7.51 Calibration Measurements (<i>Hand, 2014</i>)	145
Figure 7.52 Calibration test piece fringe order (<i>Hand, 2014</i>).....	146
Figure 7.53 CNC created model (<i>Hand, 2014</i>).....	146
Figure 7.54 Machined Test piece (<i>Hand, 2014</i>)	146
Figure 7.55 College Hurco BMC 20 CNC Mill.....	147
Figure 7.56 Machining Test Piece	147
Figure 7.57 Test piece with supports (<i>Hand, 2014</i>).....	147
Figure 7.58 Bottom holes on <i>model</i> (<i>Hand, 2014</i>)	147
Figure 7.59 Test piece in photo elastic test rig	148
Figure 7.60 Support rig for test piece	148
Figure 7.61 Testing Setup.....	149
Figure 7.62 Graphical comparison of FEA and photoelasticity results (<i>Hand, 2014</i>)	151
Figure 7.63 Graphic comparison of results.....	151
Figure 7.64 FEA parameters (<i>Hand, 2014</i>)	152
Figure 7.65 Mesh Inflation layers (<i>Hand, 2014</i>)	152
Figure 7.66 Material under low stress (<i>Hand, 2014</i>)	153
Figure 7.67 Max principal stress.....	153
Figure 7.68 Minimum principal stress	153
Figure 7.69 Deformation.....	153
Figure 7.70 Middle principal stress	153
Figure 7.71 Prototype (<i>Hand, 2014</i>).....	155
Figure 7.72 Linear, Tee and rosette strain gauges (<i>Omega, 1999</i>).....	155
Figure 7.73 Components of an LVDT (<i>Macro Sensors, 2014</i>)	156
Figure 7.74 The effect of core position the excitation signal (<i>Dally et al, 1993</i>).....	156
Figure 7.75 Prototype at Engineering Exhibition	157
Figure 7.76 Top link and bearing plates (<i>Hand, 2014</i>).....	158
Figure 7.77 Top link inserted in turnbuckle (<i>Hand, 2014</i>)	158
Figure 7.78 Turnbuckle (<i>Hand, 2014</i>)	158
Figure 7.79 Parts of strain gauge (<i>Dally et al, 1993</i>).....	159
Figure 7.80 Wheatstone bridge (<i>NI, 2014</i>).....	159
Figure 7.81 Quarter bridge circuit (<i>NI, 2014</i>).....	159
Figure 7.82 Half bridge setup (<i>NI, 2014</i>).....	160
Figure 7.83 Strain gauge orientation (L) & Lateral orientated strain gauge (R) (<i>Hand, 2014</i>)	160
Figure 7.84 Strain gauge position	161
Figure 7.85 Data logger connector.....	161

Figure 7.86 Locations of strain gauges	161
Figure 7.87 Rigid support frame (<i>Hand, 2014</i>)	162
Figure 7.88 Working Stress (MPa) (<i>Hand, 2014</i>).....	162
Figure 7.89 Displacement (mm) (<i>Hand, 2014</i>).....	163
Figure 7.90 Vishay System 7000	163
Figure 7.91 Shunt Calibration procedure in <i>Strain Smart</i> software.....	164
Figure 7.92 Strain Gauges connected to System 7000 (<i>Hand, 2014</i>).....	164
Figure 7.93 Data Acquisition (<i>Hand, 2014</i>)	165
Figure 7.94 Testing Setup (<i>Hand, 2014</i>)	165
Figure 7.95 Torque wrench on prototype	166
Figure 7.96 Axial strains.....	167
Figure 7.97 Traverse strains (negative)	167
Figure 7.98 Ratio of strains.....	167
Figure 7.99 Experimental Vs Calculated results.....	169
Figure 7.100 Scaled up results plotted on full scale (<i>Hand, 2014</i>).....	170
Figure 7.101 Plot of calculated and experimental scaled results (<i>Hand, 2014</i>)	171
Figure 7.102 Strain gauges on shaft (<i>Hand, 2014</i>)	172
Figure 7.103 GF variation with temperature for stain gauges (<i>Schukar et al, 2013</i>)	172
Figure 8.0 Project Flowchart (<i>Hand, 2013</i>)	174
Figure 8.1 Work Breakdown Schedule.....	175
Figure 9.0 Liebherr design structure (<i>Hand, 2014</i>)	178
Figure 9.1 Indicative insight to fluid structure interaction (<i>Hand, 2014</i>)	178
Figure 9.2 Engineering Ethics (<i>Carleton University, 2013</i>)	179
Figure A-1 Hinge point mechanism on boom section (<i>Hand, 2013</i>).....	A-10
Figure A-2 Derrick boom being lifted into place (<i>Liebherr Group, a 2013</i>)	A-10
Figure A-3 Trolley (<i>Liebherr Group, a 2013</i>).....	A-11
Figure A-4 Head block & spreader connected to a container (<i>Liebherr Group, a 2013</i>)....	A-11
Figure A-5 Head block (<i>Hand, 2013</i>)	A-12
Figure A-6 Operator's line of sight (<i>Liebherr Group, a 2013</i>).....	A-12
Figure A-7 Travel Unit Wheel boxes (<i>Hand,2013</i>)	A-13
Figure A-8 Crane's Travel Unit (<i>Hand,2013</i>)	A-13
Figure A-9 Cable reel drum (<i>Liebherr Group, a 2013</i>)	A-14
Figure A-10 Crane storm anchor from under sill beam (<i>Liebherr Group, a 2013</i>).....	A-14
Figure B-1 Work Breakdown Schedule (<i>Hand,2013</i>)	B-1
Figure B-2 Network Diagram (<i>Hand,2013</i>)	B-2
Figure B-3 Gantt Chart Semester 1 (<i>Hand,2013</i>)	B-3
Figure B-4 Gantt Chart Semester 2 (<i>Hand,2013</i>)	B-4
Figure C-1 Model and mesh setup (<i>Hand, 2014</i>)	C-1
Figure C.2 Model setup and settings (<i>Hand, 2014</i>)	C-2
Figure C.3 The SST k- ω turbulence model scaled residues at velocities 0-60m/s.....	C-3
Figure C-4 Reynold's number (<i>Hand, 2014</i>).....	C-4
Figure C-5 Dynamic Pressure (<i>Hand, 2014</i>).....	C-5
Figure C-6 Total Pressure Contours (<i>Hand, 2014</i>)	C-6
Figure C-7 Velocity contours (<i>Hand, 2014</i>)	C-7

Table of Tables

Table 5.0 Mesh Statistics (<i>Hand, 2014</i>).....	37
Table 5.1 Mesh Metrics (<i>Hand, 2014</i>).....	38
Table 5.2 Aspect Ratio (<i>Hand, 2014</i>).....	39
Table 5.3 Grid cells skewness.....	39
Table 5.4 Grid Orthogonal quality (<i>Hand,2014</i>).....	40
Table 5.5 Comparison of results for three models (<i>Hand,2014</i>).....	45
Table 5.6 Mass averaged y^+ values for the CFD model.....	52
Table 5.7 Drag Force Results (<i>Hand, 2014</i>).....	53
Table 5.8 Lift Force Results (<i>Hand, 2014</i>).....	53
Table 6.0 Necessary Scale factors (<i>Chakrabarti, 1994</i>).....	63
Table 6.1 ABS material properties (<i>CES, 2013</i>).....	66
Table 6.2 Stress analysis results on design (<i>Hand, 2013</i>).....	69
Table 6.3 Reynolds number values wind tunnel (<i>Hand, 2013</i>).....	73
Table 6.4 Calculated boundary layer thickness for wind tunnel (<i>Hand, 2013</i>).....	76
Table 6.5 Reynolds's number range (<i>Hand, 2014</i>).....	87
Table 6.6 Wind Tunnel Results (<i>Hand, 2014</i>).....	91
Table 6.7 CFD results for model (<i>Hand, 2014</i>).....	98
Table 6.8 Model Results Comparison.....	100
Table 6.9 Scaled up model to full scale results (<i>Hand, 2014</i>).....	102
Table 6.10 Full Scale results comparison (<i>Hand, 2014</i>).....	103
Table 6.11 Statistical Analysis of results (<i>Hand, 2014</i>).....	104
Table 6.12 Different CDvalues (<i>Hand, 2014</i>).....	107
Table 7.1 Design Selection Matrix (<i>Hand, 2014</i>).....	114
Table 7.2 Comparison of potential materials (<i>CES, 2014</i>).....	120
Table 7.3 FEA results at different mesh densities.....	136
Table 7.4 Torque applied results (<i>Hand, 2014</i>).....	141
Table 7.5 Direct tensile load results (<i>Hand, 2014</i>).....	141
Table 7.6 Calibration results for stress sensitivity (<i>Hand, 2014</i>).....	145
Table 7.7 Results of FEA and photoelasticity validation (<i>Hand, 2014</i>).....	151
Table 7.8 FEA mesh parameters (<i>Hand, 2014</i>).....	152
Table 7.9 Strain gauge specifications.....	159
Table 7.10 Results for Finite element analysis.....	162
Table 7.11 Strain gauge results.....	166
Table 7.12 Experimental Results.....	169
Table 7.13 Calculated Results.....	169
Table 7.14 Scale factors (<i>Chakrabarti, 1994</i>).....	170
Table 7.15 Prototype and full scale force and torque.....	170
Table 7.16 Experimental and Calculated results for full scale.....	171
Table B.1 Work Breakdown Schedule (<i>Hand,2013</i>).....	B-2

Nomenclature

Roman Symbols

<u>Symbol</u>	<u>Name</u>	<u>SI Unit</u>
A	<i>Area</i>	m ²
A _t	<i>Tensile area</i>	m ²
A _s	<i>Shear area</i>	m ²
c	<i>Damping Coefficient</i>	Ns/m
d	<i>Nominal diameter</i>	mm
d _m	<i>Mean diameter</i>	mm
D	<i>Distance</i>	mm
D _H	<i>Hydraulic diameter</i>	mm
E	<i>Young's Modulus</i>	GPa
F	<i>Force</i>	N
F _m	<i>Mean force</i>	N
F _{max}	<i>Maximum force</i>	N
F _{min}	<i>Minimum force</i>	N
F _D	<i>Drag force</i>	N
F _L	<i>Lift force</i>	N
F _s	<i>Nyquist frequency</i>	Hz
F _{MAX}	<i>Maximum frequency</i>	Hz
f	<i>Frequency</i>	Hz
G	<i>Shear Modulus</i>	GPa
g	<i>Gravity</i>	m/s ²
I	<i>Current</i>	Ampere
I _t	<i>Turbulence intensity</i>	%
I _m	<i>Mass moment of inertia</i>	kg/m ²
I _A	<i>Area moment of inertia</i>	m ⁴

J	<i>Polar moment of inertia</i>	m^4
k	<i>Specific turbulent kinetic energy</i>	m^2/s^2
k_s	<i>Stiffness</i>	N/m
L	<i>Characteristic length</i>	m
m	<i>Mass</i>	kg
M	<i>Moment</i>	Nm
M_t	<i>Torsional moment</i>	Nm
p	<i>Power</i>	kW
P	<i>Pressure</i>	Pa
q	<i>Dynamic pressure</i>	N/m^2
v	<i>Velocity</i>	m/s
U	<i>Velocity component</i>	m/s
u^+	<i>Friction velocity</i>	m/s
r	<i>Radius</i>	m
R	<i>Resistance</i>	Ω
S	<i>Stress sensitivity</i>	MPa
S_e	<i>Modified endurance strength</i>	MPa
S'_e	<i>Endurance strength</i>	MPa
S_y	<i>Yield strength</i>	MPa
S_{ut}	<i>Ultimate tensile strength</i>	MPa
T	<i>Torque</i>	Nm
t	<i>Time</i>	s
t	<i>Thickness</i>	m
V	<i>Voltage</i>	V
x	<i>Cartesian coordinate</i>	m
\dot{x}	<i>Velocity component</i>	m/s
\ddot{x}	<i>Acceleration component</i>	m/s^2

Dimensionless Roman Values

C	<i>Stress optic coefficient</i>
C_D	<i>Drag force coefficient</i>
C_L	<i>Lift force coefficient</i>
C_F	<i>Shape coefficient</i>
C_μ	<i>Empirical constant</i>
Ca	<i>Cauchy number</i>
e	<i>Error</i>
Fr	<i>Froude number</i>
Re	<i>Reynolds number</i>
St	<i>Strouhal number</i>
N	<i>Factor of safety</i>
k_t	<i>Stress concentration factor</i>
R^2	<i>Linear regression</i>
SS_{Error}	<i>Steady state error</i>
SS_{Total}	<i>Steady state total</i>
y^+	<i>Wall unit</i>
y	<i>Measured value</i>
\hat{y}	<i>Theoretical value</i>
\bar{y}	<i>Mean value</i>

Greek Symbols

ε	<i>Kinetic energy dissipation rate</i>	m^2/s^3
τ	<i>Shear stress</i>	MPa
τ_a	<i>Allowable shear stress</i>	MPa
τ_{Max}	<i>Maximum shear stress</i>	MPa
σ	<i>Normal stress</i>	MPa

σ_a	<i>Alternating stress</i>	MPa
σ_{avg}	<i>Average stress</i>	MPa
σ_m	<i>Mean stress</i>	MPa
σ_{max}	<i>Maximum stress</i>	MPa
σ_{min}	<i>Minimum stress</i>	MPa
σ_y	<i>Yield stress</i>	MPa
σ'	<i>Von Mises stress</i>	MPa
σ_1	<i>First principal stress</i>	MPa
σ_2	<i>Second principal stress</i>	MPa
σ_3	<i>Third principal stress</i>	MPa
ρ	<i>Density</i>	kg/m ³
δ	<i>Boundary layer thickness</i>	mm
δ^*	<i>Displacement thickness</i>	mm
ω	<i>Frequency of eddy shedding</i>	Hz
μ	<i>Dynamic viscosity</i>	Pa.s
ν	<i>Kinematic viscosity</i>	m ² /s.
θ	<i>Angle</i>	radian
η	<i>Efficiency</i>	%

Dimensionless Greek Values

Δ	<i>Difference</i>
Φ	<i>Shielding factor</i>
β	<i>Roughness coefficient</i>
∂	<i>Partial derivative</i>
γ	<i>Ratio of moments</i>
α	<i>Power-law index</i>
ζ	<i>Damping ratio</i>

λ	<i>Scale factor</i>
ν	<i>Poisson's ratio</i>
μ	<i>Frictional coefficient</i>
ϵ	<i>Strain</i>
σ	<i>Standard deviation</i>

Subscripts

i, j - The indexes i and j are used to distinguish Cartesian components

E - Enclosed

g – Gust amplitude

m – Model

m – Mean storm wind

n - Natural

P - Point

p – Prototype

W – Wind

w - wall

Ref- Reference

z - Aerodynamic roughness height

Abbreviations

BS – British Standards

CAD – Computer Aided Design

CFD- Computational fluid Dynamics

DIN- German Institute for Standardisation

FEA – Finite Element Analysis

FEM – European Federation of Materials Handling

HGV – Heavy Goods Vehicle

HV – Vickers Hardness

ISO – International Standards Organisation

SST – Shear Stress Transition

STS – Ship to Shore

WBS – Work Breakdown Schedule

1.0 Introduction

1.1 Project Motivation

This project is being carried out in conjunction with Liebherr Group, who are a worldwide leader in the design and manufacture of heavy machinery. The



Figure 1.0 Liebherr logo (Liebherr-Group-a, 2013)1

company has a reputation as a supplier of technically, innovative and user orientated products and since the company's inception in 1949 their main attribute has been their design of functional superior cranes best suited to the customer's needs. Liebherr Container Cranes a sub-division of Liebherr Group require a detailed analysis of the effect of wind induced loading on STS crane structure. Currently traditional and highly conservative standards are utilised to quantify wind loading on these structures. The traditional standards based design approach leads to high mass crane structures and creates foundation problems in many harbour and quay structures - a problem exacerbated by the increasing trend towards larger STS cranes. The complex physical geometry of modern STS cranes combined with the dynamic and unpredictable nature of wind flow poses a major challenge to the designer / analyst wishing to diverge from the standard based approach.

The crane's structure and components may be redesigned if wind loads are found to effect the crane differently compared currently which are calculated using conventional methods (FEM design standards). These standards are difficult to implement coupled with the complex geometry of a container crane and such drag



Figure 1.1 STS container cranes (Liebherr Group, a 2013)

coefficients may be found to be lower than what are currently used. The potential for design optimisation will be examined regarding the crane's tie-down anchor system which is affected by fluctuating wind loading. The crane's tie down system is the device that prevents the crane from becoming detached during high winds or storms and resists the uplift forces created from wind flow over the crane. This system has problems where it is cumbersome for the crane workers to set equal tension on these tie-down mechanisms and due to deflection of the crane from wind loading and can lead to unequal tensile loads on the turnbuckles and can be a potential failure mechanism. It is proposed to analyse the current design which is used by Liebherr and investigate possible designs which allow the development of a component which will evenly distribute the load between the two turnbuckles during operation.

1.2 Project Objectives

1.2.1 Analysis Objectives

- Carry out calculations to quantify wind loading on a STS Crane using current design standards and procedures with varied operating conditions.
- Develop CFD models to calculate wind loading on STS Crane with varied operating conditions (in-service and out-of-service conditions).
- Document CFD and wind tunnel test results, compare & contrast with analytical calculations.
- Analyse current tie down anchor system used by Liebherr using suitable analytical calculations.
- Examine new designs using appropriate calculations & FEA and document loading, deflection, stress/strain and fatigue.

1.2.2 Experimental/Validation Objectives

- Perform wind tunnel test analysis on crane section to validate CFD results using dimensional analysis techniques.
- Apply wind loads to replicate CFD model and evaluate accuracy, also flow aids will be utilised. Pressure and drag force measurements will be recorded using appropriate instrumentation.
- Validate FEA analysis using suitable experimental means such as photoelasticity testing.
- Build & test prototype of redesigned tie down mechanism to show proof of purpose.
- Develop a system to allow the crane operator to set the tension accurately in crane tie-downs with numerical feedback or some other means.
- Carry out relevant hand calculations for the design of crane tie-down system.
- Develop FEA models of crane tie-down system to analyse loadings & stresses induced from fluctuating crane loads and validate experimentally.

1.3 Chapter Descriptor

This chapter descriptor is provided to give the reader a brief introduction to each chapter, its content and the overall direction of the project.

Chapter two gives a brief and concise introduction into the concept of containerisation focusing on its developments and advancement since its establishment and reasons for introduction. Also this chapter introduces the main focus of this project which is the container crane and outlines its main function and importance in globalised world.

Chapter three outlines the many effects wind induced loading can have on container crane structures including failure initiated by storms and high winds. This chapter also outlines one of the primary crane components that is highly influenced by the dynamic nature of fluctuating wind induced loading and its reported failure in operation.

Chapter four examines the core physics behind fluid-structure interaction and its association with the dynamic nature of airflow. This chapter begins by introducing the basic concepts of lift & drag that occur when fluid interacts with a body and the formation of the boundary layer. This chapter also extends deeply into the complex nature of turbulent fluid flow and to the formation of the Navier-Stokes Equations.

Chapter five outlines the computational fluid dynamics (CFD) analysis which has been conducted by the author on a critical section of the container crane boom. This chapter also documents the process of obtaining accurate CFD results including achieving grid independent mesh to the selection of the most suitable turbulence flow model.

Chapter six introduces the methodology that was adopted to validate CFD results in the form of wind tunnel testing. It extensively outlines the manufacture of a wind tunnel test model, the utilisation of flow similarity laws, calibration procedures, flow visualisation techniques and analysis of results.

Chapter seven describes the approach that was taken on optimising the design of the crane tie-down anchor system including extensive analysis encompassing finite element analysis (FEA), photoelasticity testing, design & manufacture and testing.

Chapter eight outlines the project management of this project which documents the work breakdown schedule, semester Gantt charts and overall time management throughout the project.

Chapter nine and ten include a discussion of the project as a whole and draws conclusions & recommendations based on the analysis & experimentation with key findings addressed.

2.0 Containerisation-The Concept

Containerisation is the global storage and transportation system, where containers carrying cargo can be easily, efficiently and systematically loaded on to containerships, freight-trains and vehicles, without handling the contents individually from one mode of transfer to another (Hamedi-a, 2010). It is estimated that “Roughly ninety percent of the world’s cargo goods are transported by sea with seventy per cent as containerised cargo.” (Castonguay & Stone, 2010) Before containerisation goods were shipped across oceans from one land to another from results of foreign conquests and trading. The process of loading and unloading the ships was labour intensive. Ships spent more time in the port rather at sea while the dockworkers manually loaded cargo into tight spaces aboard ships “*what the biggest bottleneck was getting things on and off the ships*” (Krugman,2009). Before the container shipping era emerged, wooden boxes of were used for transporting cargo. This was the most logical and straightforward means of moving two items between two destinations at that time and remained the case well after the end of World War II (WSC-a, 2013)



Figure 2.0 Early shipping of goods (WSC,2013)2

Today containerisation is a well established trend in shipping both in international and domestic trade (Sople, 2007). The whole shipping process was streamlined by American entrepreneur Malcolm McLean’s Sea land Service in the 1950s which developed an intermodal structure using standardised containers that facilitated effective movement between trucks, ships, and trains through purpose built maritime terminals (Castonguay & Stone, 2010). McLean foresaw the savings in time, labour and costs if the cargo containment part of a truck trailer could be simply lifted on and off the truck chassis and moved directly by ship. McLean’s ideology was to handle cargo only twice, once at the shipper’s port and again at its final destination (Joyce, 2012). This concept seemed simple at the time but in fact it required considerable modifications to the ship and truck bodies at that time (Costamare-Inc, 2013).



Figure 2.1 McLean’s Sea-Land Service (Container-Handbook, 2013)

2.2 Economics of Containerisation

Before the inception of containerisation, international trade was a costly process where 25% of the price of goods was attributed to the insuring, transporting, loading, unloading and storing of cargo (Graham, 2005). Insurance companies could charge lower insurance premiums for containerised cargo compared with conventional cargos. This was the case because containers reduced risks such as damage, theft and non-delivery (Ismail.R, 2008). Containerisation considerably reduced the cost of freight handling, enabling logistical separation of shipping ports from industries and markets, which allowed manufacturing to relocate out of urban areas “Ultimately this slashed shipping costs, which made it affordable to haul goods over distances unimaginable at the time” stated Wayne Talley, a professor of maritime economics at Old-Dominion University, Virginia (Joyce, 2012).

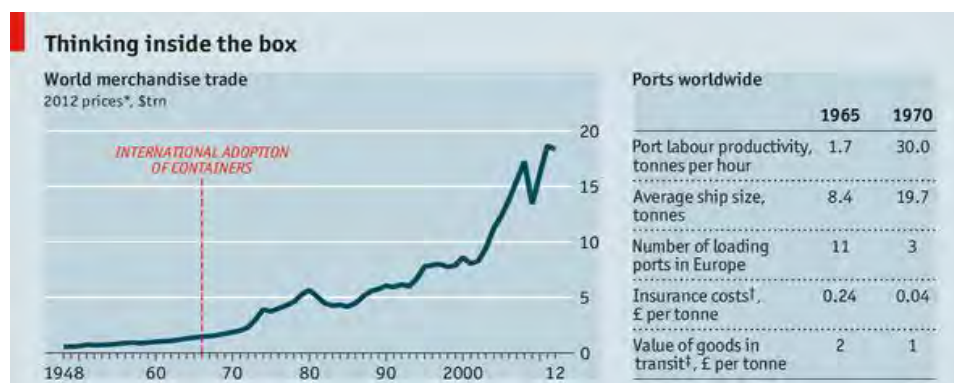


Figure 2.2 Increase in containerisation (Financial-Press, 2013)

Labour costs were significantly reduced by the implementation of containerisation, less port workers were required to work at ports due to the efficiency and time management which containerisation introduced and as a result labour costs plummeted. It opened the door for international shipping and manufacturing



Figure 2.3 Container lifted off truck (Liebherr, 2013)

industries which co-exist and meant that manufacturers could take advantage of relatively low shipping expensive (Graham, 2005). This led the foundations of the world economy we live today; manufacturers could exploit low cost labour in certain parts of the world which has led to a more globalised economy, in which manufacturing could be redirected away from the manufacturer’s homeland. China and other formerly impoverished eastern nations thus came to the fore as dominate manufacturing centres (Schiavenza, 2013).

2.3 Standardisation

2.3.1 The Container

In 1960s, international shipping groups recognised the positives that could be gained from container shipping and in deliberations with the ISO set the standard sizes for containers. The two common and most used sizes are the 20-foot and the 40-foot lengths. The 20-foot container is often referred to a Twenty-foot Equivalent Unit (TEU) and is the industry standard guide with container ships and vessel capacities are measured in TEUs. The 40-foot length container is two TEUs together and has become known as the Forty-foot Equivalent unit (FEU) (WSC-b, 2013). These containers are generally made from steel and built to the same ISO specifications regardless of where they are manufactured. The container sizes need to be identical so that the containers can be effectively stacked on top of the other aboard container ships and then be transported by crane and be mounted onto trains, trucks and HGV's (WSC-b, 2013).



Figure 2.4 Container flow chart (Hand, 2013)

Container volumes worldwide have witnessed incredible growth in the last fifty years, especially with accelerated expansion since the mid 1990s as displayed below in figure 2.6 (Rodrigue & Notteboom, 2007). According to the UN the number of containers shipped on worldwide trade routes totalled 105.2 million TEU for 2005 compared with just 28.7 million TEU in 1990. In 2015 it is forecasted that the total volume will reach 177.6 million TEU. Quantities on the east-west and north-south trade routes are expected to increase on average by 6% per annum with higher growth of 7.5% expected in the Asian trade routes (UN, 2005).

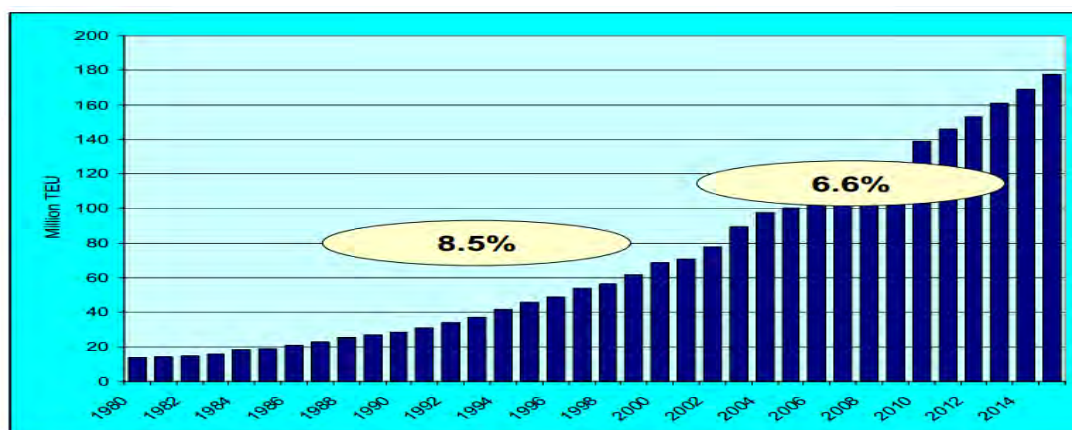


Figure 2.5 Global container volumes (UN, 2005)

2.4 The Container Crane

2.4.1 Introduction

A container crane is the biggest crane which is used in the operation sector of the shipping industry (*Marine Insight, 2010*) and is common sight in many shipping ports worldwide. It is designed and built for the main function of loading & unloading containers from a container vessel. The crane is controlled by a specially trained operator from within a cabin which is attached to the trolley suspended from a beam which traverses the span of the crane. Liebherr Group first became involved in the container crane market in 1958 (*Liebherr Group-b, 2013*) when it opened its production facility in Ireland and since then have produced many cranes of different shapes and sizes for international ports globally (See appendix-A pages A-11 to A-14 for description of crane's main components).



Figure 2.6 Liebherr container cranes (*Liebherr-Group-a, 2013*)

2.4.2 Brief History

In 1959 the world's first high speed container crane was established at Encinal Terminals in Alameda, California and was developed by PACECO due to introduction of containerisation. It considerably reduced ship turnaround time from three weeks to eighteen hours and set the design standard for future designs (*ASME-a, 2013*). Although this was a big technical advance at that time, the containerisation concept was still a long way from being ideal. One of the main setbacks facing this trend was that many ports were not equipped to manage heavy containers and many used revolving cranes which were very inefficient in that two to three minutes of the loading cycle was lost to inadequate control at the points of loading & unloading. Since the loading cycle would be repeated many thousands, reducing the length of this cycle would have direct impact on the productivity of these ports and welcomed economic outcomes (*ASME-b, 1983*).



Figure 2.7 The first container crane (*ASME-b, 1983*)

2.4.3 Evolution of the Container Crane

Since the first container crane was produced there has been significant improvements and advancements made on container cranes but all modern cranes are direct descendents of the first crane and the blueprint for later cranes has stayed relatively unchanged (Ceccarelli, 2004).

With the accelerated growth of container traffic since the first crane was produced, container vessels and cranes have together gotten larger to manage demand. In the 45 years since the first crane was designed, the dimensions of the cranes and their lifting capacities has more than doubled (Luck & Modler, 1990). The main driving force behind the expanding dimensions of the cranes has been the building of bigger container ships which can carry more containers (TEUs) and in a more efficient manner “the larger ship is cheaper per ton to build, and running costs per ton also fall as size of the vessel is increased” (Lim, 1994).

Clearly a container crane must have span wide enough to facilitate the unloading & loading of the container ship and two have evolved coherently over the past decades. The first container ships were called panamax ships and were built in line with the dimensions of the Panama Canal. The Panama Canal is a man-made canal which allows the transit of ships from the Pacific Ocean to the Atlantic Ocean without the need to travel around the most southern tip of South America (Dutemple, 2003).

In the late 1980’s panamax container ships loads increased to over 4000 TEU which put severe pressure on the Panama Canal to cope with these load increases and this coupled with the inefficient fuel consumption of these ships meant that the shipping companies opted to transport cargo using bigger ships called post-panamax ships (Van-Ham, 2005) and thus the creation of the need for bigger cranes “When you get bigger ships, you can more efficiently carry more cargo, so the fuel footprint you get per tonne of cargo is smaller” states Unni Einemo of Sustainable Shipping.



Figure 2.8 Panamax ship (Canal Museum, 2012)

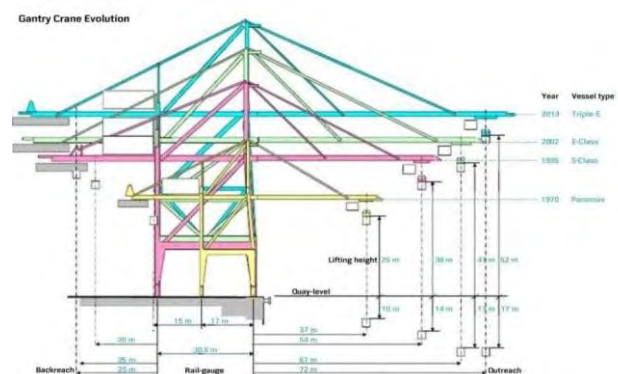


Figure 2.9 Size increases (Almeida, 2013)

3.0 Container Crane Loads

A container crane is influenced by its own static & dynamic loads and the environmental loads where it is situated. The crane's dynamic loads consist of the trolley moving containers to and from the ship which has an average frequency of 56 moves per hour or on average 1.2 million TEU per year (*Port-Technology,2012*). The trolley moving on the crane structure induces inertial loads on the crane structure which create vibrations that resonate throughout the crane. The gravitational loads are an important design constraint which can impose large fatigue and buckling stresses on the crane main structure. When the dimensions of the crane increase, the structure's weight and wheel loads become the main issue with respect to its strength.

The primary study of this report will be focussed on the wind loads on a container crane and their effect on the crane stability, see appendix-A page A-8 for visual description of the cranes loads. Storm wind is one of the many forces that is considered in the design of container cranes, to cause considerable damage and in some cases even overturning (*McCarthy & Vazifdar, 2004*). Container cranes are particularly vulnerable to adverse weather conditions due to their geometry and the fact that cranes have no shielding facility to guard against high winds "*wind load is considered the most important factor under any load conditions for container crane design*" (*Lee et al,2009*). For the purpose of this study, a Liebherr post-panamax crane will be analysed with the dimensions and specifications shown in appendix A page A-7.

3.1 Atmospheric Conditions

Wind is considered to be the movement of air over the surface of the Earth from regions of high pressure to low pressure. The larger the atmospheric pressure gradient, the higher the induced wind speed which gives rise to potential storms and hurricanes that exhibits the wind's full and often devastating forces (*Tong,2010*). Atmospheric conditions and movements determine the winds speed and direction. The atmosphere is forced to move due to the rotation of the Earth and also due to the heat absorbed from the sun through radiation. As the Earth spins on its axis it creates a circulating force more commonly known as the Coriolis Effect which pulls the atmosphere along with it. This force decreases with distance from the Earth, making wind speeds to be maximum near the Earth's surface. The difference between air speeds causes mixing to occur between the air molecules which develops

turbulence, this turbulence results in what is called wind on the Earth's surface (*Manwell et al*). Heat energy absorbed from the sun greatly influences global wind patterns. Due to the angle on which the earth rotates, this heat energy is not evenly distributed. Tropical regions receive more solar energy than that can be radiated back to back space. The amount of solar energy received at the Earth's surface reduces as one moves closer to the poles. As the air is heated it becomes less dense and rises, which causes the cooler less dense air to be pulled down by atmospheric pressure from cooler regions. This is why hurricanes and other wind driven meteorological phenomena are more common in warm climates found in the tropic regions near the equator (*Siraj, 2010*).

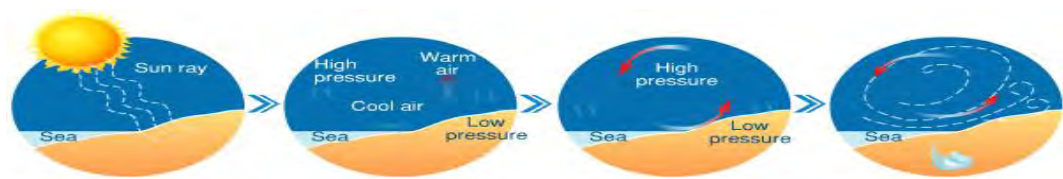


Figure 3.0 Wind formation (*Hk-Electric,2011*)3

The heated air then travels and moves by convection currents away from the warm region where it begins to cool, as the air cools it becomes denser and falls in altitude. This constant cycle of heating and cooling of air circulates warm air around the world which results in wind (*Tong, 2010*).

3.2 Wind Speed

This is ultimately one of the most dominant factors in the design of container cranes. The maximum in-service wind speed for a container crane is set at 20m/s and the maximum out-of service wind speed being 42m/s, see appendix A, page A-2. These wind speeds are set by the European Federation of Materials Handling, (FEM). Liebherr Group has to conform to these standards for crane design & manufacture, in particular for wind loading the standard FEM 1.004 (*Recommendations for the calculation of wind loads on crane structures*) is used, please note pages E-11 to E-17 of appendix E (*FEM, 2013*). The wind speed is measured during crane operation using an anemometer located at the highest point on the A-frame of the container crane. When the wind speed rises to unsafe levels, the crane is put “out-of-service” which means the crane operation is halted see appendix A page A-10 for procedure. Today precise weather forecasting

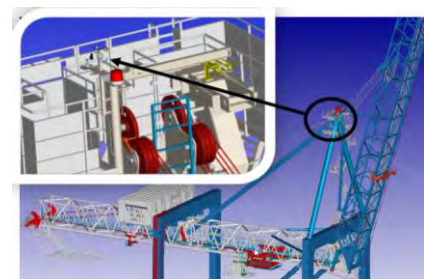


Figure 3.1 Anemometer location (*Hand,2013*)

allows crane operators to accurately predict when the crane will have to be put out-of-service. In most design standards including the FEM standard use a maximum wind speed for a given time period known as a “mean recurrence interval” (*Simlu. et al, 1998*). MRIs are established from statistical data of maximum wind speed records at particular weather observatories and in most cases, a 50-year MRI is used in container crane design. A 50 year MRI outlines that “there is 64% chance that the design speed will occur in 50 years, a 40% chance in 25 years and a 2% chance in the first or any given year” (*McCarthy & Vazifdar,2004*). Wind is naturally turbulent and it fluctuates over time, this means that the measurement of wind speed depends on the method by which the wind speed is averaged. Taking the average of wind speed over shorter periods results in a higher wind speed. The larger the crane, the less sensitive it is to gust due to the fact that it takes longer for the gust to develop around the crane. The FEM 1.004 standard takes the gust duration to be 3 seconds (*FEM,2013*) (*McCarthy & Vazifdar,2004*).

3.3 Roughness

Roughness is important parameter used to describe the friction between the wind and a surface that decreases its velocity and force. In general, the more pronounced the friction of the earth’s surface the greater the decrease in wind velocity, for the operation of container cranes in ports the sea surface has a relatively smooth surface and low friction values are utilised (Note $\alpha = 0.14$ & $\beta = 1$ in a plane area, Appendix-E page E-17). The difference of wind speeds at ground level and operation height is referred to as wind shear profile (*Roy, 2012*). *FEM 1.004* calculates wind velocity $v(z)$ at a height $z(m)$ above ground level using the Equation [3.1]:

$$v(z) = F_{ref} \times \left[\frac{v_m(z)}{v_{ref}} + \phi_8 \frac{v_g}{v_{ref}} \right] \times v_{ref} \quad [3.1]$$

Where $\frac{v_m(z)}{v_{ref}} = \beta \times \left(\frac{z}{10} \right)^\alpha$ [3.2] is the power law expression (Appendix-E page E-17 for variable denotation)

This wind shear affects the structural stability of the crane in the following way. Wind shear creates lower wind speeds closer to the ground and in-turn greater wind speeds at the top of the crane, which induces bending moments on the crane structure and excites the structure

with a dynamic frequency of vibration Equation [3.3] (Takacs & Rohal,2012). Calculation 2 shows the change in velocity with height in appendix-E page E-3.

$$f_n = \frac{1}{2\pi} \omega_n \quad [3.3]$$

3.4 Wind Induced Failure of Crane Components

Container cranes at their highest point can reach over 100m, they are especially exposed to severe windstorms such as typhoons and hurricanes and thus the wind load acting on the structure is substantial. In many cases the cranes have been damaged and even overturned due to losing their stability (Lee et al,2007). Figure 3.2 shows 8 collapsed out of 19 container cranes demolished after typhoon Maemi hit Busan, South Korea in 2003 (Ye, 2004) and figure 3.3 displays a container crane collapse in Felixstowe, UK after severe storm winds (Vertikal,2008).



Figure 3.2 Hurricane-related collapse (Ye,2004)



Figure 3.3 Toppled crane after storm (Vertikal,2008)

Hurricanes and other related storms are expected to gain considerable strength as global temperatures continue to rise due to the adverse effects of global warming. From modelling data focused on the conditions in which hurricanes develop, international researchers from the Beijing Normal University have found that for every 1°C rise in the Earth's temperature, the amount of hurricanes in the Atlantic that were as severe as Hurricane Katrina in 2005 will increase by three times (National-Geographic, 2013). "These numbers are a strong indication that climate change is a major factor in the increasing number of Atlantic hurricanes," states Greg Holland of the National Centre for Atmospheric Research (NCAR) (UCAR,2007). This means more hurricanes are

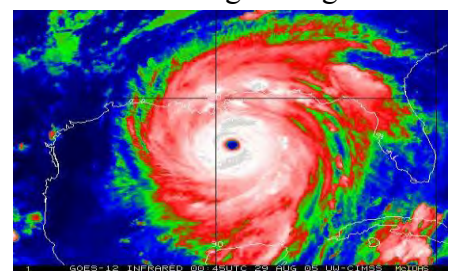


Figure 3.4 Hurricanes intensity increase (NASA,2011).

making landfall and container cranes face increasing risk of being overturned. In most hurricane related crane collapses that has been investigated by engineers and crane specialists have identified that failure commenced in the cranes tie down anchor system. These investigations showed that the tie downs were the “*weak links*” (McCarthy & Vazifdar, 2004). Although there has been no reported failure of this component on a Liebherr crane, all crane manufacturers use a similar turnbuckle type mechanism at the core of the tie down design. In some situations cranes can have ballast added to the crane to provide better stability of the crane during high winds but this has significant disadvantages such as higher wheel loads which means that the quay infrastructure has to be made stronger and also increased energy requirements for moving the crane along the quay. This would increase running costs and bigger motors would have



Figure 3.5 Tie-down system (Liebherr-Group, a 2013)

to be used instead of 40KW motors which are used presently on these cranes (Liebherr-Group, a 2013). In most cases the tie-down system is employed to prevent the corner uplift of the crane when it is out-of-service. Typically in regions where high wind speeds are expected two tie-downs are used at the corner of the crane. The main flaw with the current design of tie down’s turnbuckles is that they cannot be tightened in a manner which allows equal tension in both tie downs. It is very difficult to supply equal tension to each tie down, because a difference of a few millimetres will greatly affect the distribution of the load between the tie downs. In strong

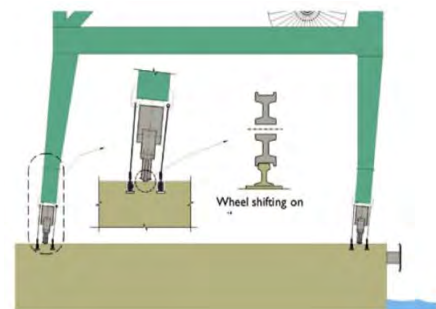


Figure 3.6 Uneven loading (Lee, 2004)

winds the crane can rotate and shift laterally and the tension in the tie downs are not equal and do not stay vertical as figure 3.6 demonstrates (Lee, 2004). In many cases the magnitude of the uplift force is transferred to one tie down which induces failure at a fraction of the design corner load. This also initiates failure in the remaining tie down before the intended design load is reached (Lee, 2004). From investigations carried out on the failure of these components, it has been reported that the tie downs failed in a brittle manner where failure was initiated at the thread



Figure 3.7 Brittle-failure (Warnes, 2006)

chest as shown in figure 3.7 and there were no indications of fatigue failure (McCarthy & Vazifdar, 2004).

3.4.1 Wind Force Calculation

Generally standards whether they are BS or DIN standards quantify wind force using the same method. The FEM 1.004 standard highlighted in Appendix-E page E-11-C-17 calculates wind force on a crane component using equation [3.4] (FEM, 2013):

$$F = C_D \times A \times q \tag{3.4}$$

$$q = \frac{1}{2} \times \rho \times v^2 \tag{3.5}$$

Bernoulli’s Equation [3.5] calculates the dynamic wind pressure at a free stream wind velocity v . The drag coefficients (C_D) used in standards such as the FEM 1.004 (Appendix E page E-15) are not completely suitable for calculating wind forces on structures such as container cranes. These shape coefficients can be conservative in their implementation coupled with difficult geometry such as a container crane to comprehend (Lee et al, 2007). Wind pressure varies with the square of wind speed and thus errors in wind speed are amplified. Taking a crane with a self weight D , a wind force F_W applied through the crane’s centre of gravity, B a distance from corner 1 to corner 4 (see Appendix-A page A-4) and A a distance between the tie downs and opposite corner as shown in figure 3.8. The ratio γ of the crane’s overturning moment to its righting moment can be expressed as: (McCarthy & Vazifdar, 2004)

$$\gamma = \frac{(F_W)(z)}{(D)\frac{B}{2}} \tag{3.6}$$

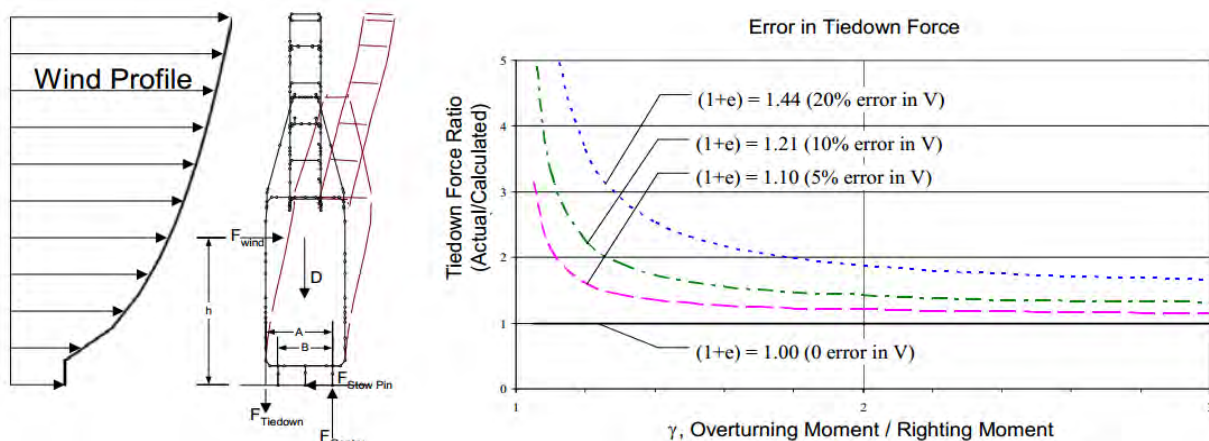


Figure 3.8 Error in tie down force (McCarthy & Vazifdar, 2004)

The variable “e” is taken to be the error in wind pressures and the ratio of the actual tie down force and the calculated tie down force is expressed in equation [3.7]:

$$\frac{F_{\text{Actaul}}}{F_{\text{Calculated}}} = \frac{\frac{1}{A}[(1+e)F_w \cdot z - D \frac{B}{2}]}{\frac{1}{A}[F_w \cdot z - D \frac{B}{2}]} = \frac{(1+e)\gamma - 1}{\gamma - 1} \quad [3.7]$$

This equation [3.7] however does not take into account the stiffness of the crane or the wind angle of attack, however it does give a good indication of how a minor error in the wind velocity can amplify the calculated tie down forces. It also displays that the crane's overturning moment becomes greater than the righting moment as the error in the tie down force approaches the error in the wind pressure, "e" (McCarthy & Vazifdar, 2004).

3.5 Wind Effects on Container Crane Structures

The interaction with a container crane and dynamic nature of wind flow can cause static, dynamic and aerodynamic effects of the crane's structure. The crane structure is mainly composed of structurally flexible members that are subject to wind induced loading along and across the direction of the wind flow. When the structure deflects in response to wind load the cranes dynamic and aerodynamics effects come into to focus (Adhikari, 2008). This structural dynamic variation is due to the buffeting effects produced by turbulence and also a phenomenon referred to as vortex shedding which will be referred to later in this report.



Figure 3.9 Exposure of cranes to wind (Liebherr, 2013)

3.5.1 Dynamic Behaviour

In its simplest form, Newton's Second Law can be used to describe the motion of crane structure mass with the differential equation [3.8] (Amirouche, 2006).

$$m\ddot{x} + c\dot{x} + kx = F(t) \quad [3.8]$$

This equation can also be expressed as shown,

$$\ddot{x} + 2\zeta\omega\dot{x} + \omega^2x = \frac{F(t)}{m} \quad [3.9]$$

Where $\omega = \sqrt{\frac{k}{m}}$ and $\zeta = \frac{c}{2m\omega}$

These above equations forms the basis for the dynamic behaviour of the crane structure in response to excitation created from vortex shedding, self-excitation and buffeting due to the turbulent nature of air flow (Selvam, 1998).

3.6 Aerodynamic Instability

Aeroelasticity is described as the interaction between the structural dynamics and the unsteady natural airflow over and around the structure. This can be considered an important aspect of crane design especially in relation to the crane boom as shown in figure 3.11 which is particularly affected by this interaction. This interaction can create both static and dynamic instabilities which if not carefully designed for can lead to failure of structural components (TU Delft, 2014)

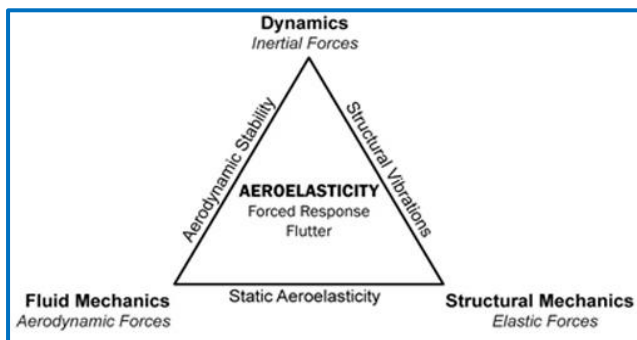


Figure 3.10 Collar Triangle of Aeroelastic Forces
(EPFL, 2011)



Figure 3.11 Crane boom is affected by aeroelastic effects (Liebherr, 2013)

Aeroelastic effects can have a detrimental effect on a structure if not treated and can increase the occurrence of fatigue stresses; therefore a reliable prediction method is required called the Collar triangle as shown above in figure 3.10. This triangle determines aeroelasticity as the interaction between inertial, aerodynamic and elastic forces (EPFL, 2011). When airflow passes through or around a structure it can deflect and vibrate also. This oscillatory motion of the structure produces a change in the flow pattern around the structure; if increasing continuous vibrations are introduced to the structure aeroelastic instability is occurring (Simiu & Scanlan, 1986). The primary causes of aeroelastic instability are vortex shedding, buffeting, galloping and flutter (Selvam & Govindaswamy, 2001). Perhaps the most well known example of failure from aeroelastic effects was the collapse of Tacoma Narrows Bridge in 1940 which failed from vibrations induced from vortex shedding around its structure which caused it to oscillate and fail (Scott, 2001)



Figure 3.12 Tacoma Bridge
(Scott, 2001)

4.0 Fluid-Structure Interaction

4.1 Introduction

The study of structures or bodies immersed in a fluid is commonly known as external flow analysis (*Young et al, 2011*) whereby the fluid flows around the body such as the case presented by the author. In situations where air is the external fluid this analysis is frequently termed aerodynamics and is the study of how airflow affects the structure and various flow phenomena that develop. As in all areas of the study of fluid mechanics principles, many methods are utilised that include hypothetical, numerical and experimental techniques which are capable of determining the forces created by a fluid in an external flow condition (*Young et al, 2011*). This approach will be adopted for the wind induced loading analysis aspect of this project.

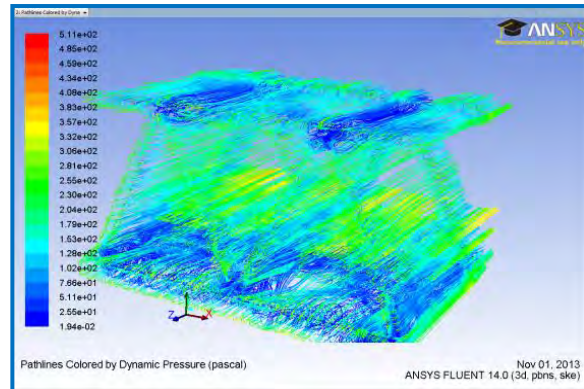


Figure 4.0 External flow shown using streamlines (*Hand, 2013*)

4.2 Drag and Lift forces on a Structure

When a structure such as a container crane comes in contact with a moving air stream, an interaction between the structural components and fluid occurs and is denoted in terms of the forces at the fluid – structural interface (*Young et al, 2011*). These forces are a result of viscous shear stresses and normal stresses due to pressure and are denoted as τ_w (wall shear stresses on the structure). The resultant force in the direction of the upstream velocity is called drag force (F_D) and the resultant force normal to the upstream velocity is termed lift force (F_L) (*Munson et al, 2012*).

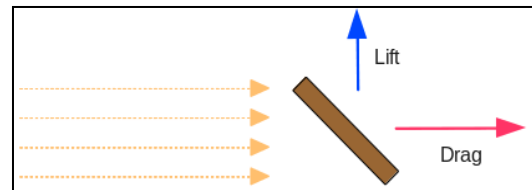


Figure 4.1 Drag & Lift forces (*Iforce2d, 2013*)

It is common in fluid dynamic problems to express these forces as non-dimensional numbers or coefficients. For drag force, the drag coefficient (C_D) is expressed as the ratio of drag force to the force produced by the dynamic pressure times the area (*Abrahamsen, 2012*). A similar approach can be taken for lift force which a dimensionless coefficient (C_L)

$$C_D = \frac{F_D}{\frac{1}{2}\rho v^2 A} \quad [4.1]$$

$$C_L = \frac{F_L}{\frac{1}{2}\rho v^2 A} \quad [4.2]$$

4.2.1 Frictional and Pressure Drag

There are two components of drag force which are frictional drag and pressure drag. Every material has its unique frictional coefficient and will oppose fluid flow to varying degrees. (Cakir, 2012). The friction coefficient of a surface effects greatly the development of a boundary layer on the surface and scales with Reynold's number (Princeton University, 2013). Pressure drag is created by eddies which are formed as the fluid flows past an obstacle. The fluid creates a space after passing the obstacle which is commonly known as a wake and is less acceptable to Reynold's number than that of frictional drag (Moffatt, 1963). Frictional drag is the primary concern where attached flows are analysed whereby there is no separation of the fluid stream. Pressure related drag is significant for separated flows and is related to the cross sectional area of the body (Princeton University, 2013).

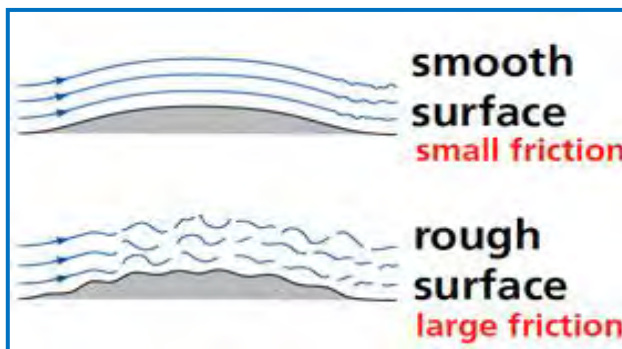


Figure 4.2 Frictional Drag (Warner, 2010)

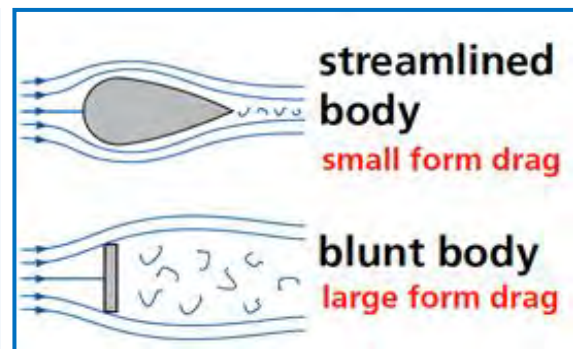


Figure 4.3 Pressure Drag (Warner, 2010)

4.3 Characteristics of Fluid Flow past a Structure

4.3.1 Fluid Shear Stress

External fluid flows create a large variety of fluid dynamic phenomena as the fluid molecules interact with the structure. The primary distinction in the mechanical performance of fluids compared with common solids is that when shear stresses are applied to a fluid it undergoes continual deformation. The fluid offers no resistance to shearing and only possesses elastic properties under direct compression (Princeton University, 2013). A fluid flowing across a surface will create a shear stress on the boundary (Stack Exchange, 2014). The theoretical no-slip condition states that the velocity of the fluid at the boundary, relative to the boundary or wall is zero. (Day, 1990). It is also stated that at some distance from the boundary the flow speed must become equal to that of the fluid. This region where the velocity distribution occurs is commonly referred to as the boundary layer and is very important occurrence in the study of fluid dynamics. Newton's Law of Viscosity states that "the rate of change in

distance between two neighbouring points moving with fluid divided by the distance between the points” (Smith, 2012) and this law is applied to Newtonian Fluids such as air in this study.

The shear stress term τ_w is imparted onto the boundary wall as a product of the loss of velocity and at a point y it can be calculated using expression [4.3].

$$\tau(y) = \mu \frac{\partial u}{\partial y} \quad [4.3]$$

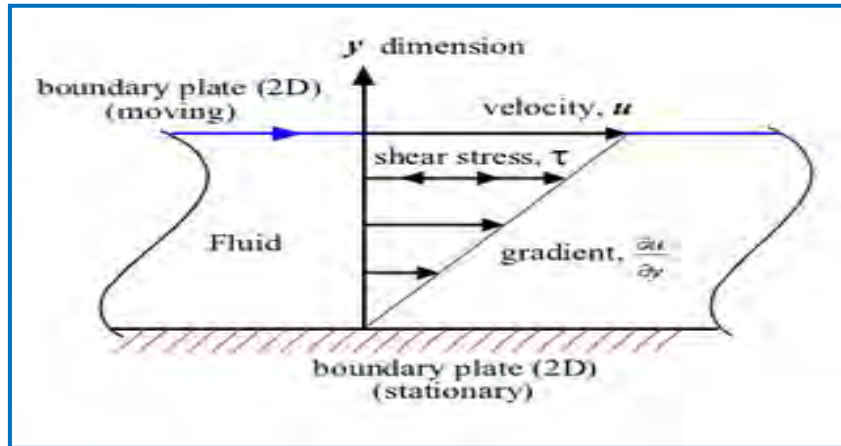


Figure 4.4 Fluid shear stress (Stack Exchange, 2014)

4.3.2 Reynolds's Number Effects

For the study of fluid induced forces on a structure the Reynold's number (Re) is significant as it describes the relationship between the inertial and viscous forces using the expression [4.4] whereby L is the characteristic length of the body or structure (HSE, 2001).

$$Re = \frac{\rho v L}{\mu} \quad [4.4]$$

In typical airflow fluid dynamic studies, upstream fluid velocities range from 0.01m/s to 100m/s (Young et al, 2011). As a result the Reynold's number (Re) can vary for flows approximately in the range of $10 < Re < 10^9$. It is considered a rule of thumb that flows with $Re > 100$ are most influenced by inertia effects and viscous effects are minimal (Young et al, 2011). This rule is an important consideration in this study as inertia effects will be more critical than viscous effects. As the velocity of the free stream increases the Reynold's number increases proportionally and the region in which the viscous effects are primary becomes less in all directions except in the downward stream as dictated in figures 4.5-4.7.

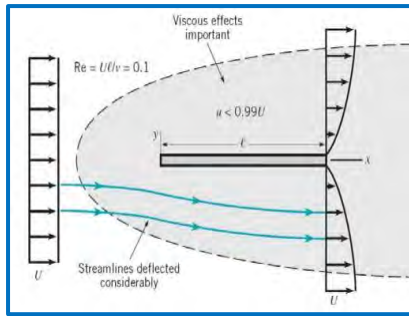


Figure 4.5 Low Re number (NTUU,2011)

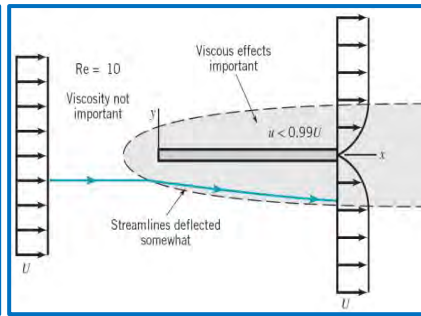


Figure 4.6 Moderate Re number (NTUU,2011)

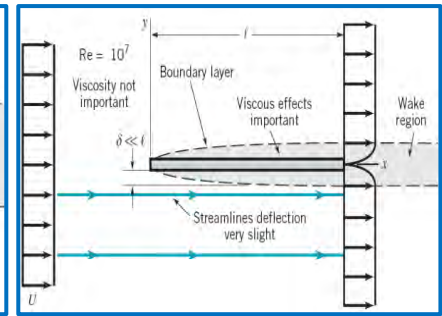


Figure 4.7 High Re number (NTUU,2011)

When the Reynolds number is very large the flow is dominated by inertial effects and the viscous effects are found to be negligible except in zones close to the plate and in the relatively thin wake region formed by the flow.

4.3.3 Boundary Layer

The term aerodynamic boundary layer was firstly defined by German engineer and aerodynamist Ludwig Prandtl in 1904 (Anderson, 2005). His theory portrayed the idea of boundary layer to be a thin region on the surface of a body in which viscous affects were important. This analogy simplified the full Navier-Stokes Equations [4.5] - [4.7] of fluid flow into two different fluid flow areas. The first accounts for inside the boundary layer where the fluid viscosity dominates the drag incurred on the body, the second accounts for the fluid flow outside the boundary layer where viscosity is considered negligible and has little influence on the solution (Sreenivasan, 2004). Prandtl's advancement meant a more simplified solution could be found too many fluid dynamic problems without resorting to the full Navier-Stokes Equations. (Anderson, 2005)

$$\frac{\partial u}{\partial x} + \frac{\partial v}{\partial y} = 0 \tag{4.5}$$

$$u \frac{\partial u}{\partial x} + v \frac{\partial u}{\partial y} = -\frac{1}{\rho} \frac{\partial p}{\partial x} + \nu \left(\frac{\partial^2 u}{\partial x^2} + \frac{\partial^2 u}{\partial y^2} \right) \tag{4.6}$$

$$u \frac{\partial v}{\partial x} + v \frac{\partial v}{\partial y} = -\frac{1}{\rho} \frac{\partial p}{\partial y} + \nu \left(\frac{\partial^2 v}{\partial x^2} + \frac{\partial^2 v}{\partial y^2} \right) \tag{4.7}$$

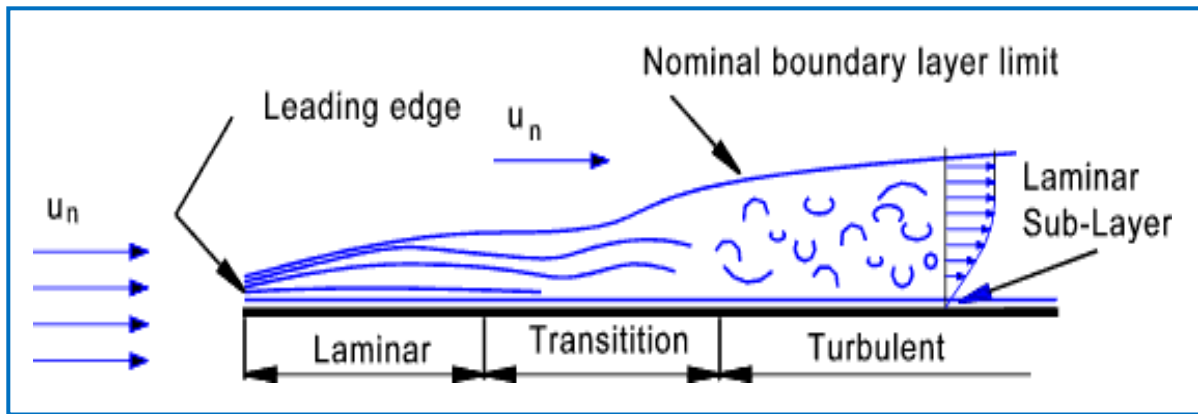


Figure 4.8 Boundary layer over a flat surface (Roymech, 2013)

There is a large diversity in the size of a boundary layer and organisation of the flow within the boundary depending on the shape of the object on which the boundary layer forms. Mainly studies have been conducted on the boundary layer formation on flat plates due to its simpler analysis and easier identification of various fluid flow conditions as shown above (Young *et al*, 2011). At the leading edge of the plate the fluid velocity is decreased as it contacts the plate and the boundary layer is initiated. As the fluid continues to flow across the plate a velocity profile is established between the plate surface and the free stream velocity indicating a laminar flow region (Roymech, 2013). As the boundary layer steadily thickens, its flow quality begins to become more unstable and the laminar region becomes less streamlined. The location where the laminar flow begins to deteriorate is called the transition point and it commences its transformation to turbulent flow which takes a specific amount of time depending on the flow velocity (Roymech, 2013).

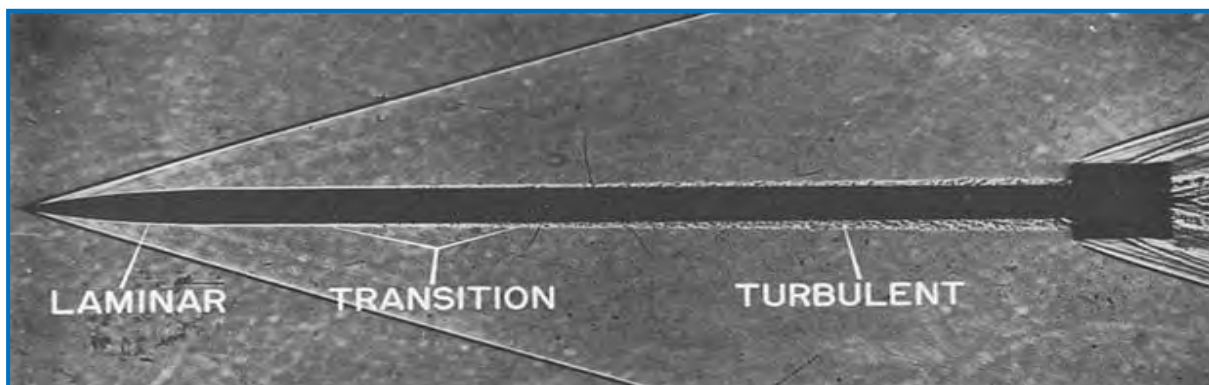


Figure 4.9 Boundary layer analyses on NASA rocket showing boundary layer transition (NASA, 2012)

The most distinguishing feature of turbulent flow is the incidence of irregular and unorganised mixing of the fluid particles. The shift of laminar region to a turbulent region happens at critical Reynolds's number range of 2×10^5 to 3×10^6 depending on such

factors such as the surface friction coefficient and the degree of turbulence present in the oncoming fluid (Young et al, 2011).

It is common in the study of boundary layer formation to establish three types of boundary-layer thickness and the most common used term is simply denoted as (δ) the boundary-layer thickness (Currie, 1993). Its definition specifies the vertical distance from the boundary where the velocity of the fluid reaches 0.99 of the free stream velocity and can be freely shown in expression [4.8] (Young et al, 2011).

$$\delta = y \quad \text{where } u = 0.99U \quad [4.8]$$

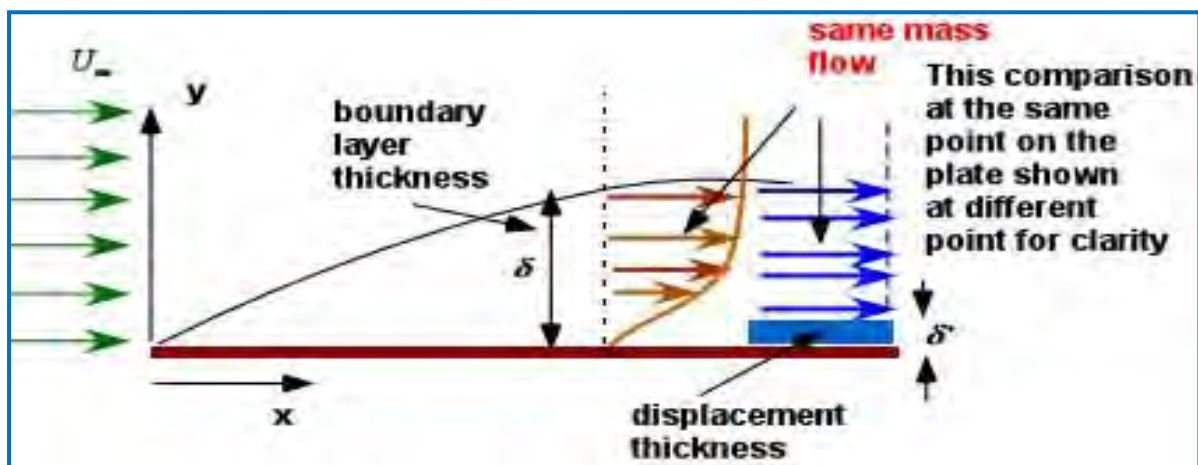


Figure 4.10 Boundary layer thickness and displacement thickness (RIT, 2013)

The next most propionate type of boundary-layer thickness that is useful for analysis is the term known as the displacement thickness(δ^*). This thickness characterises the amount that the thickness of the body must be raised so that the fictitious inviscid fluid flow has the equivalent mass flow rate properties as the actual viscous flow (Currie, 1993).

$$U\delta^* = \int_0^{\infty} (U - u)dy \quad [4.9]$$

$$\delta^* = \int_0^{\infty} \left(1 - \frac{u}{U}\right) dy \quad [4.10]$$

The momentum thickness (θ) is another term used term used in the description of boundary layer and is mainly used in the determination of drag on an object (Young et al, 2011) and is defined in relation to the momentum flow rate within the boundary layer. This rate is less than what would occur in the boundary layer did not exist (Houghton & Carpenter, 2003).

$$\int_0^{\infty} \rho u(U - u)dy = \rho U\theta \quad [4.11]$$

$$\theta = \int_0^{\infty} \frac{u}{U} \left(1 - \frac{u}{U}\right) dy \quad [4.12]$$

These three boundary layer definitions δ , δ^* and θ form the basis of boundary layer analysis (Young *et al*, 2011). The overall formation and properties of the boundary layer flow rely greatly on whether the flow is laminar or turbulent. In many engineering flow cases it is very difficult for the analyst to know whether there will be only laminar or turbulent flow, in most cases a transition between laminar to turbulent flow occurs which adds complexity to significant analytical solving of these flows. For the purpose of this study the concentration will be focused mainly on the influence of turbulent air flow, although laminar flow is evident in the formation of the boundary layer in contact with the structure its effects are found to be negligible in the grand scheme of fluid-structure interaction.



Figure 4.11 Transition of laminar flow to turbulent flow (MIT, 2002)

4.3.4 Transition from Laminar to Turbulent Flow

The transition from laminar to turbulent boundary layer flow does not occur at a single point but instead over a specific region and such factors such as surface roughness and shape of the surface effect this transition region greatly. The main way of determining if a fluid is in a state of laminar or turbulent flow is achieved by examining the Reynolds's number, "Laminar flows have a fatal weakness: poor resistance to high Reynolds numbers" (White, 1991).



Figure 4.12 Tollmien-Schlichting waves (Onera, 2006)

As already stated the fluid firstly enters a laminar condition where the fluid particles are able to damp out any instabilities induced by the factors given above. The initialisation of transition to turbulent flow is begun with the occurrence of unstable 2D Tollmien-Schlichting waves (Bainesi *et al* 1996). These waves commonly abbreviated as T-S waves steadily grow into a 3D wave structure with valleys and peaks in a spanwise direction and are characterised



Figure 4.13 Hairpin eddies (TU/e, 2013).

by Kelvin–Helmholtz instability theory which can occur when there is a velocity shear between a body and a fluid (Slangen, 2009). These waves instigate velocity and pressure fluctuations in boundary layer and form hairpin (Λ) eddies which are considered the building blocks for turbulent flow. “In wall turbulence studies much importance is attributed to the hairpin vortex for the maintenance of the turbulence” (TU/e, 2013).

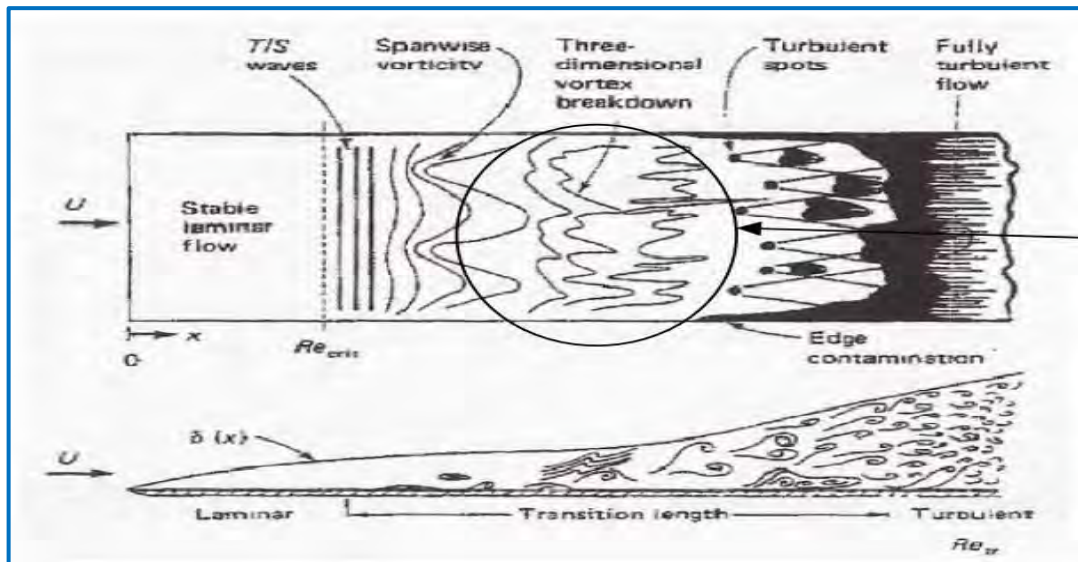


Figure 4.14 Detailed view of transition phase (White, 1991)

With the continual production of these eddies the breakdown in the organisation of the fluid continues rapidly to a complete random nature of fluid flow (Slangen, 2009). This random flow gives rise to turbulent spots that were first observed and described by H. W. Emmons in 1951 who noticed that the spots grew as the flow proceeded downstream until they merged into one another and the entire boundary layer became completely turbulent (Wallace et al, 2010).



Figure 4.15 Turbulent Spots (NTU, 2011)

4.3.5 Turbulent Boundary Layer Flow

The arrangement of the turbulent boundary layer is a very complicated, random arrangement of moving fluid flow particles. Theodore Von Kármán, the famous aerospace engineer and physicist gave the well known definition of

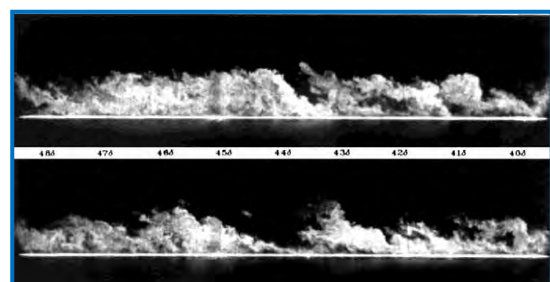


Figure 4.16 Fully developed turbulent flow (Smith et al, 1995)

turbulence “Turbulence is an irregular motion which in general makes its appearance in fluids, gaseous or liquid, when they flow past solid surfaces or even when neighbouring streams of the same fluid flow past or over one another.”(McDonough, 2007).

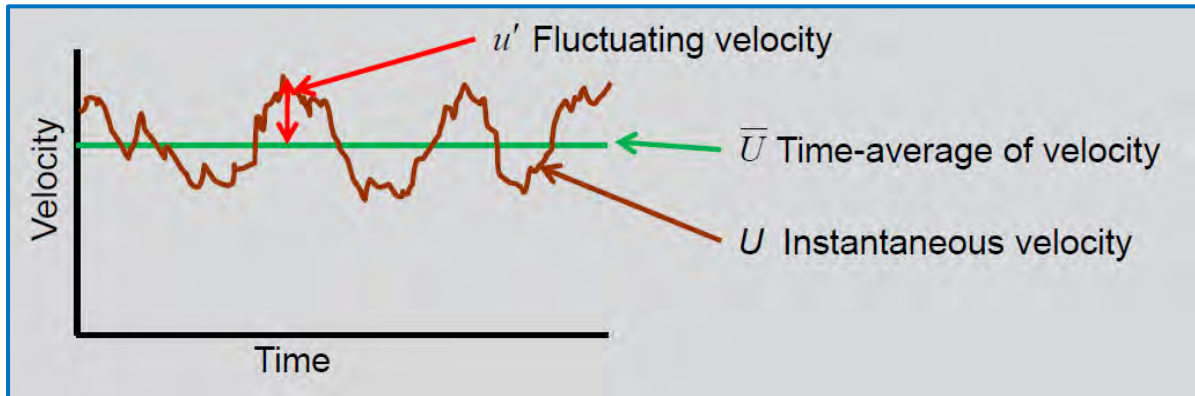


Figure 4.17 Velocity Fluctuations in turbulent flow (ANSYS, 2012)

The velocity at any point in the boundary layer is affected greatly by the fluctuations generated by the eddies present in the fluid (ANSYS, 2012). At any given time the instantaneous velocity can be calculated by [4.13]:

$$U = \bar{U} + u' \quad [4.13]$$

The eddies which are firstly generated by the transformation to turbulent flow are very unstable and break up into smaller eddies. These smaller eddies undergo the same process and in this method the energy is transferred from each eddy. This theory was firstly put forward by Kolmogorov in 1941 and it fundamentally portrays that the energy in the fluid is passed down from the large to small scale motion until a small length scale is achieved that the viscosity of the fluid can efficiently

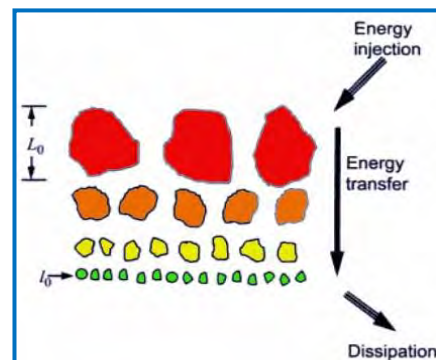


Figure 4.18 Kolmogorov's Cascade Theory of Turbulence

dissipate the kinetic energy into internal energy (PIMS 2013). The size of the largest eddies is usually denoted as (L) and the smallest eddies as (η). For high Reynold's number flows the viscous forces do become very small in relation to the inertial forces. For the energy to be dissipated successfully smaller scale motions are generated until the effects of viscosity become important (P McMurtry, 2000) and can be achieved using equation [4.14].

$$\eta = \left(\frac{v^3}{\epsilon}\right)^{1/4} \quad [4.14]$$

There is no “exact” solution to turbulent boundary layer formulation (Young et al, 2011), but it is achievable to calculate boundary layer flow for laminar flow over a flat plate using

Blasius theory but this is irrelevant to this analysis (Young *et al*, 2011). However significant progress has been made in the past few decades in obtaining accurate results with the use of computational software. These complex and extremely powerful software programs are capable of finding numerical results for many difficult engineering flow problems and use approximated shear stress relationships to obtain results for turbulent flow. This software will be closely examined in the coming chapters and purposed validation methods also.

4.3.6 Boundary Layer Separation

“separation of a boundary layer (BL) from a wall is a very important phenomenon from the practical point of view, determining force interaction between the flow and body.” (Uruba & Knob, 2009). Flow separation occurs due to the strong adverse pressure gradient (APG) or because of a sudden change in geometry of a body in a fluid. Due to the no slip condition the velocity of the fluid becomes zero at a point on the body’s surface and flow becomes detached from the surface initiating the separated region (Logdberg, 2008). Generally in terms of aerodynamics delaying the separation point or “separation bubble” can significantly reduce the pressure differential between the two ends of the body in a fluid. One of the most common applications of this technique is dimples used on golf balls which delay boundary separation in flight.

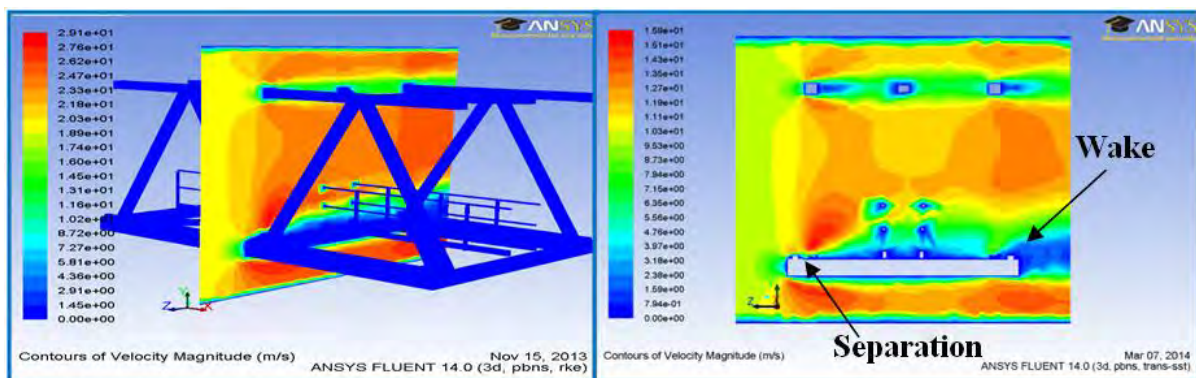


Figure 4.19 Boundary Layer Separation and Wake Region (Hand, 2014)

4.3.7 Wake Region

A wake is formed following the boundary layer separation of a flowing fluid over a body. The size of the wake region can give an analyst a lot of information about the how much drag is on the body. The wider the wake region the bigger the pressure differential will be with the front of the body and thus higher drag value. This analogy was first observed by Helm-Holtz and is sometimes referred to as Helm-Holtz flow (Douglas 2005).

5.0 Computational Fluid Dynamics

Computational fluid dynamics (CFD) is the solving of the primary equations of fluid motion using numerical methods. The section of flow and the boundaries constraining it are segregated into numerous small volumes or cells where the equations which describe the conservation of mass, momentum and energy are calculated in each cell. It is possible to obtain values for velocity, temperature, pressure and turbulence within each of these cells, and overall acquire a comprehensive overview of these variables within a specified flow domain (HSE, 2001).

Over the past ten years or so there have been increasingly rapid advances in the area of CFD, especially in the development of improved numerical algorithms which has led to a large variety of numerical methods of diverse degrees of sophistication and precision (Favier, 2010). This has been mainly pushed by the development of better & faster computing power and more advanced analysis of turbulent models to predict wind flow around structures such as container cranes (Almohammadi, 2013). CFD is based on the concept of Reynolds’s averaging of the steady Navier–Stokes Equations shown again in [5.0] & [5.1] in different form (Han et al,2011) which are considered by Leishman “to be the most appropriate method for analysing nonlinear vicious flows provided that a suitable turbulence model is employed” (Leishman,1990) (Leishman & Tyler,1992).

$$\frac{\partial U_i}{\partial x_i} = 0 \tag{5.0}$$

$$\frac{\partial}{\partial x_j} (\rho U_i U_j) = -\frac{\partial P}{\partial x_i} + \frac{\partial}{\partial x_j} \left[\mu \left(\frac{\partial U_i}{\partial x_j} + \frac{\partial U_j}{\partial x_i} \right) \right] + \frac{\partial}{\partial x_j} (-\overline{\rho u_i' u_j'}) \tag{5.1}$$

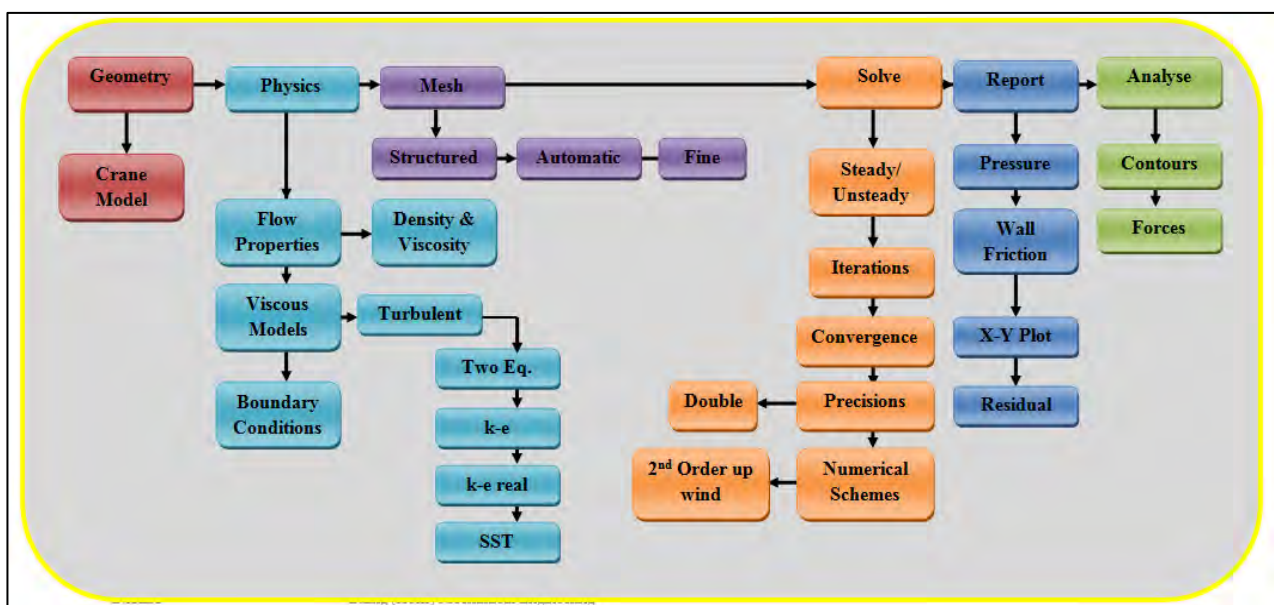


Figure 5.0 CFD model structure (Hand, 2013)

There are many advantages to using CFD; it complements experimental and analytical methods by delivering an alternative cost effective means of simulating real fluid flows. Although it does not give a fully accurate solution for common engineering flows such as fully developed turbulence flows, it does give the best approximation which is still very useful. (Cakir, 2012). “Essentially all models are wrong, but some are useful” George Box (Champkin, 2013). In particular, CFD can dramatically decrease the lead times and costs in design and production stage compared with experimental approaches and still offer the best means to solving a range of complicated flow problems where the analytical approach would be near impossible (Cakir, 2012). Although in the case of turbulence modelling it has received a negative reputation as one the notoriously unpredictable problems of classical physics and is a phenomenon that is ubiquitous and very little actually understood about it. Noble Prize winning physicist Richard Feynman quoted turbulence to be “the most important unsolved problem of classical physics” (Moin & Kim, 2012). CFD programs are becoming more powerful and poised to remain at the cutting edge of research in fluid dynamic analysis with increasing accuracy. These developments in CFD are making it a very appealing practical design tool in modern engineering practice and is steadily attracting more attention and awareness (Cakir, 2012).

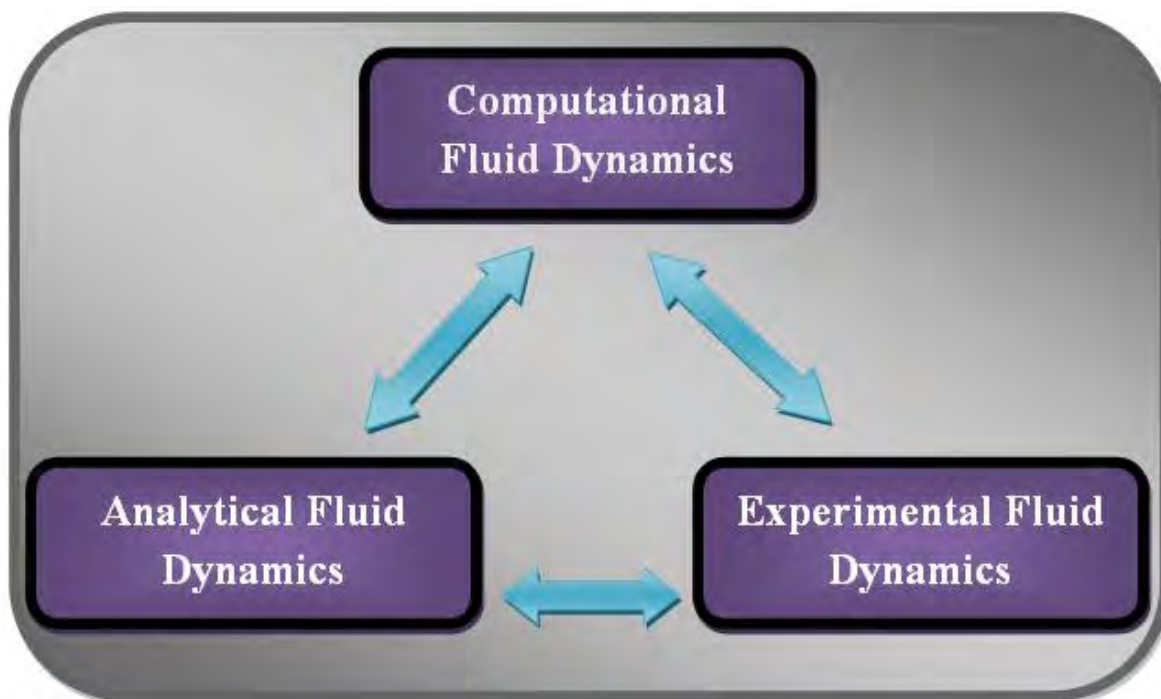


Figure 5.1 The fundamental structure to solving fluid dynamic problems (Hand, 2014)

5.1 Computational Approach

Since almost all engineering fluid flows are turbulent (*Håkansson & Lenngren, 2010*), there is a large variety in the CFD methods which can be utilised to model the fluid flow and whereby different flow equations are solved in order to simulate turbulence. The main three categories in which these models are split into what are called the Reynold's-Averaged Navier-Stokes (RANS) equations, Large Eddy Simulation (LES) and the Direct Numerical Simulation (DNS) (*Versteeg & Malalasekera, 2007*). The DNS method does not use a turbulence model, it uses discrete mathematics to model velocity fluctuations and it therefore requires more time steps and mesh cells and the end results in the need for substantial computing resources. The LES method like the DNS method requires high computational capabilities as it focuses on the large eddies in the flow (*Kandasamy et al, 2002*). The most common used method for industrial flows is the RANS method and gives reasonable approximations as it calculates the time average properties of flow such as mean pressure and velocity while not requiring huge computational capabilities (*Versteeg & Malalasekera, 2007*).

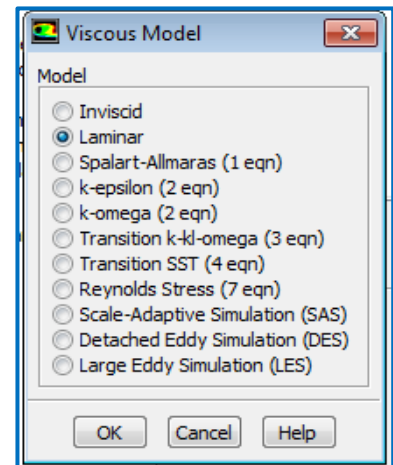


Figure 5.2 Choice of CFD models in ANSYS Fluent (*Hand, 2014*)

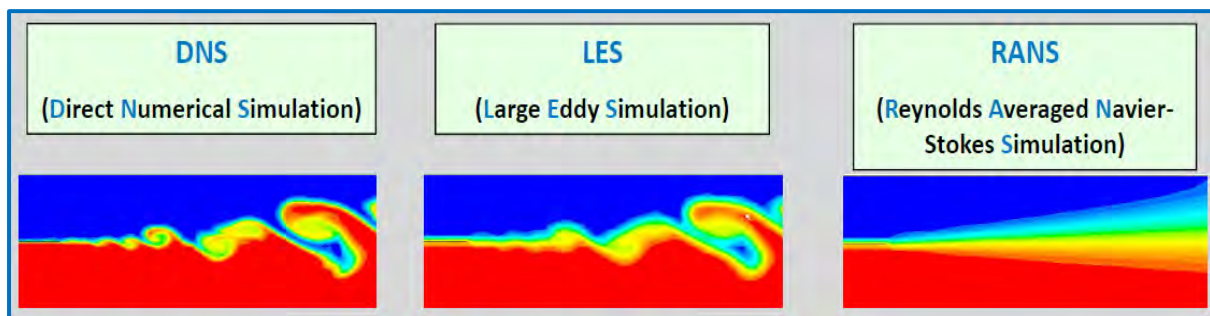


Figure 5.3 Overview of computation approaches available (*ANSYS, 2011*)

For the purpose of this analysis the RANS method will be utilised with a suitable turbulence model. This method introduces a set of unknowns referred to as Reynolds's stresses which require the use of a suitable model to be solved which will be investigated later in this chapter. The RANS equations significantly reduce the orders of magnitude that have to be solved compared with original Navier-Stokes Equations. An important advantage of this method in relation to this study is that the RANS equations for steady flow simulations allows the mean flow velocity to be computed as a direct result without the need to average the instantaneous velocity using a series of time steps (*Symscape, 2009*)

Computational Fluid Dynamics

5.2 Geometry

5.2.1 3D Model

A complete 3D parametric model of a STS container crane was obtained from Liebherr Group in ProEngineer format as shown in Appendix A page A-4. It was determined that this model contained substantial amounts of detail and would be unrealistic to model in a CFD package without the necessary computational resources being available and huge simulation times that would follow. It was therefore decided to model a unique complex section of the crane such as a section of the crane's derrick boom as displayed in figure 5.4. This section was chosen mainly because of its complex shape and the complexity involved in calculating the drag force on the structure.

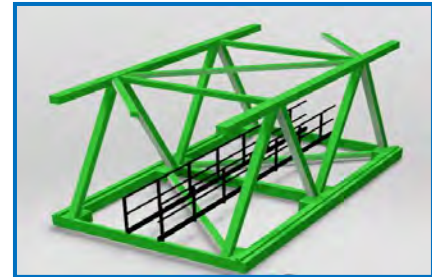


Figure 5.4 3D geometry (Hand, 2013)

The results obtained from the CFD analysis could be compared to current hand calculations using the FEM 1.004 standard (Appendix-C page C-25) and to be analysed for their accuracy. For mesh generation surface details, hollow details and other unnecessary details were refined so a clear defined mesh could be generated.

5.2.2 Computational Domain

The model was placed in a computational domain with sizing according to user guidelines of (Franke et al,2007) and (Tominaga et al,2008) which basically says the walls of the domain should not intercept with the boundary forming around the CFD model and should be kept to a reasonable size that unnecessary additional grid elements are prevented. The optimal domain size was found to be 9.43m long 6.11m high and 6.45m wide as shown below. The airflow inlet and outlet were specified as shown below.

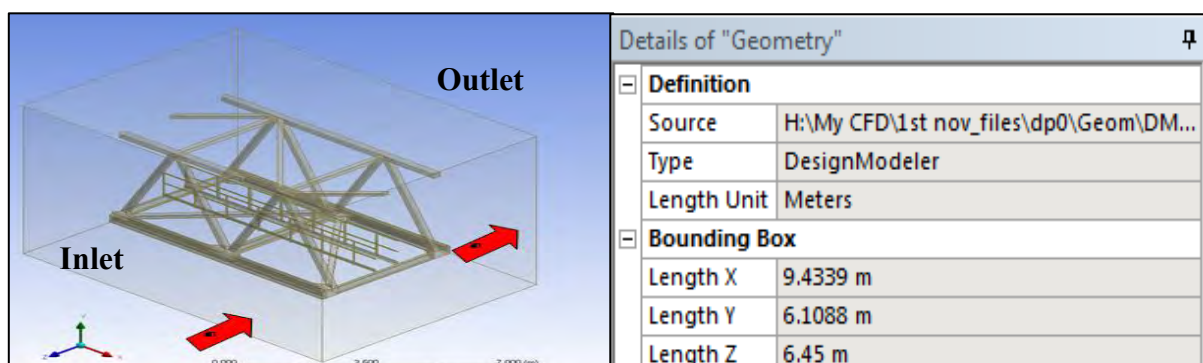


Figure 5.5 Domain Size (Hand,2014)

5.3 Discretisation

The aim of discretisation is to split up the physical space where the flow is to be computed into a large quantity of elements known as grid cells which are contained inside a predefined boundary (Rizzi, 2010) where the governing equations are solved by the chosen method for each element. The different mesh geometric types available in ANSYS mesh are shown below in figure 5.6.

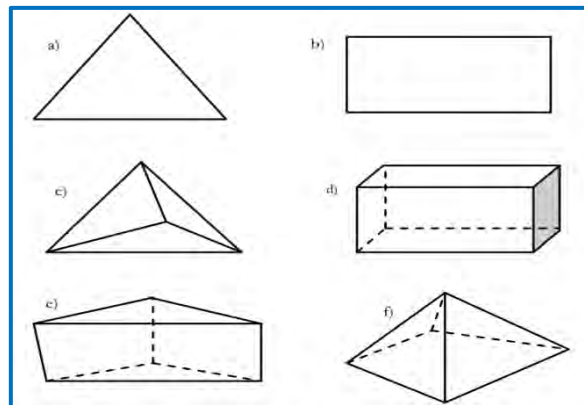


Figure 5.6 The different element types a) triangle, b) quadrilateral, c) tetrahedron, d) hexahedron, e) prismatic and f) pyramid (Nielsen, 2011)

5.3.1 Mesh Type

In the description of CFD grid types, there exists two types of mesh, structured and unstructured grids. Structured grids are seen by the regular connective pattern of cells in formal and organised manner which are advantageous as they decrease overall mesh size and produce more efficient solver processes (Innovative CFD, 2014). However these grids are limited to quadrilateral elements in 2D mesh and hexahedral elements in the 3D mesh as displayed in figure 5.6.

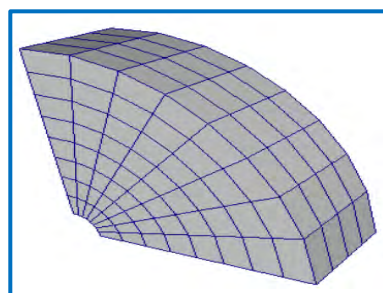


Figure 5.7 Structured Mesh (Nielsen, 2011)

Structured grid meshes do provide very accurate results, but the process of generating such a grid is a very time consuming and tedious task especially when applying to intricate geometries (Wallin, 2009). Unstructured grids as the name suggests can consist of many element types from figure 5.6 and often referred to as hybrid meshes and are mainly comprised of triangular elements on the surface mesh and tetrahedrons in the volumetric

mesh (Nielsen, 2011). Due to the structure of these grids higher grid cell counts are expected which in turn requires more memory and computing power than structured grids. The process of generating these grids has become highly automated by CFD computer packages and have good flexibility in producing local refinements to the grid without impacting on the whole grid distribution (Nielsen, 2011). An unstructured CFD mesh was chosen for this analysis mainly because of the reasons given above.

5.3.2 Mesh Requirements

Mesh generation is one of the most important steps during the pre-process stage of the CFD process because the future results depend highly on the quality of the grid (Cakir, 2012). “Both numerical stability and accuracy could be affected by a poor quality grid” (Wallin, 2009). Where grid element numbers is not limited, it is natural to keep to the resolution as high as possible but this has disadvantages whereby it costs more in computational resources and forms slower turnaround times. A primarily aspect of an accurate CFD model is to keep the element cell count as minimal as possible and use efficient grid refinement techniques to optimise the value of the elements used in the CFD grid. Furthermore to this grid cells should be clustered around areas of interest in model where boundary layers or separation points are occurring and regions where pressure gradients are taking place. It is essential also to for the transition from small to large volume elements that there is no sudden change in the volume of the grid cells (Rizzi, 2010).

5.3.3 Mesh Quality

The quality of a mesh guarantees the best analysis results for the problem being analysed which reduces the need for unnecessary additional computations (TCD, 2006). There are many common criteria used to examine the quality of the model mesh which are the skewness, aspect ratio and orthogonal quality (Plastics U, 2013).

5.3.3.1 Skewness

“Skewness is one of the primary quality measures for a mesh” (TCD, 2006). Large skewness means the accuracy of the mesh is not satisfactory and can be calculated using equilateral volume (Bakker, 2006).

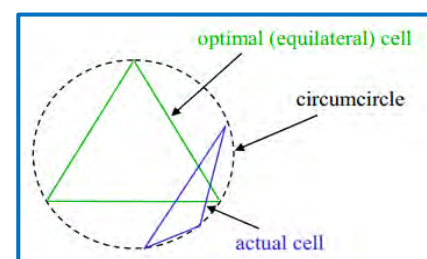


Figure 5.8 Mesh Skewness
(Bakker, 2006)

$$\text{Skewness} = \frac{\text{Optimal Cell size} - \text{Actual Cell size}}{\text{Optimal Cell size}}$$

Using this method an ideal element has a skewness of 0 and can be compared with the table below for cell quality.

Value of Skewness	0-0.25	0.25-0.50	0.50-0.80	0.80-0.95	0.95-0.99	0.99-1.00
Cell Quality	excellent	good	acceptable	poor	sliver	degenerate

Table 5.0 Grid element skewness quality (Bakker, 2006)

5.3.3.2 Aspect Ratio

The aspect ratio is established by the size of the minimum element edge length divided by the maximum element edge length. Shown in figure 5.9 below the aspect ratio can be determined by dividing A by B. A large aspect ratio can cause an interpolation error of intolerable magnitude (UTAS, 2012).

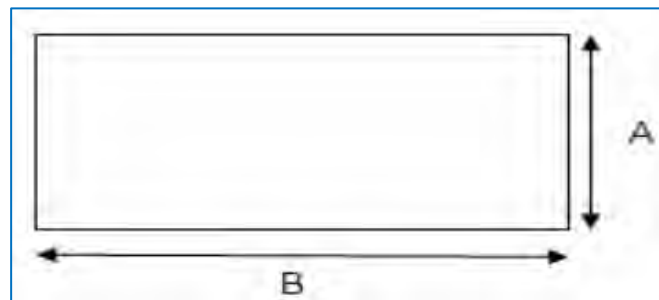


Figure 5.9 Aspect Ratio determination (UTAS, 2012)

5.3.3.3 Orthogonal quality

This is another important parameter used to describe the quality of a mesh, using CFD analysis this parameter is calculated for grid cells using a vector from the centroid of the cells to each of its faces, a face-area vector and a vector from the cell centroid to each of the centroids of the cells around that particular cell as displayed below (Oberkampf, 2010).

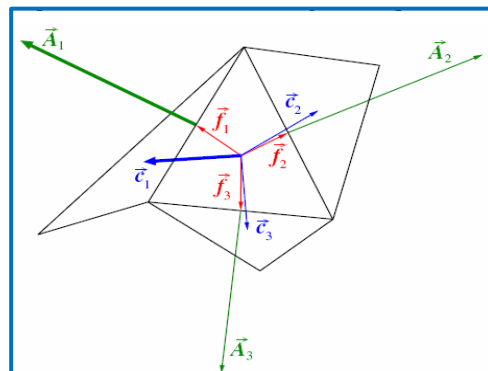


Figure 5.10 Cell Orthogonality (Virginia Tech, 2012)

5.3.4 Mesh Method

The computational fluid domain was discretised using a hybrid unstructured tetrahedral control volume mesh in the mesh generator application in ANSYS Fluent. Utilising the mesh relevance centre in the ANSYS it was possible to examine the mesh quality under three predefined mesh densities which are coarse, medium and fine and special attention was paid to parameters such grid count, element size, aspect ratio and skewness. This integrated automatic algorithm essentially increases the mesh density of the control volume and thus as an outcome, the results should become more accurate and be used as a baseline.

Defaults	
Physics Preference	CFD
Solver Preference	Fluent
<input type="checkbox"/> Relevance	0
Sizing	
Use Advanced Size Function	On: Curvature
Relevance Center	Fine
Initial Size Seed	Active Assembly
Smoothing	Medium
Transition	Slow
Span Angle Center	Fine
<input type="checkbox"/> Curvature Normal Angle	Default (18.0 °)
<input type="checkbox"/> Min Size	Default (1.8917e-003 m)
<input type="checkbox"/> Max Face Size	Default (0.189170 m)
<input type="checkbox"/> Max Size	Default (0.378350 m)
<input type="checkbox"/> Growth Rate	Default (1.20)
Minimum Edge Length	1.5418e-006 m

Figure 5.11 Parametric mesh settings (Hand, 2014)

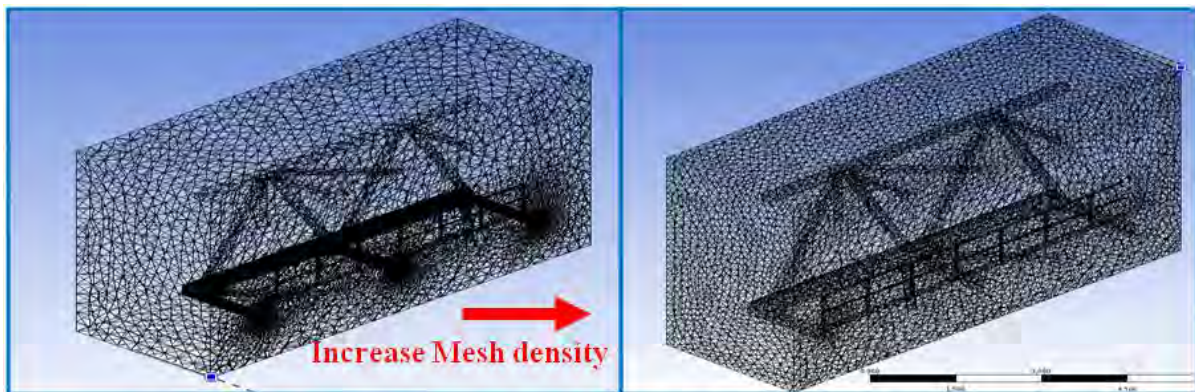


Figure 5.12 Coarse mesh (Left) and Fine mesh (right) (Hand, 2013)

The main drawback with this method even though precise results are achievable, it does not use available grid elements as efficiently as possible and this is very important where limited mesh counts are inflicted. This meant that mesh refinement techniques had to be incorporated into the mesh structure to improve the mesh quality aspects referred to as above and use minimal grid cells.

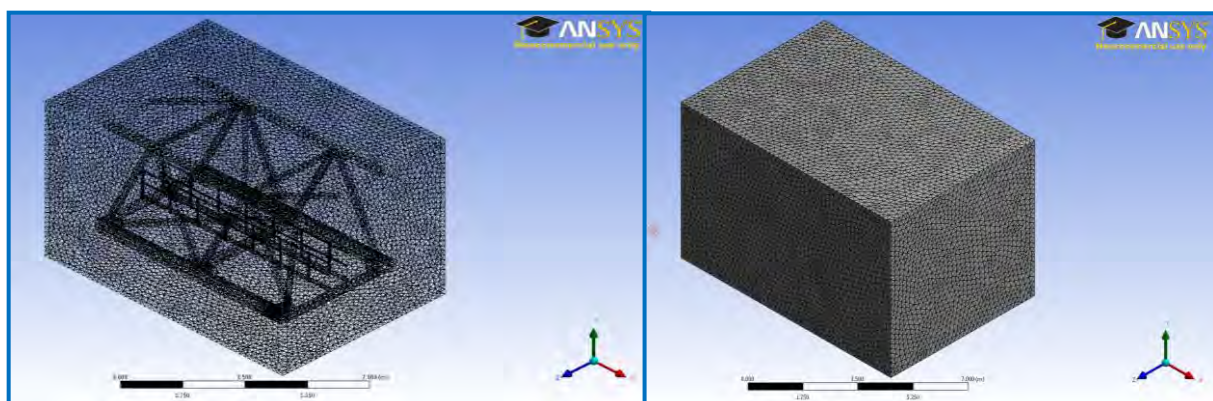


Figure 5.13 Model in mesh domain prior grid refinement (Hand, 2014)

The use of inflation layers was utilised in the model where applicable, this was done to ensure a high resolution was developed to fully resolve the thin boundary layer developed at the model walls by high Reynold's number. "Resolving the boundary layer in wall bounded flows is critical for accuracy and capturing the near wall flow physics" (CAE, 2013). This technique reduces the cell count and allows the boundary layer profile be resolved all the way to the model wall as shown in figure 5.14 (Leap,2012). This is important because boundary layer separation from a surface takes a large amount of the aerodynamic drag. The thickness of the viscous layer decreases with increasing

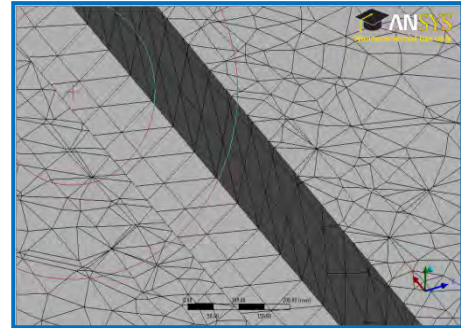


Figure 5.14 Inflation grid cells (Hand, 2013)

Reynolds's number and the Reynolds's number is generally above 10^6 for wind induced structures (Blocken et al, 2013). It proved a tedious task to apply inflation layers to all the faces of the model as it contained over 160 faces and in certain circumstances overlapping of mesh cells was occurring which would cause instabilities in numerical computations. This was overcome by independently applying suitable inflation layers to appropriate surfaces especially in regions where boundary layer was occurring and at flow separation locations.

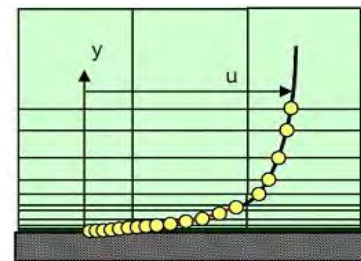


Figure 5.15 Inflation Layer (Leap,2012).

The second refinement tool implemented into the model was the use of defining mesh size in areas of interest which used the face sizing tool in the mesh generator. This allowed the mesh to be concentrated in regions of interest particularly in flow separation and the regions of wakes. The clear downside to this method was that the grid cell count was increased based on the densities of the concentrated meshes which would enlarge the computational time but this compromise had to be taken for the best accuracy. The enhanced mesh around the walls of the model did offer however mean that the main control volume mesh in the domain could be reduced in density as no intense computations were occurring in many regions of the volume mesh. It was therefore decided to change the mesh relevance from the fine setting to either coarse or medium. The medium mesh relevance was chosen because it would offer the best smoothness transition between the mesh element sizes (lower truncation errors) and the fact also there was not a huge difference between mesh totals for the coarse and medium with 119,960 and 180,067 grid cells respectively.

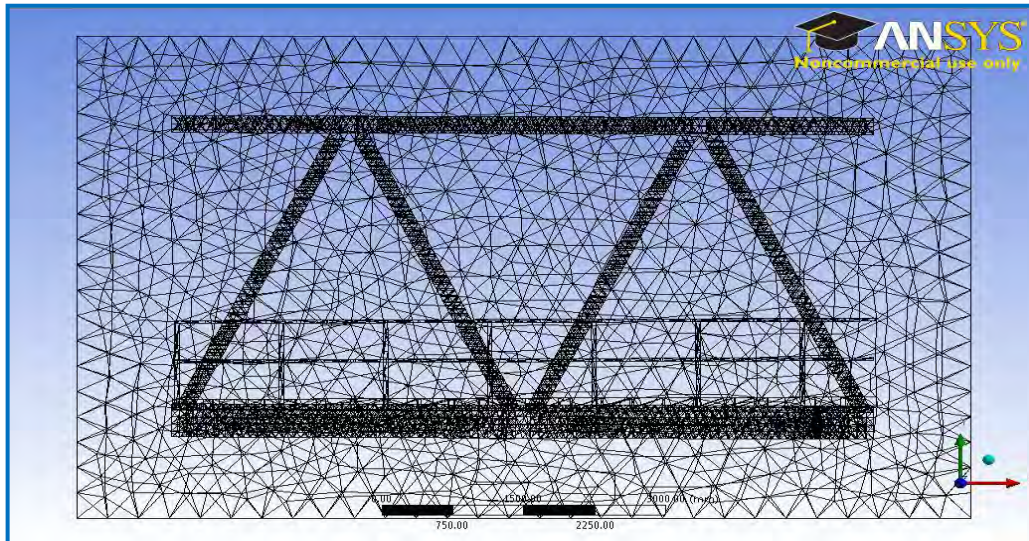


Figure 5.16 View showing mesh size difference

5.3.5 The Mesh

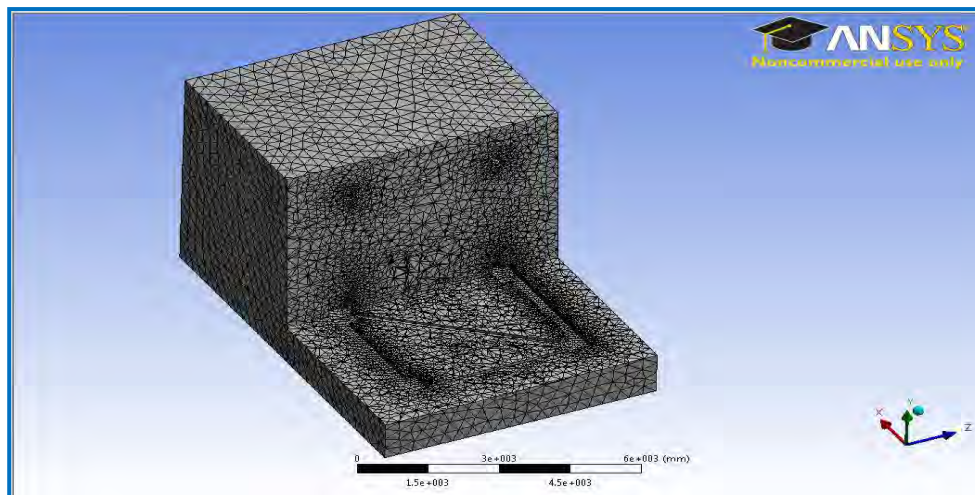


Figure 5.17 Cross section view (Hand, 2014)

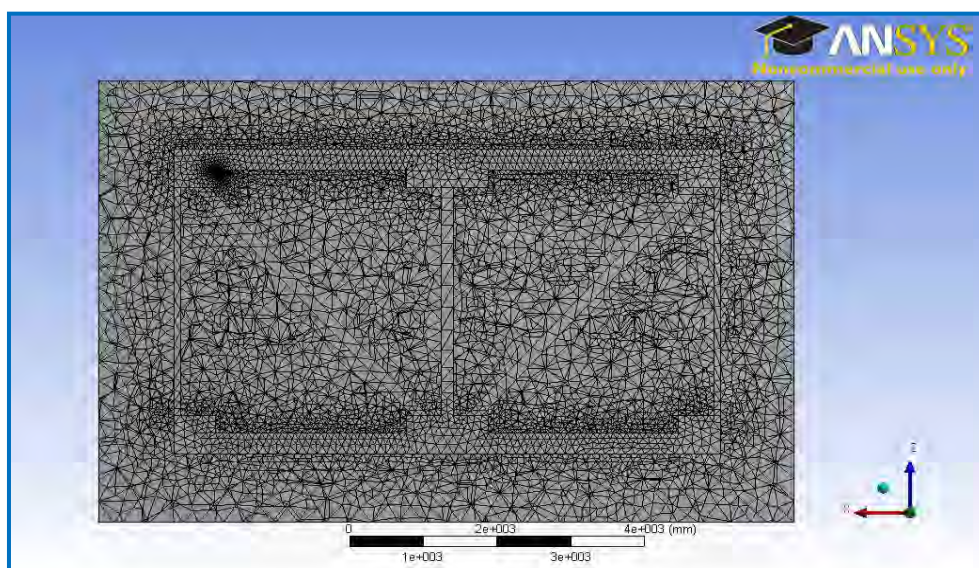


Figure 5.18 Cross Section across bottom of model (Hand, 2014)

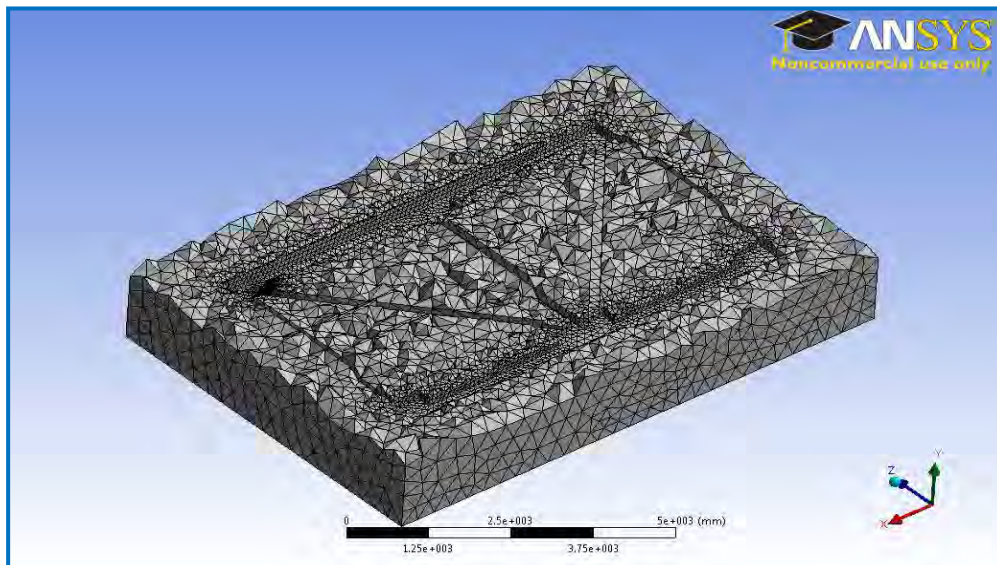


Figure 5.19 Magnified grid cells (Hand, 2014)

The refined mesh of the CFD model consisted of 87,410 nodes and 489,858 grid elements which is just under the 500,000 grid cells permitted for student academic licenses. The two graphs below in figure 5.20 & figure 5.21 show the increase in mesh size with nodes used also.

Table 5.0 Mesh Statistics (Hand, 2014)

Mesh Density	Nodes	Elements
Coarse	21465	119960
Medium	32971	180067
Fine	73649	402221
Well Refined	87410	489858

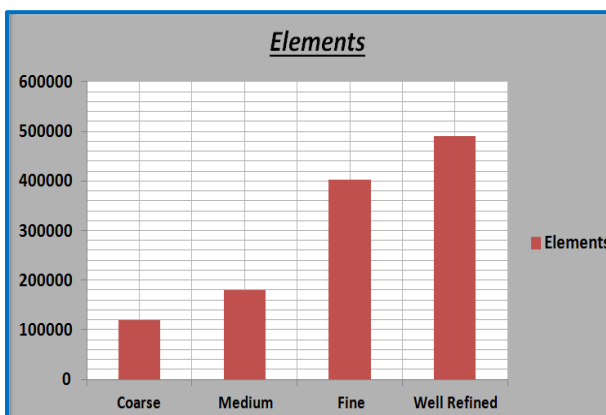


Figure 5.20 Grid elements (Hand, 2014)

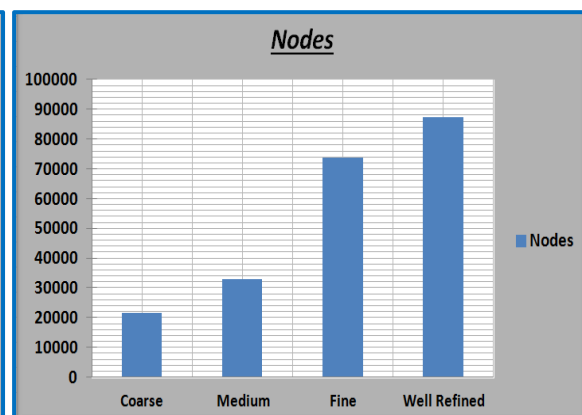


Figure 5.21 Grid nodes (Hand, 2014)

The average grid cell size was noted to be 0.82m with a standard deviation of 0.125m and was improved on the original mesh that had a standard deviation of 0.202m.

Table 5.1 Mesh Metrics (Hand, 2014)

Mesh Metric Sizes (m)				
Mesh Density	Minimum	Maximum	Average	Standard Derivation
Coarse	8.72E-04	0.999	0.725	0.202
Medium	2.44E-03	0.999	0.780	0.165
Fine	7.94E-03	1.000	0.822	0.119
Well Refined	6.72E-05	1.000	0.816	0.125

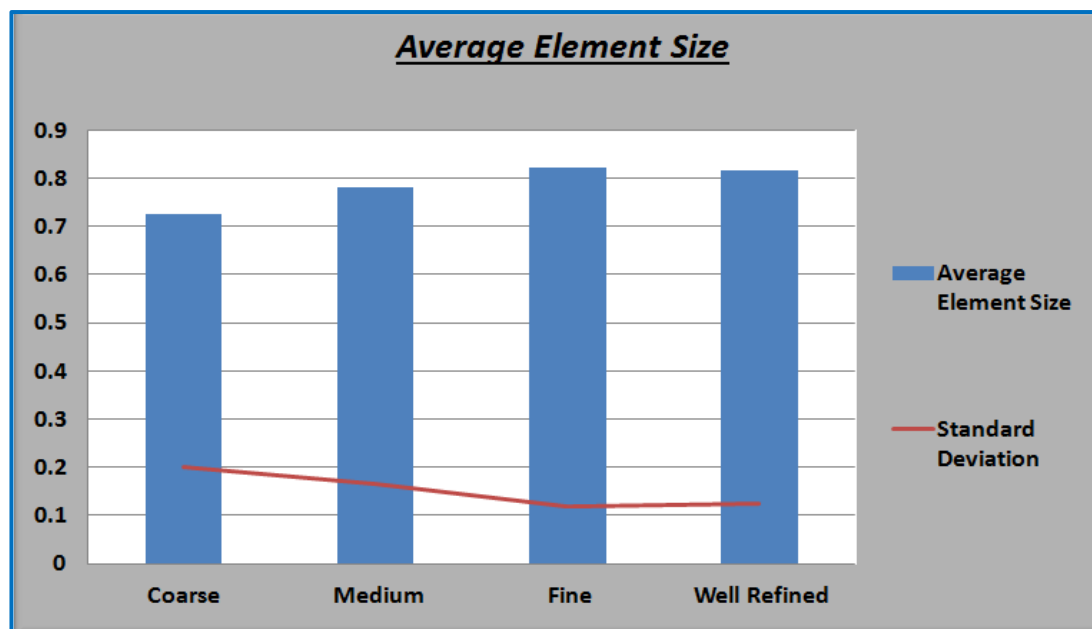


Figure 5.22 Average element sizes with standard deviation (Hand, 2014)

Particular attention was paid to the mesh quality measures especially the grid aspect ratio skewness, and orthogonal quality. In general terms if the grid elements have an acceptable level of skewness the aspect ratio will be within acceptable regions also. When refining the volume mesh extensive concentration was placed on reduced the cells with high and unsatisfactory levels of skewness. Figure 5.24 shows the level of skewness decreasing as the mesh was refined, this also effects the aspect ratio as it decreases as displayed in figure 5.23.

Table 5.3 Aspect Ratio (Hand, 2014)

Grid Elements Aspect Ratio				
Mesh Density	Minimum	Maximum	Average	Standard Derivation
Coarse	1.1706	10591	3.100	34.869
Medium	1.1669	364.85	2.288	3.248
Fine	1.1713	61642	2.119	88.095
Well Refined	1.1659	217.11	1.941	1.089

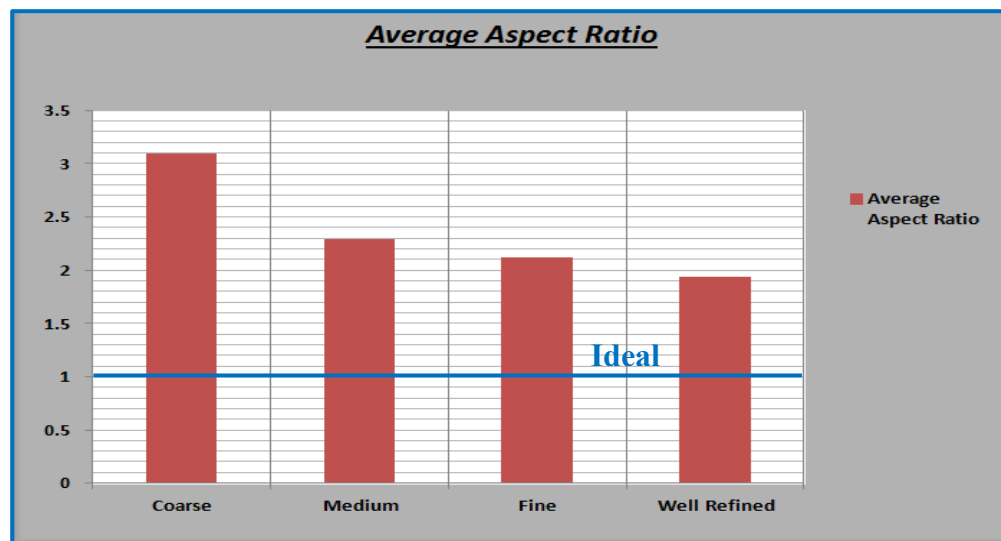


Figure 5.23 Average aspect ratio (Hand, 2014)

The refined mesh average aspect ratio was found to be 1.941 which is acceptable as 1 is ideal for an aspect ratio, this is nearly a 40% reduction in this value compared with the standard coarse mesh. The skewness value was found to be 0.246 which denotes the mesh to be of excellent quality according to the table 5.0 because it is the range of 0 - 0.25.

Table 5.4 Grid cells skewness

Grid Elements Skewness values				
Mesh Density	Minimum	Maximum	Average	Standard Derivation
Coarse	1.33E-03	1.000	0.374	0.241
Medium	2.42E-04	1.000	0.299	0.197
Fine	4.53E-04	1.000	0.255	0.153
Well Refined	1.25E-03	1.000	0.246	0.145

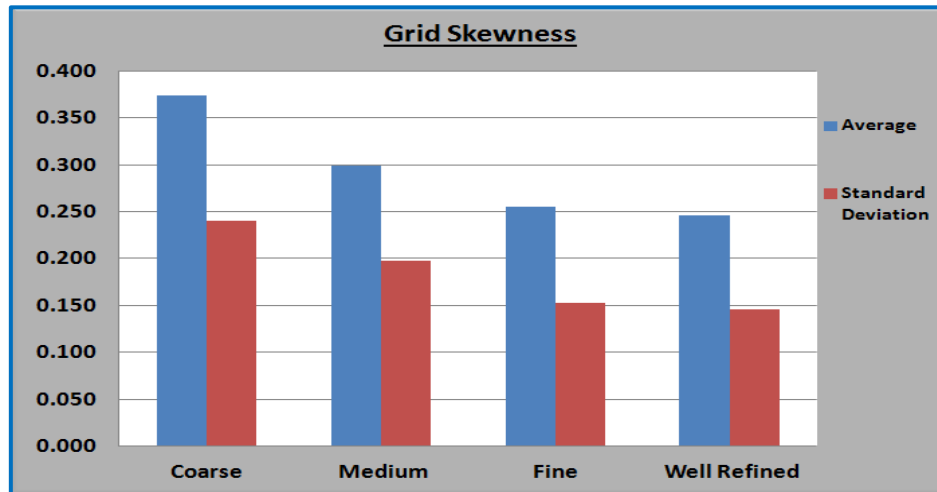


Figure 5.24 Grid Skewness (Hand, 2014)

Table 5.5 Grid Orthogonal quality (Hand,2014)

Grid Elements Orthogonal quality				
Mesh Density	Minimum	Maximum	Average	Standard Derivation
Coarse	3.42E-04	0.994	0.761	0.185
Medium	6.81E-03	0.995	0.809	0.149
Fine	1.94E-02	0.995	0.845	0.107
Well Refined	7.78E-05	0.996	0.842	0.112

To have good orthogonal quality in the element grid it is necessary to have the value close as possible to 1 and furthest from 0 (Virginia Tech, 2012). This condition has been satisfied as the average orthogonal quality in the refined mesh was recorded to be 0.842.

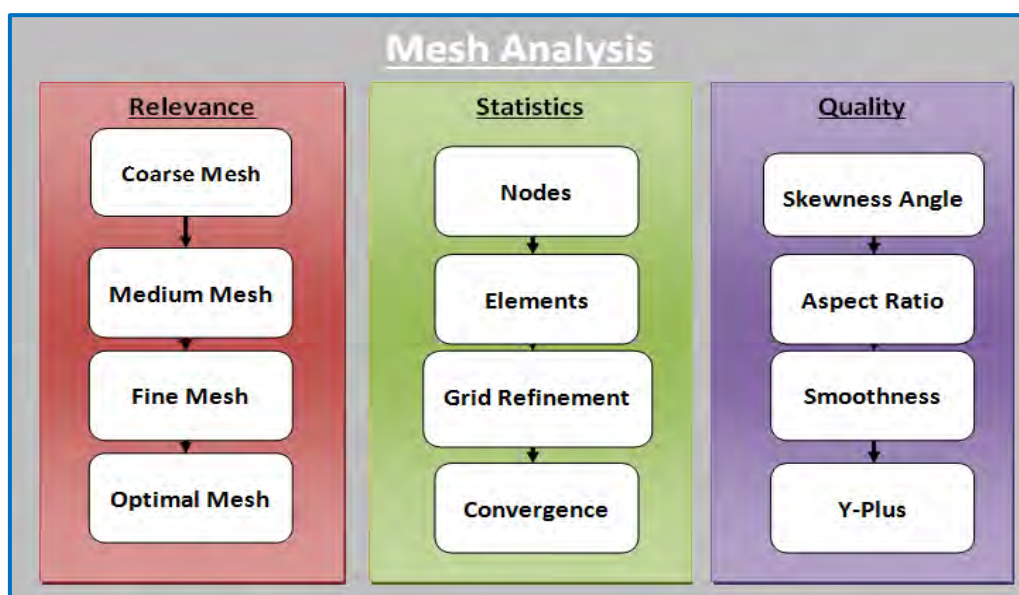


Figure 5.25 Summary of mesh analysis undertaken (Hand, 2014)

5.4 Turbulence Airflow Model

The CFD program used for this modelling to solve Reynold's averaged Navier-Stokes equations [5.0] & [5.1] was ANSYS Fluent 14.0. The accuracy and the computational power

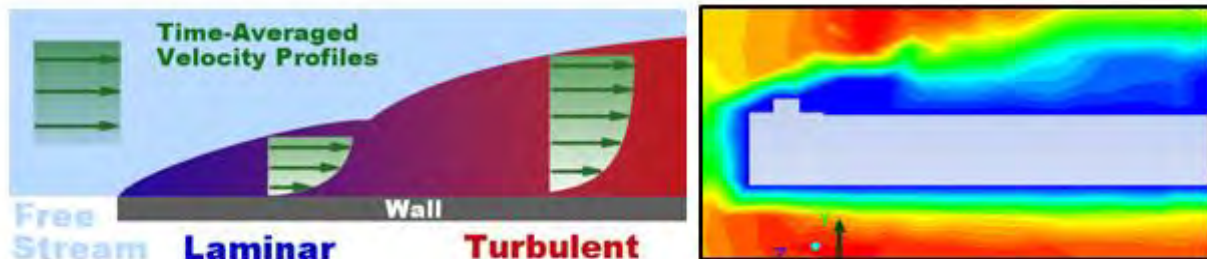


Figure 5.26 Boundary layer formation (NASA-c, 2010) & model boundary layer (Hand, 2013)

required to be used to analyse the model are critically dependent on the selection of the correct turbulent model (Almohammadi, 2013). Researchers and fluid specialists have found that CFD models have been successful in analysing airflow around bluff structures (Castro & Apsley, 1997). Flow past many object create a wide range of fluid mechanics phenomena (White, 2003) and in this CFD model it is no different. As “Air motion is invariably turbulent” (Warhaft, 1997) when it flows over a surface it creates an occurrence commonly known as a boundary layer where a series of flow transitions occur depending on the respective Reynold's number and ultimately the wind speed.

5.4.1 Applicable CFD Model

The Reynold's averaged Navier-Stokes equations (RANS) [5.0] & [5.1] are the most fundamental and commonly used approach of modelling turbulence flow in engineering. The left hand side of the equation [5.1] depicts the variation of the mean momentum of the fluid body and the right hand side accounts for the assumption of mean body force and divergence stress (Cao, 2011). The Reynold's stress term $\overline{\rho u_i' u_j'}$ is an unknown term in the equation and due to this term the RANS equation are referred to as “not closed” equation. Therefore a turbulence model is required to produce a closed system of solvable equations which is achievable with modern turbulence models (Karimi et al, 2011).

One-Equation Model
Spalart-Allmaras
Two-Equation Models
Standard k-ε
RNG k-ε
Realizable k-ε*
Standard k-ω
SST k-ω*
Reynolds Stress Model
k-k1-ω Transition Model
SST Transition Model

Figure 5.27 Available turbulence models in ANSYS Fluent (ANSYS, 2011)

It is a well established fact among CFD specialists that there is no one turbulence model universally accepted as the best for all types of problems. The selection of a turbulence model depends on many factors mainly concerning the physics encompassed in the flow, the level of accuracy needed, the time and computational facilities available. To make the most intellectual decision of the appropriate model selection an understanding of the model capability and effectiveness must be adhered (ENEA, 2001).

A comparison was therefore made between three commonly used turbulent models in engineering flow problems, the standard $k-\varepsilon$ model (SKE), the realisable $k-\varepsilon$ model (RKE) and the Shear Stress Transition (SST) $k-\omega$ model to see whether or not the presence of a complex lattice structure in the domain and laminar effects at low velocities would influence the results obtained. The convergence results when using different turbulence models would be examined and an appropriate turbulence model would be selected based on the results.

Firstly the standard $k-\varepsilon$ model was implemented which displayed promising results and efficient convergence times with 250-400 iterations, but it was noted that this model gave inaccurate results at low wind speeds 0-20 m/s and failed to converge as shown in figure 5.28 after post analysis of these results it was determined that the presence of laminar flow effects may have influenced the CFD calculations.

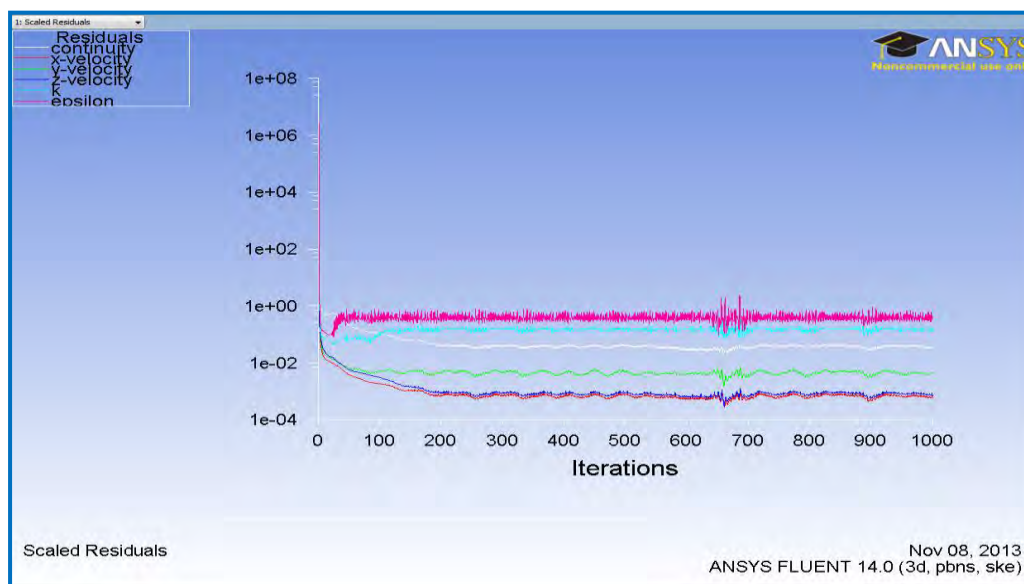


Figure 5.28 Failed convergence of $k-\varepsilon$ model at 10m/s flow velocity (Hand, 2013)

According to (Nielsen *et al*, 2007) this model has two main weaknesses, where it overestimates the shear stress in adverse gradient pressure flow due to large scale dissipation rate and also it requires near wall modifications. The realisable $k-\varepsilon$ model was then employed as a possible turbulence model “because of its improved predictive capabilities compared to the standard $k-\varepsilon$ model, and because of its ability to resolve portions of complex flows

located very close to the surface” (Han et al, 2011). This model calculated results very similar to the reference hand calculation and was more consistent than the standard $k-\epsilon$ model. To add completeness to the comparison the Shear Stress Transition (SST) $k-\omega$ model was introduced, this model is used in turbulent zones due to its good prediction of separated flow simulation and this model uses the standard $k-\omega$ model near the walls but swaps to the $k-\epsilon$ model away from the walls (Menter, 1994).

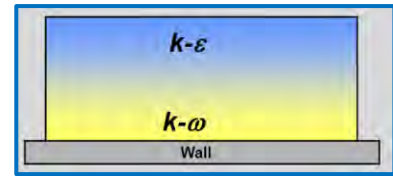


Figure 5.29 SST model switching (ANSYS, 2011)

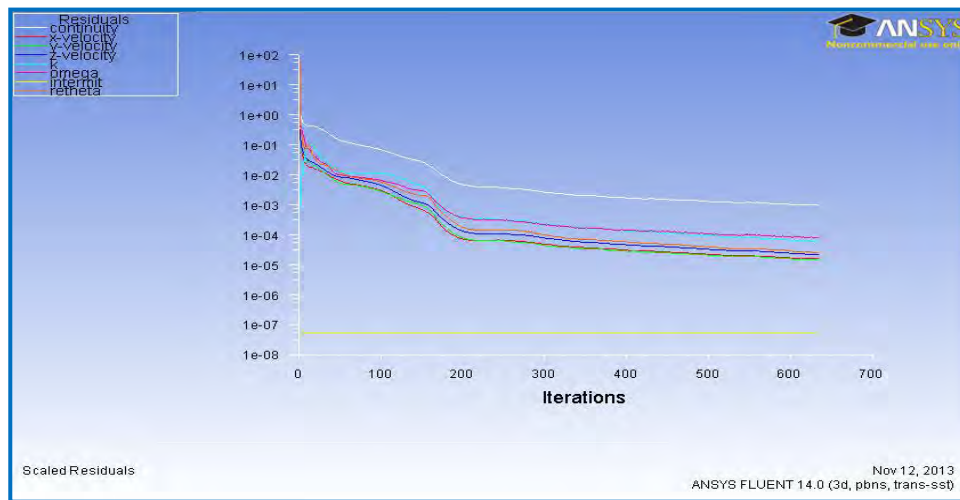


Figure 5.30 Successful convergence using the SST model at 10m/s (Hand, 2013)

This model performs a lot better than the $k-\epsilon$ models at predicting boundary layer formation and thus is widely used in industrial flow situations (Katul et al, 2004) (ANSYS, 2011). It was therefore decided that the SST $k-\omega$ model was the most appropriate model for this type of problem owing to its stability, numerical robustness and efficient computation “SST is a good compromise between $k-\epsilon$ and $k-\omega$ models” (ANSYS, 2011). Also a study carried out by (Defraeye et al, 2010) showed that this model accurately predicted aerodynamic drag on a model with an inaccuracy of just 4% of the wind tunnel result.

For the SST $k-\omega$ model CFD model that will be in this analysis, the SIMPLE algorithm was used for pressure velocity coupling, pressure interpolation was second order and second order discretisation methods were used for both the turbulent kinetic energy and specific dissipation rate terms of the core equations. Convergence was

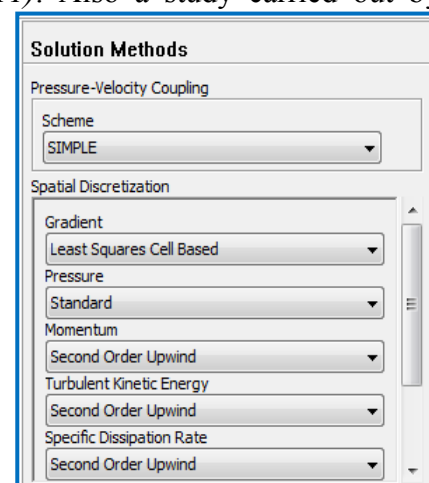


Figure 5.31 SST model solution method (Hand, 2014)

achieved using the following scaling residues levelled off and reached a minimum of 10^{-6} for x, y momentum, of 10^{-5} for y momentum and 10^{-4} for k, ϵ and continuity.

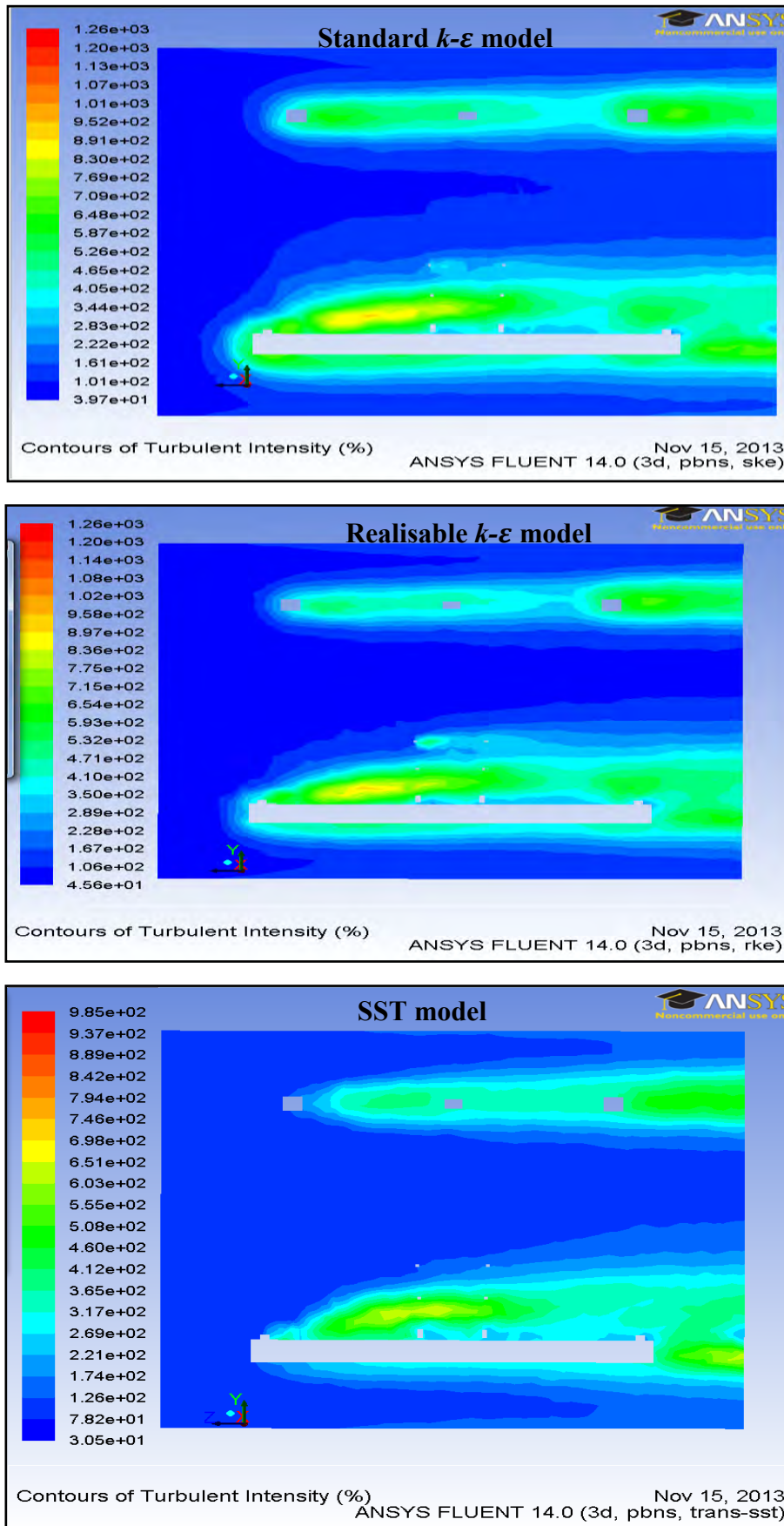


Figure 5.32 Graphic comparison of three models showing turbulence intensity (Hand, 2014)

Using the established refined mesh, these three models were compared with each other and with the reference hand calculation using the standard (FEM 1.004). Velocity intervals of 10m/s were assigned and a wind velocity range of 0 to 60m/s was defined.

Table 5.6 Comparison of results for three models (Hand,2014)

Wind velocity (m/s)	k-e (N)	(%)	k-e realisable (N)	(%)	SST (N)	(%)	Hand Calculation (FEM 1.004) (N)
5.00	484.01	24.10	401.84	3.04	398.40	2.15	390.00
10.00	1669.14	8.39	1487.83	3.39	1481.56	3.79	1540.00
20.00	5839.51	5.51	5715.08	7.52	5795.01	6.23	6180.00
30.00	12960.65	6.76	12649.44	9.00	12957.30	6.78	13900.00
40.00	22883.32	7.39	22346.4	9.57	22931.60	7.20	24710.00
50.00	35604.57	7.81	34770.32	9.97	35831.20	7.22	38620.00
60.00	51109.54	8.09	49887.15	10.29	51531.20	7.33	55610.00
Overall Percent Difference (%)		9.72		7.54		5.82	

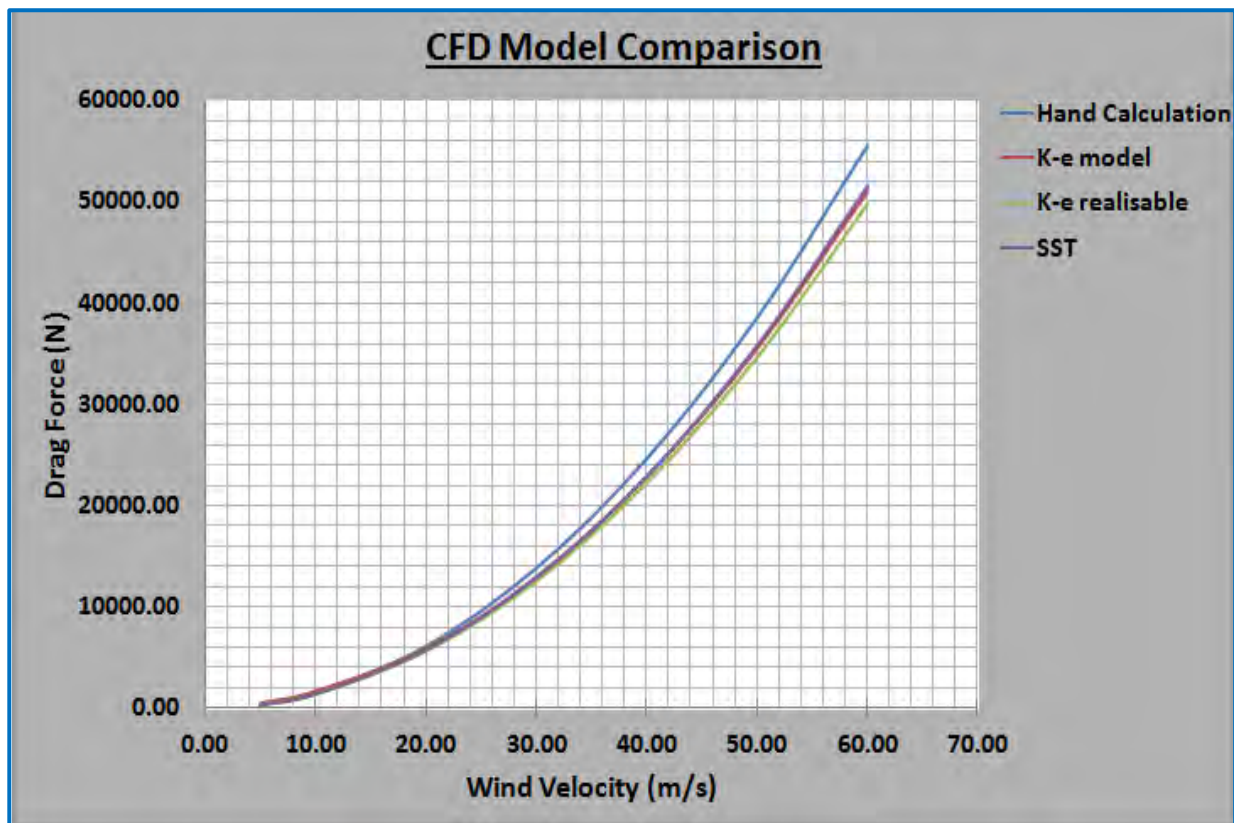


Figure 5.33 Graphical comparison of CFD results (Hand, 2014)

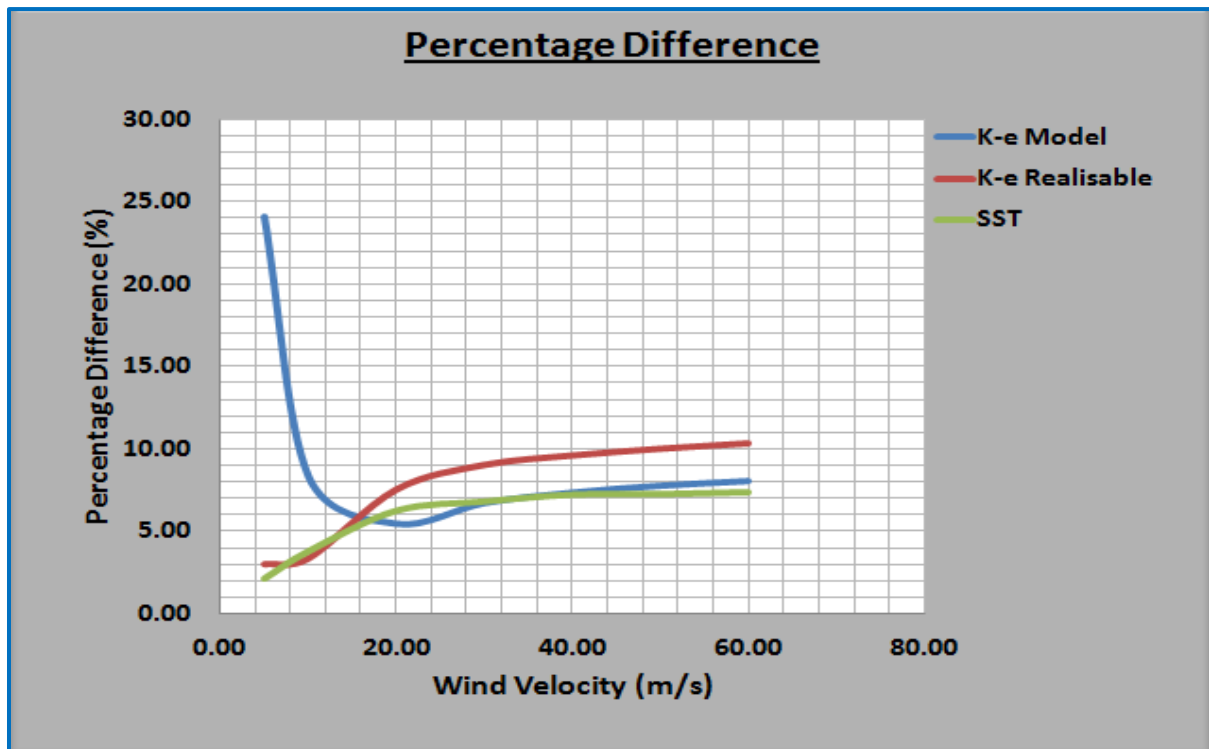


Figure 5.34 Graph showing the percentage difference for each model (Hand, 2014)

From the results of the comparison, it is clear to see that the SST $k-\omega$ model had best results of the three models as it had a average percentage difference of 5.8% in relation to the baseline calculation as shown above in table 5.6 and figure 5.34.

Analysing the properties of the boundary layer formed it is clear there is the occurrence of laminar flow particularly at lower velocities. As the air particles contact the structure surface it causes the air to act as a fluid whereby the fluid layers begin to shear over each other as described in the literature review and this is known as viscous effects. Firstly laminar flow is created at the edge of the model and then enters a transition region where it finally becomes fully turbulent flow. The length of the laminar region is fully dependent on the free stream wind velocity which is governed by Reynold's number, calculation on page C-24 of Appendix C analyses the length of this laminar region at various wind velocities over this model which is 4.45m wide and predicts the length the boundary layer using approximated derived equations. It was found that at 5m/s the laminar region length is 0.287m and at a velocity of 20m/s the length had reduced to 0.072m which indicates the laminar region is small over the model width accounting for 1.6% of the length at a velocity of 20m/s. It is generally accepted that if the laminar region is small enough it is irrelevant in the analysis of fluid flow over plate like structures (UOB, 2006) such as this case.

5.5 Numerical Simulation

The numerical simulations were conducted on the model using the preferred shear stress transition (SST) $k-\omega$ model in increments of 10m/s and in the wind velocity range of 0 – 60m/s. These numerical calculations were carried out on the four mesh types. The main reason for this is that a grid independence study could be conducted and converged solutions could be achieved. For a steady state simulation such

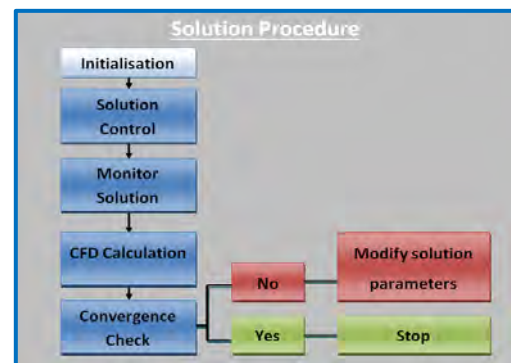


Figure 5.35 Solution Flowchart (Hand, 2014)

as this it is necessary that the solution satisfies the following conditions. The scaled residuals must have reduced to an acceptable value 10^{-4} in this case. Monitored points in the solution have reached a steady solution and the grid independence results are within a certain tolerance (Leap, 2012). Coupled with the scaled residues monitor, the mass flow rate monitor was also introduced as it offers the simplest means of observing the numerical stability of a computation. According to the conservation of mass, the mass flow rate of a fluid that enters the domain must exit also and a level line should exist in the mass flow rate graph as shown below (University of Leeds, 2008).

$$\dot{m}_1 = \dot{m}_2 \quad [5.2]$$

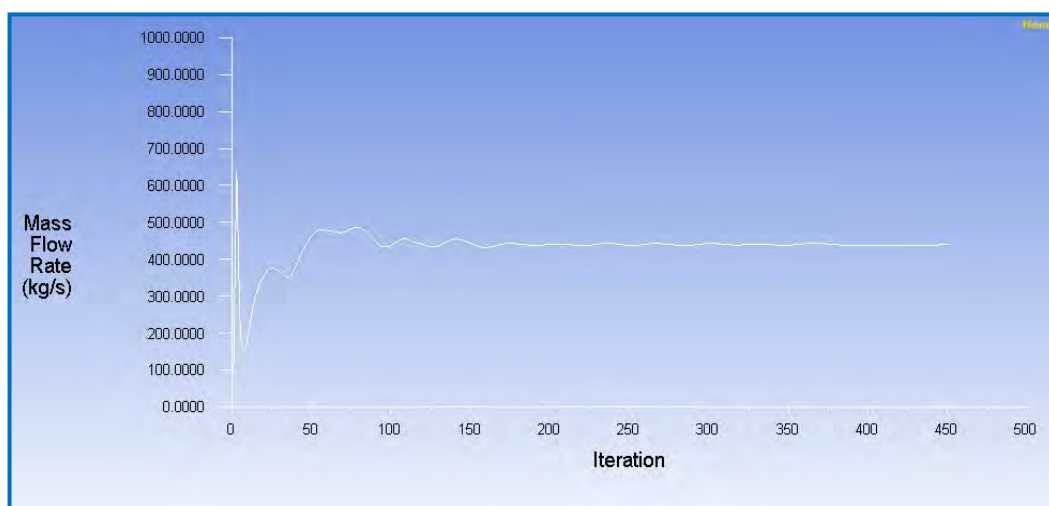


Figure 5.36 Mass flow rate solution monitor (Hand, 2014)

Convergence limitation of scaled residues was set as at 1000 iterations, but it was found that the convergence of solutions at different velocities and varied mesh density averaged between 250 and 400 iterations. Computational time also varied between one to three hours depending on the factors above.

5.6 Grid Sensitivity Analysis

A very important aspect of ensuring an accurate grid mesh is achieved is commonly conducted by carrying out a grid independence study (*Hiester, 2013*). It is imperative that a grid independence study is considered before any critical review of results is undertaken. This is the case because it is necessary to analyse the suitability of the mesh and produce an estimate of the numerical errors in the simulation in the problem (*Tu et al, 2013*). (*Roache, 1997*) outlines that grid independence can be examined by doubling the grid mesh twice in each direction and subsequently compare the fine grid numerical results with the results acquired from Richardson extrapolation of the original grid mesh. For cases where this is not feasible such as this case, it is common that grid independence is performed by running simulations at varied mesh densities with increasing grid quality. The solutions from each grid mesh are compared and grid independence is achieved when the results stop changing within a predefined accuracy tolerance (*Hiester, 2013*).

The method described above was adopted for this analysis and was performed on four varied quality meshes and the results were compared. Shown below in table is the drag values recorded at each wind velocity with varied mesh relevance. The results show the percentage difference between the well refined mesh and the other mesh densities decreasing with quality and grid element number.

Table 5.7 Grid independence study (*Hand, 2014*)

Mesh Relevance	Coarse		Medium		Fine		Well Refined
Grid Elements	119960		180067		402221		489858
Wind Velocity (m/s)	Drag Force (N)	(%)	Drag Force (N)	(%)	Drag Force (N)	(%)	Drag Force (N)
5	446.27	12.02	387.44	2.75	395.42	0.75	398.40
10	1673.28	12.94	1452.71	1.95	1442.15	2.66	1481.56
20	6482.85	11.87	5632.01	2.81	5589.32	3.55	5795.01
30	14399.70	11.13	12567.18	3.01	12508.66	3.46	12957.29
40	25518.34	11.28	22236.12	3.03	22195.76	3.21	22931.59
50	39888.49	11.32	34666.96	3.25	34683.15	3.20	35831.21
60	57211.83	11.02	49802.39	3.35	49719.48	3.52	51531.17
Overall Percent Difference (%)		11.66		2.91		2.88	

The average percentage difference decreases from 11.66% to 2.88% which means the numerical error or inaccuracy in the refined grid mesh is around 3% which is acceptable in this analysis.

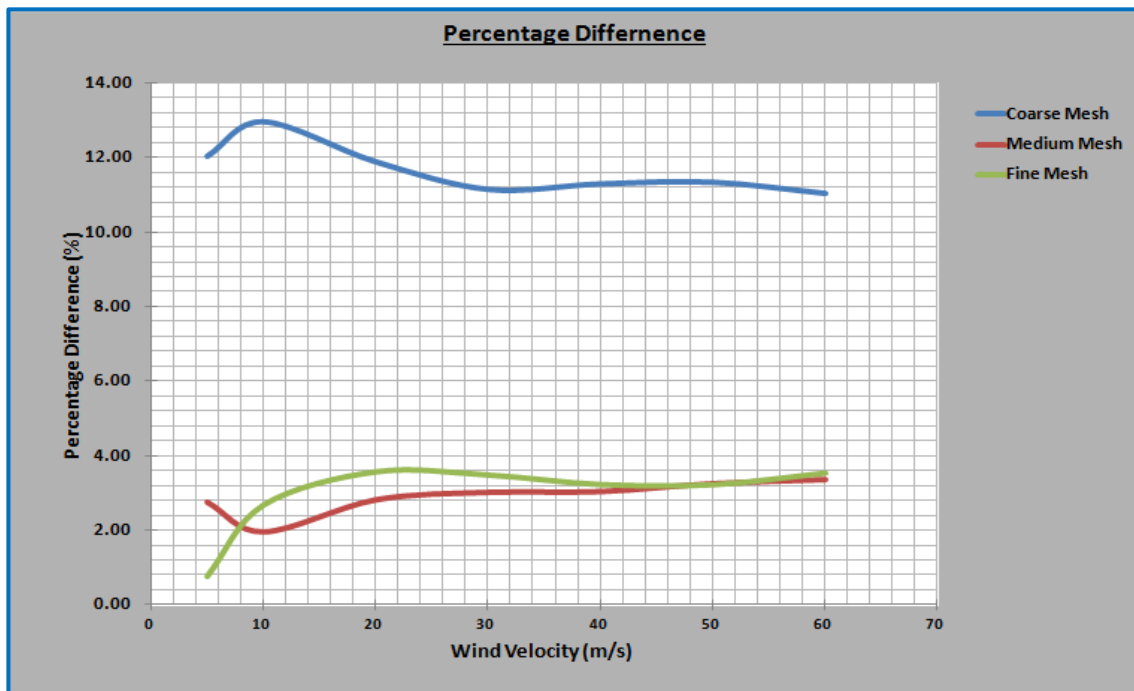


Figure 5.37 Percentage difference for three mesh types (Hand, 2014)

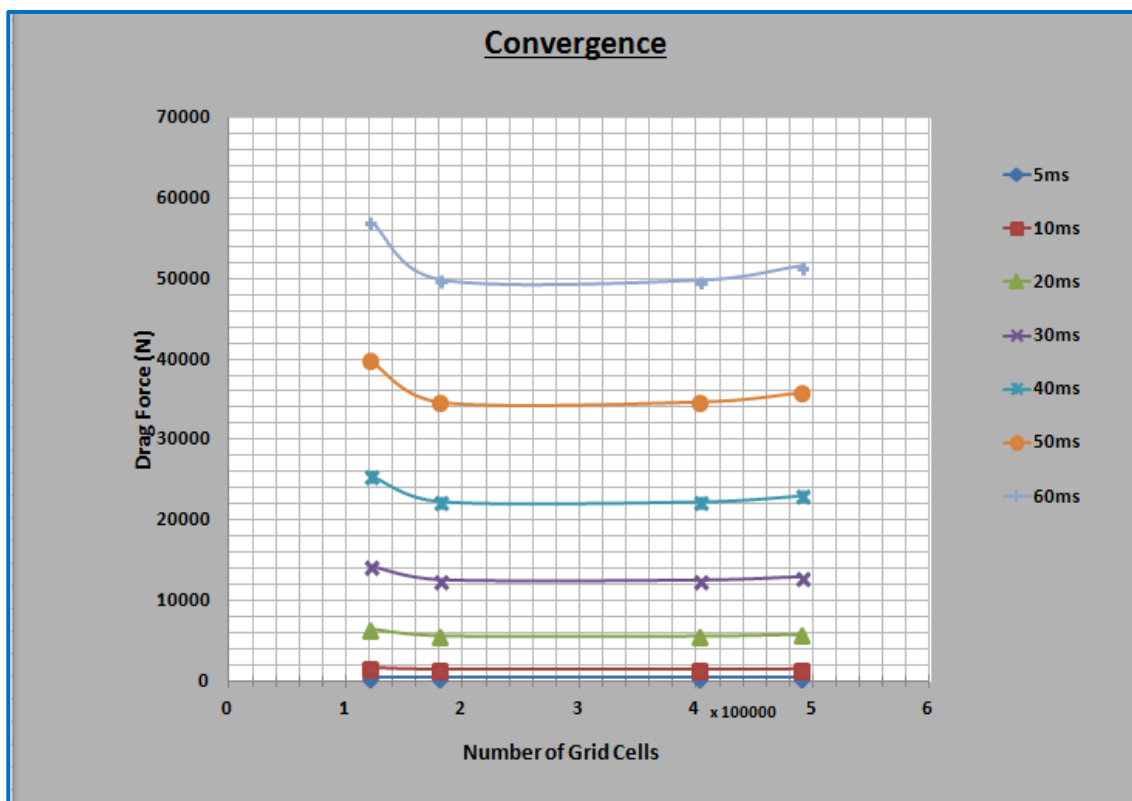


Figure 5.38 Convergence plot for analysis (Hand, 2014)

5.7 Turbulent Flows

Resolving the boundary layer properly around a model entails the fine grid resolution near the model surface. The cell density required depends on many factors mainly the boundary layer type, the CFD model used and the near wall treatments utilised (Ouazizi, 2006). The numerical results in turbulent flow are very much dependent on the mesh density due to the strong connection between turbulence and mean flow. ANSYS Fluent is constrained to the no-slip condition at the model walls which means the velocity is zero and the fluid shear stress reaches its maximum (Zhanga et al, 2010).

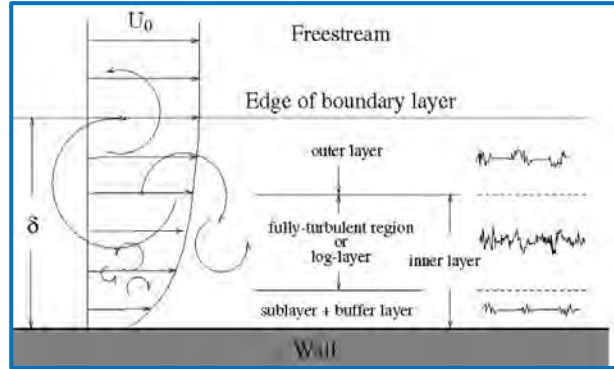


Figure 5.39 Structure of turbulent flows (ANSYS, 2011)

5.7.1 Turbulent near wall flow

Two important terms in the description of turbulent boundary layers are commonly expressed as the dimensionless velocity term u^+ [5.3] and the distance from the wall the y^+ value [5.4] (Chung, 2002).

$$u^+ = \frac{U}{u_\tau} \quad [5.3] \quad y^+ = \frac{\rho u_\tau y}{\mu} \quad [5.4] \quad (\text{Ouazizi, 2006})$$

In the equation above u_τ [5.5] is called the friction velocity and is expressed as follows

$$u_\tau = \sqrt{\frac{\tau_w}{\rho}} \quad [5.5] \quad (\text{Ouazizi, 2006})$$

It has been shown experimentally and empirically that the flow near-wall region can be subdivided into three different layers as shown below in figure 5.40 (Zhanga et al, 2010).

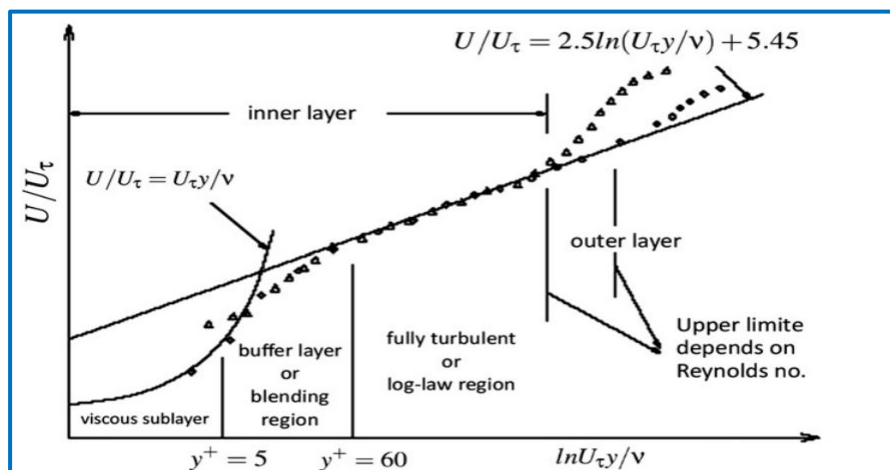


Figure 5.40 The three sub-layers of a flow field of the near wall region in semi-log plot (Zhanga et al, 2010).

Viscous sub-layer: this regions occupies the closest layers to the model wall where the flow is governed by viscous shear as the flow is stationary near the wall preventing turbulent eddies forming. The flow in this region is nearly fully laminar causing a thin viscous sub-layer with $y^+ < 5$ (Ouazizi, 2006).

Log Layer: or also known as the turbulent region ($30 < y^+ < 500$) is the next known layer from the viscous layer and involves a mixture of viscous and turbulent effects and the wall shear stress is assumed to be constant (Ouazizi, 2006).

Outer Layer: ($y^+ > 500$) is located the furthest from the wall and encloses inertia governed flow. In this region viscous effects are assumed to be negligible and the relationship between velocity and distance can be expressed in equation [5.6] (Ouazizi, 2006).

$$\frac{U_{\text{Max}} - U}{u_\tau} = \frac{1}{k} \ln \frac{y}{\delta} + A \quad [5.6] \quad (\text{Ouazizi, 2006}).$$

Where k is a universal constant that depends on the roughness of the wall and in this case as a smooth wall can be taken as $k = 0.4$ and A is a constant.

5.7.2 Near Wall Treatments

Mainly there are two approaches used for modelling the boundary layer formation near a model wall. One method is known as “near wall modelling” and is able to resolve the viscous sub layer and solve to the wall as shown in figure 5.41. The other approach does not solve the viscous inner region but uses standard “wall functions” which can be referred to as semi-empirical formulae which are used to link the viscosity affected region with the wall and the turbulent region. Using these wall functions stops the need to change the turbulence model to represent the physical wall (VT ARC, 2013).

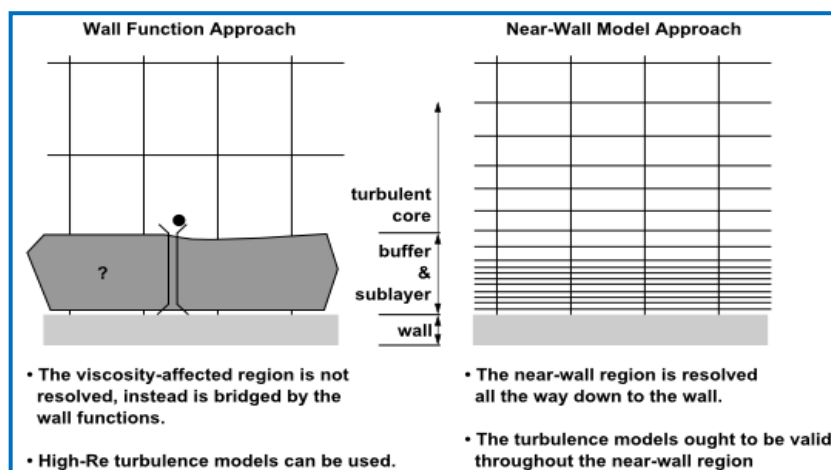


Figure 5.41 Near wall treatments (VT ARC, 2013).

For the subject of this analysis standard wall functions will be examined and the following guideline will be met. Each element centroid must be positioned within the log-layer ($30 < y^+ < 300$) and a y^+ value close to 30 is most accurate.

5.7.3 Y Plus

Y^+ characterises the local Reynold's number near the model wall and has varying definition depending on which turbulence model is being used. The $k-\omega$ SST model specifies that a Y^+ greater than 30 and less than 300 is required, with closer to 30 being the most optimal value (Botha, 2009). Table 5.8 shows the averaged y^+ values taken from the model at each relevant flow velocity interval.

Table 5.8 Mass averaged y^+ values for the CFD model

Flow velocity (m/s)	5	10	20	30	40	50	60
y^+	6	41	100	153	202	250	297

The y^+ contour plot below in figure 5.42 shows the corresponding y^+ value for all parts of the model surface. It is clearly identifiable that almost all the model surface is within the specified region for y^+ with this model but there is also some regions are above the recommended threshold. The areas within the acceptable region for y^+ are mainly the surfaces that the mesh refinement techniques were applied to using inflation and alternative face sizing techniques. The regions that are slightly above the suggested values are particular regions where the mesh was kept standardised due to precautions of exceeding mesh limits. The use of prism layers through the inflation technique considerably reduce the y^+ values as clearly shown. (Refer to Appendix C page C-21 for further Y^+ details)

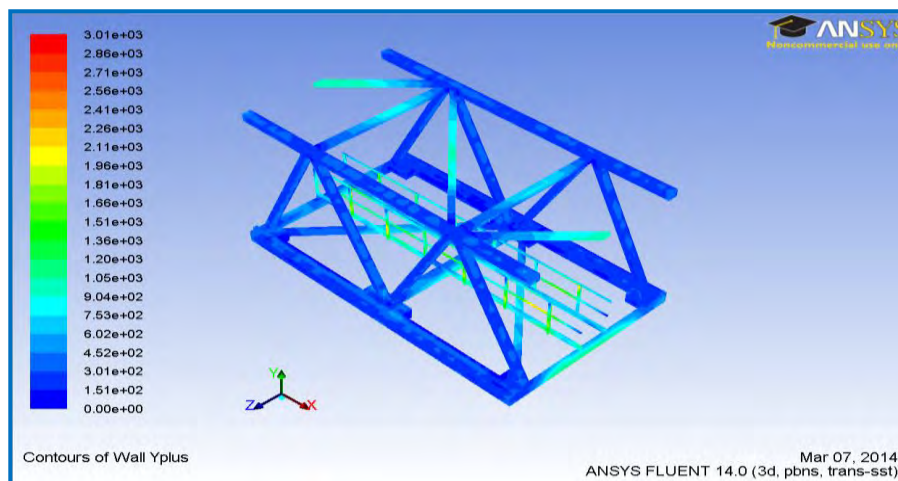


Figure 5.42 Y^+ plot for CFD model (Hand, 2014)

5.8 Numerical Results

The CFD results were acquired using the SST $k-\omega$ model and a considerable amount of data was gathered from the analysing of the raw data given from the CFD simulations. Firstly the parameters such as drag and drag-induced lift were analysed from the analysis.

Table 5.9 Drag Force Results (Hand, 2014)

Flow Velocity (m/s)	Pressure Drag (N)	Viscous Drag (N)	Total Drag (N)
5	394.27	4.13	398.40
10	1471.33	10.22	1481.56
20	5765.70	29.32	5795.01
30	12898.93	58.36	12957.29
40	22834.72	96.87	22931.59
50	35688.56	142.64	35831.21
60	51332.69	198.47	51531.17

Table 5.10 Lift Force Results (Hand, 2014)

Flow Velocity (m/s)	Pressure Lift (N)	Viscous Lift (N)	Total Lift (N)
5	8.49	0.08	8.57
10	25.11	0.23	25.34
20	64.25	0.80	65.05
30	170.28	1.69	171.98
40	286.92	2.73	289.64
50	446.36	3.97	450.33
60	491.62	5.33	496.95

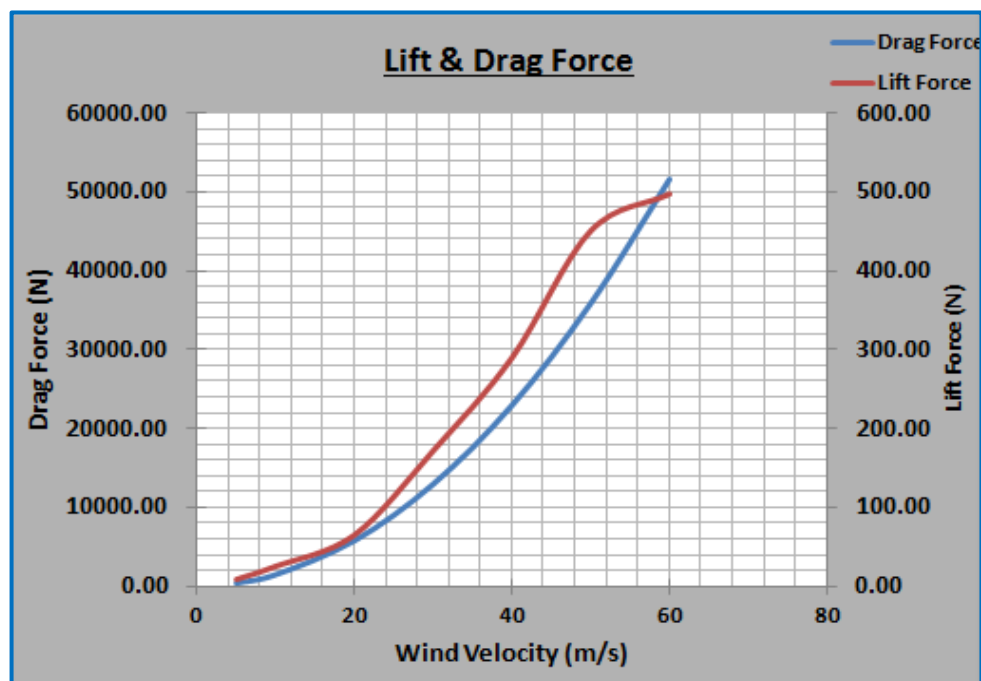


Figure 5.43 Plot of drag and lift forces on boom section

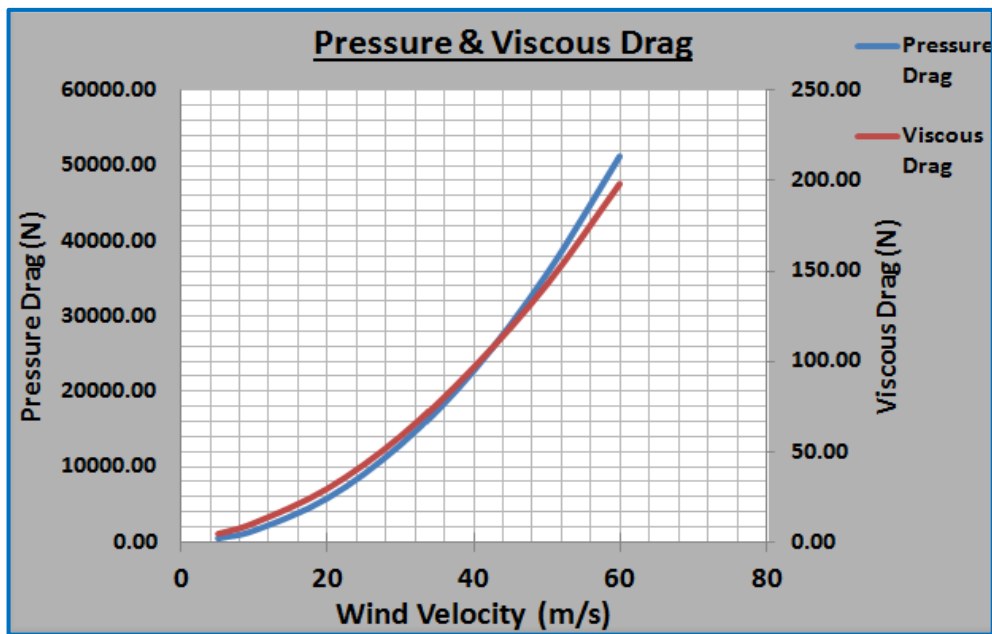


Figure 5.44 Drag induced from pressure & viscous forces (Hand, 2013)

It can be clearly seen that the forces on this boom section is predominately influenced by drag forces whereas positive lift forces are quite minimal accounting for about 1-2% of the forces on the section depending on the wind velocity. The acquired drag results do from preliminarily analysis do seem reasonable and expected as smooth curve is present in figure 5.44. It is noted from the results and that pressure induced drag is the main impacting factor for the overall drag force on the boom with viscous effects reducing with wind velocity and only accounting for less than 1% of the drag force developed. This is similar case for drag-induced lift on the boom with the positive lift generated mainly by pressure effects and to lesser degree viscous effects as shown below in figure 5.45.

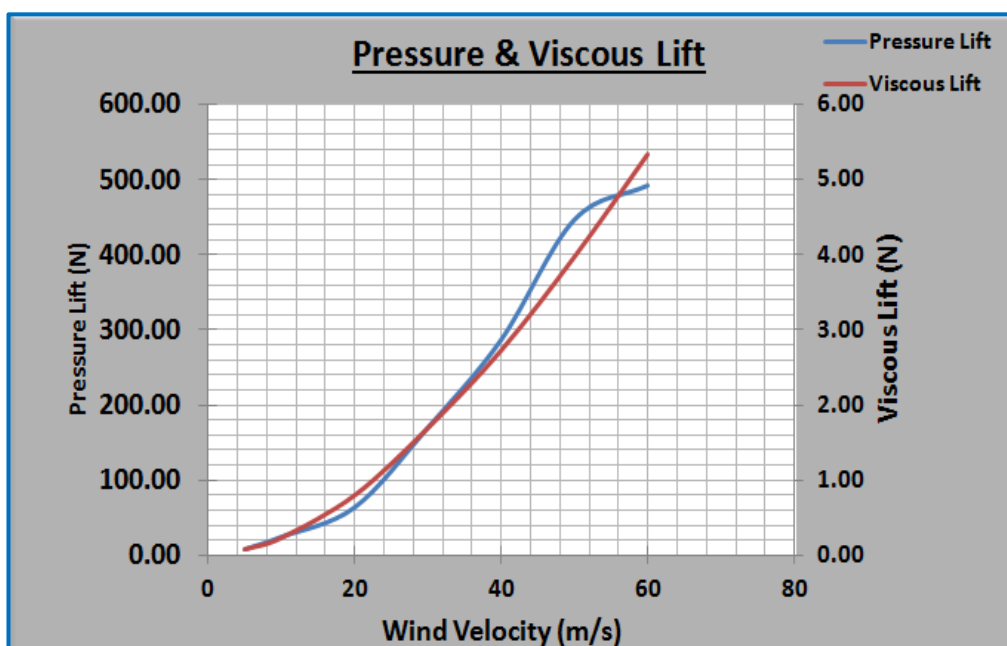


Figure 5.45 Lift induced from pressure & viscous forces

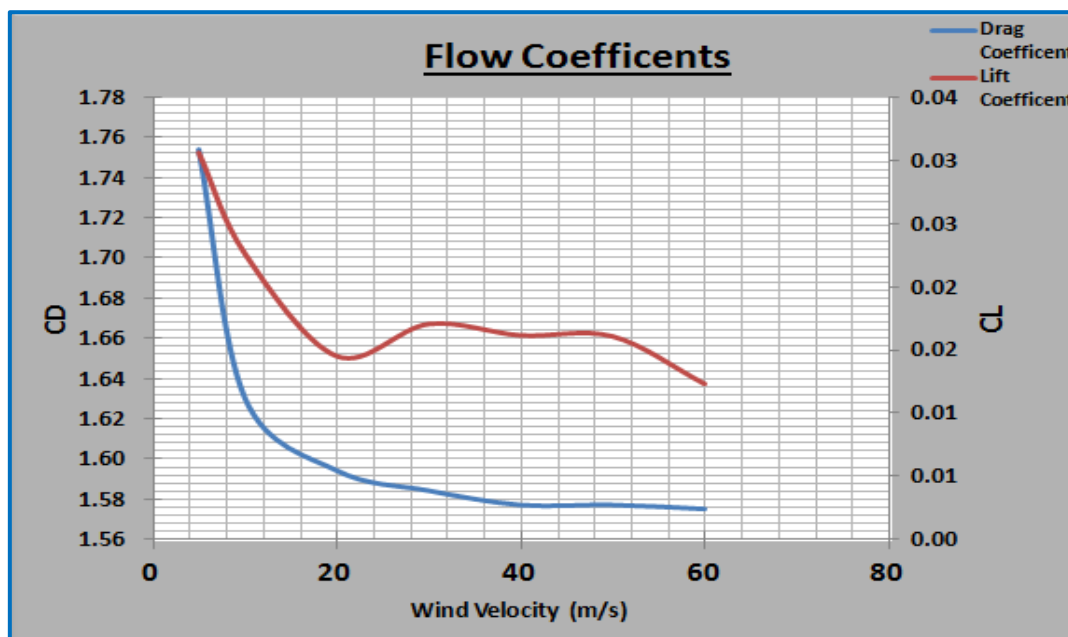


Figure 5.46 Drag and Lift Coefficients (Hand, 2014)

Figure 5.46 above shows the established drag and lift coefficients for the boom section simulated by the CFD software at various wind velocity intervals. In the current design process for these cranes drag coefficients for the structure are taken from design standards which specify a drag coefficient which cover a wide range of structure types and can be inaccurate. The current drag coefficient used for this boom structure is 1.7 taken from the FEM 1.004 design standard. The main advantage of the CFD analysis is that it that it allows the design/analyst obtain a drag of lift coefficient for various wind velocities as shown above. Taking a predefined number from a standard is a very “black box” approach and can be open to various amount of error. Obtaining the desired coefficients via CFD simulation software, the author’s believes is a more intuitive approach and could allow the designer/analyst a better picture of how the airflow interacts with the structure and make more in-depth design decisions based on this data.

In the coming pages some of the other key results of the CFD analysis are displayed with mainly contour plots of various parameters.

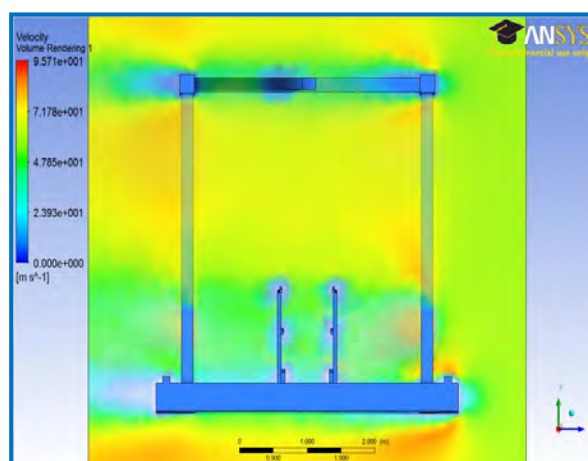


Figure 5.47 Plot showing velocity (Hand, 2014)

5.9 Graphic Results

5.9.1 Velocity Contours

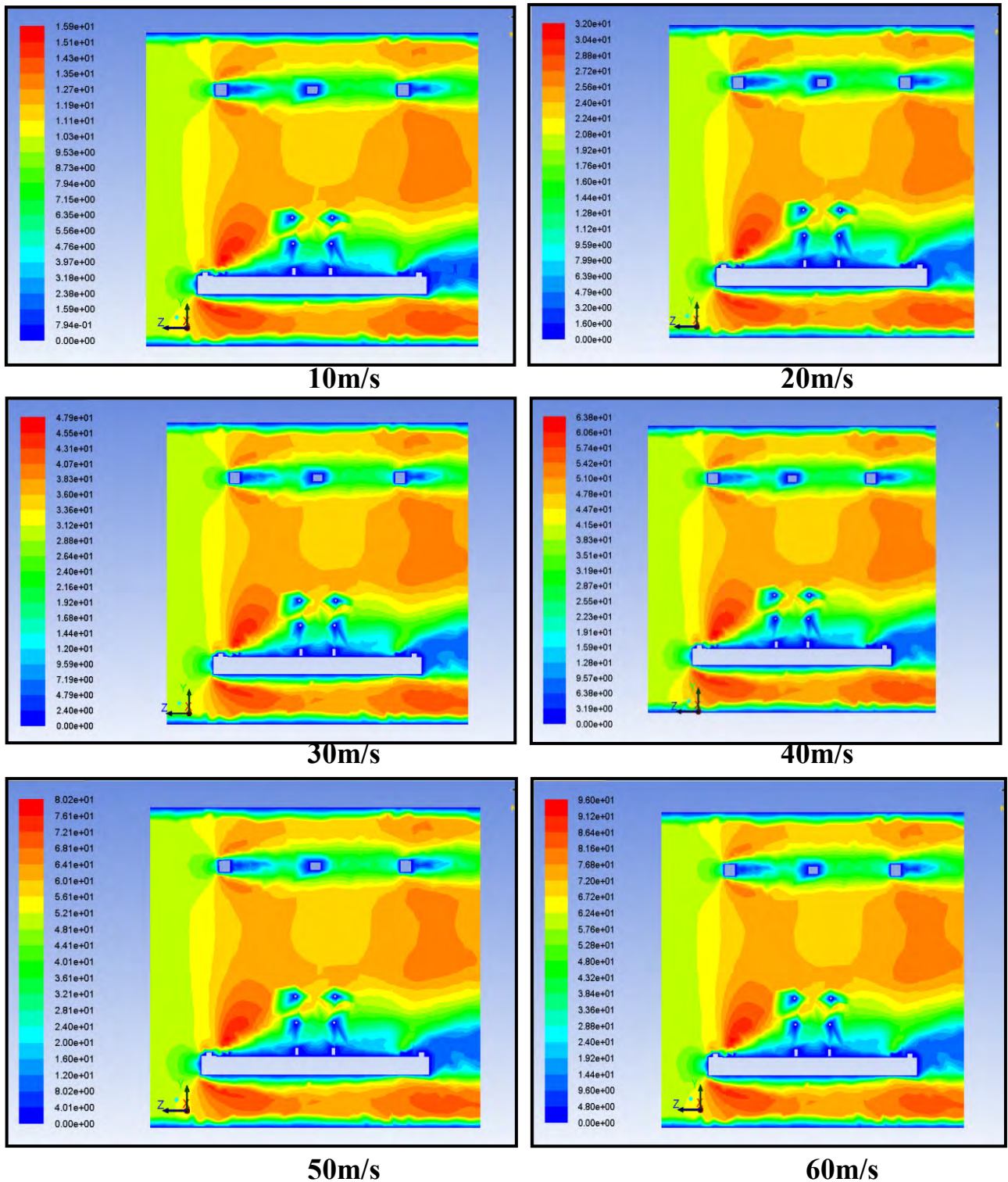


Figure 5.48 Velocity Contours (m/s) (Hand, 2014)

It can be seen from the velocity contour plots above there is wide distribution of flow velocities when the wind interacts with the structure. It is clearly seen the boundary layer developing around the structure and detached boundary layer on the bottom beam.

5.9.2 Static Pressure Contours

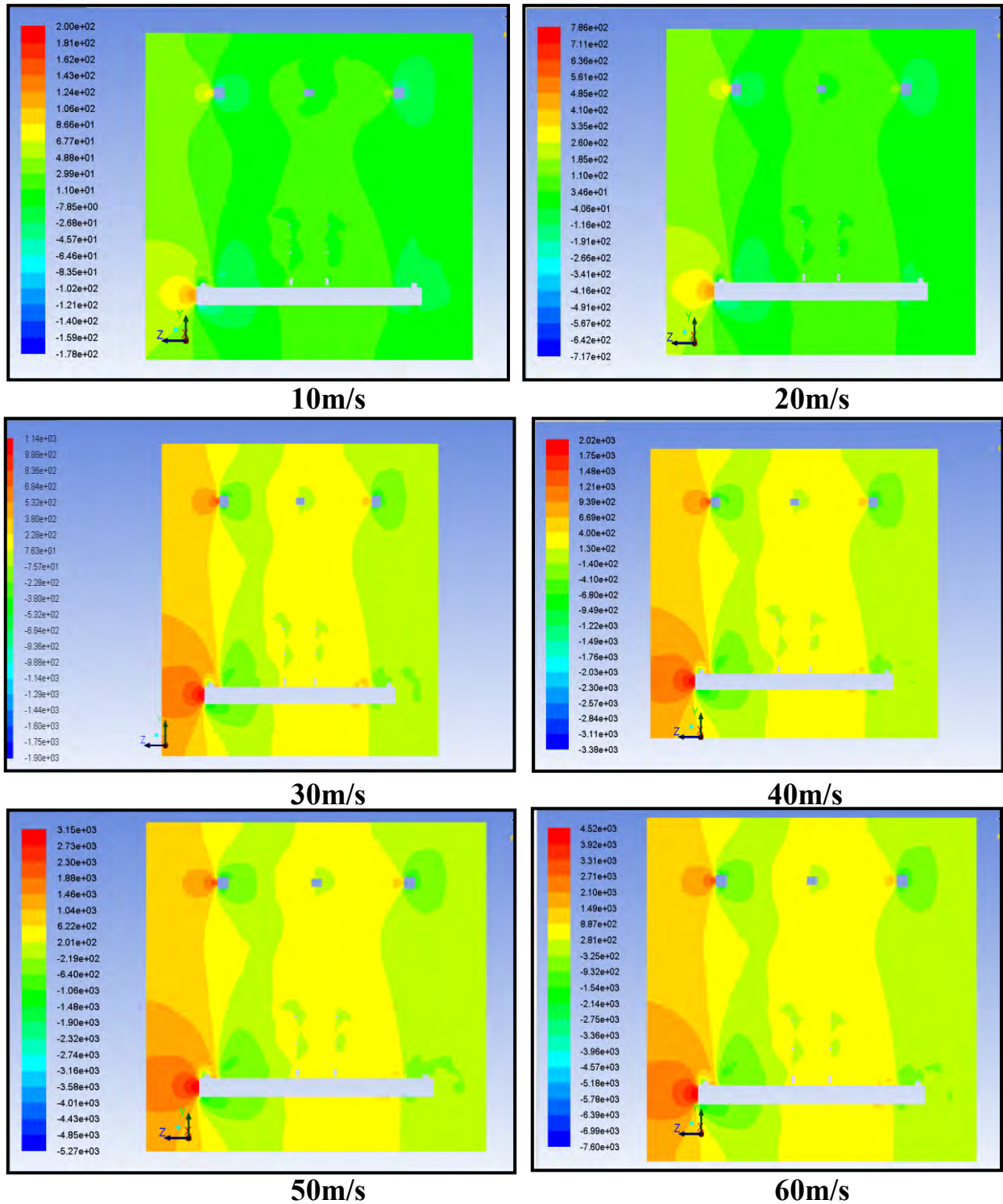


Figure 5.49 Static pressure contours (Pa) (Hand, 2014)

From the CFD analysis it has been found that significant static pressure occurring at the structural members of the structure which is what is to be expected. This static pressure increases with increasing wind velocity and contributes hugely to the drag on the structure.

5.9.3 Turbulence Intensity Contours

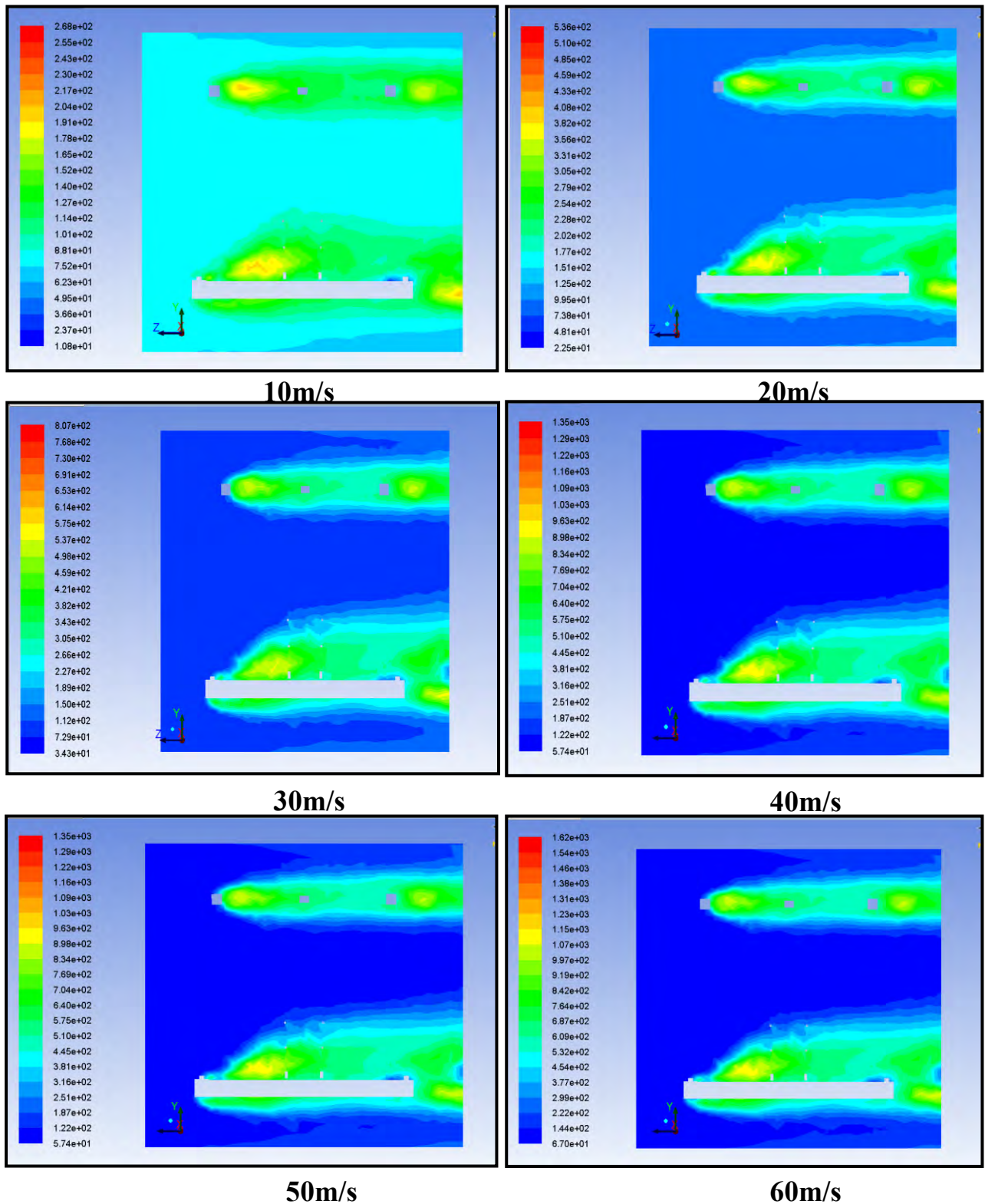


Figure 5.50 Turbulence Intensity (%) (Hand, 2014)

The above plots show the turbulence intensity on the structure with a given wind velocity. These plots show clearly the turbulent boundary layer formation occurring at the leading edges of the structure's edges.

5.9.4 Results Discussion

From examining the CFD results on this boom section, it is firstly noticed there is a considerable concentration of static pressure on the bottom section of the boom as figure 5.52 describes. This static pressure concentration is mainly caused by the shape of this section which has a rectangular face in nature and is composed of a I-beam box section which is required for the rigidity and strength of the structure as shown in figure 5.53.

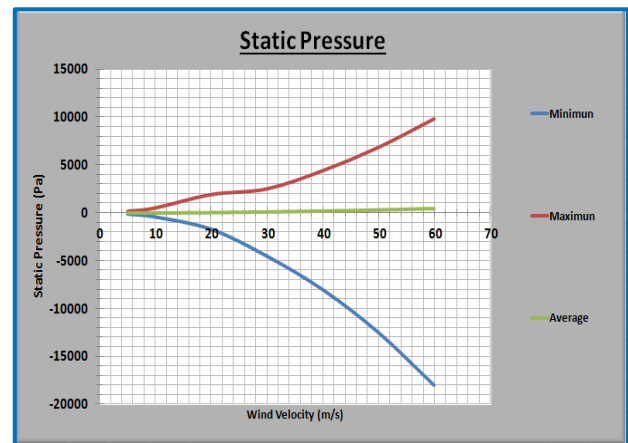


Figure 5.51 Static pressure on section (Hand, 2014)

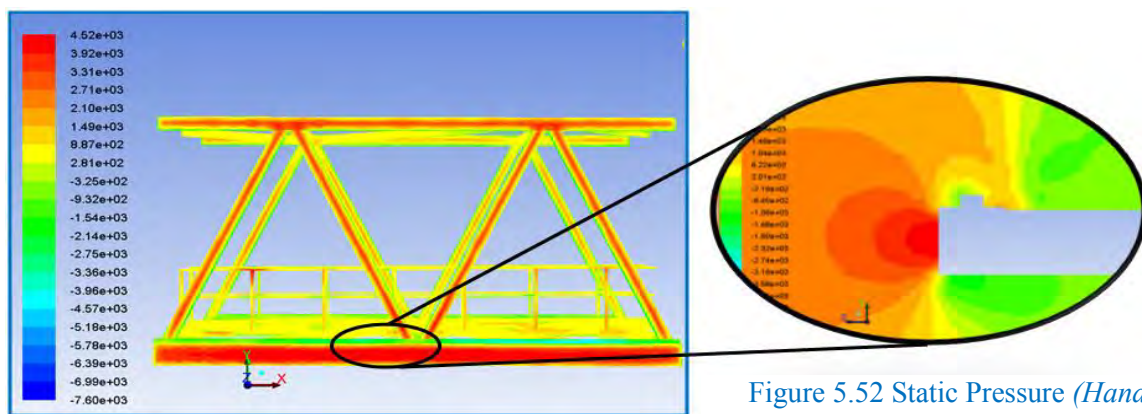


Figure 5.52 Static Pressure (Hand, 2013)

The static pressure developing on the structure vary greatly with wind velocity but at two main set points of 20m/s and 40m/s the maximum pressure is 0.78K KPa and 2.02 KPa respectively. It is witnessed also that the flow separation is mainly occurring around this part of the structure and a wake forming. From examining the contour plots of velocity and dynamic pressure it is believed that this separation is initiated by the relatively sharp corners on the beam. One minor but reasonably straightforward design modification would be to ensure a well defined filleted edge is present here, this would delay the flow separation point to further downstream and therefore improving its aerodynamics



Figure 5.53 Structure geometry (Hand, 2013)

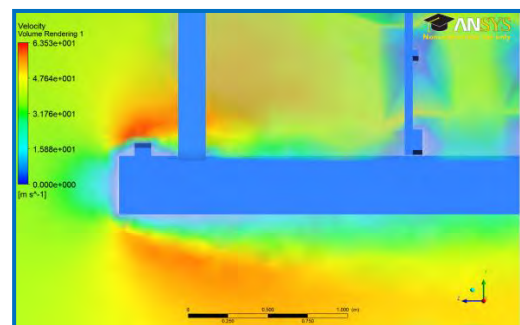


Figure 5.54 Flow separation (Hand, 2014)

6.0 Wind Tunnel Modelling

6.1 Introduction

Wind tunnel testing is a primary part of the design and analysis in many industries. Whether an item is stationary or in motion, wind tunnel testing provides insights into the effects of airflow as it moves over or around the test model in a controlled environment. Even though this type of testing has been utilised since the early twentieth century, engineers & designers today equipped with state of the art computers still rely on the testing of models to verify computer data and determine baseline aerodynamic performance (Fortus, 2010). “On the one hand, wind tunnel measurements are being used to validate CFD calculations performed with different turbulence models” (Moonena et al, 2006). It was therefore decided based on the appropriateness of wind tunnel testing it would be the most feasible means of validating the numerical simulations conducted. “Validation and assessment of data obtained using numerical simulation are recognised as crucial steps in the development of reliable Computational Fluid Dynamics (CFD) tools for engineering and academic research purposes”(Jouhaud et al, 2005).

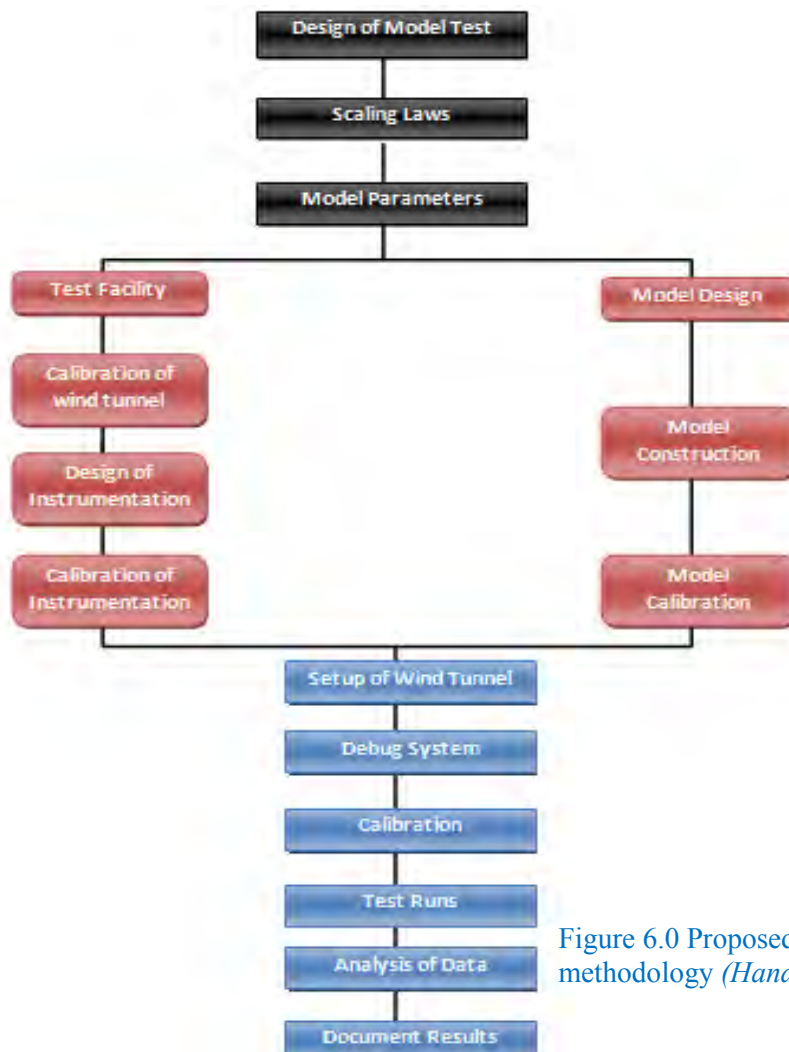


Figure 6.0 Proposed wind tunnel methodology (Hand, 2013)

6.2 Modelling Criteria

6.2.1 Background

The use of scaled models in fluid dynamics analysis offers the advantage of reproducing the way in which models interact with a fluid in a controlled environment and gives an insight into some of the fundamental fluid mechanics principles. In many occasions, such as this case the use of a scale model offers a more economical option than conducting a full-scale test. Primarily in many industrial test situations the scale model test results are used as a benchmark to compare analytical data and also allow one to make quantitative predictions about the prototype response (Zhu, 2007). “One of the first and foremost tasks in planning a model test is to investigate the modelling laws required for the system in question to be analysed” (Chakrabarti, 1998). The following paragraphs describe the theories scale modelling and elucidate on the elaborate on the scale modelling criteria for the physical test and model.

6.2.2 Theories of Scale Model Similitude

Similitude can be described as the relationship between a scale model and its corresponding prototype. A model is said to have similitude with a prototype if geometric similarity, kinematic similarity and dynamic similarity are preserved. Geometric similarity is achieved when the model and prototype have homologous physical dimensions. Kinematic similarity is attained when the model and prototype has geometric similarity and has similarity of the motion of the fluid particles around both the prototype and model. Dynamic similarity required that geometric and kinematic similarity be attained and in addition that the force ratios in the model and prototype are matched (Heller, 2012).

Scale models meet the prerequisites of similitude to the prototype to varying degrees. Specialists in fluid dynamics apply certain classification such as “true”, “adequate” and “distorted” to describe how well the model satisfies the similitude requirements. An adequate model accurately scales the primary aspects of the problem; lesser influences are allowed to deviate (Zhu, 2007). The occurrence of a distorted model is a common in fluid dynamics testing on models. Distorted models are models for which one or more of the similarity requirements are not satisfied. Distorted models still provide accurate results but are more difficult to obtain compared with a true model where all similarity conditions are set. The success of distorted models depends largely on the ability of the investigator and the analysis of the data of the model (Marin, 2014).

A more sophisticated version of dimensional analysis involves the implementation of the Buckingham Pi Theorem, which states that “*physical laws are independent of the form of units and therefore acceptable laws of physics are homogenous in all dimensions*” [6.0] (Wolfram, 2007).

$$x_0 = f(x_1, x_2, \dots, x_n) \quad [6.0]$$

It can be always written as $\frac{x_0}{f} - 1 = 0$ (Wolfram, 2007).

π terms are independent dimensionless products of the physical amounts x_1, x_2, \dots, x_n . The number of dimensionless products (m) is equal to the number of physical variables (n) taken away from the amount of fundamental measured involved in the problem. Scaling parameters can be clarified by equating the equivalent prototype and model π terms (Zhu, 2007).

6.2.3 Scaling Laws

To achieve similitude between the model and the actual structure, the following scaling laws must be ensured.

- ❖ Aerodynamic Similitude
 - Froude Number (Fr)
 - Strouhal Number (St)
 - Reynold’s Number (Re)
- ❖ Structural Similitude
 - Cauchy Number (Ca)

These scaling laws will be elaborated on in the coming sections.

6.2.1 Froude’s Number

Aerodynamic testing will be carried out on a scaled model of the crane section according primary to Froude’s scaling Law. Froude’s Law ensures that the relationship between inertial and gravitational forces is upheld when model crane section will be scaled down. Froude’s Law requires that the Froude number (Fr) [6.1] to be the same at the model (m) and prototype (p) scales [6.2] (White, 2003) where:

$$Fr = \frac{v}{\sqrt{gL}} \quad [6.1]$$

$$Fr_m = Fr_p \quad [6.2]$$

Geometric scaling will be employed throughout to ensure that the correct Froude number scaling is applied to all members of the model (HSE, 2001). “*A model and prototype are*

geometrically similar if and only all body dimensions in all three coordinates have the same linear scale ratio” (White, 2003). Also coupled with this the surface roughness of the model must be reduced with scale. Kinematic similarity has to be guaranteed that the model and the prototype have the same velocity scale ratio “The motions of two systems are kinematically similar homogenous particles lie at homogenous points at homogenous times”(Langhaar, 1980). Perfect dynamic similarity between model and prototype is very difficult to achieve in reality because both Froude and Reynold’s number can only be guaranteed if there are dramatic changes to the working fluid, but in actual experimentation air is used due to its supply and usable properties (White, 2003).

Table 6.0 gives a summary of the scale factors for the important parameters which will be used in this testing. Note λ is 28 (scale factor)

Table 6.0 Necessary Scale factors (Chakrabarti, 1994)

Variable	Unit	Scale Factor	Model : Prototype
Length	L	λ	1:28
Area	L^2	λ^2	1:784
Force	MLT^{-2}	λ^3	1:21,952
Velocity	LT^{-1}	$\lambda^{\frac{1}{2}}$	1: 5.292

6.2.2 Reynold’s Number

The Reynold’s number (Re) describes the relationship between the inertial and viscous forces [6.3], and requires that the Reynold’s number be the same for the model and prototype (HSE, 2001).

$$Re = \frac{\rho v L}{\mu} \quad [6.3] \qquad Re_m = Re_p \quad [6.4]$$

It is impossible to achieve both Froude and Reynold’s scaling simultaneously in a specific model test and in this situation the model is commonly referred to as a “distorted model”. Rearranging equations [6.1] and [6.3] shows that Froude scaling requires the model velocity to change by the square root of the length, where in the case of Reynold’s scaling requires the inverse of the relationship as shown below (HSE, 2001).

$$Re = \frac{V_m}{V_p} = \frac{L_p}{L_m} \quad [6.5]$$

$$Fr = \frac{V_m}{V_p} = \sqrt{\frac{L_m}{L_p}} \quad [6.6]$$

The Reynold's and Froude similitude problem arise because in the scaling process "the number of free parameters of the system is less than the non-dimensional numbers assumed as fundamental in the phenomenon" (Charalambos et al, 2011).

Therefore a logical compromise is taken into account so the results will be independent of Reynold's number but still taken with utmost accuracy. Differences between the model and prototype Reynold's number may not be significant as long as the following conditions are met. (1) the model will have sharp edges so flow separation occurs, (2) the flow has to be turbulent which can be achieved adding certain fixtures to the wind tunnel and (3) the Reynold's numbers of model and prototype are sufficiently high enough (HSE, 2001).

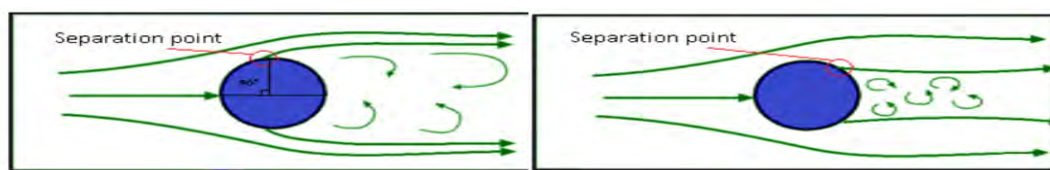


Figure 6.1 Ensure sharp edges (Abrahamsen, 2012).

6.2.3 Strouhal Similitude

Vortex shedding is a common occurrence around bluff bodies where instabilities form in the flow that result in periodic shedding of eddies and vortices as shown in figure 6.2 (White, 2003). This phenomenon gives rise to alternating forces on the body especially in the traverse direction on the body and leads to an excitation vibration on the body with a body with low damping (HSE, 2001). Previous model studies on container cranes have shown that cranes with long derrick booms would create dangerous dynamic wind loads through vortex shedding even when carried out at low wind speeds forming vortex induced vibration (Lee & Kang, 2007). The frequency of shedding is defined by the Strouhal Number (St) [6.7] (White, 2003):

$$St = \frac{\omega L}{v} \quad [6.7]$$

The Strouhal similitude ensures the similarity of the unsteady fluid flow and requires that

$$\frac{u_p T_p}{L_p} = \frac{u_m T_m}{L_m} \quad [6.8]$$

Froude similitude can comply with the Strouhal similitude which is expressed in [6.8] and expresses frequency as [6.9] (Chakrabarti, 1994).

$$f_p = \frac{f_m}{\sqrt{\lambda}} \quad [6.9]$$



Figure 6.2 Vortex Shedding (Simetrics, Inc, 2012)

6.2.4 Cauchy Number

In convectional model testing, the assumption is made that the model is fully rigid structure and the induced deflection from the interaction with the moving air is ignored. While this hypothesis is generally acceptable, for structures which are sufficiently long such as this case this simplification is not plausible. The coupling of aerodynamic load with a structure's response is referred to as aeroelasticity (*Princeton, 2012*).

Aeroelasticity accounts for problems of airflow past a structure in which the fluid dynamic forces depend on the elastic properties and dynamic response of the structure. It is often desirable from wind tunnel tests (although not in this case) to test structures to determine stresses in support members. In this case the elastic properties should be conserved in the model, to achieve this Cauchy similitude must be attained (*Chakrabarti, 1994*). Regarding the longitudinal bending of the structure, it is necessary that the model deflects the proportionally to the prototype and thus, equation [6.10] can be formulated.

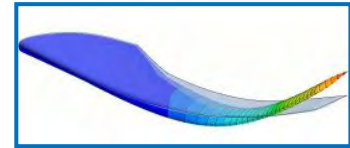


Figure 6.3 Aeroelastic analysis of a wing (*CD-Adapco, 20*

$$\left(\frac{My}{EI}\right)_m = \left(\frac{My}{EI}\right)_p \quad [6.10]$$

It is noted that the bending moment in the Froude similitude scales as λ^4 , and the Cauchy similitude criterion requires that in bending of the model and the prototype is related by expression [6.11].

$$(EI)_p = \lambda^5 (EI)_m \quad [6.11]$$

$$\text{Also } I_p = \lambda^4 I_m$$

Reducing this expression gives equation [6.12]

$$E_p = \lambda E_m \quad [6.12]$$

From expression [6.12] it shows that the Young's Modulus should be $\frac{1}{\lambda}$ times that of the prototype. As the real structure is made from structural steel with a Young's Modulus of around 200 GPa (*CES, 2014*), the model Young's Modulus should be in region of $(200 \times \frac{1}{28}) = 7.14$ GPa. Unfortunately due to the limited selection of materials to make the model a compromise had to be taken to find the material with highest E value. ABS (Acrylonitrile

Butadiene Styrene) was found to be the material with the highest E value of 3.1 GPa (CES, 2014) that could be rapid prototyped.

Table 6.1 ABS material properties (CES, 2013)

Young's Modulus (E)	Poisson's Ratio (ν)	Shear Modulus (G)	Density (ρ)	Yield Strength (S_y)	Tensile Strength (S_u)
3.1 GPa	0.38	950.277 MPa	1060 $\frac{\text{Kg}}{\text{m}^3}$	40.33MPa	40 MPa

6.3 The Model

6.3.1 Physical Model

Having determined the scaling laws which are applicable to this type of testing, the next step was to establish the size and scale of the model that would be needed to carry out the testing. The wind tunnel model scale is dictated by many conflicting issues, Firstly, the requirement for high Reynold's number implies to keep the scale as large as possible. However for measurement of forces on the model, blockage effects have to be minimised and also the model cannot intersect the boundary layer that develops at the walls (this will be discussed later in this chapter). The choice of model scale had to be a compromise between these effects and was decided that a 1/28 scale model would be suitable. Using integrated scaling features in Autodesk Inventor it was possible to scale the full scale 3D model to a 1/28 scale model as shown in figure 6.5.



Figure 6.4 Model showing clearance between wind tunnel walls (Hand, 2014)

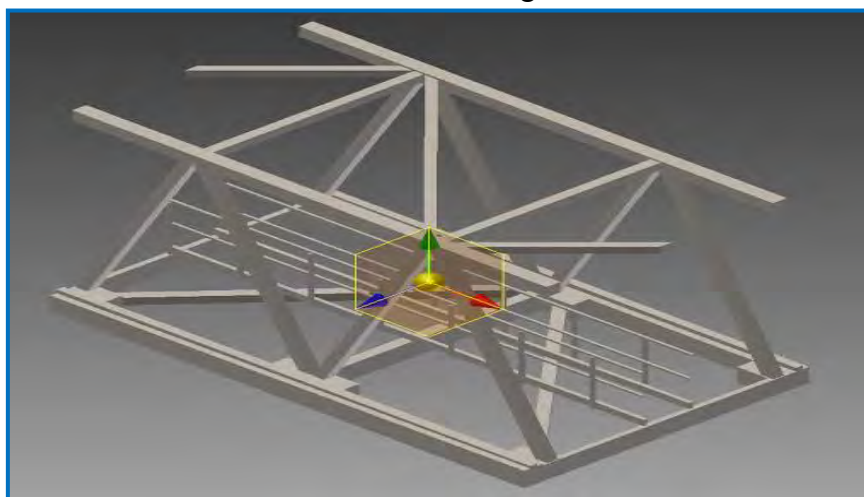


Figure 6.5 3D generated scaled model (Hand, 2013)

The next task was to integrate a design mechanism in the scaled 3D model that could be used to hold the model during testing and mainly attach it to the force balance. Inspecting the force balance used for the testing it was observed that test models were primarily held by attaching a threaded shaft that connected model to the balance. A very important design criterion for the testing primarily was that the design modification made to the model did not increase the frontal surface area which would be affected by airflow induced drag.

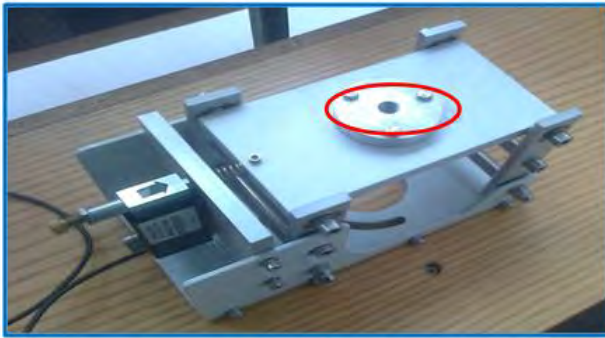


Figure 6.6 Force balance attachment (Hand, 2013)



Figure 6.7 Frontal area of model (Hand,2013)

Figure 6.8 below shows the design modifications that was made to the model so the threaded shaft could attach to the physical model as discreetly as possible. The position of where the shaft would connect with the model was also positioned where the centre of gravity was located on the model as shown in figure 6.8.

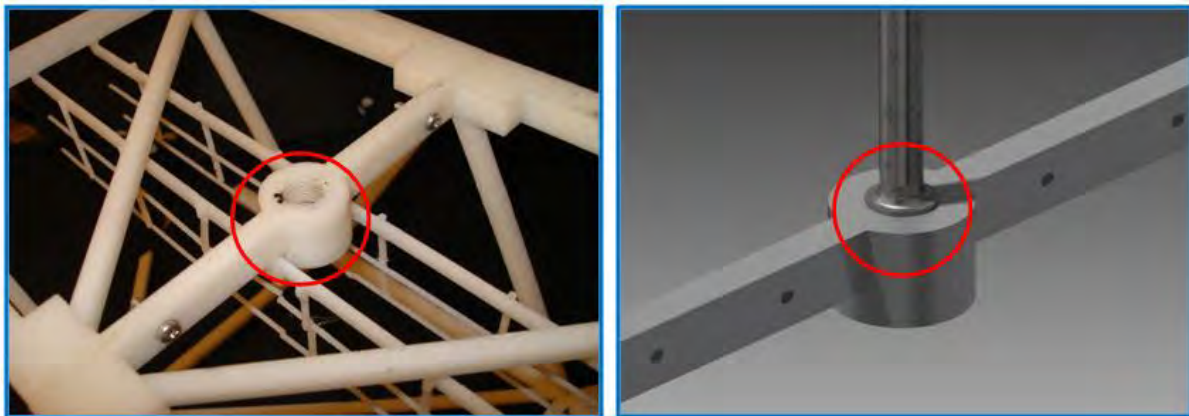


Figure 6.8 Model attachment design (Hand, 2013)

To ensure the design modification was safe and be able to withstand the drag forces within the wind tunnel it was necessary to carry out mechanical analysis of the design. The most feasible and optimal method was found to use finite element analysis (FEA) software that is enabled in Autodesk Inventor. To achieve this the CAD model shown above in figure 6.8 was analysed to ensure the ABS material did not surpass its yield point and suitable factor of safety was upheld in the design. A wide load range was implemented on the design due to the unknown drag load that the model would be put on the model during testing.

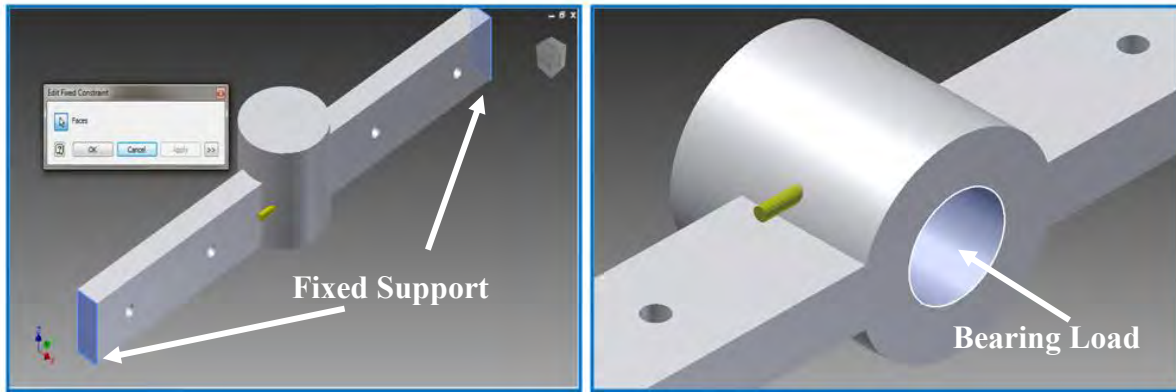


Figure 6.9 Design boundary conditions (Hand, 2013)

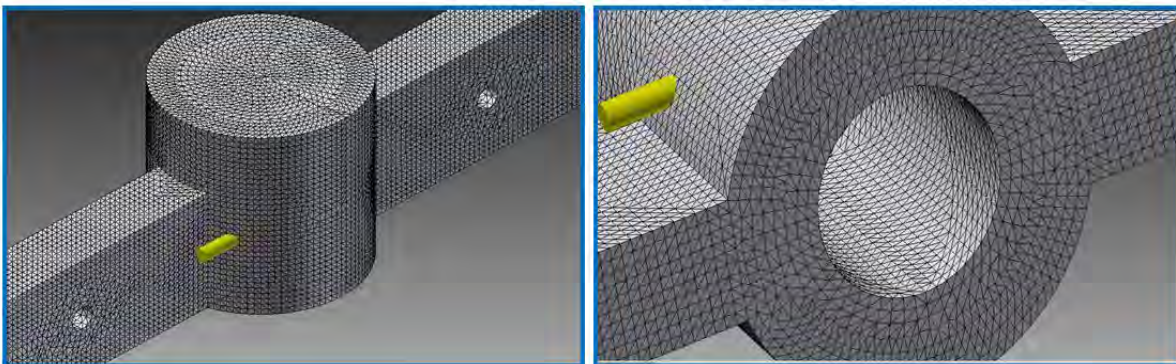


Figure 6.10 Design mesh detail (Hand, 2013)

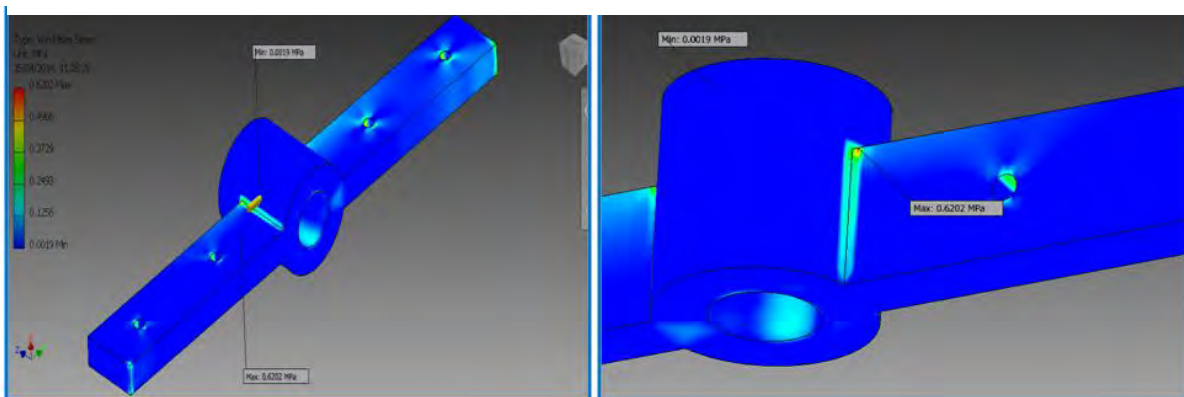


Figure 6.11 Equivalent stress on design (Hand, 2013)

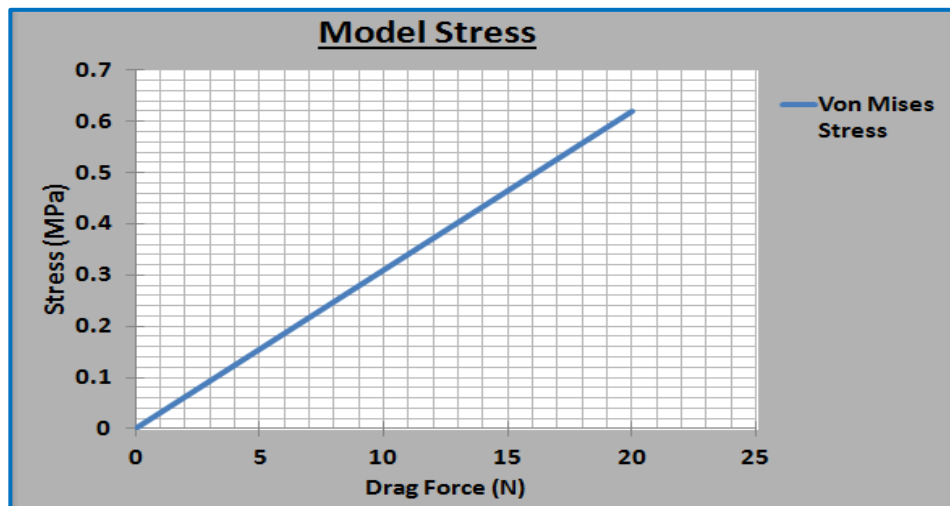


Figure 6.12 Equivalent stress vs predicted drag force for design (Hand, 2013)

Table 6.2 Stress analysis results on design (Hand, 2013)

Bearing Load (N)	Von Mises Stress (MPa)	Displacement (mm)
5	0.1551	0.0008282
10	0.3101	0.001656
15	0.4652	0.002485
20	0.6202	0.003313

A bearing load was placed where the shaft is connected with the model and the two ends of the cross beam were fixed to recreate the physical constraints in reality. A fine grid mesh was placed on the model with an average element size of 0.005 mm being implemented. The results show the values for Von Mises Stress are well under the yield stress for ABS and was considered a safe design and ready for testing.

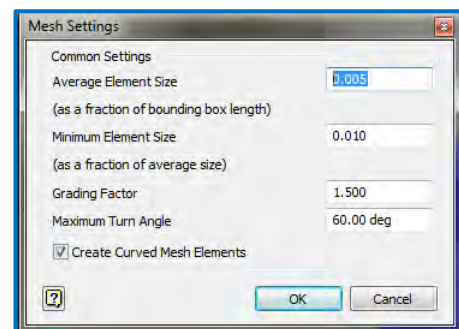


Figure 6.13 Mesh Settings (Hand, 2013)

6.3.2 Model Manufacture

6.3.2.1 Rapid Prototyping (RP)

“Wind tunnel model design and construction has traditionally been a relatively long tedious and expensive process”, (Artzi & Kroll, 2011) but since the introduction of rapid prototyping (RP) technology mainly in the past decade this has modernised the whole model manufacture procedure for wind tunnel testing “better, faster, cheaper” (Cooper, 2005). In industrial situations RP allows initial studies and analysis of baseline aerodynamic characteristics of models to be carried out at a low cost and early in the design process (Cooper, 2005).



Figure 6.14 F1 team Red Bull regularly use RP for early results for aerodynamic performance (Ridge, 2013)

The RP process is begun by the generation of a 3D parametric model using a standard solid CAD modelling software. When the design is complete the model is transferred to the printer to initiate the printing process where the model is usually printed from common plastics such as ABS. RP usually uses a construction technique known as additive fabrication whereby the material is added in layers until the 3D model is complete (*Alpha Prototypes, 2014*). The main advantage of this building technique is that it allows huge versatility in the printing of the model which is very important in this study.

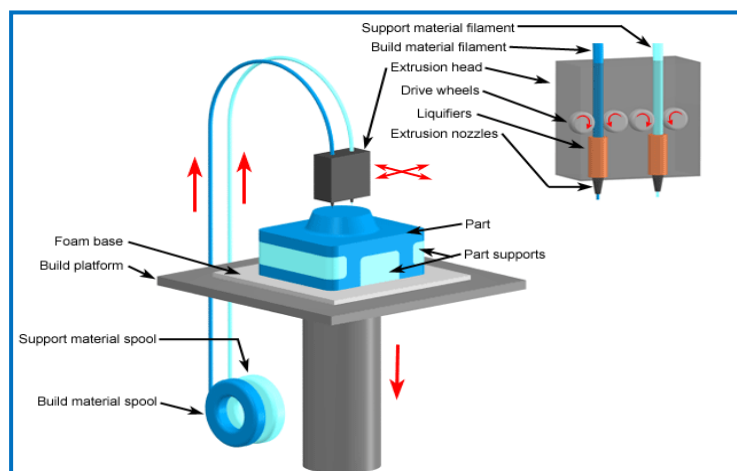


Figure 6.15 Rapid Prototyping configuration (*SRL, 2004*)

Wind tunnel models produced by RP do show promising results for the checking, validating and generating of results for drag, lift and pressure distribution on a model (*Artzi & Kroll, 2011*). Conventional building techniques for models for wind tunnel applications mainly consisted of models built from aluminium or steel by high precision machinery which took considerable amounts of time and also were expensive also (*Barlow et al, 1999*). In some experimental studies carried out, RP models have shown good results in cases where aerodynamic performances are being examined with at least a five to tenfold decrease in the model production cost and acquisition time (*Artzi & Kroll, 2011*).

A study conducted by (*Landrum et al, 1997*) was carried out on three 30 cm span by 10 cm airfoil models in a low speed subsonic wind tunnel. Two of the aerofoil models were made by RP with different plastics being used and the third model was a cast model from polyurethane. It is reported the cast model took considerable more time to produce than the RP models and different tolerances being generated. The study showed small variations for values of drag and lift for the three models which the surface roughness was attributed. The rougher surfaces of the RP models inhibited the formation of laminar separation bubbles.

To build the wind tunnel model, the college's Dimension 3D printer was used as shown in figure 6.16 which can produce fully functional ABS plastic rapid prototypes. To construct the complex geometry of the model being tested the printer uses a gel-like material which is used as a temporary support for the model during manufacturing which is necessary for over-hanging features. The printer has an accuracy of 0.05mm and a total build volume of 203mm × 203mm × 305mm which meant the model had to be printed in two parts as its longest dimension was 256.4mm. This meant the model had to be mechanically joined together using small screws and suitable adhesive where appropriate.



Figure 6.16 College RP Machine (Hand, 2013)

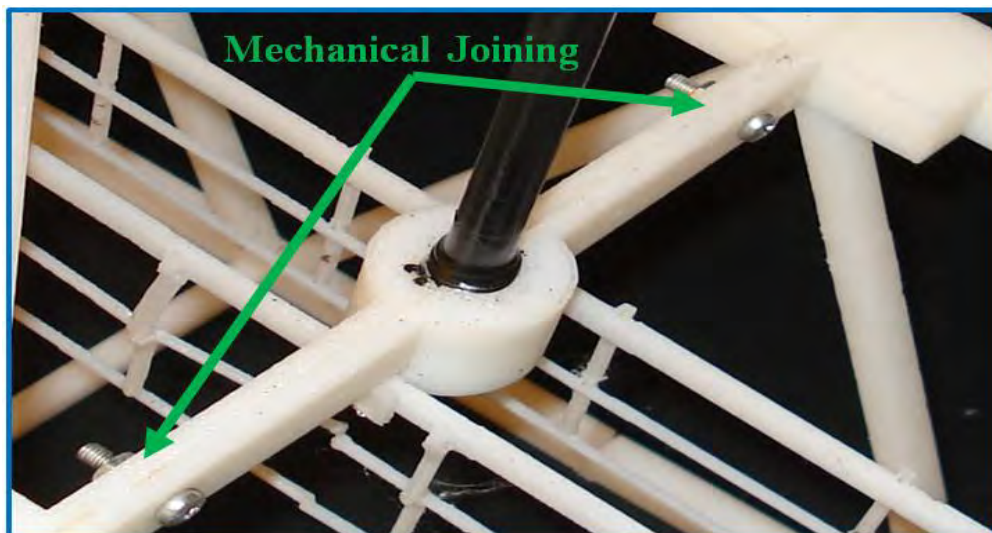


Figure 6.17 Joints used in model (Hand, 2013)

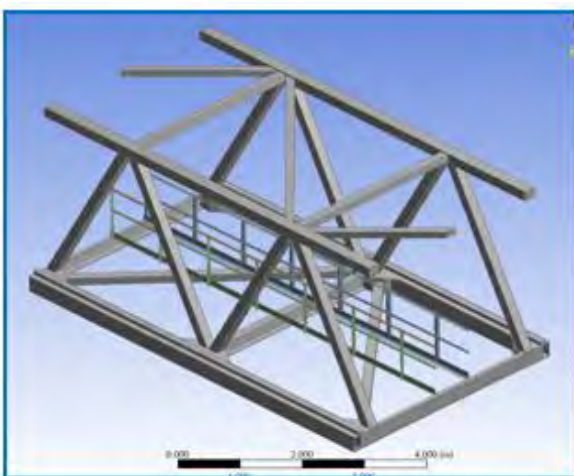


Figure 6.18 CAD generated model (Hand, 2013)

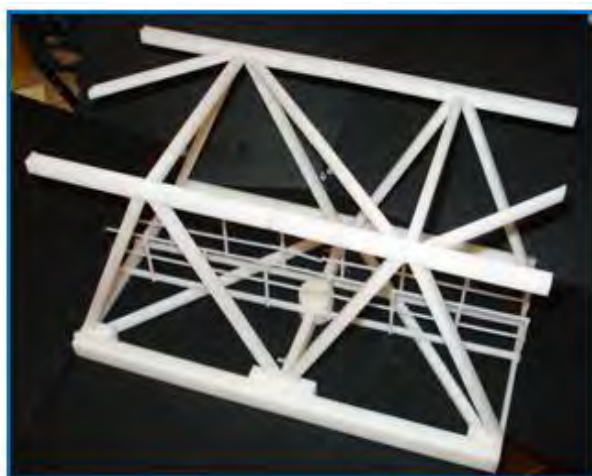


Figure 6.19 Rapid-prototype model (Hand, 2013)

6.4 The Wind Tunnel

The wind tunnel model testing was carried out using CIT's open circuit type subsonic wind tunnel with a working test section of 300mm × 300mm. The air enters the tunnel through a carefully shaped inlet and the working section is made from perspex giving full visibility during the testing as shown in figure 6.20. At the upstream end of the working section is a static

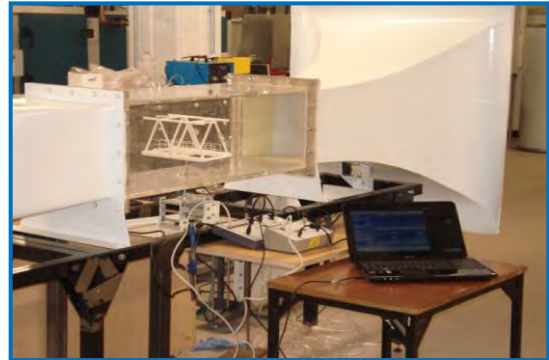


Figure 6.20 Wind tunnel (Hand, 2014)

tapping and a total head tube which may be traversed over the full height of the working section, while at the downstream end a pitot-static tube may be similarly traversed.

The wind tunnel is equipped with a Wood's Aerofoil 1.7 KW motor & fan with a max speed of 2910 RPM that is controlled by a double-butterfly valve on the fan outlet (see wind tunnel specification sheets pages D-2 & D-3 Appendix-D). The fan produces a maximum wind velocity of 20m/s that discharges through a silencer (TecQuipment, 2000). Mainly for this testing it is required to have turbulent flow to recreate the same conditions used in the CFD analysis. For internal flow through ducts such as this wind tunnel it is required to have Reynold's number above 4000 (MIT, 2002) as shown below in figure 6.21.

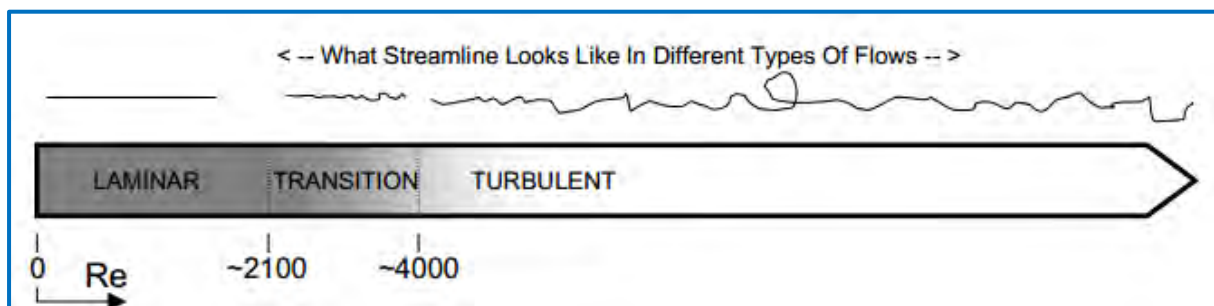


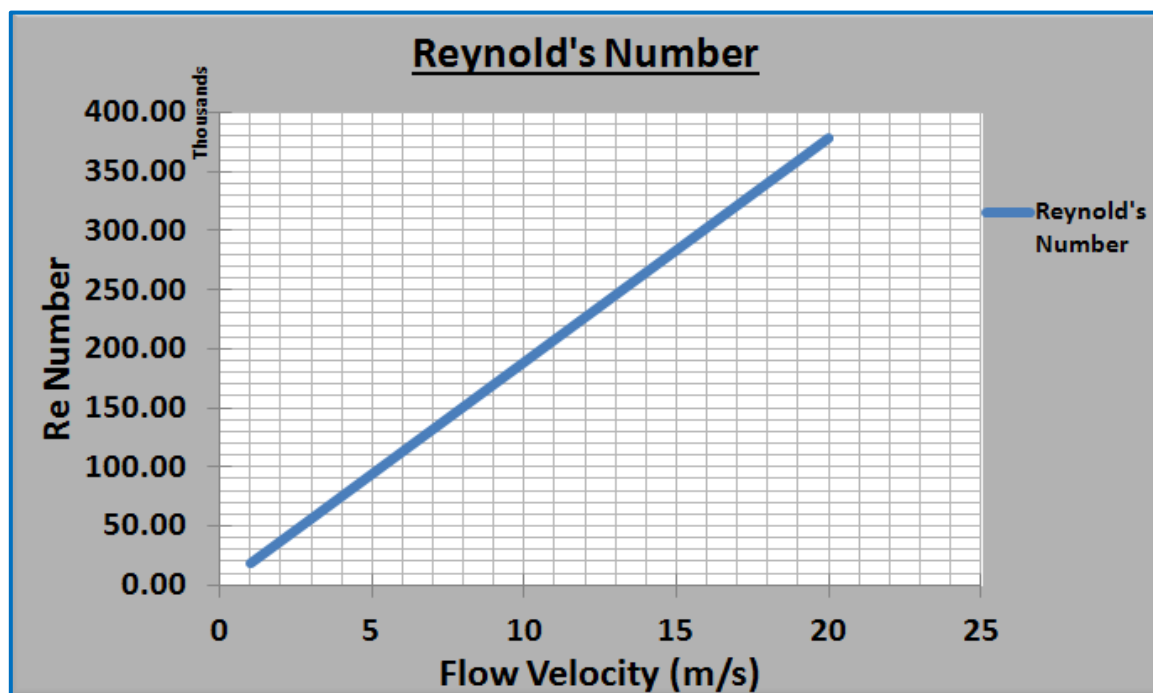
Figure 6.21 Reynold's Number range for internal flow (MIT, 2002)

For calculating the Reynolds number (Re) through the wind tunnel, equation [6.13] is used, where D_H is the hydraulic diameter or its characteristic length (L_c). As the wind tunnel cross section is a square section its characteristic length is taken as 0.3m.

$$Re = \frac{\rho v D_H}{\mu} \quad (MIT, 2002) \quad [6.13]$$

Table 6.3 Reynolds number values wind tunnel (*Hand, 2013*)

Flow Velocity (m/s)	Re Number	Flow Velocity (m/s)	Re Number
1	18910.74	11	208018.15
2	37821.48	12	226928.90
3	56732.22	13	245839.64
4	75642.97	14	264750.38
5	94553.71	15	283661.12
6	113464.45	16	302571.86
7	132375.19	17	321482.60
8	151285.93	18	340393.34
9	170196.67	19	359304.08
10	189107.41	20	378214.83

Figure 6.22 Reynold's Number vs Flow velocity (*Hand, 2013*)

As can be seen from table 6.3 and the graph above is that the Reynold's numbers are all turbulent at each incremented flow velocity which is near ideal for this testing. Table 6.4 below shows the instrumentation which is available for the testing and it is important for this type of analysis that the equipment is calibrated to ensure the highest quality of results.

Table 6.4 Wind tunnel instrumentation overview (Hand, 2013)

Name	Type of Measurement	Reference (Appendix D)
Total Head Tube	Pressure difference	Page D-5
Pitot-Static Tube	Velocity & dynamic pressure	Page D-5
Lift & Drag Balance	Lift & Drag force	Page D-7
TecQuipment's (Versatile Data Acquisition System)	Signal Converter	Page D-11

6.4.1 Calibration

One of the essential tasks that have to be carried before the experiment commences is to make sure the equipment is properly calibrated and it is important to check for linearity in the results. In an experiment it is imperative to achieve a linear regression [6.14] as close to 1 as possible as shown below in figure 6.23 with minimal scatter of results. In basic terms if the value of x is found it is possible to predict the value of y (Abrahamsen, 2012).

$$R^2 = 1 - \frac{SS_{\text{Error}}}{SS_{\text{Total}}} = 1 - \frac{\sum_i (y_i - \hat{y}_i)^2}{\sum_i (y_i - \bar{y})^2} \quad [6.14]$$

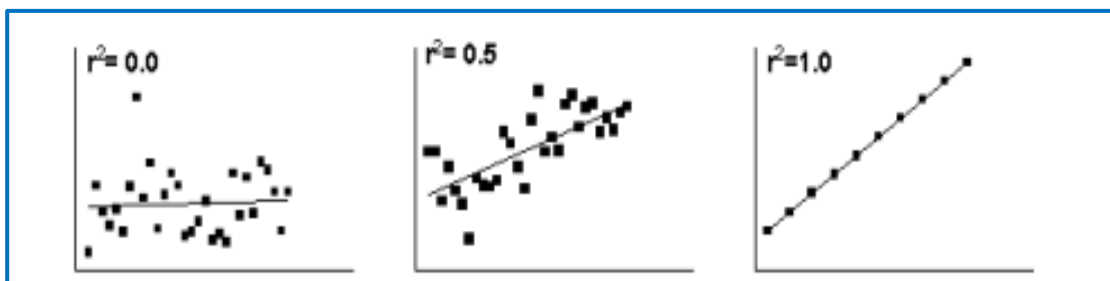


Figure 6.23 Linear Regression (Abrahamsen, 2012)

A calibration of the wind tunnel was carried out by the author to examine the thickness of the boundary layer at the wind tunnel walls because this would directly influence the scale of model that could be used and therefore was carried out before the model was made. This is necessary to ensure that the model receives the same velocity profile over its surface and not receive less towards the walls. The measurement of

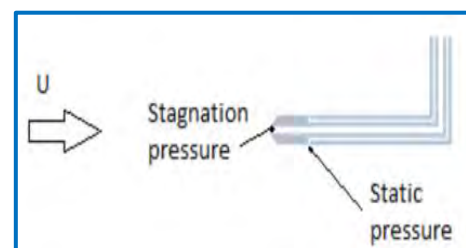


Figure 6.24 Pitot Tube (Abrahamsen, 2012)

velocity profile was achieved using a pitot-static tube as shown in figure 6.24 The pitot tube was connected to a water manometer as shown in figure 6.25 which read the difference in

head pressure (h) produced by the airflow passing through the wind tunnel. Using equation [6.15] the head pressure in meters could be related to the pressure difference in Pascal (Pa) and the velocity of airflow by using equation (Bernoulli's Principle) [6.16].

$$P = \rho gh \tag{6.15}$$

$$v = \sqrt{\frac{2(P_{\text{Stagnation}} - P_{\text{Static}})}{\rho}} \tag{6.16}$$

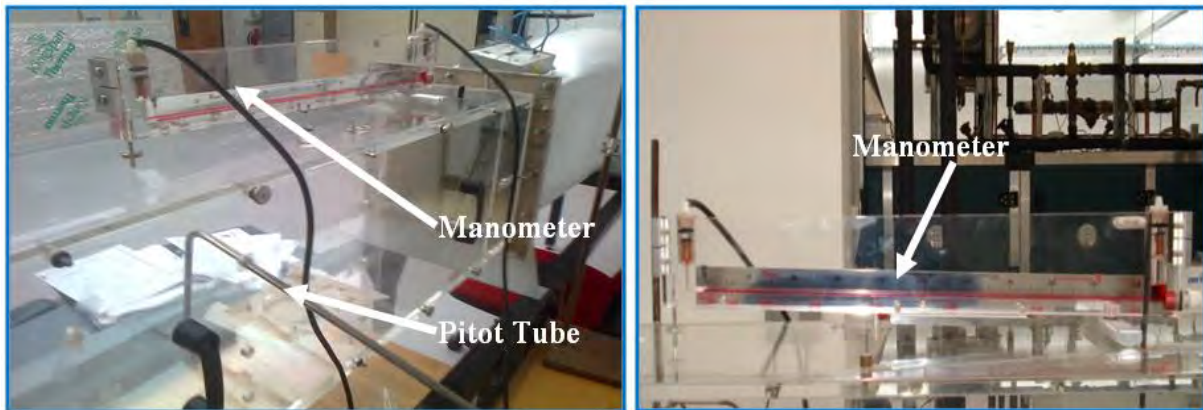


Figure 6.25 Pitot tube and water manometer (Hand, 2013)

The wind tunnel was run at maximum speed (20m/s) and pressure readings were taken at intervals over the full length of the cross section with closer readings taken near the wind tunnel walls and are shown in the graph below in figure 6.26. This procedure was carried out two times to ensure the velocity distribution in the wind tunnel was correctly represented. One main issue associated with the use of pitot-static tube is that the axis of the probe has to be orientated parallel to the flow and cannot have a misalignment of more than 5%. (Wheeler & Ganji, 1996), figure 6.26 below shows this possible occurrence taken in the first measurement.

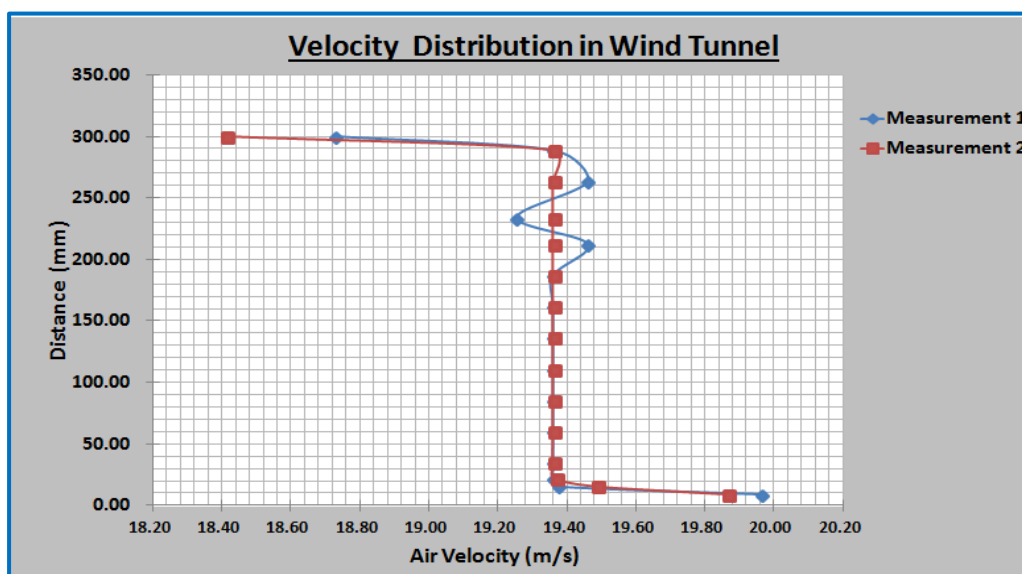


Figure 6.26 Velocity distribution inside the wind tunnel (Hand, 2013)

It is possible to make an approximation of the boundary layer thickness for a turbulent flow such as this case basing all assumptions on the $1/7^{\text{th}}$ power law which is used for estimating turbulent flows. In order to use this law it is assumed that the sides of the wind tunnel are like smooth plates (MIT, 2004). If the flow regime was laminar the Blasius boundary layer solution would be utilised which gives good accuracy but this is not the case. The thickness of the boundary layer was calculated using equation [6.17] and it is also possible to approximate the wall shear stress based on equation [6.18] also (MIT, 2004).

$$\delta \approx \frac{0.392 \times L}{Re^{\frac{1}{5}}} \quad [6.17]$$

$$\tau_w \approx 0.029 \rho U_o^2 Re^{\frac{-1}{5}} \quad [6.18]$$

Using the table below this law predicts the boundary layer to be around 15mm thick at a velocity of 20m/s which is very similar to the results which were recorded using the pitot tube and manometer which found the thickness to be around 15mm to 20mm thick also. Based on this data a 25mm clearance was ensured between the model and side of the wind tunnel.

Table 6.5 Calculated boundary layer thickness for wind tunnel (Hand, 2013)

Flow Velocity (m/s)	Re	Boundary Layer Thickness (mm)	Shear Stress at the wall (Pa)
2.00	37821.48	23.807	0.018
4.00	75642.97	20.725	0.061
6.00	113464.45	19.111	0.127
8.00	151285.93	18.042	0.214
10.00	189107.41	17.255	0.319
12.00	226928.90	16.637	0.443
14.00	264750.38	16.132	0.585
16.00	302571.86	15.707	0.744
18.00	340393.34	15.341	0.919
20.00	378214.83	15.021	1.111

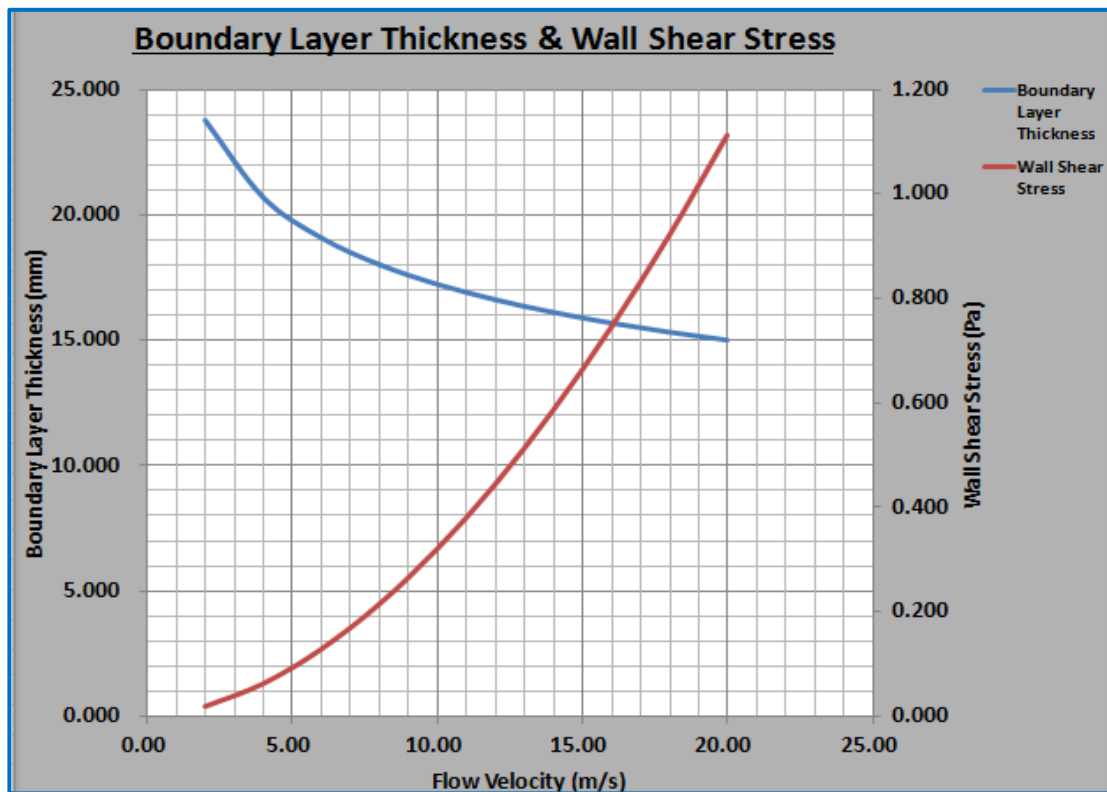


Figure 6.27 Graph of calculated boundary layer thickness and wall shear stress (Hand, 2013)

6.5 Force Balance

The force balance will be used to measure drag force induced on the model from the moving airflow. The model is connected to the force balance with a vertical slender shaft as shown in figure 6.28 through the test section floor of the wind tunnel as shown in figure 6.29. It was important that this shaft did not corrupt the drag results, so where the shaft intercepted the test section of the wind tunnel its cross section was reduced and smooth finish was applied. The forces were measured using a load cell which has a digital display output. This balance also allows the option of capturing real-time data, monitoring, and calculation using its Versatile Data Acquisition System (VDAS) system which can be used to log data (TecQuipment a, 2013).



Figure 6.28 Slender shaft (Hand, 2014)

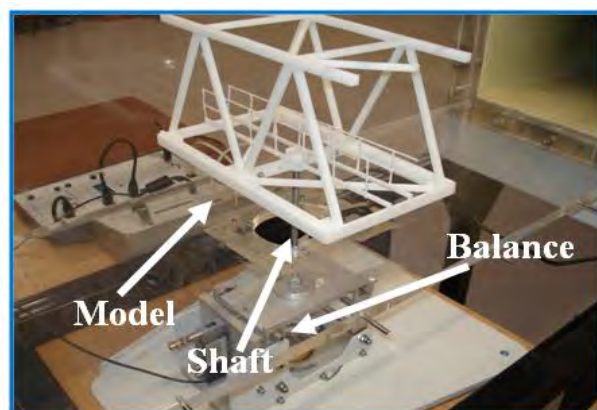


Figure 6.29 Model connected to force balance (Hand, 2014)

6.5.1 Calibration

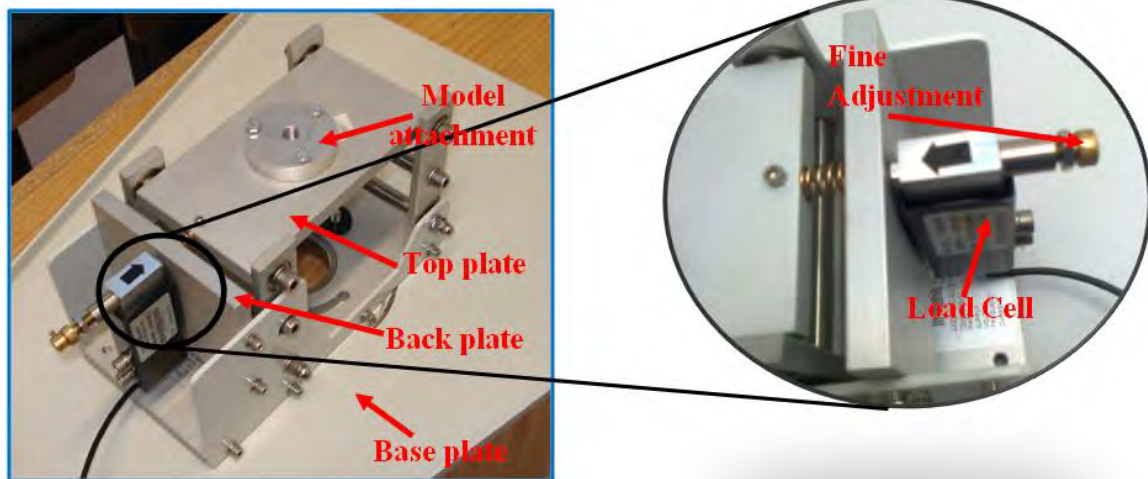


Figure 6.30 Parts of force balance (Hand, 2014)

“Accurate balance calibration is an absolute necessity for accurate wind tunnel tests” (Starcs, 2013). The balance was firstly examined to see if it was mechanically working in the way it should and to see if there was any faults in with the system. Prior to any calibration or adjustment of the balance settings small masses were placed on the balance as shown in figure 6.31 using a mass hanger. Masses were added in increments of 10g up to 250g and the corresponding force was noted from the digital display shown in figure 6.32. The force reading should be the same as the weight that was placed on the balance but this was not the case with an average of 22 % error being recorded before the calibration was conducted which is not acceptable amount of error.

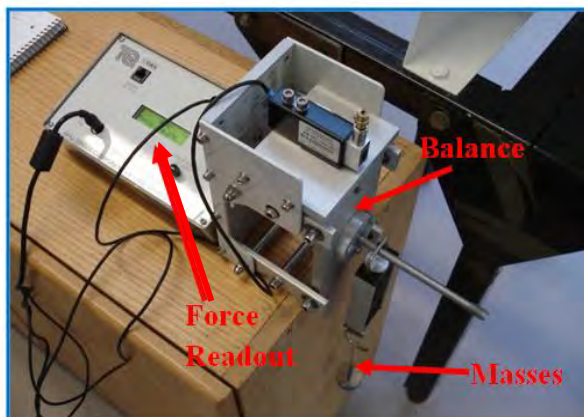


Figure 6.31 Balance calibration set-up (Hand, 2013) Figure 6.32 Force Readout (Hand, 2013)

The thumbscrew which changed the spring stiffness was then adjusted until the balance was nulled. Again the same masses were placed on the balance and this time an average of 10.8% was recorded. The spring stiffness was again modified as said above and the same process was carried out again. This time the results were more accurate and there was less error

between the reading and the actual load applied with an error of 3.4% being which was found to be best obtained for this system. The balance settlings were left unchanged for the actual testing.

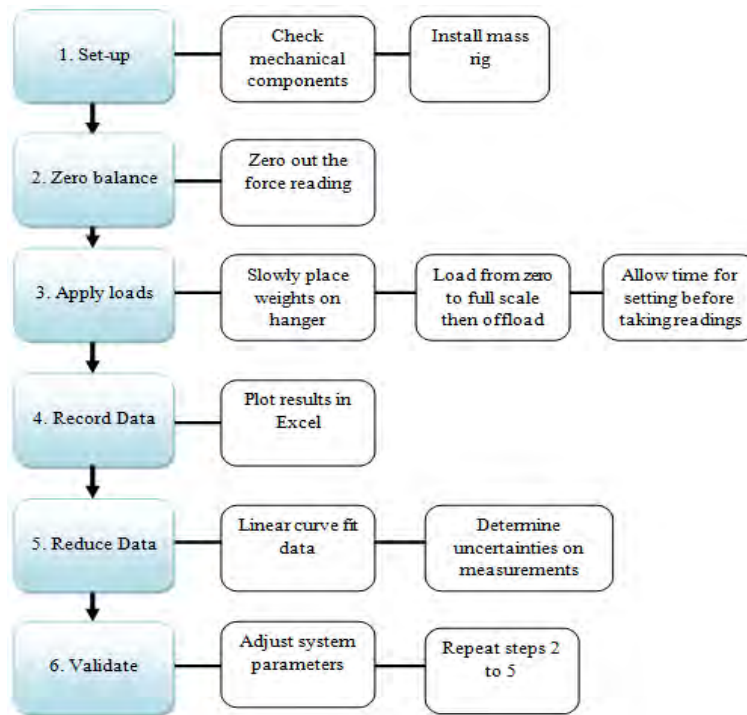


Figure 6.33 Summary of calibration process (Hand, 2014)

Table 6.6 Calibration results of force balance (Hand, 2014)

Load Applied (g)	Load Applied (N)	Reading 1 (N)	Percentage Difference (%)	Reading 2 (N)	Percentage Difference (%)	Reading 3 (N)	Percentage Difference (%)
10	0.10	0.07	28.64	0.09	8.26	0.09	8.26
20	0.20	0.15	23.55	0.14	28.64	0.18	8.26
30	0.29	0.21	28.64	0.25	15.05	0.27	8.26
40	0.39	0.28	28.64	0.31	21.00	0.38	3.16
50	0.49	0.37	24.57	0.42	14.37	0.46	6.22
60	0.59	0.46	21.85	0.5	15.05	0.56	4.86
70	0.69	0.55	19.91	0.59	14.08	0.67	2.43
80	0.78	0.61	22.27	0.71	9.53	0.74	5.71
90	0.88	0.69	21.85	0.8	9.39	0.87	1.46
100	0.98	0.75	23.55	0.89	9.28	0.98	0.10
110	1.08	0.82	24.01	0.98	9.18	1.06	1.77
120	1.18	0.89	24.40	1.07	9.11	1.15	2.31
130	1.28	0.98	23.16	1.15	9.83	1.27	0.42
140	1.37	1.04	24.28	1.3	5.34	1.35	1.70
150	1.47	1.12	23.89	1.41	4.18	1.46	0.78
200	1.96	1.86	5.20	1.98	0.92	1.94	1.12
250	2.45	2.3	6.22	2.46	0.31	2.43	0.92
Average Percentage Difference (%)			22.04		10.8		3.4

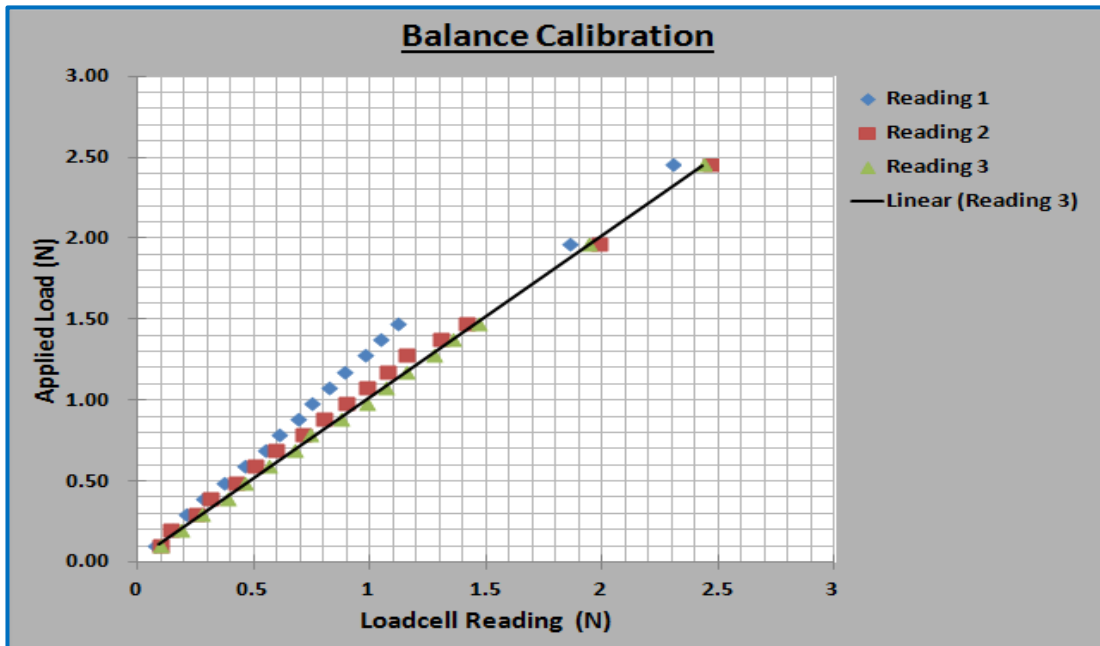


Figure 6.34 Balance calibration (Hand, 2014)

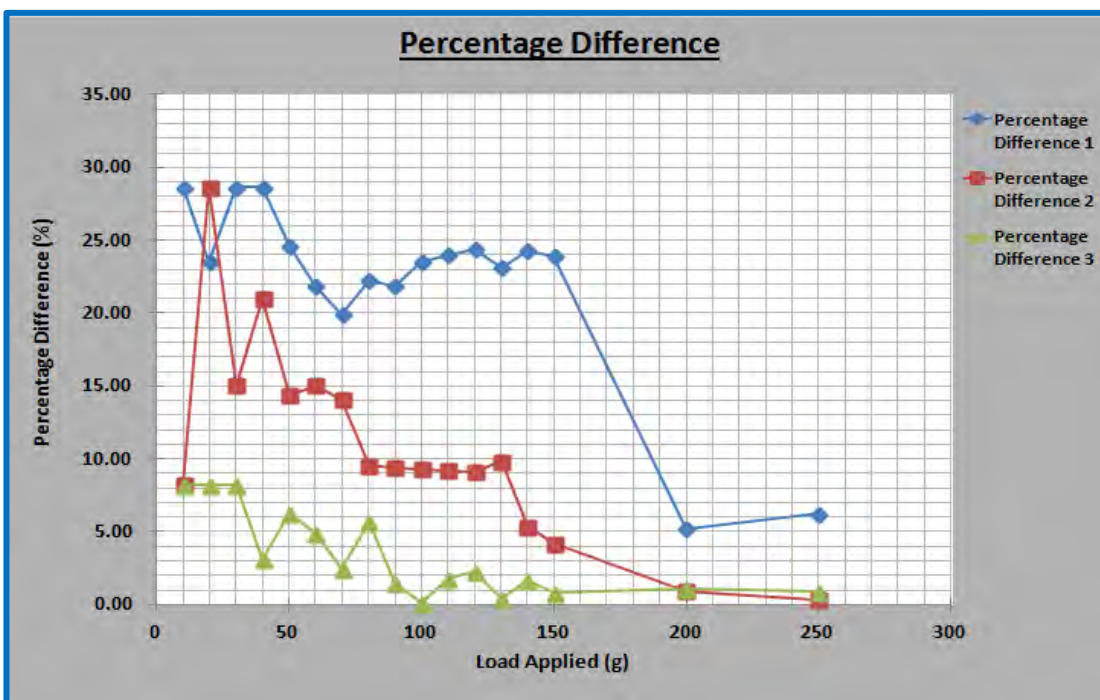


Figure 6.35 Percentage difference for each reading (Hand, 2013)

As can be seen from figure 6.34 the third reading gave almost linear relationship for the force balance which is what was required. Figure 6.35 shows the percentage difference between the three calibration attempts and shows the percentage difference dropped significantly for the third reading in contrast with the first reading. The force balance was positioned on this setting for the wind tunnel testing as it was found to be the most accurate that could be achieved using this balance.

6.5.2 Data Acquisition

“To gain accurate and trustworthy data from a testing apparatus, a proper data acquisition system is required” (Smith, 2002). Data acquisition (DAQ) is the method of measuring an electrical generated signal such as a voltage from a device known as a transducer (NI, 2014). In this case the load cell on the force balance is connected to data acquisition system which is known as the VDAS (Versatile Data Acquisition System) which is compatible with the wind tunnel load cell. This system offers many advantages such as it reduces the time needed to physically collect data and also lower the chance of errors taking place when inputting data to a computer manually. It can also allow for high speed data collection which can be important to when analysing data with respect to time.



Figure 6.36 Data acquisition system (TecQuipment, 2000)

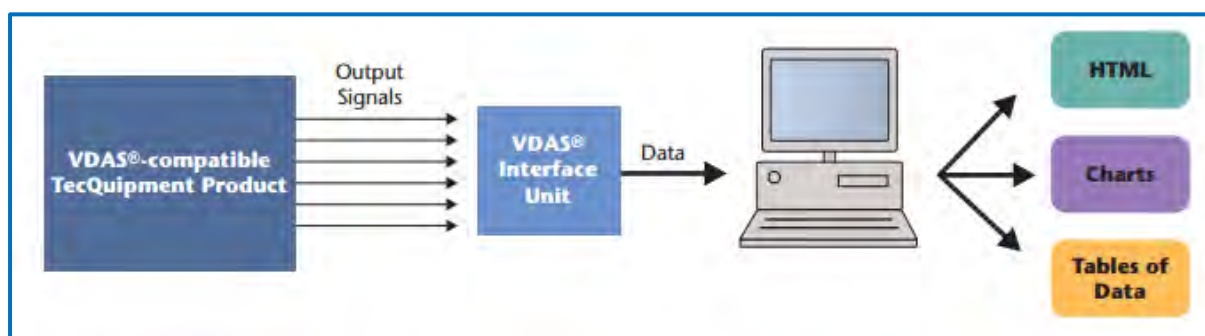


Figure 6.37 VDAS System (TecQuipment, 2000)

The data acquisition process begins with acquisition of the raw data from the sensor. Enabled in every DAQ device is a high precision clock that activates an analog-to-digital converter (ADC) on an exact time interval between each acquisition. The term sample rate is commonly referred to the amount of analog-to-digital conversions which happen per a unit time when using a DAQ device. Defining a suitable sample rate is important detail for successful data acquisition of data from a testing procedure, basically it is important not to sample at a rate too high as this can pose high demands on the computers computational resources and memory capabilities. Also it is necessary not to sample at a rate too low either as this can give a false representation of the sampled frequency and incur inaccurate results which is known as aliasing.

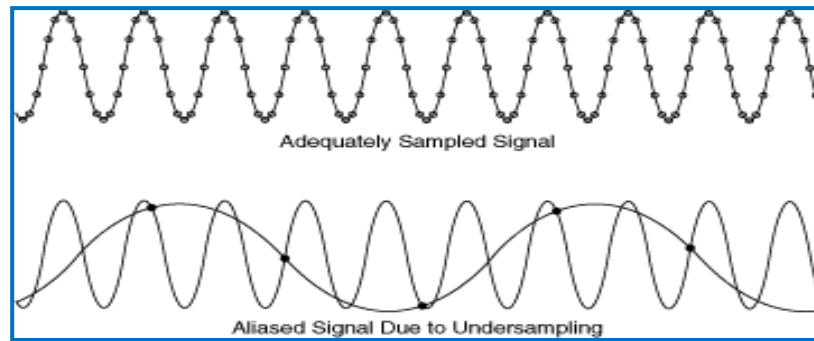


Figure 6.37 Aliased frequency (NI, 2014)

The Nyquist-Shannon sampling theorem can be used to prevent the occurrence of over and under sampling of a frequency. This theorem states that it is necessary to sample at twice the maximum frequency in order to retain all frequency components in the signal (Franz *et al*, 2011).

$$F_s > 2F_{MAX} \quad [6.19]$$

Where F_s is the sampling frequency and F_{MAX} is the maximum input frequency (also called the Nyquist frequency).

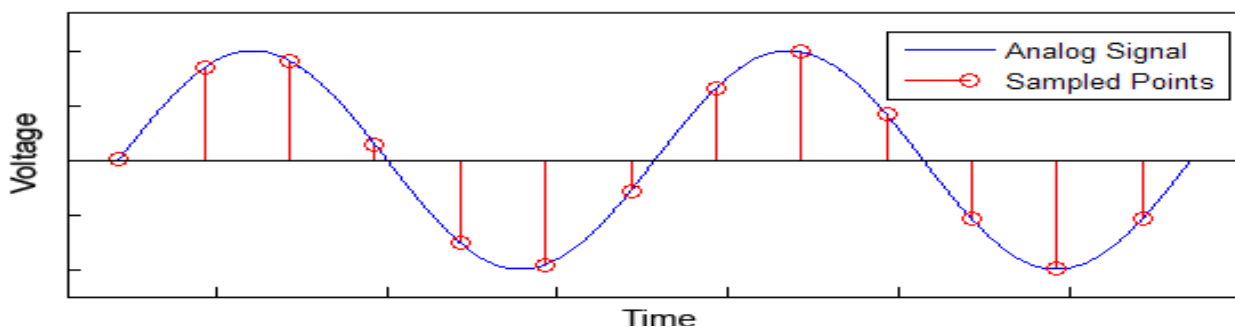


Figure 6.38 Accurate sampling of frequency (Franz *et al*, 2011)

For this testing the data acquisition device was set to record one sample every second and let run for thirty seconds. This was done for every wind tunnel airflow velocity interval from 0 – 20m/s. As the drag results on the model were not time dependent it was found that thirty samples at each airflow velocity would suffice. The drag values at each velocity should be constant but taking many samples would allow the average of the results to be taken if there were any variations in the results due to any errors in the system.



The data acquisition system software allowed the monitoring of drag values using a digital dial during the wind tunnel testing and could be data logged to allow post-processing of the results at a later date.

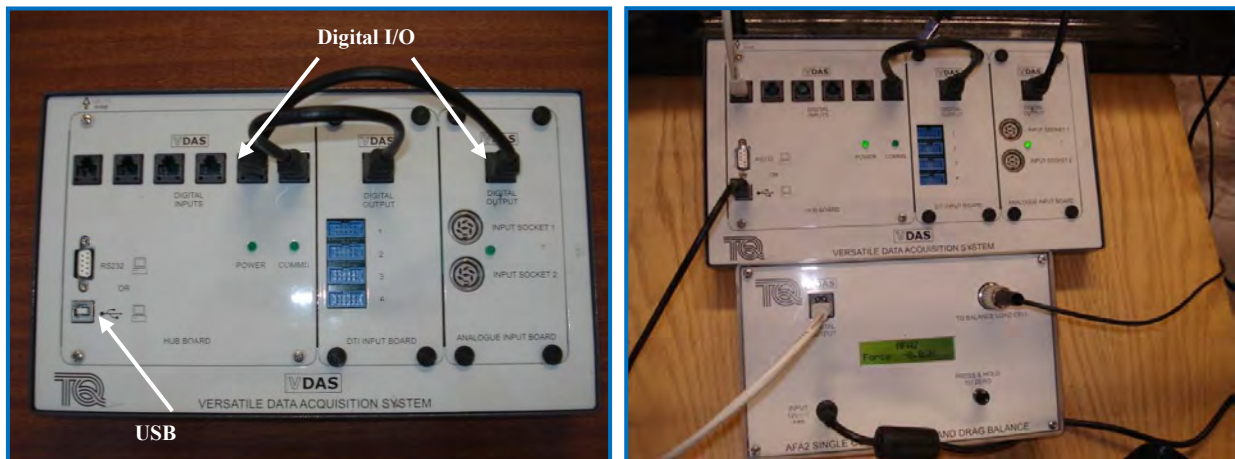


Figure 6.40 Data Acquisition set-up (Hand, 2014)

6.6 Wind Tunnel Test

6.6.1 Equipment Set-Up

- The side panel of the wind tunnel was removed and the model was placed inside the wind tunnel testing cross section. The model was then attached to the force balance via the threaded shaft.
- The height of the model was then adjusted until its centreline was aligned with the centre of the wind tunnel as shown in figure 6.41.
- Using an engineer's square the model rotated until it 90° to the direction of air flow and locked in place.



Figure 6.41 Model aligned with airflow

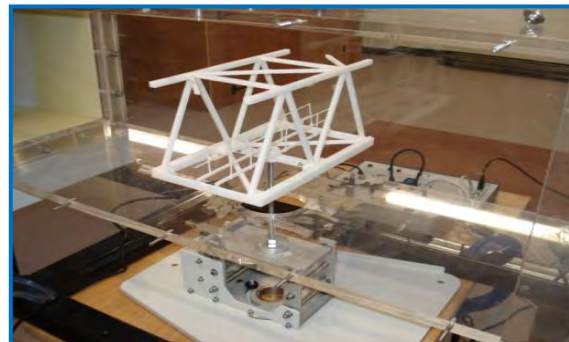


Figure 6.42 Model positioned in wind tunnel

- The panel was replaced back into the side of the wind tunnel and it was ensured there were no air gaps in the wind tunnel which may cause low pressure regions.
- The data acquisition system was connected to the force balance and also connected a laptop via a USB cable which would store the data from the wind tunnel test.



Figure 6.43 VDAS enabled with force balance and controlled with a laptop

- A pitot tube was positioned in the centreline of the wind tunnel airflow to measure head pressure using a water manometer as shown in figure 6.44. As there was no means of measuring airflow velocity in the wind tunnel, it was required to construct a chart whereby velocity could directly related to developed head pressure (Bernoulli's Principle).
- The pitot tube was held using an experimental stand and the manometer was placed on the wind tunnel and made horizontal using adjustable screws on its base.

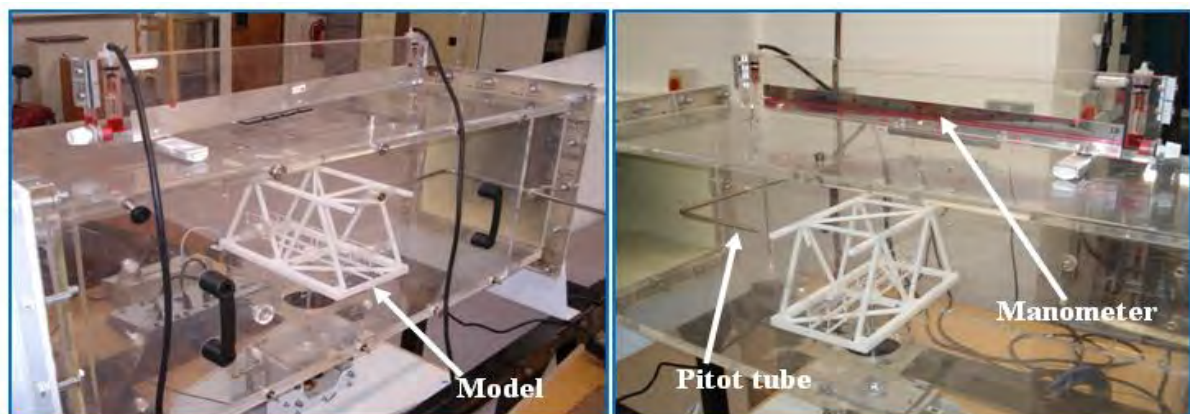


Figure 6.44 Pressure and airflow velocity measurement in wind tunnel

- All the necessary equipment was now setup and the test was ready to be commenced. Before the actual testing was begun the wind tunnel fan was turned on and a low air velocity was selected and all the systems were examined to see if they were functioning in the way they should and any problems were troubleshooted.

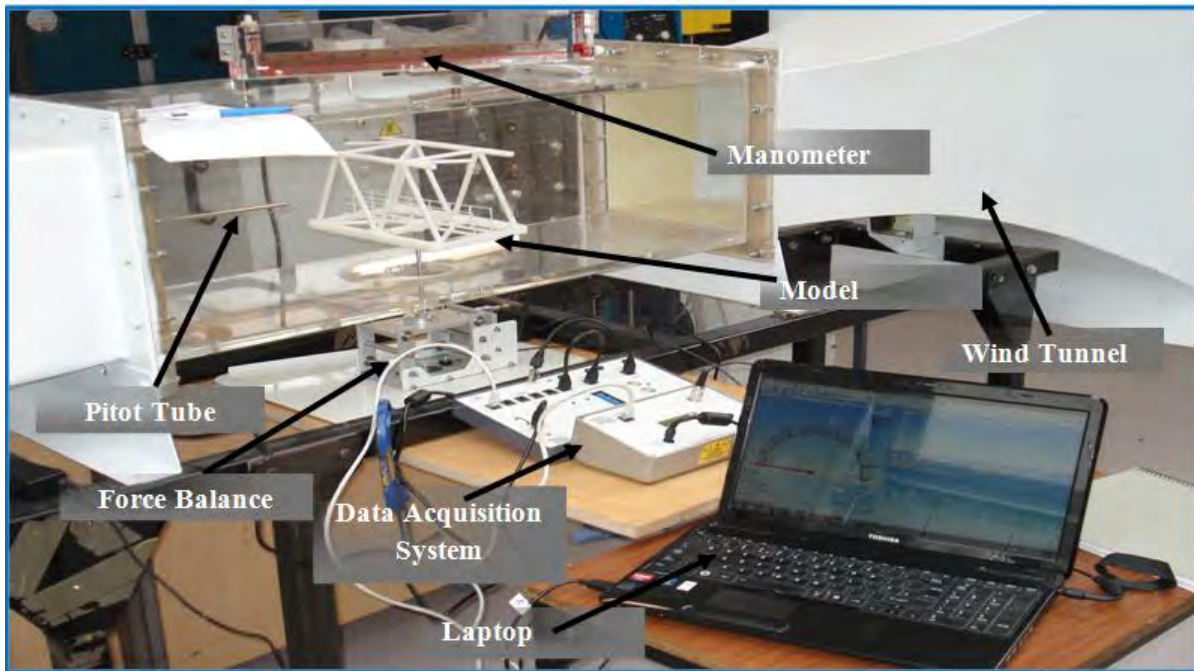


Figure 6.45 Wind Tunnel test equipment set-up (Hand, 2014)

6.6.2 Test Procedure

- The wind tunnel control systems were turned on using the main panel as shown in figure 6.46. The airflow velocity was increased by using adjusting a knob central on the panel.
- The pressure was read off the manometer scale and the corresponding velocity was found. The knob was adjusted until the pressure on the manometer corresponded with the velocity for 1m/s airflow. When this was achieved the flow was allowed to settle.
- The data acquisition software was then activated and thirty samples were taken and saved. This process was then repeated for all velocities from 1m/s to 20m/s with each taking full measurement taking about $1\frac{1}{2}$ hours to complete.
- The test was conducted three times to ensure the most accurate results were achieved from this testing. These results were critically analysed and examined which will be documented in the coming chapter.



Figure 6.46 Control Panel

6.6.3 Flow Visualisation

Flow visualisation is an experimental method of examining the flow patterns around an object or over its surface. The main benefit of this method is that it allows the ability to describe the flow over a body without the need for complicated analysis or examination (Mahmood, 2011). “Visualization of flow can provide important information on processes which are associated with many problems of fluid flow and fluid-solid interaction” (Bienkiewicz & Cermak, 1987). This technique is a central tool in experimental fluid mechanics as it can provide an overall picture of the fluid flow and has existed since the beginning of fluid flow research (Settles, 1986). As air is invisible it not possible to see the flow patterns which are happening around a model, by using a visualisation technique it is possible to witness such phenomena such vortex flows for inviscid flow and also phenomena associated by the effects of viscosity such as boundary layer, separation and wakes (Ristić, 2007).

Flow visualisation can be placed into two categories which are surface flow visualisation and off the surface visualisation both of which were utilised in this testing. Tufts are the main method used for surface visualisation in aerodynamic applications.

6.6.3.1 Flow Visualisation by Tufts

Tufts are an old visualisation tool used for wind tunnels, which consist of small lengths of wool or yarn that frayed on the ends. Tufts are attached to the model’s surface using an adhesive and when blown in the wind tunnel point downstream. Tufts are used to see surface flows in the sub region of the boundary layer and can indicate places of unsteady flow (Benson T, 2011).

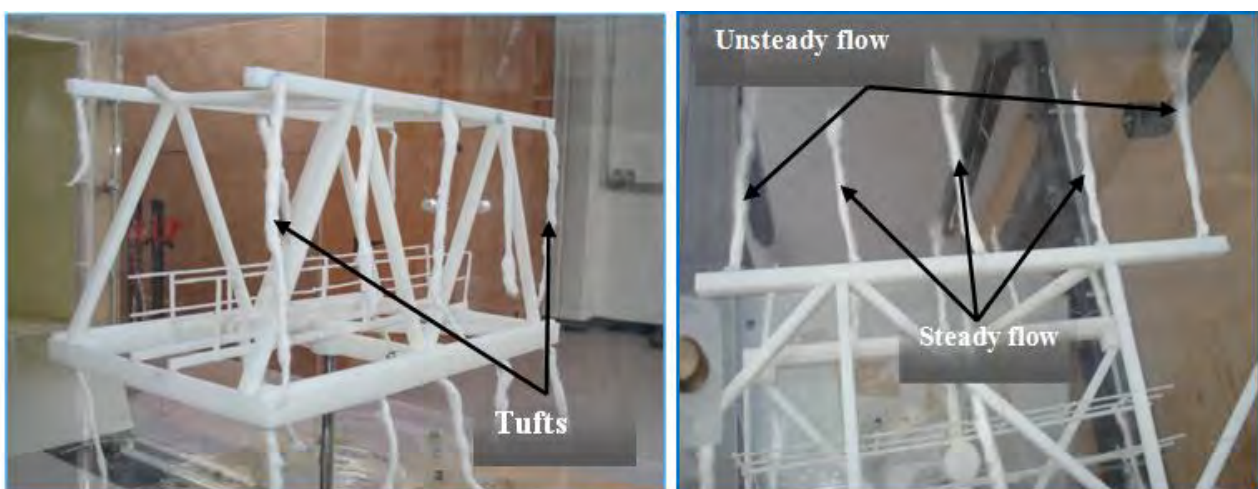


Figure 6.47 Tufts on model (Hand, 2014)

Strong centrifugal forces act on some of the tufts causing them to stick to model surface (Ristić, 2007) indicating the formation of a boundary layer, this was observed on many tufts placed on the lower edges of the bottom beam. The movement of these tufts was organised and steady which showed the laminar region. Other tufts placed on the leading edge of the model showed the presence of high turbulence region which can be seen on the top left hand corner of figure 6.48.

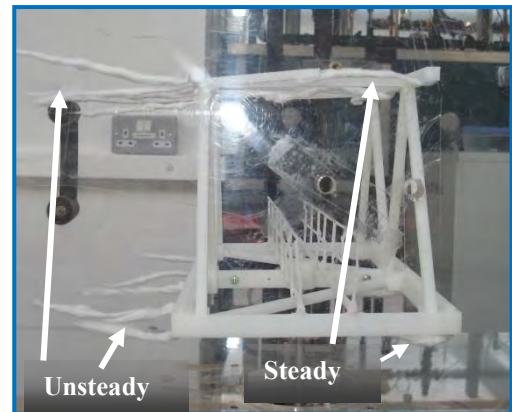


Figure 6.48 Uniform and non-uniform tufts (Hand, 2014)

6.6.3.1 Flow Visualisation by Smoke

Smoke visualisation is a primary method used for off-the-surface flow visualisation and was firstly used by Ernst Mach in the early 1900's. A.M Lippisch & F.M Brown in 1937 used the smoke visualisation technique in subsonic tunnel research and made important advances in this area which today is the current state-of-the art (Goldstein, 1996). This tool is primarily used in the study of complex dynamic phenomena around models.

It was determined that this method could be used for visualising flow around the model more precisely than the tufts indicated. To generate the necessary smoke trails to flow around the model it was found that the Reynold's number of the airflow had to be reduced in order to create organised smoke streamlines. According to (Azizi & Ginta, 2012) the Reynold's number needs to be under 2000 to minimise flow disturbance for smoke visualisation. To achieve this a flow straightener needed to be placed in the inlet to the wind tunnel to produce steady stream of airflow. A pre-manufactured bank of one inch (25.4mm) copper tubes (figure 6.49) was available which would produce the required Reynold's number for air velocity of 1m/s or less.

Table 6.7 Reynolds's number range (Hand, 2014)

Velocity (m/s)	Re				
1	1575.9		ρ	1.25	$\frac{Kg}{m^3}$
2	3151.79		μ	1.98E-05	Pa.s
3	4727.69		D	0.0254	m

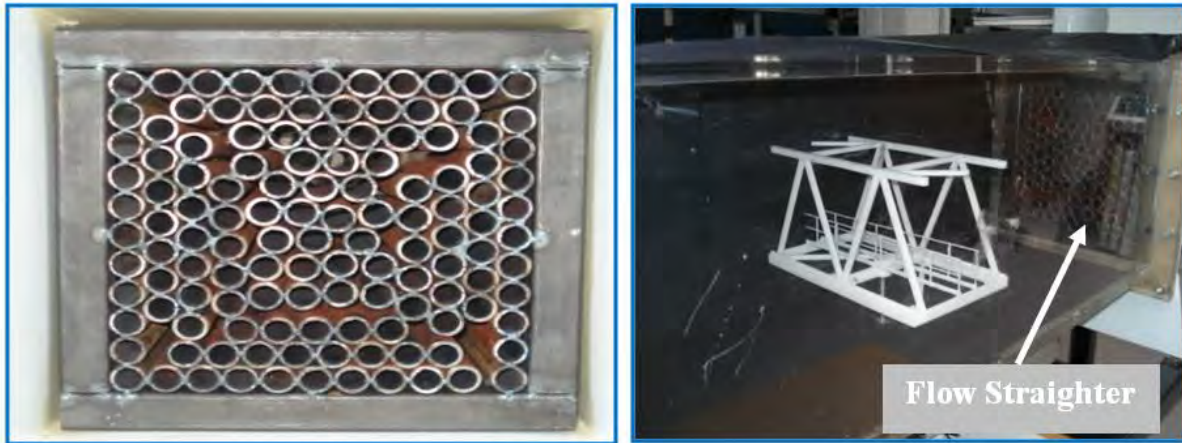


Figure 6.49 Flow straighter at the inlet of wind tunnel (Hand, 2014)

To produce the fine traces of smoke, a standalone smoke generator from Tecquipment was used (figure 6.50) (Specification Appendix D page D-9). This unit consists of a control unit which pumps oil to the tip of a probe and low voltage coil located at the probe tip heats the oil to create fine smoke trails (TecQuipment, 2000). The probe was positioned inside the wind tunnel and was located about 100mm from the closest edge of the model. To aid the optical qualities of the smoke trails, a black matted background was positioned on the floor and sides of the wind tunnel clearly seen in figure 6.51 below.



Figure 6.50 Smoke generator used (Hand, 2014)



Figure 6.51 Model background (Hand, 2014)

To record the smoke visualisation testing on the model a video camera and tripod were set up to record the footage of the smoke flowing around the model and then using slow motion software it was possible to slow the video footage down as low as 10-15 frames per second and examine the airflow over the model. The software used to achieve this was GoPro professional video slow motion editing software.



Figure 6.52 Video Camera (Hand, 2014)

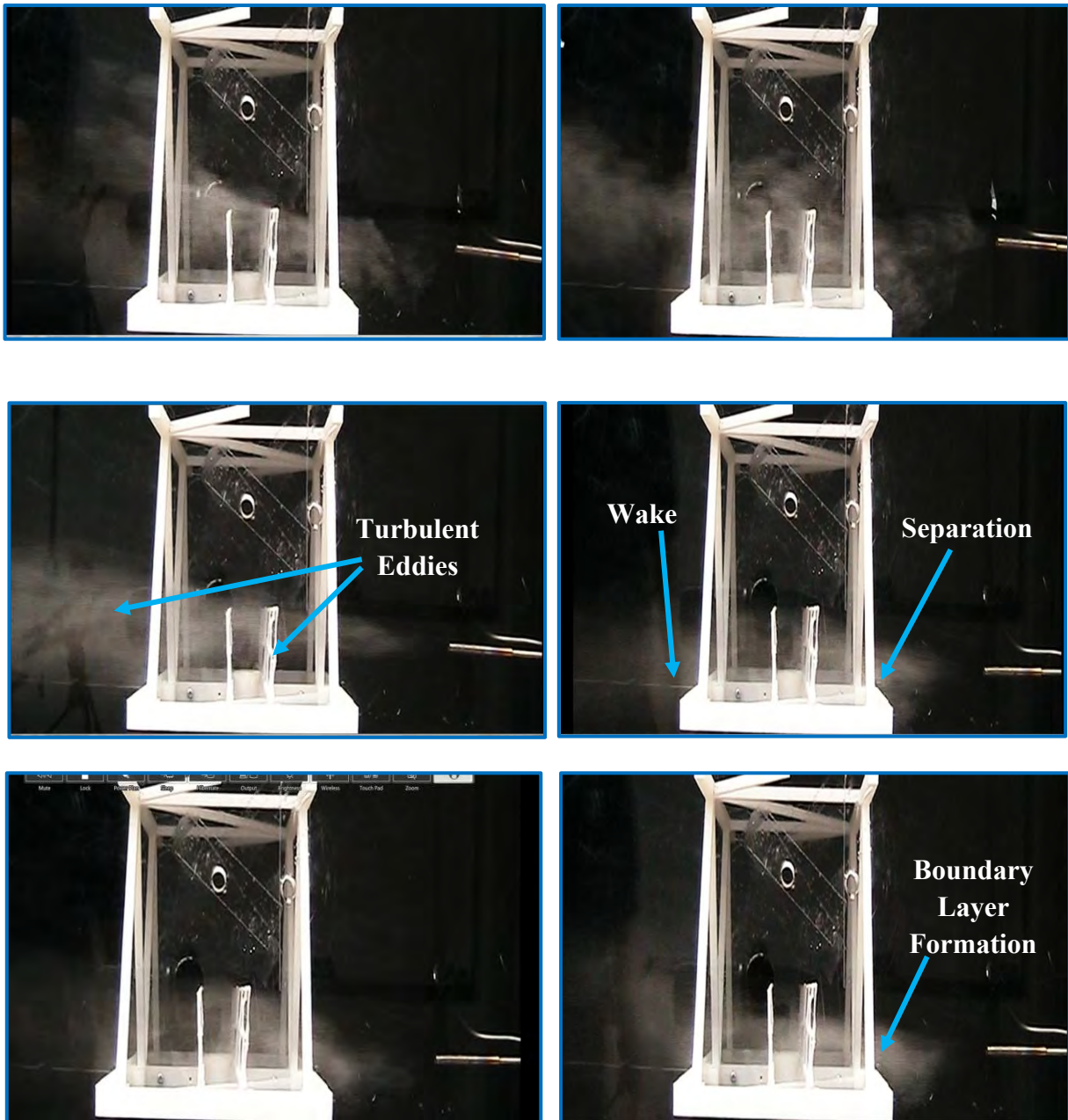


Figure 6.53 Smoke Visualisation on model

The above images show the smoke visualisation that was carried out on the model. Even though many attempts were made to produce accurate smoke streamlines the smoke trails from the probe it kept becoming turbulent and effected by eddies currents. In saying that some of the images above do show the presence of boundary layer and flow separation forming around the bottom section of the beam which is comparable with the CFD contours generated. Also a black and white filter was used to enhanced to visualisation of the smoke trails interacting with the model

6.7 Hazard Analysis for Wind Tunnel Testing

Risk Assessment											
Taken in Accordance with EN ISO 14121-1:2007											
RA #	Action	Hazard	Lo	Fe	DPH	NPR	HRN	Risk	Control	HRN with control	Risk with control
1	Setting up of Equipment	Equipment is set up incorrectly	1	1.5	0.5	1	0.75	Low	Ensure equipment is set up correctly by having a technician supervise and ensure to be fully alert.	0.5	Negligible
2	Electrical Equipment	Faults in electronic equipment, not earthed properly	2	1.5	8	1	24	Significant	Ensure all electronic equipment is operating properly before use and check with supervisor before use	0.5	Negligible
3	Electrical cables on floor	Electrical cables on the floor, major trip hazard	8	2.5	5	1	100	Very High	Ensure cables have shortest distance to socket and keep tidy	8	Low
4	Noise from fan	Excessive noise from fan can cause temporary hearing loss	8	1.5	1	1	12	Significant	Wear ear protection when using the wind tunnel	0.8	Negligible
5	Moving Equipment	Back injury/strain	1	1.5	2	1	3	Low	Ensure objects are moved correctly/ don't overload	0.5	Negligible
7	Smoke testing	Inhalation of Fumes	6	1.5	1.5	1	18	Significant	Use suitable breathing apparatus/ use for short period of time (low concentration)	2	Low
8	Smoke Testing	Turn off fire alarms (fire starts)	0.5	1.5	5	3	11.3	Significant	Have fire extinguishing nearby. Ensure fire alarms are turned back on	0.2	Very Low

6.8 Wind Tunnel Test Results

The testing on the model was conducted three times to ensure the utmost accuracy was guaranteed and possible sources of error could be eliminated. Shown in table 6.8 are the results that were recorded from the testing and mean and standard deviation between the results have been calculated.

Table 6.8 Wind Tunnel Results (*Hand, 2014*)

	Measurement 1	Measurement 2	Measurement 3	Average	Standard Deviation (σ)
Velocity (m/s)	Drag Force (N)				
1.00	0.008	0.034	0.018	0.020	0.013
2.00	0.069	0.102	0.041	0.071	0.031
3.00	0.168	0.208	0.132	0.169	0.038
4.00	0.251	0.333	0.230	0.271	0.054
5.00	0.523	0.449	0.377	0.449	0.073
6.00	0.764	0.724	0.496	0.661	0.144
7.00	0.946	1.018	0.778	0.914	0.123
8.00	1.256	1.283	0.974	1.171	0.171
9.00	1.415	1.580	1.269	1.421	0.155
10.00	1.736	1.970	1.428	1.711	0.272
11.00	2.106	2.099	1.866	2.024	0.137
12.00	2.494	2.354	2.377	2.408	0.075
13.00	2.653	2.515	2.712	2.627	0.101
14.00	3.244	3.026	2.998	3.089	0.135
15.00	3.595	3.308	3.663	3.522	0.188
16.00	4.269	4.046	3.793	4.036	0.238
17.00	4.884	4.272	4.500	4.552	0.310
18.00	5.347	5.116	5.200	5.221	0.117
19.00	5.648	5.116	5.938	5.567	0.417
20.00	5.981	5.955	5.904	5.947	0.039

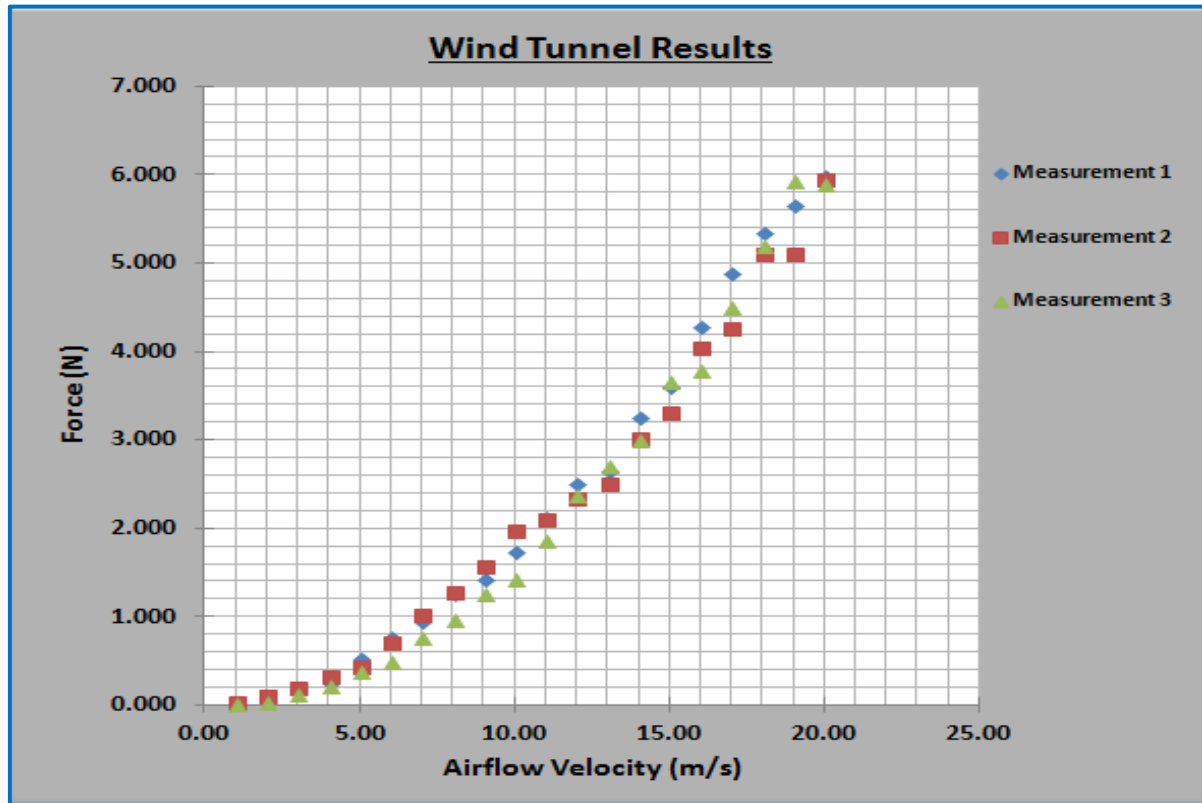


Figure 6.54 Force vs airflow velocity results (Hand, 2014)

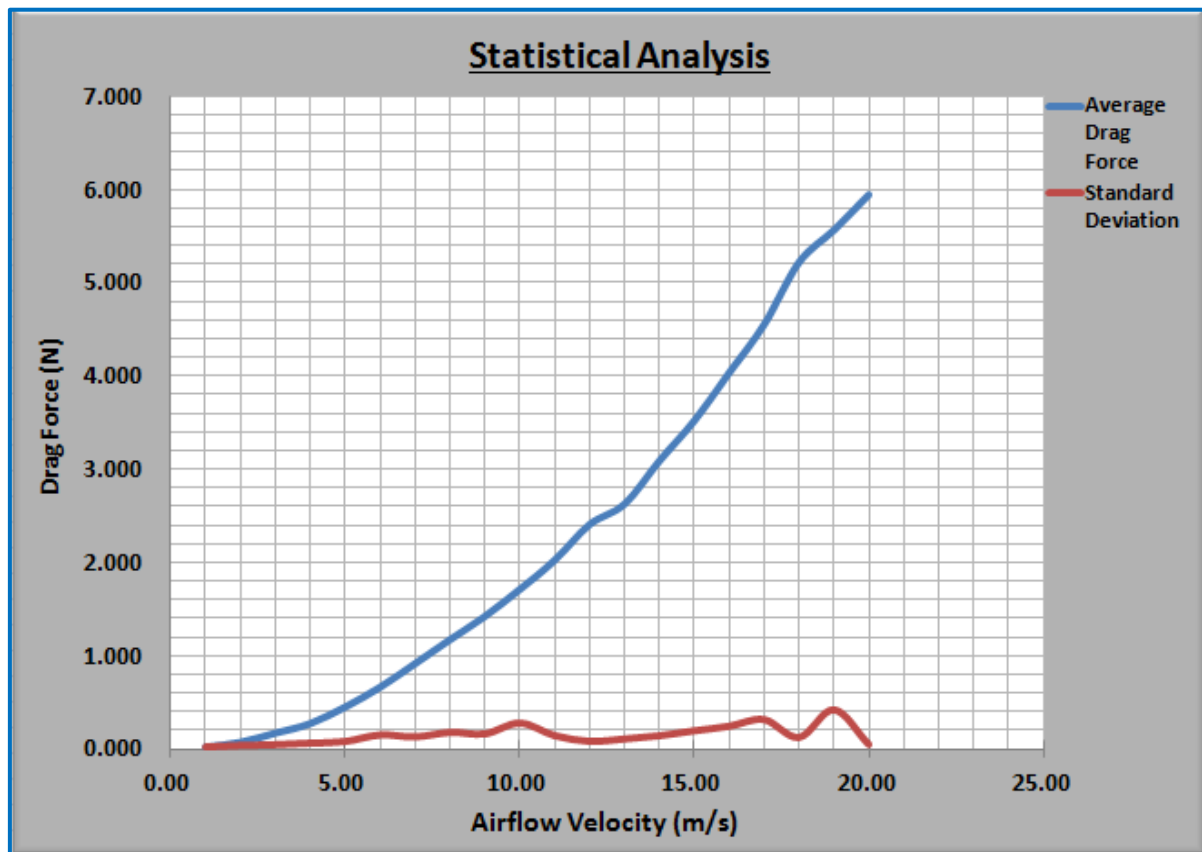


Figure 6.55 Average and standard deviation of the results (Hand, 2014)

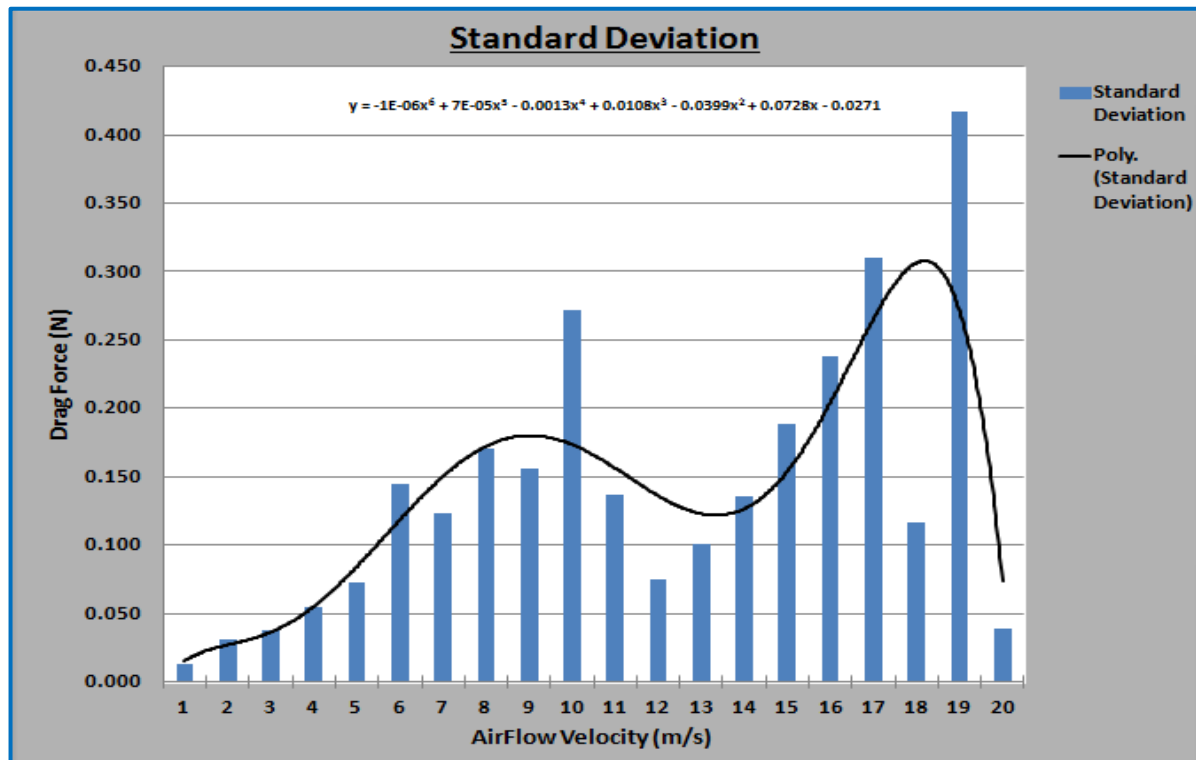


Figure 6.56 Standard deviation of results (Hand, 2014)

Examining the results obtained from the wind tunnel test from the three graphs above it shows there is a considerable amount of deviation between the results especially once the airflow was raised above 12m/s. The main suspected reason for this deviation between the results is error that was accumulated during the testing and post-processing of the results. The inaccuracies incurred during the testing phase is mainly have thought to be related to inefficiencies induced by the equipment and testing systems used rather than human error. In the forthcoming paragraphs the possible error sources during the testing will be elaborated on. Also these wind tunnel results will be compared to results taken from hand calculation and CFD analysis of the model.

An important observation made by the author during the testing was the presence of aeroelastic effects and on the model which were clearly visible at high air velocities on the model. These effects caused vertical oscillation of the model and were thought to be a result of vortex induced vibration.

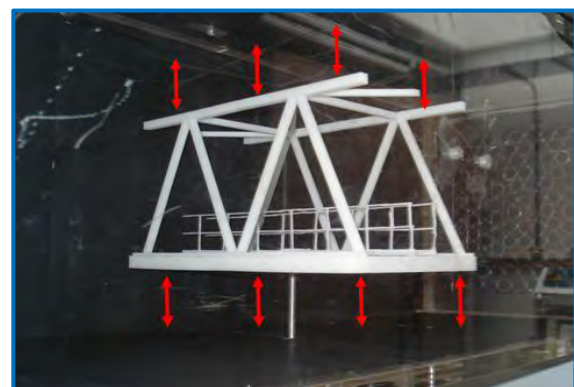


Figure 6.57 Aeroelastic effects were observed (Hand, 2014)

6.9 Experimental Uncertainty

In order to examine how accurate the gathered wind tunnel results are, it is necessary to analyse any uncertainties that could have developed in the wind tunnel test procedure. All experiments are prone to error which if the experiment is carried out accurately can be reduced. The main sources of error in experiments can be separated into three distinct groups systematic, random and human error (Abrahamsen, 2012).

6.9.1 Random Error

Random error in experimental measurements is incurred by changeable and variable nature of experimental testing (UML, 2013). In the case of wind tunnel experiments, random error can be mainly overcome by taking many data points at each testing specification which was done in this study. Taking many data points allows a better representation of the actual response and the analyst can identify inaccurate results basing it on knowledge of the trend in the experiment.

6.9.2 Systematic Error

It is strongly believed by the author that a large percentage of the error acquired in this testing was due to systematic error effects which stem mainly from the equipment that was used during the experiment.

6.9.2.1 Force Balance

From the calibration procedure carried out on the balance it was established that the force balance was difficult and set accurately and was susceptible to linearity error. Figure 6.58 shows a plot of the balance's response to drag force and time for selected velocity ranges. In theory these responses should be constant but it can be seen below there is variability in the balance's response with the unlevel lines being observed.

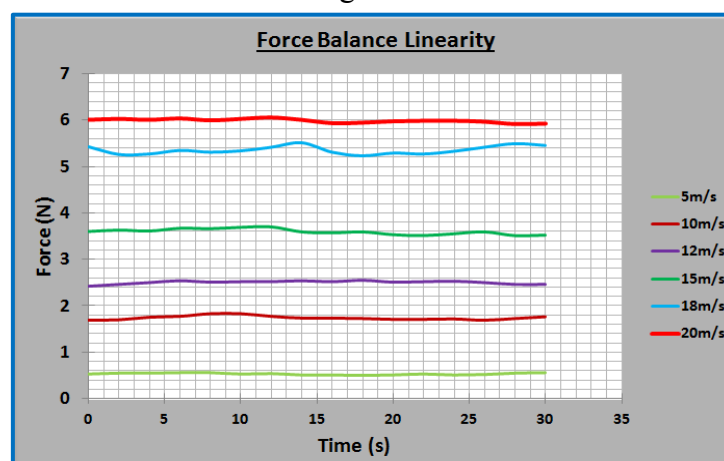


Figure 6.58 Balance error (Hand, 2014)

6.9.2.2 Wind Tunnel

The results obtained from the wind tunnel test show it was near perfect for producing turbulent flow for the model testing. However observed by the author were some events during the testing that may have influenced the quality of the recorded experimental results. It was noticed at high air flow rates through the wind tunnel that the air that exited the wind tunnel was being blown against a masonry wall which caused a high pressure region on the exit of the wind tunnel. This occurrence made reading manometer which read differential pressure a tedious task as its response became less stable with increased velocity and fluctuations in pressure were observed. Ideally the wind tunnel should exit to atmosphere or have a long duct to allow recirculation of the used air.



Figure 6.59 Wind Tunnel exit (*Hand, 2014*)

6.9.2 Human Error

Personal error may have come from biasness in the result taking, recording data or in the calculations. One primary point where human error may have affected the results taken in this testing is that when the wind tunnel velocity had to be changed, this was done based on the judgement of the author from the manometer reading to correlate the pressure difference with the velocity, also the fact that the manometer had imperial units made this a more tedious process. Repeating the test three times would have decreased the overall error in the results while also allowing the easier identification of inaccurate results.

6.10 Use of Wind Tunnel Models and CFD

“Model testing and computer simulations have always been complementary techniques” (Barltrop, 1998). In many cases of examining fluid flow over bodies it is sometimes necessary to complement model tests with analysis of another kind to gain a full understanding of the system performance. Iterative numerical software such as CFD can provide usually greater understanding of parameter variations that is not possible with wind tunnel testing. It has been quoted by many fluid flow specialists that the role of model testing has changed especially in relation to numerical simulation over the past years. Mainly today in experimental procedures, model testing is used as a validation tool and as a means of comparison (Aalbers, 1993). A correct physical model does guarantee complete modelling of the physics that happens during fluid flow although the testing does not explain why certain phenomena happen and can also be influenced by scale effects (Buchner, 1999). It is the use of numerical simulations that can aid the understanding of complex air flow and allow the behaviour to be assessed with different environmental and operating conditions (HSE, 2001). Clearly the next step in this analysis is to use CFD to analyse the scaled model in the same conditions and flow regime as to what was conducted using the wind tunnel test and see how they compare and contrast. “Wind tunnel test are a vital tool in developing and validating CFD codes and methods” (Starcs, 2013).

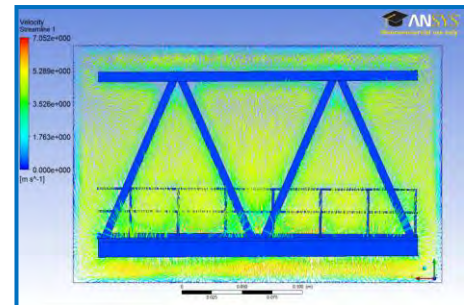


Figure 6.60 Streamlines at exit of model (Hand, 2014)

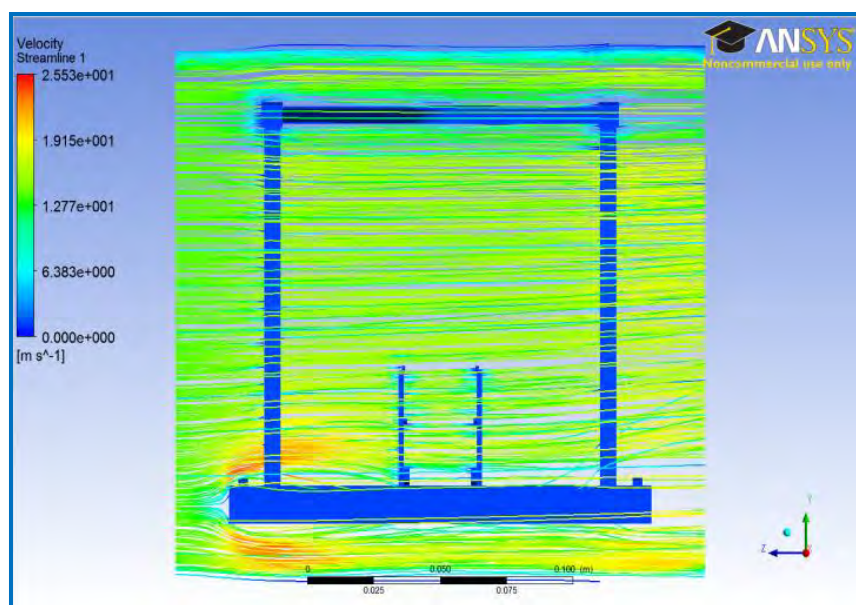


Figure 6.61 Streamlines from side of model (Hand, 2014)

6.11 Model CFD Analysis

Using the scaling capabilities in ANSYS Fluent 14 the full scale model was scaled down to the model size used in the wind tunnel by using a scaling factor of 28. This allowed all the features of the model to be scaled exactly with no distortion and the CFD mesh also. The four grid types used in the full scale analysis were scaled down also; this was done to ensure the results achieved at the model scale were grid independent like the full scale results found at the full scale.

6.11.1 Grid Independence

Table 6.9 Grid Independence study for model (Hand, 2014)

Mesh Relevance	Coarse		Medium		Fine		Enhanced
Grid Elements	119960		180067		402221		489858
Wind Velocity	Drag Force (N)	%	Drag Force (N)	%	Drag Force (N)	%	Drag Force (N)
2	0.103	2.180	0.101	1.076	0.102	0.944	0.100
4	0.405	6.073	0.379	1.404	0.387	0.735	0.382
6	0.853	7.880	0.793	1.548	0.803	0.304	0.791
8	1.474	7.835	1.366	0.885	1.379	0.066	1.367
10	2.277	8.809	2.083	0.936	2.113	0.483	2.093
12	3.240	8.640	2.955	0.570	2.999	0.926	2.982
14	4.360	8.217	3.995	0.421	4.046	0.829	4.029
16	5.684	8.516	5.189	0.515	5.265	0.932	5.238
Overall Percent Difference (%)		7.27		0.92		0.65	

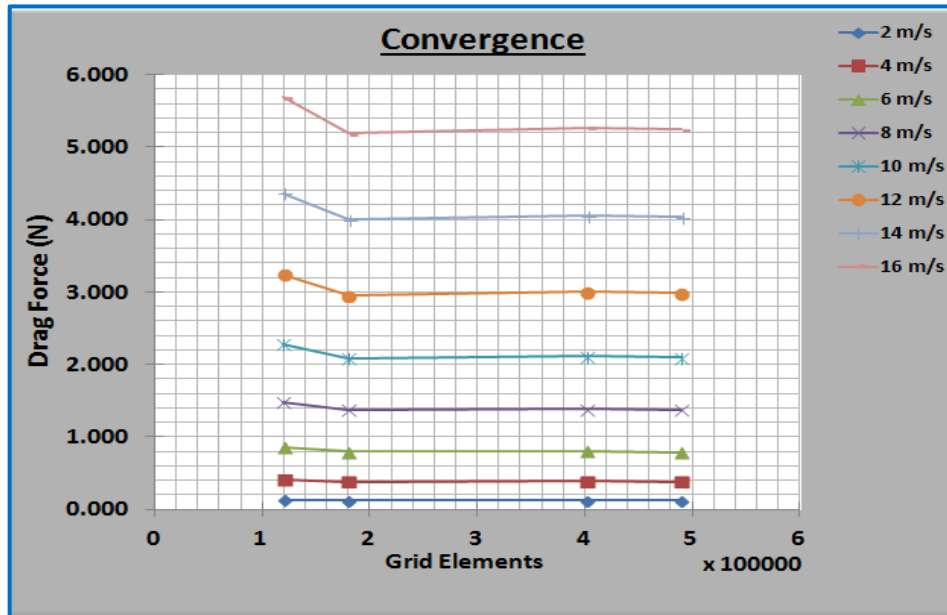


Figure 6.62 Convergence of CFD results for model scale (Hand, 2014)

Achieving converged results for the CFD analysis of the model meant these results were accurate as could be found with using the computational capabilities available. Table 6.10 below shows the primary results obtained from Fluent for drag and lift on the model.

Table 6.10 CFD results for model (Hand, 2014)

Velocity (m/s)	Drag Force (N)	Lift Force (N)	Velocity (m/s)	Drag Force (N)	Lift Force (N)
2	0.100	0.000	10	2.093	0.039
4	0.382	0.001	12	2.982	0.061
6	0.791	0.010	14	4.029	0.091
8	1.367	0.022	16	5.238	0.106

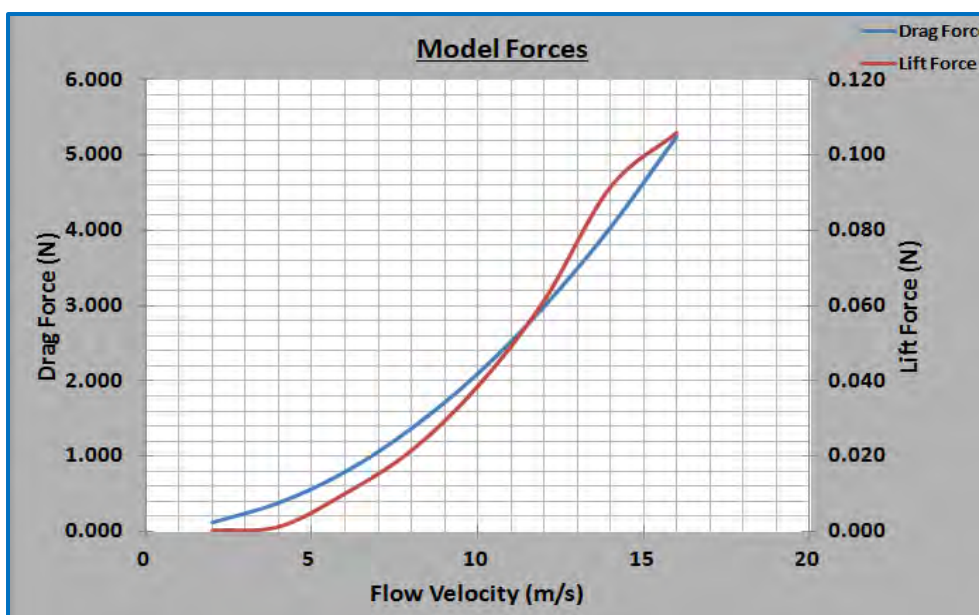


Figure 6.63 Plot CFD predicted drag and lift forces for model (Hand, 2014)

6.11.2 CFD Contour Plots

6.11.2.1 Static Pressure

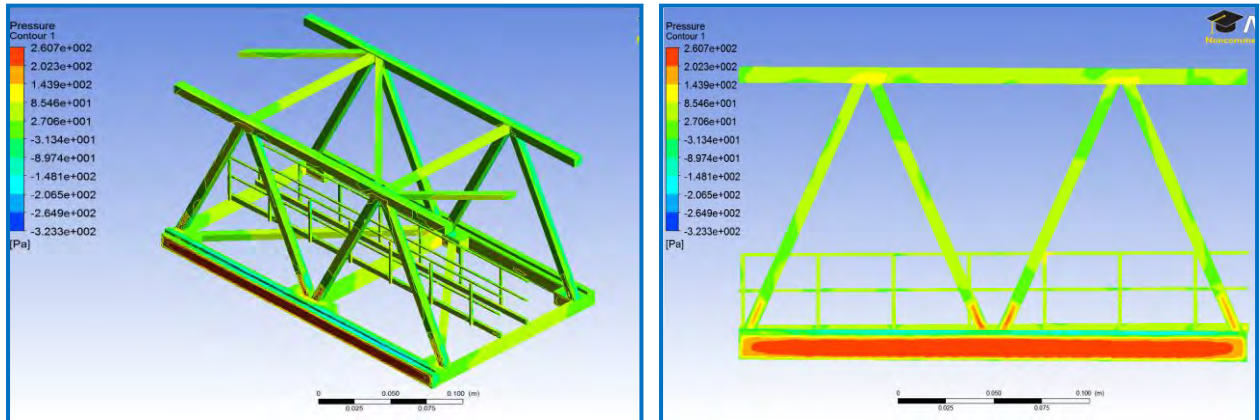


Figure 6.64 Static Pressure on Model (Pa) (Hand, 2014)

6.11.2.2 Turbulent Kinetic Energy

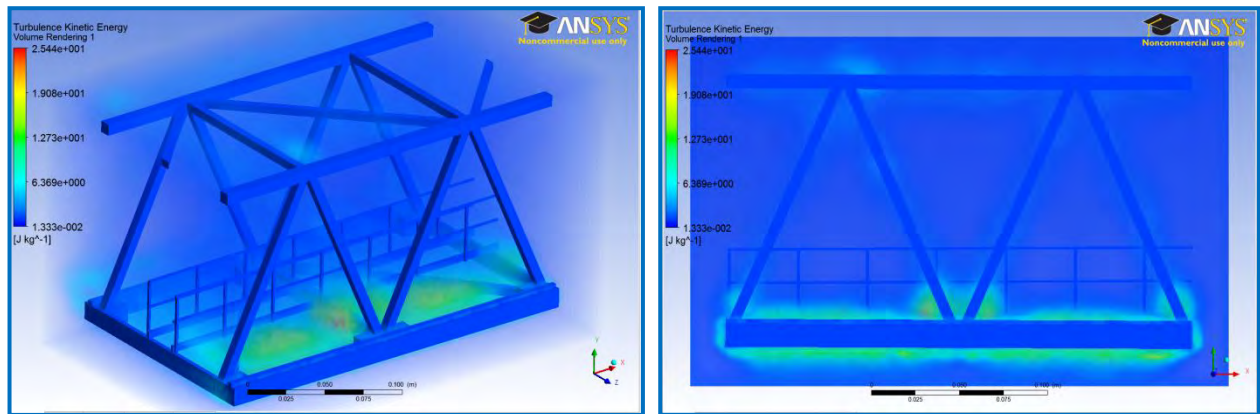


Figure 6.65 Turbulence on model (J/kg) (Hand, 2014)

6.11.2.3 Wall Shear Stress

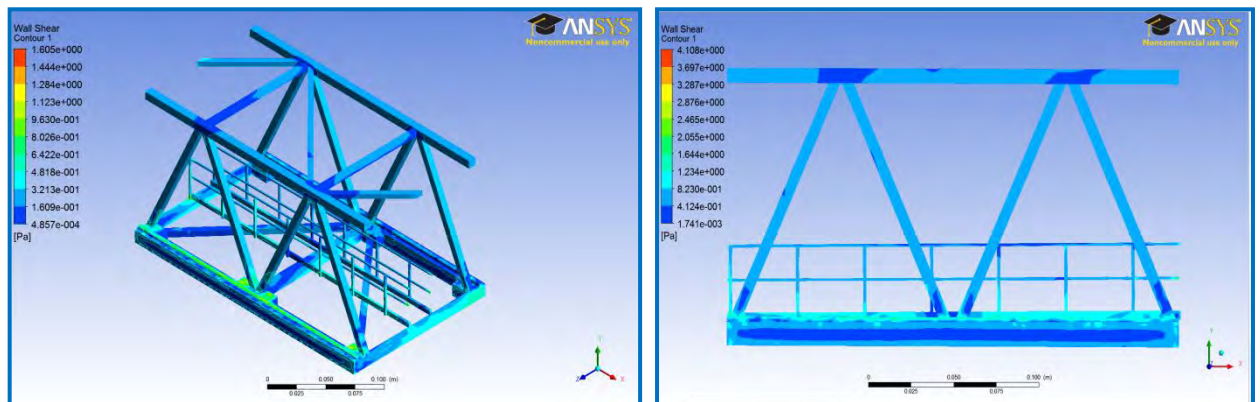


Figure 6.66 Wall shear stress on model (Pa) (Hand, 2014)

6.12 Model Results Comparison

After completing the post-processing of the results from the CFD model analysis it was now possible to compare these results from the experimentally wind tunnel testing and the reference hand calculation (Appendix C page C-25) which are documented below in table 6.11.

Table 6.11 Model Results Comparison (Hand, 2014)

Airflow Velocity (m/s)	CFD Drag (N)	Difference (%)	σ	Wind Tunnel Test (N)	Difference (%)	σ	Hand Calculation (N)
2	0.100	26.904	0.015	0.071	9.898	0.006	0.079
4	0.382	21.079	0.047	0.271	14.023	0.031	0.315
6	0.791	11.476	0.058	0.661	6.810	0.034	0.709
8	1.367	8.407	0.075	1.171	7.130	0.064	1.261
10	2.093	6.230	0.087	1.711	13.156	0.183	1.970
12	2.982	5.119	0.103	2.408	15.125	0.303	2.837
14	4.029	4.329	0.118	3.089	20.007	0.546	3.862
16	5.238	3.849	0.137	4.036	19.981	0.713	5.044
Average		10.924%	0.080N		13.266%	0.235N	

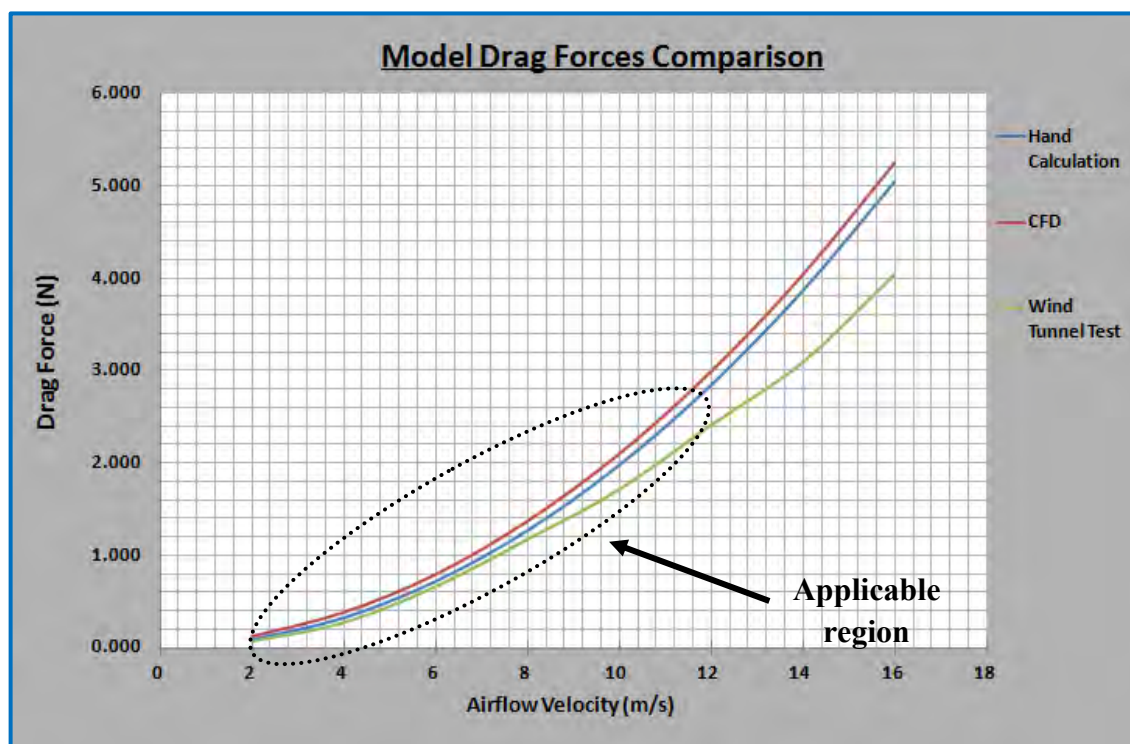


Figure 6.67 Plot of drag force on model for three techniques (Hand, 2014)

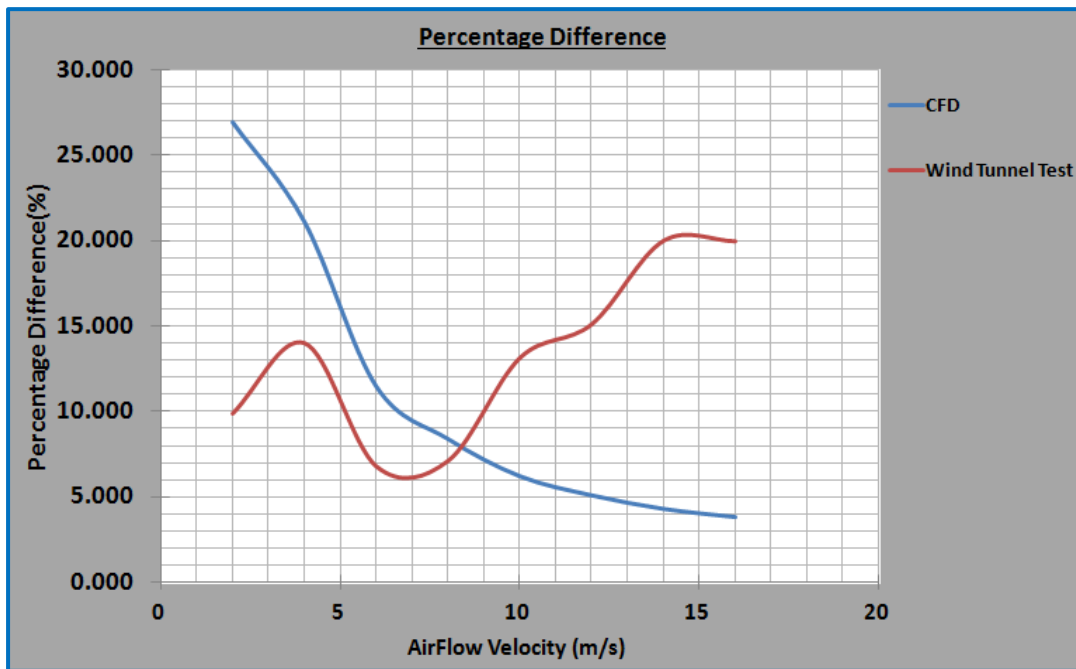


Figure 6.68 Percentage difference between hand calculation, CFD and wind tunnel results (Hand, 2014)

Figure 6.68 above shows the percentage difference between the hand calculation and the CFD and wind tunnel model results. There is a rapid decrease in the difference noted for the CFD results while the wind tunnel results stay quite uniform but show increasing percentage difference with higher velocities. The standard deviation for the wind tunnel results is considerable when observed in figure 6.69 below in relation to the CFD results. It is clear that a large amount of this deviation occurred when the airflow was increased above 12m/s and the author believes this is when the systematic error from the wind tunnel set-up mainly had an influence as previously noted in this report.

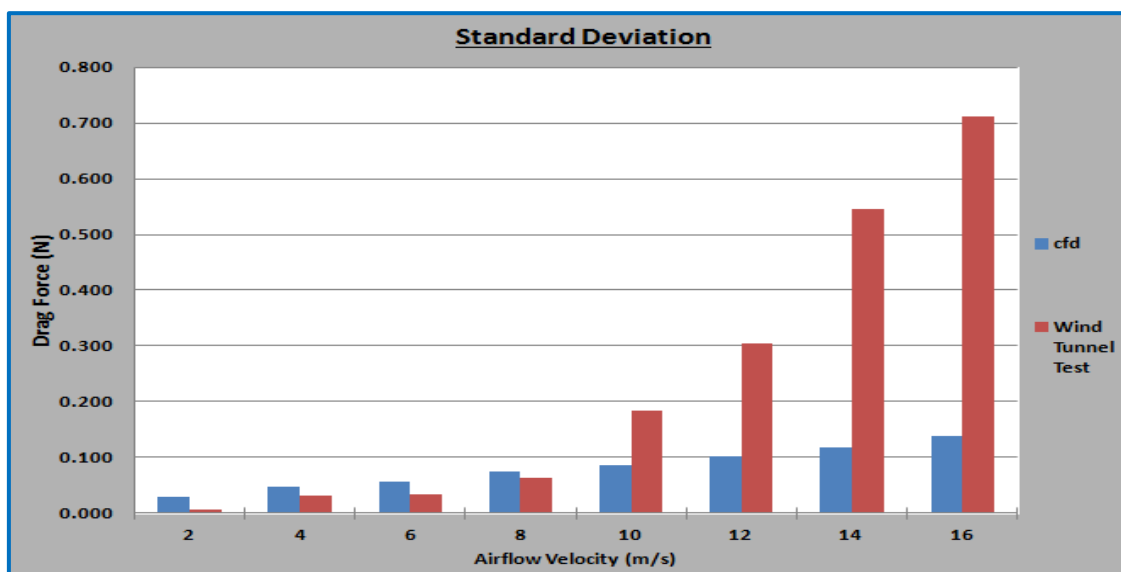


Figure 6.69 Standard deviation of results with respect to the hand calculations (Hand, 2014)

6.12.1 Results Scaling

Using Froude scaling analogy that will be used to scale these results up to the full scale only a selection of the generated data will be utilised. Figure 6.67 shows a contour band of the data that will be used, the main advantage of this that this data shows a very good correlation with each other and it is believed that systematic errors in experiment had a low influence as these results were carried out at low air velocities. The sample calculations below show the Froude technique using equations [6.20] & [6.21] in scaling the first wind tunnel test data point.

Velocity:

Note: $\lambda = 28$

$$\text{Scale factor } \lambda^{\frac{1}{2}} \qquad V_p = \lambda^{\frac{1}{2}} V_m \qquad [6.20]$$

$$V_p = (28)^{\frac{1}{2}} (2 \text{ m/s})$$

$$V_p = \underline{10.583 \text{ m/s}}$$

Force:

$$\text{Scale factor } \lambda^3 \qquad F_p = \lambda^3 F_m \qquad [6.21]$$

$$F_p = (28)^3 (0.071 \text{ N})$$

$$F_p = \underline{1,558.59 \text{ N}}$$

Using this technique both the scaled model results for the wind tunnel test and the CFD analysis were scaled up to the full prototype scale as shown in table 6.12 Therefore by doing this it is possible to compare the results with full scale CFD model which were determined earlier in this report and also compare with the standard calculations which are currently utilised (FEM 1.004).

Table 6.12 Scaled up model to full scale results (Hand, 2014)

V_m (m/s)	V_p (m/s)	F_m (CFD) (N)	F_p (CFD) (N)	F_m (Wind Tunnel Test) (N)	F_p (Wind Tunnel Test) (N)
2	10.58	0.100	2195.20	0.071	1558.59
4	21.17	0.382	8377.76	0.271	5948.99
6	31.75	0.791	17357.45	0.661	14510.27
8	42.33	1.367	30006.19	1.171	25705.79
10	52.92	2.093	45944.22	1.711	37559.87
12	63.50	2.982	65468.11	2.408	52860.42

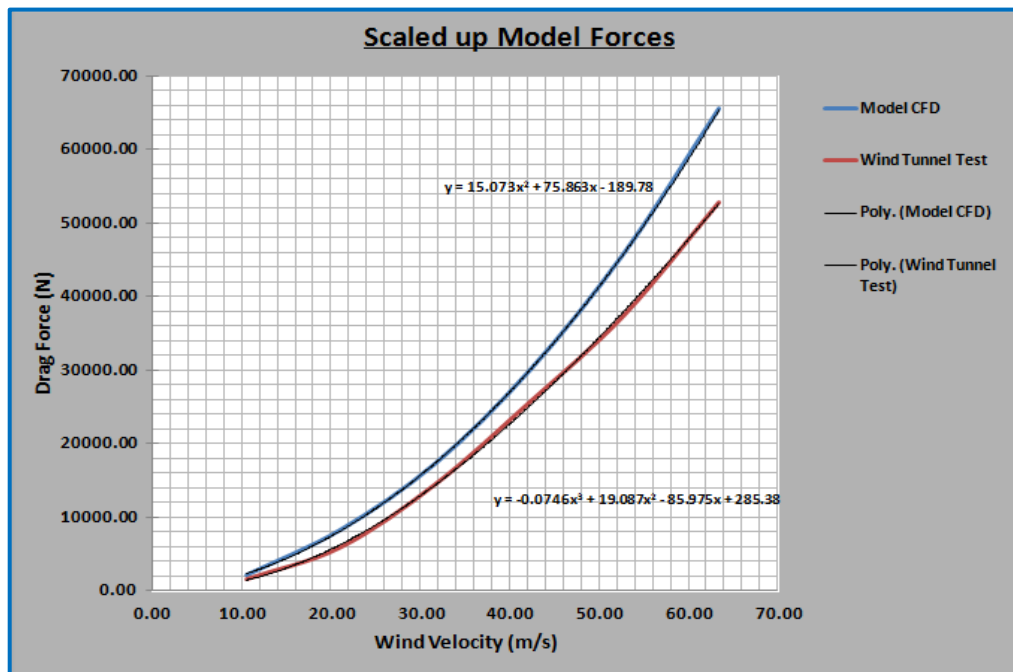


Figure 6.70 Plot of scaled up model results (Hand, 2014)

To allow the model results to be compared with the full scale generated results it was necessary to use curve fitting and extrapolation techniques to establish the drag force at defined intervals which could allow comparison with the full scale results. This was achieved by using the standard curve fitting techniques in MS Excel which it was that found a second order polynomial equation curved fitted the CFD model results very well, whereas the wind tunnel test results required a third order polynomial equation was necessary.

Which are both shown below in [6.22] and [6.23].

CFD
$$y = 15.073x^2 + 75.863x - 189.78 \quad [6.22]$$

Wind Tunnel Test
$$y = -0.0746x^3 + 19.087x^2 - 85.975x + 285.38 \quad [6.23]$$

6.13 Full Scale Results

Table 6.13 Full Scale results comparison (Hand, 2014)

Velocity (m/s)	CFD (Scaled up Model) (N)	CFD (Full Scale) (N)	Wind Tunnel Test (N)	Hand Calculation (N)
5	566.36	398.40	323.355	386.16
10	2076.15	1481.60	1259.73	1544.66
20	7356.68	5795.00	5603.88	6178.63
30	15651.81	12957.30	12870.23	13901.92
40	26961.54	22931.60	22611.18	24714.53
50	41285.87	35831.20	34379.13	38616.45
60	58624.8	51531.20	47726.48	55607.68

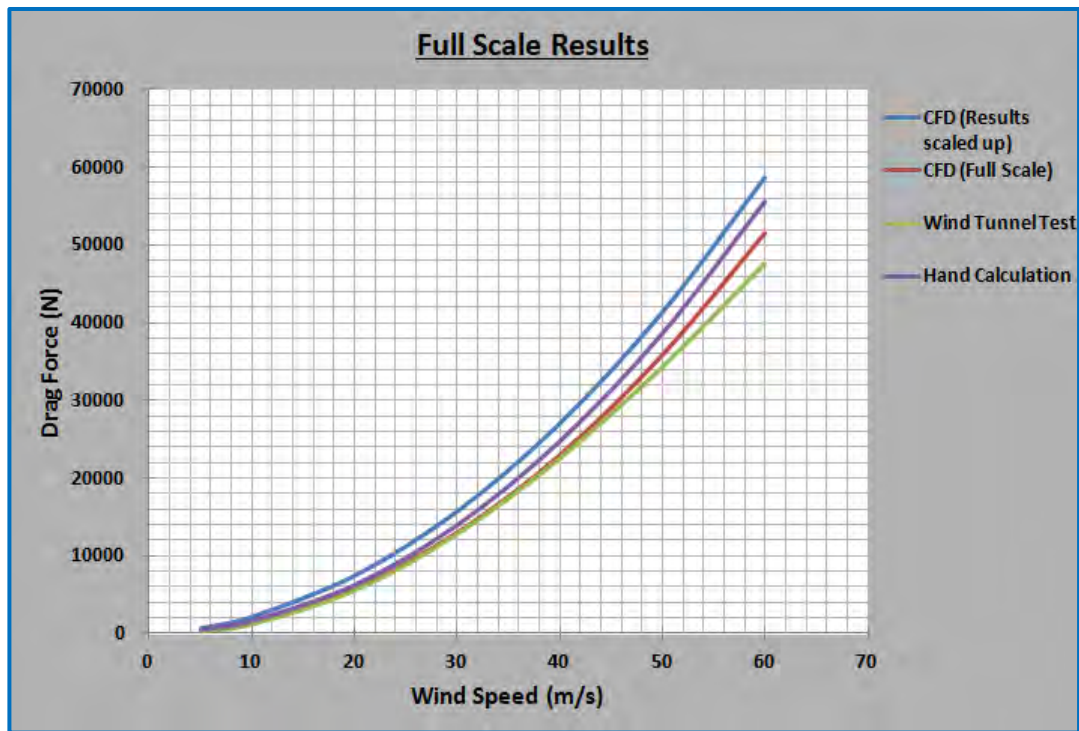


Figure 6.71 Full scale results (Hand, 2014)

The results in figure 6.71 show a good correlation with each other, it is clear the curves are not ideally rising at the same slope but the general trend in the curves are very similar. It is necessary to do a statistical analysis of these results and examine parameters such as percentage difference and standard deviation in relation to the hand calculation method.

Table 6.14 Statistical Analysis of results (Hand, 2014)

Velocity	CFD (Scaled up Model)		CFD (Full Scale)		Wind Tunnel Test	
	Difference (%)	σ (N)	Difference (%)	σ (N)	Difference (%)	σ (N)
5	46.66	127.42	3.17	8.65	16.26	44.41
10	34.41	375.82	4.08	44.59	18.45	201.47
20	19.07	833.01	6.21	271.27	9.30	406.41
30	12.59	1237.36	6.79	667.95	7.42	729.52
40	9.09	1588.88	7.21	1260.72	8.51	1487.29
50	6.91	1887.57	7.21	1969.47	10.97	2996.23
60	5.43	2133.42	7.33	2882.51	14.17	5572.85
Overall Average	19.17%	1169.07	6.00%	1015.02	12.16%	1634.03

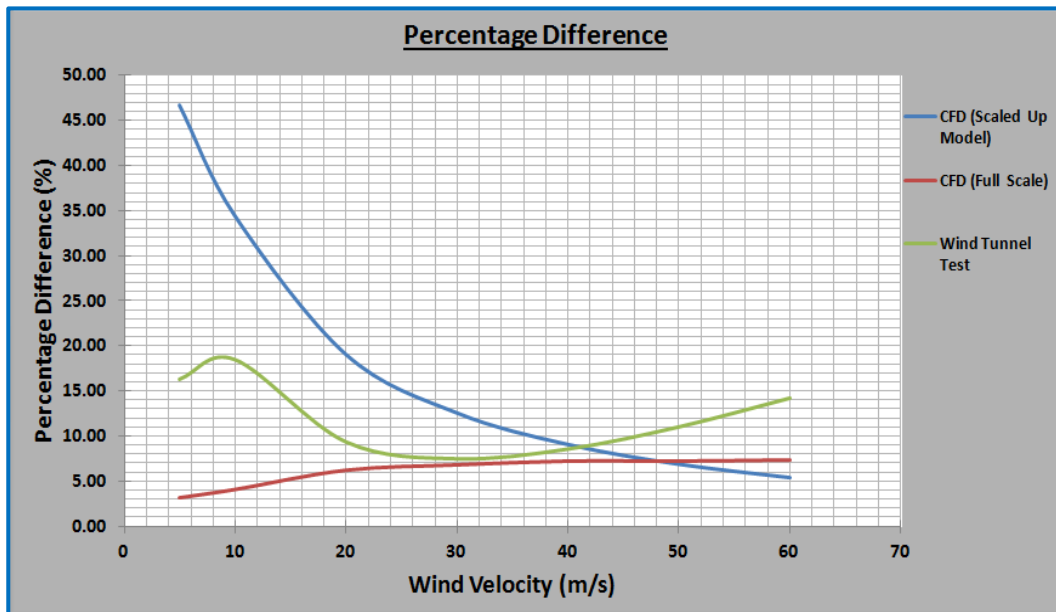


Figure 6.72 Percentage difference between results (Hand, 2014)

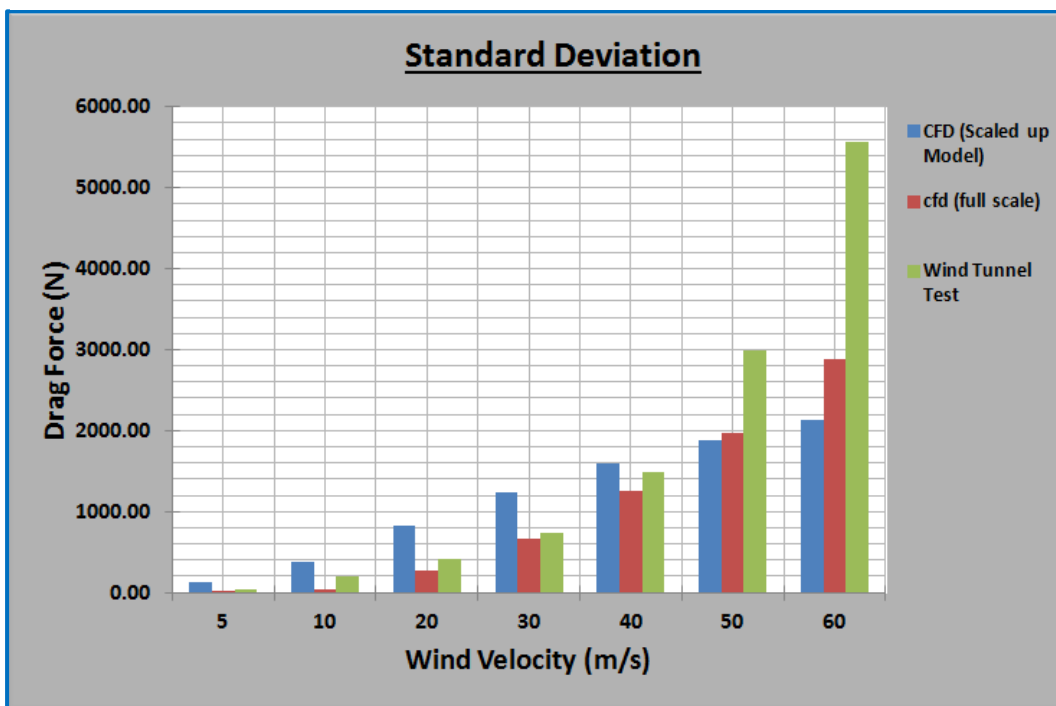


Figure 6.73 Standard Deviation for results (Hand, 2014)

In relation to the hand calculation method the results do show a significant amount of difference and deviation which is to be expected in an analysis such as this. It is largely noted that the scaled up CFD results have a significant amount of difference compared with the other two results. It is also observed there is an almost constant deviation for the results especially in the case of the wind tunnel results which becomes significant at higher speeds. These wind tunnel results deviations may have been induced by errors due the wind tunnel

set-up as already stated in this report. Also since two of these methods are scaled up from the model scale it is important to consider the presence of scale effects.

6.13.1 Scaling Effects

Scale effects can be described as the “*deviations between the model and prototype results are due to scale and model*” (Burcharth & Lykke, 2012). Scale effects arise due to the incorrect replication of ratios between forces in the model testing which can result “*in deviations between the up-scaled model and prototype observations*” (Heller, 2012). In a number of journals written by Dr Valentin Heller, a principal investigator in the Fluid Mechanics Department at the Imperial College London described scale effects as being “*complex, dependent on the involved forces and their relative importance changing from phenomenon to phenomenon*” (Heller, 2012). Dr Heller makes some important points in relation to scaling which are applicable to this study. Generally the larger the scale factor (λ) the greater the scale effects will be which is evident in this in terms of the force scaling. Force was scaled according to Froude’s Law which specifies (λ^3), this means model forces were increased by (28^3) which realistically means the utmost accuracy is required for the model forces as third and even fourth decimal places come into impact the results significantly. Dr Heller also identifies that scale effects usually do have damping effects associated with them which would not be present in the full scale. The author believes the discrepancies between the results shown clearly in figure 6.67 are a function of scale effects and any errors or inaccuracies that were accumulated during computational, test and analysis phases of this analysis.

The next appropriate point in this analysis is to determine how useful these generated results are in relation to designer/analyst examining the wind force developed on the crane structure. Generally in analytical terms the designer or analyst will mainly focus on the drag coefficient for the structure section and ultimately determine the wind force generated, so the need for accurate drag coefficients is key. Below in table 6.15 shows the calculated drag coefficients for the three methods that were utilised used in this analysis. Currently a drag coefficient of 1.7 is used (Liebherr, 2013) for this boom section from design standards of unknown accuracy or suitability for its geometry. In comparison to this now wind tunnel testing and CFD analysis have provided different C_D values for this geometry. CFD analysis of the full scale and wind tunnel test results have shown this result to be lower than what is currently used with wind tunnel results estimating the C_D to be around 1.49 and the CFD analysis

showing it to be around 1.61. The CFD analysis at the model scale does predict C_D to be higher than what is currently used, but the author deems from his judgement that these results were highly influenced by scale effects and were predicted to be higher than what is actually the case which be seen from the statistically analysis conducted. The fact that the wind tunnel C_D value is very close the computed C_D means these results have been appropriated validated to a satisfying degree.

Table 6.15 Different C_D values (Hand, 2014)

Wind Velocity (m/s)	CFD Model (Scaled up model) (C_D)	CFD (Full Scale) (C_D)	Wind Tunnel Test (C_D)	Hand Calculation (C_D)
5	2.49	1.75	1.42	1.70
10	2.28	1.63	1.39	1.70
20	2.02	1.59	1.54	1.70
30	1.91	1.58	1.57	1.70
40	1.85	1.58	1.56	1.70
50	1.82	1.58	1.51	1.70
60	1.79	1.58	1.46	1.70
Average	2.03	1.61	1.49	1.70

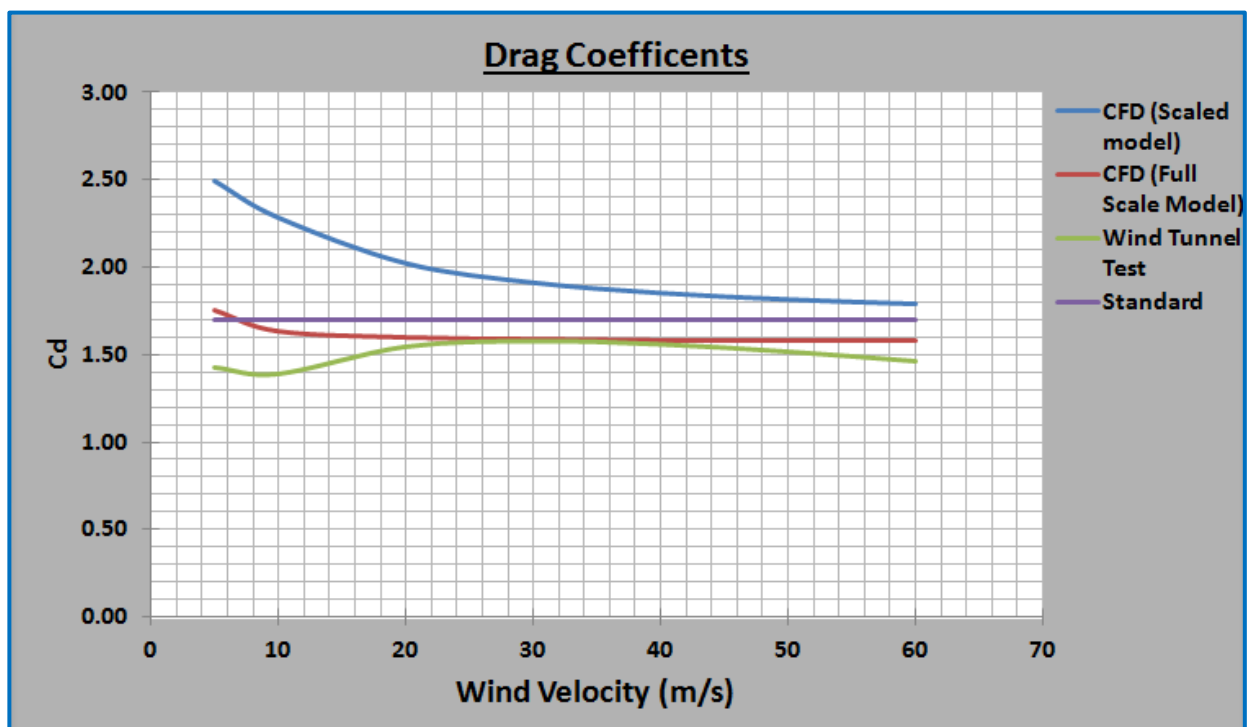


Figure 6.74 Drag Coefficients (Hand, 2014)

6.14 Benefits of this Approach

There are many advantages to be gained from a reduction of C_D values on the crane structure, as can be seen in the graph figure 6.74 above that a reduced C_D means the calculated or estimated wind force will be less than what actually occurs on this boom section which means a more efficient design can be generated from these results. The lower C_D value predicted for the boom section of the crane can be applied to the entire length of the boom and when applied will significantly reduce the force than that what was previously used. Achieving lower force values also has benefits to designer including optimal use of material and better control of factor of safety values applied to the structure. This is also advantageous to the overall the weight of the cranes, which is becoming a concern for designers of the foundations of quays and the supporting structure at the base of the cranes as these cranes continue to increase in size.

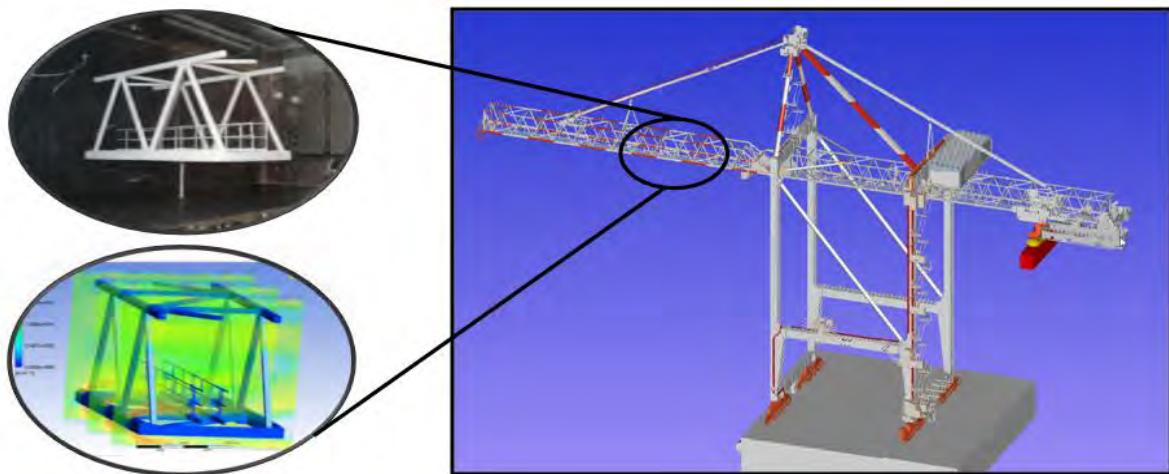


Figure 6.75 CFD and wind tunnel results have predicted lower C_D values (Hand,2014)

Optimising the C_D values for the various structural components of the crane would reduce the overall force on the base of the crane and allow for a better understanding of the forces acting the crane due to wind induced loading. From the analysis and testing carried out it is clear that the use of CFD is pivotal in this analysis and would be the most appropriate means of determining accurate wind forces on separate parts of the crane. It was found from this study that CFD is a fully capable tool of doing this analysis as it was fully validated in this analysis. Unfortunately due to computational resources and project scope calculating the overall wind force on the crane was not feasible. Integrating the use of CFD software analysis into Liebherr's current design programme would offer significant advantages and could be used as a tool to supplement the current wind flow calculations carried out. From this analysis it has been shown how powerful this analysis software could be for the design of container cranes.

7.0 Design Optimisation

7.1 Introduction

As elaborated in chapter 3 of this report excessive wind induced loading on container cranes can have many damaging and potential catastrophic effects with even collapse in some cases. It was determined from the literature research that one of the cranes' primary components of the crane storm anchor system, the tie-down system is greatly influenced by fluctuating and dynamic wind loads and in some cases failure of this component has occurred. Tie-downs are the devices fitted to the bottom sides of the crane structure at each corner. The purpose of these devices is to prevent the up lift forces of the crane during storms and strong winds because the crane can be lifted off its rail.



Figure 7.0 Current Tie down system (Hand, 2013)



Figure 7.1 Failure of tie-down system (Liftech, 2009)

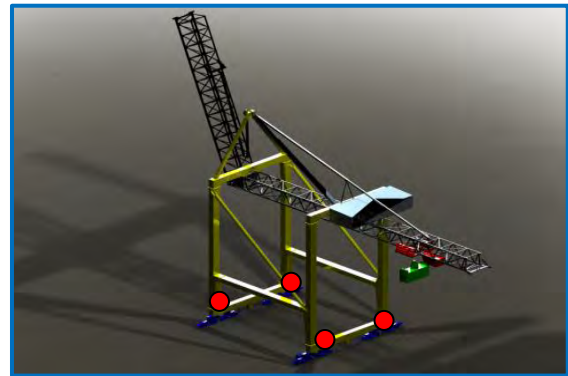


Figure 7.2 Location of tie-down anchors (Hand, 2014)

The tie-down system has two pin connections, where the first pin is connected to the crane structure at a predefined location and the second pin is connected a wharf connection on the quay interface. The tie down is then manually tightened using a turnbuckle mechanism located at the centre of the device as shown in figure 7.3. During the crane's normal operation these tie downs are not connected, but when the wind rises to unsafe working levels, these tie downs are connected to ensure the stability of the crane. In discussion with Liebherr about the operation of this



Figure 7.3 Tie down pin locations (Liebherr, 2013)

component it was found that it can be difficult to set equal tension force on two tie-downs located on the sides of cranes and it was also established from the literature review that the slightest difference in lengths of the two tie-downs can effect greatly the distribution of the load carried by these mechanisms (Lee, 2004). (Lee, 2004) noted that failure was induced by unequal loading of this system at a percentage of the design load of the system. Also a study carried out by insurance and risk related management services provider TT Club found that from over two thousand insured firms, including over four hundred ports globally that 34% of asset claims were associated to incidents involving container cranes and made recommendations for better safety of operations of these container cranes (TT-Club, 2011). It was therefore decided a redesign of this critical component was necessary to ensure the utmost safety and best working practise were upheld when using this device.

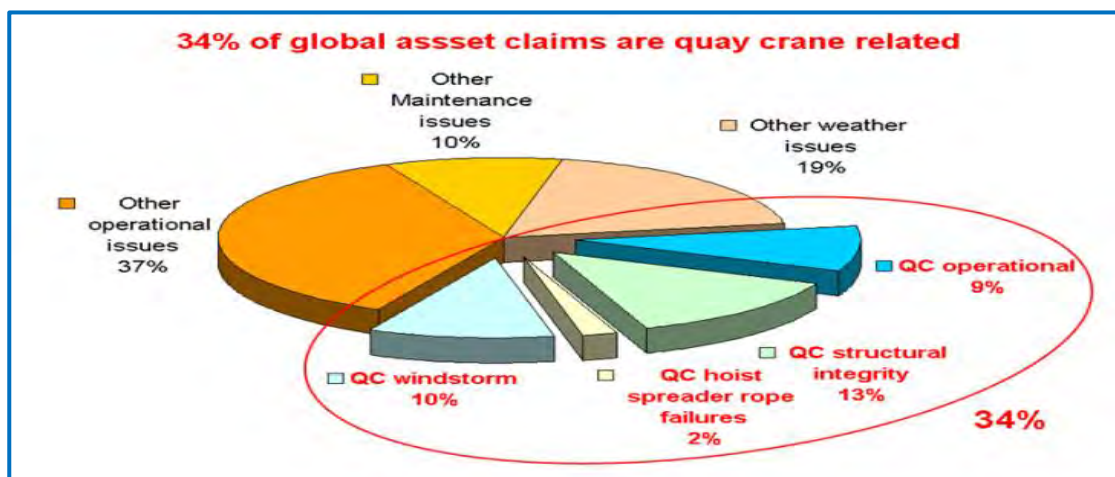


Figure 7.4 Global asset related claims in ports globally (TT-Club,2011)

7.2 Design

The following design criteria were established for the redesign of this tie-down system.

Safe

- Must be easily used without any risk of injury to user.
- Must have safety features fitted where appropriate e.g. guards, warning stickers.
- Must have correct grounding of any electronic components.

Function

- Must equally distribute tensile force when in use.
- Easily used with minimal human effort e.g. mechanical advantage.
- Allows means of communicating with user the tensile force and accurate positioning.

- Must stay vertical during operation.

Cost

- Ensure materials are cost effective and provide best Cost: Strength ratio.
- Intelligent use of material and minimise waste.
- Relatively inexpensive to manufacture and including processes used.

Performance

- Must resist impacts during use.
- Must resist deformations.
- Must operate in all weather conditions especially in salt laden atmospheres.
- Must cope with repeated use.
- Adequate lubrication system.

7.2.1 Establishing Functions

The overall function of this tie-down system is to ensure the container crane stays stationary during high wind and does not overturn; this can be considered the “black box” function. As many other mechanical systems there are sub functions which have to be carried out to achieve the overall function.

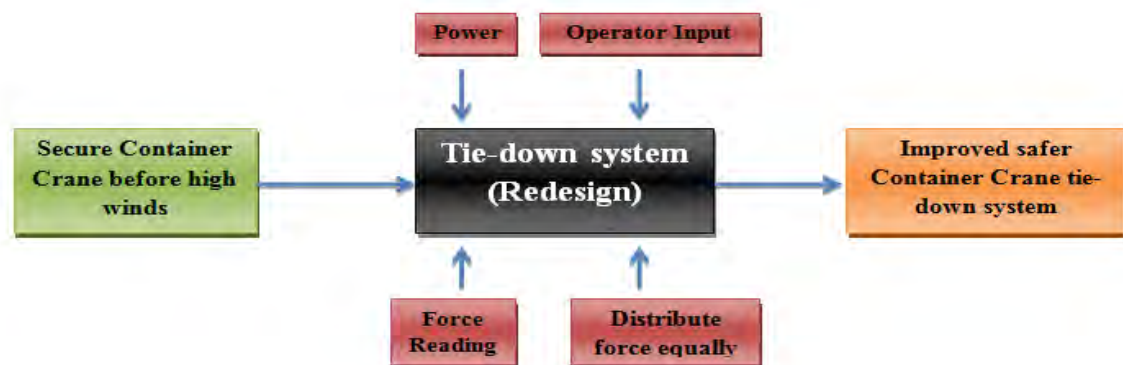


Figure 7.5 Inputs & Outputs (Hand, 2013)

7.2.1.1 Sub Functions

Predefined tension: A mechanical system will be put in place which will allow the user to set the tension accurately when using the crane tie-downs. This system will give a feedback to user to allow for precision measurement.

Equal Forces: A current design restriction with the current tie-down design is that they do not facilitate the movement of the crane during winds and therefore an integrated equaliser system would greatly improve the system's performance.

7.2.2 Setting Requirements

Table 7.0 Design Requirements (Hand, 2013)

Problem Statement: Tie-down system redesign		
#	Demand/Wish (D) / (W)	<u>Requirements</u>
Performance Requirements		
1	D	Must exert correct tensile force
2	D	Must resist deformation
3	D	Must have accurate tightening system
4	W	Must be light weight
5	W	Portable
6	W	Long service life (20 years)
7	D	Operate in all weather conditions
8	D	Must be corrosive resistant
9	D	Easily maintained (lubrication)
10	D	Must give indicated tension exerted
11	W	Easily operated
12	W	Low centre of gravity
13	D	Integrated system to allow equalizing of tensile forces
14	D	Easily adjusted for different situations
15	W	Interchangeable parts
16	D	Adequate safety features
Manufacturing Requirements		
17	D	High quality components & materials
18	D	Efficient production time
19	D	Relatively Inexpensive
20	W	Production using CNC
21	W	Minimise waste
22	W	Reduce complexity in manufacture

7.2.3 Possible Designs

7.2.3.1 Design 1

The first possible design consists of an equaliser beam coupled with turn buckles mechanisms positioned on both sides which are attached to the ends of the equaliser beam through the use of pin connections. The equaliser beam ensures the tie-down mechanisms stay vertical during operation. Each of the tie-down mechanism has an integrated mechanism which allows the connection of a wrench or a torque wrench to correctly torque each of the tie-downs during the halting procedure on the container crane. The height of the tie-down is adjusted by the use of a screw thread which can be adjusted.

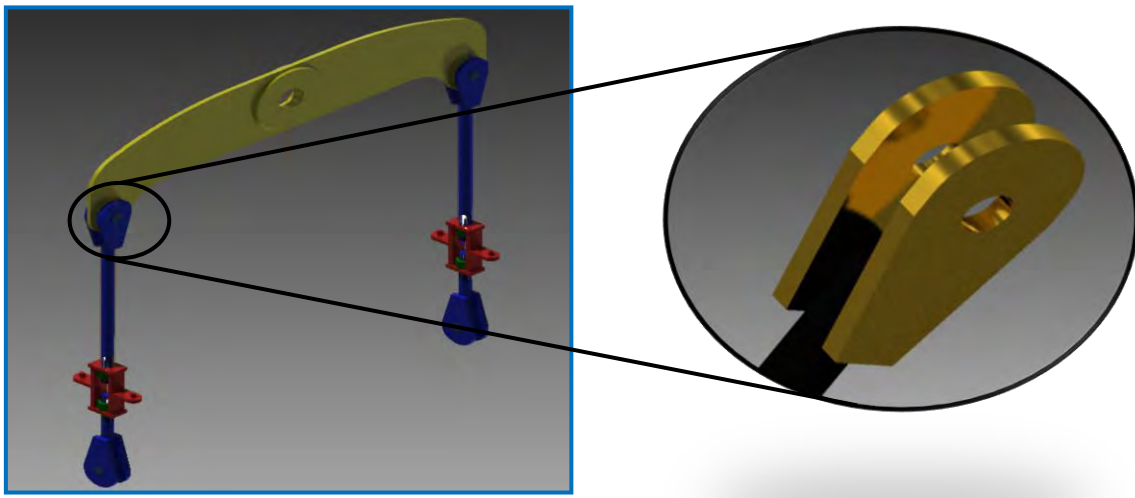


Figure 7.6 Design 1 (Hand, 2014)

7.2.3.2 Design 2

The second possible design uses primary plates instead of shafts to be manufactured. It is adjustable by the movement of one of the slider plates and a U bolt can be placed at separate intervals to accurately correct its height.

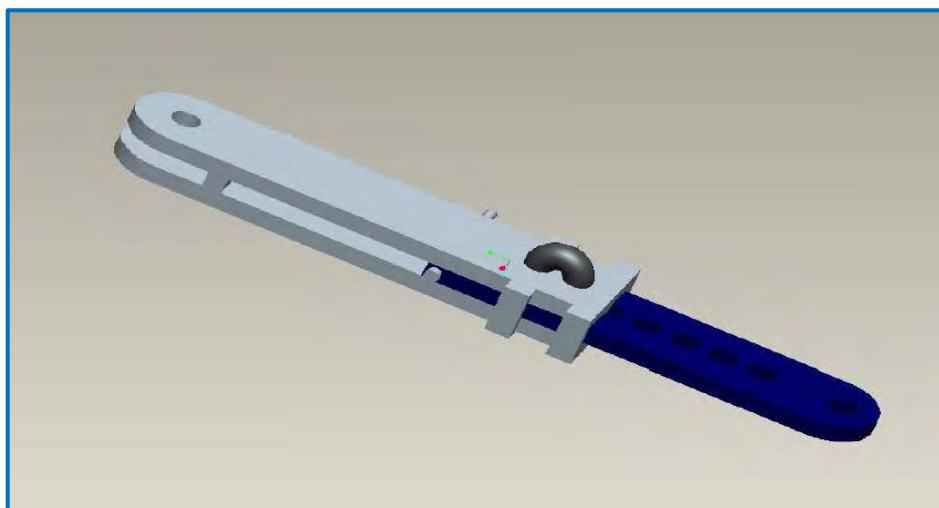


Figure 7.7 Design 2 (Hand, 2014)

7.2.3.3 Design 3

The third possible design uses a circular shaft and sleeve to connect to the crane structure and the quay structure. This design is adjustable by the use of separated slots which can change the height depending on the space increments needed. This design largely depends on the strength of the bolts in tension across their cross section which may be an issue.

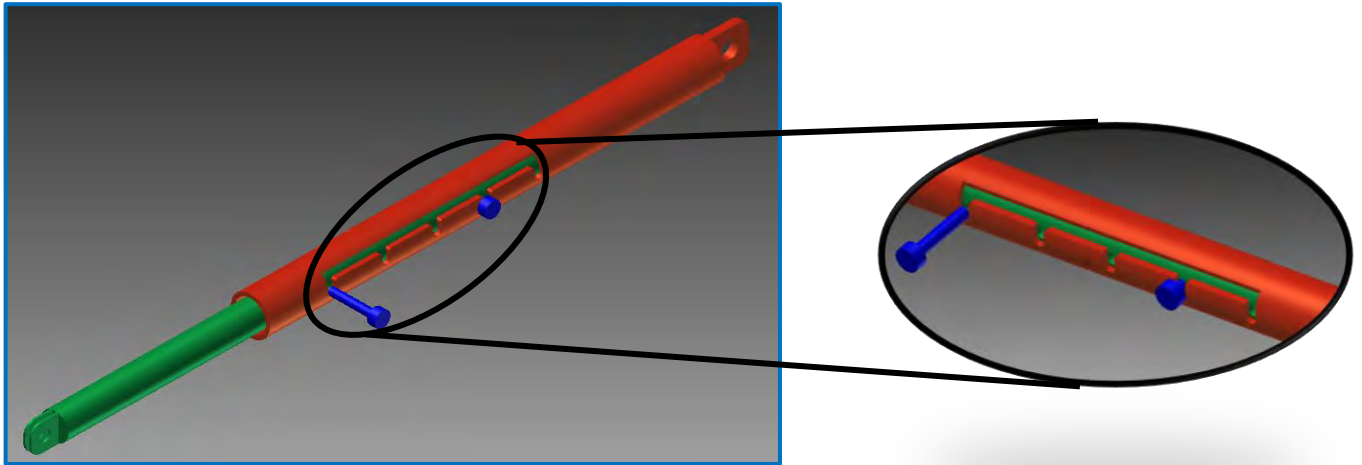


Figure 7.8 Design 3 (Hand, 2013)

7.2.4 Optimal Design

Table 7.1 Design Selection Matrix (Hand, 2014)

<u>Criteria</u>	<u>Weight</u>	<u>Rating</u>	<u>Rating</u>	<u>Rating</u>
	(1-5)	Design 1	Design 2	Design3
Safety	5	8	5	6
Adjusting	4	8	4	2
Operation	4	7	4	5
Mechanical Advantage	3	8	3	2
User Friendliness	3	8	4	2
Corrosion Protection	3	5	5	6
Complexity	2	5	7	7
Manufacture	2	6	5	5
Product Life	2	7	6	2
Effectiveness	4	8	4	3
Calculations	1	7	7	7
Total Score		77/110	54/110	47/110

The method above is used in evaluating and finding the best design solution for a selected criteria, and then rating and scoring these criteria based on their importance, for example safety is one of the most important criteria in this redesign so it will weight rating of 5.

Table 7.1 shows a list of different criteria that are important for a safe redesign of a tie-down system. These criteria are scored (1-10) and evaluated. Also a weighting factor is applied to show the particular criteria's importance in the comparison of the designs. It was found that design 1 offered the most optimal solution to this design problem as it was found it satisfied the design criteria better than other the other two possible designs. The images below show the design concept of the redesigned system.

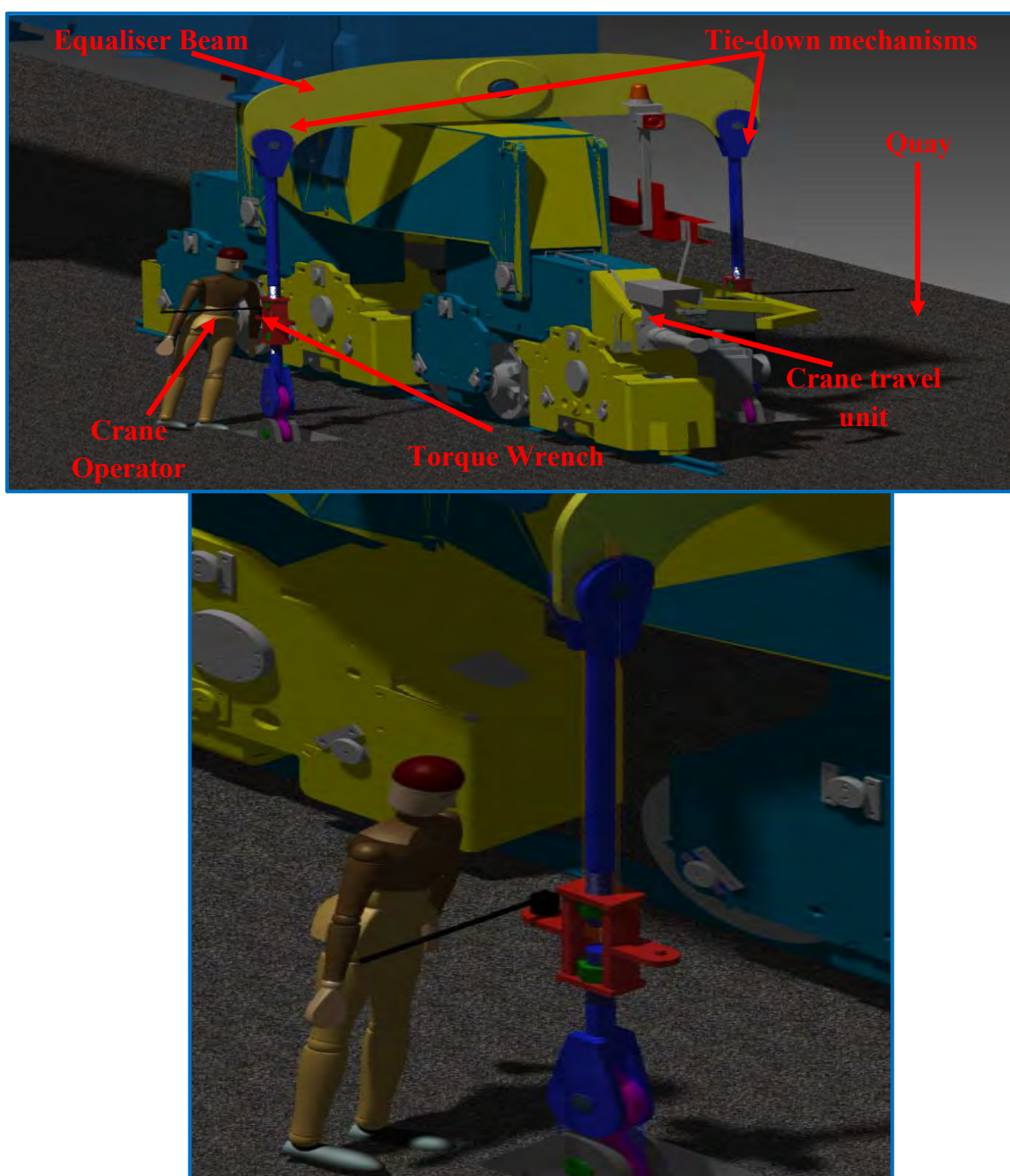


Figure 7.9 Proposed redesign of tie-down system (Hand, 2014)

7.3 Material Selection

7.3.1 Material Selection Process

Material selection is the process by which the best material is selected for a design purpose based on its properties and suitability to that application. A systematic approach is normally adopted to ensure the best materials are chosen for a particular application and firstly requirements and criteria are established primary based on its necessary performance in terms of mechanical, thermal, environmental, electrical and chemical. By using this process the choice of material is narrowed down by the process of elimination (Jayakody, 2009).

For this redesign the mechanical factors for the material such as its stiffness, tensile strength, yield strength, fatigue strength and impact strength will be important in selecting the most suitable material. Also coupled with this, environmental factors are important also as this component is placed in environment where salt laden air present with moisture which can cause significant amount of corrosion on certain materials if not properly treated or designed for. The material’s cost and availability is also an important consideration for this design whereas the material’s mass is not a very important factor but it is reduced where applicable. (Mangonon, 1999), a well-known design engineer, outlines five main aspects that effect material selection: “(1) physical factors, (2) mechanical factors, (3) processing and fabricability, (4) life of component factors, (5) cost and availability and (6) codes, statutory, and others”.

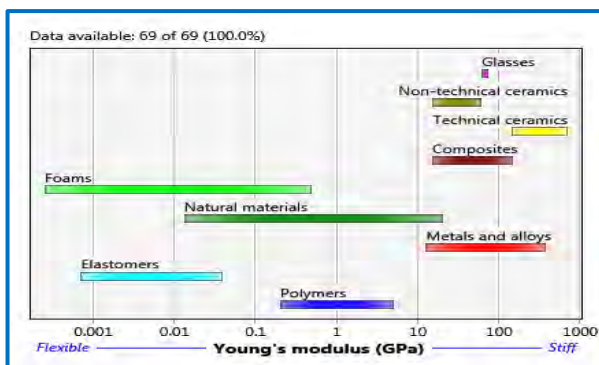


Figure 7.10 Material E performance limits (CES, 2014).

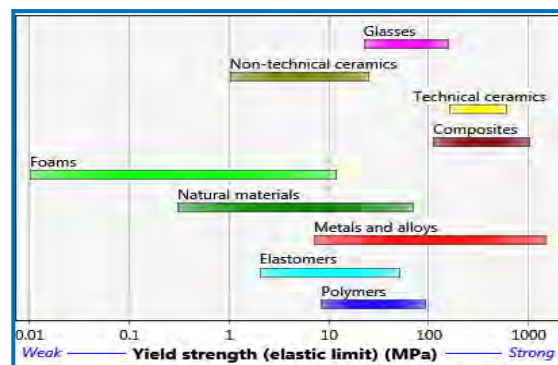


Figure 7.11 Material σ range limits (CES, 2014).

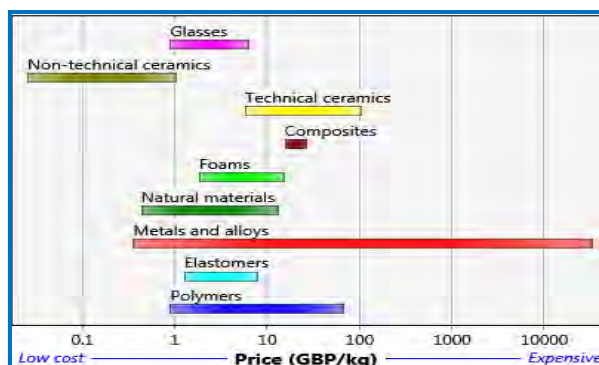


Figure 7.12 Material cost ranges (CES, 2014).

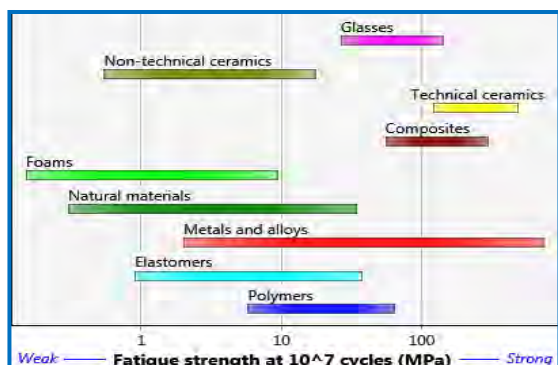


Figure 7.13 Material cycling fatigue (CES, 2014).

The most efficient and effective of means of determining the most suitable material was done using the assistance of the CES Selector Material software package which allows the user to select a material that is most suited to producing a product. This software has the advantage whereby it is a database of all materials and allows the user input necessary material properties and parameters to it, to refine the material selection process. This technique was adopted for this material selection aspect of the redesign.

Shown in figure 7.10 to figure 7.13 is a simple but effective comparison of the primary material properties that will need to be addressed for this design. Firstly the material properties such as yield strength (S_y), Young's Modulus (E) and fatigue strength (S_{Nf}) were examined and cost being a significant factor also. It was determined from observing these plots that metals and alloys had a good association with all these material parameters especially in the terms of yield strength and cost. The primary focus was mainly determined that a suitable metal or alloy which would suit this design.

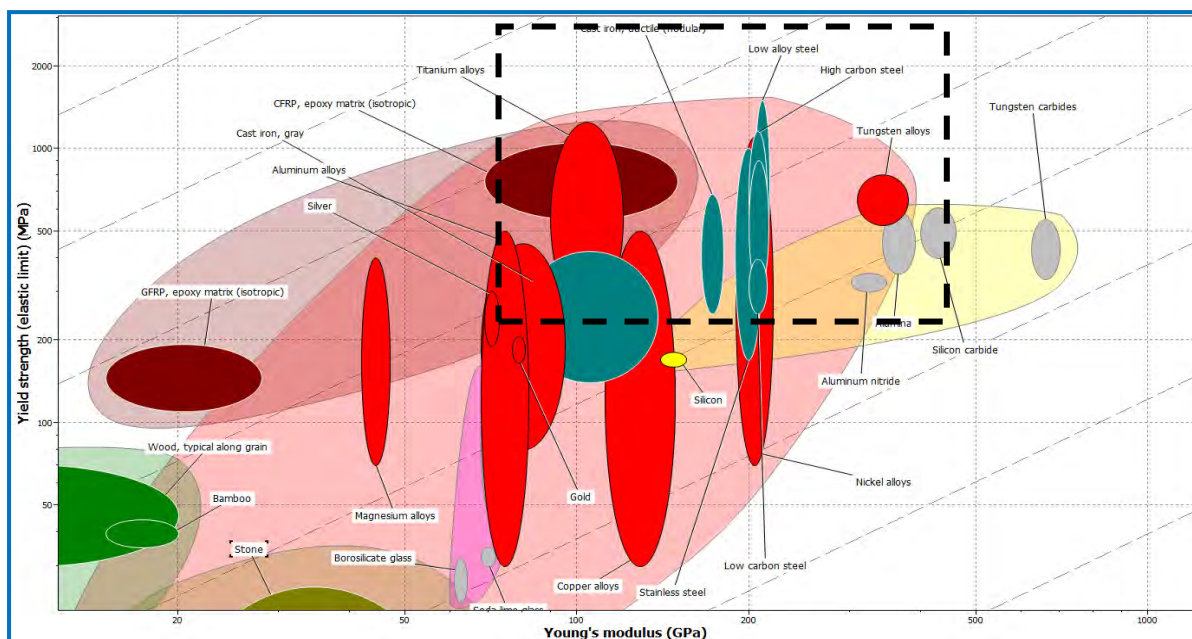


Figure 7.14 Yield strength versus Young's Modulus (CES, 2014)

The material's plot above of yield strength versus Young's Modulus shows there is suitable of range of materials which would be applicable to this design. A high yield strength and tensile strength is necessary for this design as tensile loads will be significant. The plot shows a range of steel alloys which may be applicable to this design such as stainless steel alloys and medium & high carbon steel alloys.

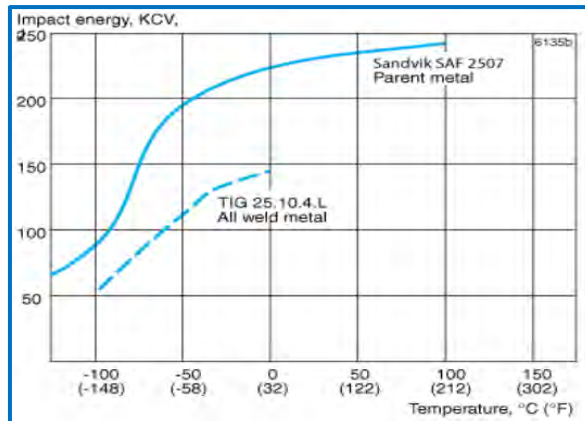


Figure 7.16 Impact energy for SAF 2507
(Sandvik, 2014)

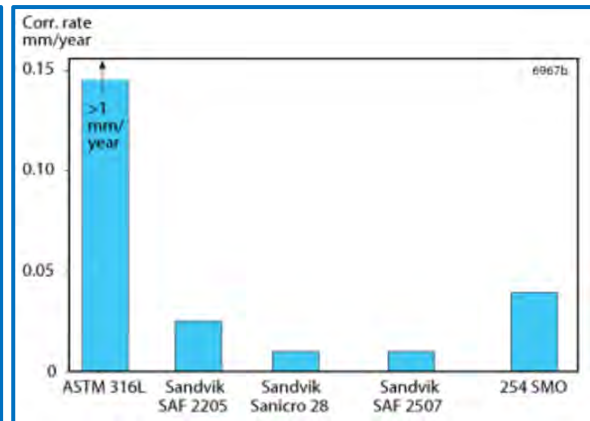


Figure 7.17 Corrosion resistance of SAF 2507
(Sandvik, 2014)

The cost of stainless steel is significantly higher than ordinary steels and therefore would increase manufacturing costs. A common alternative to using stainless steel for an application such as this is to use a suitable carbon steel with a corrosion prevention measure such as galvanising or painting.

High Carbon Steel

If the dimensions of the turnbuckle redesign are to be small, a suitable high carbon steel may be used to facilitate smaller cross sections of material required. A problem with this type of steel is that galvanising can cause damaging effects to the material's surface and is mostly not suitable (Olsson, 2006). Also any machining or cutting processes on this material will be more tedious and costly to produce. A common high carbon steel used in high tensile loading situations is SS 2541 (34CrNiMo6+QT) (Olsson, 2006).

Medium Carbon Steel

The use of medium carbon steel is already commonly used in the construction of cranes and is often denoted as structural steel. It notable has a lower price per unit than high carbon and stainless steel and is easier to machine and weld and process. Also coupled with this, this material has very good reaction with surface treatments such as galvanising. Medium carbon steel is widely available in plate sizes and shaft sizes also with shafts up to 200mm available (Olsson, 2006). Currently Liebherr uses medium carbon steel for crane component manufacture which is called S355 (DIN 1623(86) S355J2G3) (Germany) and is equivalent EN10029 (Europe), this material offers the best mechanical responses of possible structural

steels and has a yield strength for medium carbon steel (Appendix E page E-25 for material specification).

Galvanising

Is the process by which a coating of zinc is placed over ferrous components in order to prevent corrosion, it is normally achieved by placing the metal components in a bath of molten zinc and therefore creating a protective layer between the surface of the component and air (*Shifler, 2005*). For maritime application the cost of galvanising is less than any other corrosion prevention measures (*Olsson, 2006*). The Swedish standard BSK-99 for maritime design states that galvanising is the most appropriate surface treatment in environments of where a high deposition of salt is expected and galvanising provides the longest lasting finish. Also this standard states that external threads should have a reduced dimension before galvanising due to the thickness of the zinc layer applied and internal threads shall be required to be nominal size after the galvanising process (*Boverket, 2003*).

Table 7.2 Comparison of potential materials (*CES, 2014*)

Material	Tensile Strength (S_{ut}) (MPa)	Yield Strength (S_y) (MPa)	Shear Modulus (G) (GPa)	Hardness (HV)	Cost per kg (€)
SAF 2507 Stainless Steel	950	550	84	302	4.59
SS 2541 High Carbon Steel	900	700	80	650	0.494
S355 Medium Carbon Steel	535	355	84	165	0.494

It was found that the medium carbon steel would be best suited to this application, which can be mainly seen from the comparison above in table 7.2. The main factors that determined decision was the material's cost, availability and suitability to the application. Refer to Appendix E page E-25 for the full material specification.

7.4 Design Calculations

7.4.1 Direct Loading

The first and foremost safe design requirement for this redesign is that it must be able to withstand uplift forces during a maximum storm condition exposed to the crane during an out-of-service period. Using the current wind loading calculations specifications (*FEM 1.004*) and new drag values derived from the wind tunnel testing and computational fluid dynamics analysis carried out it was possible to calculate the maximum wind force generated on the crane in various positions and angles as described in Appendix E. The maximum uplift load calculated at one of the crane base corners was found to be 14.3 metric tons in a full storm condition. This load does seem significant and large, but one has to remember the size of the structure that the wind force is being calculated on and the corresponding overturning moments generated as a result which are very significant.

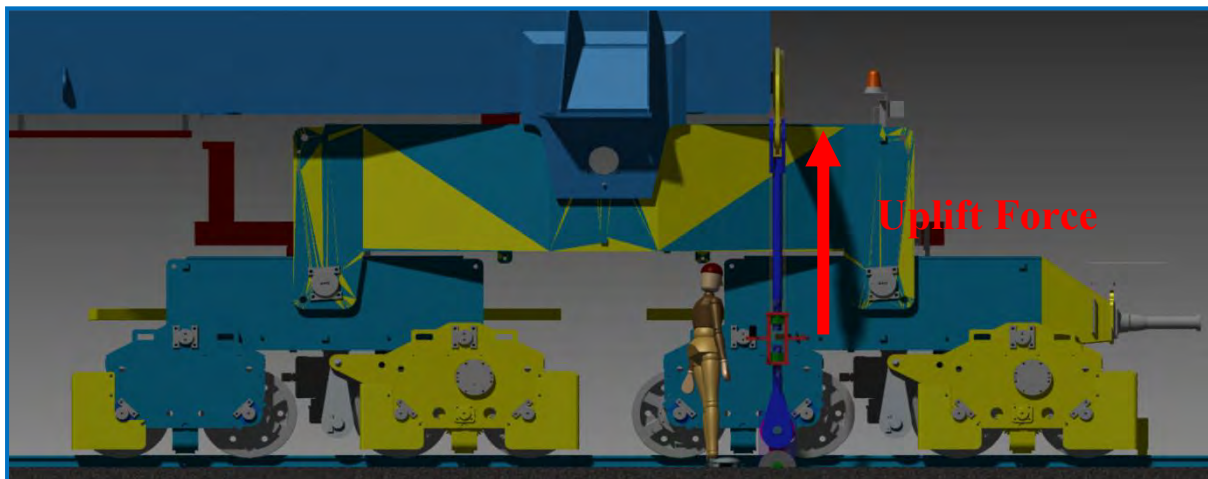


Figure 7.18 Uplift Force at crane corner base unit (*Hand, 2014*)

It is necessary that the redesigned tie-down system is able to withstand this force with a suitable factor of safety. A factor of safety of between 2 and 3 was found to be the most suitable to an application such as this based the criteria described in the standard BS 2573 Pt 1: 1983 Rules For Design of Cranes : Specification for Classification stress Calculations and design criteria for structures. This standard contains a set of rules for carrying out calculations and applying factors for allowable stresses to be used for the grade of materials. This also outlines the factor of safety requirements needed for different types of loading which will be investigated in the following pages.

General Considerations

By their use, turnbuckles can be subjected to rough handling while in use and in some cases examples of misuse can occur by workers using a pipe to tighten the turnbuckle and other cases also using a hammer to apply impact force. These are some of the other considerations that have taken in account when determining a suitable factor of safety.

For the thread used in this design an ISO metric coarse will be used mainly because of these advantages (*Bhandari, 2008*).

- Coarse threads are easier to machine than fine threads.
- There is a more distribution of stress in the threads.
- The thread profile is less likely to seize during tightening compared with a fine thread.

The tension arms are tightened by applying a torque about the turnbuckle which creates a tension in the tension arms which is denoted by P and the equation [7.0] shows the relationship between torque and the tension created (*Bhandari, 2008*).

$$M_t = \frac{Pd_m}{2} \times \frac{(\mu \sec\theta + \tan\alpha)}{(1 - \mu \sec\theta + \tan\alpha)} \quad [7.0]$$

For ISO metric threads:

$$\theta = 30^\circ \qquad \alpha = 2.5^\circ \qquad d_m = 0.9d$$

d is the nominal diameter of the threads

The coefficient of friction can vary on the conditions especially in a maritime location due to weathering and the values mainly range from 0.12 to 0.20. In this case coefficient will be taken as $\mu = 0.15$.

This simplifies equation [7.0] to:

$$M_t = \frac{Pd_m}{2} \times \frac{(0.15 \sec(30) + \tan(2.5))}{(1 - 0.15 \sec(30) + \tan(2.5))}$$

$$M_t = 0.098Pd$$

This will give the torsional moment required at one end of the turnbuckle.

To determine the maximum torque that could be applied to the turnbuckle, certain guidelines had to be accounted for. According to the BS EN 1005-3:2002, Safety of machinery- Human physical performance – Part 3, it gives the force limits for machinery operations. This standard presents the isometric force limits for professional workers to 15th percentile values for the adult working population. It was found the maximum design push force should be 200 N or 20.4 Kg (*HSE, 2004*).

In working situations such as this a standard 1m torque wrench is most suitable for this operation. The maximum torque that can be generated will be assumed to 200Nm and a 50% clamping load will suffice.

Total uplift force = 14.3 Ton = 140.283 kN

There are two tie-down per corner, the design load = $\frac{140.283 \text{ kN}}{2} = \underline{70.14 \text{ kN}}$

The nominal diameter thread will be found by:

$$200\text{Nm} = 0.098 (70.14 \times 10^3)d$$

$$D = 30\text{mm}$$

Thread Specification:

ISO coarse thread M30 3.5 Pitch (*Steel Masters, 2014*).

Core diameter (d_c) = 26.21 mm

Shear Area = 561 mm²

Pitch diameter (d_p) = 27.77mm

Nominal diameter (d) = 30 mm

Material S355 Steel

Mechanical Properties

UTS = 535 MPa $\sigma_y = 355 \text{ MPa}$

Direct Stress

$$\sigma_t = \frac{P}{\frac{\pi}{4}(d_c)^2} [7.1] \text{ (Mott, 2006)} = \frac{70.14 \times 10^3}{\frac{\pi}{4}(26.21)^2} = 130\text{MPa}$$

Shear Stress

$$\tau = \frac{16M_t}{\pi d_c^3} [7.2] \quad (Mott, 2006) \quad \frac{16(200,000)}{\pi(26.21)^3} = 56.58\text{MPa}$$

The principal shear stress is given by:

$$\tau_{Max} = \sqrt{\left(\frac{\sigma_t}{2}\right)^2 + \tau^2} [7.3] \quad (Mott, 2006)$$

$$\tau_{Max} = \sqrt{\left(\frac{130}{2}\right)^2 + 56.58^2}$$

$$\tau_{Max} = 86.176 \text{ MPa}$$

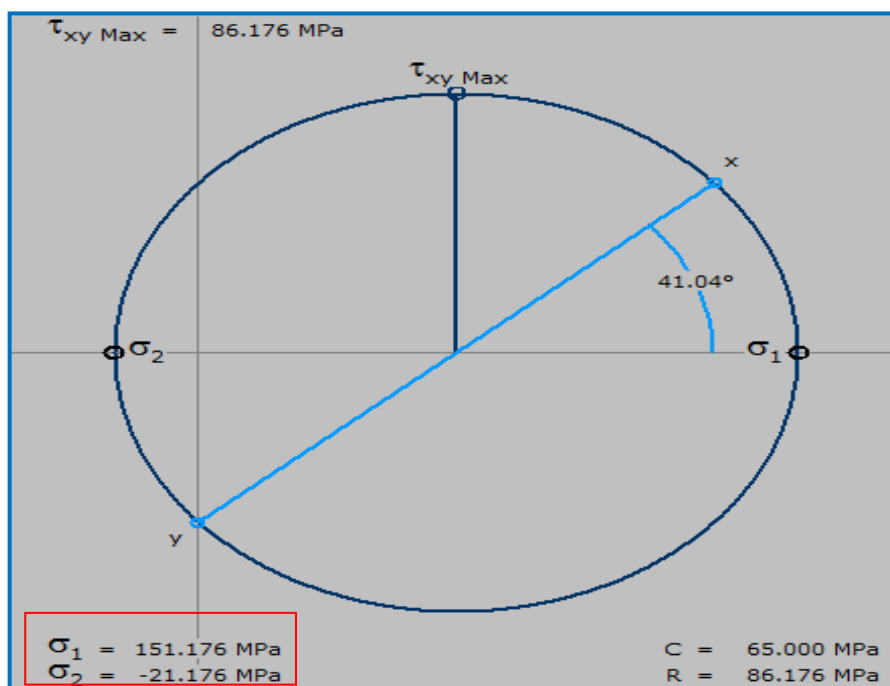


Figure 7.19 Mohr's Circle of Stress (MD Solids, 2012)

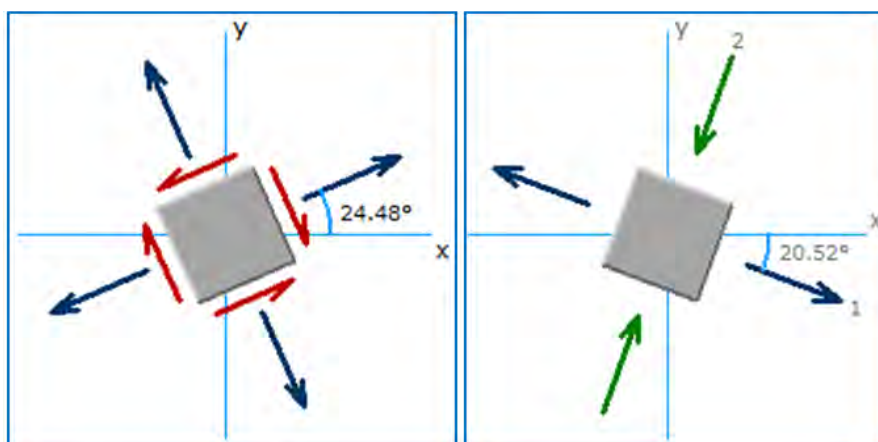


Figure 7.20 Max in plane shear stress direction (L) Principal stress direction (R) (MD Solids, 2012)

(Von Mises Criterion)

$$\sigma' = \sqrt{\frac{(\sigma_1 - \sigma_2)^2 + (\sigma_2 - \sigma_3)^2 + (\sigma_1 - \sigma_3)^2}{2}} \quad [7.4]$$

$$\sigma' = \sqrt{\frac{(151.17 - (-21.17))^2 + (-21.17)^2 + (151.17)^2}{2}}$$

$$FOS = \frac{181.486 \text{ MPa}}{86.176 \text{ MPa}} = 2.180 \text{ (Satisfactory)}$$

L_e = Length of Thread Engagement required.

$$\text{Tensile Stress Area of male thread} = A_t = \frac{\pi}{4} (D - 0.938094 \times p)^2 \quad [7.5] \quad (\text{Roymech, 2013})$$

$$= A_t = \frac{\pi}{4} (30 - 0.938094 \times 3.5)^2$$

$$A_t = 561 \text{ mm}^2 \text{ (same as shear area)}$$

Minimum Thread Engagement (L_e)

$$L_e = \frac{2 \times A_t}{0.5 \times \pi \times D_p} \quad [7.6]$$

$$L_e = \frac{2 \times 561 \text{ mm}^2}{0.5 \times \pi \times 27.77 \text{ mm}} = 25.722 \text{ mm}$$

In practise the length varies from d to $1.25d$ (Bhandari, 2008).

$$d = 30 \text{ mm}$$

$$1.25(d) = 1.25(30) = 37.5 \text{ mm (both larger)}. \quad [7.7]$$

Design for Fatigue

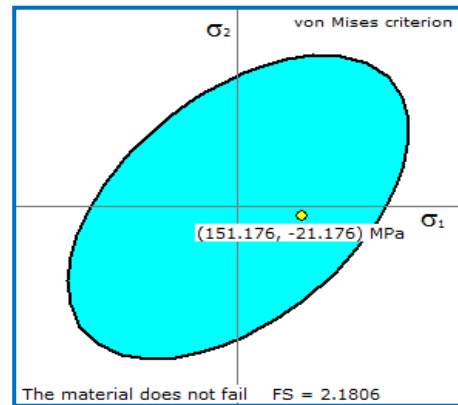


Figure 7.21 Von Mises Criterion (MD Solids, 2012)

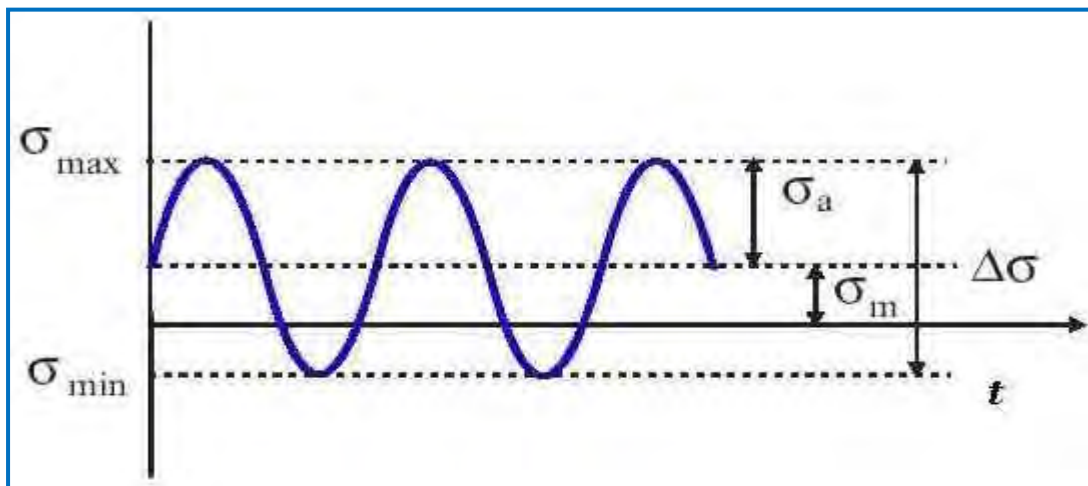


Figure 7.22 Alternating and mean stresses (Materials Engineer, 2012)

$$\sigma_{\text{mean}} = \frac{\sigma_{\text{Max}} + \sigma_{\text{min}}}{2} \quad [7.8]$$

$$F_{\text{mean}} = \frac{F_{\text{Max}} + F_{\text{min}}}{2} \quad [7.9] \text{ (Mott, 2006)}$$

$$\sigma_{\text{alt}} = \frac{\sigma_{\text{Max}} - \sigma_{\text{min}}}{2} \quad [7.10]$$

$$F_{\text{alt}} = \frac{F_{\text{Max}} - F_{\text{min}}}{2} \quad [7.11] \text{ (Mott, 2006)}$$

$$F_{\text{Max}} = 70.14 \text{ kN} \quad F_{\text{Min}} = 0$$

$$F_m = F_a = 35.07 \text{ kN}$$

$$\sigma_m = \sigma_a = \frac{F}{\frac{\pi}{4}(d_c)^2} = \frac{35.07 \times 10^3}{\frac{\pi}{4}(26.21)^2} = 66.11 \text{ MPa}$$

$$\text{Endurance Limit } (S'_e) = \frac{S_{Ut}}{2} = \frac{535}{2} = 267.5 \text{ MPa} \quad [7.12]$$

$$\text{Modified Endurance Strength } (S_e) = k_a \cdot k_b \cdot k_c \cdot k_d \cdot k_e S'_e \text{ (Mott, 2006)} \quad [7.13]$$

$$k_a = a(S_{Ut})^b \text{ (Surface finish factor) (Machined surface } a = 4.51 \text{ \& } b = -0.265) \quad [7.14]$$

$$k_a = 4.51(535)^{-0.265} = 0.853$$

k_b (size factor) for axial loading $k_b = 1$

k_c (Reliability factor) = 0.868 for 95% Reliability

k_d (Temperature Factor) = 1

k_e (Impact Factor) = 0.8

$$(S_e) = k_a \cdot k_b \cdot k_c \cdot k_d \cdot k_e S'_e = (0.853)(1)(0.868)(1)(0.8)(267.5 \text{ MPa}) = 158 \text{ MPa}$$

$$\text{Modified Goodman Equation} = \frac{\sigma_a}{S_e} + \frac{\sigma_m}{S_{ut}} = \frac{1}{N} \quad \frac{66.11}{158} + \frac{66.11}{535} = \frac{1}{N} \quad \underline{N = 2} \text{ (Satisfactory)}$$

Top Pin Size

This is the point where the tie-down connects with the crane structure.

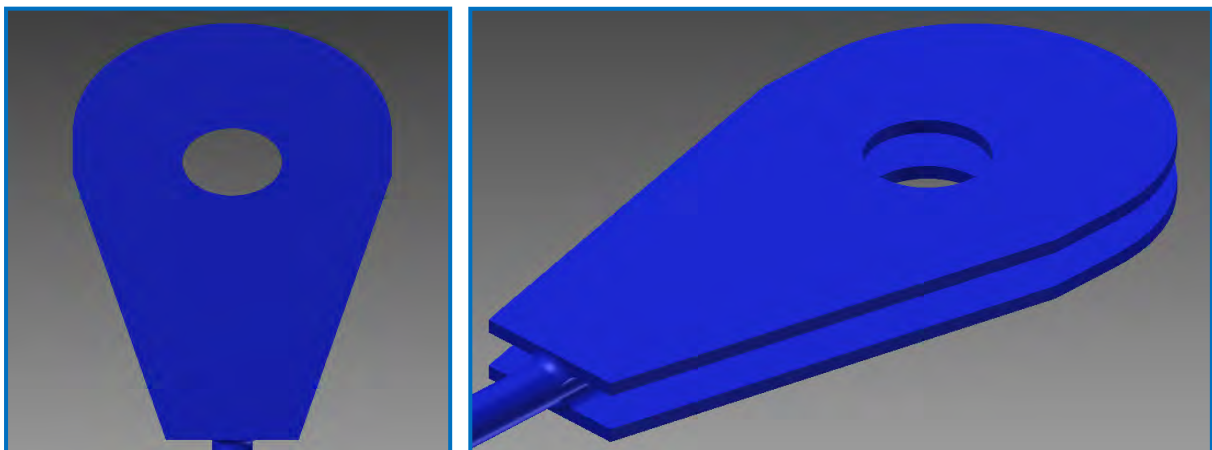


Figure 7.23 Attachment area (Hand, 2014)

Material S355 Steel

Mechanical Properties

$$\text{UTS} = 535 \text{ MPa} \quad \sigma_y = 355 \text{ MPa} \quad \text{FOS} = 3$$

$$\tau_{\text{Max}} = 0.5 \cdot \sigma_y \text{ (Von Mises Criterion)} \quad (\text{Mott, 2006})$$

$$\tau_{\text{Max}} = 0.5 \times 355 \text{ MPa} = 177.5 \text{ MPa}$$

Pin in Double Shear

$$\text{Allowable shear stress} \quad \tau_a = \frac{177.5 \text{ MPa}}{3} = 59.16 \text{ MPa}$$

$$\text{Total uplift force} = 14.3 \text{ Ton} = 140.283 \text{ kN}$$

$$\text{There are two tie-down per corner, the design load} = \frac{140.283 \text{ kN}}{2} = \underline{70.14 \text{ kN}}$$

Current Size pin must be used to connect with crane structure $D = 76 \text{ mm}$

$$\sigma = \frac{F}{A} \quad (\text{Mott, 2006})$$

$$\sigma = \frac{70.14 \text{ kN}}{2 \cdot \frac{\pi(0.076)^2}{4}} \quad \sigma = 7.73 \text{ MPa}$$

$$\underline{7.73 \text{ MPa} < 59.16 \text{ MPa}} \text{ (Acceptable)}$$

Top Connection Bearing Plates

Material S355 Steel

Mechanical Properties

$$\text{UTS} = 535 \text{ MPa} \quad \sigma_y = 355 \text{ MPa} \quad \text{FOS} = 3$$

$$\tau_{\text{Max}} = 0.5 \sigma_y \text{ (Von Mises Criterion)} = 0.5 \times 355 \text{ MPa} = 177.5 \text{ MPa}$$

Double Shear Connection, Load is halved between two bearing plates

$$\text{Allowable direct stress} \quad \sigma_a = \frac{355 \text{ MPa}}{3} = 118.3 \text{ MPa}$$

$$\sigma = \frac{F}{A} \quad \sigma = \frac{F}{A} \quad 118.3 \text{ MPa} = \frac{35.07 \text{ kN}}{A} \quad A = \frac{35.07 \text{ kN}}{118.3 \text{ MPa}}$$

$$D \times t = \frac{35.07 \times 10^3}{118.3 \times 10^6} \quad D \times t = 0.000296 \text{ m} \quad 0.076 \times t = 0.000296 \text{ m}$$

$$\text{Thickness (t) required} = t = \frac{0.000296 \text{ m}}{0.076 \text{ m}} = 0.0039 \text{ m} \quad t = 3.9 \text{ mm}$$

Use standard size 10 mm plate.

Stress Concentration at the hole in the plates:

Assumption:

Stress concentration factor based on rectangular plate with central hole

$$\frac{d}{b} = \frac{78 \text{ mm}}{180 \text{ mm}} = 0.433 \quad K_t = 2.2$$

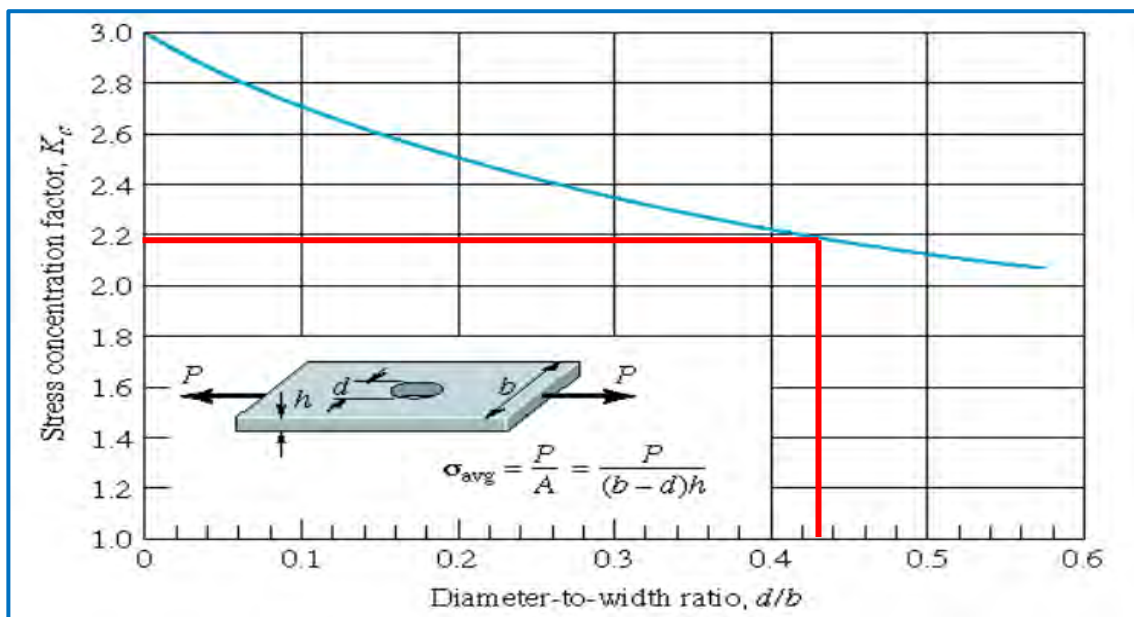


Figure 7.24 Stress Concentration factor for a circular hole in a rectangular plate (Huston & Harold, 2011)

$$\sigma_{avg} = \frac{p}{A} = \frac{p}{(b-d)h} \quad [7.15] = \frac{35.07 \text{ kN}}{(0.180 - 0.078)0.03} = 11.46 \times 10^6 \text{ Pa} = 11.46 \text{ MPa}$$

11.46 MPa < 118.3 MPa (Acceptable)

$$\sigma_{max} = K_t \times \sigma_{avg} \quad [7.16] = 2.2 \times 11.46 = 25.212 \text{ MPa}$$

25.212 MPa < 118.3 MPa (Acceptable)

Note: These calculations are the same for opposite connection of tie-down.

Turnbuckle

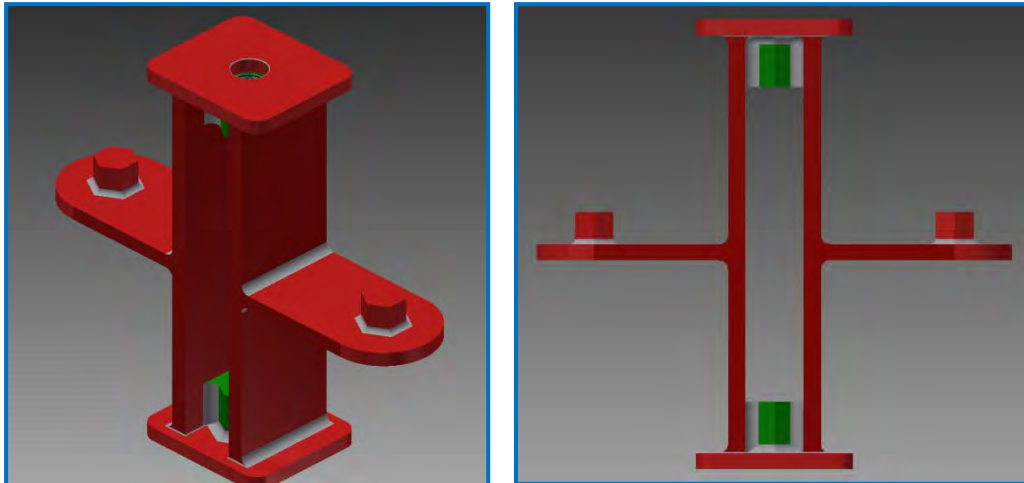


Figure 7.26 Turnbuckle weld detail (Hand, 2014)

Side plate width (W) necessary

Two plates required, each takes halve of the load

$$A = \frac{F}{\sigma} = \frac{35.07 \text{ kN}}{118.3 \text{ MPa}} = 0.000296 \text{ m}^2$$

$$W \times t = 0.000296 \text{ m}^2 \quad (\text{Use plate thickness } 30 \text{ mm})$$

$$(0.010)(W) = 0.000296 \quad L = 0.02964 \text{ m} \quad L = 30 \text{ mm}$$

Two welds required per plate, each weld has to take $\frac{F}{4} = \frac{70.14 \text{ kN}}{4} = 17.535 \text{ KN}$

$$F = 1.414(h)(L)(\tau) \quad (\text{Bhandari, 2008})$$

$h = 8 \text{ mm}$ (width of weld)

$$\text{Allowable shear stress} \quad \tau_a = \frac{177.5 \text{ MPa}}{3} = 59.2 \text{ MPa}$$

$$17.535 \text{ kN} = 1.414 \times 0.008 \text{ m} \times L \times 59.2 \text{ MPa}$$

$$17.535 \times 10^3 = 0.669 \times 10^6 \cdot L$$

$$L = \frac{17.535 \times 10^3}{0.669 \times 10^6} = 0.026 \text{ m} = 26 \text{ mm (Length of Weld required)}$$

Torque Wrench Attachment

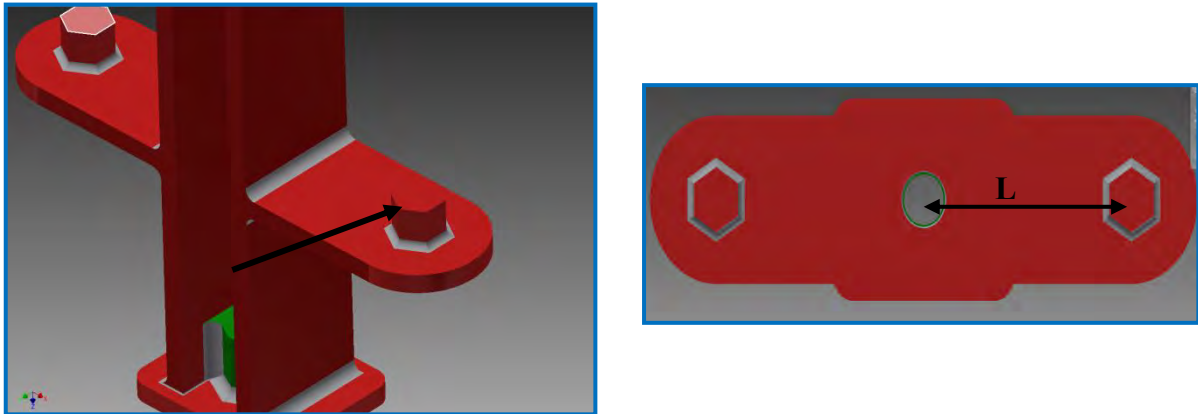


Figure 7.27 Torque Wrench attachment (Hand, 2014)

Torque wrench fitting size to attach to the turnbuckle has been chosen to be 35mm. Check ensure shear stress is within the FOS region or lower.

Assumption:

Model the hexagonal connection as a cylinder (this will give a slight difference in results but will give a reasonable prediction)

$$\frac{T}{J} = \frac{\tau}{r} = \frac{G\theta}{L} \quad \text{(Torsion equation)} \quad [7.18]$$

$$T = 200 \text{ Nm}$$

$$r = \frac{D}{2} = \frac{35 \text{ mm}}{2} = 17.5 \text{ mm}$$

$$J = \frac{\pi D^4}{32} = \frac{\pi(0.035)^4}{32} = 147 \times 10^{-9} \text{ m}^4$$

$$\tau = \frac{T \cdot r}{J} = \frac{(200) \cdot (0.0175)}{147 \times 10^{-9}} = 23.81 \times 10^6 \text{ Pa} = 23.81 \text{ MPa}$$

Allowable shear stress (τ_a) = 59.16 MPa

$$\text{FOS} = \frac{59.16 \text{ MPa}}{23.81 \text{ MPa}} = 2.48 \text{ (Satisfactory)}$$



Figure 7.28 Torque applied

The design of the turnbuckle shows the torque wrench connection offset from the centre of the shaft as shown above. This length (L) is 60mm and accounts for an amplification factor on the torque applied on such inefficiencies such thread friction and wear. For a 1m torque wrench this increases torque applied by 6%.

7.4.2 Torque-Tightening Method

An important design feature of the redesigned turnbuckle is that it allows the crane operator or user to accurately set a torque value in the tie-down turnbuckle and therefore creating a tensile force or preload clamping load which can be equally set on every turnbuckle on the crane. This is important because it therefore establishes that each tie-down is under the same clamping load and this significantly reduces the possibility of unequal loading occurring between opposite tie-downs on a crane.

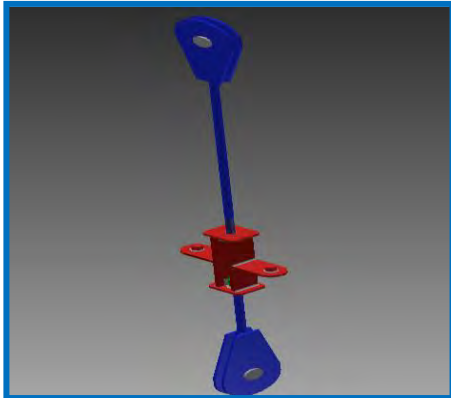


Figure 7.31 Redesigned tie-down



Figure 7.32 Tightening procedure (Liebherr, 2014)

This design also poses many advantages in the area of working health and safety which is the primary concern for this design. Existing designs meant that these tie-downs were tightened by the users in way that unequal tensile forces were generated in the tie-downs. This could lead to the user overstraining oneself and lead to injuries and disorders such as musculoskeletal disorders (MSDs) which would have mainly affected the user's back due to the pulling technique involved "Between 9 and 20 per cent of the injury claims for low back pain are a result of pulling activities" (GV Safety, 2004) This redesign however offers the attachment of a torque wrench or some other applicable tool to the turnbuckle centre (figure 7.33) and a set desired torque value can be applied by the user involving a pushing technique instead of pulling technique. Researchers have found that specifically in Manual Material Handling (MMH) it is the horizontal push force that matters the most in design (Darcor, 2014). Pushing is a preferred action for many reasons, if a person is pulling their arms are out stretched beyond their body and their shoulder and back are in a mechanically awkward position increasing the chance of debilitating injury. Researchers have established that higher force can be generated by a pushing force and this has been incorporated into this design.



Figure 7.33 Turnbuckle centre (Hand, 2014)

7.4.3 Hazard Analysis for Redesign of Tie-down

Risk Assessment											
											Taken in Accordance with EN ISO 14121-1:2007
RA #	Action	Hazard	Lo	Fe	DPH	NPR	HRN	Risk	Control	HRN with control	Risk with control
1	Connecting tie-down to crane	Improper lifting (back strain)	2	1	1	1	2	Low	Ensure correct manual handling is done.	1	Very Low
2	Contact with threads	Cuts/mild lacerations	2	1	0.5	1	1	Low	Ensure hand protection is worn by worker	0.2	Negligible
3	Contact with threads	Contact with oils/grease (skin dermatitis)	2	1	0.3	1	0.6	Very Low	Wear adequate hand protection/barrier cream	0.1	Negligible
4	Tightening turnbuckle	Improper technique/pulling (back strain injury)	1	1	5	1	5	low	Ensure crane workers know correct tightening procedure	0.5	Low
5	Tightening turnbuckle	Torque wrench slips off seating. Worker hits crane structure	0.5	1	5	1	2.5	Low	Ensure good connection is made between torque wrench and turnbuckle	0.5	low
7	Tightening turnbuckle	Quay surface slippy (moisture,oil,residues). Worker slips when pushing	1	1	6	1	6	Significant	Ensure good traction footwear is worn	1	Low
8	Inexperienced user	Incorrect use of equipment/injury occurs	1	1.5	5	1	7.5	Significant	Ensure have experienced persons supervising/ Consult user manual	1	Low

7.5 Finite Element Analysis (FEA)

7.5.1 Introduction

Finite element analysis (FEA) was carried out on the redesigned turnbuckle in two loading situations using ANSYS 14 static structural through the Workbench framework. The design was structurally analysed in direct loading situation while under a tensile load and during the tightening phase where a torque would be applied on the turnbuckle. This analysis allows examination of the stresses and deflections in the design and see are they within acceptable limits for the design.

7.5.2 Methodology

Figure 7.34 below shows the methodology that was implemented to undertake the finite element analysis. Firstly the 3D CAD model was refined which meant that any sharp corners or edges in the model were smoothed out to ensure the closest representation to the physical model existed. The model was transferred to the ANSYS workbench and its material properties were modified to the chosen medium carbon steel which is shown in figure 7.35 below.

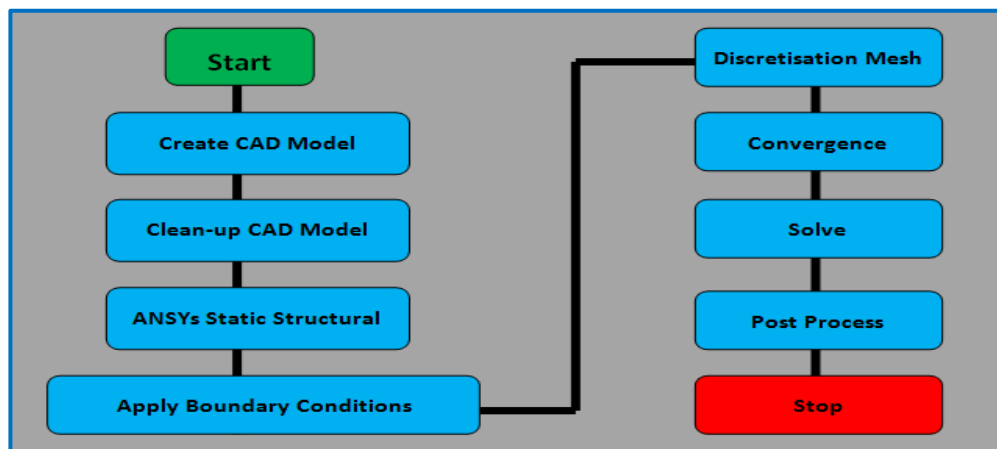


Figure 7.34 Finite element analysis flowchart (Hand, 2014)

Properties of Outline Row 3: Structural Steel			
	A	B	C
1	Property	Value	Unit
2	Density	7850	kg m ⁻³
3	Isotropic Secant Coefficient of Thermal Expansion		
6	Isotropic Elasticity		
12	Alternating Stress Mean Stress	Tabular	
16	Strain-Life Parameters		
24	Tensile Yield Strength	3.55E+08	Pa
25	Compressive Yield Strength	3.55E+08	Pa
26	Tensile Ultimate Strength	5.35E+08	Pa
27	Compressive Ultimate Strength	5.35E+08	Pa

Figure 7.35 Modified material properties (ANSYS, 2014)

7.5.3 Mesh

In similarity with the CFD section in chapter 5 of this report the FEA analysis was also carried out using an unstructured hybrid mesh with primary tetragonal and hexagonal elements. To ensure the most optimal and most accurate results were generated from the FEA model a convergence check was conducted to ensure the results were grid independent. Also particular concentration was placed on the grid quality techniques outlined in chapter 5 such as aspect ratio, skewness and orthogonal quality.

Table 7.3 FEA results at different mesh densities

Mesh Relevance	Nodes	Elements	Equivalent Stress (MPa)	Shear Stress (MPa)	Deformation (mm)	Average Aspect Ratio	Average Skewness	Average Orthogonal Quality
Coarse	17577	9434	134.98	76.788	2.5632	4.434	0.650	0.562
Medium	21852	11777	114.13	65.878	2.5601	3.816	0.614	0.599
Fine	21161	11265	88.355	51.004	2.6028	3.820	0.627	0.593
Refined	441772	234232	87.988	50.796	2.7091	2.584	0.345	0.815

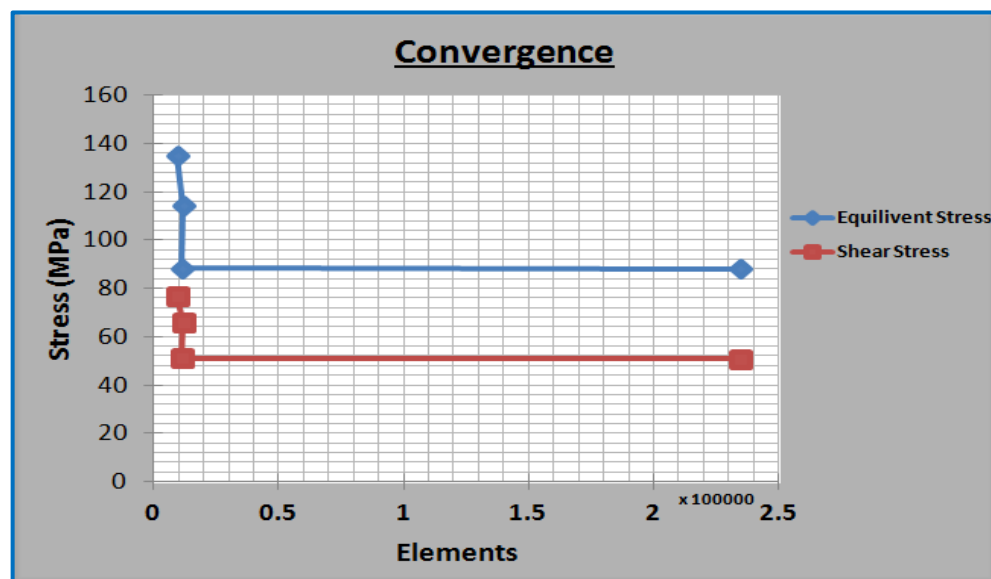


Figure 7.36 Grid independent mesh (Hand, 2014)

The graph above shows the converged results for the refined mesh density which has 441,772 nodes and 234,232 elements. These results were taken when an applied torque was placed on the model and shows the Von Mises and shear stress to be around 88MPa and 50.8MPa respectively. It is noticed there is little difference between the refined mesh results and the fine mesh relevance for results, therefore grid independence is achieved. It is also observed that the mesh quality parameters are growing in quality as the mesh density was increased.

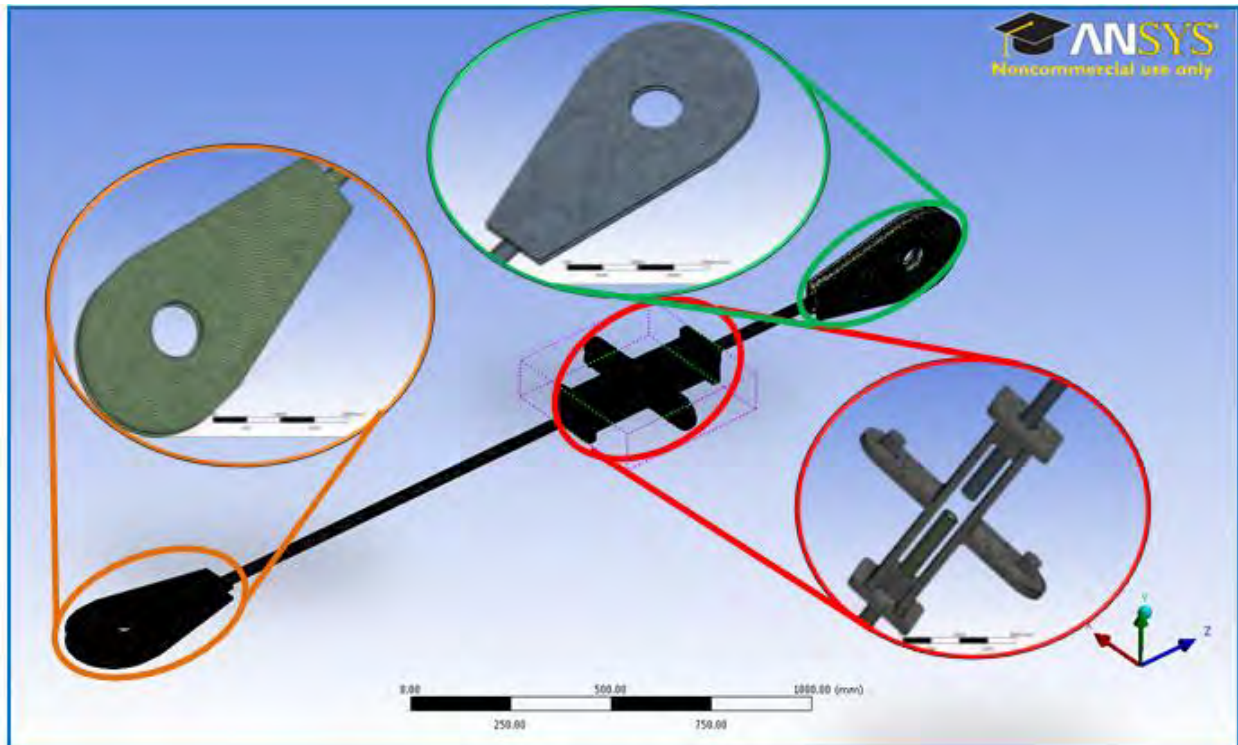


Figure 7.37 FEA mesh detail (Hand, 2014)

7.5.4 Torque Applied

7.5.4.1 Boundary Conditions

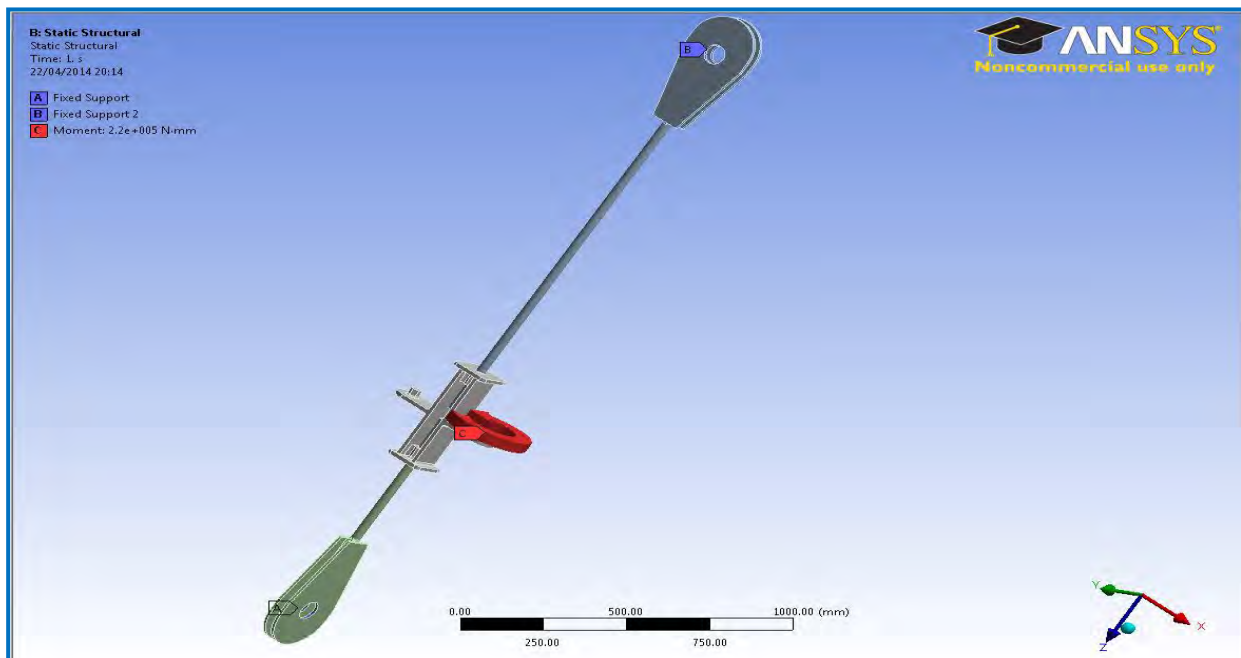


Figure 7.38 Boundary Conditions (Hand, 2014)

Figure 7.38 above shows the boundary conditions that were placed on the FEA model to see what stresses and displacements occurred when a 200Nm torque was placed on the turnbuckle centre. The two pins are placed as fixed constraints.

7.5.4.2 Graphic Results

Equivalent Stress

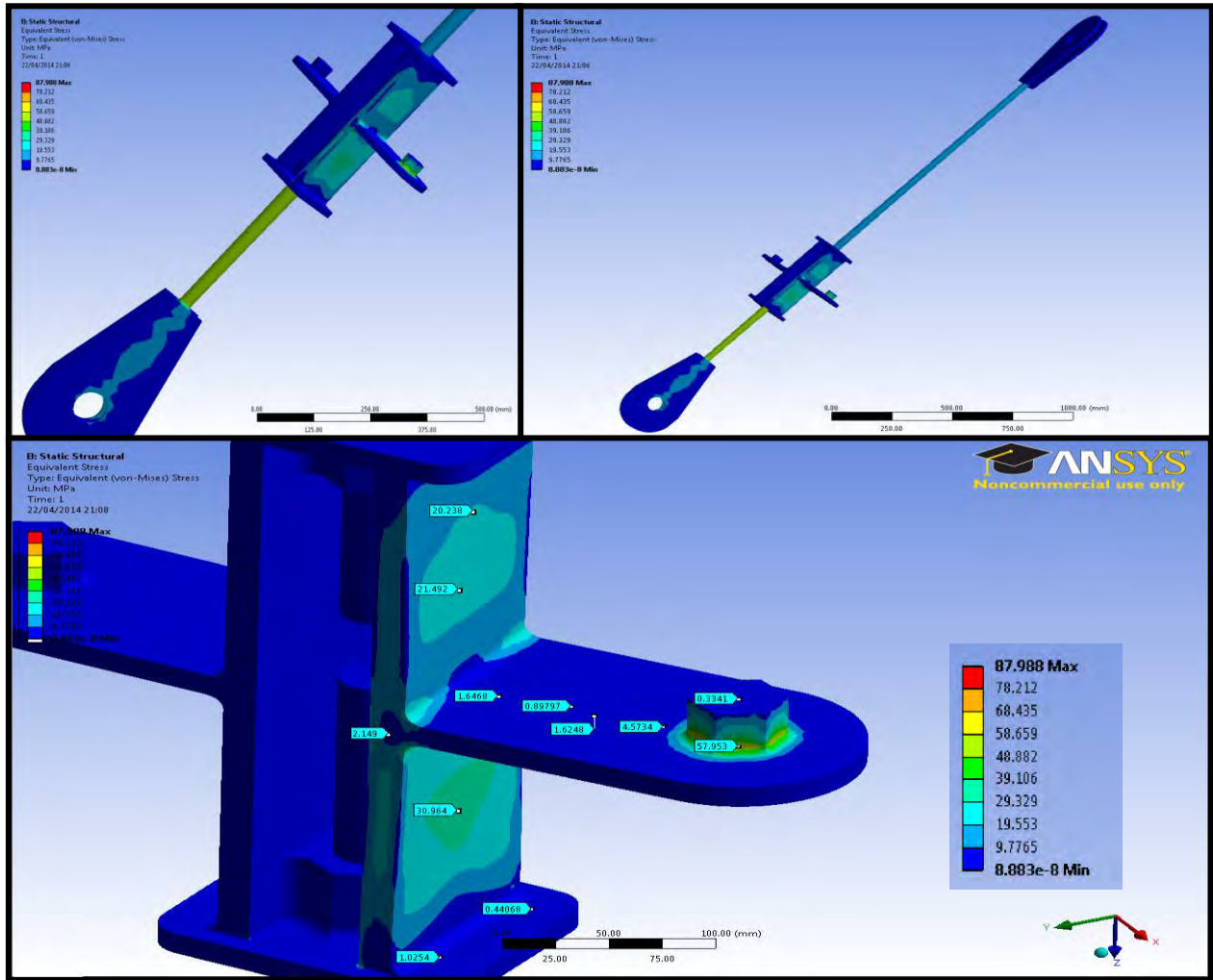


Figure 7.39 Equivalent Stress (MPa) (Hand, 2014)

Maximum Shear Stress

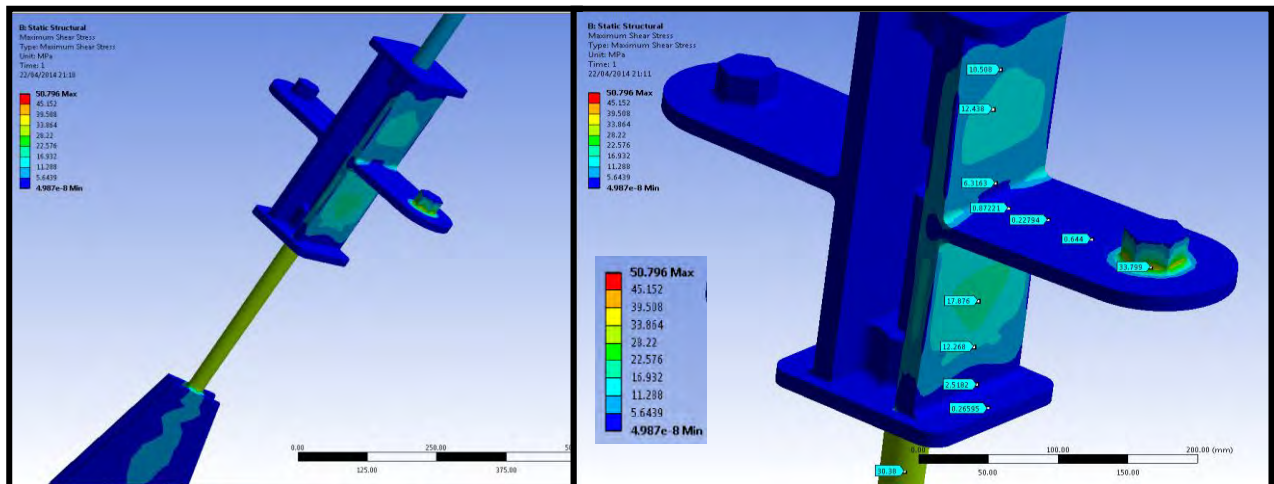


Figure 7.40 Maximum Shear Stress (MPa) (Hand, 2014)

Displacement

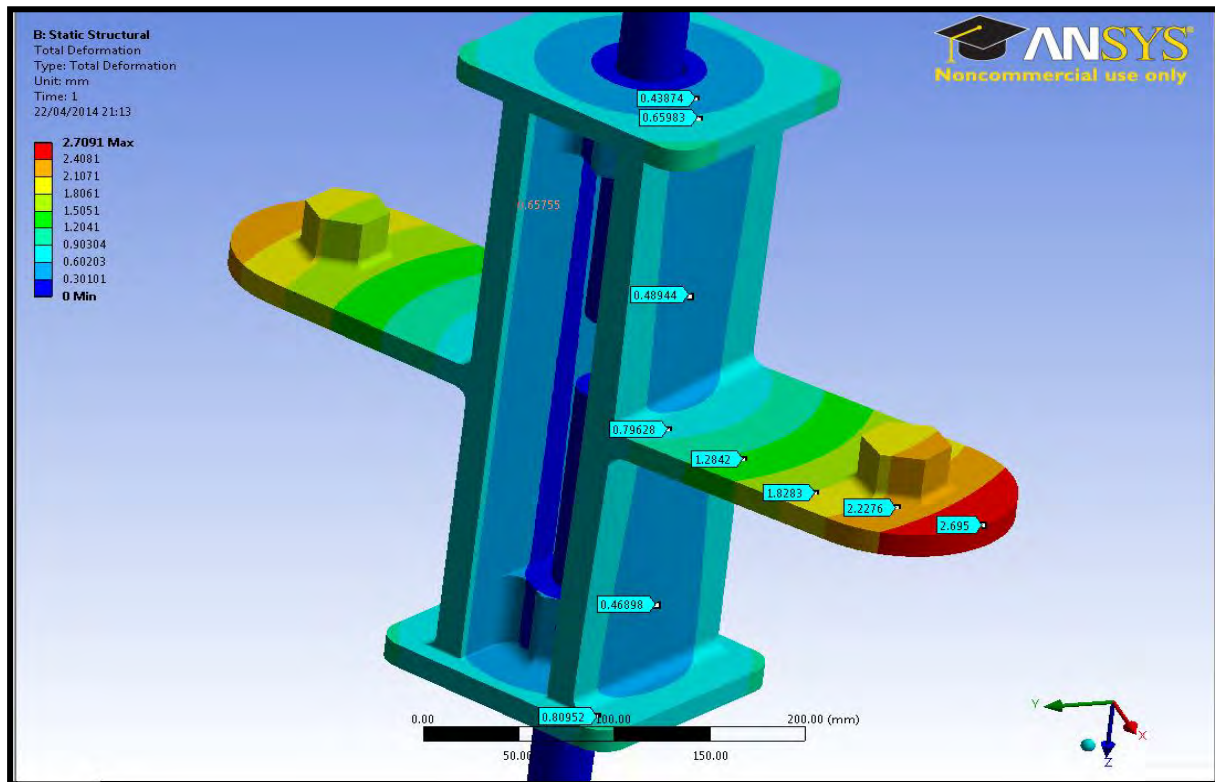


Figure 7.41 Displacement (mm) (Hand, 2014)

7.5.5 Direct Tensile load

7.5.5.1 Boundary Conditions

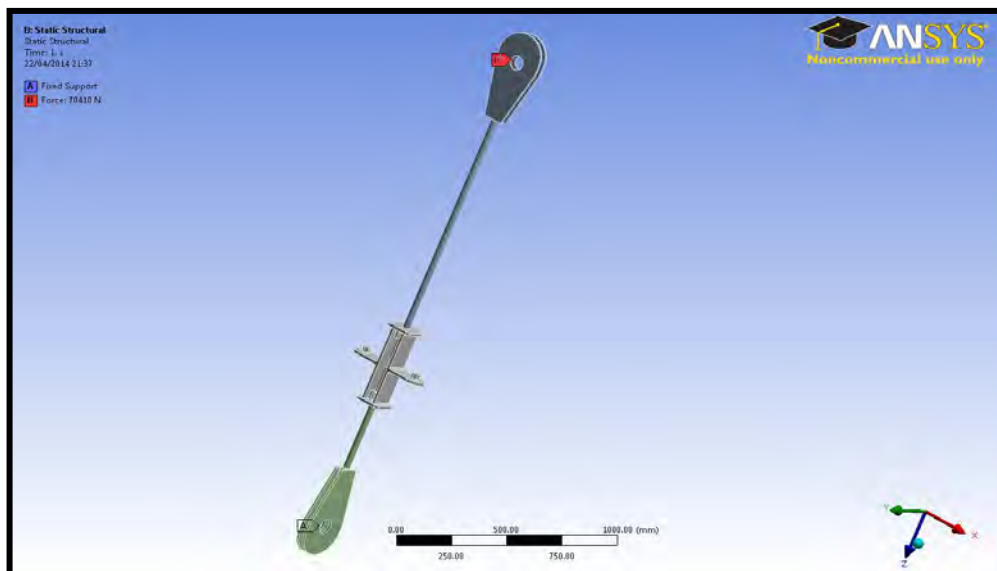


Figure 7.42 Boundary Conditions (Hand, 2014)

Figure 7.42 above shows the boundary conditions for the direct tensile axial load of 70.14kN on the top pin and other end has a fixed support. This is to recreate the largest calculated tensile load applied to the mechanism during operation.

7.5.5.2 Graphic Results

Equivalent Stress

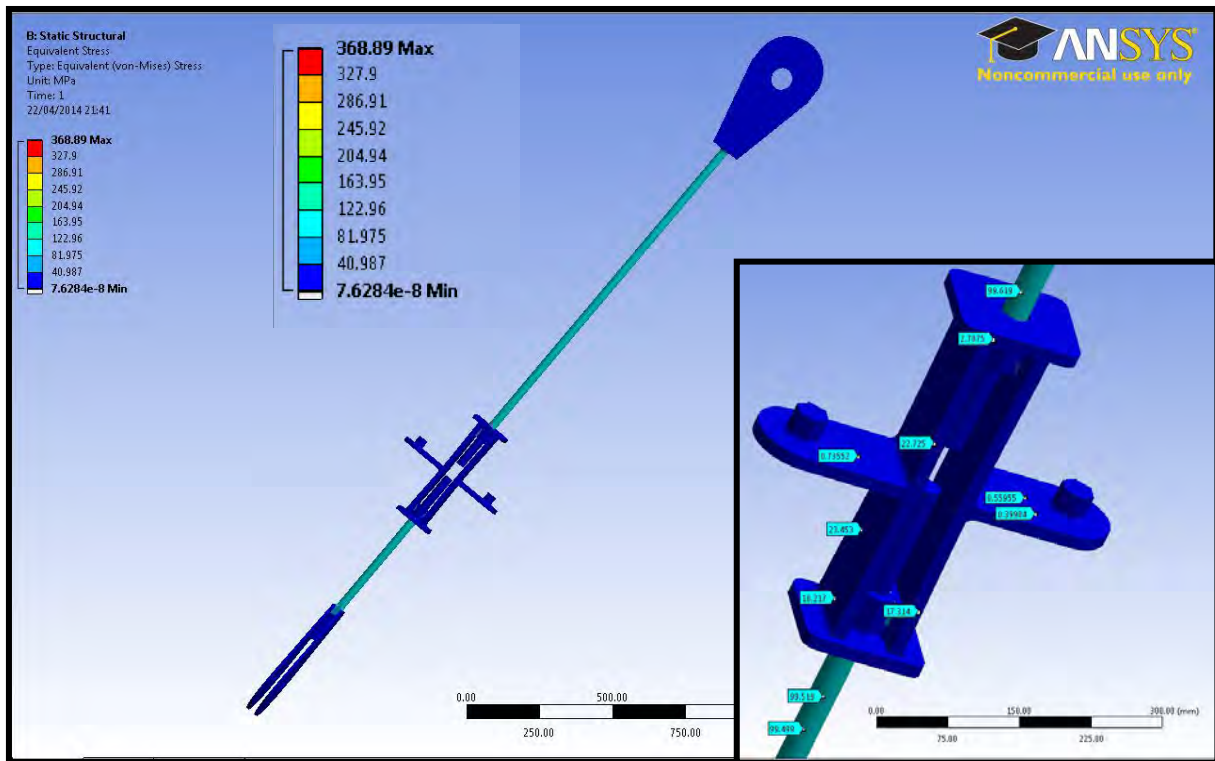


Figure 7.43 Equivalent Stress (MPa) (Hand, 2014)

Maximum Shear Stress

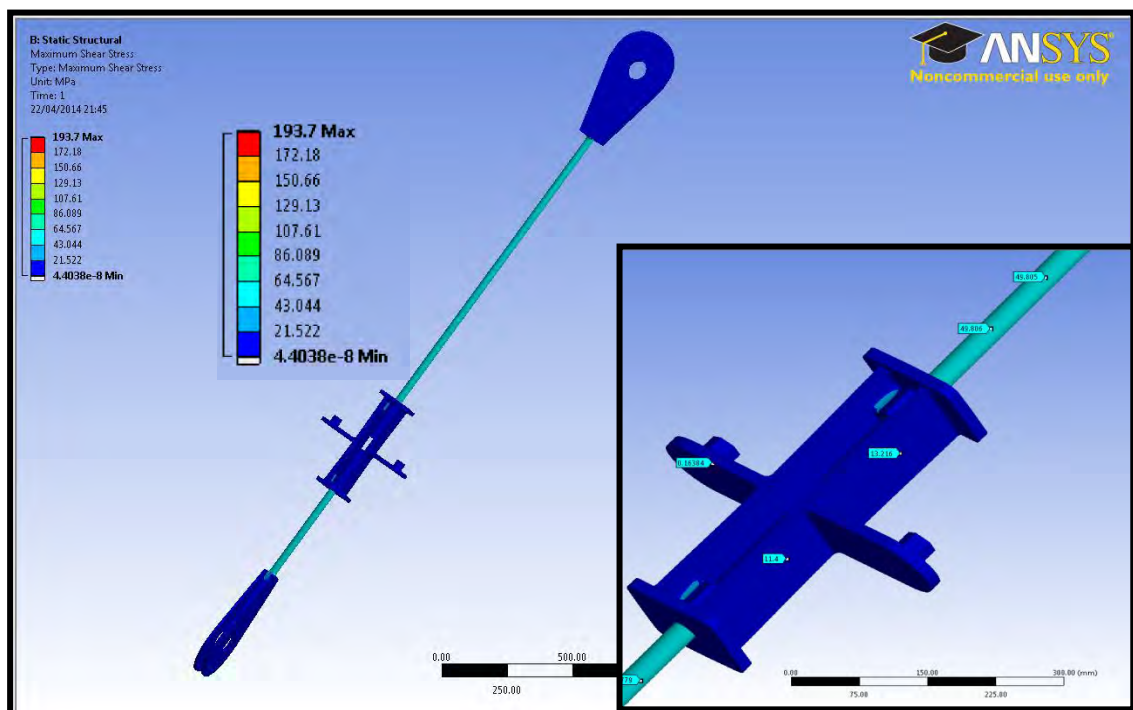


Figure 7.44 Maximum Shear Stress (MPa) (Hand, 2014)

Displacement

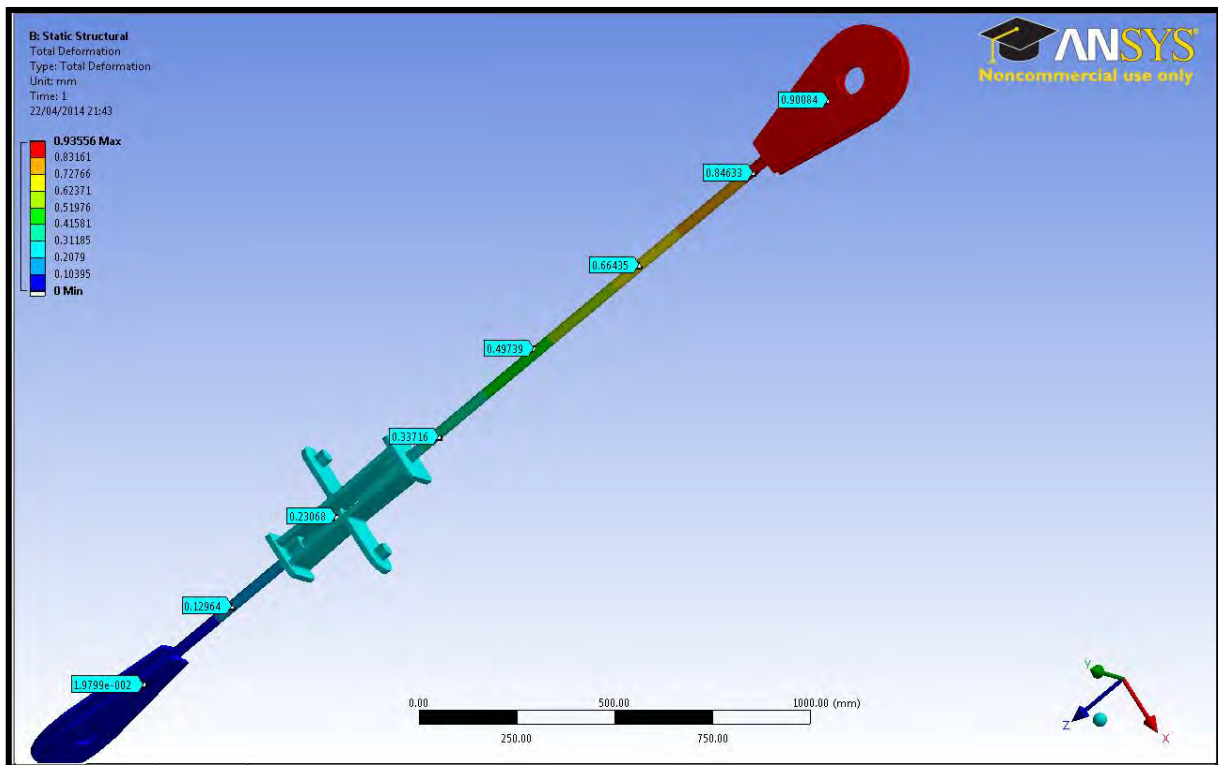


Figure 7.45 Displacement (mm) (Hand, 2014)

Table 7.4 Torque applied results (Hand, 2014)

Torque Applied			
Parameter	Equivalent Stress	Maximum Shear Stress	Displacement
Magnitude	87.98 MPa	50.796 MPa	2.709 mm
Location	Root of weld on torque wrench attachment area	Root of weld on torque wrench attachment area	Supporting plate for torque wrench fitting device

Table 7.5 Direct tensile load results (Hand, 2014)

Direct Tensile Load Applied			
Parameter	Equivalent Stress	Maximum Shear Stress	Displacement
Magnitude	96.619 MPa	49.806 MPa	0.9356 mm
Location	Tensile stress on bottom link shaft	Shear stress on bottom link shaft	Top link connection plates

It was determined from closely examining the results from the FEA analysis that all the stresses and displacements on the component were within the factor of safety region and that displacements were very low. To ensure these results were accurate a commonly used validation method was utilised for this purpose which is called photoelasticity testing.

7.6 Photoelasticity Testing

To validate the stress analysis conducted on this component using FEA it was now necessary to use a means of experimentally predicted the stresses in this component. A critical part of the redesigned tie-down system is the four bearing plates which are used to attach it to the structure of the crane and to the quay with two bearing plates on opposite ends. Therefore it was necessary to get an accurate representation of the stress on these parts of the design and the most applicable method was found to be a technique known as photoelasticity testing. Due to the bearing plates 2D shape but also curved geometry photo elasticity would provide most visually accurate results in comparison with other experimentally methodologies for the stress concentration in the part.

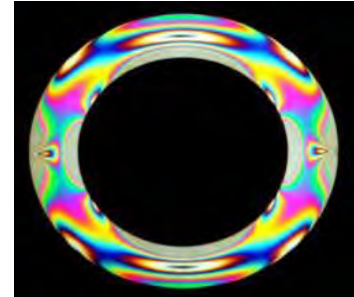


Figure 7.46 Photoelasticity (Wang,2008)

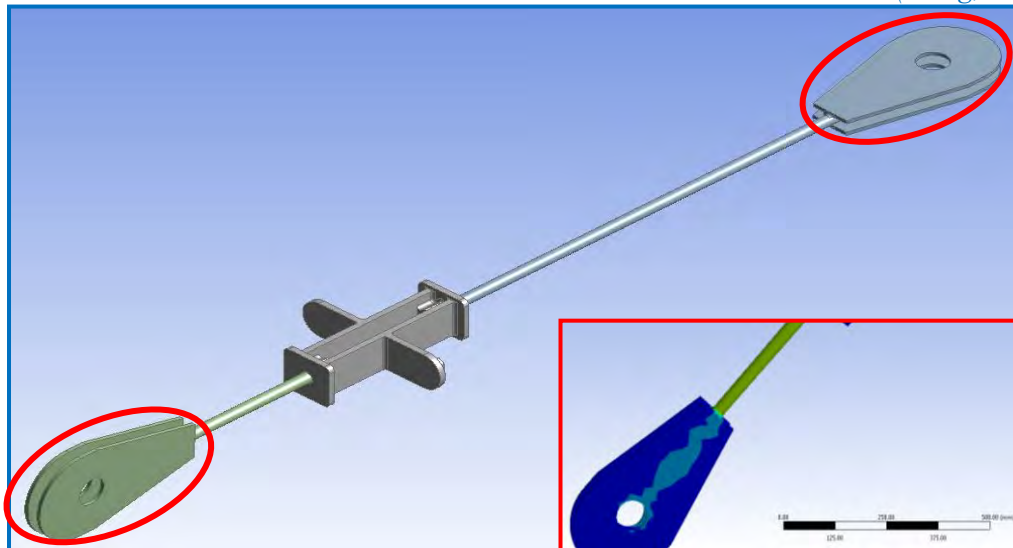


Figure 7.47 Critical sections (Hand, 2014)

Photoelasticity is an experimental technique used to determine the stress distribution in a part where common mathematical procedures can become tedious and unpredictable (Li, 2010). Photoelasticity gives a full picture of the stress distribution in a component unlike that possible with analytical calculations. One of the primary advantages of this method is that it is a full field measurement and allows the determination of the critical stress concentration points in a model and is very much suited to irregular shapes and geometries such as in this case (Phillips, 2006). The theory of photoelasticity is based on the occurrence of birefringence fringes in certain transparent materials. Birefringence is a property whereby a ray of light passing through a material causes two refractive light indices to occur, and when the material is stressed these fringes concentrate on areas of maximum stress (Li, 2010).

When a beam of light passes through a photoelastic material, the light is split into two principal stress directions and each experience diverse refractive indices (Dally & Riley, 1993). The variation in the refractive indices produces a phase retardation between the two component waves. The stress optic's law can be used to quantify the magnitude of the relative retardation of the waves with equation [7.22] (Uddanwadiker, 2011).

$$R = Ct(\sigma_1 - \sigma_2) \quad [7.22]$$

Where R is the induced retardation, C is the stress optic coefficient, t is the thickness and σ_1 & σ_2 are the first and second principle stresses (Uddanwadiker, 2011).

7.6.1 Circular Polariscopes

For the photoelastic testing the college Terco circular polariscopes were used as shown in figure 7.49. This polariscopes have a light source at the back of the unit which passes a light rays through a plane-polarising filter followed by a circular polarising filter. The light beams that emerge from the circular polarising filter pass through the model constrained in a loading device. Then the light rays pass through another circular polarising filter and then finally by a analyser screen. There are two light sources available one is a linear polarised light that shows stress fringes as black and white fringes, the other light source uses a monochromatic light to shows stress fringes in a rainbow pattern.

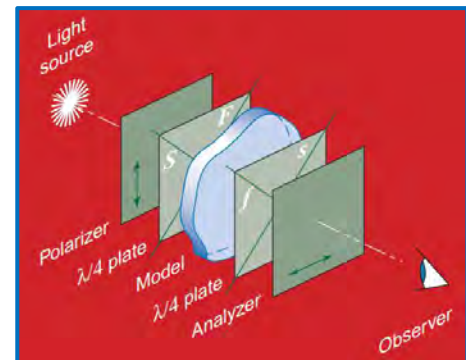
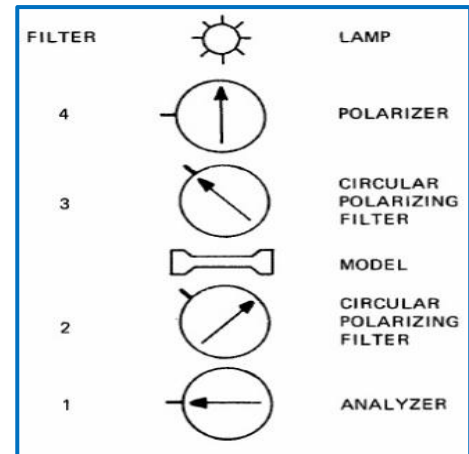


Figure 7.48 Circular Polariscopes (Phillips, 2006).



Figure 7.49 College circular polariscopes equipment (Hand, 2014)

Attached to the photoelastic rig is a cross member used for loading the model during testing which is equipped with a strain gauge and indicator to record the loads placed on the model and has a maximum load capacity of 600N (TERCO AB, 1977). The photoelastic rig filters was setup as shown in figure 7.50 and according to its manual specifications. The polarising filter and analyser filter were put the extreme left position. The two circular



polarising filters were placed at right angles to each other but also to create linear polarised light from the polariser it was necessary to have a 45° offset between the two circular polarising filters.

Figure 7.50 Polariscope filters set up (TERCO AB, 1977)

7.6.2 Calibration

Before any testing of the photoelastic model could be conducted it was necessary to determine the stress sensitivity (S) of the photoelastic material. This is essentially done to find the stress value per fringe for the material. The photoelastic material used for this testing was called PSM-1 which is a specially produced birefringent polycarbonate plastic from Vishay Micro Measurements (Data sheet Appendix page E-28 & E-29). A rectangular test piece was made from this material as shown below with a 6 mm hole on each end to allow it to be held in the photo elastic rig.



Figure 7.51 Calibration test piece (Hand, 2014)



Figure 7.52 Measuring test piece (Hand, 2014)

The following steps were taken to find the sensitivity of the material:

1. The cross section was measured at the hole location
2. The calibration piece was fixed to the photo elastic setup
3. Load was applied until the first fringe appeared
4. The load magnitude was recorded and steps 2-4 were repeated.
5. Carry out calibration test two times and compare values.

The stress sensitivity (S) can be calculated using equation [7.23]

$$S = \frac{\text{Load 2} - \text{Load 1}}{\text{CSA}} \quad [7.23]$$

The fringe concentration was taken near the holes where the cross section area (CSA) was:

$$\begin{aligned} \text{CSA} &= (L \times T) - (l \times t) \\ (0.021 \times 0.006) - (0.006 - 0.006) &= 9 \times 10^{-5} \text{m}^2 \end{aligned}$$

Sample Calculation

The first fringe was recorded at a load of 59.1N

$$S = \frac{59.1 - 0}{9 \times 10^{-5}} = 656,666.67 \text{ Pa} = 0.657 \text{ MPa}$$

Table 7.6 Calibration results for stress sensitivity (Hand, 2014)

<u>Measurement 1</u>			<u>Measurement 2</u>		
Fringe	Load(N)	Sensitivity (MPa)	Fringe	Load(N)	Sensitivity (MPa)
1	59.1	0.657	1	59.7	0.663
2	107.6	0.539	2	102.5	0.476
3	209.1	1.128	3	197.5	1.056
4	303.5	1.049	4	264.5	0.744
5	394.7	1.013	5	364	1.106
6	470	0.837	6	455.4	1.016
	Average	0.870		Average	0.843

Total Average S = 0.857 MPa per fringe

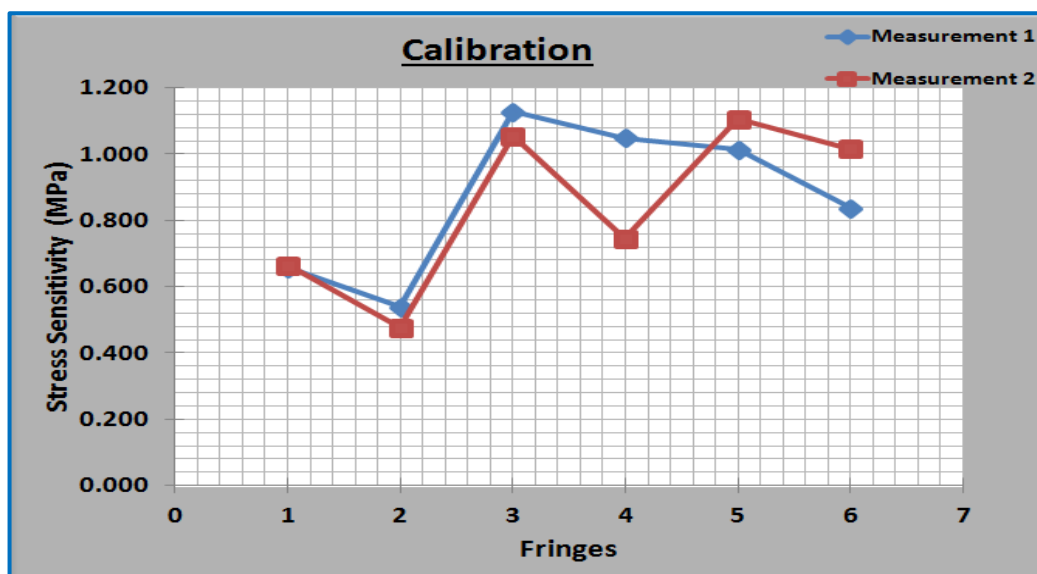


Figure 7.53 Calibration Measurements (Hand, 2014)

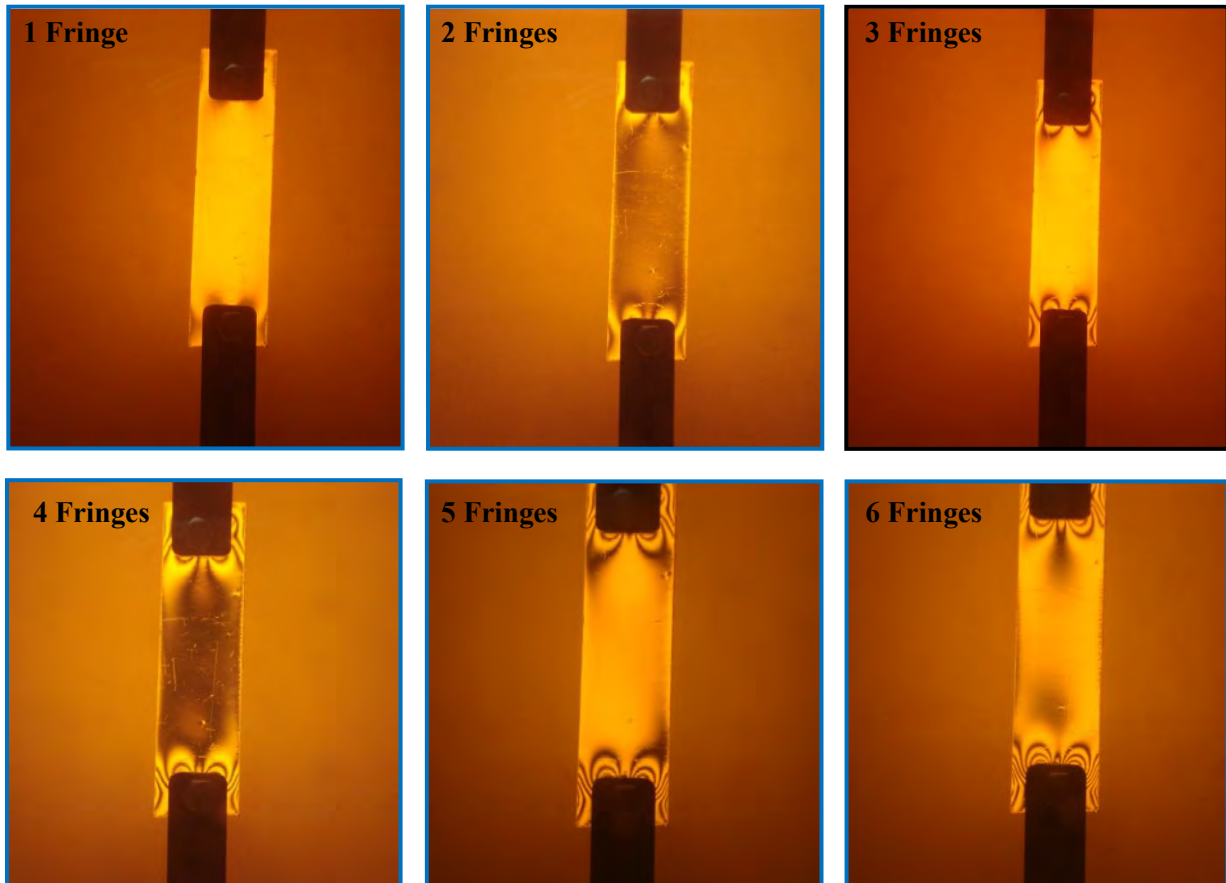


Figure 7.54 Calibration test piece fringe order (Hand, 2014)

7.6.3 The Test Piece

Figure 7.55 and figure 7.56 below show the physical and CNC represented test piece that was tested using the photoelasticity method. This test piece was produced by CNC machining the photoelastic material into the required shape as below (Appendix E page E-30 for CNC codes). The machining of the material was done using a high speed carbide router machining tool and light cuts were taken to avoid chipping of the material which can cause stress raisers in the material. Also sufficient coolant was used during machining operation to dissipate heat from the test piece and avoid the possibility of thermal stresses (residual stresses) being induced on the test piece especially along its edges.

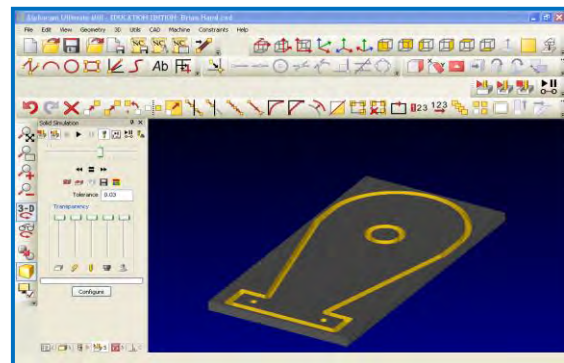


Figure 7.55 Machined Test piece (Hand, 2014) Figure 7.56 CNC created model (Hand, 2014)



Figure 7.57 College Hurco BMC 20 CNC Mill



Figure 7.58 Machining Test Piece

7.6.4 Test Piece Support Rig

This was a very important part of the experimental setup to design & create a rig to load and constrain the test piece in the same way as in the realistic manner. Also another design constraint was the support rig blocked as little of the polarised light as possible through the loaded test piece and had to be safe also. To secure the test piece to the floor of the photoelastic test rig, two 6 mm holes were designed into the test piece as shown in figure 7.59 and two rectangular plates secured it to the bottom support on the photoelastic rig. To ensure these holes did not disrupt the stress distribution in the test piece it was believed by the author that Saint Venant's principle would be effective here which states that *“The stresses and strains in a body at points that are sufficiently remote from points of application of load depends only on the static resultant of the loads and not on the distribution of loads”* (Whelan, 2010). As this is loaded in axial tension the point of load application is sufficiently far enough from the supporting bottom holes.



Figure 7.59 Bottom holes on model (Hand, 2014)



Figure 7.60 Test piece with supports (Hand, 2014)

To create the bearing load through the centre of the test piece, a reduced section of a shaft was machined and was locked together with two shackle plates. These two shackle plates had

the material removed from their centres which removed to allow the passage of light through the test piece.

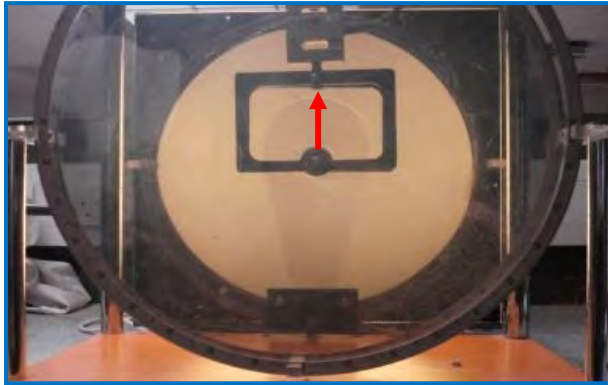


Figure 7.61 Test piece in photo elastic test rig

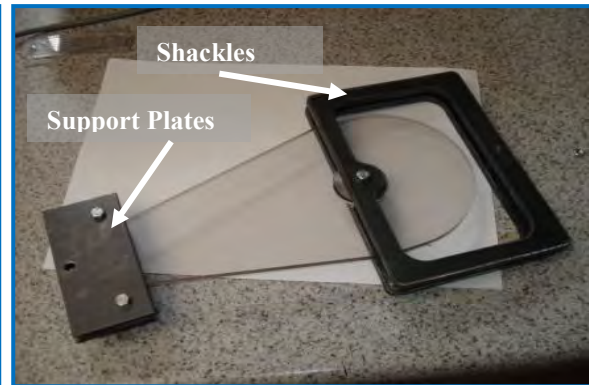


Figure 7.62 Support rig for test piece

For safety reasons it was necessary to establish a factor of safety for this testing. Examining the test piece it was established that the two fixed holes on the bottom of the test piece would be first to yield if too much load was placed on the test piece. Therefore a high factor of safety of 4 was placed on the testing procedure for extra safety considerations. From this it could be determined what the maximum load applied could be.

$$F = \sigma A$$

Failure would occur in direct shear at the bolt connections at the bottom of the test piece.

Yield strength of polycarbonate = 59 MPa (CES, 2014)

Area = 2A (two bolts holding test piece) = 2 (0.006 × 0.006) = 72 × 10⁻⁶ m²

$$F = \frac{59 \times 10^6}{4} (72 \times 10^{-6}) = 1,062 \text{ N}$$

Maximum design load is well over the rig's maximum load (600N) with a FOS of 4.

7.6.5 Test Procedure

- The test piece was placed in the photoelastic test rig and the load cell was calibrated by placing a mass and on it and the indicator gave the same reading.
- It was ensured that the test piece was under no stress from the support rig or apparatus as shown in figure 7.63.
- Carefully apply a load to the test piece by twisting the adjustment knob on the top of the cross beam
- Examine the test piece for stresses and record the load per additional fringe.
- Compare these results with FEA analysis on the same test piece.

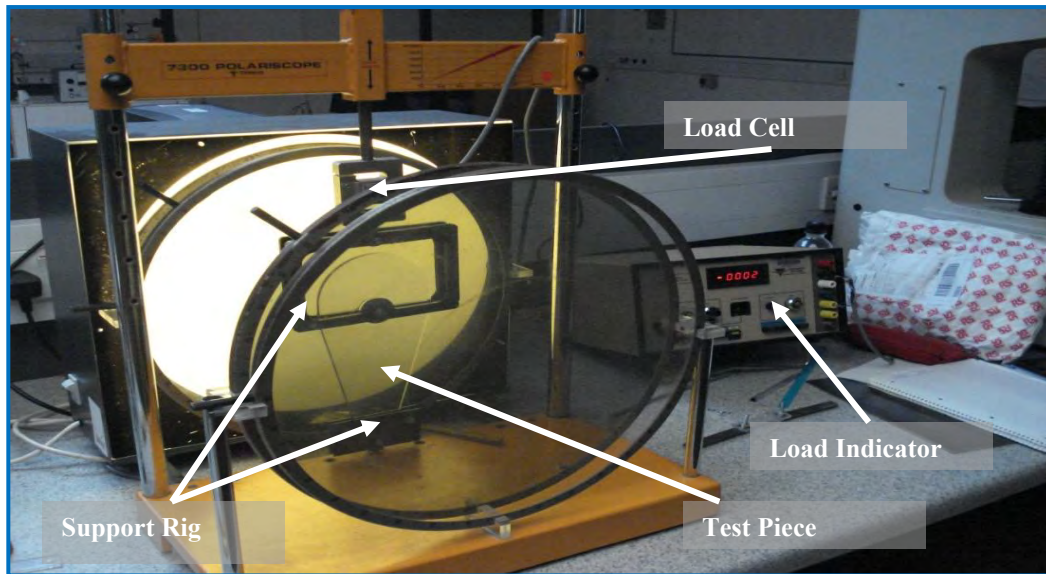
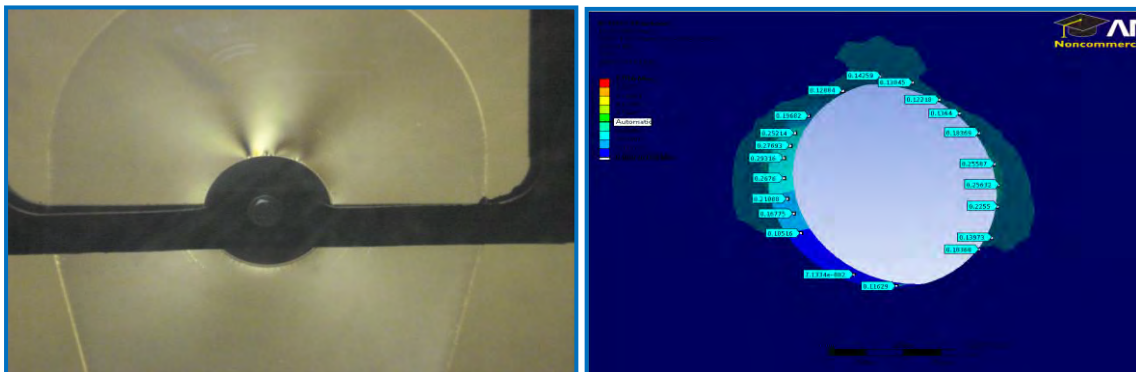


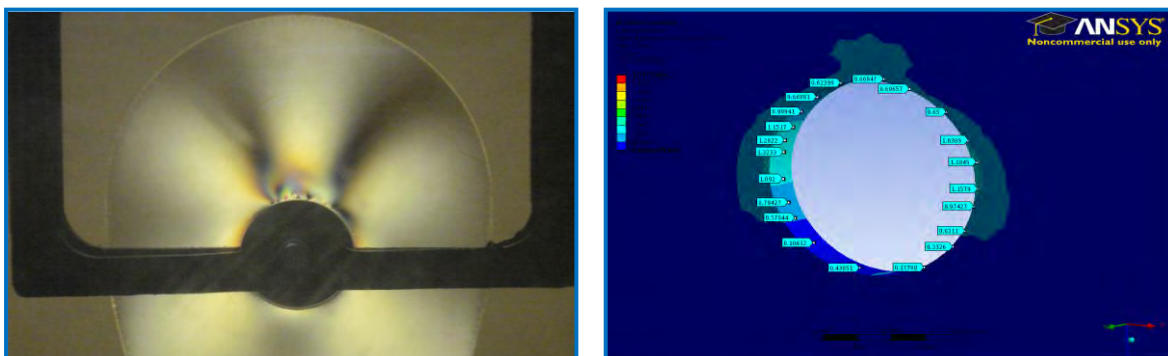
Figure 7.63 Testing Setup

The stress concentration was mostly concentrated around the hole in the test piece and the stress fringes were found to be starting from this location. The load was recorded for a stress fringe in the test piece and using finite element analysis software through ANSYS Workbench these same loads were applied to the same model to allow for a comparison.

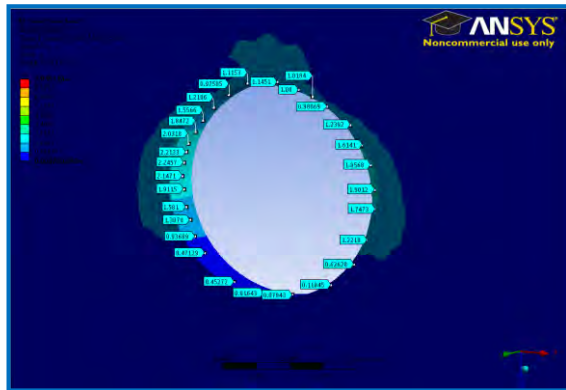
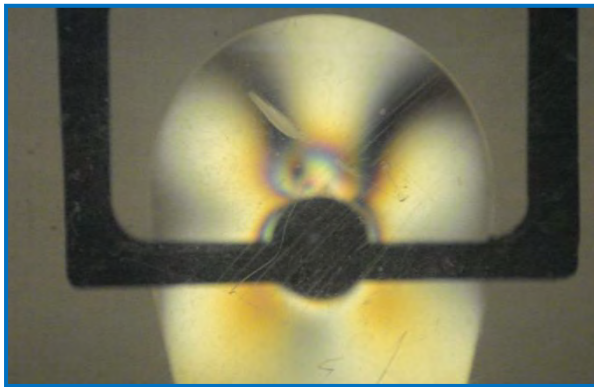
1 Fringe 30.3N Load



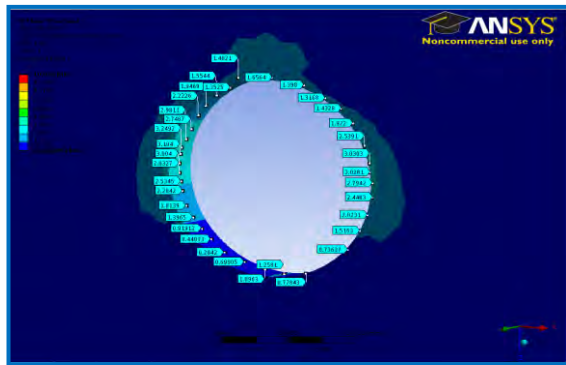
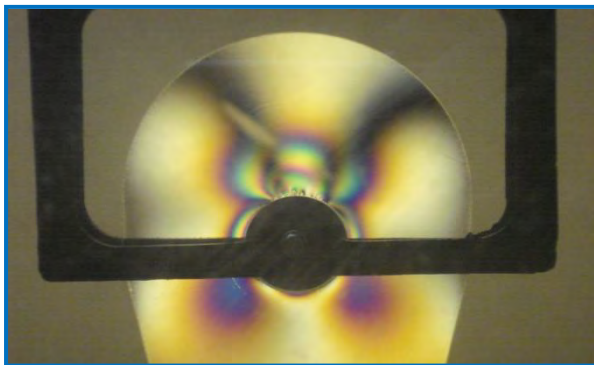
2 Fringes 138.3N Load



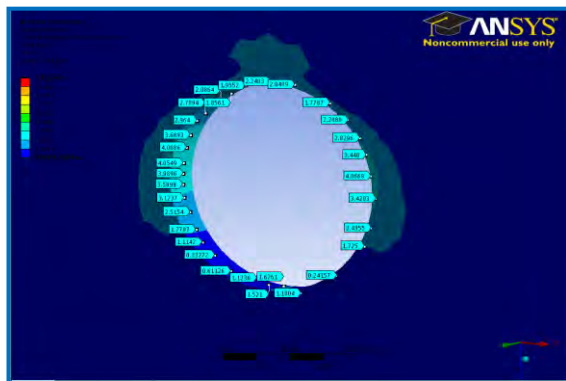
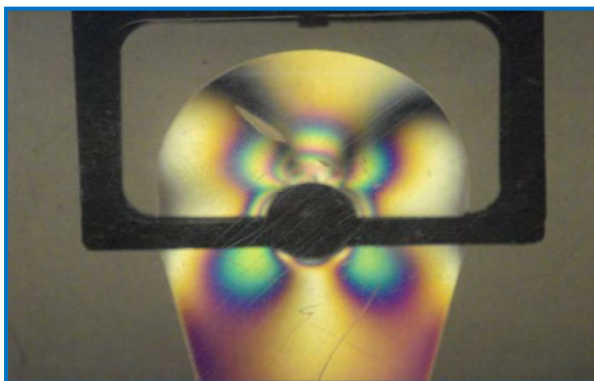
3 Fringes 234N Load



4 Fringes 326.4N Load



5 Fringes 436N Load



6 Fringes 562.3N Load

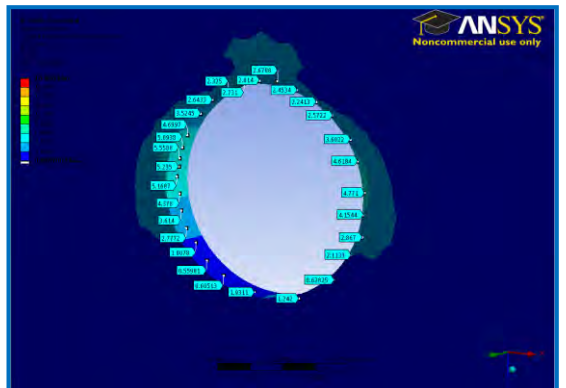
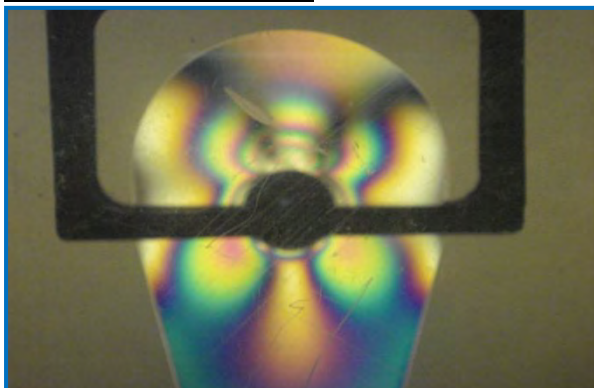


Table 7.7 Results of FEA and photoelasticity validation (Hand, 2014)

Load Applied (N)	Fringes	Maximum Stress (Fringes × Material Sensitivity) (MPa)	Maximum Stress of polycarbonate (FEA) (MPa)	Deflection (mm)
30.3	1	0.857	0.276	0.009
138.3	2	1.714	1.323	0.041
234	3	2.571	2.245	0.069
326.4	4	3.427	3.249	0.097
436	5	4.284	4.089	0.130
562.3	6	5.141	5.552	0.168

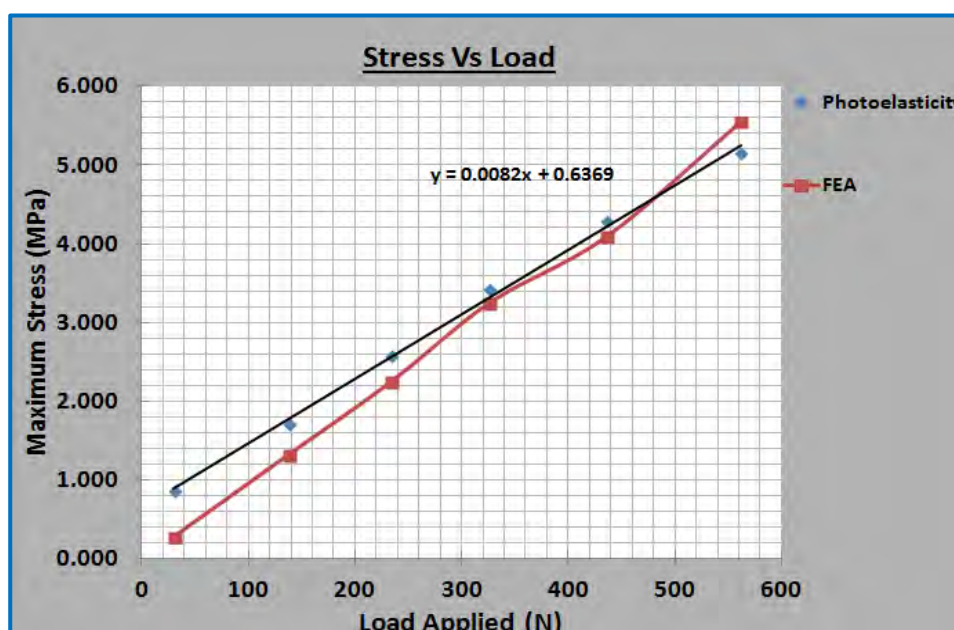


Figure 7.64 Graphical comparison of FEA and photoelasticity results (Hand, 2014)

Examining the results both from the FEA and the photoelasticity testing they show a good correlation each other especially shown in figure 7.65 below. This field experimental testing shows a very good association with the computer generated stress model and has put a large degree of trust in its accuracy. Examining the graph above it shows the maximum stress at higher magnitudes shows a higher degree of correlation; this is to be anticipated as the photoelastic material sensitivity effects increase with low levels.

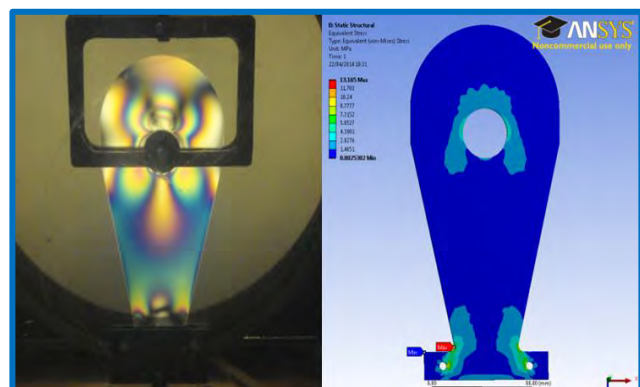


Figure 7.65 Graphic comparison of results

7.6.6 Photoelasticity FEA

This short section outlines the FEA model that was generated to compare with the photoelastic test piece results. To ensure an accurate model was generated close attention was paid to the mesh quality parameters when making the mesh more. As can be seen in the table below these parameters increased in quality. In similarity with the CFD method inflation layers were also utilised here as shown below to improve mesh quality.

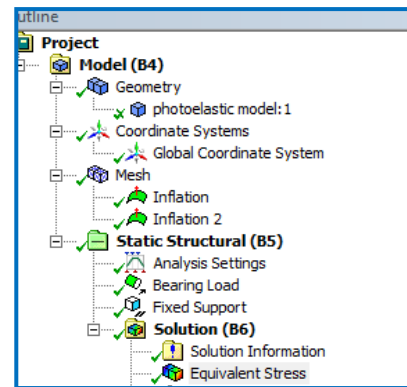


Figure 7.66 FEA parameters

Table 7.8 FEA mesh parameters (Hand, 2014)

Mesh Relevance	Elements	Nodes	Max Stress (MPa)	Average Aspect ratio	Average Skewness	Average Orthogonal
Coarse	165	1344	18.856	9.192	0.432	0.882
Medium	510	3909	14.561	3.001	0.31	0.764
Fine	2282	13413	14.161	1.733	0.158	0.968
Inflation	7069	22982	13.165	1.414	0.159	0.963

Note: Results were taken at highest load and max stress occurred at fixed locations, not at load applied location.

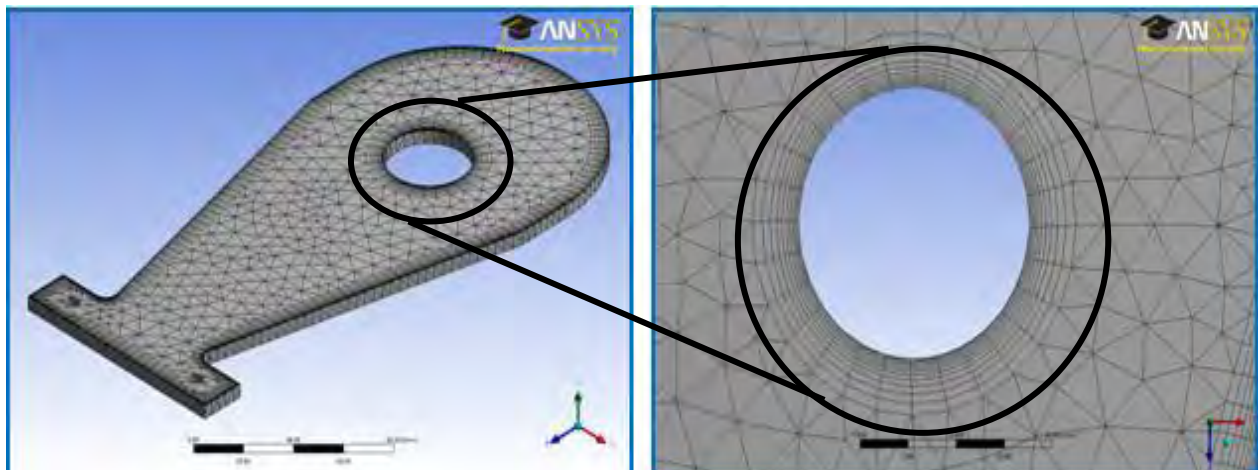


Figure 7.67 Mesh Inflation layers (Hand, 2014)

In figure 7.68 below the FEA plot of stress and the visual photoelasticity image show a good representation of where material is under low stress in comparison with the rest of the model. This noticeable in the photoelastic image where clear portions are present as clearly depicted in figure 7.68.

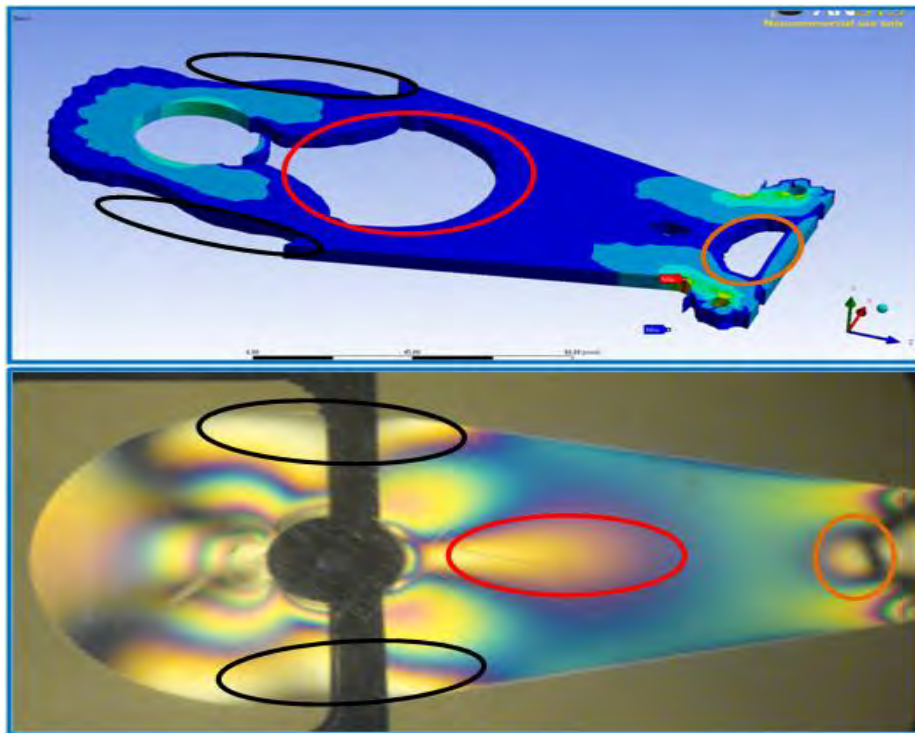


Figure 7.68 Material under low stress (Hand, 2014)

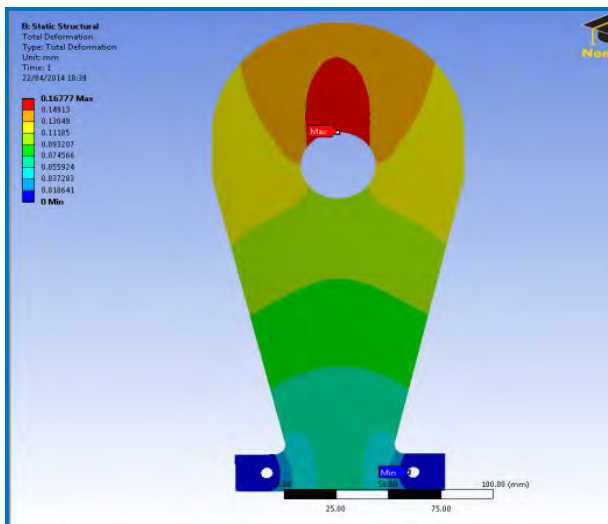


Figure 7.69 Deformation (mm)

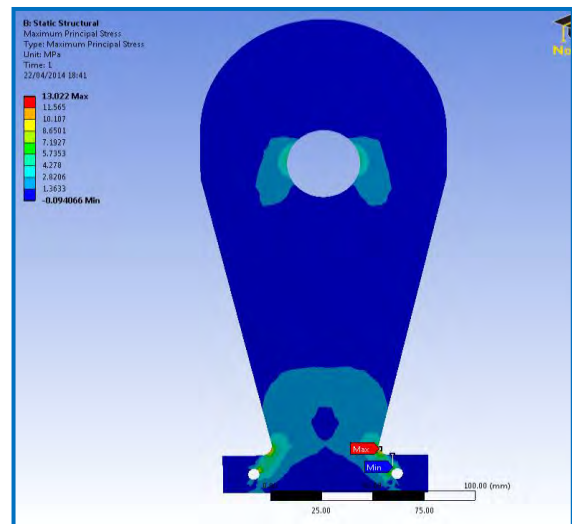


Figure 7.70 Max principal stress (Pa)

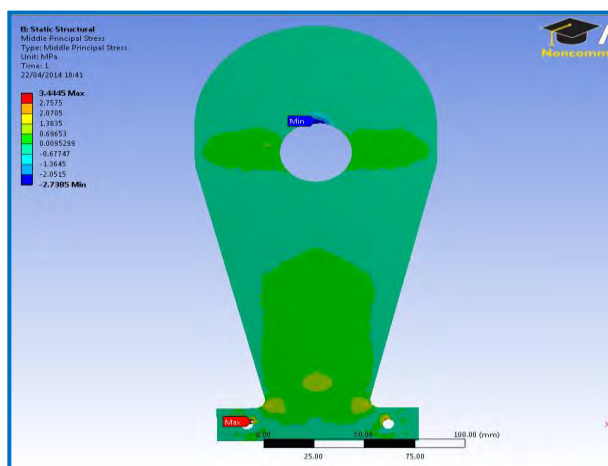


Figure 7.71 Middle principal stress (Pa)

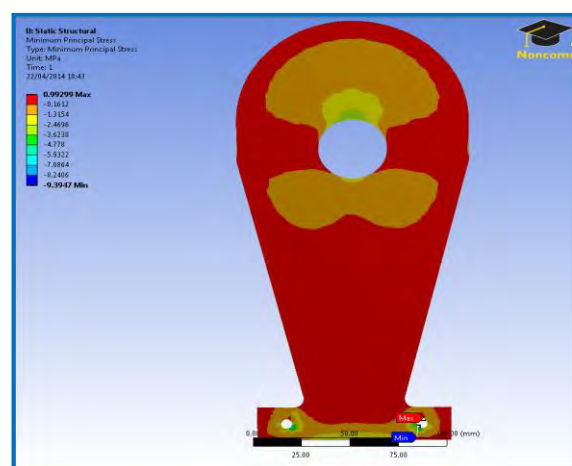


Figure 7.72 Minimum principal stress (Pa)

7.6.7 Hazard Analysis for Photoelasticity Testing

Risk Assessment											
											Taken in Accordance with EN ISO 14121-1:2007
RA #	Action	Hazard	Lo	Fe	DPH	NPR	HRN	Risk	Control	HRN with control	Risk with control
1	Setting up of Equipment	Equipment is set up incorrectly	1	1.5	0.5	1	0.75	Low	Ensure equipment is set up correctly by having a technician supervise and ensure to be fully alert.	0.5	Negligible
2	Electrical Equipment	Faults in electronic equipment, not earthed properly	2	1.5	8	1	24	Significant	Ensure all electronic equipment is operating properly before use and check with supervisor before use	0.5	Negligible
3	Adjusting of test piece	Cuts from sharp edges/ crushing of fingers	2	2	0.5	1	2	Low	Remove burrs on manufactured pieces, ensure machine is stopped	0.5	Negligible
4	Test piece failing in rig	Material hitting user	1	1.5	1	1	1.5	low	Establish a FOS and any faults with design or equipment	0.5	Negligible
5	Excessive heat from lamp	Heat burns to user	1	1.5	2	1	3	Low	Ensure guard around light source is in place	0.5	Negligible
7	Tempering with/fault in machine	Electrocution/burns	1	1.5	8	1	12	Significant	Have supervision using test equipment/ report faults	1	Low
8	Inexperienced user	Incorrect use of machine cause of injuries to user	1	1.5	1	1	1.5	Low	Ask experienced persons	1	Low

7.7 Prototype Testing

Having conducted extensive FEA and experimental analysis it was now suitable to manufacture a prototype of the purposed redesigned tie-down system and examine its performance and functionality. It was necessary to examine how well the design functioned in reality and compare these results with hand calculations. This meant that the tensile force generated by the design had to be experimentally measured using some type of transducer or equipment. The following gives an account of the different sensors that were considered to achieve this.

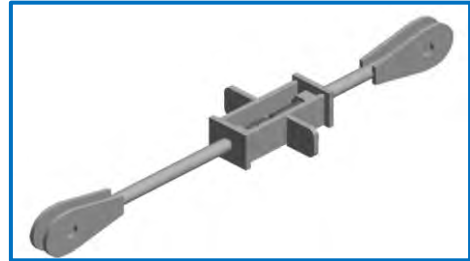


Figure 7.73 Prototype (Hand, 2014)

7.7.1 Force Measurement

Load Cell

A load cell is a direct measuring force transducer and many types exist such as strain gauged load cells, hydraulic load cells, pneumatic load cells and piezoelectric load cells. The most used is the wire based strain gauge. This type of strain gauge converts the load generated in a member into an electrical resistance that can be data logged and processed (Omega, 1999). There are many different variations of strain gauges available including linear gauges, Tee gauges, and rosette strain gauges. The different variations allows strains to be measured in different directions which is necessary in some applications.

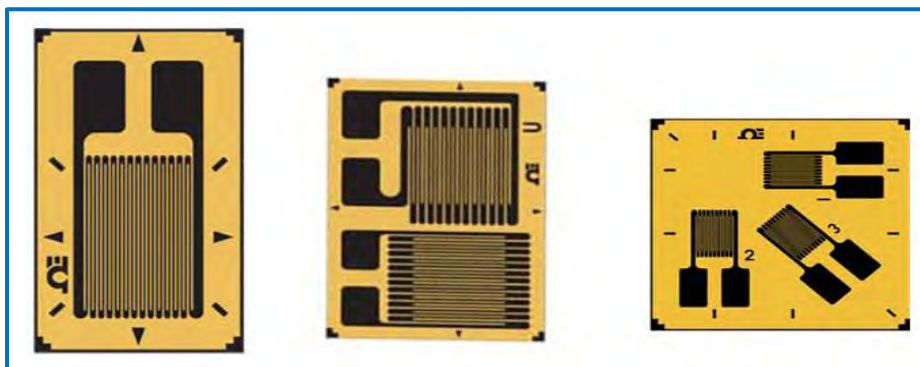


Figure 7.74 Linear, Tee and rosette strain gauges (Omega, 1999).

The bonded strain gauge consists of a metallic foil organised in a grid pattern which deforms when the component or part is stress causing the metallic wires to become strained. These strains create a small voltage which can be amplified and converted into a force reading (NI, 2014).

Linear Variable Differential Transducer (LVDT)

An LVDT is electromechanical transducer which converts linear motion of an object into a corresponding electrical signal (Macro Sensors, 2014). Figure 7.75 below shows the primary components of a LVDT.

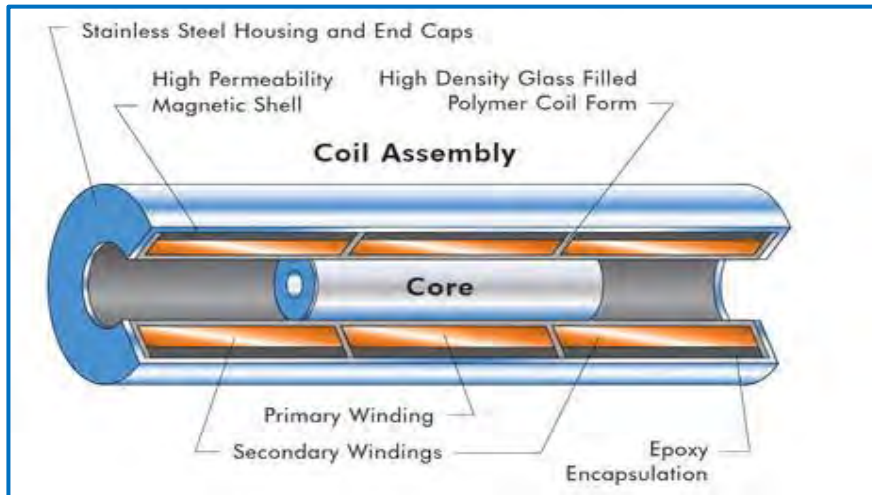


Figure 7.75 Components of an LVDT (Macro Sensors, 2014)

The LVDT works using 3 coils, a primary coil and two secondary coils. The transfer of current between the primary and the secondary coils of the LVDT is controlled by the position of a magnetic core called the armature. As the LVDT's armature moves away from the centre, the result is an increase in one of the position sensor secondary coils and a decrease in the other, this results in an output from the measurement sensor. The main advantage of this sensor is clean precise data, infinite resolution and long life (RDP, 2009). The change in distance voltage measured can be manipulated into a corresponding force reading.

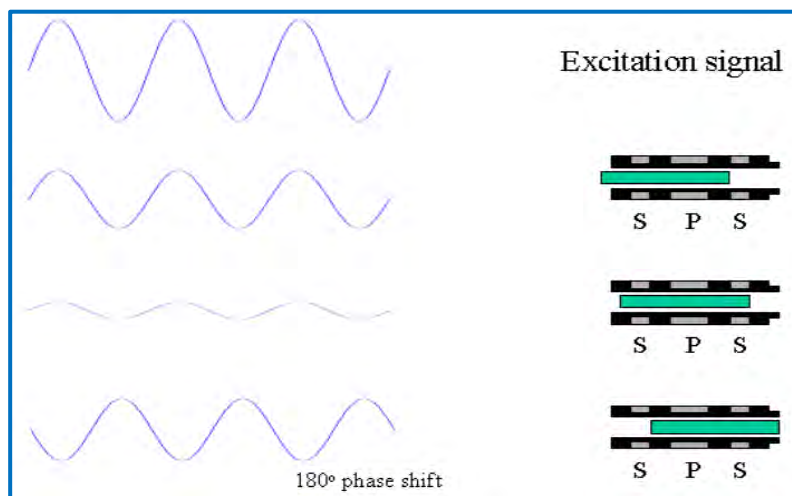


Figure 7.76 The effect of core position the excitation signal (Dally et al, 1993)

Both strain gauges and an LVDT were the two main types of transducers mainly considered for the force measurement in this testing of the prototype. It was found that strain gauges would be applicable to this testing as they could be easily located in areas of interest on the prototype rather than an LVDT which is much larger in dimension and also a number of strain gauges could be used to give a better insight into the forces generated. Both the strain gauges and the LVDT have around the same resolution but the LVDT would be more difficult to position near a body that moves at the rate as the rest of the prototype. Cost also was significant factor and LVDTs are considerable more expensive than strain gauges. Weighting up the positives and negatives of both transducers it was determined that strain gauges would be most suited to this application.

7.7.2 Prototype Manufacture

Figure 7.77 below shows a picture of the completed testing prototype that was manufactured at the CIT workshops. Due to the large dimension of the redesigned tie-down created it was



Figure 7.77 Prototype at Engineering Exhibition (Hand, 2014)

necessary to scale down the dimensions in order to manufacture a prototype of proposed redesigned system. This was also done because of the availability of suitable materials in the mechanical stores. The sizes of shafts used in the tie-down links were reduced from 30mm to 20mm and their lengths reduced overall to facilitate testing of the prototype. All other parts of the prototype were scaled accordingly to ensure an accurate representation was got. The following page shows some of the manufacturing stages of the prototype.



Figure 7.78 Top link and bearing plates (Hand, 2014)



Figure 7.79 Turnbuckle (Hand, 2014)

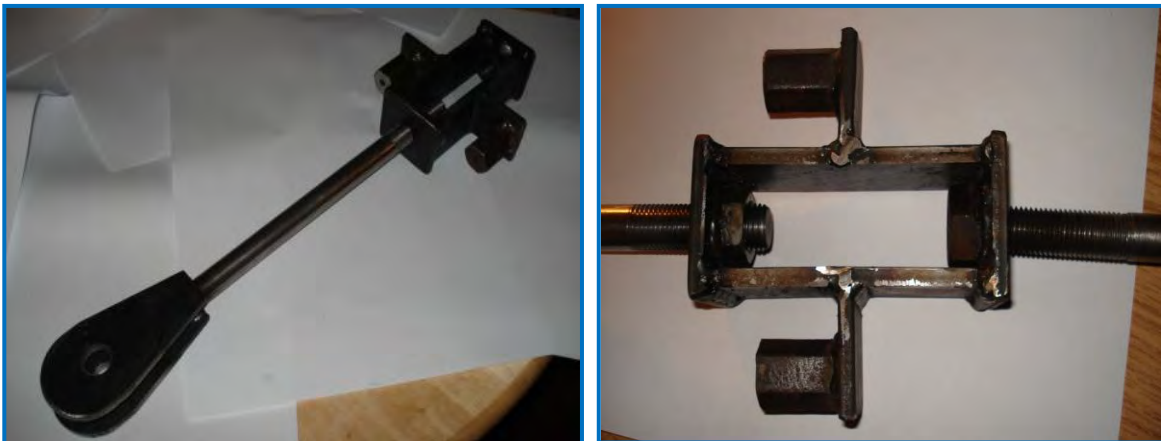


Figure 7.80 Top link inserted in turnbuckle (Hand, 2014)

Having completed manufacturing the prototype the next step was to add the strain gauges to the prototype in strategic locations to accurately measure the generated tensile force which was chosen to be the ends of the shafts. The type of strain gauges used for this testing were linear strain gauges with the following specifications as shown below in table 7.9 . An important parameter of the strain gauges is their sensitivity to strain which is referred to as the gauge factor (GF). The gauge factor is classified as the change in electrical resistance to the fractional change in length and is expressed in equation [7.24] (NI, 2014).

$$GF = \frac{\frac{\Delta R}{R}}{\frac{\Delta L}{L}} \quad (NI, 2014). \quad [7.24]$$

Table 7.9 Strain gauge specifications

Supplier	Radionics
Gauge Factor	2.1
Gauge Length	5mm
Gauge Resistance	120Ω
Length	9.5mm
Width	3.5mm

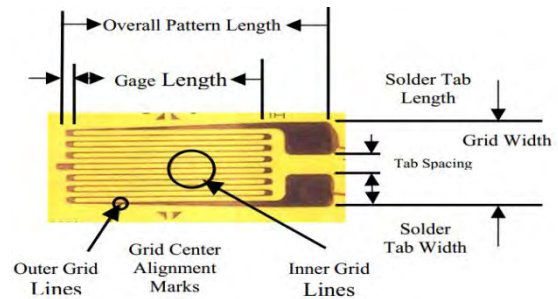
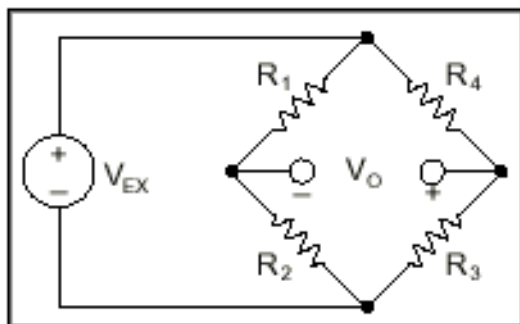


Figure 7.81 Parts of strain gauge (Dally et al, 1993)

The wiring and application of the strain gauges is based on the Wheatstone bridge theory as presented below in figure 7.82. A voltage is passed through the bridge and any change in the resistance of one of the four resistors (R1, R2 R3, and R4) will cause a change in the return voltage in proportion to the change in the resistance. The output voltage V_o is equal to,



$$V_o = \left[\frac{R_3}{R_3+R_4} - \frac{R_2}{R_1+R_2} \right] V_{EX} \quad [7.25]$$

Figure 7.82 Wheatstone bridge (NI, 2014).

In most cases one strain gauge is entered into the circuit in parallel replacing R4 in figure 7.82. This method of gauging is referred to as a quarter bridge circuit and is represented below in figure 7.83.

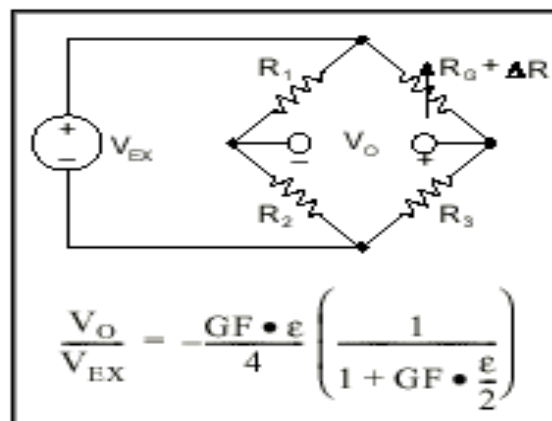


Figure 7.83 Quarter bridge circuit (NI, 2014).

In some cases to improve the gauges sensitivity the quarter bridge circuit can be changed by adding another strain gauge to record the tension and the compression force of the member and replacing R3 in figure 7.84. The measured resistance will then be an average of the two recorded values from the gauges, therefore improving the resolution of the measurement. This strain gauge configuration is known as half bridge circuit and is displayed in figure 7.83 below.

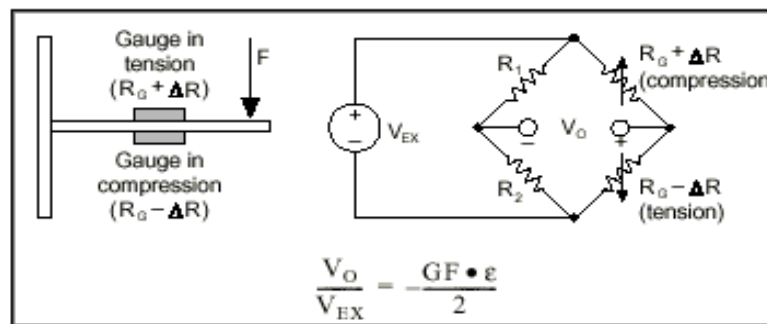


Figure 7.84 Half bridge setup (NI, 2014).

For the purpose of this testing the quarter bridge circuit will be used as shown in figure 7.83. Before any of the strain gauges could be bonded to the steel surface of the prototype it was necessary to carry out preparation measures beforehand.

- Firstly where the strain gauges were being bonded to the surface acetone was used to remove any residues or contaminants such as grease or oil.
- Then using fine sand paper (400 grit) the surface was smoothed down to smooth finish.
- Using a pencil and ruler the positions of the gauges were determined.
- Using specialised cyanoacrylate adhesive the gauges were carefully bonded to the surface of the shaft and special attention was taken to make sure the gauges were aligned properly.

A total of eight strain gauges were bonded to both the shafts, four gauges were placed on each shaft with the orientation shown below in figure 7.85 on each side of the shaft.



Figure 7.85 Strain gauge orientation (L) & Lateral orientated strain gauge (R) (Hand, 2014)

Signal and receiver wires for the data logging system were then soldered on to strain gauges tabs as shown in figure 7.85. These wires transfer the resistance readings from the gauges to the data logger which converts the readings to strain. Two receiver wires are used to increase accuracy and for simplicity the signal and receiver wires were colour coded red and blue respectively as displayed in figure 7.86. Each cable was taped into place to prevent damage during movement. The wires were connected to plastic connectors (figure 7.86) that plugged into the data logger. These connectors are designed for signal cables used in telecommunications.

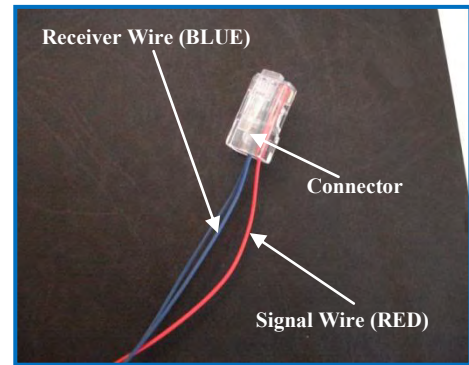


Figure 7.86 Data logger connector

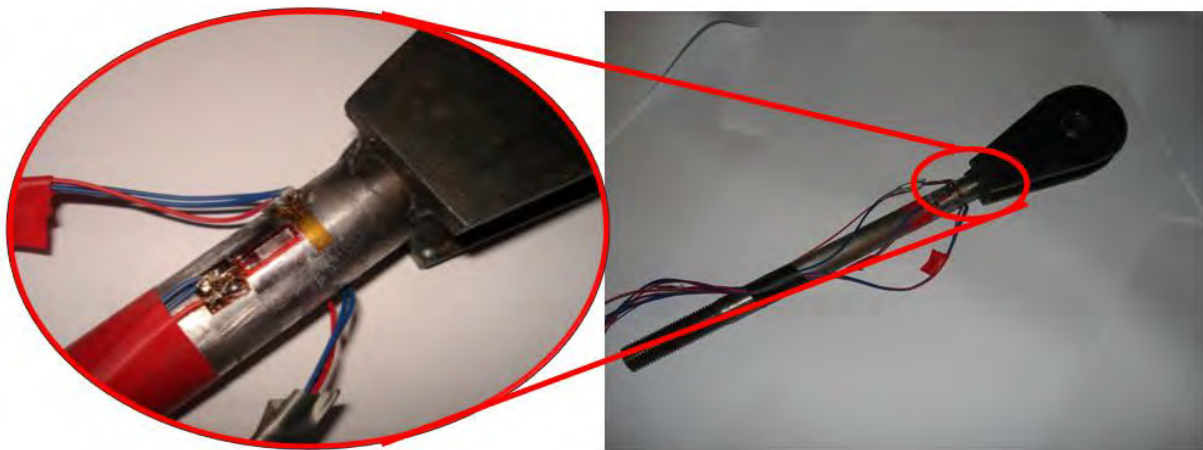


Figure 7.87 Strain gauge position

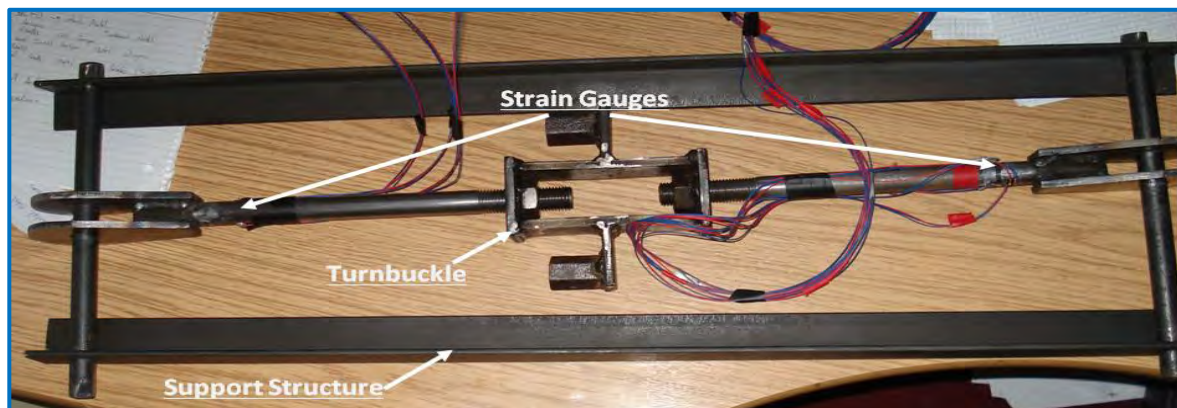


Figure 7.88 Locations of strain gauges

Figure 7.87 and figure 7.88 above shows where the strain gauges were attached to the prototype for testing. The next important consideration was that a rigid frame or structure had to be made in order to test the prototype and put in under a tensile load. Shown in figure 7.88 above and figure 7.89 below was a purposed rigid frame that would achieve this. It consisted

of two rigid angle sections of equal length constrained together with two shafts that would act as stiff supports for the tie-down during testing.

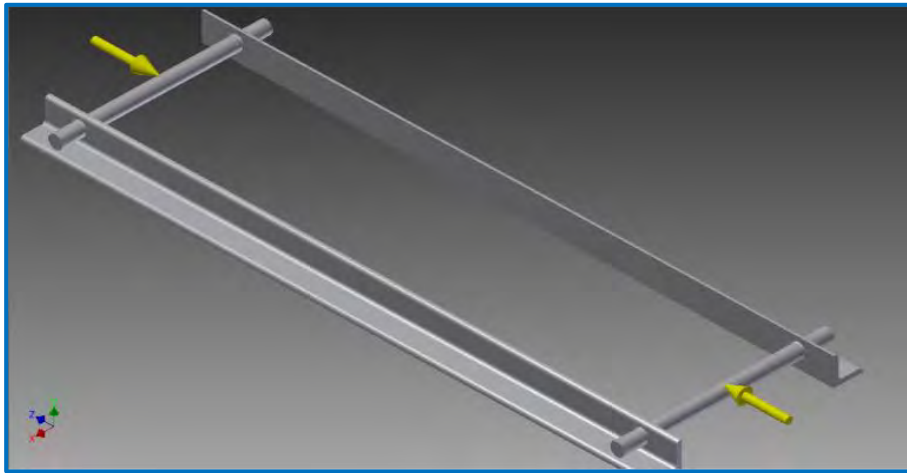


Figure 7.89 Rigid support frame (Hand, 2014)

To ensure the frame was safe for testing and an adequate factor of safety was upheld, appropriate FEA analysis was conducted to ensure that stress limits were within acceptable values.

Table 7.10 Results for Finite element analysis

FEA			
Tensile load (N)	Von Mises Stress (MPa)	Displacement (mm)	FOS
2500	26.3	0.063	5.9
5000	72.4	0.124	3.8
7500	101.1	0.186	2.86
10000	144.3	0.255	2.2

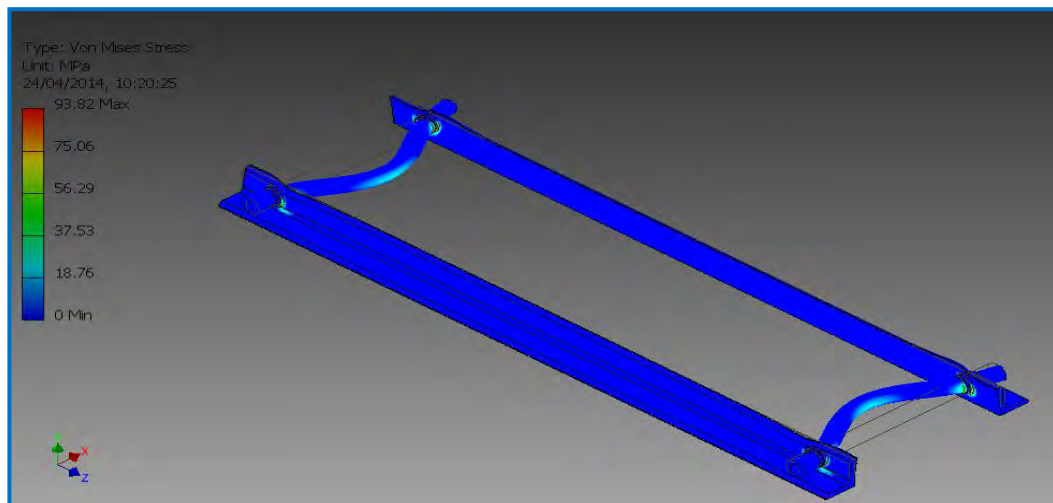


Figure 7.90 Working Stress (MPa) (Hand, 2014)

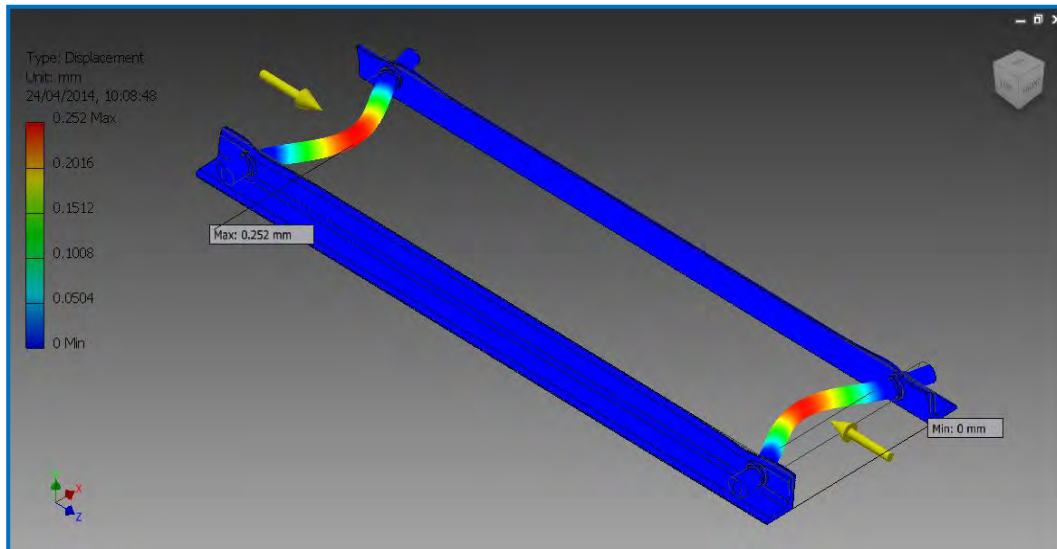


Figure 7.91 Displacement (mm) (Hand, 2014)

7.7.3 Prototype Testing

7.7.3.1 Data Management System

The Vishay Micro-Measurement System 7000 (figure 7.92) that was kindly loaned from the CIT Department of Structural Engineering was used to measure and interpret the data from the strain gauges in the testing of the prototype. All the data was measured and monitored using compatible software with the system 7000 called “*Strain Smart*” which ensures the highest accuracy and data traceability. The use of this system is



Figure 7.92 Vishay System 7000

important as the measurement from strain gauges involve sensing very small changes in resistance and therefore the best choice of signal conditioning and data acquisition is critical for reliable results (NI, 2014). This system amplifies the output of the strain gauges which can be in region of less than 10mV/V. For example with a 10V excitation the output signal becomes 100mV which improves measurement resolution and also the signal-to-noise ratio (Vishay, 2011). This data acquisition module also encompasses filtering apparatus in the form of lowpass filters which can remove high frequency noise mainly caused by electromagnetic waves from other electrical equipment. The system 7000 also includes a shunt calibration procedure before taking readings from the strain gauges; this procedure verifies the output of a strain gauge reading to some predefined mechanical input or strain (Vishay, 2011). This is primary done to reduce span errors for the entire measuring time period and verify the setup.

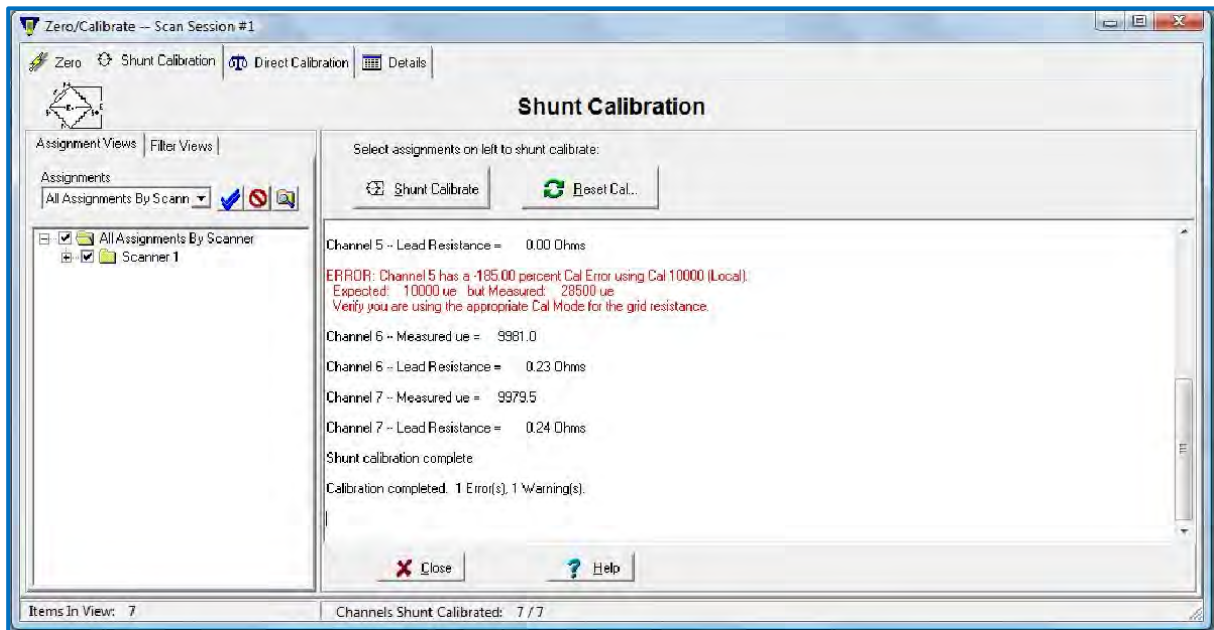


Figure 7.93 Shunt Calibration procedure in *Strain Smart* software

7.7.3.2 Test Procedure

Firstly for safety reasons a hazard analysis was conducted on the testing procedure to ensure all safety regulations were fulfilled. It was necessary to constrain the frame and prototype onto a firm lab bench before any testing could commence to ensure it did not move during the testing procedure, this was achieved by using G-clamps to apply a suitable force constrain it to a laboratory bench. To start with, the strain gauge connectors were attached to the System 7000 data acquisition model.

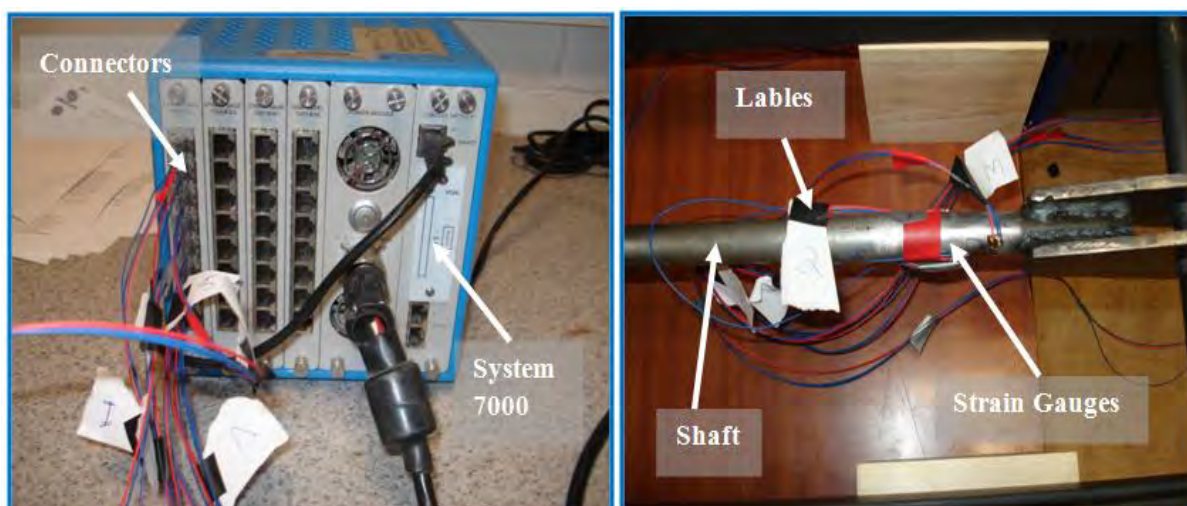


Figure 7.94 Strain Gauges connected to System 7000 (Hand, 2014)

The data logger was connected to a laptop and a shunt calibration procedure was initiated (figure 7.95) and it was determined that one of the gauges was faulty. The bonding of the strain gauge to the shaft and its connector were examined and calibration was conducted again, unfortunately the problem with the gauge could not be rectified and the test continued.

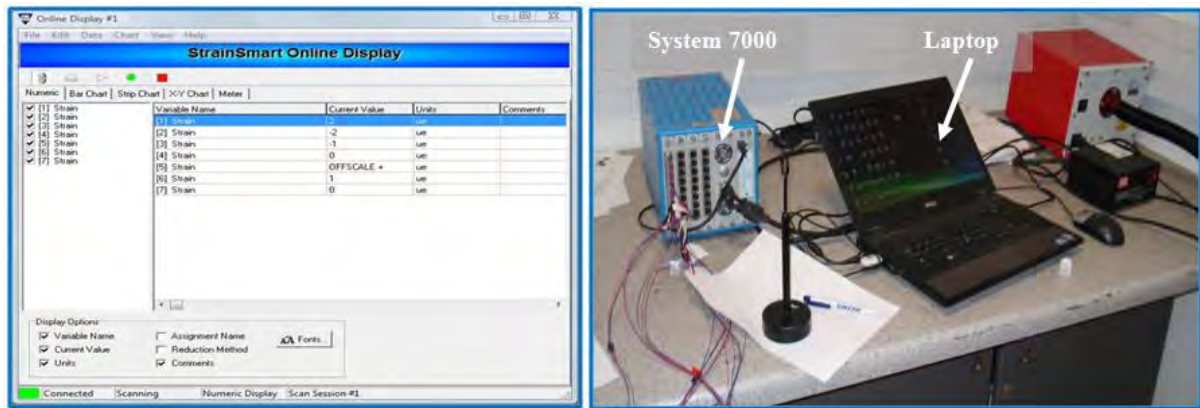


Figure 7.95 Data Acquisition (Hand, 2014)

Having completed the calibration procedure all of the strain gauge values was nulled and the test was setup as shown below.

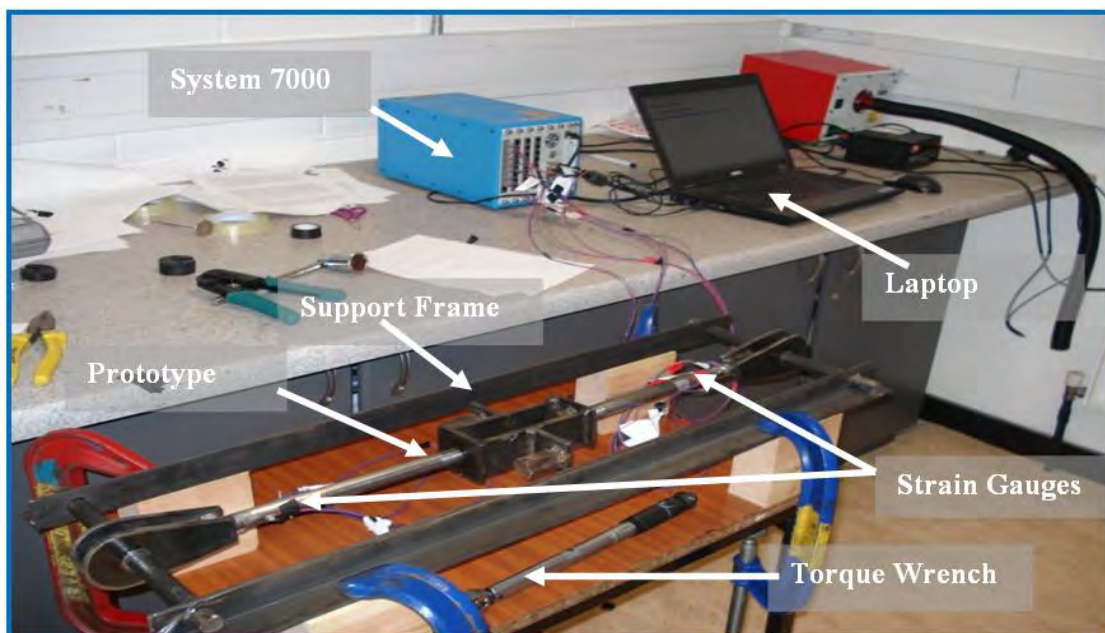


Figure 7.96 Testing Setup (Hand, 2014)

The length of the lever was measured and was found to be 0.36m. Weights were placed on the end of the torque wrench increasing in magnitude of 10N. The data acquisition system was set to record 10 samples per second and the corresponding



strains were recorded and exported to MS Excel. Weights were added for the range of 10 - 80N.



Figure 7.97 Torque wrench on prototype & Masses and mass hanger (Hand,2014)

7.7.3 Results

Table 7.11 Strain gauge results

	Effort (N)	10	20	30	40	50	60	70	80
L= 0.36m	Torque (Nm)	3.6	7.2	10.8	14.4	18	21.6	25.2	28.8
	Torque on each screw (Nm)	1.8	3.6	5.4	7.2	9	10.8	12.6	14.4
Location	Gauge & Type**	μϵ							
RHS	1 (long)	2.0E-05	2.2E-05	3.1E-05	5.3E-05	7.3E-05	8.5E-05	1.0E-04	1.3E-04
RHS	2 (long)	2.2E-05	2.5E-05	3.2E-05	4.6E-05	6.6E-05	8.2E-05	1.1E-04	1.2E-04
RHS	3 (Lat)	-7.0E-06	-8.0E-06	-1.1E-05	-2.0E-05	-2.6E-05	-3.5E-05	-4.7E-05	-6.0E-05
RHS	4 (Lat)	-8.0E-06	-9.0E-06	-1.4E-05	-2.4E-05	-3.4E-05	-4.6E-05	-5.9E-05	-6.6E-05
LHS	6 (Long)	9.0E-06	2.4E-05	4.0E-05	5.5E-05	7.7E-05	9.3E-05	1.1E-04	1.2E-04
LHS	7 (Lat)	-3.0E-06	-7.0E-06	-1.3E-05	-2.3E-05	-3.3E-05	-4.0E-05	-5.2E-05	-7.0E-05
	*AVG(long)	1.7E-05	2.4E-05	3.4E-05	5.1E-05	7.2E-05	8.7E-05	1.1E-04	1.2E-04
	*AVG(Lat)	-6.0E-06	-8.0E-06	-1.3E-05	-2.2E-05	-3.1E-05	-4.0E-05	-5.3E-05	-6.5E-05

** Strain Gauge number and type (long = longitudinal gauge) (Lat = Lateral gauge)

*AVG = Average strain reading **Note:** Strain gauge 5 failed to function during testing

Above in table 7.11 shows the key results that were recorded using the data acquisition system for the longitudinal and lateral strain gauges positioned on the tie-down shafts with the longitudinal strain and lateral strains corresponding to axial and traverse strains respectively. Firstly it was observed that the ratio of traverse strain to axial strain was averaged to be about 0.35 which is close to published value for Possion’s ratio for steel which is 0.30 (CES, 2014) which initially checked during the testing phase put initial confidence in the results.

$$\text{Possion’s Ratio } (\nu) = \frac{-\epsilon_{Traverse}}{\epsilon_{Axial}} \quad [7.26] \quad (\text{Gere \& Goodno, 2012})$$

As the strain gauges were strategically positioned on both shafts of the tie-down mechanism, the corresponding strains should be the same as the material elastically deforms at the same rate as equal tensile force is generated. Below in figure 7.98 and figure 7.99 shows the graphically results of the respective strains recorded.

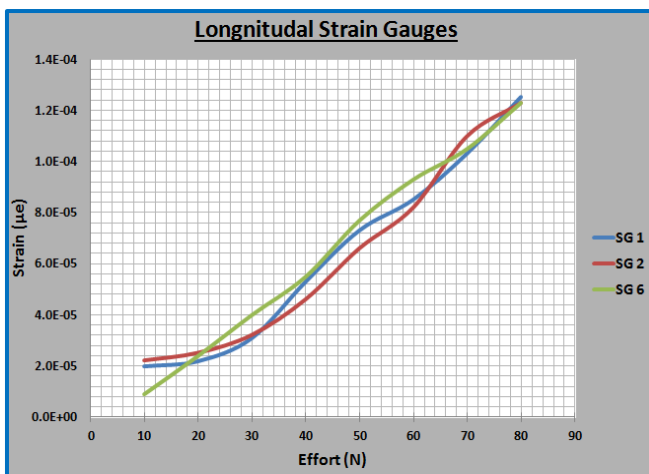


Figure 7.98 Axial strains

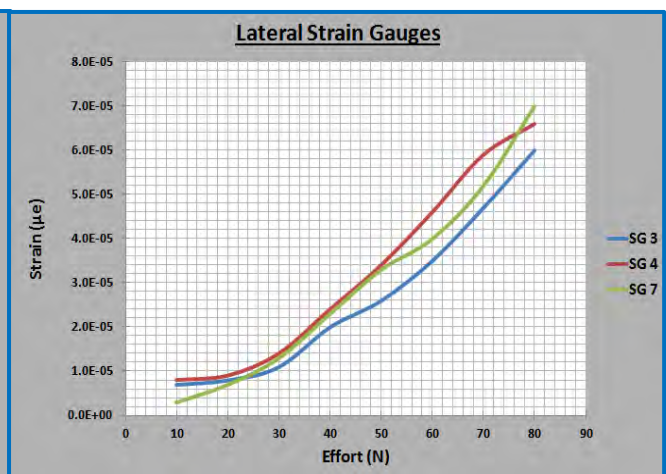


Figure 7.99 Traverse strains (negative)

It is clearly seen that there is deviations between the strain gauge results which is to be expected when using strain gauges mainly due to their sensitivity and resolution. Although the gauge results do show a good correlation with each other and similar slope. At this point the axial strains were mainly considered, knowing the strain values allowed the determination of the shaft axial force by utilising some fundamental principles of mechanics.

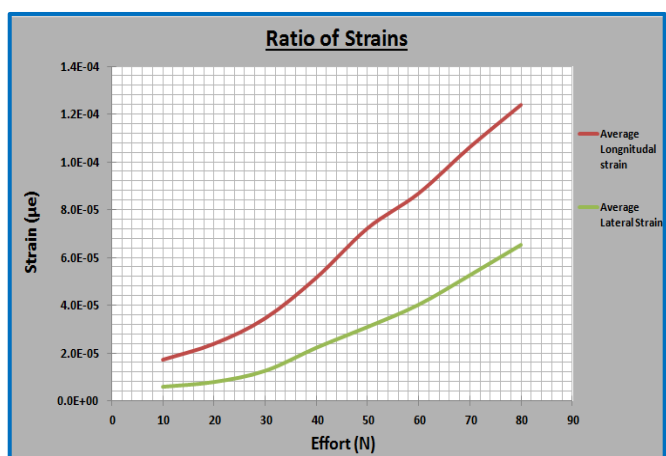


Figure 7.100 Ratio of strains

$$\text{(Normal Stress)} \sigma = \frac{F}{A} \text{ (Mott, 2006)}$$

$$\text{(Strain)} \epsilon = \frac{\Delta L}{L} \text{ (Mott, 2006)} \quad [7.27]$$

$$\text{(Young's Modulus)} E = \frac{\sigma}{\epsilon} \text{ (Mott, 2006)} \quad [7.28]$$

An average was taken of the axial strain gauge readings to increase the overall accuracy of the results. Using the above 3 formulae the following was calculated.

Sample Calculation

Take first averaged axial strain result (17 $\mu\epsilon$)

Diameter shaft = 20mm

$$A = \frac{\pi D^2}{4} = \frac{\pi 0.02^2}{4} = 3.14 \times 10^{-4} m^2$$

$$F = \sigma \cdot A \quad F = \sigma \cdot (3.14 \times 10^{-4})$$

$$\sigma = E \cdot \epsilon \quad (E = 210 \text{ GPa for Steel}) \text{ (Mott, 2006)}$$

$$\sigma = (210 \times 10^9)(17 \times 10^{-6}) = 3.57 \text{ MPa}$$

$$F = (3.57 \times 10^6) \cdot (3.14 \times 10^{-4}) = \underline{1,121 \text{ N (Tensile force)}}$$

$$\text{Mechanical Advantage (MA)} = \frac{\text{Load}}{\text{Effort}}$$

$$\text{Mechanical Advantage} = \frac{1,121 \text{ N}}{10 \text{ N}} = 112.1$$

$$\text{Velocity Ratio (VR)} = \frac{\text{Distance moved by effort}}{\text{Distance moved by Load}} \quad \frac{2\pi L}{P}$$

$$\text{Lever arm (L)} = 0.36 \text{ m}$$

$$\text{Thread Pitch (P)} = 2.5$$

$$\text{Velocity Ratio (VR)} = \frac{2\pi(0.36)}{(2.5 \times 10^{-3})} = 904.77$$

$$\text{Efficiency } (\eta) = \frac{\text{MA}}{\text{VR}}$$

$$\text{Efficiency } (\eta) = \frac{112.1}{904.77} = 0.12 \times 100\% = 12\%$$

Table 7.12 contains the above calculated values for each averaged axial strain

Table 7.12 Experimental Results

Effort (N)	10	20	30	40	50	60	70	80
Normal Stress (MPa)	3.6	5.0	7.2	10.8	15.1	18.2	22.3	26.0
Tensile Force (N)	1121.0	1560.6	2263.9	3384.9	4747.7	5714.8	6989.6	8154.6
MA	112.1	78.0	75.5	84.6	95.0	95.2	99.9	101.9
Efficiency (η)	0.12	0.09	0.08	0.09	0.11	0.11	0.11	0.11

These results were then compared with the calculated results for this mechanism which was used at the start of this chapter as equation [7.0] and is shown again below. The following results were calculated using equation [7.29] and are tabulated in table 7.13.

$$M_t = 0.098Pd \quad [7.29]$$

Table 7.13 Calculated Results

Effort (N)	10	20	30	40	50	60	70	80
Torque (Nm)	3.6	7.2	10.8	14.4	18	21.6	25.2	28.8
Torque on each screw (Nm)	1.8	3.6	5.4	7.2	9	10.8	12.6	14.4
Tensile Force (N)	918.4	1836.7	2755.1	3673.5	4591.84	5510.20	6428.57	7346.94
IMA	91.84	91.84	91.84	91.84	91.84	91.84	91.84	91.84
Efficiency	0.10	0.10	0.10	0.10	0.10	0.10	0.10	0.10

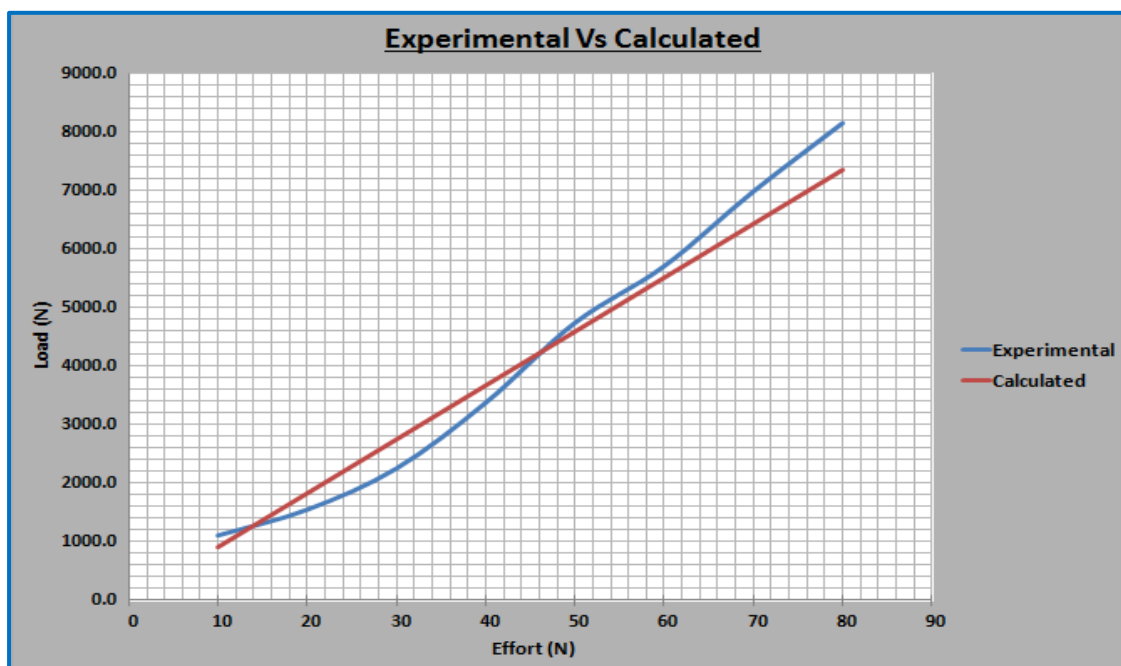


Figure 7.101 Experimental Vs Calculated results

It can be seen from figure 7.101 above is that there is a very similar response from the axial loaded strain gauges to the theoretical calculations for this prototype and this puts a huge degree of confidence in the functionality of the redesigned tie-down mechanism. Having achieved a very accurate response from the scaled prototype it was now possible to scale these results and compare with the full scale response which was shown in figure 7.30 on page 132 and is shown below in figure 7.102 . The two scale factors (λ) required here are torque and force. The scale factor $\lambda = 1.5$ (Shaft diameters were reduced from 30mm in full scale to 20mm in prototype and other dimensions were scaled appropriately)

Table 7.13 Scale factors (Chakrabarti, 1994)

Variable	Unit	Scale Factor	Model : Prototype
Force	MLT^{-2}	λ^3	1:3.375
Torque	ML^2T^{-2}	λ^4	1:5.063

Table 7.14 Prototype and full scale force and torque

Torque prototype (Nm)	3.6	5.0	7.2	10.8	15.1	18.2	22.3	26.0
Force prototype (N)	1121.0	1560.6	2263.9	3384.9	4747.7	5714.8	6989.6	8154.6
Torque full scale (Nm)	18.1	25.2	36.5	54.6	76.5	92.1	112.7	131.5
Force full scale (N)	3783.31	5266.96	7640.80	11424.11	16023.42	19287.45	23590.04	27521.71

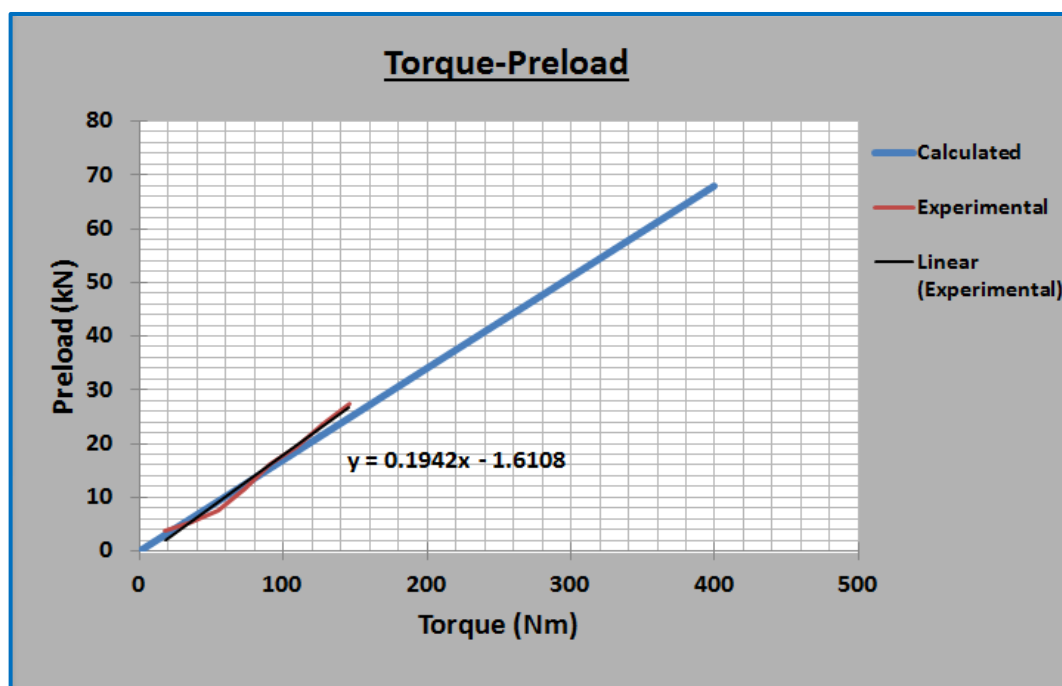


Figure 7.102 Scaled up results plotted on full scale (Hand, 2014)

Curving fitting techniques had to be utilised here to plot a full response of the data from the testing of the prototype, it was determined that a linear trend line would be most applicable here a linear relationship was required. Using MS Excel commands a linear equation [7.30] was found to fit the experimental results adequately.

$$y = 0.1942x - 1.6108 \tag{7.30}$$

This allowed the full range of scaled values to be plotted against the full scale calculated values. These results are given below in table 7.15.

Table 7.15 Experimental and Calculated results for full scale

Torque (Nm)	50	100	150	200	250	300	350	400
Calculated force (kN)	8.5	17.0	25.5	34.0	42.5	51.0	59.5	68.0
Experimental force (kN)	8.1	17.8	27.5	37.2	46.9	56.6	66.4	76.1
Percentage Difference (%)	4.8	4.7	7.9	9.5	10.4	11.0	11.5	11.8

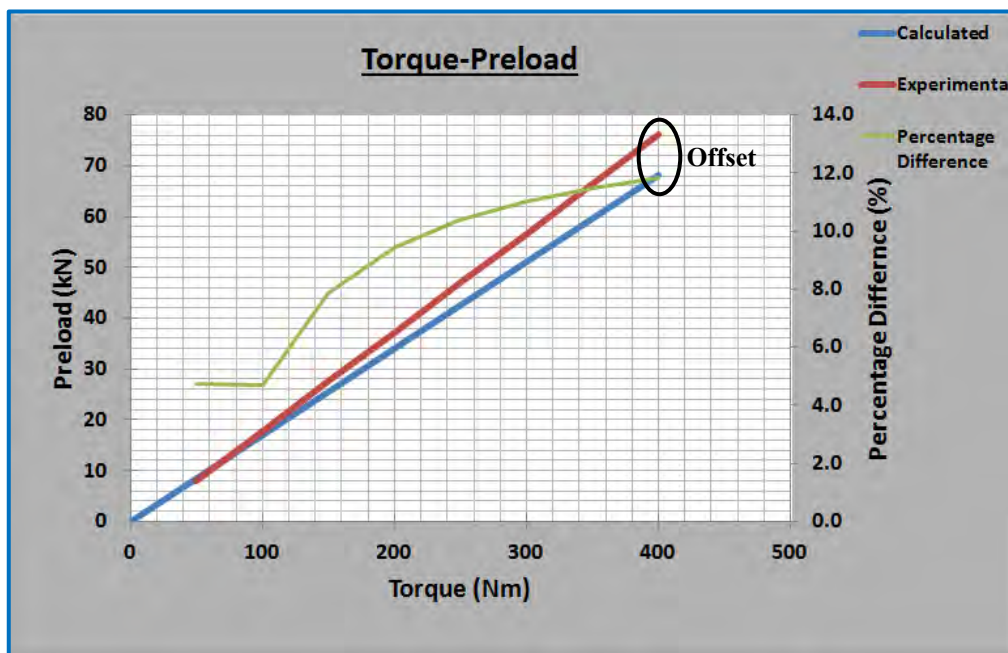


Figure 7.103 Plot of calculated and experimental scaled results (Hand, 2014)

The graph above in figure 7.103 does show a very good correlation for the experimental scaled results and the calculated results for the tensile generated by each torque. It is observed however there is significant offset between the lines in the graph above accounting for about 12% difference in values. This is believed to be primary caused by experimental errors that

occurred during the testing of the prototype and also scale effects may have enhanced this difference. One of the main drawbacks with using strain gauges is that their sensitivity can often create errors in experimental testing. The most common and most difficult error to remove in testing is temperature effects on the strain gauges. Any increase in temperature can alter the resistance of the strain gauge element and change its gauge factor (Rangan, 1997) as shown in figure 7.104. The strain gauges used in this testing had a quoted gauge factor variation with temperature of $\pm 0.015\%/^{\circ}\text{C}$ (Radionics, 2014).

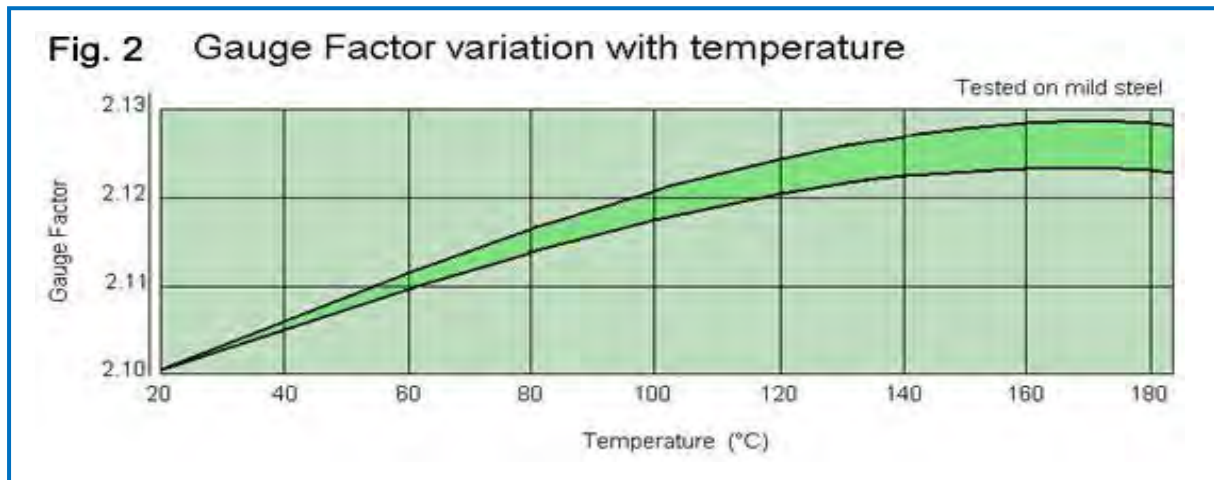


Figure 7.104 GF variation with temperature for strain gauges (Schukar et al, 2013)

An error also difficult to remove from this testing was misalignment error of the strain gauges. As the gauges were very small in size it was very difficult to align the gauges exactly with the axis of the shaft. If one of the gauges was misaligned it would cause an angular error in the strain readings. Traverse gauges were added to the prototype before testing as a means of establishing the accuracy of the results, as the ratio of the traverse and axial strains should be similar to the Poisson's ratio for the material. The difference in values for the graph above may have been caused by undefined factors

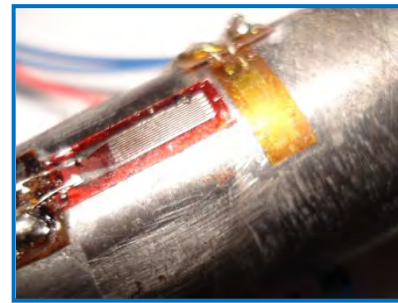


Figure 7.105 Strain gauges on shaft (Hand, 2014)

in the calculations that may have been present in the testing. The calculations do take account of frictional resistances between the screw thread and turnbuckle, but these resistances may have varied with the length of the machined thread causing variable resistance which may explain the oscillation of the experimental curve in figure 7.103. The author considers the use of a modern and accurate data acquisition greatly influenced the accuracy of these results as calibration and signal conditioning were automatically conducted by the equipment. The influence of noise on the testing would be substantial without the integrated signal filtering

7.6.7 Hazard Analysis for Prototype Testing

Risk Assessment											
											Taken in Accordance with EN ISO 14121-1:2007
RA #	Action	Hazard	Lo	Fe	DPH	NPR	HRN	Risk	Control	HRN with control	Risk with control
1	Apply torque to prototype	Causes support frame to lift and hit user	10	5	3	1	150	Very High	Use a suitable method to clamp/constrain the prototype to ensure no movement	5	Low
2	Electrical Equipment	Faults in electronic equipment, not earthed properly	2	1.5	8	1	24	Significant	Ensure all electronic equipment is operating properly before use and check with supervisor before use	0.5	Negligible
3	Adjusting of prototype	Cuts from sharp edges/ crushing of fingers	2	2	0.5	1	2	Low	Remove burrs on manufactured pieces, ensure no moving parts	0.5	Negligible
4	Applying weights	Weight hits user's foot	3	1.5	1	1	4.5	low	Wear suitable footwear during testing	1	Very Low
5	Exposed contact wires	Electrocution/shock	3	1.5	1	1	4.5	Low	Ensure any exposed contact wires are insulated adequately	0.5	Negligible
7	Lifting of weights	Back strain/muscle injury	2	1.5	2	1	12	Significant	Ensure correct material handling techniques are used	1	Low
8	Wires leading to plug sockets	Trip hazard/ Fall	3	1.5	2	1	9	Significant	Ensure cables are kept organised and remove obstacles	1	Low

8.0 Project Management

8.1 Introduction

The key to a successful project is to ensure effective time management is ensured and that the individual elements of the project are achieved during the project. As this project had a duration of two academic semesters it is therefore necessary to have a realistic and feasible plan in place before the project commenced, which will take account of potential setbacks throughout the project and allow adequate time to guarantee the author's best effort was put into the project. The author also had to be practical about how much time and attention could be given to the project also, as other course work is running in parallel with the project which require equally amount of concentration. Shown below in figure 8.0 is a simplified predicted work flowchart for the two semesters, the project had been split in two to allow a better comprehension of the necessary elements which have to be completed for the project to be finished. The first semester dealt with a large amount of the literature research and examining of the state of the art. In semester 2, primarily the core analysis and testing was performed with an emphasis on validation procedures based on research conducted in semester 1

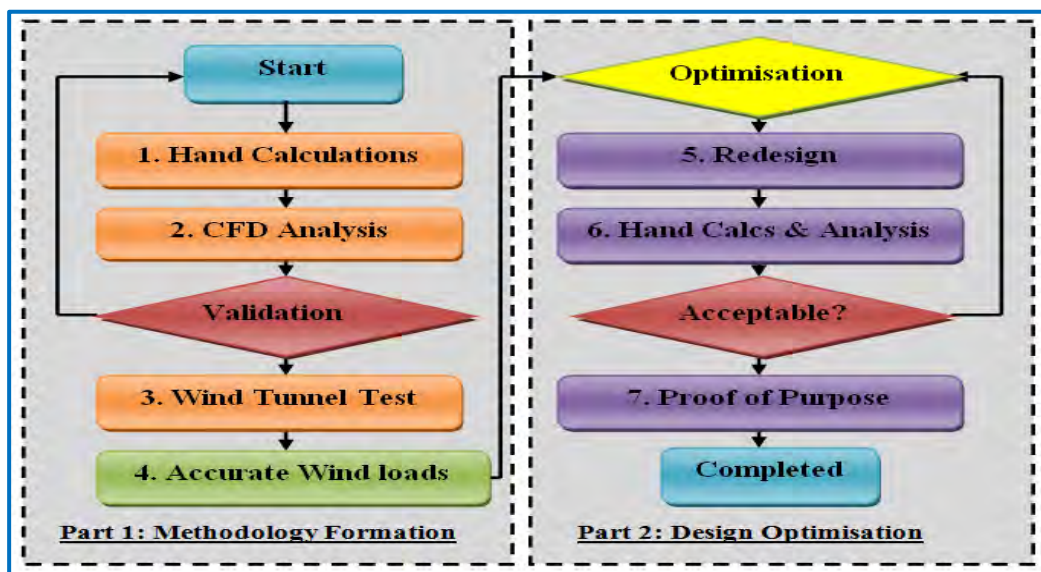


Figure 8.0 Project Flowchart (Hand, 2013)

8.2 Time Management Techniques

To ensure the most efficient time management was achieved in this project three project management techniques were utilised which involved the use of Gantt charts, work

breakdown schedules (WBS's) and PERT (Project Evaluation and Review Technique) network charts all of which are clearly shown in appendix A.

Firstly the WBS technique was utilised when beginning this project and each part of the project was broken down into sizeable tasks which had defined deliverables for the project as whole. Figure 8.1 below shows a short version of the WBS that was created at the beginning of this project (see Appendix A for full WBS). Breaking the project up into different tasks allowed different time periods for each deliverable to be accomplished.

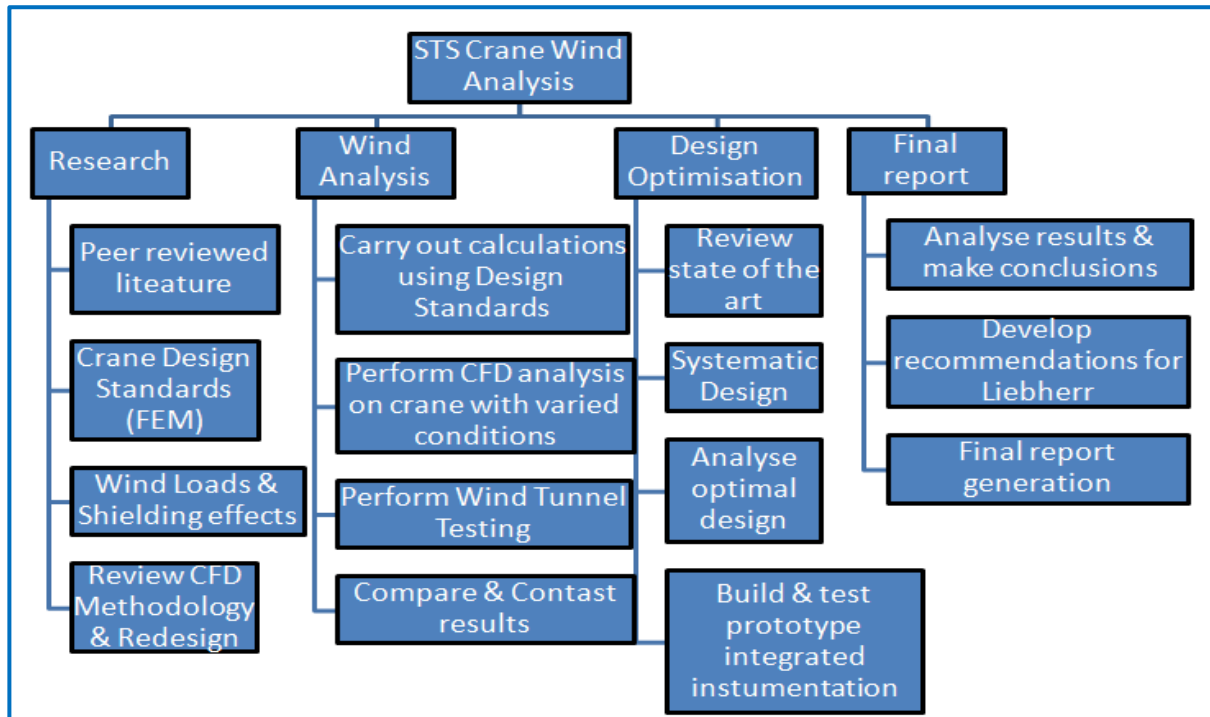


Figure 8.1 Work Breakdown Schedule

Using both the PERT network diagrams and Gantt charts allowed these tasks to be broken down further and the period of time to be spent doing each task was calculated. To ensure an efficient project plan was put in place a total of two weeks were defined as “slippage” at the end of each semester, which meant that if any tasks took longer than originally thought they could be compensated in this time period. The use of the Gantt charts and PERT diagrams allowed the time in days and weeks that could be spent on each task, throughout the project these were consulted to ensure the project was running on schedule. It also allowed the determination of the critical path in the project which means a period of time whereby numerous tasks had to be completed.

8.3 Overview of Work Complete

The following discusses the project as whole over the two semesters and outlines the tasks done by the author to complete this project. It also outlines any difficulties or obstacles the author faced during this project, how these were overcome and how they effected the overall time plan.

8.3.1 Semester 1

Primarily this time period focused mainly on the literature research aspect of the project, it was important that an in-depth research was carried out of the state of the art primary on the effects of wind loading on these structures. From this study it allowed the author determine the main focal points of the project and establish a clear agenda for the project. In parallel with this significant progress was made in the understanding of CFD analysis software for the project. It was critical that this was started early in the project because a software program like CFD takes a sizeable amount of time to understand and use properly as the author became firmly aware of. It is well known among specialists in this software that experience accounts heavily on the accuracy of results that are generated. The author did have past experience with ANSYS from work placement and third year mechanical material's module, but did find the use of this software a challenge at the beginning of the project.

This challenge was overcome by doing background reading about how the software operated and the use of tutorials and supervisor assistance overcame this obstacle. In this semester also significant progress was made into the validation technique for the CFD analysis which was the wind tunnel testing. In reflecting on the course of the project the author believes that having the wind tunnel model made before the break between semesters was pivotal in the project's success. Initially it was proposed that the testing completed before the break but due to time constraints from the model manufacture difficulties it had to be pushed to start of the second semester. But having the physical model made at the start of the second semester gave the project momentum as calibration and the setup procedures for experimentation were carried out much earlier than expected allowing more time in the Gantt chart for semester 2.

8.3.2 Semester 2

As stated above having the model made early allowed the wind tunnel testing to be conducted on week 2 of semester 2. This allowed these results to be used a bench mark for the CFD results and examine how accurate the results were. From this it was determined that grid mesh in the CFD model had to be modified and grid refinement techniques were integrated to

ensure the utmost accuracy was guaranteed. This process was found to be very consuming as when the mesh parameters were altered simulations had to be conducted at various velocities to plot a defined curve of the simulation results. Each simulation on average took about two hours to complete and it was found difficult to carry out these simulations during lecture hours in the college, so this obstacle was overcome by allowing simulations generally run overnight and the data could be processed in the mornings. To aid the wind tunnel testing to be carried out flow visualisations techniques such as smoke streamlines were utilised, an important but unforeseen obstacle that was encountered here was that smoke alarms had to be decommissioned for the period of this testing

Having obtained the most accurate results from the CFD analysis and wind tunnel analysis the focus of the project now shifted to the design optimisation part of the project which carried out on the crane tie-down system as outlined in chapter 7 of this report. The results obtained from the CFD analysis and wind tunnel testing were used with the current standards to calculate the maximum uplift force on the crane during its “out of service” phase. Following this extensive finite element analysis was conducted and validated using the photoelastic technique on the redesigned tie-down mechanism. One significant obstacle that was met with the photoelasticity testing was the significant lead time to acquire the photoelastic material which was over six weeks, fortunately this material was ordered at the beginning of semester 2 and meant it arrived in time to allow sufficient time to carry out the necessary testing to validate the FEA analysis as documented in chapter 7. Another significant bottleneck in this project was that the manufacture of components for the prototype and experimental rigs could be only done in a limited amount of time each week due to the availability of workshop hours which meant time had to be used very efficiently and wisely.

8.4 Project Constraints

The most primary constraint in this project was the limited analysis that could be conducted using the standard licenses for the CFD analysis. The grid mesh limits severely restrict the possibilities of doing very detailed modelling using this software simulation available. Although this was a considerable limitation in the project, it did have significant learning outcomes for the author especially with the use of effective meshing techniques that enabled detailed analysis to be conducted with effective mesh in place. The second most influential project constraint was the effectiveness of the wind tunnel as a testing platform. The wind tunnel was found to be limited in the amount of testing that could be conducted.

9.0 Discussion

This section gives a brief discussion of the intervening segments of this report. It was established from the CFD analysis and experimental testing that lower drag values were found in comparison with the standardised approach. It was found that CFD as a design tool would allow designers to accurately predict regions of high pressure and wind loading forming on the crane structure and allow design changes to be made based on the significance of the data and an important parameter of this software is that it allows the designer to visually see this which is not the case with the standardised approach. CFD would enable the designer to simulate different environmental conditions depending on what part of the world the crane is going to be in-service and operating. In a recent survey conducted by TechNavio a market research company found that the CFD applications for industrial companies is set “to grow at 16.5% per year” (Cranfield, 2014) due to its increasing computational capabilities and due to its suitable integration into the design process (Cranfield, 2014).



Figure 9.0 Liebherr design structure (Hand, 2014)

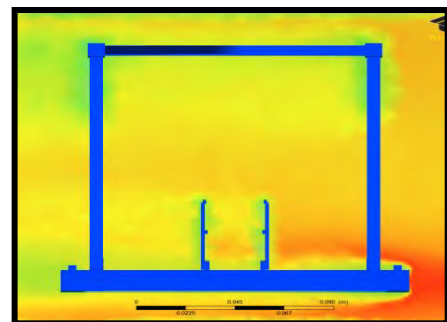


Figure 9.1 Indicative insight to fluid structure interaction (Hand, 2014)

The purposed design optimisation of the crane’s tie-down system was approached with a systematic design methodology which outlined the primary needs for the redesign overall requirements. Suitable material selection procedure was adopted and based on the use of advanced material selection software an appropriate material was determined that fulfilled the needs of the design and Liebherr’s quality specifications. Combining the use of the derived drag coefficients from numerical and experimental analysis with the use of standards the largest design loads were established for this component. The utilisation of ANSY’s FEA application proved very beneficial in the analysing the structural response of the design under various different loading scenarios and allowed the procurement of the factor of safety for the design in potential high locations of stress in the design which were found to acceptable. To ensure that these FEA results were accurate, the photoelastic technique was employed which

provides the most useful means of optical and interferometric measurements for stress in a component which was conducted on a potential location of stress concentration in the design. Results from the stress-induced birefringence load testing of the photoelastic test piece were found to be very similar to the predicted FEA results and visually the occurrences of radial stresses of similar magnitudes were observed in both cases. This analysis and experimentation allowed the foundation for the testing of the redesigned prototype which was comprehensively performed with the use resistance bonded strain gauges mounted to the surface of the artefact at spatially defined points. The results were empirically scaled using scaling factors and were found to have good association with the predicted performance for the design.

9.1 Ethical Considerations

The whole subject matter of ethics is a very important consideration in any engineering project especially in any work undertaken that has direct influence on the operation or design of machinery and components that people will be in contact with on a regularly basis “*engineers shall hold paramount the safety, health and welfare of the public*” (ASME, 2012). Particularly in this project with respect to the redesign of the crane components it is important to take into account the effects that these design modifications will have on the people using them.

Outlined in this report already are some of the core safety criteria that have been put in place for the use of the redesigned system. This purposed design reduces greatly the possible safety hazards with its use compared with the original design which is a very important ethical design consideration, “*the complete rational and licensing of engineers emanates from the fact that engineers are involved in a technical and specific profession having serious impact on the well being of all members of the general public*” (Srinivasan & Halada, 2012).



Figure 9.2 Engineering Ethics
(Carleton University, 2013)

10.0 Conclusions

At the beginning of this report a series of defined objectives were stated in order to achieve the overall aims of this project. The primary aim of this project was to analyse wind flow on a container crane structure and examine the effectiveness of current standards used in quantifying wind induced loading on these detailed engineered structures. This was numerically analysed using detailed CFD analysis and experimentally utilising wind tunnel testing on a complex critical section of the crane structure. The results from both of these methods showed a very good association with each other and the numerical analysis was appropriately validated. A principle finding from this investigation was found that both of the employed numerical and experimental methodologies predicted the drag coefficients to be lower for this type of structure than what are presently used. This finding raises a significant question mark in relation to the suitability of the current standards in relation to their accuracy of quantifying wind loading on these structures. One of the primary reasons for carrying out this project in the first instance was the belief among engineers that used these standards was that they were overestimating the magnitude of wind load on the crane structural components. This conclusion from this study puts reinforcement behind these uncertainties as has been discussed in this report that these standards are not entirely suitable for container crane geometry. Whereas in this study the analysis and experimentation has been performed on the actual crane geometry which is significant for the reduced drag coefficients. It has also been shown how accurate CFD analysis can be in the application of crane design and many benefits associated with this software for an engineer or designer wishing to diverge from the standardised approach.

The secondary aim of this project was the investigation into design optimisation which was conducted on a critical crane component which was the crane's tie-down system. The author's extensive literature research of these components and previous experience of use showed there was an underlying opportunity to improve the operational functionality of these components and the overall working safety criteria. Therefore a comprehensive systematic design, material selection and design requirements analysis was thoroughly examined for the purpose of the redesign of this component. The use of the finite element analysis technique coupled with photoelastic testing as an applicable validation tool showed reasonable working stresses in the redesigned component together with acceptable deflections under associated design loads and alternating load situations. The manufactured and tested prototype of the redesign corresponded very well to predicted performance established for this design. The

prevailing and overall conclusion which can be drawn from this project as a whole is that significant progress has been made in modernising the current methods for predicting wind loads on these structures and also considerable advancement made in improving the design and safety of a critical crane component.

10.1 Recommendations

Within the scope of this project there is a significant opportunity for future work especially in the area of CFD analysis for improved wind loading computation on these crane structures, which has been clearly seen from the extensive work carried out in this project. This may suitably take the form of a master's research project or equivalent where prior knowledge of CFD software would be crucial in the study as the one the next steps would involve transient analysis. Coupled with this also access to powerful computational facilities would be a requirement and unlimited grid cell capabilities for analysis purposes. Alternatively as ready stated in this report, there may be a prospect that Liebherr may integrate the use of CFD into its design procedure and could be used as a means of complementing the current standards in situations where current standards accuracy could be called into judgement. Having seen the validity of the CFD results obtained from this analysis there could be huge potential and advantages for the company both design wise and financially. This can be reinforced by the fact that the CFD results from this analysis were validated by wind tunnel testing and showed corresponding results which is key.

The author would propose the following recommendations to improve the performance of the wind tunnel test unit in CIT for further testing. (1) Ideally the wind tunnel should be positioned somewhere there is no obstruction to its exit flow as this can disrupt results (2) integrate a airflow velocity measurement system into the wind tunnel, this will significantly improve the accuracy of result recording and user efficiency

With respect to the design optimisation criteria of this project all work carried out by the author both analytically and experimentally will be presented to Liebherr following the closing of this project. It is hoped that full scale testing of the redesigned tie-down prototype could be carried out, to fully test its operational functionality and safety of the design. It would also be a prerequisite that this design conforms to Liebherr's quality control procedures. Further analysis into stress distribution on the design can be conducted by Liebherr with the availability of a commercial FEA license which will allow much more analysis to be conducted.

11.0 References

Aalbers A.B, 1993. *Mooring and Offloading: Model Testing for Design*: Paper No 23:Texas Section SNAME: Third Offshore Symposium-FPSO Technology, Houston

Abrahamsen L.S, 2012. *Wind tunnel model testing of offshore platforms*: NTNU-Trondheim: Norwegian University Science and Technology: Master of Science in Product Design and Manufacturing: 2.5 Atmospheric boundary layer
Available Online at: <http://www.diva-portal.org/smash/get/diva2:566139/FULLTEXT01.pdf>. [Accessed 13th November 2013].

Achterberg F.F, 2012. TU Delft: Delft University of Technology: Faculty Mechanical, Maritime, and Materials Engineering. Department Marine and Transport Technology: Literature Assignment: Trends in ship-to-shore container cranes: *Introduction to STS cranes: 2.2.2 Trolley*. Page 10.

Adhikari S,2008. Effect of wind on structure. Indian Structural Engineers.

Anderson, J D 2005. Physics Today: *Ludwig Prandtl's Boundary Layer*. Page 42. Available Online at: http://www.aps.org/units/dfd/resources/upload/prandtl_vol58no12p42_48.pdf. [Accessed 9th April 2014].

Alibaba, 2013. *Hydraulic Cylinders*: Available Online at http://www.alibaba.com/product-gs/497663730/Telescopic_and_hydraulic_cylinder_for_tipper.html. [Accessed 29th November 2013].

Alpha Prototypes, 2014. How the Rapid Prototyping Process Works: Available Online at:<http://www.alphaprototypes.com/How-Does-Rapid-Prototyping-Work.aspx>. [Accessed 15th April 2014].

Almeida. R, 2013. gCaptain: *Bigger Containerships Means Bigger Gantry Cranes*. Available Online at. <http://gcaptain.com/bigger-containerships-gantry-cranes/>. [Accessed 2nd November 2013].

ANSYS, 2012. Lecture 6: Turbulence: Introduction to Ansys Fluent: Mean and Instantaneous Velocities.

Amirouche F, 2006. Fundamentals of Multibody Dynamics: Theory and Applications: Particle Dynamics: The Principle of Newton's Second Law: Published by Springer

Almohammadi. K.M, Inghama D.B, Maa. L & Pourkashana M, 2013. *Computational fluid dynamics (CFD) mesh independency techniques for a straight blade vertical axis wind turbine: Energy* 58 (2013) Page 483-493: Introduction: Published by Elsevier.

Artzi D & Kroll E, 2011. Lesson from wind tunnel models made by rapid prototyping: Faculty of Aerospace Engineering: Technion-Israel Institute of Technology: Rapid Prototyping Journal: ISSN 1355-2546: Volume 17 Number 5 2011. Page 2.

Azizi M.N.B & Ginta T.L,2012 Design and Construction Smoke Wire Apparatus for Wind Tunnel Flow Visualization: Int. J. of Mechanical Computational and Manufacturing Research, Vol.1. No.3, (2012) 79 – 86, ISSN: 2301-4148 Department of Mechanical Engineering, Universiti Teknologi PETRONAS, Bandar Seri Iskandar, 31750, Tronoh, Perak Darul Ridzuan, Malaysia

ASME (The American Society of Mechanical Engineers) a, 2013. About ASME: Who we are: Engineering history: Landmarks: *PACECO Container Crane*. Available Online at <https://www.asme.org/about-asme/who-we-are/engineering-history/landmarks/85-paceco-container-crane>. [Accessed 23th October, 2013].

ASME (The American Society of Mechanical Engineers) b, 1983. Dedicates an International Historic Mechanical Engineering Landmark: *The PACECO container crane: The World's First High Speed, Dockside Container Crane*: Encinal Terminals – Alameda, California: May 5th 1983: Introduction. Pages 3-5.

ASME (American Society of Mechanical Engineers) c, 2012. *Setting the Standard*: Society Policy: Ethics: Code of Ethics of Engineers: The Fundamental Canons: Available Online at :<http://files.asme.org/asmeorg/governance/3675.pdf>. [Accessed 7th of November].

Atro, 2013. Engineered Systems: *Cast Equalizer Beam w/Bushing*. Available Online at: <http://www.atrobushing.com/item/eq53-35701/>. [Accessed 28th November 2013].

Bainesi, P G Majumdar S J. & Mitsudera, H 1996. *The mechanics of the Tollmien-Schlichting wave*: 1 CSIRO Division of Atmospheric Research, Aspendale, Australia: 2 Department of Applied Mathematics and Theoretical Physics, University of Cambridge, Silver Street, Cambridge, CB3 9EW, UK: *J. Fluid Mech* (1996), vol 312. Page 107-124. Published by Cambridge University Press.

Bakker A, 2006. Lecture 7 – Meshing: Applied Computational Fluid Dynamics: Mesh quality: skewness: Page 24. Available Online at: <http://www.bakker.org/dartmouth06/engs150/07-mesh.pdf>. [Accessed 13th April 2014].

Barltrop N.D.P, 1998. Floating Structures: *A Guide for Design and Analysis*, Centre for Marine and Petroleum Technology.

Barlow J B, Rae W H & Pope A, 1999. A Low speed wind tunnel testing: 3rd Edition. Published by John Wiley & Sons.

Benson T, 2011. Smoke and Tufts: NASA Official: NASA, Available Online at: <https://www.grc.nasa.gov/www/k-12/airplane/tunvsmoke.html>. [Accessed 15th April 2014].

BETA, 2012. Flow Induced Vibration (FIV): Available Online at <http://www.betamachinery.com/flow-induced-vibration.aspx>. [Accessed 18th April 2014].

Blocken B, Defraeye T, Koninckx E, Carmeliet J & Hespel P, 2013. *CFD simulations of the aerodynamic drag of two drafting cyclists*: 3. Numerical simulations: computational settings and parameters: Page 435-445: Published by Elsevier.

Bienkiewicz B, Cermak J. E, 1987. Experiments in Fluids: A flow visualization technique for low-speed wind-tunnel studies: Volume 5, Issue 3 pp 212-214: ISSN 0723-4864: 1. Civil Engineering Department, Colorado State University, 80523, Fort Collins, CO, USA

Bhandari.V.B, 2008. Design of Machine Elements, Second Edition. Chapter 8: *Welded Joints*: 8.7 Strength of Parallel Fillet Welds: Equation 8.7. ISBN 978- 0-07-061141-2. Published by McGraw Hill

Boverket, 2003. About the National Housing Board: the writers: Swedish Regulations for Steel Structures - BSK 99 Swedish Regulations for Steel Structures - BSK 99: Available

Online at <http://www.boverket.se/Om-Boverket/Webbokhandel/Publikationer/2003/Swedish-Regulations-for-Steel-Structures--BSK-99//>. [Accessed 18th April 2014]

Botha M, 2009. A Comparative study of Reynolds-Averaged Navier-Stokes and Semi-Empirical Thermal Solutions of a Gas Turbine Nozzle Guide Vane: University of Pretoria: Available Online at: <http://upetd.up.ac.za/thesis/available/etd-06222009-123554/unrestricted/dissertation.pdf>. [Accessed 13th April 2014].

Buchner.B,1999. *Numerical Simulation and Model Test Requirements for Deep Water Developments*: Proc.Conf.Deep and Ultra Deep Water Offshore Technology: Newcastle: Institute of Maritime Engineers: Volume 111:No 1:Part 1:Page 97-107.

Burcharth, H. F. & Lykke Andersen, T, 2012. Scale effects related to small scale physical modelling of overtopping of rubble mound breakwaters: Aalborg University.

CAE, 2013. Resources: *Generating Inflation Layers for CFD* - ANSYS e-Learning: Available Online at: <https://caeai.com/resources/generating-inflation-layers-cfd-ansys-e-learning>. [Accessed 13th April 2014].

Canal Museum, 2012. *Images of Panamax Ships in the Panama Canal Locks*. Available Online at: <http://www.canalmuseum.com/canalphotos/panamax.htm>. [Accessed 2nd November 2013].

Cao H, 2011. Aerodynamics Analysis of Small Horizontal Axis Wind Turbine Blades by Using 2D and 3D CFD Modelling: 2.3 Computational fluid dynamics (CFD): 2.3.2 Turbulent models. Page 14.

Carleton University, 2013. *Psychology: Ethics*: Available Online at <http://carleton.ca/psychology/ethics/>: [Accessed 22th of November].

Cakir,M 2012. CFD Study on Aerodynamic Effects of a Rear Wing/Spoiler on a Passenger Vehicle: Master Thesis: Submitted in Partial Fulfilment of the Requirements For the Degree of Master of Science In Mechanical Engineering In the School of Engineering at Santa Clara University, December 2012 Santa Clara, California: Chapter 1: Automobile Aerodynamics: 1.4.3 *Friction Drag*. Page 7.

Castro I P & Apsley DD, 1997. *Flow and dispersion over topology: a comparison between numerical and laboratory data for two dimensional flows*. Atmospheric Environment 31, Page 839–850.

Castonguay.J & Stone.L, 2010. Witness – An online magazine: *International Shipping: Globalization in Crisis*. Page 2

CD-Adapco, 2014. Aerospace & Defense Aerospace – Application: Aeroelasticity Aeroelastic studies are critical to ensure structural and lift requirements are met in flight Available Online at: <http://www.cd-adapco.com/industries/aeroelasticity>. [Accessed 14th April 2014].

Ceccarelli. M, 2004. International Symposium on History of Machines and Mechanisms. Coulomb and applied Mechanics: *Evolution of Container Crane Industry*: Page 231-232 ISBN 1-4020-2203-4. Printed by Kluwer Academic Publishers.

Container Handbook, 2013. 1 History : 1.1 *History of the Container*. Available Online at: http://www.containerhandbuch.de/chb_e/stra/index.html?/chb_e/stra/stra_01_01_00.html. [Accessed 22nd October, 2013].

Corsa-Technic, 2013. *Sensors-Position, Linear: Products: Linear Potentiometer* Available Online at: http://www.corsa-technic.com/category.php?category_id=65[Accessed 22nd November, 2013].

Costamare Inc, 2013. Industry: History of Shipping: *The Inventor*. Available Online at http://www.costamare.com/industry/shipping_container_history. [Accessed 18th October, 2013].

Champkin J, 2013. Significance Magazine. George Box, (1919-2013): a wit, a kind man and a statistician: Available Online at: <http://www.significancemagazine.org/details/webexclusive/4566511/George-Box-1919-2013-a-wit-a-kind-man-and-a-statistician.html>. [Accessed 12th April 2014].

Chung TJ, 2002. *Computational fluid dynamics*. Cambridge University Press, ISBN 0521594162; 2002, Available Online at: <http://www.amazon.ca/exec/obidos/redirect?tag%2Fciteulike09-20%2Fpath%2FASIN%2F0521594162;2002> [Accessed 13th April 2014].

Chakrabarti S, 1998. Dynamic positioning conference: Physical Model Testing of Floating: Offshore Structures: *Offshore Structure Analysis, Inc.: 2.0 modelling criteria*: Page 4: DP Conference, Houston

Charalambos C. Baniotopoulos, Claudio Borri, Theodore Stathopoulos, 2011. Environmental Wind Engineering and Design of Wind Energy Structures: Aero-Servo-Elastic Design of Wind Turbines: ISBN 978-3-7091-0952-6: Published by Springer

Cranfield, 2014. Cranfield University:Msc In Computational Fluid Dynamics: Available Online at <https://www.cranfield.ac.uk/courses/masters/files/msc-cfd-soe1181.pdf>. [Accessed 20th April 2014].

Currie, IG 1993. Fundamental Mechanics of Fluids, Third Edition: Chapter 9: Boundary Layers: *9.1 Boundary Layer Thicknesses*. ISBN 0-203-91054-0: Published by Marcell Dekker.

Cooper K, 2005. Rapid Prototyping Technology: Selection and Application: National Aeronautics and Space Administration: Marshall Space and Flight centre: Huntsville: Case Study: wind tunnel testing with Rapid Prototyped Models. Page 147 ISBN 0-203-91079-6: Published by Marcel Dekker, Inc.

Day, M A 1990. The no-slip condition of fluid dynamics: 1.Dept. of Physics, Lebanon Valley College, 17003, Annville, PA, U.S.A: November 1990: Volume 33: Issue 3: Pages 245-296. Published by Springer.

Dally J. W. & Riley W. F, 1993. "Experimental Stress Analysis," Springer Publisher, New York.

Darcor, 2014. Casters and Wheels:The Ergonomics of Manual Material Handling: Pushing and Pulling Tasks. Available Online at

http://www.darcor.com/public/File/pdf/Darcor_Casters_WhitePaper.pdf. [Accessed 20th April 2014].

Defraeye T, Blocken B, Koninckx E, Hespel P, Carmeliet J, 2010. *Computational fluid dynamics analysis of cyclist aerodynamics: performance of different turbulence-modelling and boundary-layer modelling approaches.* J Biomech ; 43(12):2281–7.

Direct Industry, 2013. *The Online Industry Exhibition:* Digital LVDT displacement transducer. Available Online at: <http://www.directindustry.com/prod/solartron-metrology/digital-lvdt-displacement-transducers-4818-632022.html>. [Accessed 18th November, 2013].

Douglas J F, 2005. Fluid Mechanics: 5th Edition: Chapter 12: Incompressible Flow around a body: 12.9 Wakes and Drag: page 430 :ISBN 978-0-13-129293-2: Published by Pearson Education

Dutemple.L.A, 2003. *The Panama Canal.* Chapter 1: The Path Between Two Oceans: Page 8:ISBN: 0-8225-0079-5

Duthinh.D & Simiu.E, 2011. *The Use of Wind Tunnel Measurements in Building Design, Wind Tunnels and Experimental Fluid Dynamics Research,* Prof. Jorge Colman Lerner (Ed.), ISBN: 978-953-307-623-2, InTech, Available from: <http://www.intechopen.com/books/wind-tunnels-and-experimental-fluid-dynamicsresearch/the-use-of-wind-tunnel-measurements-in-building-design>

El-Sahli.Z, 2012. *Estimating the Effects of Containerisation on World Trade:* The University of Nottingham: Chapter 1: Introduction.

ENEA-GRID, 2001. Fluent: Chapter 10. Modelling Turbulence. Available Online at: <http://www.afs.enea.it/fluent/Public/Fluent-Doc/PDF/chp10.pdf>. [Accessed 13th April 2014].

Engineering Toolbox, 2014. Modulus of Elasticity - Young Modulus for some common Materials: Available Online at: http://www.engineeringtoolbox.com/young-modulus-d_417.html. [Accessed 14th April 2014].

EPFL (école polytechnique fédérale de lausanne), 2011. Aeroelasticity in turbomachines Introduction to Aeroelasticity Available Online at <http://gtt.epfl.ch/page-63561-fr.html>. [Accessed 18th April 2014].

Favier. D, 2010. *The Role of Wind Tunnel Experiments in CFD Validation:* Institute of Movement Sciences, University of Mediterranean, Marseille, France: Introduction: Encyclopaedia of Aerospace Engineering: Published By John Wiley & Sons, Ltd

FEM (European Federation of Materials Handling), 2013. Technical Documents: Technical Documents & Publications: Heavy Lifting and Handling Equipment: FEM 1.004 (07.2000): *Recommendation for the calculation of wind loads on crane structures.* Available Online at: <http://www.fem-eur.com/index.php>. [Accessed 9th November 2013].

Fortus, 2010. 3D Production Systems: By Dave Campo, Stratasys, Inc: *Wind Tunnel Testing: Overview:* Page 1. Available Online at: <http://cimetrixsolutions.com/downloads/AG-WindTunnel.pdf>. [Accessed 13th November 2013].

- Financial Press, 2013.** *Economy: Free exchange: The humble hero.* Available Online at: <http://financialpress.com/2013/05/19/free-exchange-the-humble-hero/>. [Accessed 21th October, 2013].
- Franke.J, Hellsten. A, Schlünzen. H, Carissimo. B, 2007.** *Best practice guideline for the CFD simulation of flows in the urban environment*, COST Action 732: quality assurance and improvement of micro scale meteorological models. Germany: Hamburg
- Franz B, Ameika K, Reeber J, 2011.** DSP CON: A CDI Company Protection from Aliasing in Data Acquisition Systems Available Online at: http://www.dspcon.com/LinkClick.aspx?fileticket=a0eld_2Yqd0%3D&tabid=132. [Accessed 15th April 2014].
- Gere J, & Goodno B, 2012.** *Mechanics of Materials: Page 54: Chapter 1 Tension Compression and Shear*: ISBN: 978:111:57773-5: Published by Cengage Learning
- GD International, 2013.** *China Trade: Electronic Parts: Motor*: Available Online at: <http://www.gd-wholesale.com/chinaproduct/mf58d/av2794to1bv/eg-series-three-phase-industrial-motor-m128466.html>. [Accessed 21th November, 2013].
- Goldstein R 1996.** *Fluid Mechanics Measurements, Second Edition: Flow Visualisation by Direct Injection: Aerodynamic Flow Visualisation*: page 369 Published by CRC Press
- Graham.C, 2005.** *Containerization and the Decline of South Street Seaport*: Fordham University: The Jesuit University of New York: Decline 1870-1960. Available Online at: http://www.fordham.edu/academics/colleges__graduate_s/undergraduate_colleg/fordham_college_at_1/special_programs/honors_program/seaportproject/decl/containerization.html. [Accessed 21th October, 2013].
- GV Safety, 2004.** *Workplace Health and Safety: Push it or Pull it?:* Available Online at: <http://gvsafety.com/Documents/SAFETY%20HANDOUTS/Ergonomics/Ergonomic%20Equipment/Pushing%20vs.%20Pulling%20Objects.pdf>. [Accessed 20th April 2014].
- Han. D.S, S.W Yoo, H.S Yoon, M.H Kim, S.H Kim, J.M Lee, 2011** *Coupling analysis of finite element and finite volume method for the design and construction of FPSO crane.* Automation in Construction: Published by Elsevier.
- Hand.B, 2013.** Material generated by Brian Hand (Author).
- Håkansson C & Lenngren M J., 2010.** *CFD Analysis of Aerodynamic Trailer Devices for Drag Redution of Heavy Duty Trucks: Master's Thesis 2010:10*: Master's thesis in the Master's programme of Automotive Engineering: 2.3 Computational fluid Dynamics: Page 6:
- Hamedi. M a, 2010.** *Containership Load Planning With Crane Operations*: Faculty of the Graduate School of the University of Maryland: Chapter 1: Introduction: *Containerisation*. Page 1
- Hamedi.M b, 2010.** *Containership Load Planning With Crane Operations*: Faculty of the Graduate School of the University of Maryland: Chapter 1:1.1 The Container. Page 13
- Heller V,2012.** Imperial College London: *Model---Prototype Similarity Prototype Similarity*: Fluid Mechanics Section, Department of Civil and Environmental Engineering4: the Coast Lab Teaching School, Wave and Tidal Energy, Porto, 17-20th January

2012. Available Online at:

http://www.drvalentinheller.com/Dr%20Valentin%20Heller_files/Heller_Model-Prototype%20Similarity.pdf. [Accessed 13th April 2014].

Heller, V. 2012, Three Replies to Discussions of „Scale effects in physical hydraulic engineering models“ by Pfister, M., and Chanson, H.; Tafarjnoruz, A., and Gaudio; Echávez, G., R. *Journal of Hydraulic Research* 50(2):246; 248; 249-250.

HK Electric, 2011. About Us: Lamma Wind Power Station: *Exhibition on Renewable Energy*. Available Online at http://www.hkelectric.com/web/AboutUs/RenewableEnergy/ExhibitionCentre/WindEnergy_en.htm. [Accessed 6th November 2013].

Houghton E. L & P. W. Carpenter, 2003 Aerodynamics for Engineering Students, 5th Edition: Viscous Flow and Boundary Layers: *Momentum Thickness*: Page 387. Published by Butterworth-Heinemann

Hiester P, 2013. Computational Fluid Dynamic Simulation of a Straight Labyrinth Seal for Leakage and Thermal Characterization: Rensselaer Polytechnic Institute Hartford, Connecticut: 2. Methodology / Approach: 2.3 *Meshing*: Page 25.

HSE (Health & Safety Executive), 2001. *Review of model testing requirements for FPSO's*: Prepared by BMT Fluid Mechanics Ltd for the Health and Safety Executive: Offshore Technology Report 2000/123: ISBN 0 7176 2046 8: Printed and Published by the Health & Safety Executive.

HSE, 2004. Review of the risks associated with pushing and pulling heavy loads: Prepared by Health and Safety Laboratory for the Health and Safety Executive 2004 RESEARCH REPORT 228: J.J. Ferreira, M.G. Boocock and M.I. Gray: Page 9: ISBN 0 7176 2845 0 Available Online at <http://www.hse.gov.uk/research/rrpdf/rr228.pdf>. [Accessed 20th April 2014].

Huston R & Harold J, 2011. Practical Stress Analysis in Engineering Design 3rd Edition, Third Edition: Published by CRC Press. ISBN 978-1-57444-713-2.

Ismail, R, 2008. Logistics Management: Chapter 8: Containerisation: *Benefits of Trade*: Page 131. ISBN: 978-81-7446-627-3. Printed by Excel Books.

Oberkampf W L & C J Roy, 2010. Verification and Validation in Scientific Computing: 8.7 Mesh Refinement Techniques. Published by Cambridge University Press,

Olsson J, 2006. Karlstad University: Safety Turnbuckle: Page 7

Omega, 1999. Practical Strain Gage Measurement: Available Online at: http://www.omega.com/techref/pdf/StrainGage_Measurement.pdf. [Accessed 20th April 2014].

Onera, 2006. The French Aerospace Lab: Science Pictures: *Transitional Flow along a Sheet* Available Online at: <http://onera-windtunnel.com/photos-en/tunnel/turbulence-1.php>: [Accessed 11th April 2014].

Iforce2d, 2013. Crushing Immovable objects since 2011: Box2D C++ tutorials – Buoyancy: Lift: Available Online at: <http://www.iforce2d.net/b2dtut/buoyancy>. [Accessed 16th November 2013].

- Innovative CFD, 2014.** Making Sense of CFD Grid Types: *Structured Grids*; Available Online at: <http://www.innovative-cfd.com/cfd-grid.html>. [Accessed 12th April 2014].
- Jayakody S, 2009.** Bright Hub Engineering: Mechanical Engineering: Manufacturing Technology. Available Online at <http://www.brighthubengineering.com/manufacturing-technology/57192-why-is-selection-of-engineering-materials-important/>. [Accessed 18th April 2014].
- Joyce.B, 2012.** Federal Reserve Bank of Richmond: Publications: Current Publications: Economic History: *The Voyage to Containerization*: How a North Carolina trucker freed world trade. Page 39.
- Jouhaud J.C, Sagaut P & Labeyrie B, A Kriginh 2005.** Approach for CFD/Wind Tunnel Data Comparison: Journal of Fluids Engineering: Introduction: Page 3
- Kandasamy S. H. Cheng R.Lietz, S. Mallick, 2002.** *Exterior airflow simulations using a lattice Boltzmann approach*. SAE, 2002-01-0596, 2002.
- Karimi, M Akdogan G & Bradshaw S M., 2011.** *Effects of different mesh schemes and turbulence models in cfd modelling of stirred tanks*: Department of Process Engineering, Stellenbosch University, Private Bag X1, Matieland 7602, Stellenbosch, South Africa: Physicochemical Problems of Mineral Processing: ISSN 1643-1049: 2.1. RANS based turbulence mode: Page 516.
- Katul, G.G., Mahrt, L., Poggi, D., Sanz, C., 2004.** *One- and two-equation models for Canopy turbulence*. Boundary-Layer Meteorol. Pages 113, 81–109.
- Krugman, P, 2009.** Citigroup Foundation Special Lecture, Festschrift paper in Honour of Alan V. Deardorff, University of Michigan IPC working paper 91.
- Landrum, D.B., Beard, R.M., LaSarge, P.A. & von Sprecken, N.,1997.** Evaluation of Stereolithography Rapid Prototyping for Low Speed Airfoil Design, 35th Aerospace Sciences Meeting & Exhibit, Reno, NV, Jan. 6-9.
- Langhaar H.L, 1980.** *Dimensional Analysis and Theory of Models*: Robert E. Krieger Publishing Co, Malabar,FL.,1980. Published by Wiley & Sons Inc, New York 1951.
- Leap, 2012.** *Computational Fluid Dynamics: Tips & Tricks*: Inflation Layer Meshing in ANSYS: Available Online at: <http://www.computationalfluidynamics.com.au/tips-tricks-inflation-layer-meshing-in-ansys/>: [Accessed 18th November 2013].
- Lee.K, 2004.** Ductile link tie-down systems for quay cranes: Port Technology International: liftech Consultants Inc, Oakland, California, USA: Introduction: *Tie-down failures*. Available Online at: http://www.porttechnology.org/images/uploads/technical_papers/PT31-10.pdf. [Accessed 11th November 2013].
- Lee .S.J & Kang .J, H,2007.** *Wind Load on a container crane located in atmospheric boundary layers*: Journal of Wind Engineering and Industrial Aerodynamics 96 (2008) 193-208: Department of Mechanical Engineering, Pohang University of Science and Technology, Hyoja-dong, Pohang 790-784, South Korea: 1 Introduction: Published by Elsevier Ltd.
- Lee S.W, Kim Y, Han D.S, Han G.J, 2007.** Proceedings of the 4th WSEAS International Conference on Fluid Mechanics, Gold Coast, Queensland, Australia, January 17-19, 2007:

Page 64. Wind Tunnel Study on the Structural Stability of a Container Crane According to the Boom Shape. *Introduction*.

Leishman J, 1990. *Dynamic stall experiments in the NACA 23012 aerofoil*. Experiments in Fluids. Page 49-58.

Leishman J & Tyler J.C, 1992. *Analysis of pitch and plunge effects on unsteady airfoil behaviour*: Journal of the American Helicopter Society: Pages 37-69.

Levinson. M, 2006. *The Box: How the Shipping Container Made the World Smaller and the World Economy Bigger*. Page 2. ISBN: 987-0-691-12324-0. Printed by Princeton University Press.

Lim.S.M, 1994. Economics of container ship size: a new evaluation: Department of International Trade, Handshin University, 411 Yangsan-Dong Osan-Si, Kyungki-Do, Republic of Korea: *1. Introduction*: Volume 21, Number 2: Page 149.

Linn Gear, 2013. All Products: Gears: *Bevel Gears*. Available Online at: <http://www.linngear.com/part-type/bevel/>. [Accessed 10th November 2013].

Lloyd's Register, 2012. Info sheet No 30: *Modern Ship Size definitions*. Available Online at: http://www.lr.org/Images/30%20ship%20sizes_tcm155-173543.pdf [Accessed 2nd November 2013].

Liebherr Group, a 2013. Material obtained from Liebherr Group.

Liebherr Group, b 2013. Production site in Killarney (Ireland): Liebherr Container Cranes. Available Online at <http://www.liebherr.com/en-GB/35279.wfw>. [Accessed 24th October, 2013].

Li F, 2010. Study of Stress Measurement Using Polariscope: A Thesis Presented To The Academic Faculty Georgia Institute of Technology

Logdberg O, 2008: Turbulent boundary layer separation and control: Technical Reports from: Royal Institute of Technology: KTH Mechanics: SE-100 44 Stockholm, Sweden

Luck.K & Modler.L, 1990. *Getriebetechnik- Analyse, Synthese, Optimierung*. Printed by Springer –Verlag Wien, New York.

Manwell .J.F, McGown J.G, Rogers A.L, 2009. *Wind Energy Explained: Theory Design and Application: Second Edition: Chapter 2: Wind Characteristics and Resources: 2.2 General Characteristics of the Wind Resource: 2.2.1 Wind Resource: Global Origins: 2.2.1.2 Mechanics of Wind Motion*. Page 24. ISBN: 978-0-470-01500-1. Published by Wiley.

Macro Sensors, 2014. LVDT Basics: What is an LVDT. Available Online at: http://www.macrosensors.com/lvdt_tutorial.html. [Accessed 23th April 2014].

Mahmood M, 2011. Flow Visualization in Wind Tunnels King Fahd University of Petroleum & Minerals Kingdom of Saudi Arabia: Wind Tunnels and Experimental Fluid Dynamics Research: ISBN: 978-953-307-623-2. Page 6

Mangonon, Pat L. 1999. *The Principles of Material Selection for Engineering Design* Prentice- Hall, New Jersey, USA pp 430-435

- Marin L E., 2014:** Fluid Mechanics: Available Online at: <http://blogs.uprm.edu/inqu4010fluids/files/2010/03/Chapter-7-Dimensional-Analysis-Modeling-and-Similitude.pdf>. [Accessed 13th April 2014].
- Marine Insight, 2010.** *Container-Gantry-Crane-Construction-and-Operation*. Available Online at <http://www.marineinsight.com/marine/container-gantry-crane-construction-and-operation/>. [Accessed 24th October, 2013].
- Materials Engineer, 2012.** Metallurgical Consultants: Fatigue Failures Available Online at <http://www.materialsengineer.com/CA-fatigue.htm> . [Accessed 22th April 2014].
- McCarthy. P & Vazifdar.F, 2004.** Liftech Consultants: ASCE PORTS 2004 Conference :Houston, Texas. *Securing Cranes for Storm Wind: Uncertainties and Recommendations: Background: Page 1.*
- McDonough J. M., 2007.** Introductory Lectures on Turbulence: Physics, Mathematics and Modelling Departments of Mechanical Engineering and Mathematics: University of Kentucky: Chapter 1. Fundamental Considerations: 1.2 Some Descriptions of Turbulence
- McMurtry P, 2000.** Professor: Mechanical Engineering: Associate Dean, Graduate School University of Utah, Turbulence: Class Notes: Length and Time Scales: Available Online at: <http://www.eng.utah.edu/~mcmurtry/Turbulence/turbflt.pdf>. [Accessed 11th April 2014].
- Menter,F.R.,1994.***Two-equation eddy-viscosity turbulence models for engineering applications.* AIAA Journal 32 (8), Page 1598–1605.
- MIT, 2002.** Open Course Ware: Mechanical Engineering: Turbulent Flow: Available Online at: <http://ocw.mit.edu/courses/mechanical-engineering/2-000-how-and-why-machines-work-spring-2002/study-materials/TurbulentFlow.pdf>. [Accessed 15th April 2014].
- MIT,2004.** Marine Hydrodynamics, Fall 2004: Lecture 17: Department of Ocean Engineering: Available Online at: <http://web.mit.edu/13.021/demos/lectures/lecture17.pdf>. [Accessed 15th April 2014].
- MIT (Massachusetts Institute of Technology), 2002.** OpenCourseWare: Civil and Environmental Engineering: Transport Processes in the Environment, Fall 2002: *7. Velocity Profiles and Turbulence:* Available Online at:<http://dspace.mit.edu/bitstream/handle/1721.1/37147/1-061Fall-2002/OcwWeb/Civil-and-Environmental-Engineering/1-061Transport-Processes-in-the-EnvironmentFall2002/LectureNotes/detail/7-lec.htm>: [Accessed 11th April 2014].
- Moffatt, H K 1963.** Viscous and resistive eddies near a sharp corner; Journal of Fluid Mechanics, Volume 18, part 1,pp 1-18. Trinity College, Cambridge. Printed by University Printing House, Cambridge Brooke Crutchley, University Printer.
- Moonena P, Blockena. B, Roelsa S. & Carmelieta J., 2006.** *Numerical modelling of the flow conditions in a closed-circuit low-speed wind tunnel:* Journal of Wind Engineering and Industrial Aerodynamics 94 (2006) 699–723. Introduction. Published by Elsevier Ltd.
- Moin P & Kim J, 2012.** Stanford University: Centre for Turbulence Research: Tackling Turbulence with Supercomputers: Available Online at: <http://www.stanford.edu/group/ctr/articles/tackle.html>. [Accessed 12th April 2014].

Mott, R., 2006. *Machine Elements in Mechanical Design, Fourth Edition in SI units*. Page 141, 185, Appendix 3. Published by Pearson Education, Inc

Munson, B.R, Rothmayer, A.P & Okiishi T.H, 2012. *Fundamentals of Fluid Mechanics 6Ed*: Chapter 9: Flow over immersed Bodies: Page 478-482. ISBN: 978-0-470-47103-6: Printed by Wiley Global Education.

National Geographic, 2013. Daily News: Environment: Rising Temperatures May Cause More Katrinas: *Small increases in temperature found to add power to storms in the Atlantic*: Daniel Stone: National Geographic News: Published March 19, 2013. Available Online at: <http://news.nationalgeographic.com/news/2013/03/130319-hurricane-climate-change-katrina-science-global-warming/>. [Accessed 10th November 2013].

NASA a (National Aeronautics and Space Administration), 2011. Precipitation Measurement Missions: *Visualisations of Hurricane Floyd*: Available Online at: <http://pmm.nasa.gov/node/225>. [Accessed 10th November 2013].

NASA b (National Aeronautics and Space Administration), 2008. Centers: Ames Research Centre: News: Releases: NASA Tunnels Test Tennis Balls: Available Online at: <http://www.nasa.gov/centers/ames/news/releases/2000/00images/tennisball/Tennispage.html>. [Accessed 17th November 2013].

NASA c (National Aeronautics and Space Administration), 2010. *Boundary Layer*: Glenn Research Centre: Available Online at: <http://wright.nasa.gov/airplane/boundlay.html>. [Accessed 20th November 2013].

NASA (National Aeronautics and Space Administration), 2012: SP-4302 Adventures in Research: A History of Ames Research Center 1940-1965: PART II : A NEW WORLD OF SPEED : 1946-1958: Boundary Layer, Skin Friction, and Aerodynamic Heating: Available Online at: <http://history.nasa.gov/SP-4302/ch2.12.htm>. [Accessed 9th April 2014].

NI (National Instruments), 2014. Measuring Strain with Strain Gages: 2. The Strain Gage: Available Online at: <http://www.ni.com/white-paper/3642/en/>: [Accessed 22th April 2014].

NTUU (National Tsing Hua University), 2011. Open Course Ware: Chapter 9: *Flow over Immersed Bodies*: Available Online at: <http://ocw.nthu.edu.tw/ocw/upload/2/183/Flow%20over%20Immersed%20Bodies.pdf>. [Accessed 9th April 2014].

Nielsen P V, Allard F, Awabi H B, Davidson L, Schaalin A, 2007. *Computational fluid dynamics in ventilation design*. REHVA (Federation of European Heating and Air-conditioning Associations) Guidebook, Finland.

Nielsen P, 2011. 3D CFD-analysis of conceptual bow wings: 070 7 – 384496: Master Thesis: Ver. 0.1: KTH Center for Naval Architecture

Pennstate CICTR (The Centre for Information and Communications Technology Research), 2008. Kolmogorov Cascade Theory of Turbulence. Available Online at: <http://cictr.ee.psu.edu/research/pcs/index.html>. [Accessed 11th April 2014].

Port Technology, 2012. News: *Liebherr delivers first STS cranes to Brazil*. . Available Online at: http://www.porttechnology.org/news/liebherr_delivers_first_sts_cranes_to_brazil. [Accessed 9th November 2013].

PIMS (Pacific Institute for the Mathematical Sciences), 2013. Lectures: Kolmogorov's 1941 Theory Introduction: Available Online at: <https://www.pims.math.ca/files/Hydro-Sverak-Lecture2.pdf>. [Accessed 11th April 2014].

Phillips JW, 2006. University of Sao Paulo: TAM 326—Experimental Stress Analysis Available Online at <http://www.ifsc.usp.br/~lavfis2/BancoApostilasImagens/ApEfFotoelastico/photoelasticity.pdf> ./. [Accessed 20th April 2014].

Plastics U, 2013. Mesh quality Definition: Mesh Quality *Definition: Mesh Quality* Overview: Available Online at: <http://help.plastics-u.com/online-help/moldex3d-pre-processing-tools/moldex3d-mesh/mesh-quality-definition/>. [Accessed 12th April 2014].

Princeton University, 2013. Aerodynamics of Bicycles: Drag of Blunt Bodies and Streamlined Bodies Available Online at: http://www.princeton.edu/~asmits/Bicycle_web/blunt.html. [Accessed 8th April 2014].

Princeton, 2012. Aeroelasticity: Available Online at: <http://www.princeton.edu/~achaney/tmve/wiki100k/docs/Aeroelasticity.html>. [Accessed 14th April 2014].

Ouazizi A e, 2006. CFD based aerodynamic redesign of a marcos lm600: Delft University of Technology Aerospace Engineering Department Chair of Aerodynamics: Chapter 2: Grid Generations: 2.2.7 *Turbulent flows*: Page 10.

Rangan CS, 1997. Instrumentation Devices and Systems 2nd Edition: Page 62: Instrumentation and Device: Temperature Effects ISBN 0-07-463350-3: Published by Tata McGraw-Hill Education

RDP, 2009: LVDT: How it works: Available Online at: <http://www.rdpe.com/displacement/lvdt/lvdt-principles.htm>, [Accessed 23th April 2014].

Rizzi, A, 2010: *Background documentation for software & labwork*. Course SD2610 Computational Aerodynamics in Aircraft Design. KTH, Dept. of Aeronautical and Vehicle Engineering, Stockholm.

Ridge, 2013. Red Bull Racing Wind Tunnel, Bedford. : Available Online at: www.ridge.co.uk/Ridge/SectorsAndProjects/MotorSport/RedBullF1RacingWindTunnel.html. [Accessed 15th April 2014].

Ristić S, 2007. Flow Visualisation Techniques in Wind Tunnels :Scientific Technical Review, Vol.LVII,No.1,2007 39: UDK: 533.6.07: 532.529 COSATI: 01-01 :Part I – Non optical Methods

Roymech.2012. *Basic Notes on Factor of Safety*. [Online] Available at: http://www.roymech.co.uk/Useful_Tables/ARM/Safety_Factors.html [Accessed 03 March 2014].

Rodrigue. JP & Notteboom. T, 2007. The future of containerization: Box logistics in light of global supply chains: Proceedings of the 2007. International Association of Maritime Economists (IAME) Conference, July, Athens: 1.Introduction: *1.1 Looking Back at Fifty Years of Containerization*. Page 2.

Roy,A, 2012. *Derivation of Surface Roughness and Capacity Factor from Wind Shear Characteristics*: INTERNATIONAL JOURNAL of RENEWABLE ENERGY RESEARCH Apratim Roy, Vol.2, No.2, 2012: 3. Derivation of Wind Shear Characteristics. Page 349.

Schiavenza.M, 2013. *The Atlantic: China: China's Dominance in Manufacturing—in One Chart*. Available Online at: <http://www.theatlantic.com/china/archive/2013/08/china-dominance-in-manufacturing-in-one-chart/278366/>. [Accessed 21th October, 2013].

Scott R, 2001. In the Wake of Tacoma: Suspension Bridges and the Quest for Aerodynamic Stability Chapter 8: The Problematic Plate Girder: Page 351 Published by ASCE Publications

Schukar V, Kusche N, Kalinka G& Habel W, 2013. Field Deployable Fiber Bragg Grating Strain Patch for Long-Term Stable Health Monitoring Applications BAM Federal Institute for Materials Research and Testing, Unter den Eichen 87, D-12205 Berlin, Germany: applied sciences ISSN 2076-3417: www.mdpi.com/journal/applsci

Settles,G.S, 1986. Modern Developments in Flow Visualization, AIAA: Journal, 1986, Vol.24, No.8, pp.1313-1323

Selvam, R.P., 1998, “Computational Procedures in Grid Based Computational Bridge Aerodynamics”, in Larsen, A., and Esdahl, S. (eds), Bridge Aerodynamics, A.A Balkema, Rotterdam, pp. 327-336.

Selvam R P & Govindaswamy S, 2001. A Report on aeroelastic analysis of bridge girder section using computer modeling for Mack Blackwell Transportation Center May 2001: University of Arkansas

Sandvick, 2014. Home: Materials center: Material datasheets: Tube and pipe, seamless: Sandvik SAF 2507: Available Online at <http://www.smt.sandvik.com/en/materials-center/material-datasheets/tube-and-pipe-seamless/sandvik-saf-2507/>. [Accessed 18th April 2014].

Shifler D. A, 2005. Corrosion in Marine and Saltwater Environments II: Proceedings of the International Symposium: Electrochemical Society. Corrosion: Introduction: Page 84: ISBN 1-56677-457-8.

Steel Masters, 2014. ISO Coarse Threads: Available Online at http://www.steelmasters.co.nz/webfiles/SteelmastersNZ/files/Internal_Thread_Dimensions_for_Metric_Coarse_Pitch_Screw_Thread.pdf. [Accessed 20th April 2014].

Simlu.E, Heckert.N.A & Whalen.T.M, 1998. National Institute of Standards and Technology (NIST): Publications: *Mean Recurrence Intervals of Ultimate Wind Loads*. 17th International Conference on Offshore Mechanics and Arctic Engineering: ASME: OMAE98-1218: Introduction:

Simerics, Inc, 2012. Simerics Gallery: Classic Fluid Problems: Benchmark & Validation: VORTEX STREET. Available Online at: http://www.simerics.com/gallery_vortex. [Accessed 14th November 2013].

SRL, 2004. The Georgia Institute of Technology The Systems Realization Laboratory: the George W. Woodruff School of Mechanical Engineering: education: me6105: projects: fall 2011 projects: simulation-based design study of a rapid prototyping machine: Available Online at:

<http://www.srl.gatech.edu/education/ME6105/Projects/Fa11/rapidprototyping/>. [Accessed 15th April 2014].

Srinivasan.V & Halada.G, 2012. Department of Materials Science and Engineering State University of New York at Stony Brook: *Engineering Disasters and Learning from Failure: Engineering Ethics*: Available Online at : <http://www.matscieng.sunysb.edu/disaster/>. [Accessed 22th of November 2013].

Starcs, 2013. Aerodynamics Research and Analysis: Facilities: Balance Calibration Rigs Available Online at: http://www.starcs.se/balance_calibration_rigs.aspx. [Accessed 15th April 2014].

Smith S, 2002 . Recent advances in digital data acquisition technology. *Sound and Vibration*, 36(3), Pages 18-21.

Siraj.A, 2010. *Wind Energy : Theory And Practice*, 1st Edition: Chapter 2: *Wind Resource Assessment: 2.1 Introduction*. Page 8 ISBN: 978-81-203-4066-4. Published by PHI Learning.

Sople.V, 2007. *Logistics Management: The Supply Chain Imperative*. Page 108. 8.6 *Containerisation*. ISBN 81 317-1055-6. Printed by Pearson Education.

Symscape, 2009. *Computational Fluid Dynamics: Articles: Reynolds-Averaged Navier-Stokes Equations*: Available Online at :<http://www.symscape.com/reynolds-averaged-navier-stokes-equations>. [Accessed 12th April 2014].

Takacs.G & Rohal-Ilkiv.B, 2012. *Damped Mechanical Structures: Chapter 2: Basics of Vibration Dynamics: Free Vibration Damping*: Page 29: ISBN: 978-1-4471-2332-3. Published by Springer.

TCD (Trinity College Dublin), 2006: *Fluent: 14.1 Mesh Quality*: Available Online at: http://www.tchpc.tcd.ie/fluent/Unpacked_ISO/TGrid__4.0_Documentation/tgrid4.0/help/html/ug/node314.htm. [Accessed 12th April 2014].

TecQuipment, 2000. *TQ-Plint TE54: 300mm×300mm Subsonic Suction Tunnel Operating Manual*: TQ Education and Training Ltd: Products Division: PW/MP?ajp/0398.

TecQuipment a, 2013. *Aerodynamics: Basic Lift and Drag Balance: AFA2*: Measures lift and drag forces on models in a TecQuipment Subsonic Wind Tunnel (AF100): PE/bs/db/0313.

TecQuipment b, 2013. *Supporting Products: VDAS (Versatile Data Acquisition System)*: Page 2: Description: PE/db/1013.

TERCO AB, 1977. *TERCO Polariscope MT7300 Manual*: 525 091/01

Tong.W, 2010. *Wind Power Generation and Wind Turbine Design: Chapter 1: Fundamentals of wind energy: Wind Energy: 2. Wind Generation*. Published by WITpress: ISBN: 978-1-84564-205-1.

Tominaga Y, Mochida A, Yoshie R, Kataoka H, Nozu T, Yoshikawa M, 2008. *AIJ guidelines for practical applications of CFD to pedestrian wind environment around buildings*. *J Wind Eng Ind Aerodyn*;96(10–11):1749–61.

TU Delft, 2014. Aerospace Engineering: Study: Online Education: Online MSc courses in Aerospace Engineering: Aeroelasticity: Available Online at <http://www.lr.tudelft.nl/en/study/online-education/online-msc-courses-in-aerospace-engineering/aeroelasticity/>. [Accessed 18th April 2014].

Tu J, Yeoh G H, & Liu C, 2013. Computational Fluid Dynamics: A Practical Approach 2nd Edition Chapter 6: Guidelines on Grid Generation: Page 237 Published by Butterworth-Heinemann: ISBN: 978-0-08-098243-4

TT Club, 2011. *Recommended minimum safety specifications for quay container cranes* A joint initiative from TT Club, ICHCA International and Port Equipment Manufacturers Association: 1 Introduction: Page 6. ISBN 978-1-85330-0349 Available Online at: http://www.ttclub.com/fileadmin/uploads/tt-club/Publications___Resources/Annual_Reports/Recommended%20minimum%20safety%20specifications%20for%20quay%20cranes%2020110607.pdf. [Accessed 28th November 2013].

UCAR (University Corporation for Atmospheric Research), 2007. News Centre: News Releases: NCAR News Release: *Frequency of Atlantic Hurricanes Doubled Over Last Century; Climate Change Suspected*: Greg Holland: Available Online at: <http://www.ucar.edu/news/releases/2007/hurricanefrequency.shtml>. [Accessed 10th November 2013].

Uddanwadiker R, 2011. Stress Analysis of Crane Hook and Validation by Photo-Elasticity: Department Mechanical Engineering, Visvesvaraya National Institute of Technology, Nagpur, India: Published by Scientific Research.

Verschoof, J, 2002. *Cranes - Design, practice and maintenance*, 2nd edition, Professional Engineering Publishing Limited.

UOB (University of Babylon), 2006. Downloads: *External Forced Convection: Parallel Flow over Flat Plates*. Available Online at: http://www.uobabylon.edu.iq/uobColeges/ad_downloads/7_9866_900.pdf. [Accessed 27th November 2013].

UN (United Nations), 2005. Economic and Social Commission for Asia and the Pacific: monograph Series on Managing Globalization: Regional Shipping and Port: Development strategies: (Container Traffic Forecast): Container Trade Growth 3.2 *Global Container Forecasts*. Page 28-29.

University of Leeds, 2008. Institute of Engineering Thermofluids, Surfaces and Interfaces; school of mechanical engineering: Continuity and Conservation of Matter: 1. Mass flow rate: Available Online at: <http://www.efm.leeds.ac.uk/CIVE/CIVE1400/Section3/continuity.htm> [Accessed 13th April 2014].

UML (University of Maryland) 2013. Physics: Random vs Systematic Error Available Online at: <http://www.physics.umd.edu/courses/Phys276/Hill/Information/Notes/ErrorAnalysis.html>: [Accessed 15th April 2014].

Young, D.F. Munson, B.R. Okiishi, T.H. Huebsch, W.W. 2011 A Brief Introduction To Fluid Mechanics: 5th Edition. Chapter 9: *Flow over Immersed Bodies*: pp 321-322. ISBN 13 978-0470-59679-1: Published by John Wiley and Sons.

- Van Ham, J.C, 2005.** The feasibility of mega container vessels: Faculty of Technology, Policy and Management, Delft University of technology, The Netherlands. 2.2 *The Panamax age*. Page 91.
- UTAS (University of Tasmania), 2012.** 3 Meshing Strategy: 3.4 Mesh Quality: 3.4.2 Aspect Ratio. Available Online at: <https://elibrary.utas.edu.au/utas/file/006d5bf6-eae3-e24e-adf8-33a169744809/1/Fell%20Chapter%203.PDF>. [Accessed 13th April 2014].
- (VT ARC, 2013).** Virginia Tech, Advanced Research Computing: Turbulence Modelling: 4.13.1.Overview. Available Online at: http://www.arc.vt.edu/ansys_help/flu_th/flu_th_sec_turb_near_wall_overview.html. [Accessed 13th April 2014].
- Virginia Tech, 2012.** Advanced Research Computing: ANSYS: 5.2.2.*Mesh Quality*: Available Online at:http://www.arc.vt.edu/ansys_help/flu_ug/flu_ug_mesh_quality.html. [Accessed 15th April 2014].
- Uruba V & Knob M, 2009.** Dynamics of a boundary layer separation: Separation
- Vishay, 2011.** System 7000: StrainSmart® Available Online at: Data Acquisition System <http://www.vishaypg.com/docs/11271/syst7000.pdf>. [Accessed 23th April 2014].
- Vertikal, 2008.** News: Story: *Cranes damaged at Felixstowe*: March 1, 2008. Available Online at: <http://www.vertikal.net/en/news/story/5498/> [Accessed 10th November 2013].
- Wallin S, 2009:** *Notes for: Applied Computational Fluid Dynamics (5C1213)*. KTH, Dept. of Mechanics and Systems Dept. FOI. Stockholm.
- Wang, J, 2008.** University of Washington: *Laboratory of Nanomechanics of Complex Material Systems* .Available Online at: <http://depts.washington.edu/nanomech/teaching.html>. [Accessed 27th November 2013].
- Warhaft, Z, 1997.** *The Engine and the Atmosphere: An Introduction to Engineering*, Cambridge University Press: Transition and Turbulence. Available Online at: http://www.princeton.edu/~asmits/Bicycle_web/transition.html. [Accessed 10th November 2013].
- Warnes, W. H, 2006.** Oregon State University: ENGR322: Final Exam: Spring 2006: Fractography. Available Online at: <http://oregonstate.edu/instruct/engr322/Exams/AllExams/S06/ENGR322-Final.html>. [Accessed 11th November 2013].
- Whelan, 2010.** UNCC (University of North Carolina Charlotte): ES222 Strength of Materials Spring 2010 Available Online at http://coefs.uncc.edu/mwhelan3/files/2010/10/ICD_Saint_Venant1.pdf. [Accessed 20th April 2014].
- Wheeler A.J & Ganji A.R, 1996.***Introduction to Engineering Experimentation*: Chapter 10: Measurement of Fluid Flow Rate: Fluid Velocity: Fluid Level, and Combustion: Subchapter 10.2: Systems for the Measurement of Fluid Velocity Pollutants: 10.2.1 Pitot-Static Probe: Page 305-306. ISBN: 0-13-337411-4: Published by Prentice Hall, Inc.
- White F.M, 2003.***Fluid Mechanics 3rd Edition*: Dimensional Analysis and Similarity: Page 251-308: ISBN: 0071333126: Publied by Tata McGraw: Hill Education.

Wolfram, 2007. Research: Units and Dimensional Analysis Dimensionless Parameters: Buckingham Pi Theorem: Available Online at: <http://scienceworld.wolfram.com/physics/BuckinghamsPiTheorem.html>. [Accessed 14th April 2014].

World Shipping Council (WSC) a, 2013. About the Industry: History of Containerization: *Before Container shipping*. Available Online at <http://www.worldshipping.org/about-the-industry/history-of-containerization/before-container-shipping>. [Accessed 16th October, 2013].

World Shipping Council (WSC) b, 2013 About the Industry: History of Containerization: The Birth of Intermodalism: *The Container*. Available Online at: <http://www.worldshipping.org/about-the-industry/history-of-containerization/the-birth-of-intermodalism> [Accessed 22nd October, 2013].

Ye. Q, 2004. *Typhoon Rusa and Super Typhoon Maemi in Korea*. Chapter 4: 4.2 Super Typhoon Maemi Impacts :*Impacts of the national economy*: Page 18:

Zarius D, 2012. Online Textbook: Chapter 34: Concept 34.2: *Climate determines global wind patterns in the biosphere*: Page 750- 752. Figure 34-7. . Available Online at: <http://biologytb.net23.net/text/chapter34/concept34.2.html>. [Accessed 6th November 2013].

Zhu N, 2007. Wind tunnel test for guyed mast dynamic characteristics under wind loads: Department of Civil and Geological Engineering University of Saskatchewan Saskatoon: Mast Modelling Page: 56: 3.3.3.1 Overview: 3.3.3.2 Scaling of Structural Stiffness

Zhanga R, YZhang, K P Lama, & D H. Archer 2010. A prototype mesh generation tool for CFD simulations in architecture domain: 4. *CFD simulations*: Page 2257. Building and Environment 45 (2010) 2253e2262

12.0 Bibliography

- Andersson. B, Andersson. R, Hakansson. L, Sudiyo.R, Wachem. B.V & Hellstorm.L, 2012.** *Computational Fluid Dynamics for Engineers*, Chapter 4: Turbulent Flow Modelling: 4.1 The Physics of fluid turbulence: 4.1.1 Characterises features of turbulent flow: Page 63-66: ISBN 978-1-107-01895-2 Printed by Cambridge University Press
- Ai Z.T & Mak C.M. 2013.** *CFD simulation of flow and dispersion around an isolated building: Effect of inhomogeneous ABL and near-wall treatment*: Department of Building Services Engineering, The Hong Kong Polytechnic University, Hong Kong: 3. Near-wall treatments 3.1. Wall functions modified for rough surfaces: Page 570. Published by Elsevier:
- Altekar R.V, 2005.***Supply Chain Management: Concepts and Cases: Concept of Containerisation*: Page 266: Published by PHI Learning Pvt. Ltd.
- ASCE (American Society of Civil Engineers), 2012.** *Wind Tunnel Testing for Buildings and Other Structures*: Chapter 6 Extreme Wind Climate: C 6.1.4 Hurricanes: ISBN 978-0-78-1228-2: Published by the American Society of Civil Engineers (ASCE)
- Bansal R. K, 2005.** Text Book of Fluid Mechanics and Hydraulic Machines: Model Laws or Similarity: 12.9.2 Froude Model Law: Page 583: ISBN 81-7008-311-7: Published by Firewall Media:
- Bireswar M 2011.***Fluid Mechanics with Laboratory Manual*: Chapter 12 Dimensional Analysis and Similitude:12.3 Physical Similarity: Page 377-378: ISBN 978-81-203-4034-3: PHI Learning Pvt. Ltd.
- Bosniakov .S, 1998.** *Experience in integrating CFD to the technology of testing models in wind tunnels*: Progress in Aerospace Sciences 34 (1998) 391-422: Power Unit Department, TsAGI, Zhukovsky 3, Moscow Region, Russia.
- Cebeci T, 2004.***Analysis of Turbulent Flows: 2nd Edition Revised Edition*: Chapter 4: General Behaviour of Turbulent Boundary Layer: 4.2 Composite Nature of Turbulent Boundary layer: Page 81-89: Published by Elsevier: ISBN 0-08-044350-8
- Coronado D, 2006.***Economic Impact of the Container Traffic at the Port of Algeciras Bay*: 1.2 Containerisation Process: Concepts, Resources and Relationships:1 Container Traffic from an economic perspective: 1.2.1 Containerisation and Intermodality Page 6: ISBN 978-3-540-36788-8: Published by Springer
- Defraeyea T, Blockenb B, Koninckxc E, Hespel P & Carmeliet J, 2010** *Aerodynamic study of different cyclist positions: CFD analysis and full-scale wind-tunnel tests*: 5 Conclusions. Page 1267: Published by Elsevier:
- Glabeke, G,2011.** The influence of wind turbine induced turbulence on ultra light aircraft, a CFD Analysis: The Von Karmen Institute for Fluid Mechanics: Chapter 4 Turbulence: What is Turbulence: Pages 4-9.

Gray D, 2000 *A First Course in Fluid Mechanics for Civil Engineers*: Chapter 15: Physical Models and Similarity: 15.1 Scale Model Testing: Page 437-439: ISBN 1-887201-11-4: Published by Water Resources Publications.

Pickering M, 2009. *Human Powered Submarine Hull CFD*: Final Year MEng Engineering University of Bath: Department of Mechanical Engineering: Chapter 19. Accuracy Discussion: 19.1 Effectiveness of the CFD Model: Page 79.

Samardžić M, Isaković J, Anastasijević Z & Marinkovski D, 2013. *Apparatus for measurement of pitch and yaw damping derivatives in high Reynolds number blow down wind tunnel*: *Measurement* 46 (2013) 2457–2466:

Stathopoulos T, Charalambos C, & Baniotopoulos, 2007. *Wind Effects on Buildings and Design of Wind-Sensitive Structures*: 1. Introduction: Page 2-3 ISBN: 978-3-211-73075-1. Published by Springer.

Szirtes T, 2007. *Applied Dimensional Analysis and Modelling, 2nd Edition*: 7.2 The Dimensional Matrix: Page 134: ISBN 978-0-12-370620-1 Published by Elsevier:

Tabrizi A.B, Whalea J, Lyons T, & Urmeea T, 2013. *Performance and safety of rooftop wind turbines: Use of CFD to gain insight into inflow conditions*. 3.2 Computational Fluid dynamic model: 3.2.1. Navier Stokes equations and turbulence models: Page 5. Published by Elsevier:

Tavoularis S, 2005 *Measurement in Fluid Mechanics*: Chapter 6: Wind Tunnels : Fluid Mechanical Apparatus: ISBN 978-0-521-81518-5 : Page 155-156: Published Cambridge University Press.

Tu J, Yeoh J, & Liu C, 2012 *Computational Fluid Dynamics: A Practical Approach 2nd Edition*: Chapter 6: Practical Guidelines for CFD Simulation and Analysis: 6.1 Introduction: Pages 219-220: ISBN: 978-0-08-098243-4 Printed by Butterworth-Heinemann

Versteeg, H & Malaasekera, W, 2007: *An Introduction Computational Fluid Dynamics, the Finite Volume Method*: Chapter 3 Turbulence and its Modelling: Descriptors of Turbulent Flow ISBN 978-0-13-127498-3: Published by Pearson Education

Zikaov O, 2010. *Essential Computational Fluid Dynamics*: Chapter 5 The Finite Volume Method ISBN 978-0-470-42329-5 Published by John Wiley & Sons.

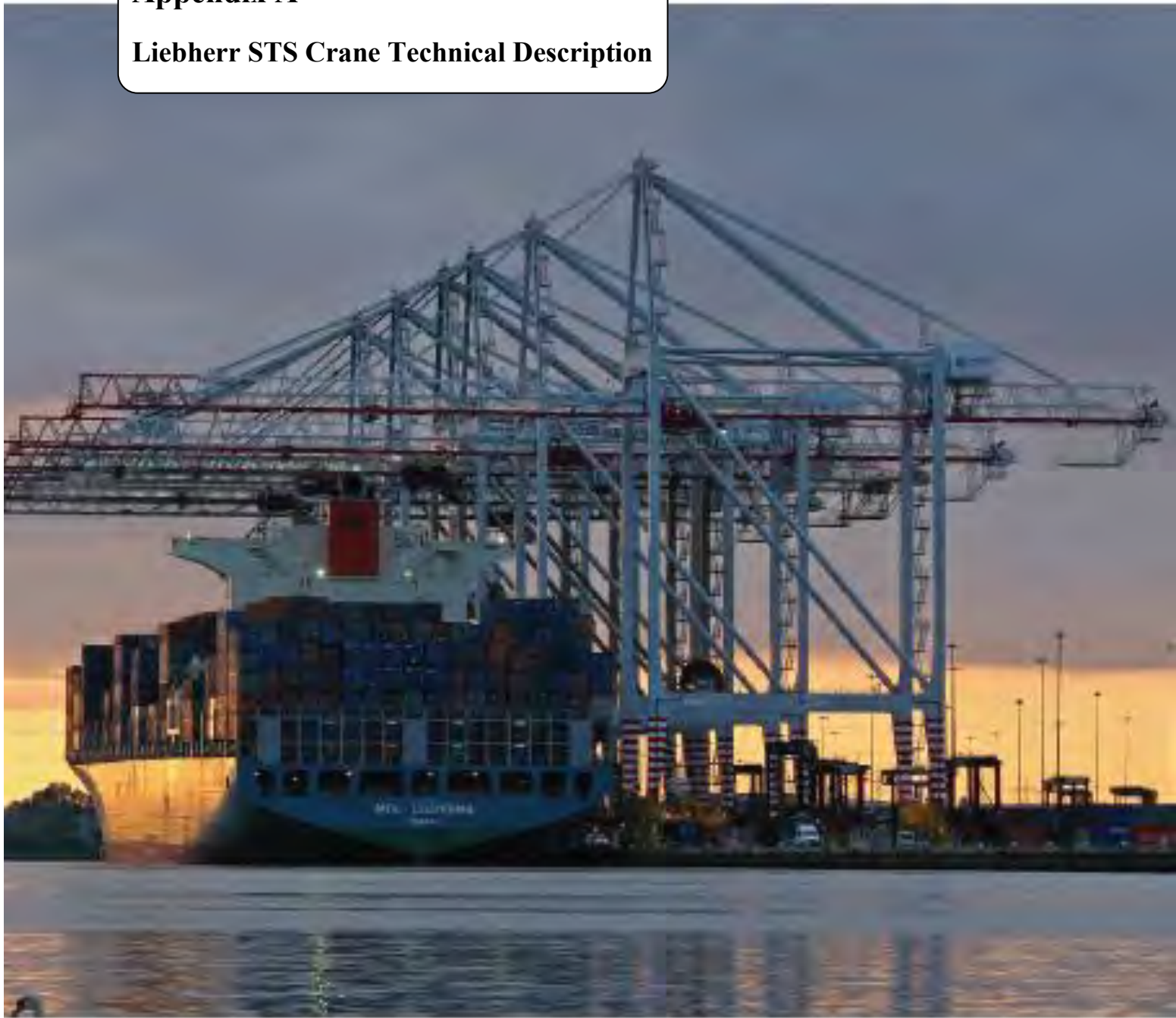
Wanga M, Linb C.H, & Chena Q, 2011. *Advanced turbulence models for predicting particle transport in enclosed environments*: 2.1. Modelling airflow: 2.1.1. RANS: Page 41. Published by Elsevier:

Xu Y.L, 2013. *Wind Effects on Cable-Supported Bridges*: Chapter 8: Computational Wind Engineering: 8.4.9 Verification and Validation: Page 319: ISBN 978-1-118-18828-6 Published by John Wiley & Sons

Technical Description Ship To Shore Gantry Cranes (STS)

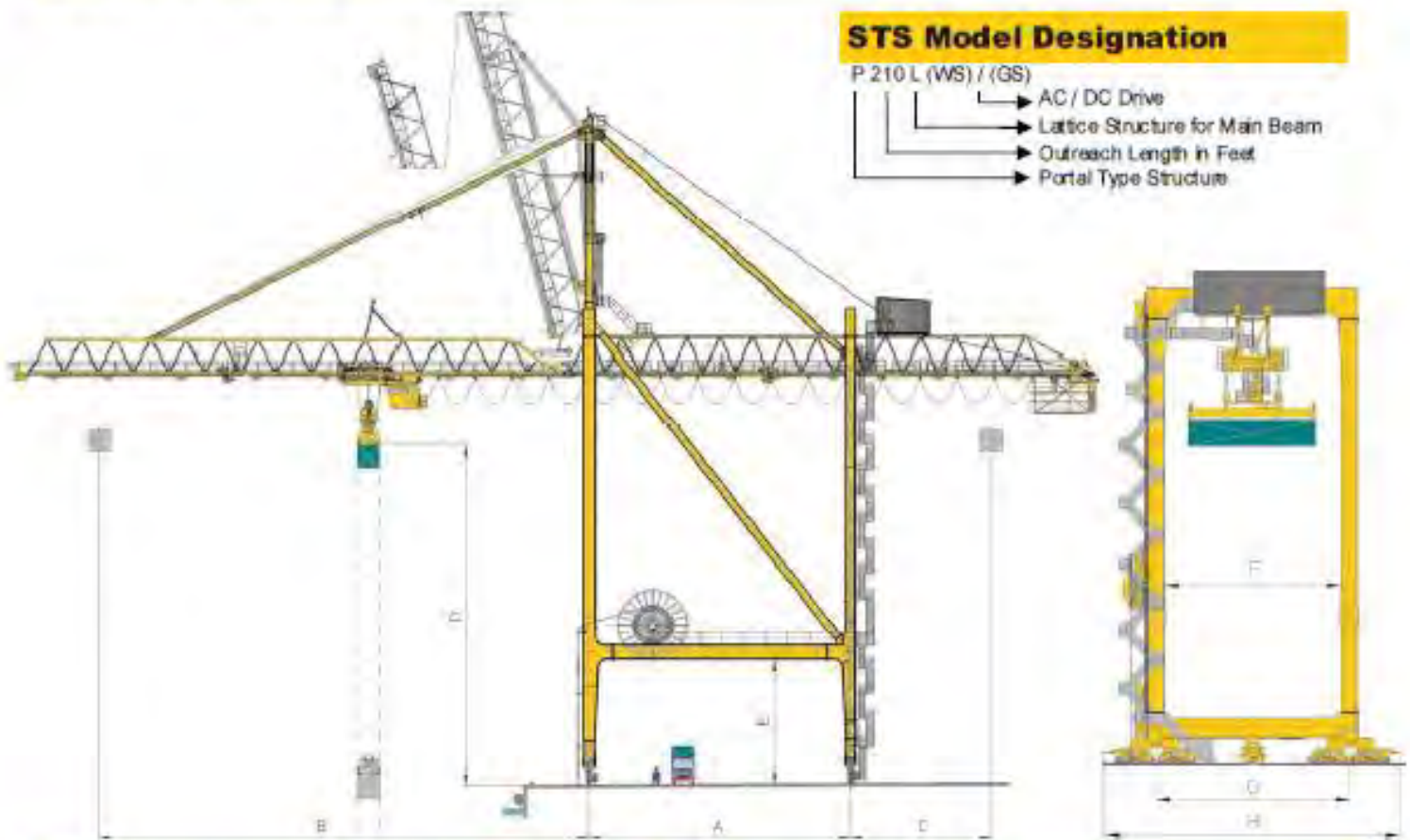
Appendix A

Liebherr STS Crane Technical Description



LIEBHERR

Dimensions



Typical Quayside Crane *

A Gantry Span	15.00 - 35.00m
C Backreach	0.00 - 25.00m
E Clearance Under Sil Beam	12.00 - 18.00m
G Travel Wheel Gauge **	18.20m
H Buffer to Buffer	27.00m
Wheel Spacing **	1.00 - 2.00m
Wheels per Corner **	8 / 12 - Seaside
Wheels per Corner **	8 / 12 - Landside
Max. Width Trolley & Main Beam/Bloom	7.50m

** Dependant on Required Wheel Loads

Typical Feeder - Panamax Crane *

B Outreach	30.00 - 40.00m
D Lift Height	24.00 - 30.00m
SWL Capacity	40/50T Single - 65T Twin
Hoisting Speed	50 / 125 m/min
Trolley Speed	150 - 180 m/min
Travel Speed	45 m/min
Wheel Load **	30 - 45T Per Meter

** Based on 8 Wheels per Corner at 1.00m Spacing

Typical WideSpan Crane *

A Gantry Span	35.00 - 50.00m
B Outreach	30.00 - 40.00m
C Backreach	15.00 - 30.00m
D Lift Height	20.00 - 25.00m
SWL Capacity	40/50T Single - 65T Twin
Hoisting Speed	50 / 125 m/min
Trolley Speed	180 m/min
Travel Speed	100 - 140 m/min
Wheel Load per Meter **	40 - 50T Per Meter

** Based on 8 Wheels per Corner at 1.00m Spacing

Typical Post Panamax Crane *

B Outreach	40.00 - 46.00m
D Lift Height	30.00 - 35.00m
SWL Capacity	40/50T Single - 65T Twin
Hoisting Speed	60 / 150 m/min
Trolley Speed	180 - 210 m/min
Travel Speed	45 m/min
Wheel Load **	40 - 55T Per Meter

** Based on 8 Wheels per Corner at 1.00m Spacing

Typical Design Parameters *

Classification according F.E.M.	U7-Q2-A7
In service wind Speed	72km/h (20m/s)
Out of service wind Speed	151.2km/h (42m/s)
Ambient Temperature Range	- 40°C to +50°C
Frequency	50Hz to 60Hz
Voltage	3.3kV to 20kV

Typical Super Post Panamax / Megamax *

B Outreach	46.00 - 69.00m
D Lift Height	35.00 - 49.00m
SWL Capacity	65T Twin - 80T Tandem
Hoisting Speed	70 / 175 m/min
Trolley Speed	210 - 240 m/min
Travel Speed	45 m/min
Wheel Load **	60 - 80T Per Meter

** Based on 8 Wheels per Corner at 1.00m Spacing

* Other Features, Dimensions and Design Parameters Also Available

Single Beam Lattice Construction

Main Beam & Derrick Boom



Description

- Single Beam of Monobox Lattice Construction for Main Beam and Boom, where the Individual Members are of Box Type Rectangular Section.
- Used on All Liebherr High Performance Container Cranes for Over Forty (40) Years
- Welded Down Solid Member Trolley Rails (S160.2 Quality)
- Members of the Boom & Beam are Made from High Tensile Steel S355J2G3 to DIN 17100.

Advantages by Design

- Reduced Crane Deflection / Structural Sway
- Maximum Boom & Beam Rigidity Levels Achieved (Without a Weight Penalty while Giving Considerable Increases in Operational Performance)
- More Precise Container Handling & Driver Comfort
- Reduced Boom Width - Allowing Quick & Efficient Handling of Containers, close to the Ship's Superstructure & On-Board Ship Cranes.
- Ideally Suited for Eccentrically Loaded Containers.
- High Tensile Steel, allows a Lighter Overall Construction and a Reduced Wind Area.
- Reduces Overall Crane Self Weight, Minimises Wheel Loads and Assists in Ensuring Crane Stability in Out-of-Service Conditions
- The Monobox Design Ensures that the Trolley Travel Path is Parallel Throughout
 - Eliminating the Possibility of Trolley Travel Deviations.
 - Eliminating Side Forces Associated with Other Forms of Design.

Boom / Beam Hinge Point

- Unique Concept Developed over 25 Years & Refined Over That Period
- Hinge Point Section of the Trolley Rail has a Specialty Machined Profile, Bored into Position.
- Low Stressed Hinge Pin Connection which is Below and Close to the Rail Transition area.
- Designed to Provide Shock-Free Transfer from Boom to Beam & Vice-Versa (Regardless of Climatic Conditions & With Full Trolley Speed and Max. Trolley Load)
- Reduces Driver Fatigue, Improved Performance & Extends the Life-Time of the Trolley, Wheels, Bearings etc.



Self Powered Trolley

Description

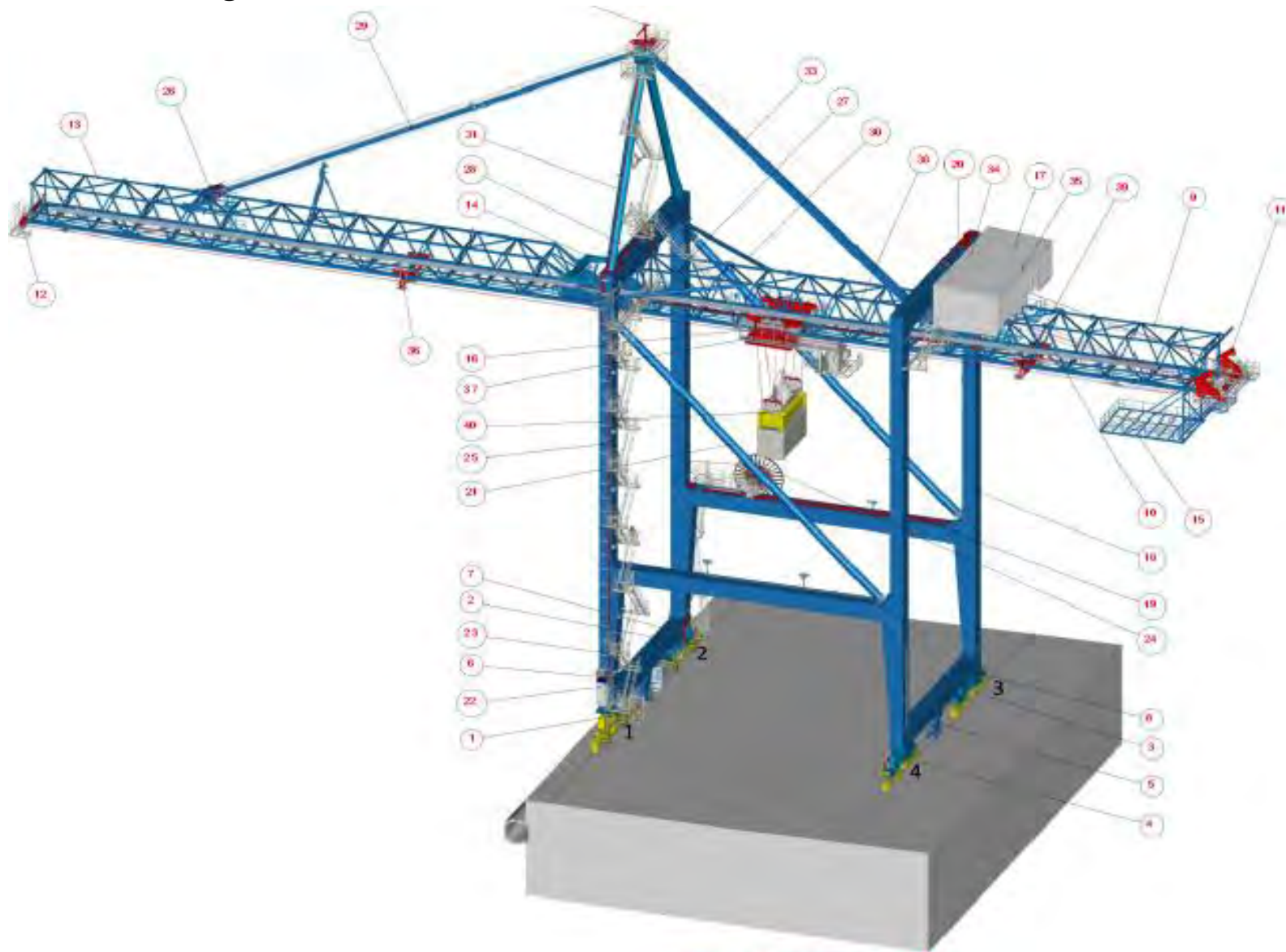
- Fabricated Structure with Machining after Welding, Ensuring Correct Alignment of Wheels & Drive System.
- Easy Replacement & Alignment of Trolley Travel Wheels.
- Machined Pads Throughout to Aid Alignment and Dimensional Checks.

Advantages By Design

- Fine Positioning / Inching Accurately - All Wheels are Direct Driven with Individual Braking Systems
- All Components are Easily Accessible for Maintenance.
- Extended Trolley Wheel Lifetime (Due to Non-Skewing Trolley & Accurate Alignment)
- In Event of One Motor Failing - The Trolley can Continue Working at reduced speed with 2 Motors.



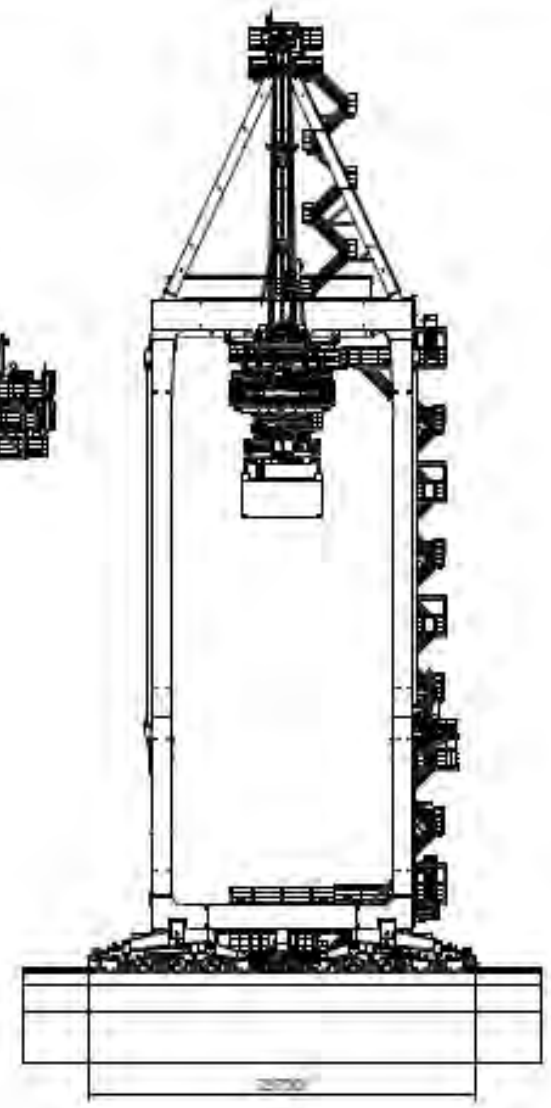
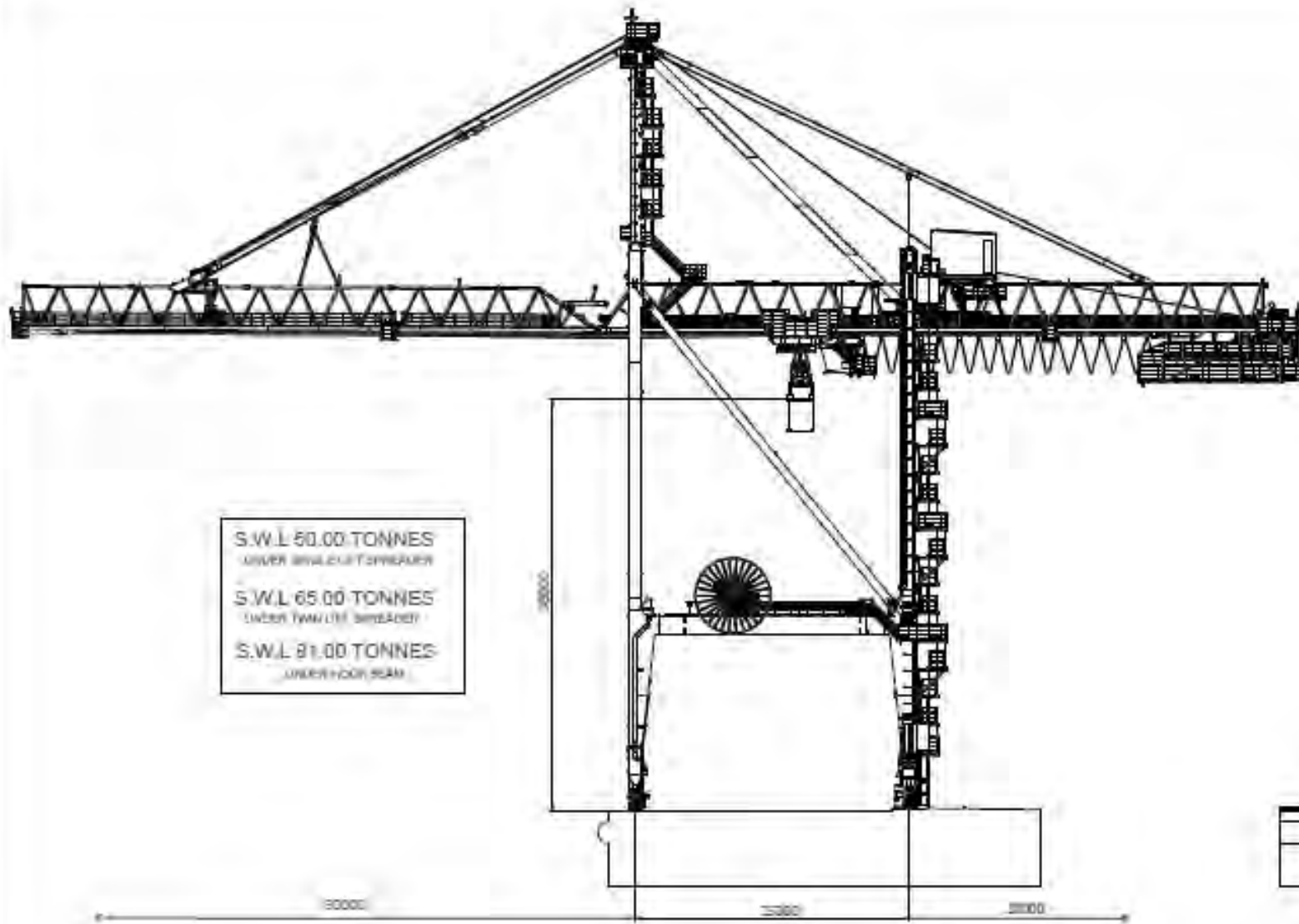
STS Crane Legend



DESCRIPTION	DRAWING NUMBER
1. TRAVEL UNIT 1	-110.000
2. TRAVEL UNIT 2	-120.000
3. TRAVEL UNIT 3	-130.000
4. TRAVEL UNIT 4	-140.000
5. RAIL CLAMPS + STORM PIN	-160.000
6. CHECKERS CABIN	-170.000
7. END-CARRIAGE (SEASIDE)	-180.000
8. END-CARRIAGE (LANDSIDE)	-190.000
9. MAIN BEAM	-210.000
10. ENERGY CHAIN	-220.000
11. TRANSLATOR + PLATFORM	-230.000
12. HOIST OVERLOAD SYSTEM	-240.000
13. DERRICK BOOM	-250.000
14. HOIST ROPE DEFLECTION ARM	-260.000
15. CABIN CLEANING PLATFORM	-270.000
16. TROLLEY TRAVEL UNIT SWITCHES	-276.000
17. MACHINELECT HOUSE	-290.000
18. LANDSIDE LEG	-310.000
19. GILL BEAMS	-321.000
20. LANDSIDE CARRIER	-380.000
21. PORTAL DIAGONAL	-361.000
22. PERSONNEL LIFT	-370.000
23. MAIN ENTRY	-380.000
24. CABLE REEFING DRUM	-364.000
25. SEASIDE LEG	-410.000
26. DERRICK BOOM CROSS BEAM	-430.000
27. A-FRAME ACCESS	-440.000
28. SEASIDE CARRIER	-450.000
29. HOLDING ARM	-480.000
30. CARRIER FLAT BRACING	-470.000
31. A-FRAME CPL	-480.000
32. ANEMOMETER	-464.000
33. A-FRAME BACK TIE	-490.000
34. DERRICK GEAR	-530.000
35. HOIST GEAR	-540.000
36. SECONDARY TROLLEY SEASIDE	-540.000
37. TROLLEY	-560.000
38. CABIN + ENTRY PLATFORMS	-570.000
39. SECONDARY TROLLEY LANDSIDE	-580.000
40. ANTI SWAY HEAD BLOCK	-900.000

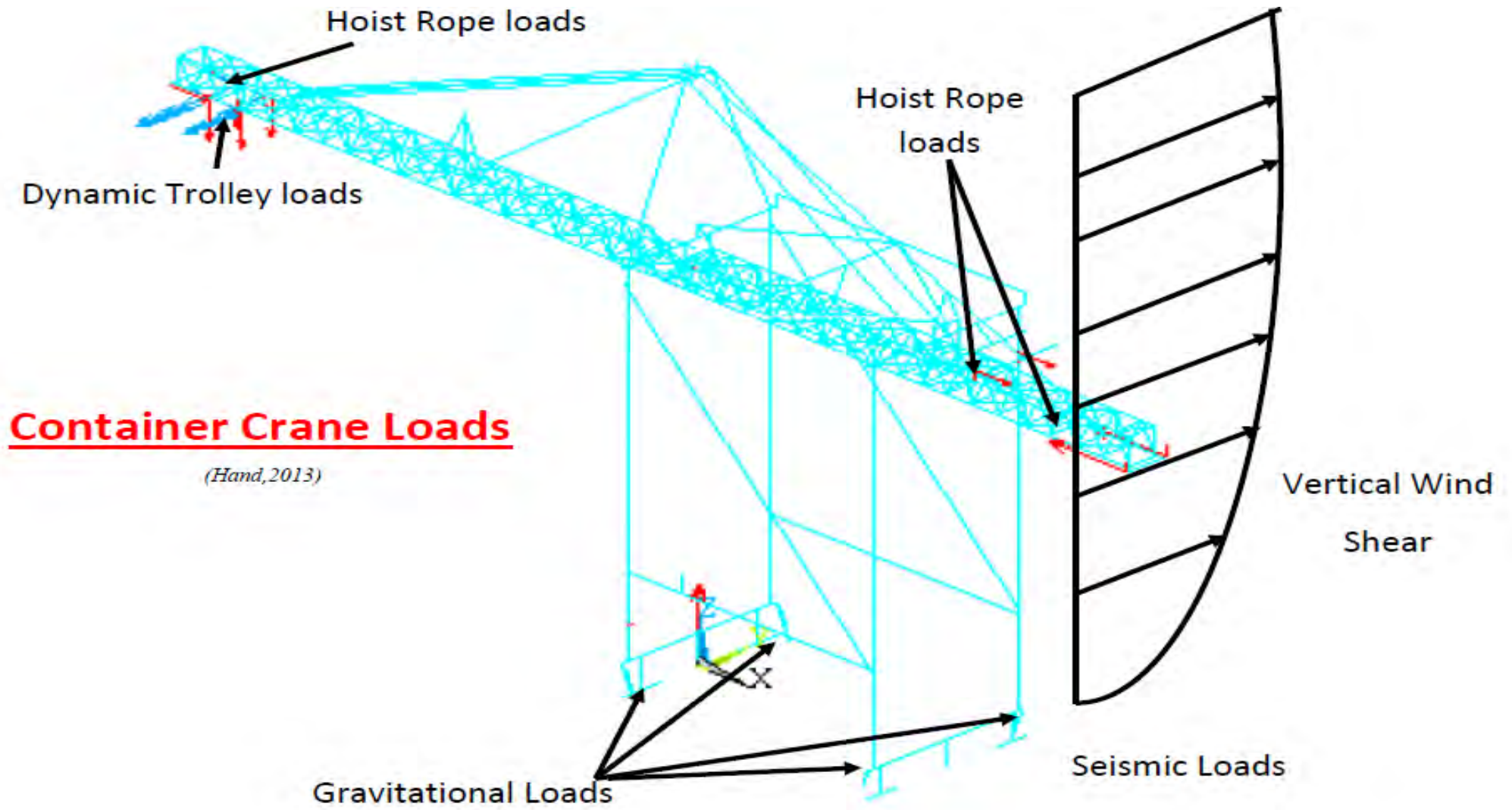
STS CRANE LEGEND





PROJECT NO.		
DATE		
DRAWN BY		
CHECKED BY		
APPROVED BY		
NO.	REV.	DATE
1		
SCALE		1:200
PROJECT NAME		ALUMINUM TOWER
DRAWING NO.		

Container Crane Loads



Crane Overall Dimensions

3.1.5 PHYSICAL DIMENSIONS

Span	25.30m
Outreach on Waterside (From Waterside Rail Centre)	50.00m
Outreach on Landside (From Landside Rail Centre)	20.00m
Spreader Height above Seaside Rail	38.00m
Lowest point of Spreader below seaside rail	16.00m
Total Spreader Hoisting / Lowering Path	54.00m
Wheel Gauge	
Seaside rail	16.20m
Landside rail	17.50m
Overall length Buffer to Buffer (Buffers uncompressed)	29.70m
Clearance under Sill Beam	16.00m
Clearance between Portal Legs	16.76m
Distance Waterside Rail to Front Face of Fender	3.475m
Average Rail level difference: Landside Rail is Higher	0.254m

3.1.6 TRIM SYSTEM ($\pm 5^\circ$) / LIST SYSTEM ($\pm 5^\circ$) / SKEW SYSTEM ($\pm 5^\circ$)

1 x 18.5kW A.C. Squirrel Cage Motor, which operates hydraulic system controlling all motions

3.1.7 NUMBER OF CRANE WHEELS AND MAX. WHEEL LOADS (IN-SERVICE) *

Seaside Rail	10 wheels/corner, wheel diameter 710mm 43.05 tonnes/wheel, 33.1 tonnes/metre
Wheel Centres	1300/1300/1300/1300/1300/1300/1300/1300
Landside Rail	8 wheels/corner, wheel diameter 710mm 43.30 tonnes/wheel, 33.3 tonnes/metre
Wheel Centres	1300/1300/1300/1300/1300/1300/1300

* Wheel loads consider a total self weight of 18 tonnes for the lifting equipment (i.e. Headblock and Spreader).



Both rails are 73KG/M BHP with a head width of 73mm.

6 PUTTING THE CRANE OUT OF SERVICE

The Crane must be taken "Out Of Service" if the Wind Speed Exceeds 22m/s (79.2km/h).



Audio and visual warning devices indicate if this maximum wind speed has been reached or exceeded.

When putting the crane out of service for any period, however short, the following procedure must be strictly adhered to. Only then can it be properly ensured that the crane is safely parked and is capable of withstanding the forces imposed by strong winds.

1. Remove load from lifting equipment.
2. Raise lifting equipment to the park position, above the 50% pre up limit.
3. Bring the trolley to the park position, **TROLLEY PARK** position lamp on swivel panel is ON.
4. Bring crane to the storm anchor position, **STORM PIN POSITION** lamp is on if applicable.
5. Press **CRANE OFF** pushbutton on swivel panel.
6. Switch on boom drive, **BOOM ON** on side panel and raise boom, **BOOM UP** to the locked position, 75 Degrees.
7. Ensure Trolley Lock Pin is manually engaged. Trolley Lock Pin is located on the main beam and can be reached via the top of the cabin stairs at trolley parked location.
8. Insert storm anchors into the corresponding ground pockets. **STORMPINS UP** status light is switched OFF.

The storm anchors cannot be raised or lowered until the crane is in the parking area, i.e. **STORM PIN POSITION** status light is switched on.

9. Switch OFF as follows at the **Gantry Console P20 Panel** at ground level:
 - o Switch OFF keyswitch **CRANE DISABLE** by inserting the key and turning Anti-clockwise to dis-engage. Remove key and store in a safe place.
 - o Close cover of Control Panel and lock.
10. The following equipment on the crane is fitted with **Anti-Condensation Heating**:
 - o Electrical Switchgear / Electronic regulator panels. These heaters are thermostatically controlled.
 - o All Drive motors. These heaters come on when the crane drive goes off.
 - o Cable Reeling Drum Motor / Slipping Assembly. These heaters come on when the crane drive goes off.
 - o High Tension Switches

The Anti-Condensation heating system is powered via the high-tension supply switches. Ensure the H.T. supply remains ON even when the crane is out of service.

Container Crane Components

A container crane is composed of many different components which have to interact and function with each other to carry the crane's objective in the most effective manner. A detailed illustration of a STS crane is displayed on page A-4 and in the following a brief overview is given of the crane's main components.

Main beam and Derrick Boom

Essentially these two components make up a horizontal beam which spans the length of the crane which changes depending on the size of crane required at a port for example panamax or super post-panamax. The main beam is the section of the beam which is connected to the crane structure and is suspended over the quay. The derrick boom (see figure A-1) is the part



Figure A-1 Derrick boom being lifted into place
(Liebherr Group, a 2013)



Figure A-2 Hinge point mechanism on boom
section (Hand, 2013)

of the beam which is over the ship during operation and is joined to the main beam through a mechanism known as a hinge point as shown in figure A-2. This hinge point allows the derrick boom to be lifted from its horizontal position to allow for ships to berth at the quay and also allow the crane to be put out-of-service. The term out-of-service for a container crane means when the crane is shut down mainly due to unsafe working wind speed which exceeds a certain threshold for its design, in this condition the derrick boom is raised 75° from the horizontal. Liebherr manufactures the main beam and boom using a technique called monobox lattice construction which allows it to have a higher strength to weight ratio compared with other crane manufacturers (Liebherr Group, b 2013).

Trolley

This component of the crane traverses the length of the main beam and boom moving containers from the ship to quay and vice versa. The trolley is the supporting structure for the spreader and the crane operator's cabin. The trolley has to support the hoisting mechanism as shown in figure A-3 and the mechanism which allows the trolley to manoeuvre along the beam which are motors (Achterberg, 2012). Liebherr uses a system known as a "direct driven trolley" which results in better positioning of the trolley and greater accuracy during operation.

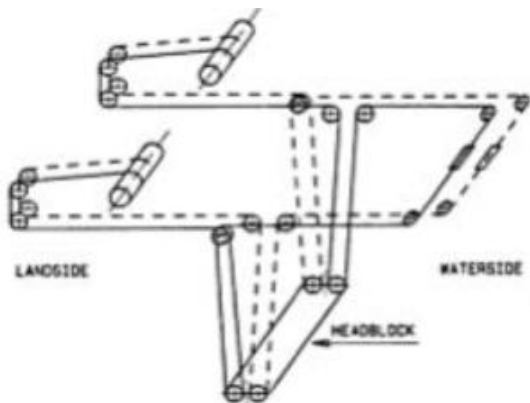


Figure A-3 Standard hoisting mechanism (Verschoof, 2002)



Figure A-4 Trolley (Liebherr Group, a 2013)

Spreader & Head block

The connection between the container and the container crane is achieved by using a head block and a spreader. The head block shown in figure A-5 is the component that is connected with the trolley using hoisting cables and connected to the head block using twist lock mechanisms is the spreader. Every container is fitted with the same lifting points and using a spreader with an integrated twist lock system allows the crane operator to connect and disconnect with the container in the most efficient manner (Achterberg, 2012).



Figure A-5 Head block (Hand, 2013)



Figure A-6 Head block & spreader connected to a container (Liebherr Group, a 2013)

Cabin

The cabin is the location where the central operations of the crane are carried out and is undertaken by the crane operator. The cabin is accessed from stairways and platforms which run up the sides of the crane to the cabin from the quay or the cabin can be accessed from a service elevator. The cabin is fixed onto the trolley which allows the operator the best line of sight for the movement of the containers (see figure A-7) especially when looking deep into big storage bays of ships.



Figure A-6 Cabin (Hand, 2013)



Figure A-7 Operator's line of sight (Liebherr Group, a 2013)

Travel Units

The static & dynamic forces of the crane on the quay are transferred by the crane travel unit's and wheels of the crane. The travel unit (figure A-8) is the part of the crane which supports each leg of the crane and therefore there are four travel units in a container crane. The main function of these travel units is to allow the crane to move along the quay and be fixed in one position. The travel units are integrated with motors and drum brakes to allow accurate



Figure A-8 Crane's Travel Unit (Hand,2013)



Figure A-9 Travel Unit Wheel boxes (Hand,2013)

positioning of the crane. Typically a Liebherr crane has eight wheels per corner which means the total loads of one corner have to be supported by eight wheels. If the quay is insufficiently

strong crane travel units with more wheels are produced. In most cases it is the sea-side part of the crane where corner travel units are fitted with ten wheels, this allows a wider distribution of the crane's forces (*Liebherr Group, a 2013*).

Cable reel and Power Supply

To provide the most time efficient unloading and loading procedure involves the crane has to move along the quay during operation. The cranes are electrically powered and therefore are connected to the grid and this is achieved by large cables which lie in channels over the quay. When the crane has to move, the cable is rolled on or off a large motorised reel as shown in figure A-9 which is attached to the side of the crane. This system ensures that the cable is kept at the correct tension and to avoid the cable becoming tangled (*Liebherr Group, a 2013*).

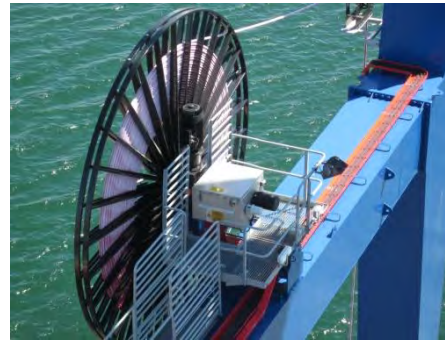


Figure A-9 Cable reel drum (*Liebherr Group, a 2013*)

Storm Anchor

Storm anchors are the components fitted to the underneath the sill beams on the container cranes. The purpose of these devices is to prevent the lateral movement of the crane during storms and high winds. In the case of when the crane is put out-of-service, claps are manually pushed out of the storm anchor and into predefined slots in the quay interface.



Figure A-10 Crane storm anchor from under sill beam (*Liebherr Group, a 2013*)

Appendix B – Project Management

Work Breakdown Structure

Work Breakdown Schedule

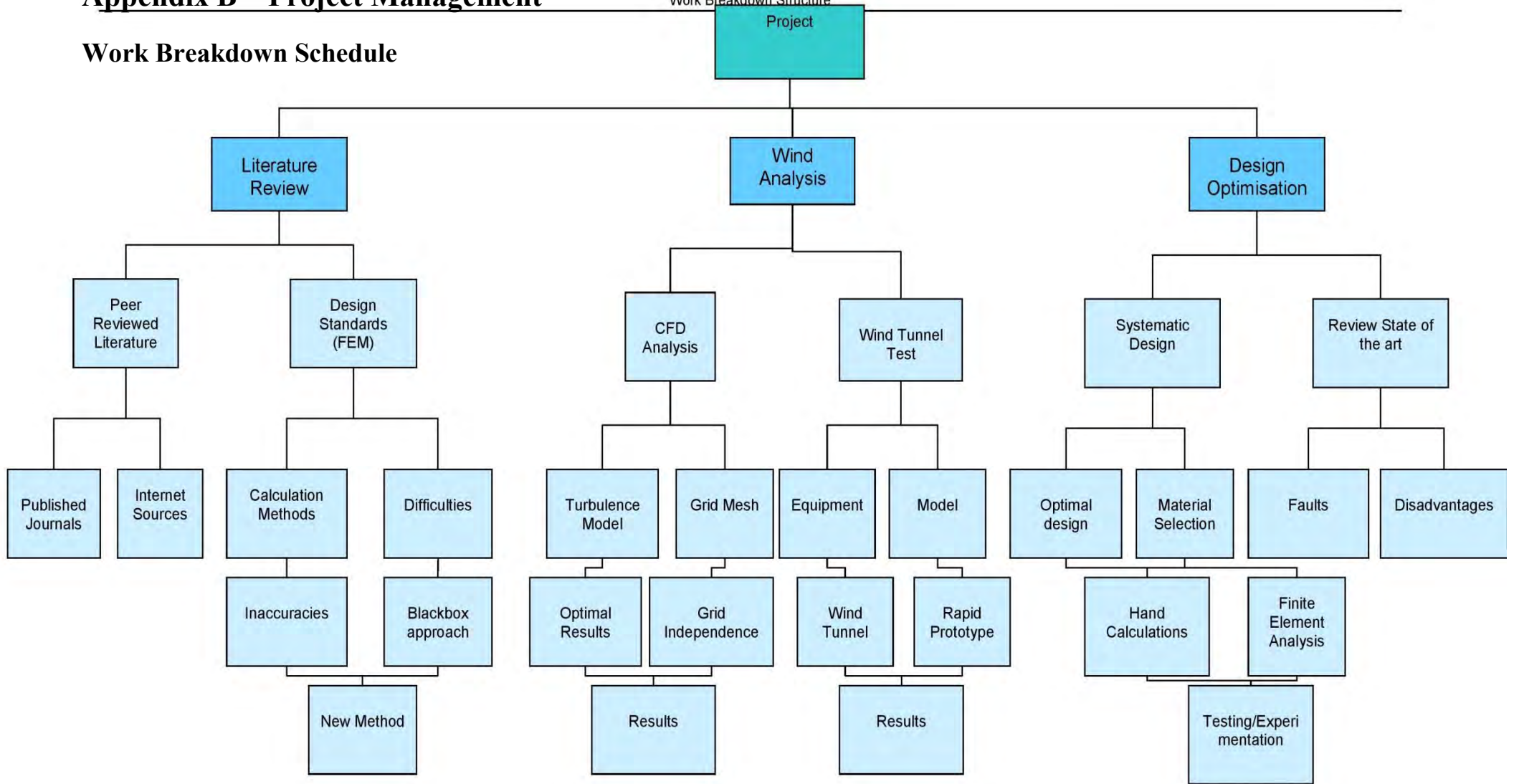


Table: B-1 Tasks Description (Hand,2013)

	Activity	Predecessors	Duration(days)
SEMESTER 1			
A	Research crane loads & wind flow effects	none	14
B	Review crane design standards & procedures	none	14
C	Carry out wind load calculations using FEM standards on pivotal section of crane boom	A,B	28
D	Familiarise oneself with ANSYS CFD software using tutorials	none	14
E	Create accurate CFD model of pivotal boom section	D,C	21
F	Rapid Prototype model for wind tunnel test	C	7
G	Setup equipment & instrumentation for wind tunnel test	F	10
H	Perform Wind tunnel testing	G,E	3
I	Critically analyse & compare results of analytical ,CFD and wind tunnel testing	H	14
J	Using results gathered, calculate total wind loads on the crane to obtain crane wheel loads	I	10
SEMESTER 2			
K	Review & analyse tie-down anchor systems in cranes	J	7
L	Carry out systematic design of the components of the tie-down system	K,I	14
M	Perform analytical calculations & FEA to examine optimal design	J	10
N	Research instrumentation for reading design tensile forces	L	7
O	Purchase necessary materials, components, electronics	N,L	14
P	Build prototype	M,O	14
Q	Laboratory testing of data acquisition system	P	7

Network Diagram

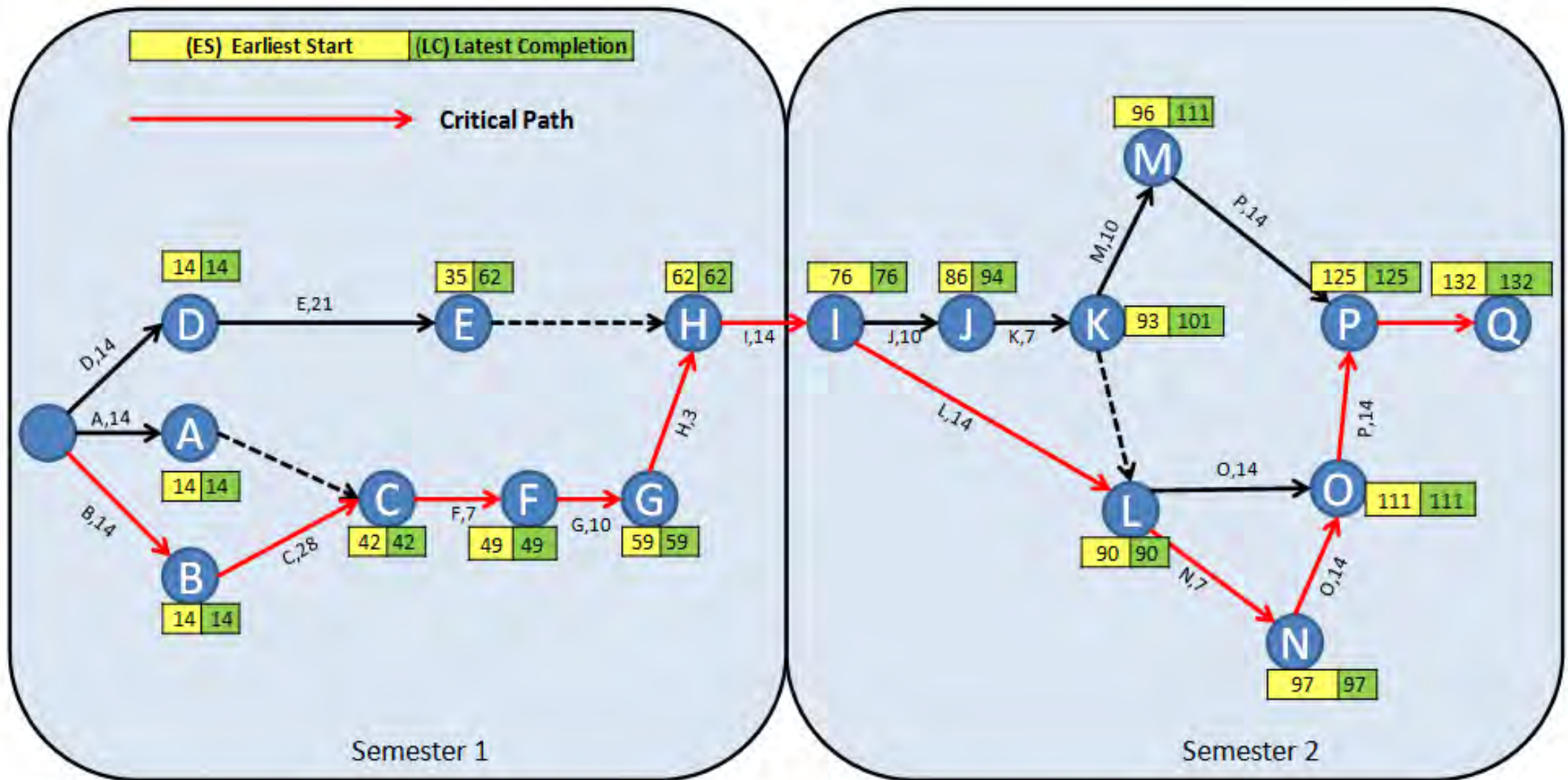


Figure B-2 Network Diagram (Hand,2013)

STS Crane Wind Analysis

Liebherr Group
Gantt Charts

Today's Date: 12/04/2014 Saturday
(vertical red line)

Semester 1 Project Lead: Brian Hand
Start Date: 23/09/2013 Monday

First Day of Week (Mon=2): 2

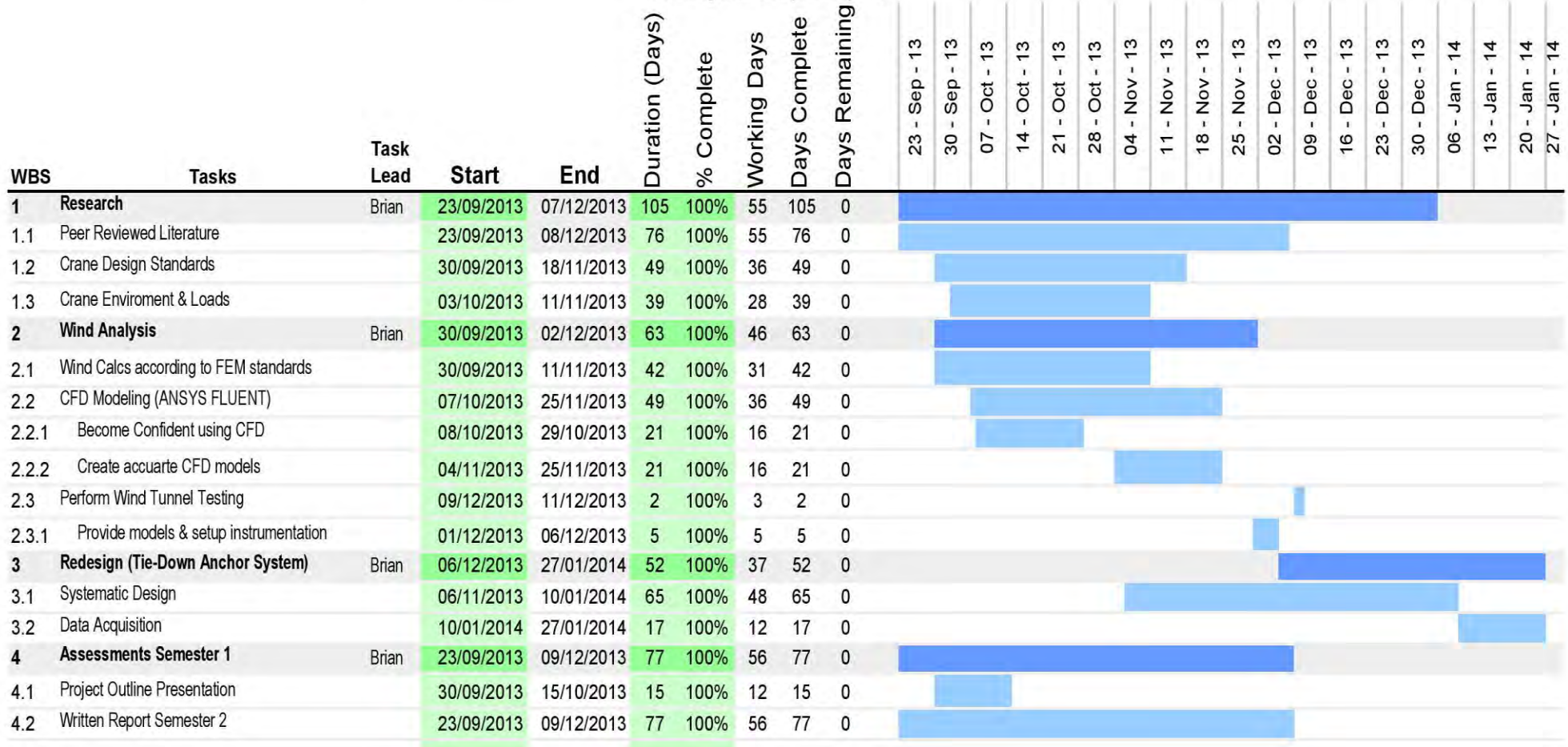


Figure B-3 Gantt Chart Semester 1 (Hand, 2014)

STS Crane Wind Analysis

Liebherr Group

Semester 2

Today's Date: 12/04/2014 Saturday

(vertical red line)

Project Lead: Brian Hand

Start Date: 06/01/2014 Monday

First Day of Week (Mon=2): 2

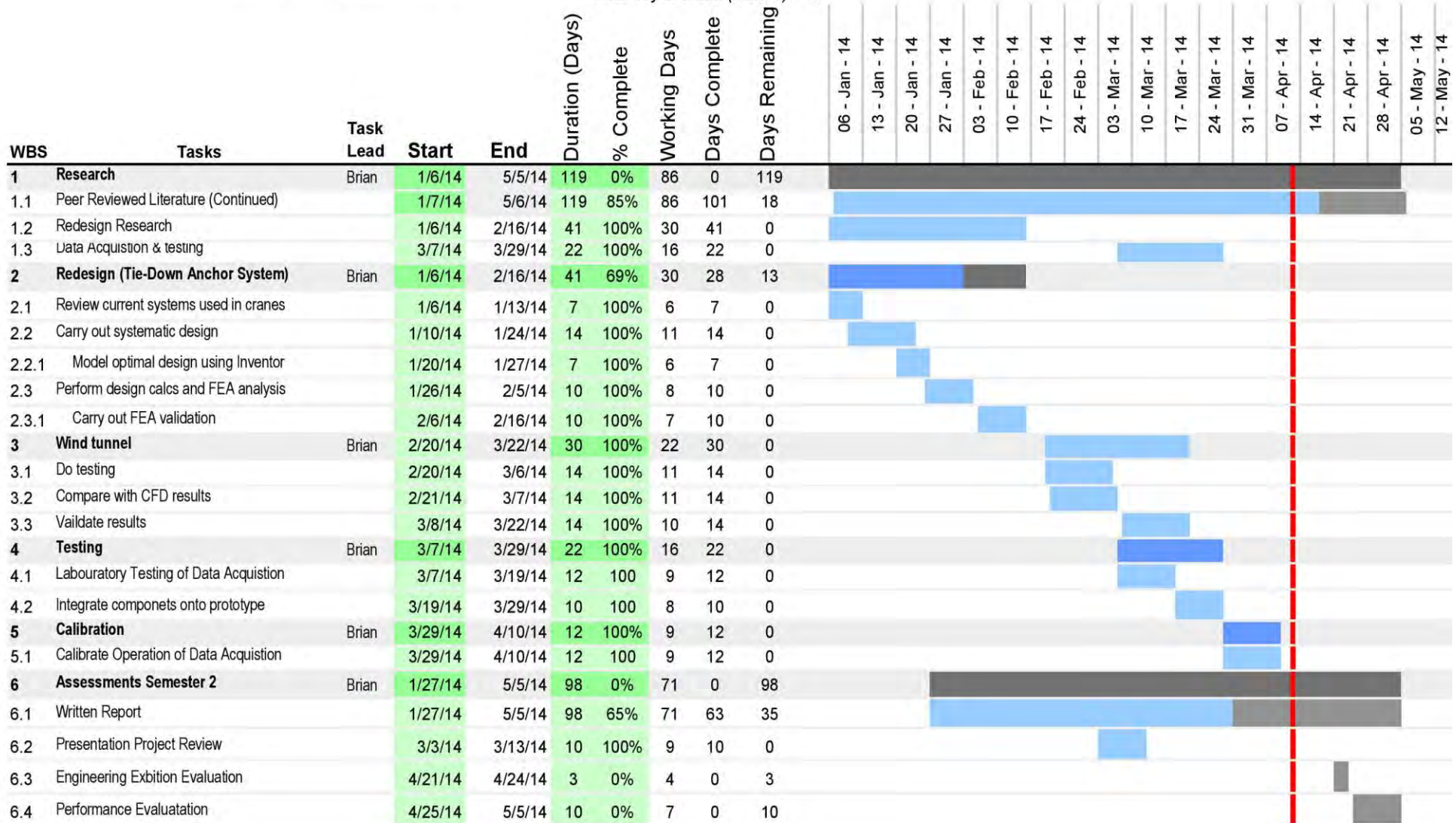


Figure B-4 Gantt Chart Semester 2 (Hand,2014)

Resources

Wind Analysis

- **Computational Fluid Dynamics (CFD):** support from supervisor, online user support & forums from ANSYS and high availability of software in college computer labs.
- **Wind Tunnel Testing:** Wind tunnel is equipped with a load cell which can measure aerodynamic lift. Pressure can be measured using a series of manometers which incorporated pressure tapings for static pressure measurement. There is also a pilot tube with inclined manometer to measure dynamic pressure and ultimately calculate wind velocity. There are also flow aids such as smoke available to categorise the air flow and also a high speed camera available in the mechanical department for recording this for post analysis.
- **Sterolithography:** For the production of wind tunnel models there is a rapid prototyping machine available.

Design Optimisation

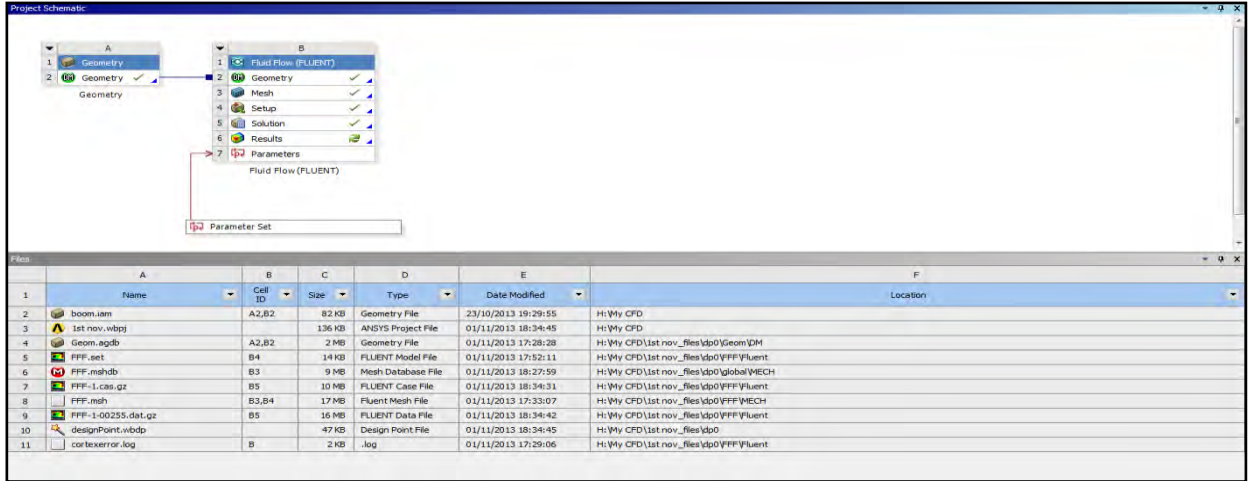
- **Experience:** There is a wide range of experience in systematic design and design manufacture in the mechanical department.
- **Finite Element Analysis (FEA):** Wide availability of software in college computer labs and experienced personal in this area and in validation tools such photo-elasticity.
- **Workshop facilities:** Fully equipped mechanical workshops and experienced technicians in prototype manufacture.
- **Electronic/Instrumentation:** For electronics in my project, I am currently studying the “Instrumentation for Sensors” module conducted by Emmanuel Pican which prove very beneficial when doing the instrumentation and using Labview for my project.

Limitations/Constraints

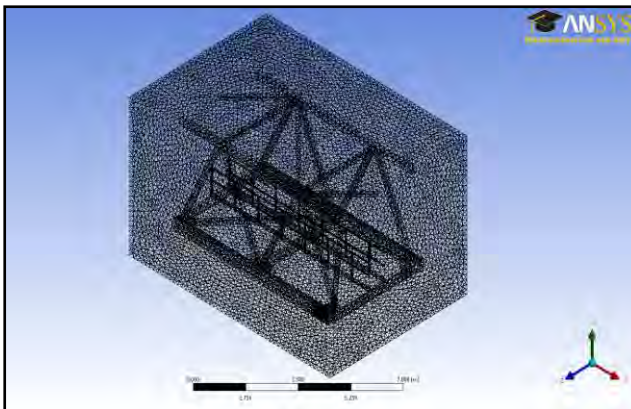
- **FEA Software:** This software provided by ANSYS has a non-commercial license at the college and is limited in how much analysis can be done due to the number of cells which can be generated for finite element analysis.
- **Wind Tunnel:** The models that can be tested in the wind tunnel have to fit the wind tunnel cross section which is 300mm × 300mm which limits the scales that can be used. Also the air velocity which can be generated in the wind tunnel is limited at 16m/s. The use of the high speed camera may be limited if there is high demand for its use.
- **Sterolithography:** The rapid prototyping (RP) is limited to producing models which are 200mm × 200mm and the minimum thickness of features is 1mm. There is also the case that demand for RP will increase the delay for models to be produced.
- **Photo-Elasticity:** Used for validating FEA models this uses optical plastic to display stresses, use is limited with this testing because it can only be used on 2D models thus excluding 3D model

Appendix C – Computational Fluid Dynamics

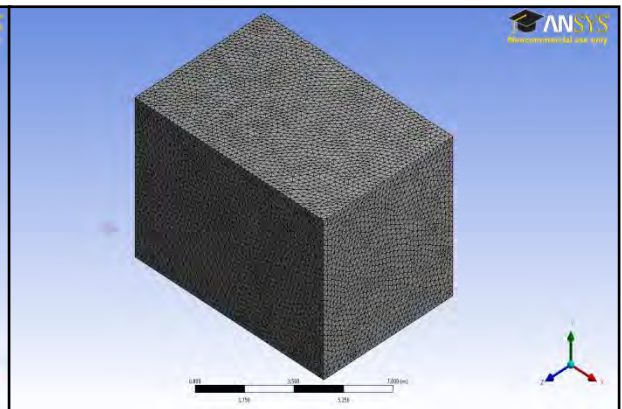
Model & Mesh Setup



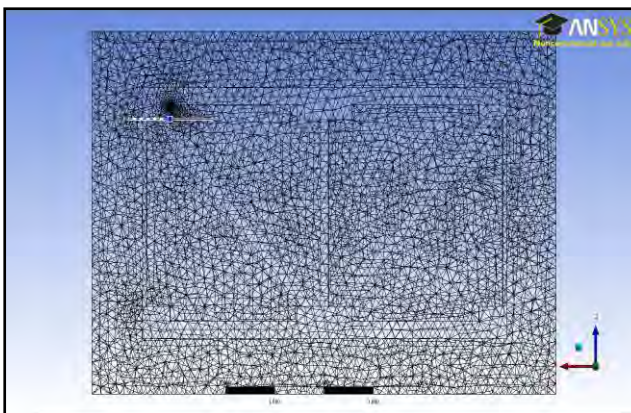
ANSYS Workbench Schematic



Wire frame mesh



Domain Mesh



Mesh detail on bottom panel

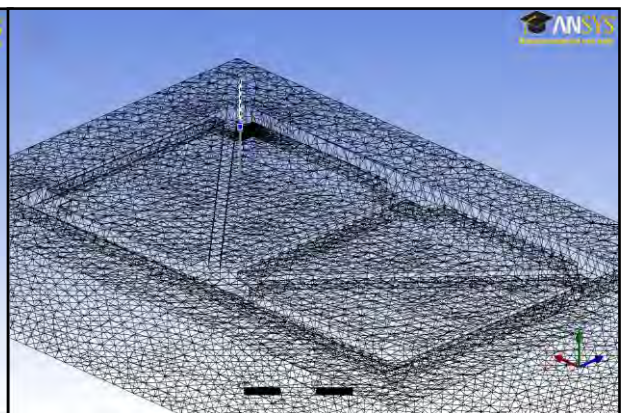
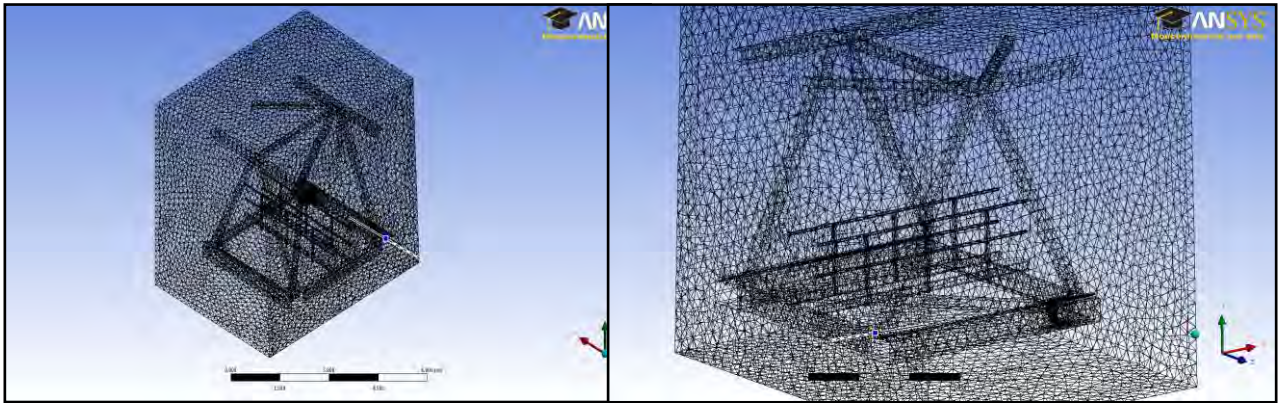
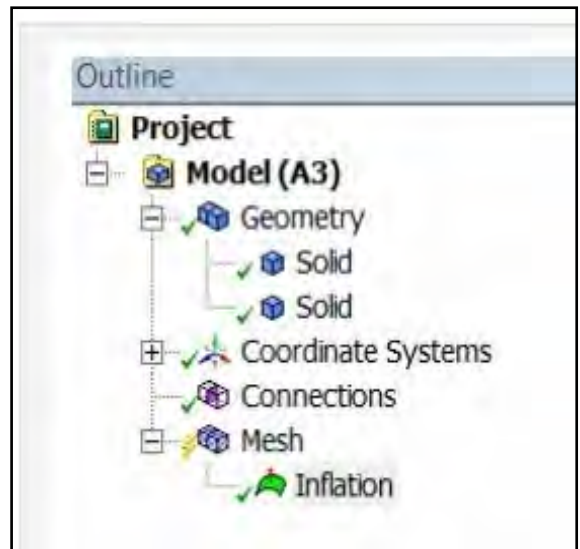


Figure C-1 Model and mesh setup (Hand, 2013)



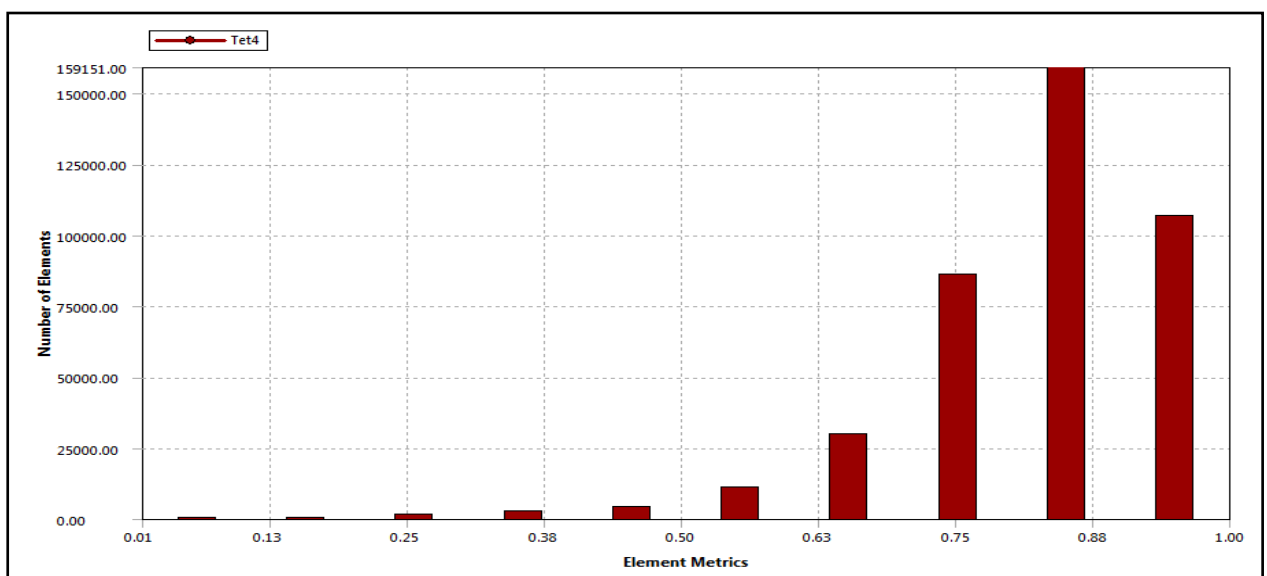
Cross section mesh detail

Sizing	
Use Advanced Size Function	On: Curvature
Relevance Center	Fine
Initial Size Seed	Active Assembly
Smoothing	Medium
Transition	Slow
Span Angle Center	Fine
<input type="checkbox"/> Curvature Normal Angle	Default (18.0 °)
<input type="checkbox"/> Min Size	Default (1.8917e-003 m)
<input type="checkbox"/> Max Face Size	Default (0.189170 m)
<input type="checkbox"/> Max Size	Default (0.378350 m)
<input type="checkbox"/> Growth Rate	Default (1.20)
Minimum Edge Length	1.5418e-006 m
Inflation	
Assembly Meshing	
Method	None
Patch Conforming Options	
Triangle Surface Mesher	Program Controlled
Advanced	
Defeaturing	
Statistics	
<input type="checkbox"/> Nodes	73649
<input type="checkbox"/> Elements	402221
Mesh Metric	
Element Quality	
<input type="checkbox"/> Min	7.93904849432458E-03
<input type="checkbox"/> Max	0.99969987937557
<input type="checkbox"/> Average	0.822060913905032
<input type="checkbox"/> Standard Deviation	0.118973541713037



Inflation Layer

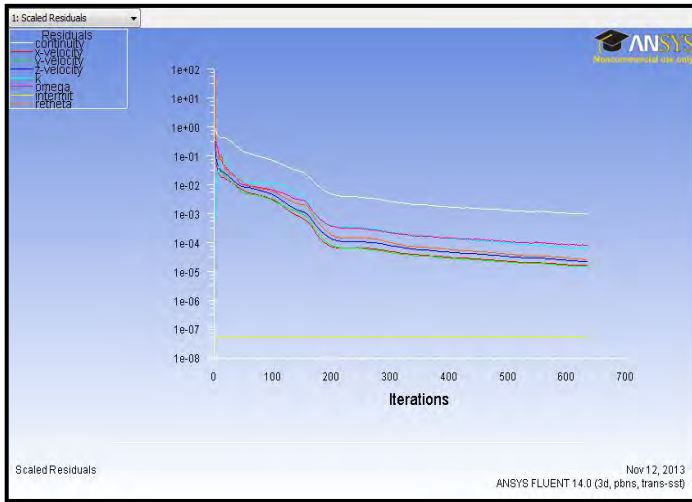
Model Statistics & Sizing



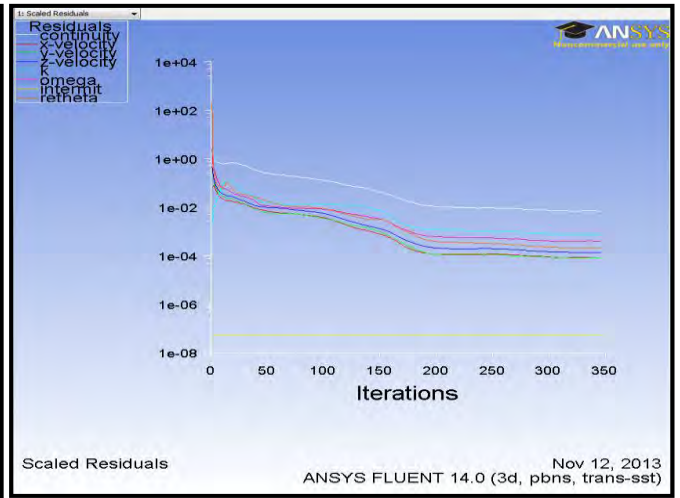
Element quality

Figure C-2 Model setup and settings (Hand, 2013)

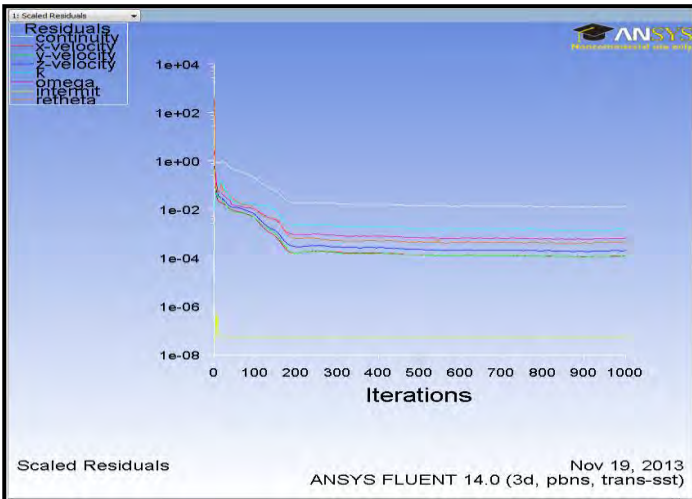
SST k- ω model Scaled Residuals



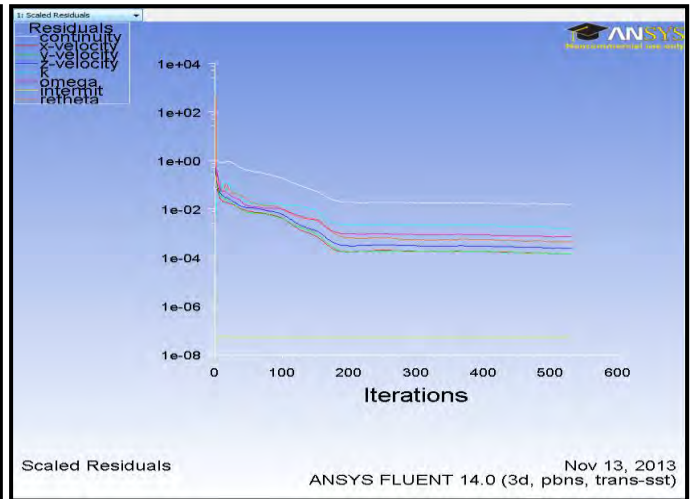
10m/s



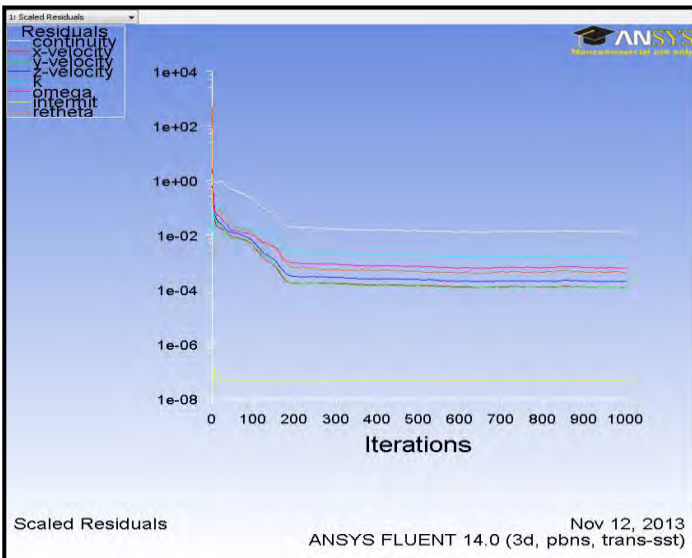
20m/s



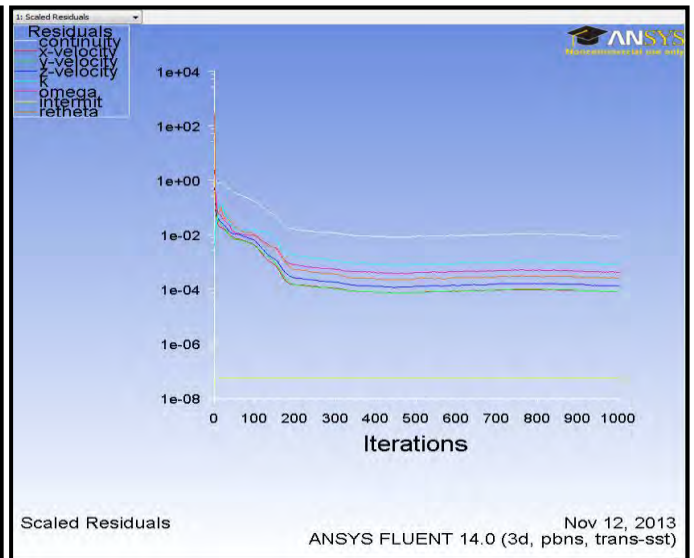
30m/s



40m/s



50m/s



60m/s

Figure C-3 The SST k- ω turbulence model scaled residues at velocities 0-60m/s (Hand,2013)

SST k- ω model Computed Results (Full Scale)

SST CFD Model Results (Full Scale)

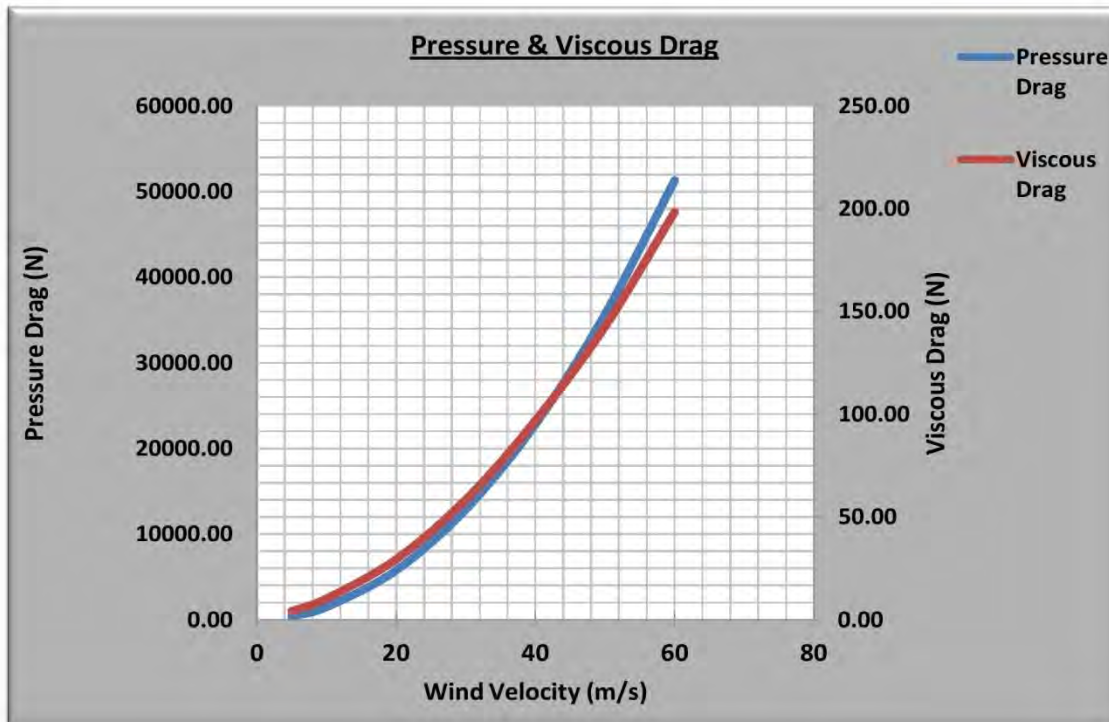
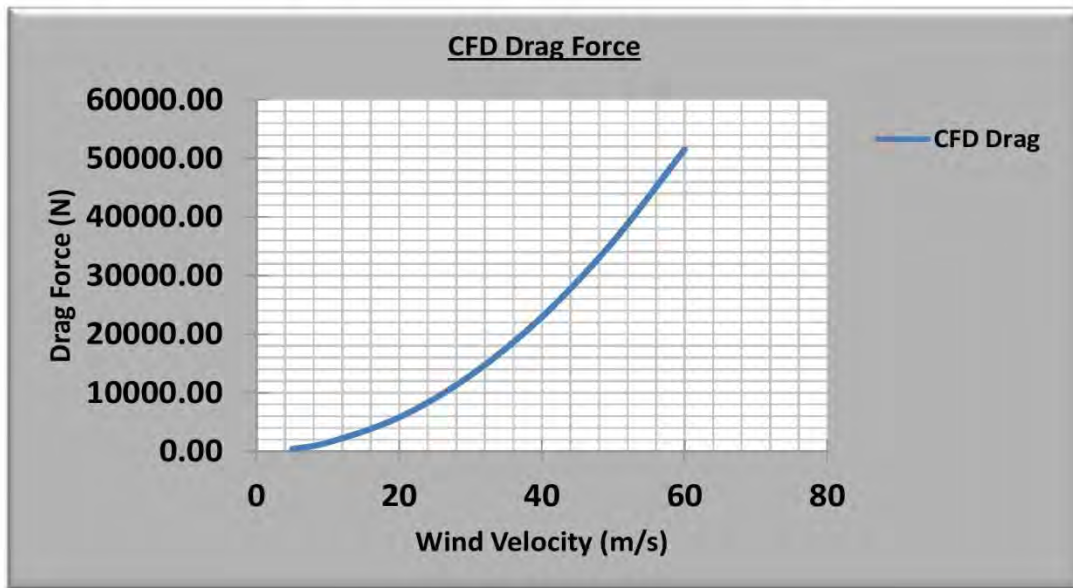
Flow Velocity		DRAG FORCES			
		Mesh Relevance			
5m/s	Parameter	Coarse	Medium	Fine	Enhanced
	Grid Elements	119960	180067	402221	489858
	Pressure	440.3439	238357.88	390.10272	394.271
	Viscous	5.9248176	100124.48	5.3166084	4.12585
	Total	446.268718	387.441	395.41933	398.397
10m/s	Parameter	Coarse	Medium	Fine	Enhanced
	Grid Elements	119960	180067	402221	489858
	Pressure	1658.694	1439.256	1429.2249	1471.33
	Viscous	14.590776	13.451059	12.922285	10.2242
	Total	1673.28478	1452.707059	1442.1472	1481.56
20m/s	Parameter	Coarse	Medium	Fine	Enhanced
	Grid Elements	119960	180067	402221	489858
	Pressure	6445.9473	5596.7354	5554.3467	5765.7
	Viscous	36.903759	35.27309	34.973595	29.3156
	Total	6482.85106	5632.00849	5589.3203	5795.01
30m/s	Parameter	Coarse	Medium	Fine	Enhanced
	Grid Elements	119960	180067	402221	489858
	Pressure	14333.512	12502.146	12442.428	12898.9
	Viscous	66.190262	65.037033	66.229538	58.3556
	Total	14399.7023	12567.18303	12508.658	12957.3
40m/s	Parameter	Coarse	Medium	Fine	Enhanced
	Grid Elements	119960	180067	402221	489858
	Pressure	25415.77	22133.303	22089.631	22834.7
	Viscous	102.57423	102.8207	106.13116	96.8721
	Total	25518.3442	22236.1237	22195.762	22931.6
50m/s	Parameter	Coarse	Medium	Fine	Enhanced
	Grid Elements	119960	180067	402221	489858
	Pressure	39743.367	34518.828	34527.723	35688.6
	Viscous	145.11948	148.12852	155.42404	142.643
	Total	39888.4865	34666.95652	34683.147	35831.2
60m/s	Parameter	Coarse	Medium	Fine	Enhanced
	Grid Elements	119960	180067	402221	489858
	Pressure	57018.227	49601.949	49507.574	51332.7
	Viscous	193.59819	200.44104	211.90866	198.473
	Total	57211.8252	49802.39004	49719.483	51531.2

SST CFD Model Results (Full Scale)

LIFT FORCES					
Flow Velocity	Mesh Relevance				
	Parameter	Coarse	Medium	Fine	Enhanced
5m/s	Grid Elements	119960	180067	402221	489858
	Pressure	-12.962878	4.96E+08	5.7561221	8.41089
	Viscous	0.07768291	520418.66	0.0504095	0.07809
	Total	-12.885195	496224958.7	5.8065316	8.48898
10m/s	Grid Elements	119960	180067	402221	489858
	Pressure	-57.635361	-26.588366	17.186069	24.8803
	Viscous	0.20184797	0.23638335	0.1838404	0.23225
	Total	-57.433513	-26.3519827	17.369909	25.1126
20m/s	Grid Elements	119960	180067	402221	489858
	Pressure	-234.12218	-74.729355	26.69606	63.4547
	Viscous	0.53537279	0.65776068	0.5371524	0.79799
	Total	-233.58681	-74.0715943	27.233212	64.2527
30m/s	Grid Elements	119960	180067	402221	489858
	Pressure	-541.87164	-180.84059	45.591366	168.587
	Viscous	0.88981009	1.2261318	1.2610761	1.69456
	Total	-540.98183	-179.614458	46.852442	170.282
40m/s	Grid Elements	119960	180067	402221	489858
	Pressure	-937.37323	-309.845	170.82127	284.193
	Viscous	2.0363355	2.011941	2.0298634	2.72615
	Total	-935.33689	-307.833059	172.85113	286.919
50m/s	Grid Elements	119960	180067	402221	489858
	Pressure	-1506.546	-507.97513	428.48883	442.387
	Viscous	2.8339043	2.6727254	3.2094524	3.97086
	Total	-1503.7121	-505.302405	431.69828	446.358
60m/s	Grid Elements	119960	180067	402221	489858
	Pressure	-2157.9058	-694.77765	274.8287	486.282
	Viscous	3.3124731	3.8987527	4.6624346	5.3348
	Total	-2154.5933	-690.878897	279.49113	491.617

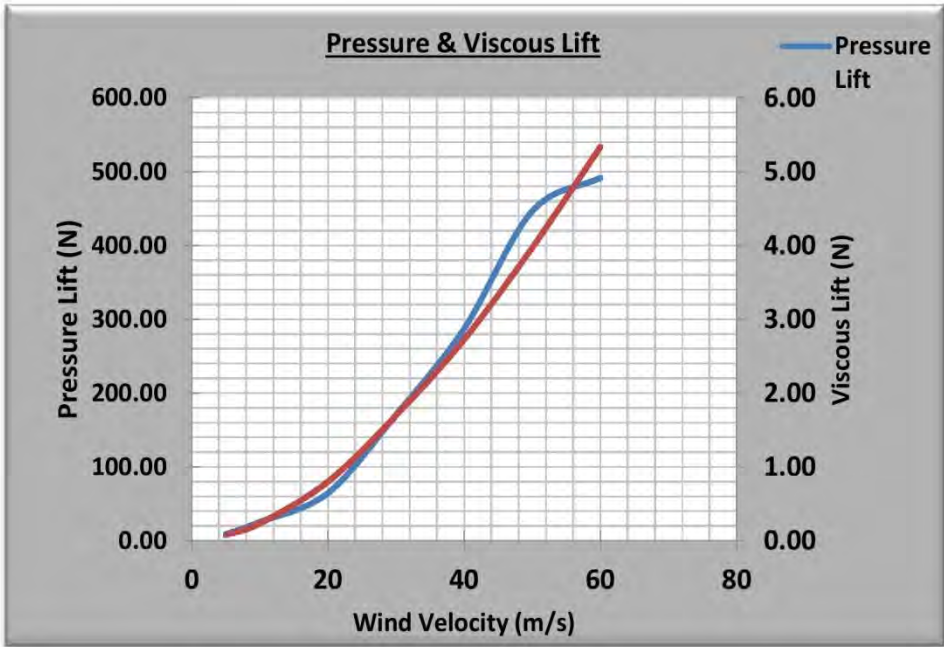
SST CFD Model Results (Full Scale)

Flow Velocity	Pressure Drag	DRAG FORCES	
		Viscous Drag	Total Drag
5	394.27	4.13	398.40
10	1471.33	10.22	1481.56
20	5765.70	29.32	5795.01
30	12898.93	58.36	12957.29
40	22834.72	96.87	22931.59
50	35688.56	142.64	35831.21
60	51332.69	198.47	51531.17



SST CFD Model Results (Full Scale)

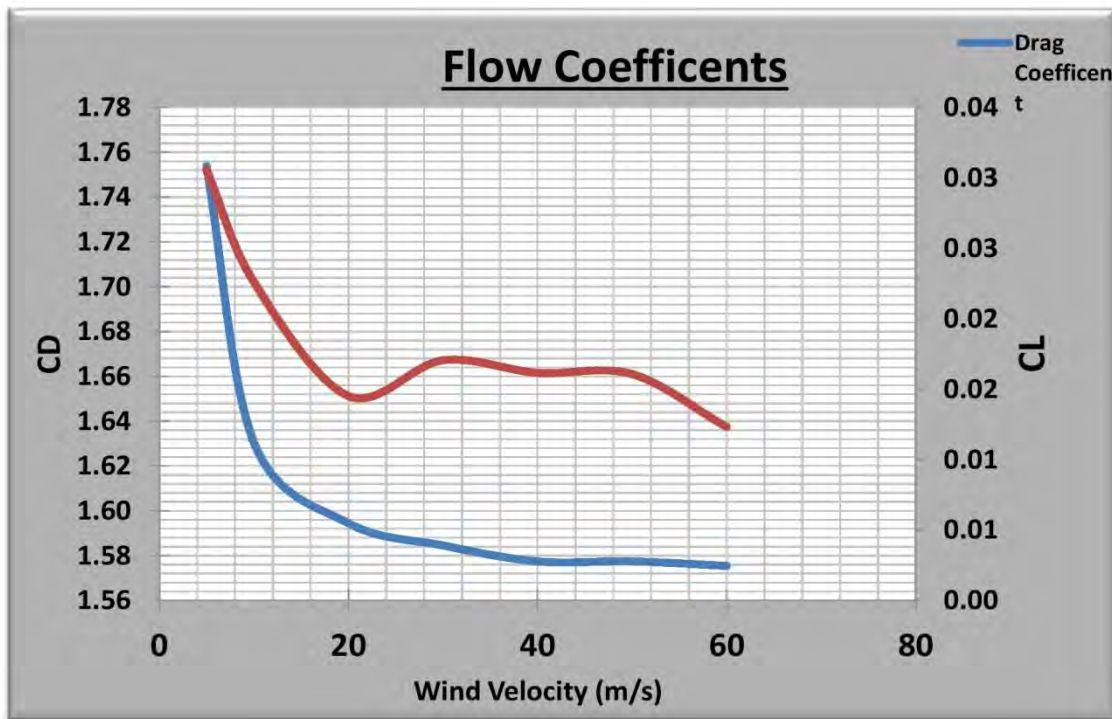
Flow Velocity	Pressure Lift	LIFT FORCES	
		Viscous Lift	Total Lift
5	8.49	0.08	8.57
10	25.11	0.23	25.34
20	64.25	0.80	65.05
30	170.28	1.69	171.98
40	286.92	2.73	289.64
50	446.36	3.97	450.33
60	491.62	5.33	496.95



SST CFD Model Results (Full Scale)

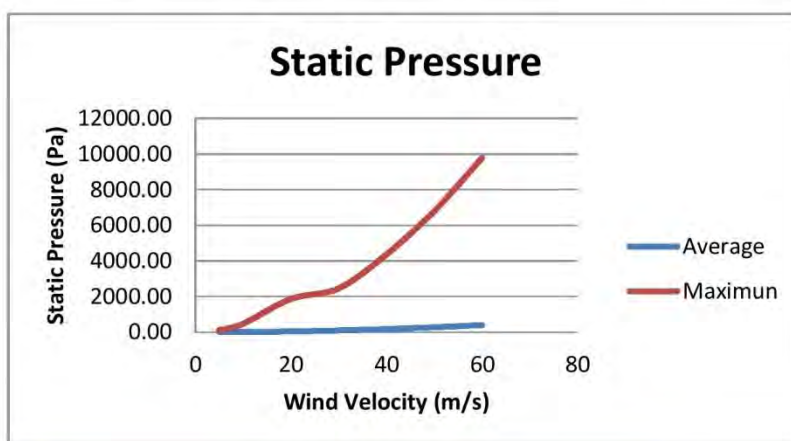
		FLOW COEFFICIENTS	
Flow Velocity	Cd	Cl	
5	1.75	0.03	
10	1.63	0.02	
20	1.59	0.01	
30	1.58	0.02	
40	1.58	0.02	
50	1.58	0.02	
60	1.58	0.01	
AVG	1.61	0.02	

Drag Area	12.917m ²
Lift Area	17.93m ²

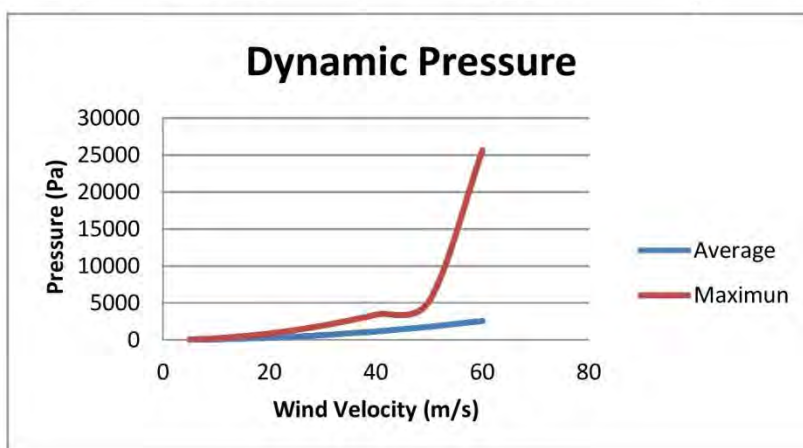


SST CFD Model Results (Full Scale)

STATIC PRESSURE			
Wind Velocity (m/s)	Minimum Static Pressure (Pa)	Maximum Static Pressure (Pa)	Average Static Pressure (Pa)
5	-108.96	115.67	3.08
10	-422.4413	472.221	11.23778
20	-1704.107	1865.917	44.49938
30	-4521.844	2456.829	101.4674
40	-8027.294	4356.778	176.2354
50	-12517.87	6791.571	272.7982
60	-18056.64	9771.718	392.5923

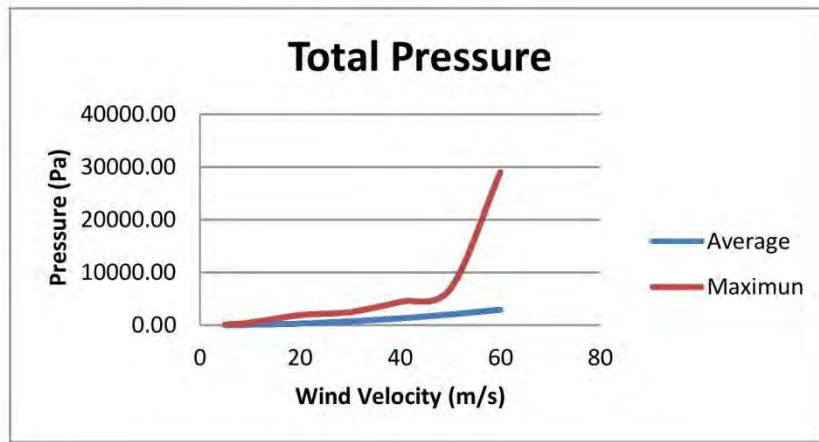


DYNAMIC PRESSURE			
Wind Velocity (m/s)	Minimum Dynamic Pressure (Pa)	Maximum Dynamic Pressure (Pa)	Average Dynamic Pressure (Pa)
5	2.32E-04	50.78723	17.20651
10	2.17E-04	212.9718	69.8332
20	1.62E-03	855.6563	280.9796
30	1.76E-02	1922.188	632.9092
40	8.91E-03	3405.615	1124.863
50	4.91E-02	5276.391	1759.156
60	1.80E-02	25704.18	2533.394

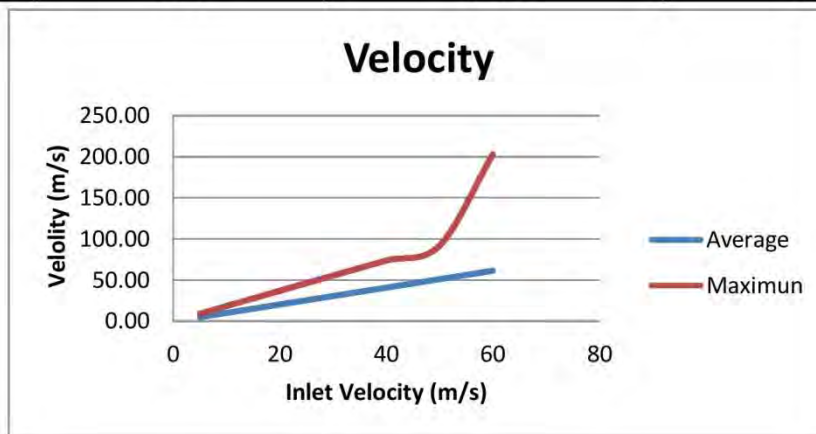


SST CFD Model Results (Full Scale)

TOTAL PRESSURE			
Wind Velocity (m/s)	Minimum Total Pressure (Pa)	Maximum Total Pressure (Pa)	Average Total Pressure (Pa)
5	-86.44	120.49	20.28
10	-327.73	487.51	81.07
20	-1319.81	1919.03	325.48
30	-3651.34	2497.03	734.38
40	-6492.04	4429.26	1301.10
50	-10126.72	6905.68	2031.95
60	-14613.59	29059.61	2925.99

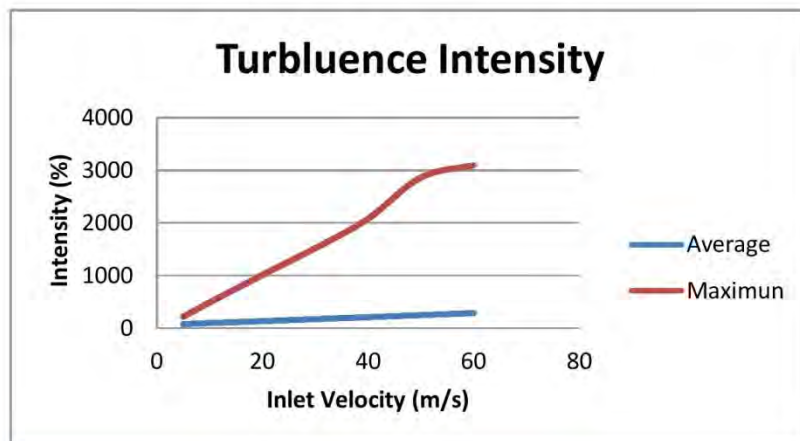


VELOCITY			
Wind Velocity (m/s)	Minimum Velocity	Maximum Velocity	Average Total Velocity
5	0.02	9.01	5.10
10	0.02	18.46	10.23
20	0.05	37.00	20.47
30	0.17	55.46	30.72
40	0.12	73.82	40.95
50	0.28	91.88	51.20
60	0.17	202.80	61.44

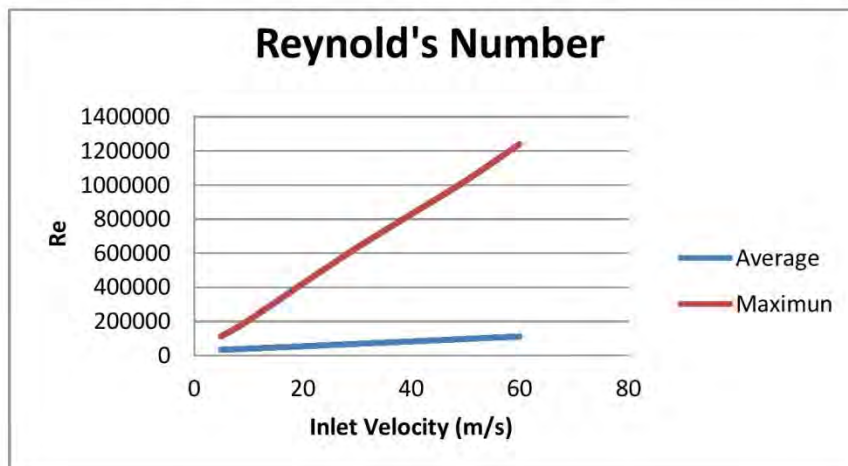


SST CFD Model Results (Full Scale)

Wind Velocity (m/s)	TURBLUENCE INTENSITY		Average Total turbulence
	Minimum Turbluence	Maximum Turbluence	
5	8.139003	216.2393	75.04875
10	9.752604	489.1886	95.15477
20	21.57549	1009.721	132.9499
30	32.3111	1516.678	171.0392
40	43.39405	2075.209	208.4789
50	52.74936	2859.65	248.1391
60	62.07439	3094.78	287.2455

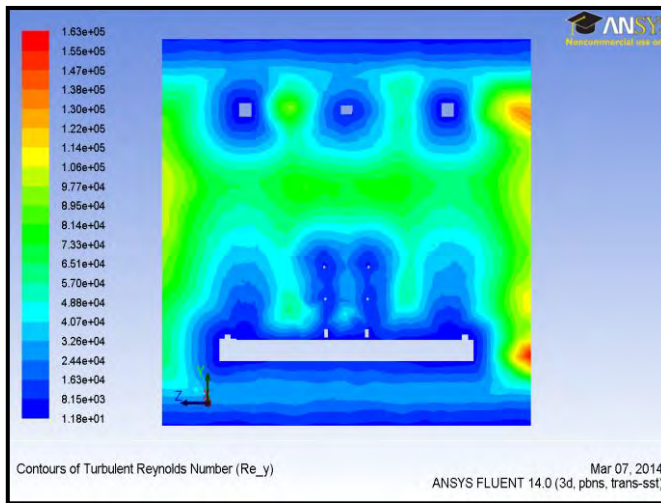


Wind Velocity (m/s)	REYNOLD'S NUMBER		Average Total Re
	Minimum Re	Maximum Re	
5	9.716767	111183	31917.55
10	5.345204	204431.5	39339.39
20	12.21827	420709	53281.01
30	18.12949	631826	67433.05
40	24.02784	828410.2	81482.77
50	29.36466	1023965	96316.48
60	35.3457	1241006	111021.4

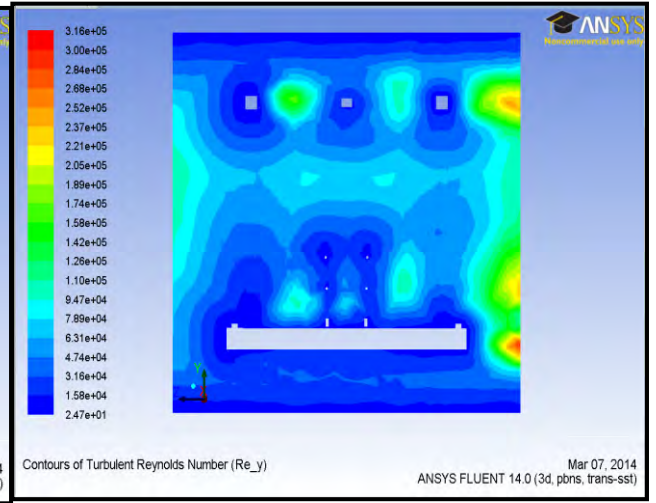


SST k- ω model Graphic Results (Full Scale Model)

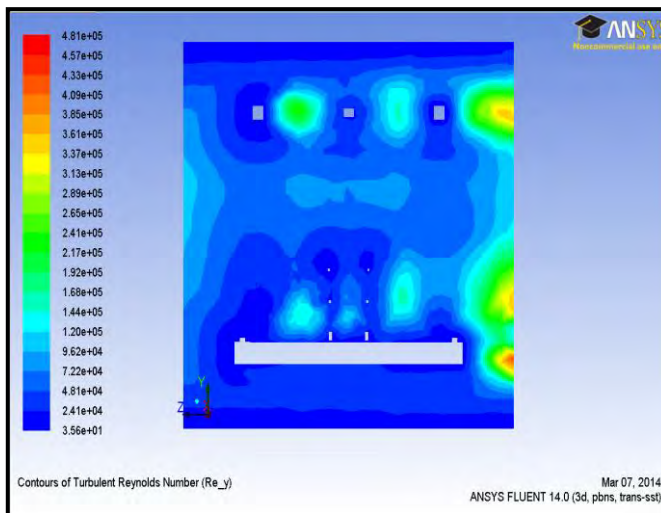
Reynold's Number



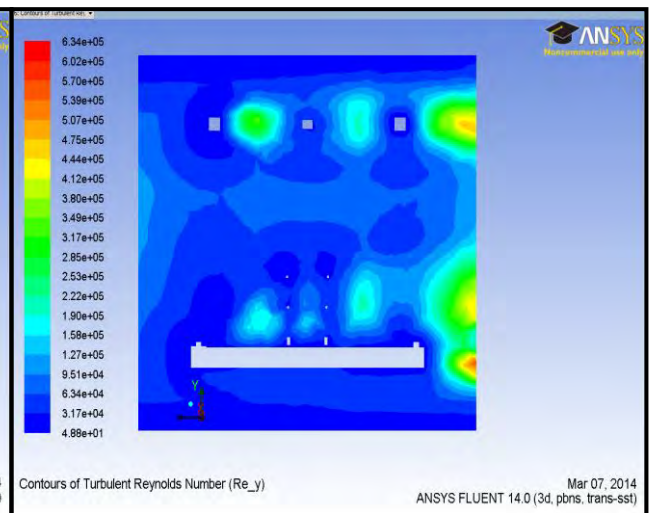
10m/s



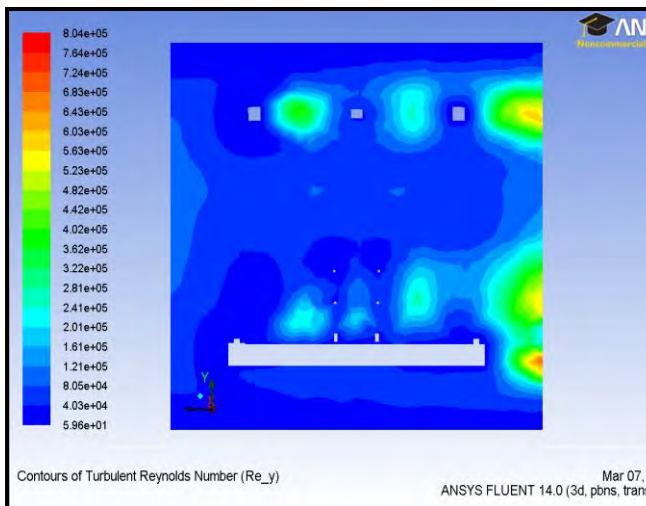
20m/s



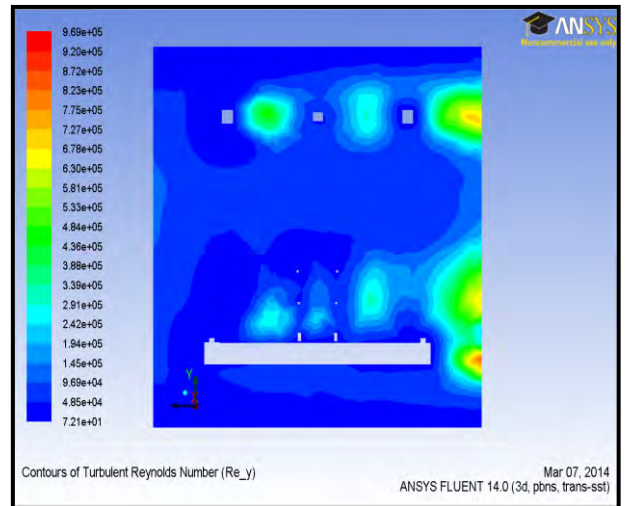
30m/s



40m/s



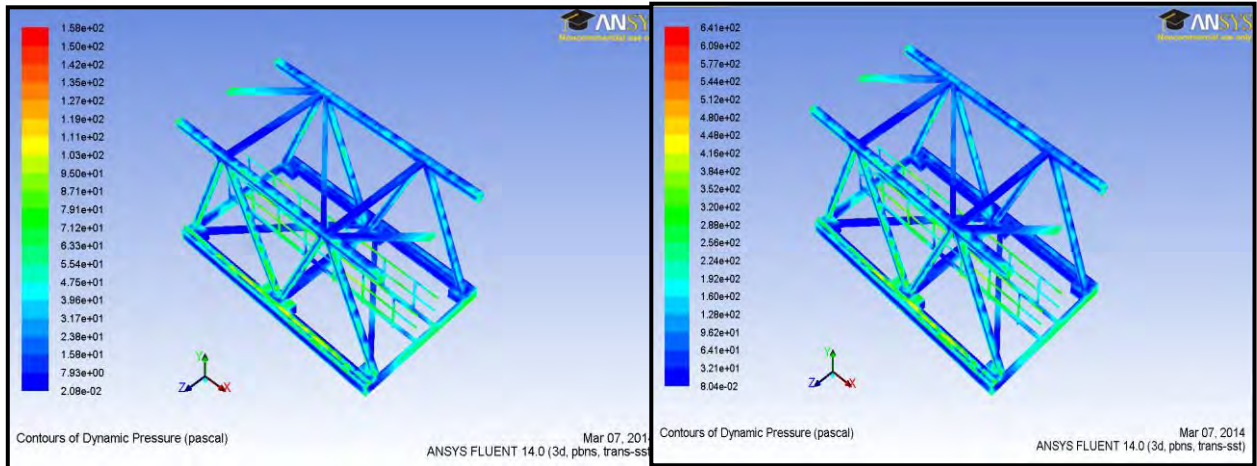
50m/s



60m/s

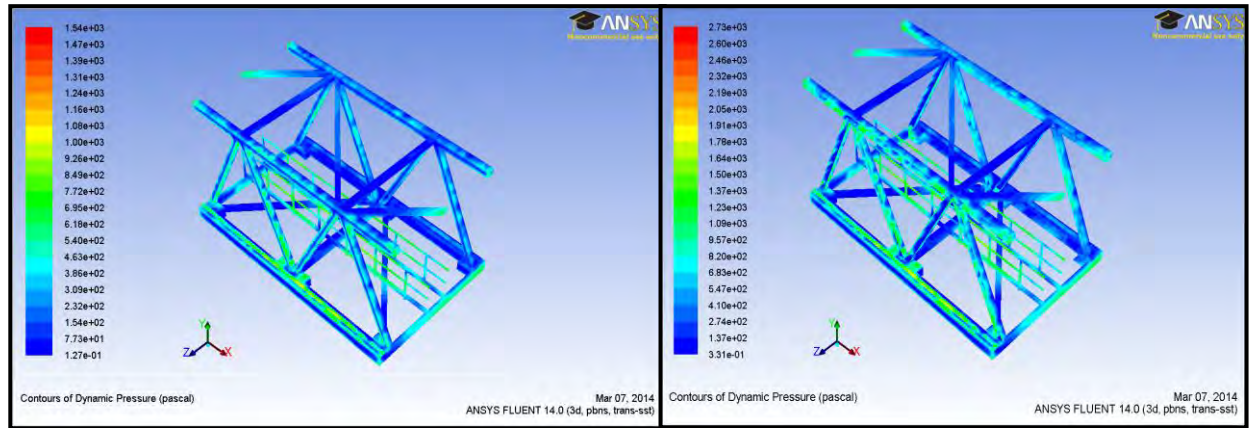
Figure C-4: Reynold's number (Hand, 2014)

Dynamic Pressure



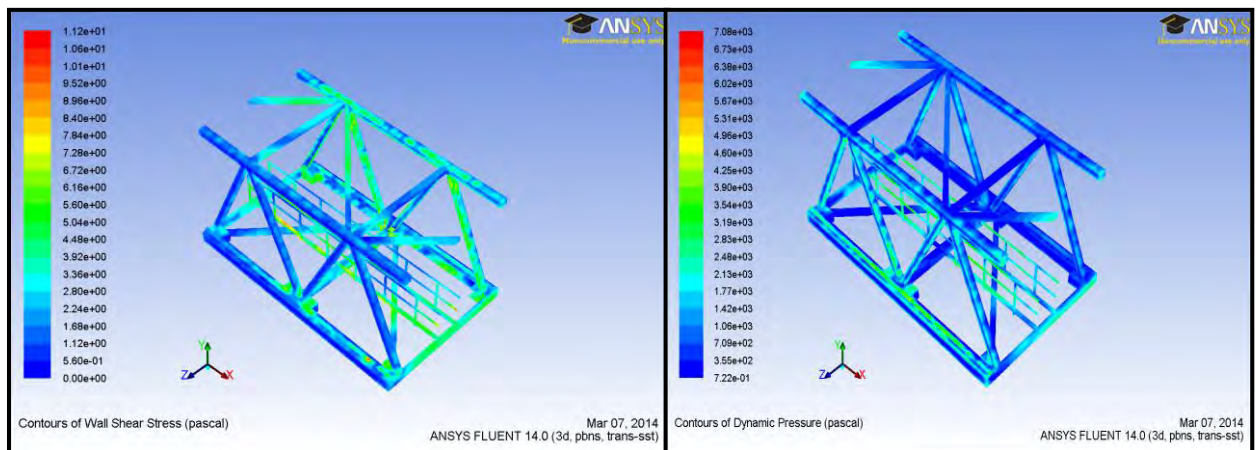
10m/s

20m/s



30m/s

40m/s

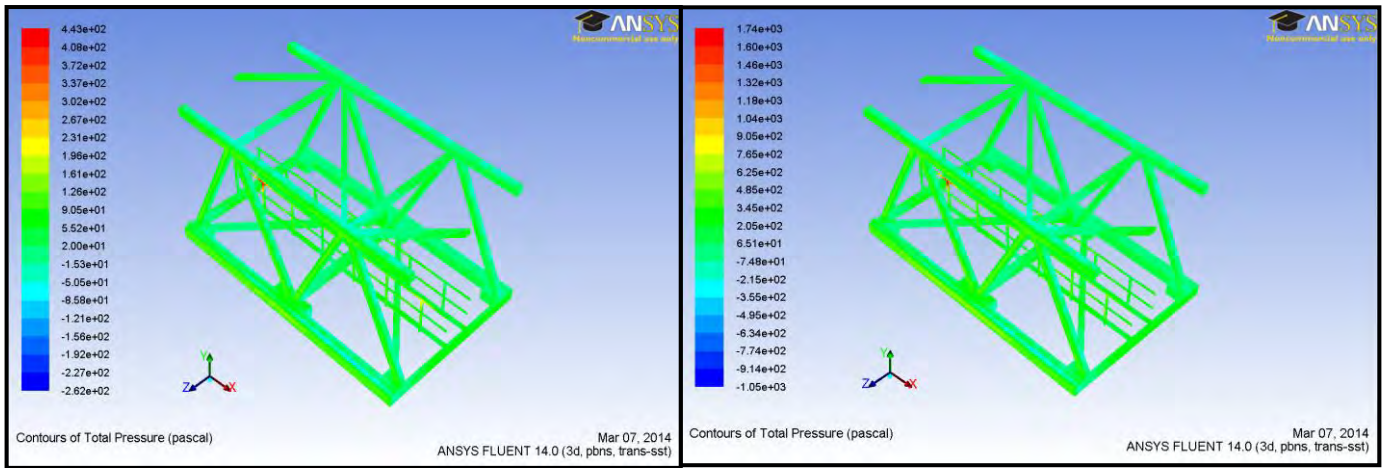


50m/s

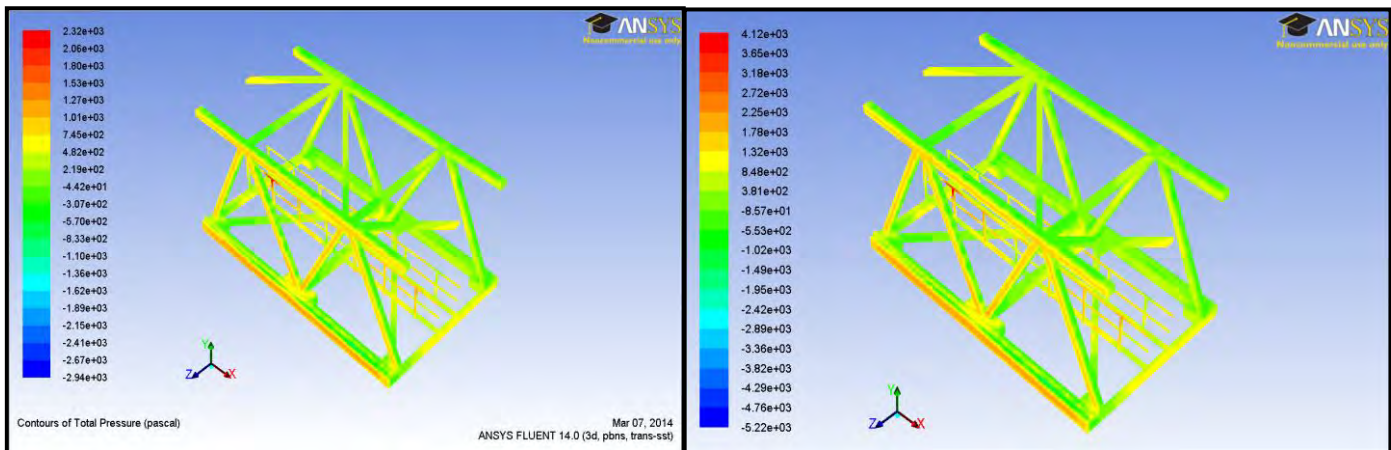
60m/s

Figure C-5 Dynamic Pressure (Hand, 2014)

Total Pressure

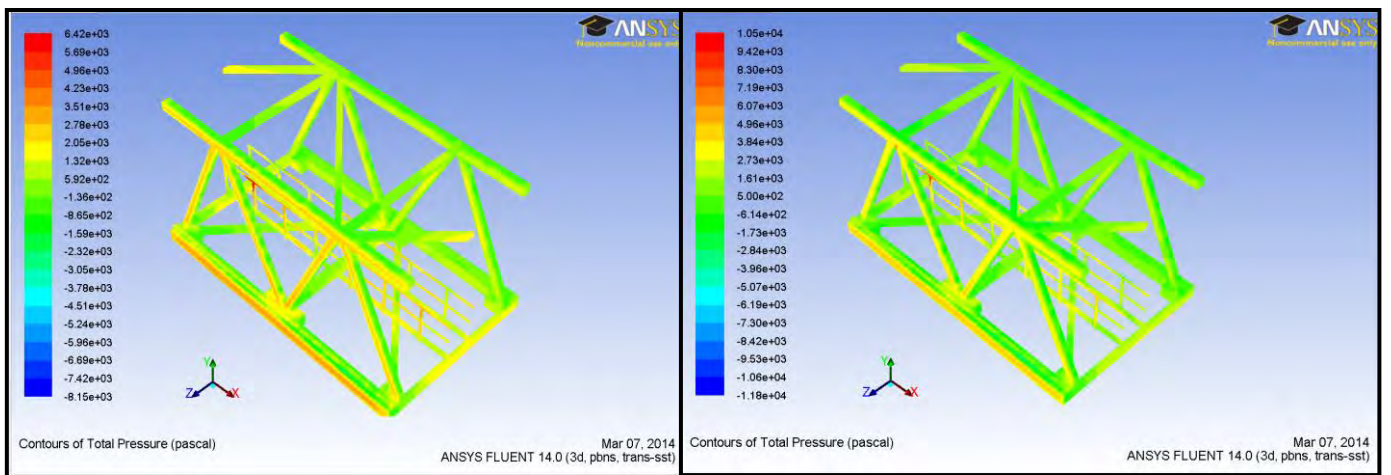


10m/s



30m/s

40m/s



50m/s

60m/s

Figure C-6 Total Pressure Contours (Hand, 2014)

SST k- ω model Computed Results (Model Scale)

SST CFD Model Results (Model scale)

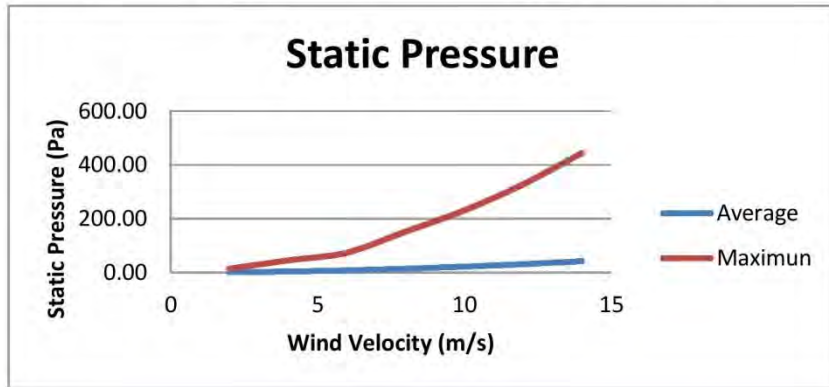
		DRAG FORCES			
Flow Velocity	Parameter	Mesh Relevance			
		Coarse	Medium	Fine	Enhanced
2m/s	Parameter	Coarse	Medium	Fine	Enhanced
	Grid Elements	119960	180067	402221	489858
	Pressure	0.101	0.101	0.102	0.101
	Viscous	0.004	0.004	0.004	0.004
	Total	0.123	0.120	0.122	0.121
4m/s	Parameter	Coarse	Medium	Fine	Enhanced
	Grid Elements	119960	180067	402221	489858
	Pressure	0.395	0.369	0.787	0.373
	Viscous	0.009	0.010	0.016	0.008
	Total	0.405	0.379	0.803	0.382
6m/s	Parameter	Coarse	Medium	Fine	Enhanced
	Grid Elements	119960	180067	402221	489858
	Pressure	0.840	0.777	0.787	0.777
	Viscous	0.010	0.016	0.016	0.014
	Total	0.853	0.793	0.803	0.791
8m/s	Parameter	Coarse	Medium	Fine	Enhanced
	Grid Elements	119960	180067	402221	489858
	Pressure	1.451	1.365	1.359	1.347
	Viscous	0.020	0.024	0.020	0.020
	Total	1.474	1.388	1.379	1.367
10m/s	Parameter	Coarse	Medium	Fine	Enhanced
	Grid Elements	119960	180067	402221	489858
	Pressure	2.245	2.051	2.081	2.064
	Viscous	0.032	0.032	0.031	0.029
	Total	2.277	2.083	2.113	2.093
12m/s	Parameter	Coarse	Medium	Fine	Enhanced
	Grid Elements	119960	180067	402221	489858
	Pressure	2.246	2.913	2.959	2.945
	Viscous	0.031	0.041	0.041	0.037
	Total	2.277	2.955	2.999	2.982
14m/s	Parameter	Coarse	Medium	Fine	Enhanced
	Grid Elements	119960	180067	402221	489858
	Pressure	4.309	3.944	3.995	3.982
	Viscous	0.051	0.051	0.051	0.047
	Total	4.360	3.995	4.046	4.029
16m/s	Parameter	Coarse	Medium	Fine	Enhanced
	Grid Elements	119960	180067	402221	489858
	Pressure	5.623	5.127	5.203	5.181
	Viscous	0.061	0.062	0.062	0.057
	Total	5.684	5.189	5.265	5.238

SST CFD Model Results (Model scale)

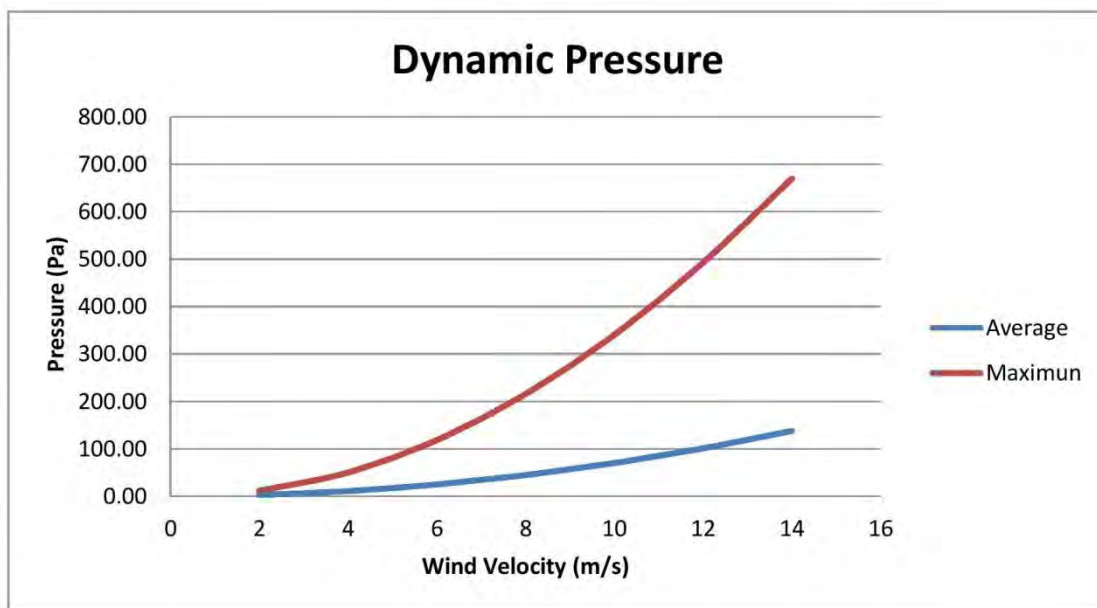
		LIFT FORCES			
Flow Velocity	Parameter	Mesh Relevance			
		Coarse	Medium	Fine	Enhanced
2m/s	Grid Elements	119960	180067	402221	489858
	Pressure	-0.0010	0.0017	0.0036	0.0003
	Viscous	0.0001	0.0001	0.0001	0.0001
	Total	-0.0008	0.0017	0.0037	0.0005
4m/s	Grid Elements	119960	180067	402221	489858
	Pressure	-0.0055	0.0042	0.0108	-0.0010
	Viscous	0.0003	0.0002	0.0005	0.0003
	Total	-0.0052	0.0044	0.0113	-0.0007
6m/s	Grid Elements	119960	180067	402221	489858
	Pressure	0.0108	0.0002	0.0108	0.0096
	Viscous	0.0005	0.0004	0.0005	0.0007
	Total	0.0000	0.0006	0.0113	0.0103
8m/s	Grid Elements	119960	180067	402221	489858
	Pressure	-0.012	0.009	0.024	0.021
	Viscous	0.001	0.000	0.001	0.001
	Total	-0.011	0.010	0.025	0.022
10m/s	Grid Elements	119960	180067	402221	489858
	Pressure	-0.0319	-0.0278	0.0228	0.0370
	Viscous	0.0011	0.0008	0.0009	0.0017
	Total	-0.0308	-0.0270	0.0237	0.0386
12m/s	Grid Elements	119960	180067	402221	489858
	Pressure	373.8178	-0.0363	0.0408	0.0591
	Viscous	-3.9673	0.0012	0.0014	0.0023
	Total	369.8506	-0.0351	0.0422	0.0613
14m/s	Grid Elements	119960	180067	402221	489858
	Pressure	-0.0746	-0.0205	0.0447	0.0886
	Viscous	0.0018	0.0013	0.0018	0.0029
	Total	-0.0728	-0.0192	0.0464	0.0915
16m/s	Grid Elements	119960	180067	402221	489858
	Pressure	-0.1032	-0.0194	0.0521	0.1022
	Viscous	0.0020	0.0017	0.0022	0.0037
	Total	-0.1012	-0.0177	0.0542	0.1059

SST CFD Model Results (Model scale)

STATIC PRESSURE			
Wind Velocity (m/s)	Minimum Static Pressure (Pa)	Maximum Static Pressure (Pa)	Average Static Pressure (Pa)
2	-12.07	14.65	1.18
4	-50.38	45.48	4.14
6	-117.91	74.32	8.34
8	-213.66	152.21	14.46
10	-336.65	230.95	22.06
12	-486.95	327.75	31.01
14	-662.86	443.92	41.89

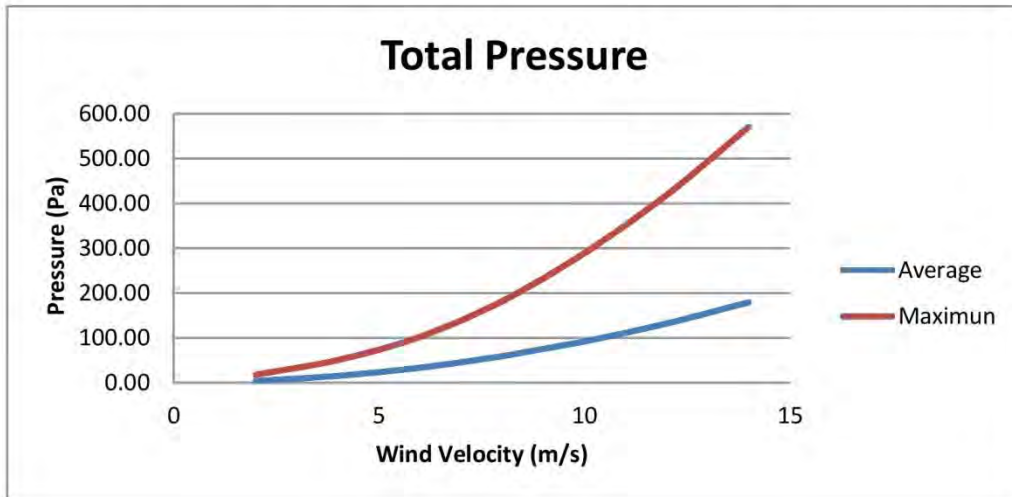


DYNAMIC PRESSURE			
Wind Velocity (m/s)	Minimum Dynamic Pressure (Pa)	Maximum Dynamic Pressure (Pa)	Average Dynamic Pressure (Pa)
2	4.52E-06	11.78	2.73
4	4.90E-05	50.36	11.05
6	2.05E-04	118.59	25.06
8	5.96E-04	215.80	44.76
10	6.40E-04	340.55	70.11
12	2.60E-04	492.85	101.11
14	7.90E-04	669.79	137.78

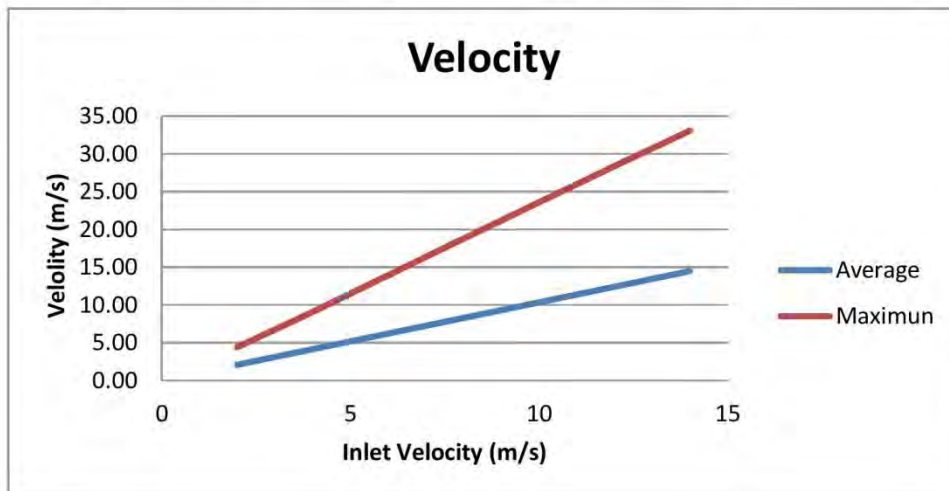


SST CFD Model Results (Model scale)

Wind Velocity (m/s)	TOTAL PRESSURE		
	Minimum Total Pressure (Pa)	Maximum Total Pressure (Pa)	Average Total Pressure (Pa)
2	0.00	17.74	3.90
4	-28.09	50.63	15.18
6	-65.05	102.32	33.40
8	-115.55	181.75	59.21
10	-181.26	288.91	92.17
12	-265.82	418.37	132.12
14	-361.85	570.50	179.67

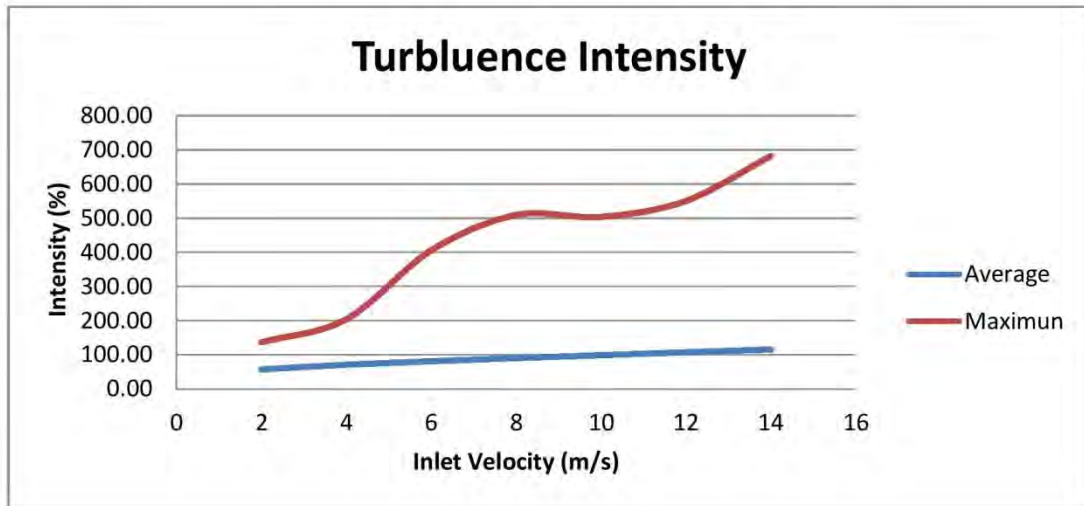


Wind Velocity (m/s)	VELOCITY		
	Minimum Velocity	Maximum Velocity	Average Total Velocity
2	0.00	4.39	2.06
4	0.00	9.07	4.12
6	0.00	13.91	6.19
8	0.03	18.77	8.25
10	0.03	23.58	10.32
12	0.02	28.37	12.39
14	0.04	33.07	14.46

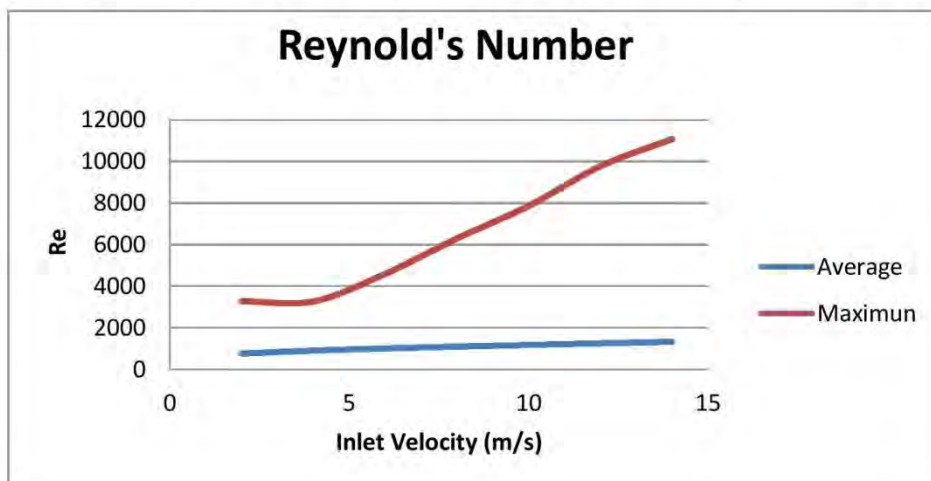


SST CFD Model Results (Model scale)

	TURBLUENCE INTENSITY		
Wind Velocity (m/s)	Minimum Turbluence	Maximum Turbluence	Average Total turbulence
2	2.72	136.75	57.44
4	3.30	204.30	70.90
6	0.01	405.87	80.92
8	0.00	509.28	90.03
10	0.00	503.73	98.58
12	0.00	550.18	107.00
14	0.00	681.60	115.09



	REYNOLD'S NUMBER		
Wind Velocity (m/s)	Minimum Re	Maximum Re	Average Total Re
2	0.05623193	3272.539	756.0659
4	0.066775873	3265.0186	900.5936
6	0.003940336	4592.816	1001.243
8	0.000205825	6297.645	1088.689
10	2.77E-06	7864.686	1169.748
12	2.77E-06	9778.896	1.25E+03
14	2.84E-06	11087.74	1324.736



SST k- ω model Graphic Results (Scale Model)

Velocity

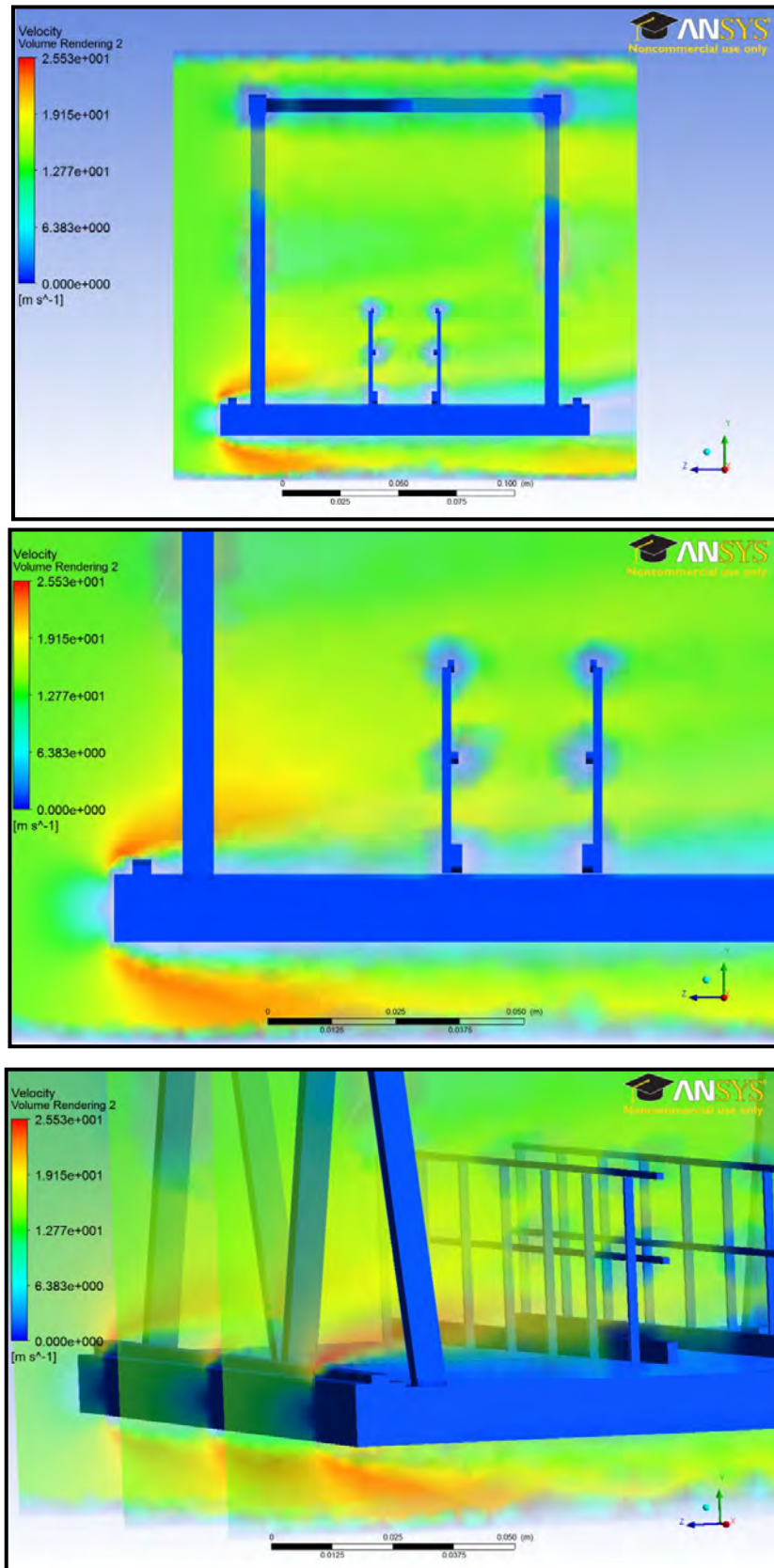


Figure C-7 Velocity contours (*Hand, 2014*)

Y Plus

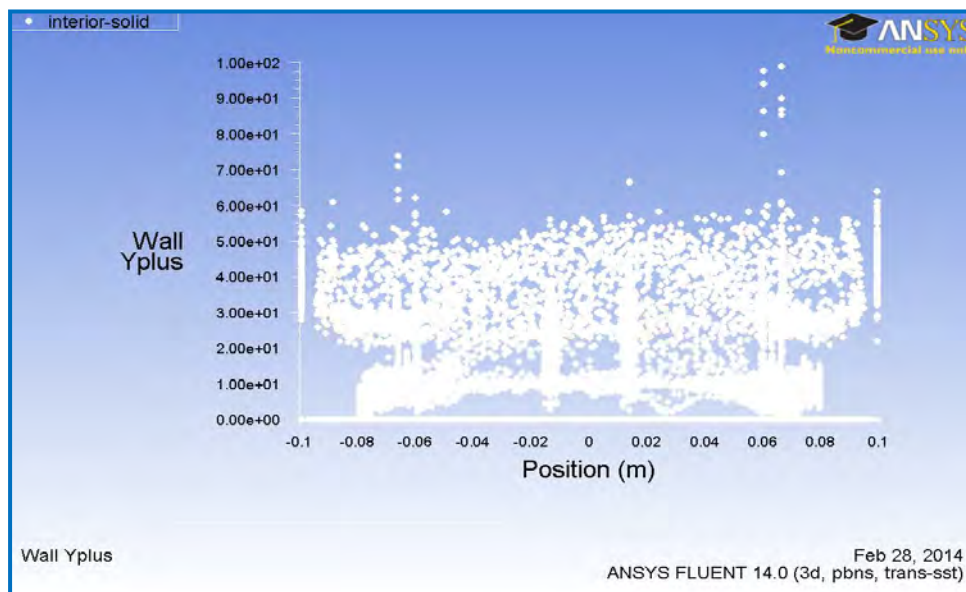
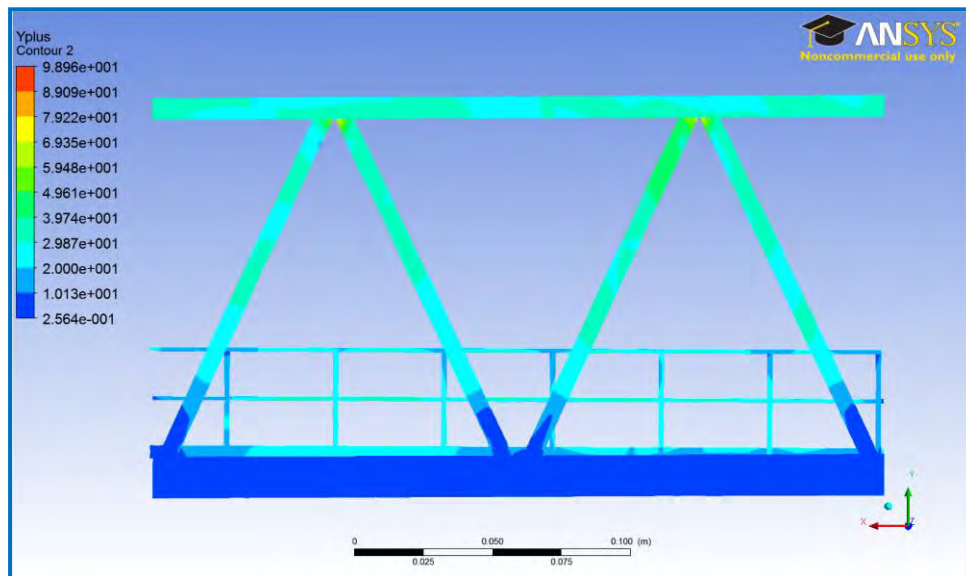
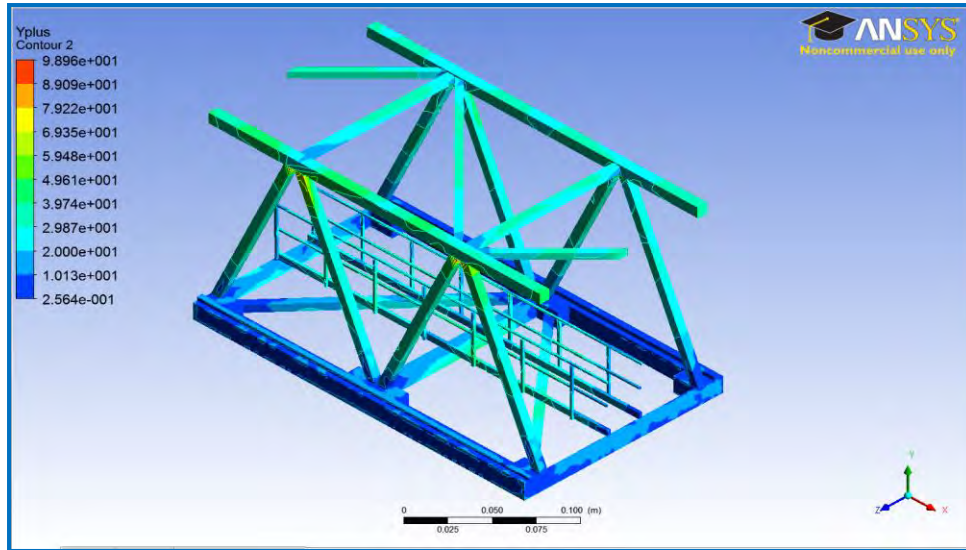
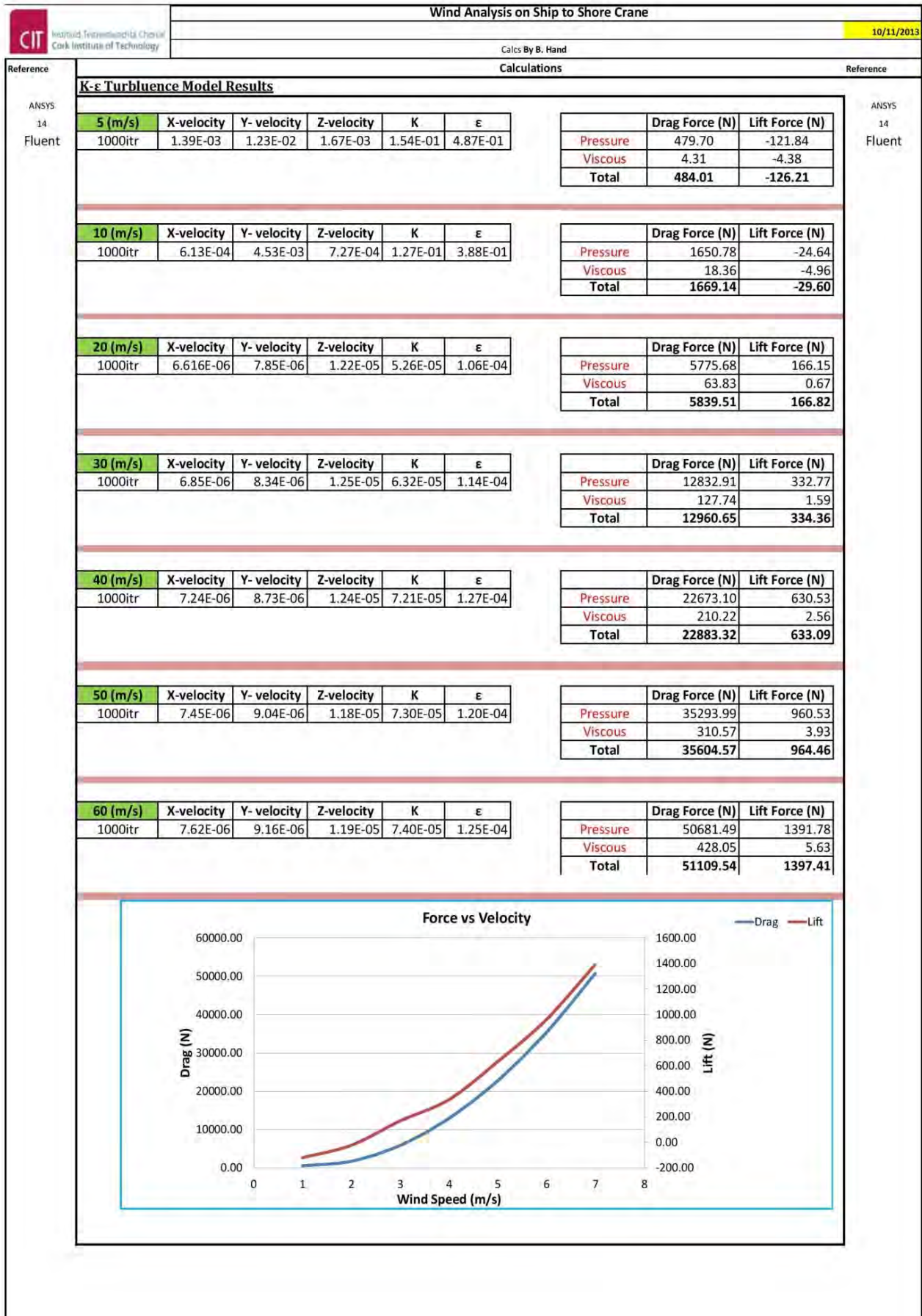


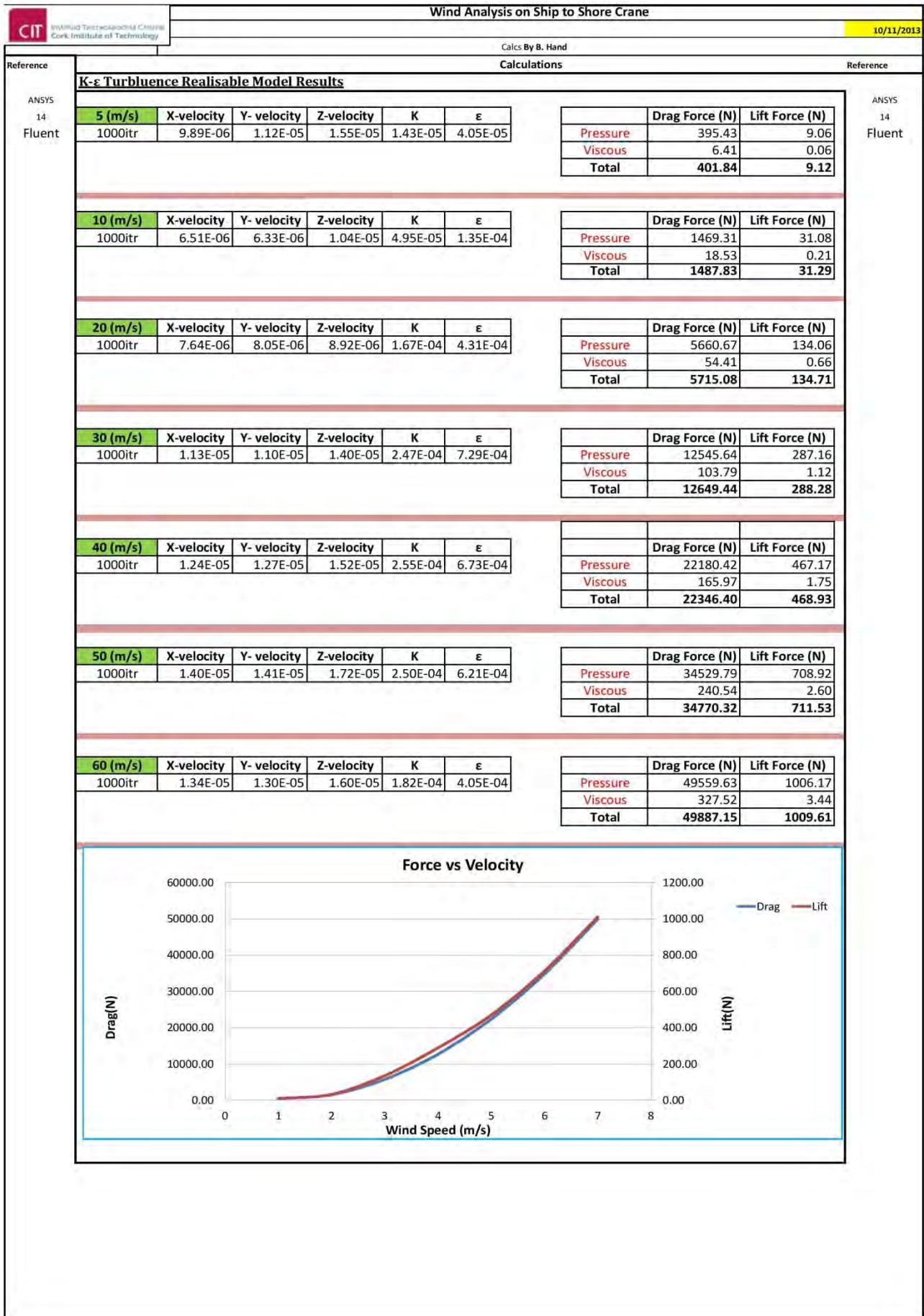
Figure C-8 Y Plus parameters (Hand, 2014)

CFD Model Selection Computations

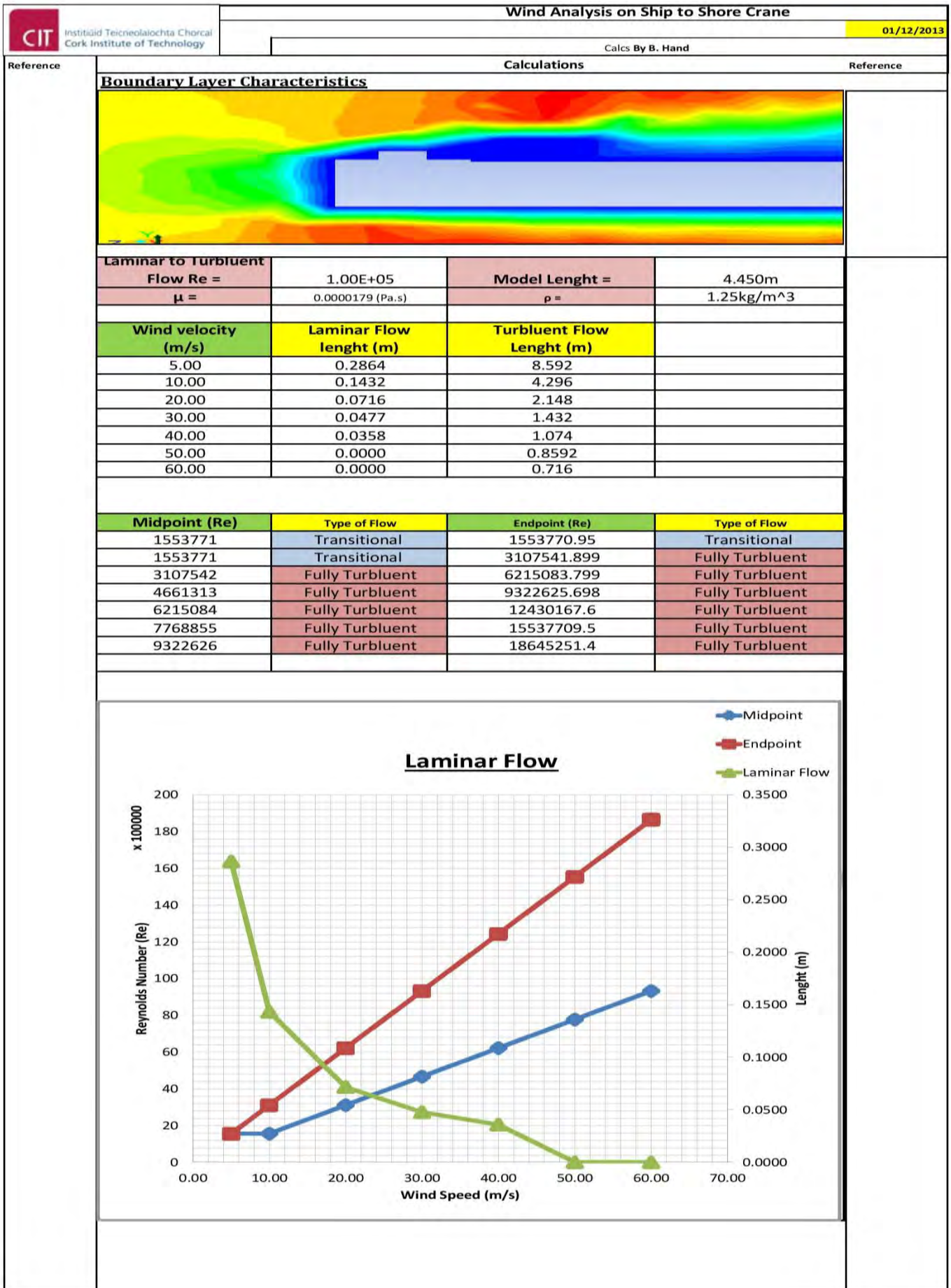
K-ε Model



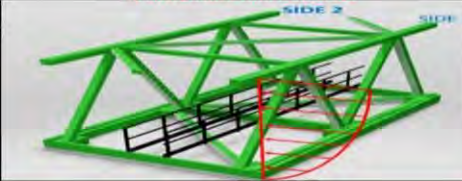
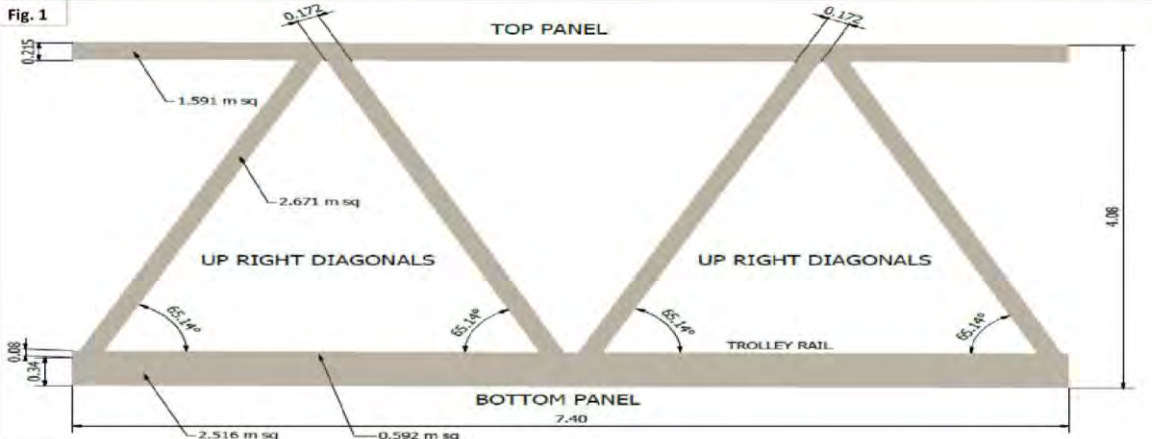
K-ε Realisable model



Air Flow Type Approximation

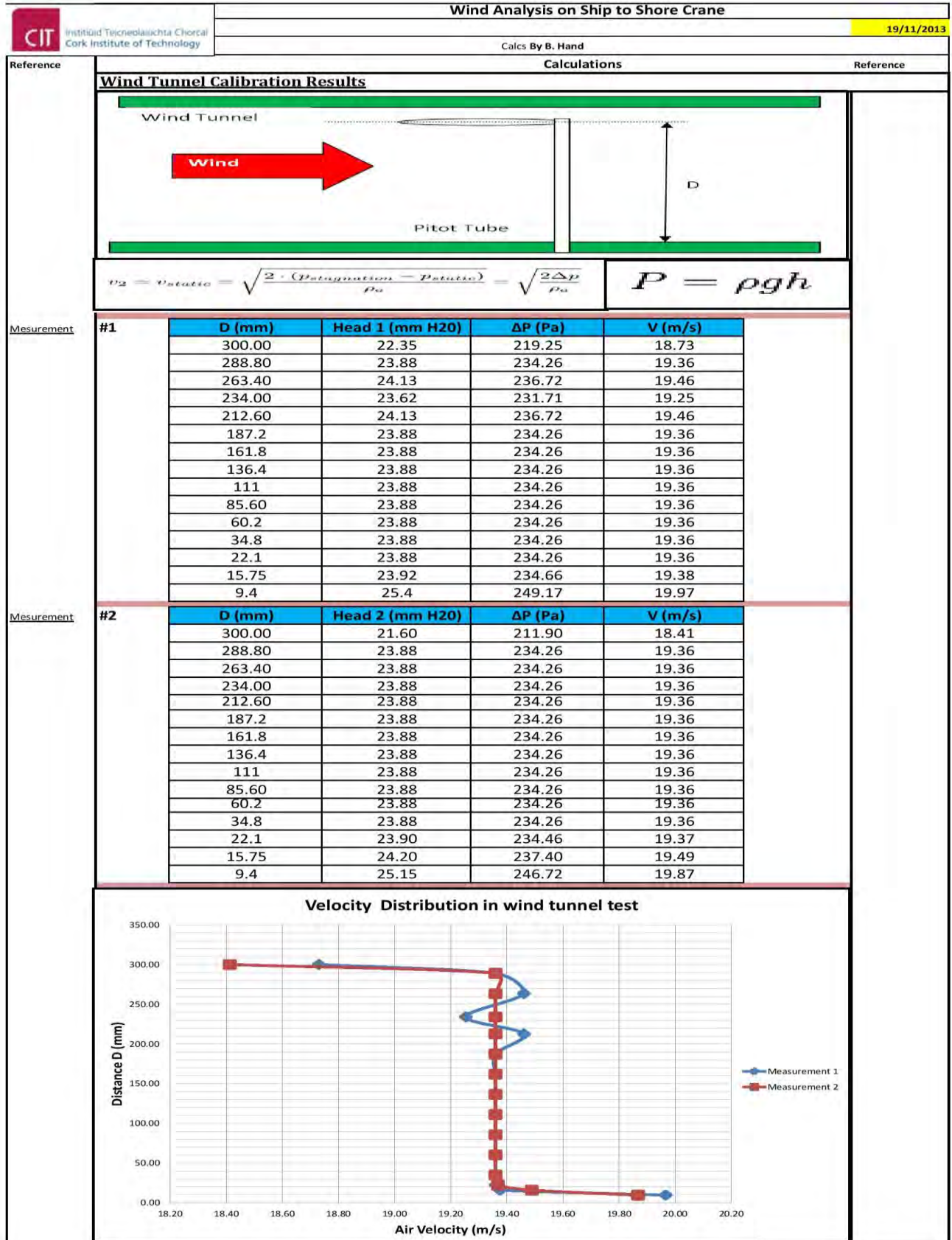


Hand Calculation

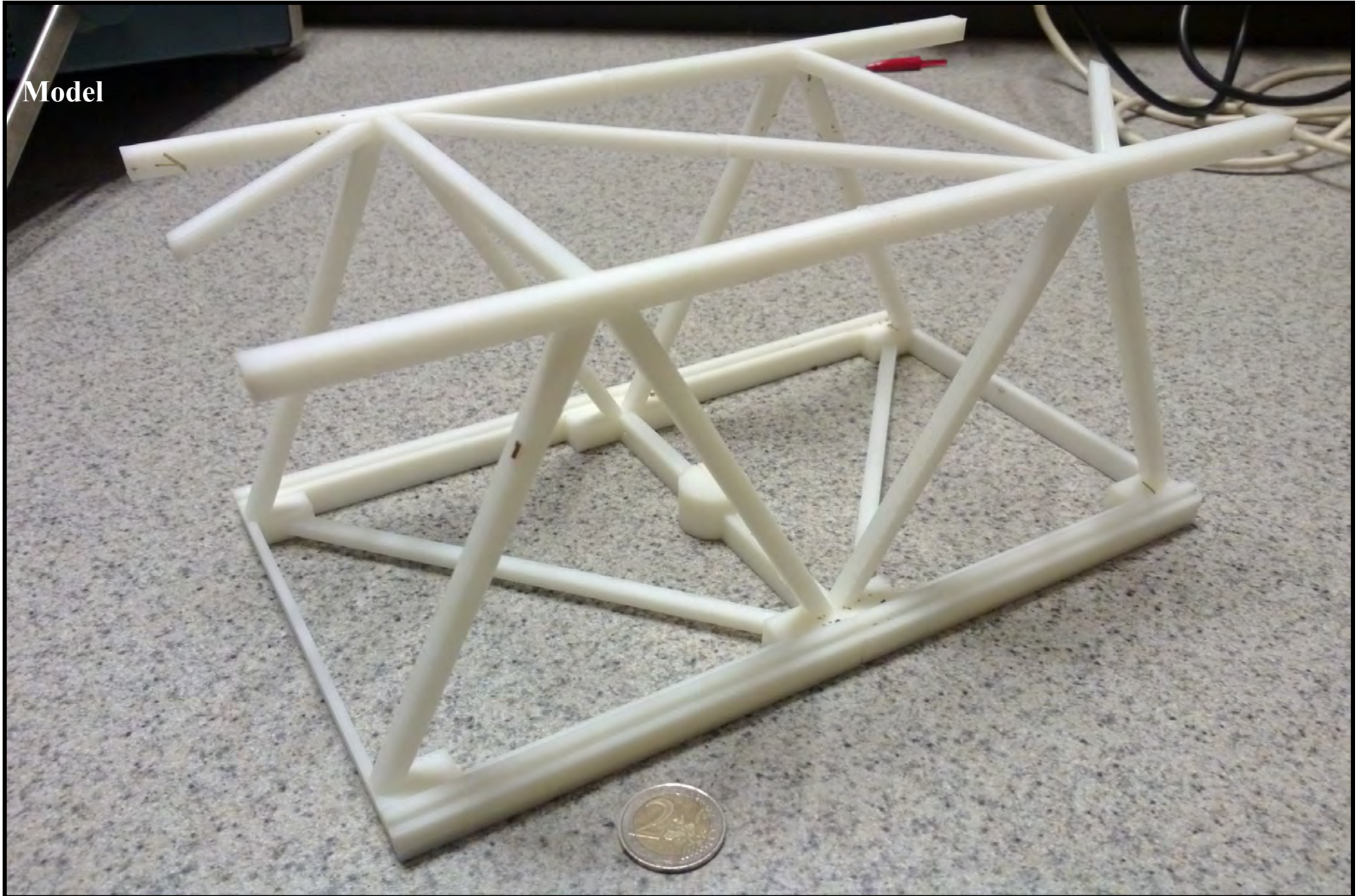
CIT		Wind Analysis on Ship to Shore Crane		31/10/2013
Institiúid Teicneolaíochta Chorcaí Cork Institute of Technology		Calcs By B. Hand		
Reference	Calculations	In Accordance with FEM 1.004	Reference	
	Wind Forces on Derrick Boom Section (Corner 1 to 2)			
	Wind Speed (v) = 42 m/s = 151.2 km/hr Wind Pressure (q): 1102.5 N/m ² Out-of-Service			
	Length L (m) = 7.4 (2 Bays of Lattice Structure) A is the effective frontal area of the part under consideration (m ²) A' is effective area influenced by shielding (m ²)			
Fig. 1	Lattice Structure Area (2 Bays) Bottom Panel IPB340 RSJ = 2.516 m ² Trolley Rail = 0.592 m ²	Lattice Structure Wind Force (Side 1) Shape Coefficient (Cf) = 1.7 Wind Pressure (q) = 1102.5 N/m ² Wind Effected Area (A) = 7.37 m ² Wind Force (F) = 13.81 KN	T 5.1.b	Chpt 3.1
Fig. 1	Top Panel Hollow 215mm Sq.section = 1.591 m ²	Platform Wind Force (Side 1) Shape Coefficient (Cf) = 1.7 Wind Pressure (q) = 1102.5 N/m ² Wind Effected Area (A) = 1.8611 m ² Wind Force (F) = 3.49 KN	T 5.1.b	Chpt 3.1
Fig. 1	Up Right Diagonals 4 Hollow 172mm Sq sections = 2.671 m ² 0.6677m ² × 4 = 2.671 m ² TOTAL A = 7.37 m ²	Shielded Lattice Structure Wind Force (Side 2) Enclosed area of 2 bays = 30.17 m ² Ae = 7.40 × 4.077 = 30.17 m ² Area of Solid parts (A') = 7.37 m ² Solidity Ratio, A'/Ae = 0.2442824 Spacing Ratio, a/b = 3.534/4.077 = 0.867 Shielding Factor, Φ = 0.5938 Shape Coefficient (Cf) = 1.7 Wind Pressure (q) = 1102.5 N/m ² Wind Force (F) = 8.20 KN	Chpt 5.1	Chpt 5.1
Fig. 2	Platforms Area Horizontal Kick Plates = 0.962 m ² Vertical Rail Supports = 0.3367 m ² Handle Rails = 0.5624 m ² (7.40 × 0.038) × 2 = 0.5624 m ² TOTAL A = 1.86 m ²	Shielded Platform Wind Force (Side 2) Enclosed area of 2 bays = 8.362 m ² Ae = 7.40 × 1.130 = 8.362 m ² Area of Solid parts (A') = 1.8611 m ² Solidity Ratio, A'/Ae = 0.22256637 Spacing Ratio, a/b = 0.767/1.14 = 0.6728 Shielding Factor, Φ = 0.5 Shape Coefficient (Cf) = 1.7 Wind Pressure (q) = 1102.5 N/m ² Wind Force (F) = 1.74 KN	Chpt 5.1	Chpt 5.1
	Total Calculated Wind Force 13.81 KN 3.49 KN 8.20 KN (Shielded) 1.74 KN (Shielded) TOTAL F = 27.25 KN Wind Force per unit length = 3.68 KN/m			
Fig. 1				
Fig. 2				

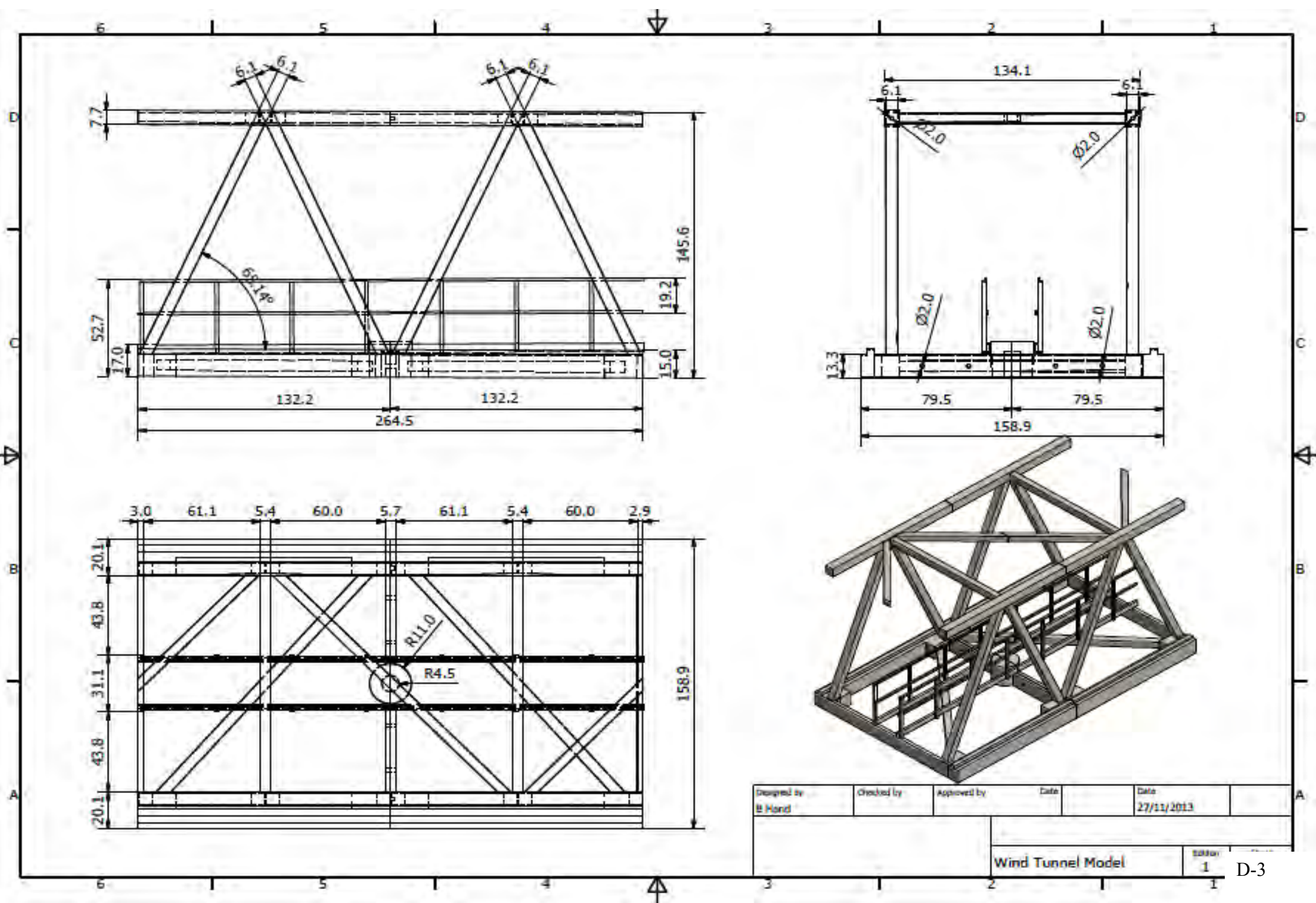
Appendix D - Wind Tunnel Testing

Wind Tunnel Calibration

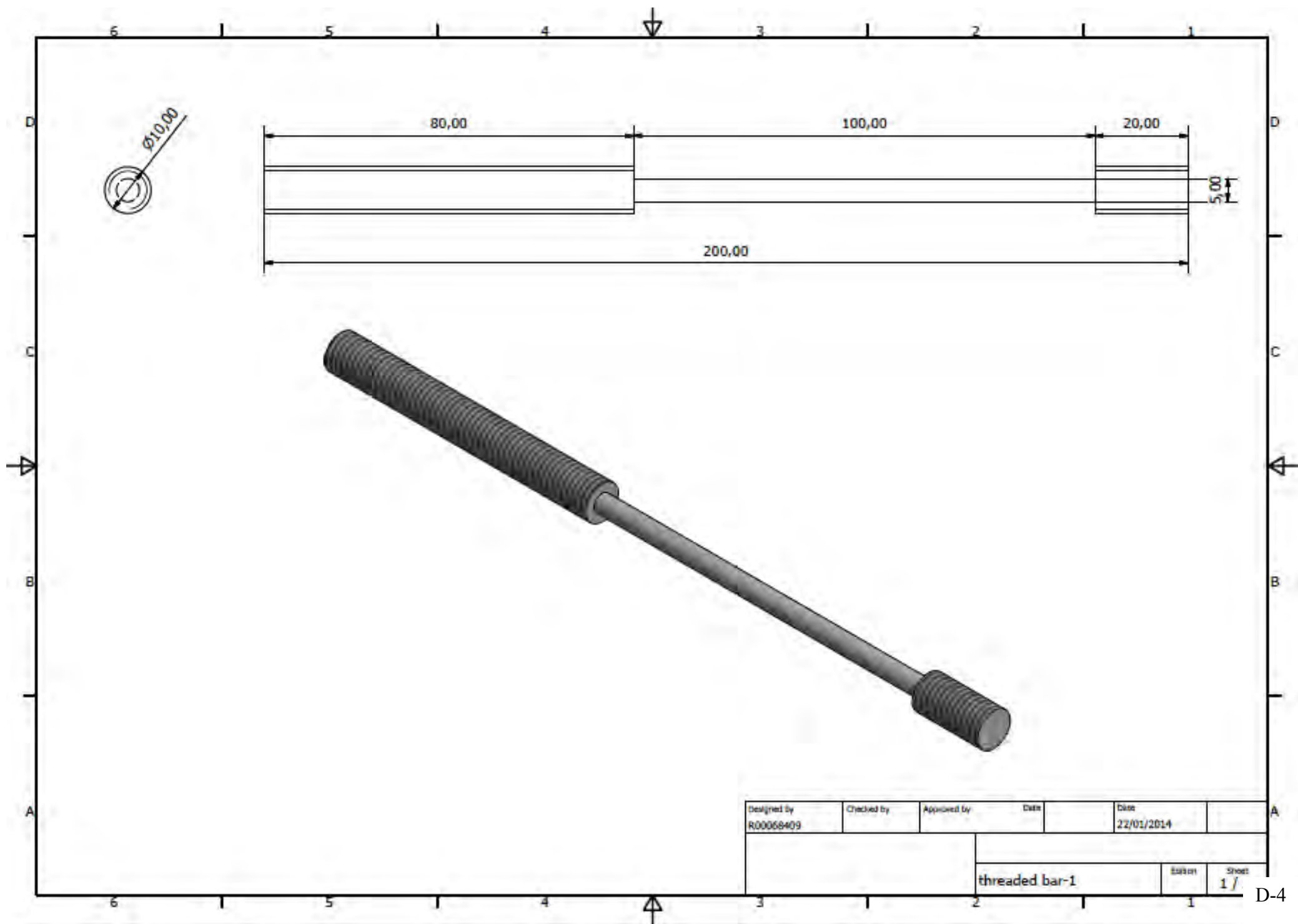


Model





Designed by B Hand	Checked by	Approved by	Date	Date 27/11/2013
Wind Tunnel Model				Issue 1



Designed by R00068409	Checked by	Approved by	Date	Date 22/01/2014
			threaded bar-1	Sheet 1 / 1

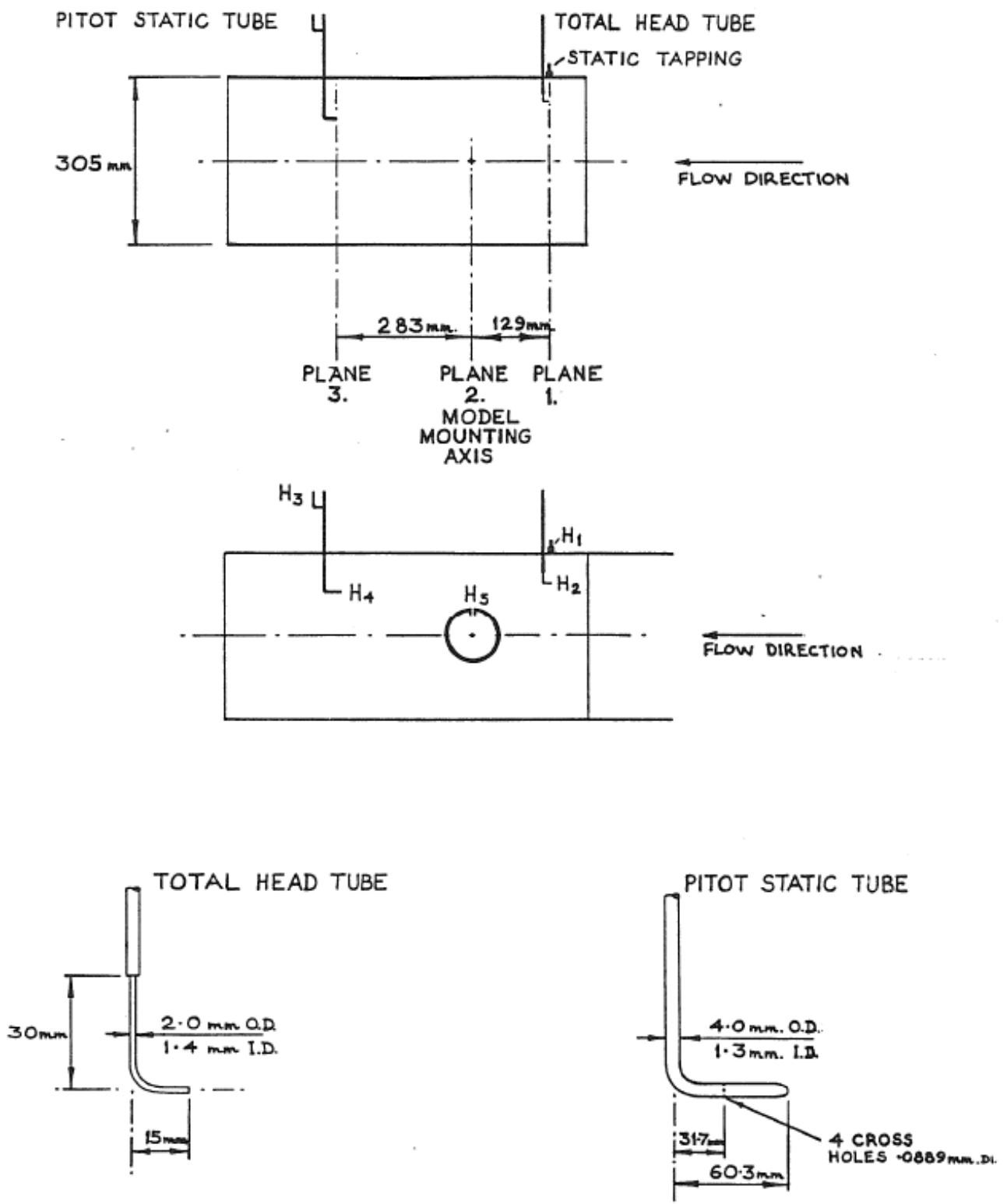
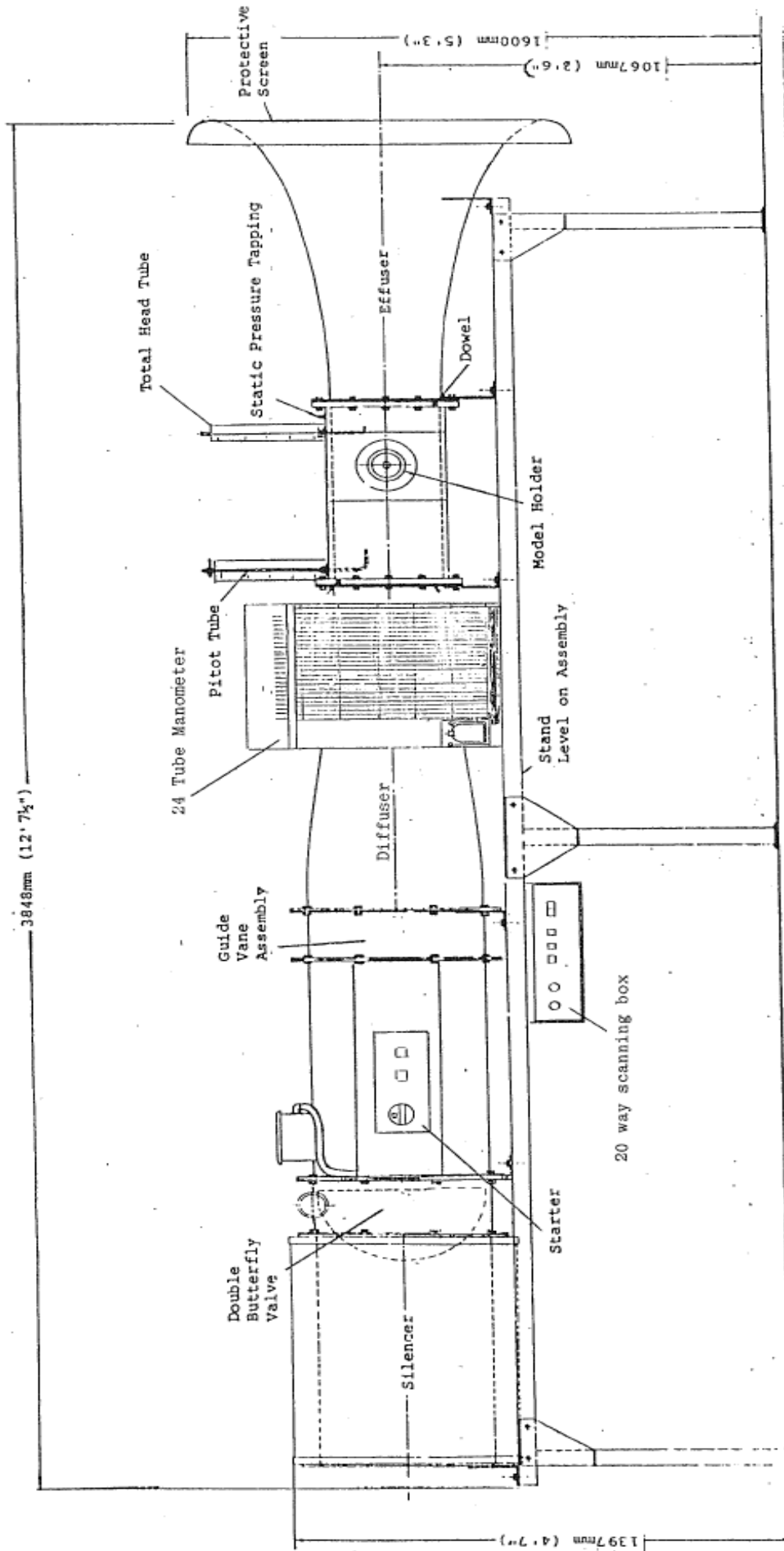


Figure 2a Working Section and Instruments



Note: Stamp up all legs and brackets on assembly in their respective positions, to ease installation

Figure 14 300mm x 300mm Wind Tunnel - TE 54 (reduction of dwg. 50130)

AFA2

Basic Lift and Drag Balance

Measures lift and drag forces on models mounted in a TecQuipment Subsonic Wind Tunnel (AF100)

Works with
VDAS®



Base mounted with model car to measure drag



Mounted on side of wind tunnel to measure both lift and drag. Shown fitted with the protractor from the Wind Tunnel.



- Optional ancillary to TecQuipment's modular Subsonic Wind Tunnel (AF100)
- Single-component balance to measure lift and drag forces on models mounted in the tunnel
- Transmits the force on the model directly to a strain gauged load cell with digital display
- Fully compatible with TecQuipment's Versatile Data Acquisition System (VDAS®) to enable accurate real-time data capture, monitoring and display on a computer
- Includes power supply

- TecQuipment Ltd, Bonsall Street, Long Eaton, Nottingham NG10 2AN, UK
- T +44 115 972 2611 • F +44 115 973 1520 • E info@tecquipment.com • W www.tecquipment.com
- An ISO 9001 certified company
- VDAS is a registered trademark of TecQuipment Ltd

TecQuipment

DE 800746 3/03 13

AFA2

Basic Lift and Drag Balance

Description

A single-component balance which measures the lift and drag forces on models mounted in TecQuipment's Subsonic Wind Tunnel (AF100).

The balance mechanism enables test models with a rigid support arm to be mounted and held securely in position in the working section of the wind tunnel. The arm transmits the force on the test model directly to a strain gauged load cell. The load cell is connected to a readout unit with a digital display, which is powered by a desktop power supply (included).

In addition, the equipment is fully compatible with TecQuipment's Versatile Data Acquisition System (VDAS®) and can quickly and conveniently connect to the frame-mounting interface unit (VDAS-F, not included). Using VDAS® enables accurate real-time data capture, monitoring, display, calculation and charting of all relevant parameters on a suitable computer (computer available separately).

To measure the lift and drag forces on models (airfoils for example, available separately), the balance mounts on the side of the working section of the wind tunnel. The drag force is measured first, then students rotate the balance mechanism through 90 degrees and repeat the test to measure the lift force. When mounted in the base of the wind tunnel working section, the balance measures the drag force only. This is useful for a variety of investigations such as wind loadings on tall buildings. It can also be used to measure drag forces on model vehicles enabling students to determine and compare coefficients of drag.

Note: For experiments requiring measurement of pitching moment as well as drag and lift forces, a three-component balance, such as TecQuipment's AFA3, is required.

Standard Features

- Supplied with comprehensive user guide
- Two-year warranty
- Made in accordance with the latest European Union directives

Ancillary for:

- Subsonic Wind Tunnel (AF100)
- Cylinder Model with Pressure tapping (AF101)
- 150 mm Chord NACA0012 Airfoils (AF104)
- 100 mm Diameter Flat Plate (AF105)
- Three-dimensional Drag Models (AF109)

Operating Conditions:

Operating environment:

Well ventilated laboratory environment

Storage temperature range:

-25°C to +55°C (when packed for transport)

Operating temperature range:

+5°C to +40°C

Operating relative humidity range:

80% at temperatures < 31°C decreasing linearly to 50% at 40°C

Essential Services:

Electrical supply:

100 V a. c. to 240 V a. c., 50 Hz to 60 Hz

Note: A suitable electrical supply outlet is included at the rear of the Wind Tunnel controller

Specification:

Dimensions (packed for export):

0.045 m³

Weight:

Nett: 6 kg

Packed: 12 kg

Maximum load:

10 kg (100 N)

Power supply output:

12 V d.c.

Typical scale for models:

1/18th

- TecQuipment Ltd, Bonsall Street, Long Eaton, Nottingham NG10 2AN, UK
- T +44 115 972 2611 • F +44 115 973 1520 • E info@tecquipment.com • W www.tecquipment.com
- An ISO 9001 certified company
- VDAS is a registered trademark of TecQuipment Ltd



AFA10

Smoke Generator

Produces a fine trace of smoke to allow students to see air flow in subsonic wind tunnels and other air flow products



- Produces a smooth, fine trace of smoke
- Probe shaped to minimise wake generation
- Low oil consumption
- Fully adjustable smoke strength
- Supplied with smoke oil and a spare heater tip

- TecEquipment Ltd, Bonsall Street, Long Eaton, Nottingham NG10 2AN, UK
- T +44 115 972 2611 • F +44 115 973 1520 • E info@tecequipment.com • W www.tecequipment.com
- An ISO 9001 certified company



IND 413 112

AFA10

Smoke Generator

Description

A smoke generator and probe that allows students to see air flow in subsonic wind tunnels and other low flow rate air flow products.

It is a control unit that pumps oil to the tip of a probe. A low-voltage electrical coil at the probe tip heats the oil to produce a fine smoke trail. The smoke moves into the air stream smoothly and steadily. Students can adjust the controls of the control unit to change the smoke strength to suit the air flow conditions.

The apparatus includes an integral reservoir bottle. Low oil consumption allows approximately six hours of use on one filling of the bottle.

Supplied with instructions, smoke probe, spare heater tip and oil.

AERODYNAMICS

AFA10

latest European

Description

A smoke generator and probe that allows students to see air flow in subsonic wind tunnels and other low flow rate air flow products.

It is a control unit that pumps oil to the tip of a probe. A low-voltage electrical coil at the probe tip heats the oil to produce a fine smoke trail. The smoke moves into the air stream smoothly and steadily. Students can adjust the controls of the control unit to change the smoke strength to suit the air flow conditions.

The apparatus includes an integral reservoir bottle. Low oil consumption allows approximately six hours of use on one filling of the bottle.

Supplied with instructions, smoke probe, spare heater tip and oil.

Standard Features

Supplied with operating instructions

Two-year warranty

Manufactured in accordance with the latest European Union directives

Ancillary For

- Subsonic Wind Tunnel (AF100)
- Flight Demonstration Wind Tunnel (AF41)

Operating Conditions

Operating environment:

Well Ventilated Laboratory environment

Storage temperature range:

-25°C to +55°C (when packed for transport)

Operating temperature range:

+5°C to +40°C

Operating relative humidity range:

80% at temperatures < 31°C decreasing linearly to 50% at 40°C

Essential Services

Electrical supply:

Single-phase, 230 V/110 V, 50/60 Hz

Ventilation:

Use this smoke generator in an area that has good ventilation and an air extraction system

Specifications

Nett dimensions:

180 mm x 240 mm x 370 mm

Approximate Packed Dimensions and Weight:

0.06 m³ and 15 kg

tec, Nottingham NG10 2AN, UK

Tel: +44 115 972 2611 • Fax: +44 115 973 1520 • E: info@tecquipment.com • W: www.tecquipment.com

TecEquipment Ltd, Boxall Street, Long Eaton, Nottingham NG10 2AN, UK
T: +44 115 972 2611 • F: +44 115 973 1520 • E: info@tecquipment.com



VDAS

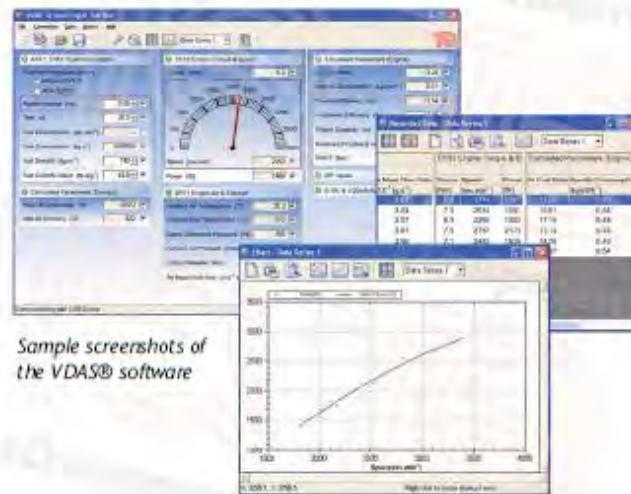
Versatile Data Acquisition System

Enables high-capacity, accurate, efficient and user-friendly digital automatic data acquisition for a wide range of TecQuipment products

Works with
VDAS®



Versatile Data Acquisition System Frame-mounting Interface (VDAS-F)



Versatile Data Acquisition System Bench-top Interface (VDAS-B)

- Modern, cost-effective digital automatic data acquisition hardware, software and accessories to enhance teaching and laboratory sessions
- Highly versatile system for use with equipment from many TecQuipment product ranges
- Enables real-time data capture, monitoring and display of all relevant parameters on a computer (PC)
- Highly accurate and noise-resistant
- Software is intuitive and easy to use, with clear and convenient data display options
- Fast and convenient automatic calculation, recording, charting and export of relevant data and parameters makes efficient use of students' and lecturers' time
- Compact interface units available in both frame-mounting and bench-top options
- User-friendly software is similar for all VDAS® compatible products – students do not have to learn to use new software when changing experiments

- TecQuipment Ltd, Bonsall Street, Long Eaton, Nottingham NG10 2AN, UK
- T +44 115 972 2611 • F +44 115 973 1520 • E info@tecquipment.com • W www.tecquipment.com
- An ISO 9001 certified company
- VDAS is a registered trademark of TecQuipment Ltd



PE/db/1013

VDAS

Versatile Data Acquisition System

Essential Services

Electrical supply (for VDAS Hardware):

- VDAS-B 90 VAC to 264 VAC, 50 Hz to 60 Hz
- VDAS-F 90 VAC to 250 VAC, 50 Hz to 60 Hz

Recommended computer hardware:

- Intel® Pentium® 4 or equivalent processor operating at 2 GHz
- 512 MB of RAM
- SVGA monitor that works with 16-bit colour, 1024 x 768 resolution
- CD-ROM drive
- USB 2 port
- 500 MB of hard disc space
- Standard two-button mouse (three-button mouse with scroll wheel is better)

Recommended PC operating systems:

- Microsoft® Windows XP, Vista and 7

Operating Conditions

Operating environment: Laboratory environment

Storage temperature range:

-25°C to +55°C (when packed for transport)

Operating temperature range: +5°C to +40°C

Operating relative humidity range:

30% to 95% (non-condensing)

Specifications

Frame-Mounting Interface Unit (VDAS-F):

Nett Dimensions and Weight:

Width 190 mm x depth 130 mm x height 445 mm and 4.5 kg

Approximate Packed Volume and Weight:

0.07 m³ and 9 kg

Bench Top Interface Unit (VDAS-B):

Nett Dimensions and Weight:

Width 305 mm x depth 180 mm x height 40 mm and 2 kg

Approximate Packed Volume and Weight:

0.05 m³ and 9 kg

Computer connection:

- USB (lead included)
- or
- RS 232 D-type 9-pin port (lead available separately)

Accessories (supplied):

- All mains connectors and cables
- STP leads for equipment connection

- TecEquipment Ltd, Bonsall Street, Long Eaton, Nottingham NG10 2AN, UK
- T +44 115 972 2611 • F +44 115 973 1520 • E info@tecequipment.com • W www.tecequipment.com
- An ISO 9001 certified company
- VDAS is a registered trademark of TecEquipment Ltd



Appendix E – Design Optimisation

Crane Wind Load Calculation

 Institiúid Teicneolaíochta Chorcaí Cork Institute of Technology		<u>Wind Analysis on to Ship Shore Crane</u>	
Name: B.Hand		Date: 19/01/2014	
Crane Weight			
Note: The following crane component mass were obtained from Liebherr Group			
Description		Tonnes	Tonnes
Derrick Boom			
Derrick Boom Steel (Welded Rail 105 × 80)	(53.50 m)	77.00	
Cable Rail & Electrics		1.50	
Boom Platform		4.50	
Latching Device		2.00	
Pivot Block		4.00	
Holding Arm		12.00	
Hoist Overload & Platforms		2.50	
Rope Deflection Device		2.50	
			106.00
Main Beam			
Main Beam Steel (Welded Rail 105 × 80)	(61.70 m)	100.00	
Cable Rail & Electrics		2.00	
Beam Platforms		5.00	
Cable Rail Extension & Electrics		10.00	
Hoist Trim/List/Skew & Platforms		12.00	
			129.00
Seaside Portal (Ø710 mm drive wheels) 10 Wheels			
A-Frame Compression Legs		19.00	
A-Frame Platforms & Stairways		2.50	
Seaside Carrier		26.00	
Seaside Legs Upper		38.00	
Seaside Legs Lower		32.00	
Seaside Endcarriage		28.00	
Primary Rocking Beam		13.00	
Intermediate Rocking Beam		7.00	
Secondary Rocking Beam		8.00	
Driven Wheelbox (Includes 4 × 40kW AC Motors)		18.00	
Non-Driven Wheelbox		14.00	
Storm Anchors & Buffers etc		4.00	
Electrics & Miscellaneous items		2.50	
Cable Reeling Drum		5.00	
			217.00
Landside Portal (Ø710 mm drive wheels) 8 Wheels			
Landside Carrier		27.00	
Landside Legs Upper		37.00	
Landside Legs Lower		32.00	
Landside Endcarriage		25.00	
Primary Rocking Beam		13.00	
Secondary Rocking Beam		8.00	
Driven Wheelbox (Includes 4 × 40kW AC Motors)		18.00	
Non-Driven Wheelbox		9.00	
Stairs & Platforms		19.00	
Storm Anchors & Buffers etc		4.00	
Personnel Lift		4.00	
Electrics & Miscellaneous items		3.00	
Rear Tie Support		1.00	
Work Cage Platform		3.00	
			203.00

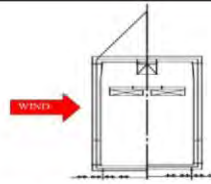
<u>Description</u>	<u>Tonnes</u>	<u>Tonnes</u>
Intermediate Bracing		
Back Tie	12.00	
Portal Diagonals	19.00	
Sill Beam	32.00	
Carrier Plan Bracing	3.00	
Backreach Tie	11.00	
		77.00
Machinery/Electrical House		
Base Frame	18.00	
Cladding Frames & Cladding	10.00	
Hoist Unit (Includes 2 × 500kW AC Motors)	27.00	
Derrick Unit (Includes 180 kW AC Motor)	8.00	
Overhead Crane	3.00	
Switchgear	6.00	
Transformer	5.00	
Miscellaneous Items	1.50	
Supports and Access Platforms	1.50	
		80.00
Hoist Rope Support Trolley		
		5.00
Trolley		
Trolley Material (Steel)	11.00	
Trolley Drives (Includes 4 × 35 kW AC motors)	6.50	
Trolley Fittings	3.00	
Cabin & Holding Arms	4.00	
Cabin Entrance	0.50	
		25.00
Total Crane Mass (Excluding Spreader & Ballast)		842.00
Telescopic Spreader		
Puley Frame	4.80	
Twin lift Spreader	13.20	
		18.00
Ballast		
Seaside	50.00	
Landside	35.00	
		85.00
Total In Service Mass (Unloaded)		945.00

Reference

Calculations

Wind Shear Profiles

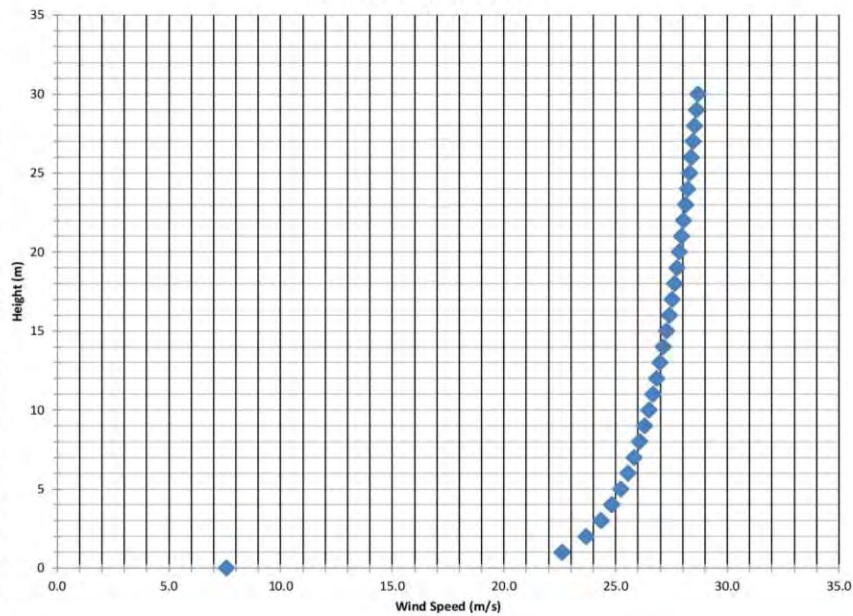
pg 18	α [-]	0.1
pg 18	β [-]	1.0
pg 18	ϕ_B [-]	1.1
pg 18	F_{rec} [-]	0.9463 (25 years)
pg 17	v_{ref} [m/s]	20 (Maximum In-Service Speed)
pg 18	v_g [m/s]	7.27 (= 0.36332 * v_{ref})



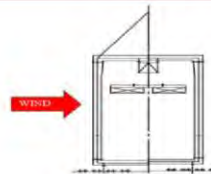
q [N/m²] = 0.625 * (F_{rec} * ((β *z/10)² + ϕ_B * v_g / v_{ref})* v_{ref})²

z [m]	V(Z) m/s
0	7.6
1	22.6
2	23.7
3	24.3
4	24.8
5	25.2
6	25.5
7	25.8
8	26.1
9	26.3
10	26.5
11	26.7
12	26.8
13	27.0
14	27.1
15	27.3
16	27.4
17	27.5
18	27.6
19	27.7
20	27.8
21	27.9
22	28.0
23	28.1
24	28.2
25	28.3
26	28.4
27	28.5
28	28.5
29	28.6
30	28.7

In-Service Wind Speed



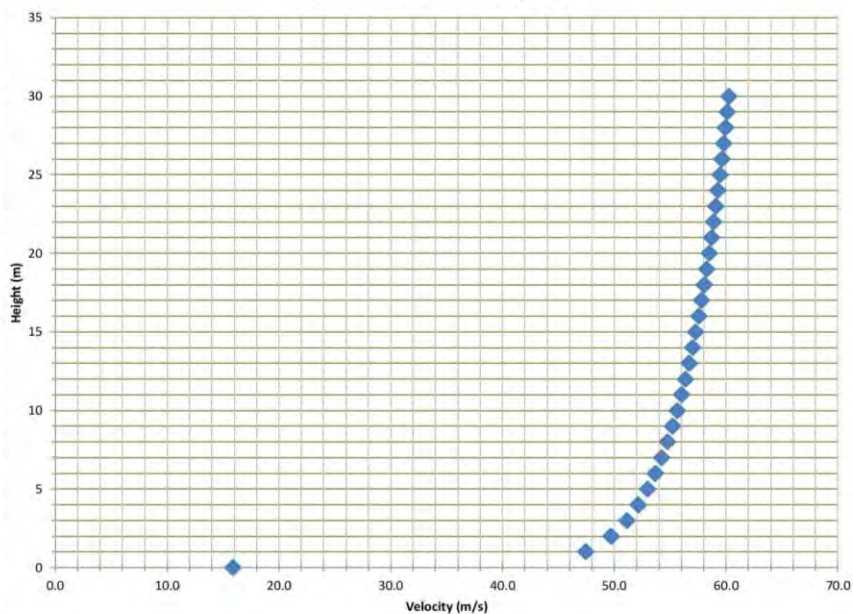
pg 18	α [-]	0.1
pg 18	β [-]	1.0
pg 18	ϕ_B [-]	1.1
pg 18	F_{rec} [-]	0.9463 (25 years)
pg 17	v_{ref} [m/s]	42 (Maximum Out-of-Service Speed)
pg 18	v_g [m/s]	15.26 (= 0.36332 * v_{ref})



q [N/m²] = 0.625 * (F_{rec} * ((β *z/10)² + ϕ_B * v_g / v_{ref})* v_{ref})²

z [m]	V(Z) m/s
0	15.9
1	47.5
2	49.7
3	51.1
4	52.1
5	53.0
6	53.6
7	54.2
8	54.8
9	55.2
10	55.6
11	56.0
12	56.4
13	56.7
14	57.0
15	57.3
16	57.5
17	57.8
18	58.0
19	58.3
20	58.5
21	58.7
22	58.9
23	59.1
24	59.3
25	59.4
26	59.6
27	59.8
28	59.9
29	60.1
30	60.2

Out-of-Service-Wind Speed



Wind Analysis on Ship-to-Shore Crane

Name: **B.Hand** Date: **22/02/2014**

Crane Wind Forces

Wind Speed (v) **20** m/s
 Wind Pressure (q): **250** N/m²
 Air Density (ρ) **1.25** kg/m³

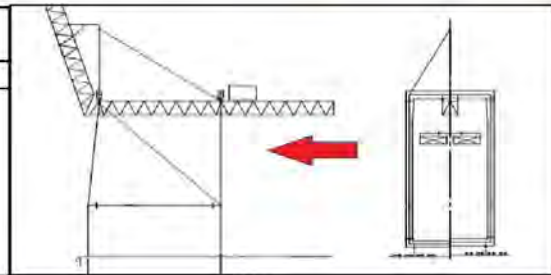
72 km/hr
 $q = 0.5 \times \rho \times v^2$

X-Direction (Sea / Land)

Derrick Boom

Up

In-Service



In Accordance with FEM 1.004

Table T 5.1.b $F = A \times q \times Cr$

	Component	L (m)	b (m)	d (m)	$\frac{L}{b}$	$\frac{b}{d}$	Force Coefficient (Cr)	Effective Area (A) (m ²)	Total Force (kN)	Force / Length (kN/m)
Seaside Portal:	End Carriage	18.700	2.420	1.225	7.727	1.976	1.693	45.254	19.154	1.024
	Leg 1 Lower leg	4.550	1.790	1.217	2.542	1.471	1.506	8.145	3.066	0.674
	Leg 1 Upper Leg	38.940	1.530	1.208	25.451	1.267	1.824	59.578	27.168	0.698
	Leg 2 Lower Leg	4.550	1.790	1.217	2.542	1.471	1.506	8.145	3.066	0.674
	Leg 2 Upper Leg	38.940	1.530	1.208	25.451	1.267	1.824	59.578	27.168	0.698
	Carrier	20.200	2.410	1.220	8.382	1.975	1.685	48.682	20.507	1.015
	Long Travel System	11.000	2.500				1.500	27.500	10.313	0.938
	Storm-Anchors	2.500	1.600	0.828	1.563	1.932	1.500	4.000	1.500	0.600
Landside Portal:	End Carriage	18.700	2.420	1.225	7.727	1.976	1.693	45.254	19.154	1.024
	Leg 3 Lower Leg	4.550	1.790	1.217	2.542	1.471	1.506	8.145	3.066	0.674
	Leg 3 Upper Leg	38.940	1.530	1.208	25.451	1.267	1.824	59.578	27.168	0.698
	Leg 4 Lower Leg	4.550	1.790	1.217	2.542	1.471	1.506	8.145	3.066	0.674
	Leg 4 Lower Leg (Stairs & Lift)	4.550	0.725				1.400	3.299	1.155	0.254
	Leg 4 Upper Leg	38.940	1.530	1.208	25.451	1.267	1.824	59.578	27.168	0.698
	Leg 4 Upper Leg (Stairs & Lift)	38.940	0.725				1.400	28.232	9.881	0.254
	Carrier	20.200	2.410	1.220	8.382	1.975	1.685	48.682	20.507	1.015
	Long Travel System	11.000	2.500				1.500	27.500	10.313	0.938
	Storm-Anchors	2.500	1.600	0.828	1.563	1.932	1.500	4.000	1.500	0.600
	Checkers Cabin	2.500	1.600	1.200	1.563	1.333	1.383	4.000	1.383	0.553
Portal:	Portal Diagonal (Near)	35.200	0.762	0.762			0.400	0.023	2.253	0.064
	Portal Diagonal (Aft)	35.200	0.762	0.762			0.400	0.023	2.253	0.064
	Sill Beam (Near)	20.900	1.598	1.510	13.079	1.058	0.000	0.000	0.000	0.000
	Sill Beam (Aft)	20.900	1.598	1.510	13.079	1.058	0.000	0.000	0.000	0.000
	Sill Beam (Aft) Platforms	20.900	0.175				0.000	0.000	0.000	0.000
	A-Frame Leg (Aft)	11.950	0.864	0.864			0.400	10.325	1.032	0.086
	A-Frame Leg (Near)	11.950	0.864	0.864			0.400	10.325	1.032	0.086
	A- Frame Ladders & Platforms	11.950	0.550				0.700	6.573	1.150	0.096
	Holding Arm	22.700	0.260	0.475	87.308	1.827	1.406	5.902	2.075	0.091
	Back Tie	21.788	0.850	0.826	25.633	0.972	1.800	18.520	8.334	0.383
	Rear Tie	21.788	0.405	0.530	53.798	1.309	1.297	8.824	2.861	0.131
	Machinery house	15.840	4.800	5.900	3.300	0.814	1.100	76.032	20.909	1.320
Derrick Boom:	Bottom Panel Members	44.200					1.490	185.540	46.400	1.266
	Top Panel Members	44.113					1.490	106.175	21.235	1.266
	Upright Diagonals									
Main Beam:	Bottom Panel Members	4.450	0.340				1.490	6.000	1.500	
	Top Panel Members	3.754	0.215				1.490	6.000	1.500	
	Upright Diagonals	3.500	0.344				1.490	1.204	0.000	
	Back Tie Connection							0.000	0.000	
TOTAL WIND FORCE ON CRANE (UNLOADED):								998.76	348.84	
Auxiliary Items:	Trolley							29.760	7.440	
	Spreader							41.760	10.440	
	Load (Container)							0.000	0.000	
TOTAL WIND FORCE ON TROLLEY + SPREADER + LOAD:								71.52	17.88	
TOTAL WIND FORCE ON CRANE (LOADED) :								1070.28	366.72	

35.56 [t]

37.38 [t]

Wind Analysis on Ship-to-Shore Crane

Name: **B.Hand**

Date: **22/02/2014**

Crane Wind Forces

Wind Speed (v) **20** m/s
 Wind Pressure (q): **250** N/m²
 Air Density (ρ) **1.25** Kg/m³

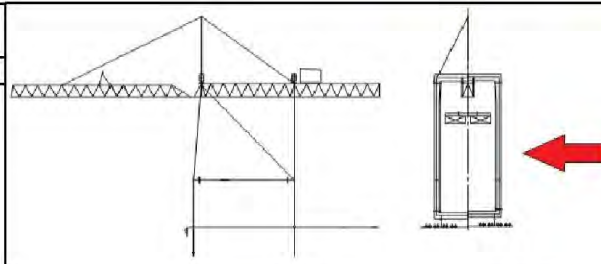
72 km/hr
 $q = 0.5 \times \rho \times v^2$

Y-Direction (Along Track)

Derrick Boom

Up/Down

In-Service



In Accordance with FEM 1.004

Table

T 5.1.b

$F = A \times q \times Cr$

	Component	L (m)	b (m)	d (m)	$\frac{L}{b}$	$\frac{b}{d}$	Force Coefficient (Cr)	Effective Area (A) (m ²)	Total Force (kN)	Force / Length (kN/m)
Seaside Portal:	End Carriage	18.700	2.420	1.225			0.000	0.000	0.000	0.000
	Leg 1 Lower leg	14.660	2.750	1.800	5.331	1.528	1.475	40.315	14.866	1.014
	Leg 1 Upper Leg	14.400	1.208	1.208	11.921	1.000	1.570	17.395	6.828	0.474
	Leg 2 Lower Leg	14.660	2.750	1.800	5.331	1.528	1.475	40.315	14.866	1.014
	Leg 2 Upper Leg	14.400	1.208	1.208	11.921	1.000	1.570	17.395	6.828	0.474
	Carrier	20.200	2.410	1.220			0.000	48.682	0.000	0.000
	Long Travel System	4.340	0.964				1.500	4.184	1.569	
	Storm-Anchors	2.500	0.828	1.600			1.500	2.070	0.776	0.311
Landside Portal:	End Carriage	18.700	2.420	1.225			0.000	0.000	0.000	0.000
	Leg 3 Lower Leg	14.660	2.750	1.800	5.331	1.528	1.475	40.315	14.866	1.014
	Leg 3 Upper Leg	14.400	1.208	1.208	11.921	1.000	1.570	17.395	6.828	0.474
	Leg 4 Lower Leg	14.660	2.750	1.800	5.331	1.528	1.475	40.315	14.866	1.014
	Leg 4 Lower Leg (Stairs & Lift)	14.660	0.725				1.400	10.629	3.720	0.254
	Leg 4 Upper Leg	14.400	1.208	1.208	11.921	1.000	1.570	17.395	6.828	0.474
	Leg 4 Upper Leg (Stairs & Lift)	38.940	0.725				1.400	28.232	9.881	0.254
	Carrier	20.200	2.410	1.220			0.000	0.000	0.000	0.000
	Long Travel System	4.340	0.964				1.500	4.184	0.000	
	Storm-Anchors	2.500	0.828	1.600			1.500	2.070	0.776	0.311
Checkers Cabin	2.500	1.200	1.600			1.500	3.000	1.125	0.450	
Portal:	Portal Diagonal (Near)	35.700	0.762	0.762			0.400	27.203	2.720	0.076
	Portal Diagonal (Aft)	35.700	0.762	0.762			0.400	27.203	2.720	0.076
	Sill Beam (Near)	20.900	1.630	1.530	12.822	1.065	1.606	34.067	13.678	0.654
	Sill Beam (Aft)	20.900	1.630	1.530	12.822	1.065	1.606	34.067	13.678	0.654
	Sill Beam (Aft) Platforms	20.900	0.250				1.550	5.225	2.025	0.097
	A-Frame Leg (Aft)	18.200	0.864	0.864			0.400	15.725	1.572	0.086
	A-Frame Leg (Near)	18.200	0.864	0.864			0.400	15.725	1.572	0.086
	A-Frame Ladders & Platforms	18.200	0.356				0.700	6.479	1.134	0.062
	Holding Arm	45.374	0.475	0.260	95.524	0.547	1.427	21.553	7.692	0.170
	Back Tie	35.700	0.826	0.850	43.220	1.029	1.251	29.488	9.221	0.258
	Rear Tie	49.845	0.530	0.405	94.047	0.764	1.424	26.418	9.403	0.189
	Machinery house	5.900	4.800	15.840	1.229	0.303	1.100	28.320	7.788	1.320
Derrick Boom:	Bottom Panel Members	53.700	0.420	0.300	127.857	1.400	1.499	22.554	8.450	0.157
	Top Panel Members	48.310	0.215	0.215	224.698	1.000	1.490	10.387	3.869	0.080
	Upright Diagonals	53.700					1.490	21.563	8.032	0.150
Main Beam:	Bottom Panel Members	61.995	0.420	0.300	147.607	1.400	1.490	26.038	9.699	0.156
	Top Panel Members	59.100	0.215	0.215	274.884	1.000	1.490	12.707	4.733	0.080
	Upright Diagonals	61.995					1.490	29.570	11.015	0.178
	Back Tie Connection							0.000	0.000	
TOTAL WIND FORCE ON CRANE (UNLOADED):								728.18	223.62	
Auxiliary Items:	Trolley							35.520	8.880	
	Spreader							28.000	7.000	
	Load (Container)							21.400	5.350	
TOTAL WIND FORCE ON TROLLEY + SPREADER + LOAD:								84.92	21.23	
TOTAL WIND FORCE ON CRANE (LOADED) :								813.10	244.85	

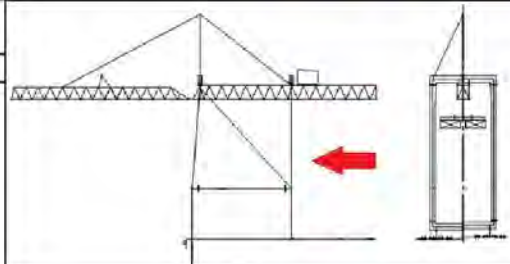
22.80 [t]

24.96 [t]

Crane Wind Forces

Wind Speed (v) 42 m/s
 Wind Pressure (q): 1102.5 N/m²
 Air Density (ρ) 1.25 Kg/m³
 X-Direction (Sea / Land) Down
 Derrick Boom Out-of-Service

151.2 km/hr
 $q = 0.5 \times \rho \times v^2$



In Accordance with FEM 1.004

Table T 5.1.b $F = A \times q \times C_f$

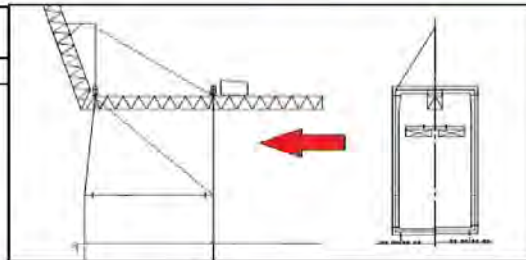
	Component	L (m)	b (m)	d (m)	$\frac{L}{b}$	$\frac{b}{d}$	Force Coefficient (C _f)	Effective Area (A) (m ²)	Total Force (kN)	Force / Length (kN/m)
Seaside Portal:	End Carriage	18.700	2.420	1.225	7.727	1.976	1.693	45.254	84.468	4.517
	Leg 1 Lower leg	4.550	1.790	1.217	2.542	1.471	1.506	8.145	13.523	2.972
	Leg 1 Upper Leg	38.940	1.530	1.208	25.451	1.267	1.824	59.578	119.809	3.077
	Leg 2 Lower Leg	4.550	1.790	1.217	2.542	1.471	1.506	8.145	13.523	2.972
	Leg 2 Upper Leg	38.940	1.530	1.208	25.451	1.267	1.824	59.578	119.809	3.077
	Carrier	20.200	2.410	1.220	8.382	1.975	1.685	48.682	90.437	4.477
	Long Travel System	11.000	2.500				1.500	27.500	45.478	4.134
	Storm-Anchors	2.500	1.600	0.828	1.563	1.932	1.500	4.000	6.615	2.646
Landside Portal:	End Carriage	18.700	2.420	1.225	7.727	1.976	1.693	45.254	84.468	4.517
	Leg 3 Lower Leg	4.550	1.790	1.217	2.542	1.471	1.506	8.145	13.523	2.972
	Leg 3 Upper Leg	38.940	1.530	1.208	25.451	1.267	1.824	59.578	119.809	3.077
	Leg 4 Lower Leg	4.550	1.790	1.217	2.542	1.471	1.506	8.145	13.523	2.972
	Leg 4 Lower Leg (Stairs & Lift)	4.550	0.725				1.400	3.299	5.092	1.119
	Leg 4 Upper Leg	38.940	1.530	1.208	25.451	1.267	1.824	59.578	119.809	3.077
	Leg 4 Upper Leg (Stairs & Lift)	38.940	0.725				1.400	28.232	43.575	1.119
	Carrier	20.200	2.410	1.220	8.382	1.975	1.685	48.682	90.437	4.477
	Long Travel System	11.000	2.500				1.500	27.500	45.478	4.134
	Storm-Anchors	2.500	1.600	0.828	1.563	1.932	1.500	4.000	6.615	2.646
Checkers Cabin	2.500	1.600	1.200	1.563	1.333	1.383	4.000	6.099	2.440	
Portal:	Portal Diagonal (Near)	35.200	0.762	0.762			0.400	0.023	4.731	0.134
	Portal Diagonal (Aft)	35.200	0.762	0.762			0.400	0.023	4.731	0.134
	Sill Beam (Near)	20.900	1.598	1.510	13.079	1.058	0.000	0.000	0.000	0.000
	Sill Beam (Aft)	20.900	1.598	1.510	13.079	1.058	0.000	0.000	0.000	0.000
	Sill Beam (Aft) Platforms	20.900	0.175				0.000	0.000	0.000	0.000
	A-Frame Leg (Aft)	11.950	0.864	0.864			0.400	10.325	4.553	0.381
	A-Frame Leg (Near)	11.950	0.864	0.864			0.400	10.325	4.553	0.381
	A- Frame Ladders & Platforms	11.950	0.550				0.700	6.573	5.072	0.424
	Holding Arm	22.700	0.260	0.475	87.308	1.827	1.406	5.902	9.149	0.403
	Back Tie	21.788	0.850	0.826	25.633	0.972	1.800	18.520	36.753	1.687
	Rear Tie	21.788	0.405	0.530	53.798	1.309	1.297	8.824	12.618	0.579
Machinery house	15.840	4.800	5.900	3.300	0.814	1.100	76.032	92.208	5.821	
Derrick Boom:	Bottom Panel Members	4.450	0.340				1.490	6.000	5.369	
	Top Panel Members	3.754	0.215				1.490	6.000	5.369	
	Upright Diagonals	3.500	0.344				1.490	1.204	1.978	
Main Beam:	Bottom Panel Members	4.450	0.340				1.490	6.000	5.369	
	Top Panel Members	3.754	0.215				1.490	6.000	5.369	
	Upright Diagonals	3.500	0.344				1.490	1.204	1.978	
	Back Tie Connection							0.000	0.000	
TOTAL WIND FORCE ON CRANE (UNLOADED):								720.25	1241.89	
Auxiliary Items:	Trolley							29.760	32.810	
	Spreader							41.760	46.040	
	Load (Container)							0.000	0.000	
TOTAL WIND FORCE ON TROLLEY + SPREADER + LOAD:								71.52	78.85	
TOTAL WIND FORCE ON CRANE (NO LOAD) :								791.77	1320.74	

126.59 [t]

134.63 [t]

Crane Wind Forces

Wind Speed (v)	42	m/s	151.2	km/hr
Wind Pressure (q):	1102.5	N/m ²	q = 0.5 × ρ × v ²	
Air Density (ρ)	1.25	Kg/m ³		
X-Direction (Sea / Land)	Sea			
Derrick Boom	Up			



In Accordance with FEM 1.004

Table T 5.1.b F = A × q × Cf

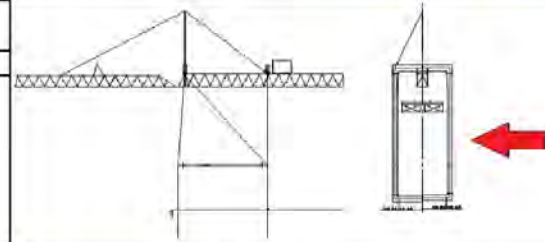
	Component	L (m)	b (m)	d (m)	$\frac{L}{b}$	$\frac{b}{d}$	Force Coefficient (Cf)	Effective Area (A) (m ²)	Total Force (kN)	Force / Length (kN/m)
Seaside Portal:	End Carriage	18.700	2.420	1.225	7.727	1.976	1.693	45.254	84.468	4.517
	Leg 1 Lower leg	4.550	1.790	1.217	2.542	1.471	1.506	8.145	13.523	2.972
	Leg 1 Upper Leg	38.940	1.530	1.208	25.451	1.267	1.824	59.578	119.809	3.077
	Leg 2 Lower Leg	4.550	1.790	1.217	2.542	1.471	1.506	8.145	13.523	2.972
	Leg 2 Upper Leg	38.940	1.530	1.208	25.451	1.267	1.824	59.578	119.809	3.077
	Carrier	20.200	2.410	1.220	8.382	1.975	1.685	48.682	90.437	4.477
	Long Travel System	11.000	2.500				1.500	27.500	45.478	4.134
	Storm-Anchors	2.500	1.600	0.828	1.563	1.932	1.500	4.000	6.615	2.646
Landside Portal:	End Carriage	18.700	2.420	1.225	7.727	1.976	1.663	45.254	82.961	4.436
	Leg 3 Lower Leg	4.550	1.790	1.217	2.542	1.471	1.506	8.145	13.523	2.972
	Leg 3 Upper Leg	38.940	1.530	1.208	25.451	1.267	1.824	59.578	119.809	3.077
	Leg 4 Lower Leg	4.550	1.790	1.217	2.542	1.471	1.506	8.145	13.523	2.972
	Leg 4 Lower Leg (Stairs & Lift)	4.550	0.725				1.400	3.299	5.092	1.119
	Leg 4 Upper Leg	38.940	1.530	1.208	25.451	1.267	1.824	59.578	119.809	3.077
	Leg 4 Upper Leg (Stairs & Lift)	38.940	0.725				1.400	28.232	43.575	1.119
	Carrier	20.200	2.410	1.220	8.382	1.975	1.685	48.682	90.437	4.477
	Long Travel System	11.000	2.500				1.500	27.500	45.478	4.134
	Storm-Anchors	2.500	1.600	0.828	1.563	1.932	1.500	4.000	6.615	2.646
	Checkers Cabin	2.500	1.600	1.200	1.563	1.333	1.383	4.000	6.099	2.440
Portal:	Portal Diagonal (Near)	35.200	0.762	0.762			0.400	0.023	4.731	0.134
	Portal Diagonal (Aft)	35.200	0.762	0.762			0.400	0.023	4.731	0.134
	Sill Beam (Near)	20.900	1.598	1.510	13.079	1.058	0.000	0.000	0.000	0.000
	Sill Beam (Aft)	20.900	1.598	1.510	13.079	1.058	0.000	0.000	0.000	0.000
	Sill Beam (Aft) Platforms	20.900	0.175				0.000	0.000	0.000	0.000
	Carrier Bracing (Near)	20.900	0.660	0.660				0.000	0.000	0.000
	Carrier Bracing (Aft)	20.900	0.660	0.660				0.000	0.000	0.000
	A-Frame Leg (Aft)	11.950	0.864	0.864			0.400	10.325	4.553	0.381
	A-Frame Leg (Near)	11.950	0.864	0.864			0.400	10.325	4.553	0.381
	A-Frame Ladders & Platforms	11.950	0.550				0.700	6.573	5.072	0.424
	A-frame Cross Beam	3.540	1.360	1.100	2.603	1.236	1.436	4.814	9.058	1.025
	Holding Arm	22.700	0.260	0.475	87.308	1.827	1.406	5.902	9.149	0.403
	Back Tie	21.788	0.850	0.826	25.633	0.972	1.800	18.520	36.753	1.687
	Rear Tie	21.788	0.405	0.530	53.798	1.309	1.297	8.824	12.618	0.579
	Latching Device							3.000	4.689	
	Machinery house	15.840	4.800	5.900	3.300	0.814	1.100	76.032	92.208	5.821
	Cable Reeling Drum						1.500	3.333	7.185	
Derrick Boom:	Bottom Panel Members	44.200						185.540	46.400	1.266
	Top Panel Members	44.113						106.175	21.235	1.266
	Upright Diagonals							0.000	0.000	
Main Beam:	Bottom Panel Members	4.450	0.340				1.490	6.000	5.369	
	Top Panel Members	3.754	0.215				1.490	6.000	5.369	
	Upright Diagonals	3.500	0.344				1.490	1.204	0.000	
	Back Tie Connection							0.000	0.000	
TOTAL WIND FORCE ON CRANE (UNLOADED):								1009.90	1314.26	
Auxiliary Items:	Trolley							29.760	32.810	
	Spreader							41.760	46.040	
	Load (Container)							0.000	0.000	
TOTAL WIND FORCE ON TROLLEY + SPREADER + LOAD:								71.52	78.85	
TOTAL WIND FORCE ON CRANE (NO LOAD) :								1081.42	1393.11	

133.97 (t)

142.01 (t)

Crane Wind Forces

Wind Speed (v) 42 m/s 151.2 km/hr
 Wind Pressure (q): 1102.5 N/m² q = 0.5 * rho * v²
 Air Density (rho) 1.25 Kg/m³
 Y-Direction (Along Track) Up
 Derrick Boom Out of Service



In Accordance with FEM 1.004

Table T 5.1.b F = A x q x Cr

Component	L (m)	b (m)	d (m)	L/b	b/d	Force Coefficient (Cr)	Effective Area (A) (m ²)	Total Force (kN)	Force / Length (kN/m)	
Seaside Portal:										
End Carriage	18.700	2.420	1.225			0.000	0.000	0.000	0.000	
Leg 1 Lower leg	14.660	2.750	1.800	5.331	1.528	1.475	40.315	65.560	4.472	
Leg 1 Upper Leg	14.400	1.208	1.208	11.921	1.000	1.570	17.395	30.110	2.091	
Leg 2 Lower Leg	14.660	2.750	1.800	5.331	1.528	1.475	40.315	65.560	4.472	
Leg 2 Upper Leg	14.400	1.208	1.208	11.921	1.000	1.570	17.395	30.110	2.091	
Carrier	20.200	2.410	1.220			0.000	48.682	0.000	0.000	
Long Travel System	4.340	0.964				1.500	4.184	6.919		
Storm-Anchors	2.500	0.828	1.600			1.500	2.070	3.423	1.369	
Landside Portal:										
End Carriage	18.700	2.420	1.225			0.000	0.000	0.000	0.000	
Leg 3 Lower Leg	14.660	2.750	1.800	5.331	1.528	1.475	40.315	65.560	4.472	
Leg 3 Upper Leg	14.400	1.208	1.208	11.921	1.000	1.570	17.395	30.110	2.091	
Leg 4 Lower Leg	14.660	2.750	1.800	5.331	1.528	1.475	40.315	65.560	4.472	
Leg 4 Lower Leg (Stairs & Lift)	14.660	0.725				1.400	10.629	16.405	1.119	
Leg 4 Upper Leg	14.400	1.208	1.208	11.921	1.000	1.570	17.395	30.110	2.091	
Leg 4 Upper Leg (Stairs & Lift)	38.940	0.725				1.400	28.232	43.575	1.119	
Carrier	20.200	2.410	1.220			0.000	0.000	0.000	0.000	
Long Travel System	4.340	0.964				1.500	4.184	0.000		
Storm-Anchors	2.500	0.828	1.600			1.500	2.070	3.423	1.369	
Checkers Cabin	2.500	1.200	1.600			1.500	3.000	4.961	1.985	
Portal:										
Portal Diagonal (Near)	35.700	0.762	0.762			0.400	27.203	11.997	0.336	
Portal Diagonal (Aft)	35.700	0.762	0.762			0.400	27.203	11.997	0.336	
Sill Beam (Near)	20.900	1.630	1.530	12.822	1.065	1.606	34.067	60.320	2.886	
Sill Beam (Aft)	20.900	1.630	1.530	12.822	1.065	1.606	34.067	60.320	2.886	
Sill Beam (Aft) Platforms	20.900	0.250				1.550	5.225	8.929	0.427	
A-Frame Leg (Aft)	18.200	0.864	0.864			0.400	15.725	6.935	0.381	
A-Frame Leg (Near)	18.200	0.864	0.864			0.400	15.725	6.935	0.381	
A-Frame Ladders & Platforms	18.200	0.356				0.700	6.479	5.000	0.275	
Holding Arm	45.374	0.475	0.260	95.524	0.547	1.427	21.553	33.920	0.748	
Back Tie	35.700	0.826	0.850	43.220	1.029	1.251	29.488	40.663	1.139	
Rear Tie	49.845	0.530	0.405	94.047	0.764	1.424	26.418	41.469	0.832	
Machinery house	5.900	4.800	15.840	1.229	0.303	1.100	28.320	34.345	5.821	
Derrick Boom:										
Bottom Panel Members	53.700	0.420	0.300	127.857	1.400	1.490	22.554	37.050	0.690	
Top Panel Members	48.310	0.215	0.215	224.698	1.000	1.490	10.387	17.062	0.353	
Upright Diagonals	53.700					1.490	21.563	35.421	0.660	
Main Beam:										
Bottom Panel Members	61.995	0.420	0.300	147.607	1.400	1.490	26.038	42.773	0.690	
Top Panel Members	59.100	0.215	0.215	274.884	1.000	1.490	12.707	20.873	0.353	
Upright Diagonals	61.995					1.490	29.570	48.575	0.784	
Back Tie Connection							0.000	0.000		
TOTAL WIND FORCE ON CRANE (UNLOADED):							728.18	985.97		
Auxiliary Items:										
Trolley							35.520	39.161		
Spreader							28.000	30.870		
Load (Container)							0.000	0.000		
TOTAL WIND FORCE ON TROLLEY + SPREADER + LOAD:							63.52	70.03		
TOTAL WIND FORCE ON CRANE (NO LOAD) :							791.70	1056.00		

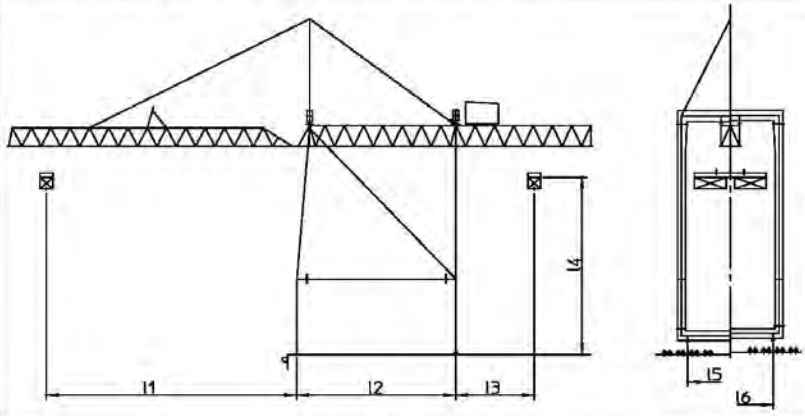
100.51 [t]

107.65 [t]

Wind Analysis on to Ship Shore Crane

Name	B.Hand	Date:	23/02/2014
------	--------	-------	------------

Estimated In-Service Wheel Loads



l1 [m]:	50.00	(FEM 1.001)
l2 [m]:	25.00	
l3 [m]:	20.00	
l4 [m]:	38.00	
l5 [m]:	16.20	
l6 [m]:	17.50	

Load: [t]	65.0	0.0
Spreader: [t]	18.0	18.0
Trolley: [t]	25.0	25.0
Total: [t]	108.0	43.0
Stability Factor	2.0	2.0
Factored Load [t]	191.0	61.0

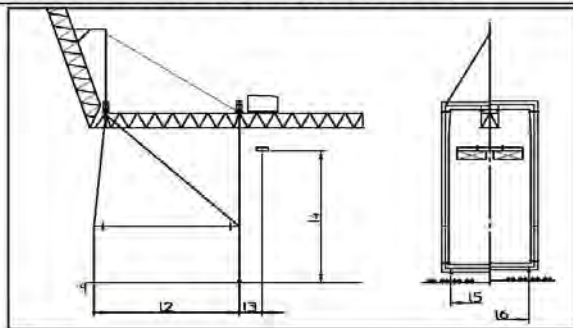
Wind Speed (v)	72	km/hr
Wind Speed (v)	20	m/s
Wind Pressure (q):	250	N/m ²
Air Density (ρ)	1.25	Kg/m ³

Standard values obtained from Liebherr

Wheels per Corner:			
Seaside:	10	Spacings [m]:	1.30
Landside	8	Spacings [m]:	1.30

Boom Position	Load Position	Rail	Crane Weight [t]	Crane Weight [t]	Load & Trolley [t]	Wind (Y Direction) (Along Track) [t]	Wind (X Direction) (Sea/Land) [t]	Corner Load [t]	Wheel Load [t]	Wheel Load [t/m]	Load & Trolley [t]	Stability Check / Corner [t]
Down	Max. Outreach	Seaside.	478.10	162.00	24.96	32.11	665.06	66.51	51.16	286.50	739.64	
		Landside.	418.90	-108.00	24.96	32.11	335.86	41.98	32.29	-191.00	202.94	
Down	Max. Backreach	Seaside.	478.10	-43.20	24.96	32.11	459.86	45.99	35.37	-76.40	376.74	
		Landside.	418.90	97.20	24.96	32.11	541.06	67.63	52.02	171.90	565.84	
Up	Max. Backreach (No Load)	Seaside.	478.10	-17.20	24.96	37.38	485.86	48.59	37.37	-24.40	428.74	
		Landside.	418.90	38.70	24.96	37.38	482.56	60.32	46.40	54.90	448.84	

Estimated Out of Service Wheel Loads



L2 [m]:	25.00
L3 [m]:	4.80
L4 [m]:	38.00
L5 [m]:	16.20
L6 [m]:	17.50

	151.2	km/hr
Wind Speed (v)	42	m/s
Wind Pressure (q):	1102.5	N/m ²
Air Density (ρ)	1.25	Kg/m ³

Wheels per Corner:			
Seaside:	10	Spacings [m]:	1.30
Landside:	8	Spacings [m]:	1.30

Values obtained from Liebherr

Vertical Storm Load				Min	Max.		
Rail	Crane & Trolley [t]	Storm (Y) Along Track [t]	Storm (X) Sea/Land [t]	Corner Load [t]	Corner Load [t]	Wheel Load [t]	Wheel Load [t/m]
Storm (Y) Along Track	Seaside	201.4	107.6	72.2	309.0	30.9	23.8
	Landside	264.4	107.6	135.2	372.0	46.5	35.8
Storm (X) Sea/Land	Seaside	201.4		142.0	31.0	343.4	26.4
	Landside	264.4		142.0	94.0	406.4	39.1

	Seaside	Landside
L1 [m]	16.2	17.5
L2 [m]	20.4	20.4
L3 [m]	2.1	1.4
L4 [m]	18.3	18.9

Includes Stability Factor (1.2) (FEM 1.001)

Storm along Track (Y)
Storm Sea/land (X)

Tie Force/Corner [t]		
Sideside	Landside	
8.7	14.3	Max Tie down force
5.0	10.7	

Storm Along Track (Y)

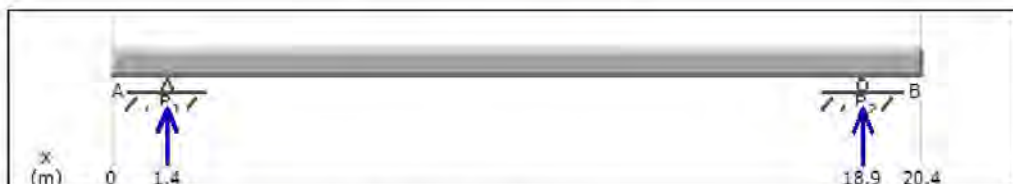
Seaside [t] Landside [t]

Uplift Forces from Storm [t]:	P1 =	107.6	107.6
Uplift Forces due to crane geometry	P2 = P1 * L1 / L4	95.4	99.5

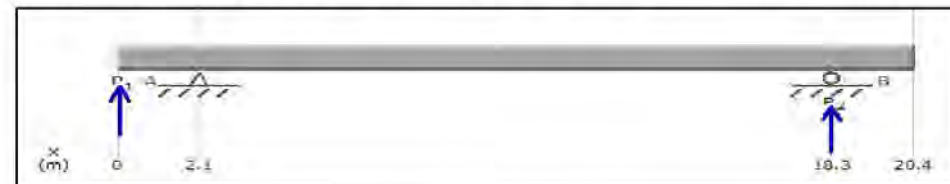
Storm Sea/land (X)

Seaside [t] Landside [t]

Uplift Forces from Storm [t]:	P1 =	142.0	142.0
Uplift Forces due to crane geometry	P2 = P1 * L1 / L4	125.9	131.3



Landside Endcarriage



Seaside Endcarriage

Relevant FEM 1.004 Standard Sections for Calculations

1. GENERAL

This document relates to wind loads on crane structure.

It gives a simplified method of calculation and assumes that the wind can blow horizontally from any direction, that the wind blows at a constant velocity.

2. WIND PRESSURE – REYNOLDS NUMBER

The dynamic wind pressure (or wind pressure) is calculated by:

$$q = \frac{1}{2} \times \rho \times V^2$$

where

q is the dynamic wind pressure N/m^2

ρ is the air density in kg/m^3 (except particular specifications it is given by $\rho = 1,25 \text{ kg/m}^3$)

V is the design wind speed in m/s .

The flow conditions are mainly characterized by the Reynolds number.

The Reynolds number is defined in appendix 1.

3. DESIGN WIND CONDITIONS

Two design wind conditions are taken into account in calculating wind loads on cranes.

3.1. In-service wind

This is the maximum wind in which the crane is designed to operate. The wind loads are assumed to be applied in the least favourable direction in combination with the appropriate service loads.

In-service design wind pressures and corresponding speeds are given in table T.1

They are assumed to be constant over the height of the appliance¹.

NOTE: It is assumed that the operating speeds and nominal accelerations are not necessarily reached under extreme wind conditions.
(FEM,2013)

¹ Where a wind speed measuring device is to be attached to an appliance it shall normally be placed at the maximum height of the appliance. In cases, where the wind speed at a different level is more significant to the safety to the appliance, the manufacturer shall state the height at which the device shall be placed.

Table T.1 — In-service design wind pressure

Type of appliance	Design wind pressure in service q N/m ²	Wind speed in service v(3) m/s	Wind pressure in service q(3) N/m ²
Lifting appliance easily protected against wind action or designed for use exclusively in light wind. Erection operations.	125	12,86	103
All normal types of crane installed in the open	250	18,18	207
* Appliances which must continue to work in high winds	500	25,71	413
* For example appliances of type 12a in table T.2.1.2.5. (F.E.M. 1.001 booklet 2).			

q is the in-service design wind pressure. It is determined from the relationship:

$$q = \phi_g^2 \times q(3)$$

where

ϕ_g is the gust response factor $\phi_g = 1,1$

q(3) is the wind pressure at v (3) $q(3) = \frac{1}{2} \times \rho \times v(3)^2$

v(3) is the gust wind velocity averaged of a period of 3 seconds.

• **Action of wind on the load**

The action of the wind on the hook load for a crane that handles miscellaneous loads shall be determined from the relationship:

$$F = c \times A \times q$$

where

F is the force exerted by the wind on the hook load in N,

q is the in-service wind pressure from table T.1 in N/m²,

(FEM,2013)

- A is the maximum area of the solid parts of the hook load in m² ⁽²⁾. Where this area is not known, a minimum value of 0,5 m² per tonne of safe working load shall be used,
- c is the aerodynamic coefficient of the gross load in direction of the wind velocity, which in absence of detailed information should be assumed to c = 2,5.

Where a crane is designed to handle loads of a specific size and shape only, the wind loading shall be calculated for the appropriate dimensions and configurations.

3.2. Out-of-service wind

This is a maximum (storm) wind for which the lifting machine is designed to remain stable in out-of-service conditions as indicated by the manufacturer.

The speed varies with the height of the apparatus above the surrounding ground level, the geographical location and the degree of exposure to the prevailing winds.

The figure F.A.2. of the appendix 2 gives a storm-wind map of Europe, roughly indicating the regions where the same reference storm-wind velocities are applicable.

When calculating wind loads for out-of-service conditions, if the machine is located in A, B, C areas, the speed and the pressure may be:

- taken as constant as to the table T.3.2. or,
- calculated according to appendix 2.

Table T.3.2 — Out-of-service wind speed and pressure

Height above ground level	Approximate wind speed out of service	Approximate wind pressure out of service
m	m/s	N/m ²
0 to 20	36	800
20 to 100	42	1100
more than 100	46	1300

The out-of-service wind pressure must be calculated according to appendix 2, if the lifting machine is located in D, E, F, G areas.

In a first approximation, the maximum wind speed at the top of the machine can be assumed constant over the total height of the structure.

Where cranes are to be permanently installed or used for extended periods in areas where wind conditions are exceptionally severe, the above values may be modified by agreement between the manufacturer and purchaser in the light of local meteorological data.

The Davenport law may be used.

⁽²⁾ Where, exceptionally, a crane is required to handle loads of large surface area, it is admissible for the manufacturer to determine a wind speed less than that specified in table T.1 above which such loads shall not be handled.

For certain types of appliance of which the jib can be quickly lowered (such as a tower crane which can be easily lowered by a built-in mechanism), the out-of-service wind need not be taken into consideration provided the machine is intended for lowering after each working day.

4. WIND LOAD CALCULATIONS

For most complete and part structures, and individual members used in crane structures the wind load is calculated from:

$$F = A \times q \times C_f$$

where

F is the wind load in N,

A is the effective frontal area of the part under consideration in m²,

q is the wind pressure corresponding to the appropriate design condition in N/m²,

C_f is the shape coefficient in the direction of the wind for the part under consideration.

The total wind load on the structure is taken as the sum of the loads on its component parts.

In determining strength and stability requirements of the appliance the total wind load shall be considered.

The magnitude of the wind load to be allowed for in the design of a mechanism, in determining the motor and brake requirements for the mechanism and to provide for the safety of the appliance in the wind, are given in the chapter dealing with the design of mechanisms.

5. SHAPE COEFFICIENTS

For a given Reynolds number (or given D×V), the shape coefficient varies according to:

- the aerodynamic slenderness λ defined in figure F.5.1.b,
- the wind turbulence

$$I = \frac{|u|}{V}$$

Where

I is the turbulence intensity,

u is the speed fluctuation with regard to a speed V. This quantity characterizes the atmospheric turbulence,

$$u = \frac{1}{T} \sqrt{\int_0^T u_{(t)}^2 dt}$$

V is the mean wind speed, averaged over a period of 10 minutes.

b) for $Re > 3 \cdot 10^5$ (or $D \times V > 4,5 \text{ m}^2/\text{s}$)

In a critical regime, the following values for the cylindrical section may be assumed:

$$C_{i0} = 0,4$$

$$K_x = 1$$

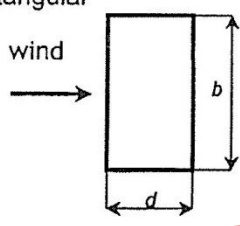
$$K_l = 1$$

$$K_r = 1$$

Where a lattice frame is made up of flat-sided and circular sections, or of circular sections in the critical regime ($D \times V > 4,5 \text{ m}^2/\text{s}$), the appropriate shape coefficients are applied to the corresponding frontal areas.

For all other sections, in the absence of information, the values of table T.5.1.b may be taken into account:

Table T 5.1.b — Shape coefficients

Type	Description		Aerodynamic slenderness l/b or l/D						
			≤ 5	10	20	30	40	50	> 50
Individual member	Sections and circular sections where : $D \times V > 4,5 \text{ m}^2/\text{s}$		0,4	0,4	0,4	0,4	0,4	0,4	0,4
$D \times V > 4,5 \text{ m}^2/\text{s}$ $Re > 3 \cdot 10^5$	Hollow sections for a section $\geq 356 \text{ mm}$ square and $254 \times 457 \text{ mm}$ rectangular 	b/d							
		2	1,55	1,75	1,95	2,10	2,20		
		1	1,40	1,55	1,75	1,85	1,90		
		0,5	1,0	1,20	1,30	1,35	1,40		
		0,25	0,80	0,90	0,90	1,0	1,0		
Single lattice frames	Flat-sided sections		1,70						
	Circular sections where : $D \times V > 4,5 \text{ m}^2/\text{s}$		0,40						
Machinery houses etc.	Rectangular clad structures on ground or solid base		1,10						

APPENDIX 2

OUT OF SERVICE WIND

For the calculation of loads acting on a crane due to out-of-service wind (storm-wind), it is assumed that the wind blows horizontally from any direction at a velocity increasing with the height above the surrounding ground level.

The mean storm-wind velocity with a recurrence interval of once in 50 years, measured at 10 m above flat open country, averaged over a period of 10 minutes, is defined as reference storm-wind velocity v_{ref} . It describes the level of storm-winds in relation of the different geographical regions and varies in Europe between 20 to 36 and more than 36 m/s.

In figure F.A.2, a storm-wind map of Europe is given, roughly indicating the regions where the same reference storm-wind velocities are applicable.

Where available, more detailed (national) storm-wind maps or local meteorological data should be used as sources for the reference storm-wind velocities v_{ref} , taking into account the requirements of the second paragraph of the present appendix.

NOTE: National storm-wind maps can be used from the appendix A of the ENV 1991-2-4.

For crane design, the following reference storm-wind velocities are mostly applicable:

Region	A-B	C	D	E
v_{ref} [m/s]	24	23	32	36

For safety reasons, the region A is assimilated to region B.

Special conditions have to be agreed upon for cranes used in regions F and G, where $v_{ref} \geq 36$ m/s.

Cranes likely to be used in different regions shall be verified in their configurations for the conditions applicable in those different regions.

The equivalent static storm-wind velocity $v(z)$ at the height z [m] above the surrounding ground level shall be calculated by the relation :

$$v(z) = F_{rec} \times \left[\frac{v_d(z)}{v_{ref}} + \psi_s \frac{v_d}{v_{ref}} \right] \times v_{ref}$$

where :

$\frac{v_m(z)}{v_{ref}} = \beta \times \left(\frac{z}{10}\right)^\alpha$ = a roughness coefficient, which gives the relation of the 10 minutes mean storm-wind v_m in the height z to the reference storm-wind velocity v_{ref} .

α , β , are numbers without dimension characterizing the site :

$\alpha = 0,14$	$\beta = 1$	in plane area
$\alpha = 0,25$	$\beta = 0,65$	in wooded area or suburbs
$\alpha = 0,36$	$\beta = 0,41$	in urban area, densely built.

The above mentioned values of α and β can be replaced by experimental or theoretical values, especially when the site is critical, those values should be adjusted to the real situation. In this case the value of α can be determined inferior to 0,14.

$v_g = 2 \times \sqrt{6 \times K} \times v_{ref}$ = a 3 second gust amplitude beyond the 10 minutes mean storm-wind, which may be considered independent of the height and proportional to the reference storm-wind velocity.

Where :

$K = 0,0055$

$\phi_s = 1,10$ = a factor to consider the response of the elastic crane system caused by the gusts.

F_{rec} = a factor depending on the recurrence interval R , which allows to adapt the reference storm-wind velocities v_{ref} to other recurrence intervals than 50 years.

For crane calculation, the designer may select a recurrence interval comprise between 5 and 25 years ($R = 5$ to $R = 25$).

For those intervals factors coming from Eurocode for Actions on Structures, Chapter 8 : Wind Loads – A.2. are the following:

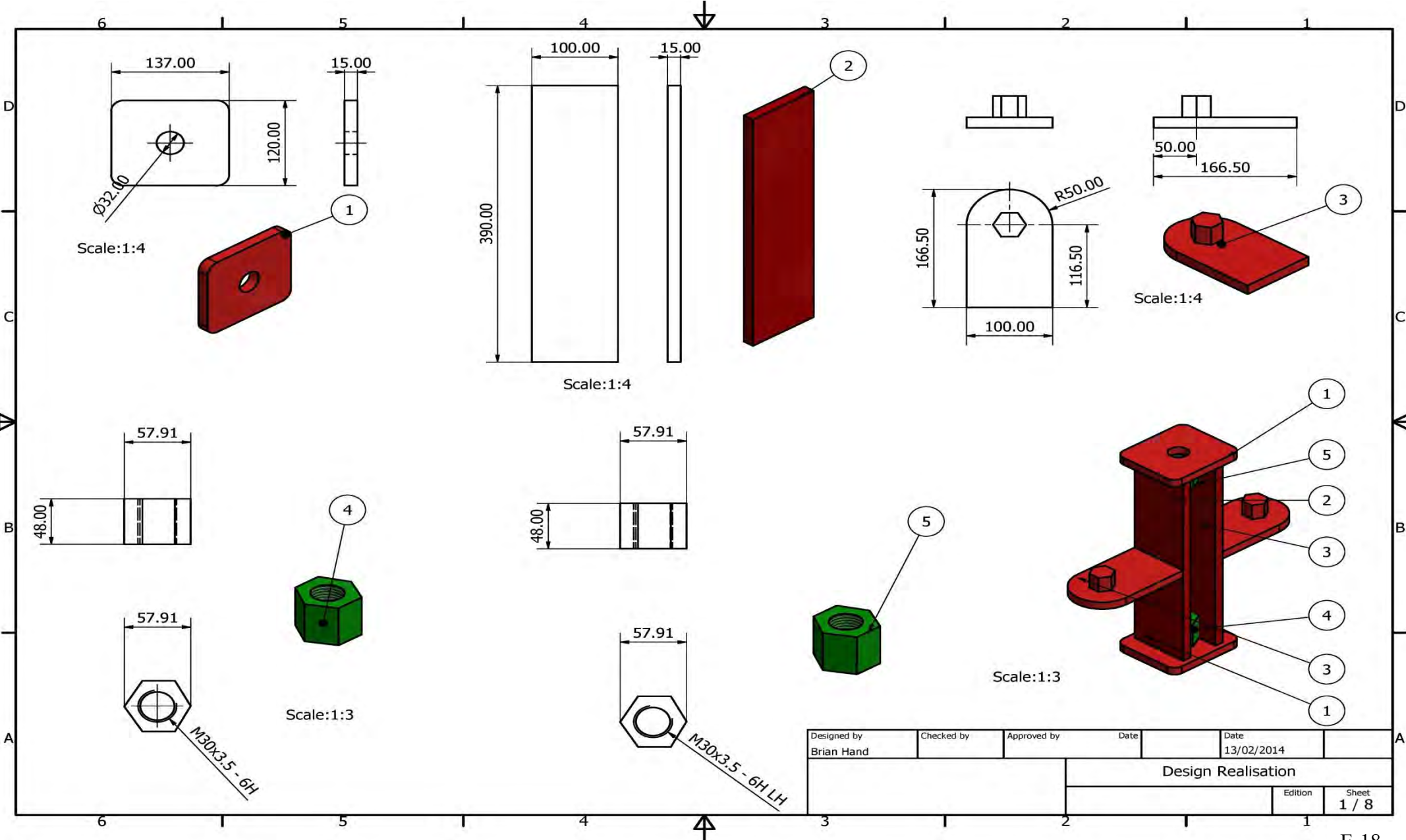
$R=5: F_{rec} = 0,8155$ $R=10: F_{rec} = 0,8733$ $R=25: F_{rec} = 0,9463$

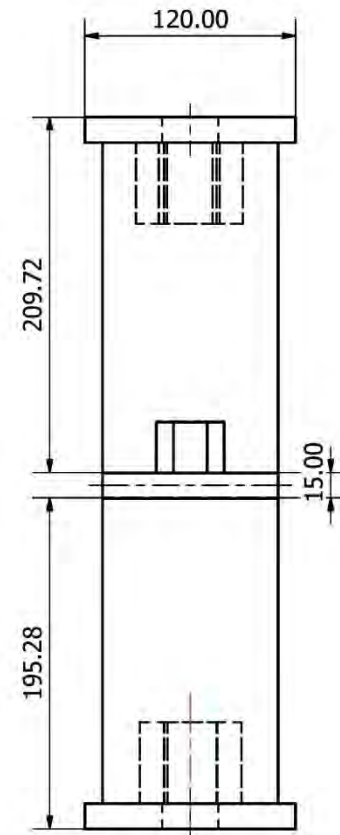
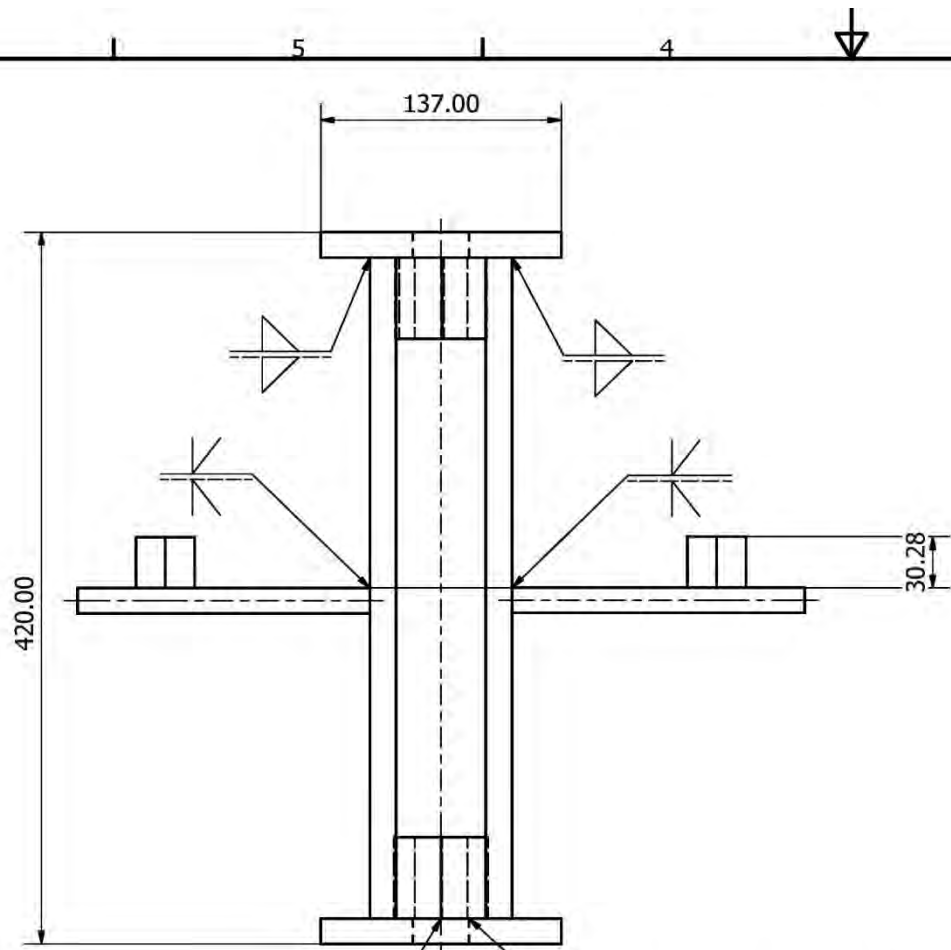
The equivalent static storm-wind pressures $q(z)$ follows from the equivalent static storm wind velocities $v(z)$ from :

$$q(z) = 0,625 \times v^2(z)$$

In table T.A.2 for illustration, equivalent static wind pressures $q(z)$ are given for $R=10$ in relation to the height z and the European storm-wind region E.

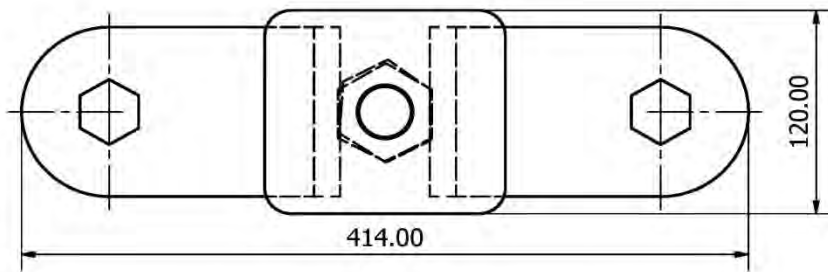
Redesign Drawings



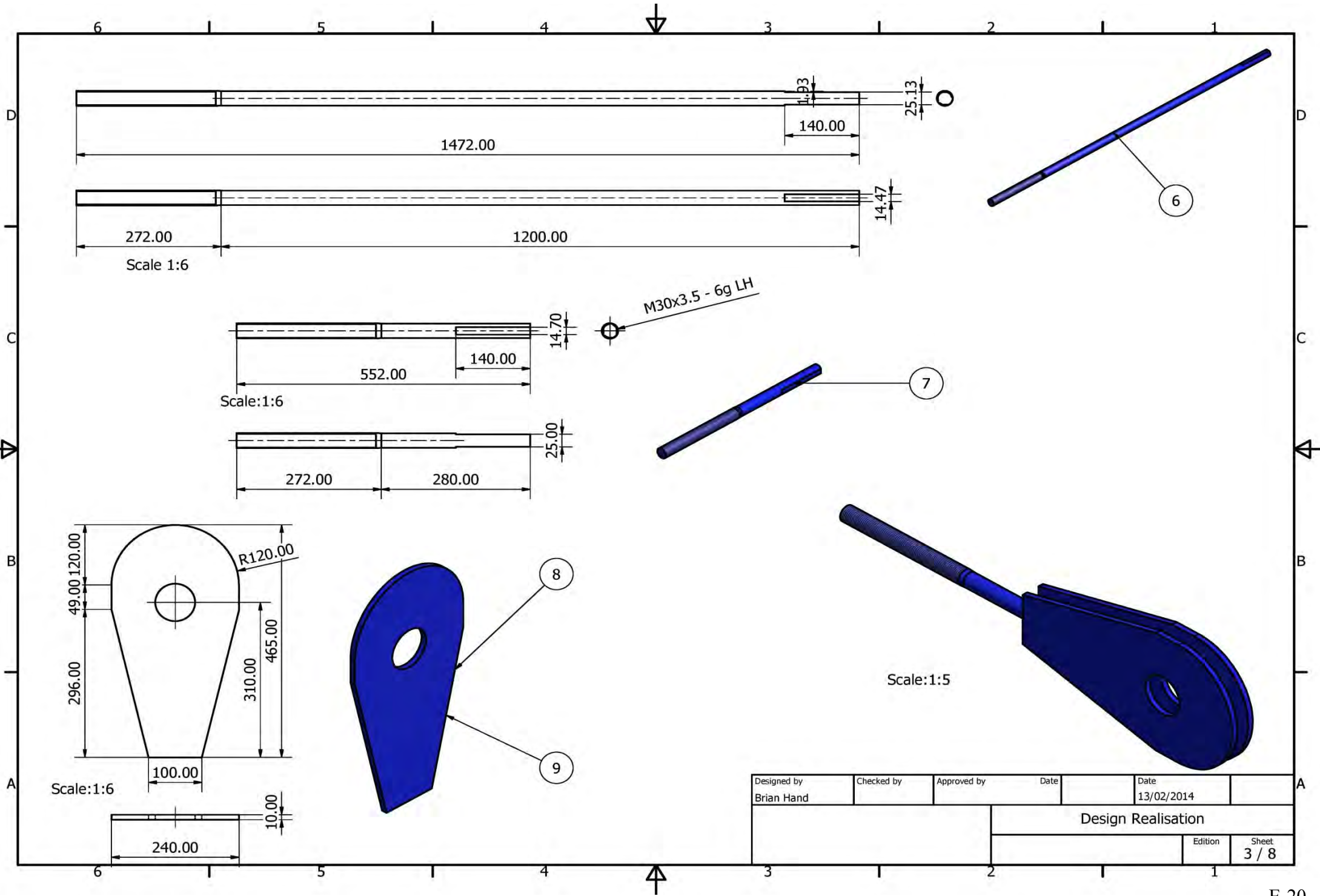


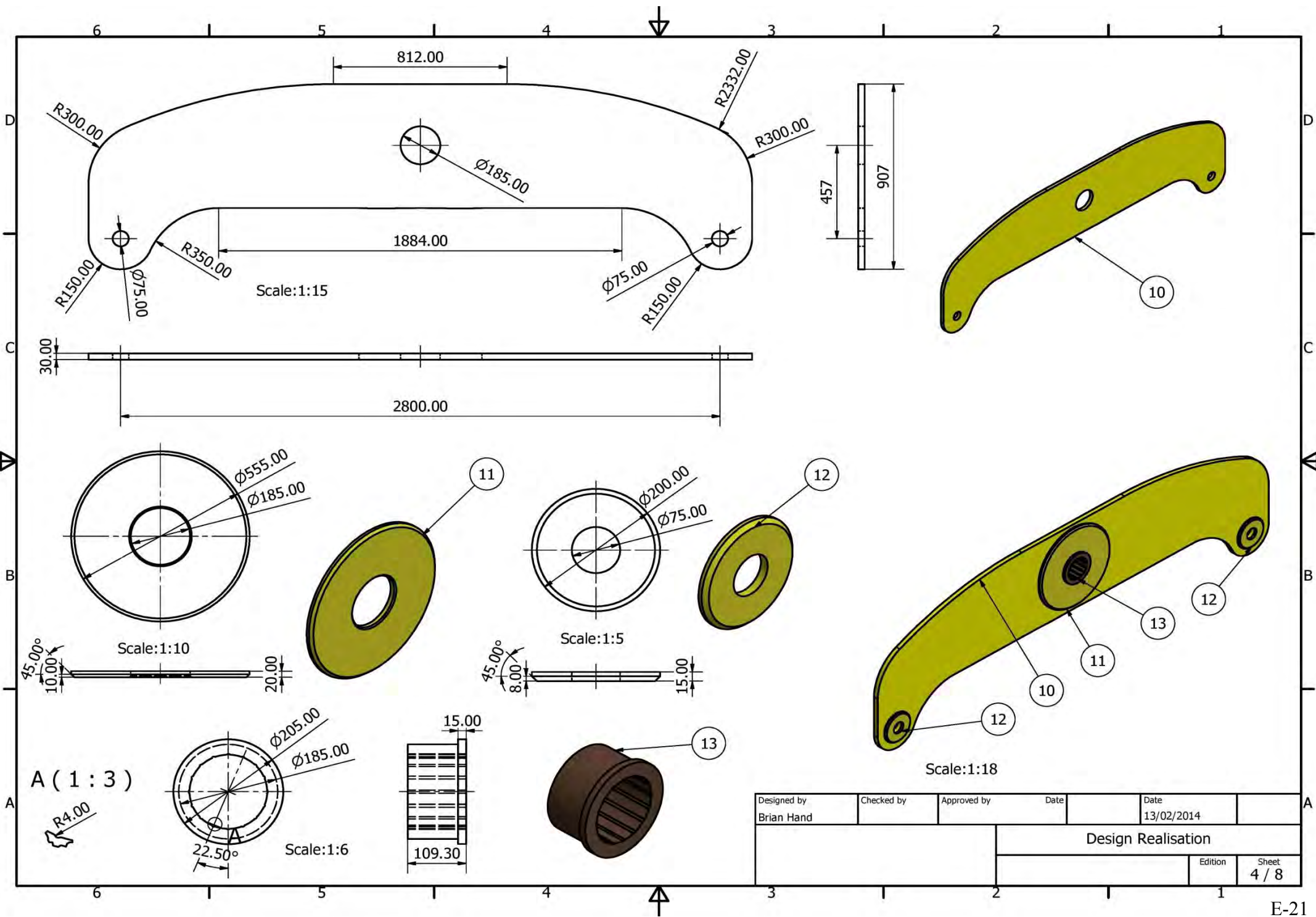
Scale 1:3

Note: Weld nut to plate before attaching side plates

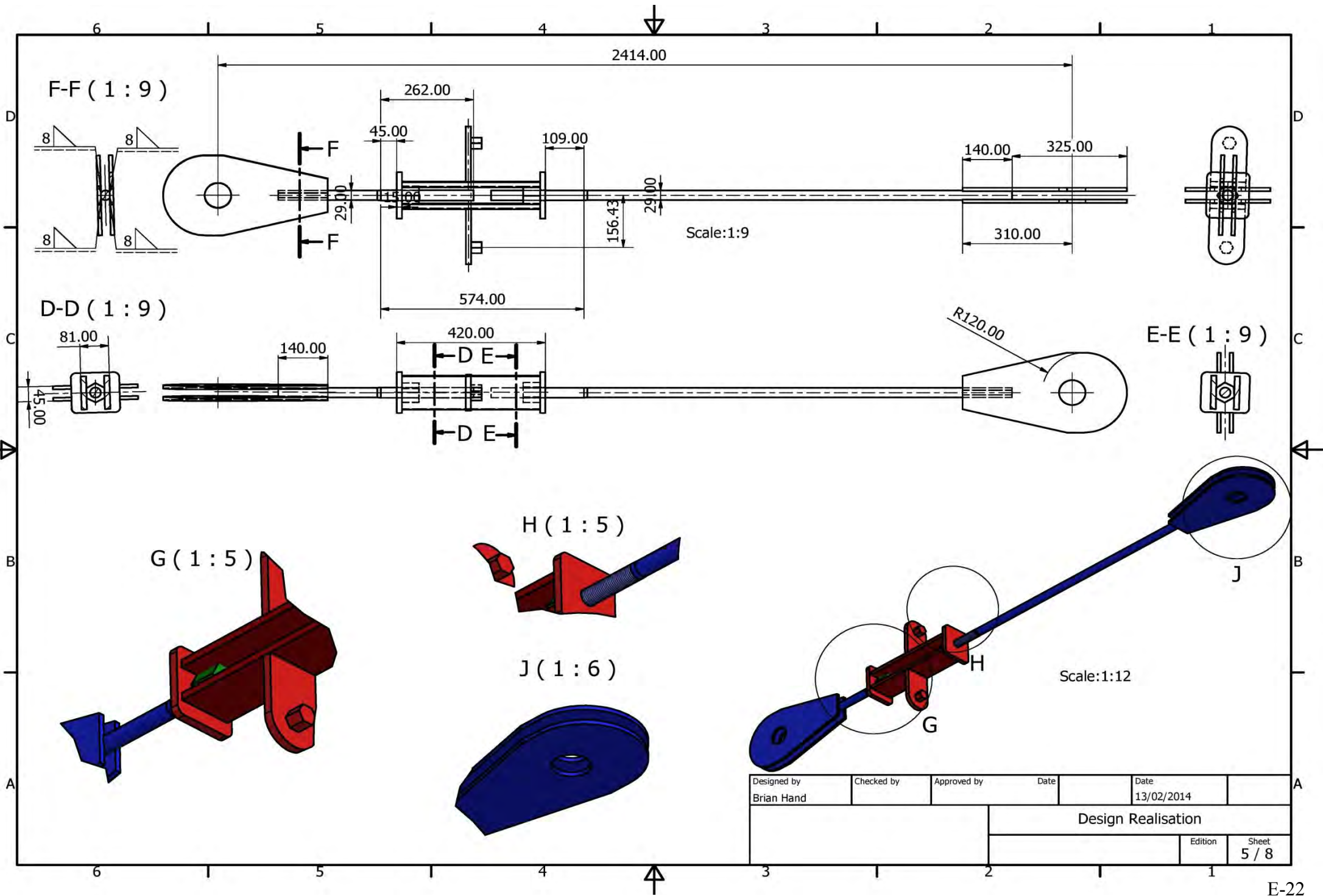


Designed by	Checked by	Approved by	Date	Date
Brian Hand				13/02/2014
			Design Realisation	
			Edition	Sheet
				2 / 8



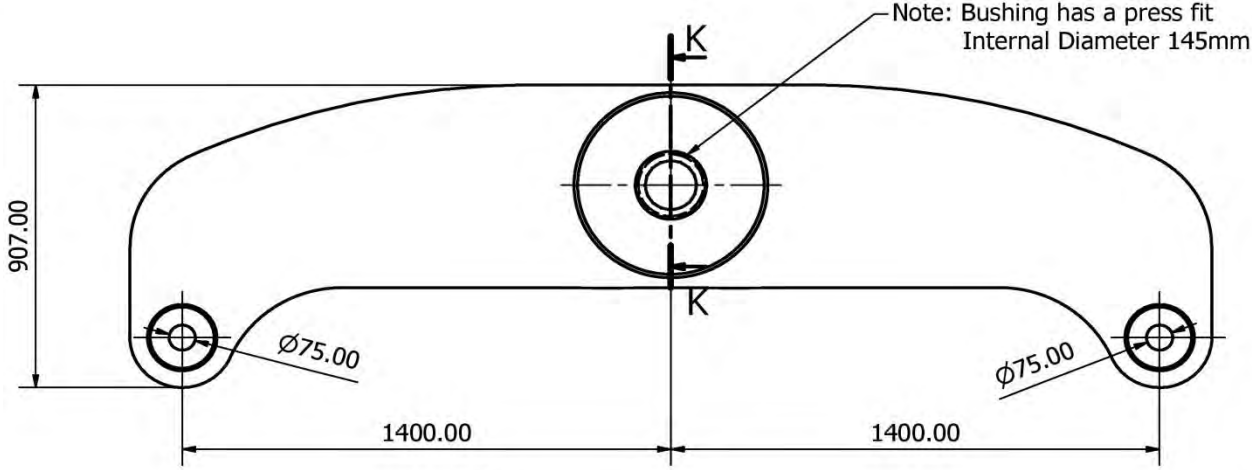


Designed by Brian Hand	Checked by	Approved by	Date	Date 13/02/2014
			Design Realisation	
			Edition	Sheet 4 / 8

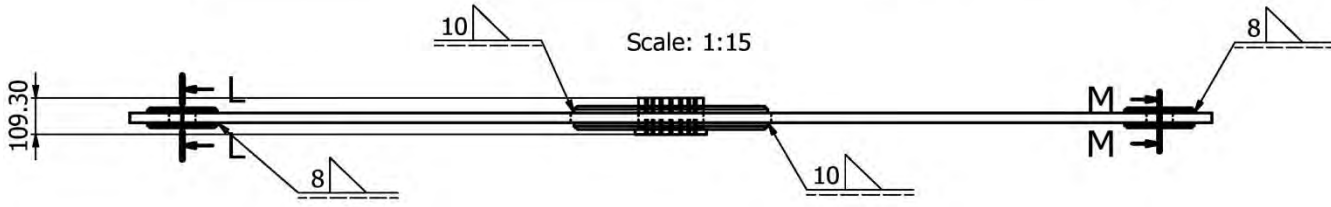


Designed by Brian Hand	Checked by	Approved by	Date	Date 13/02/2014
Design Realisation			Edition	Sheet 5 / 8

K-K (1 : 15)



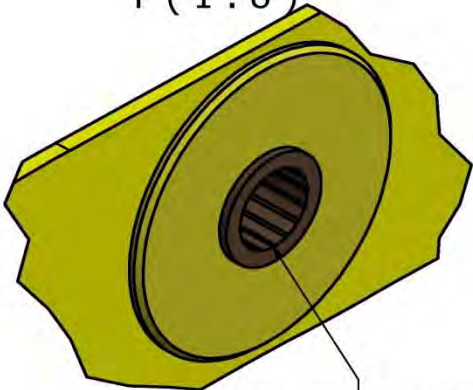
L-L (1 : 15)



M-M (1 : 15)

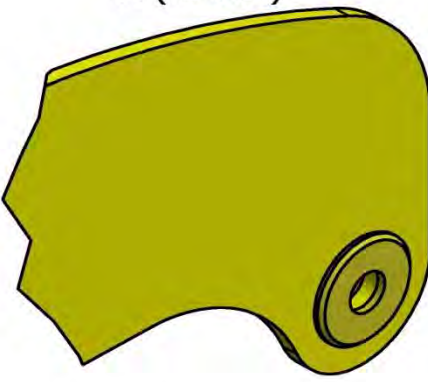


P (1 : 8)

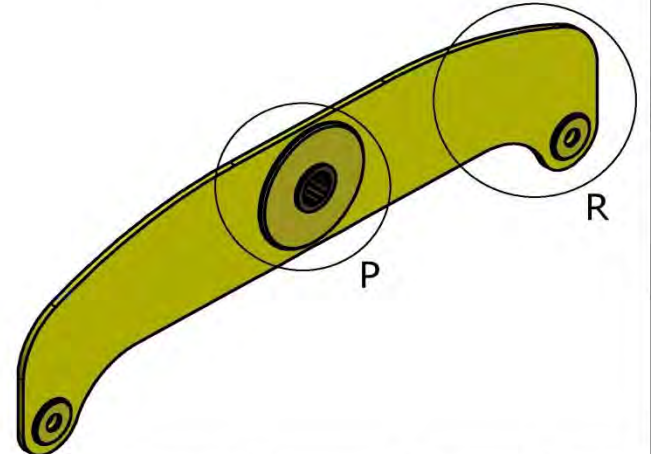


Scale:1:8

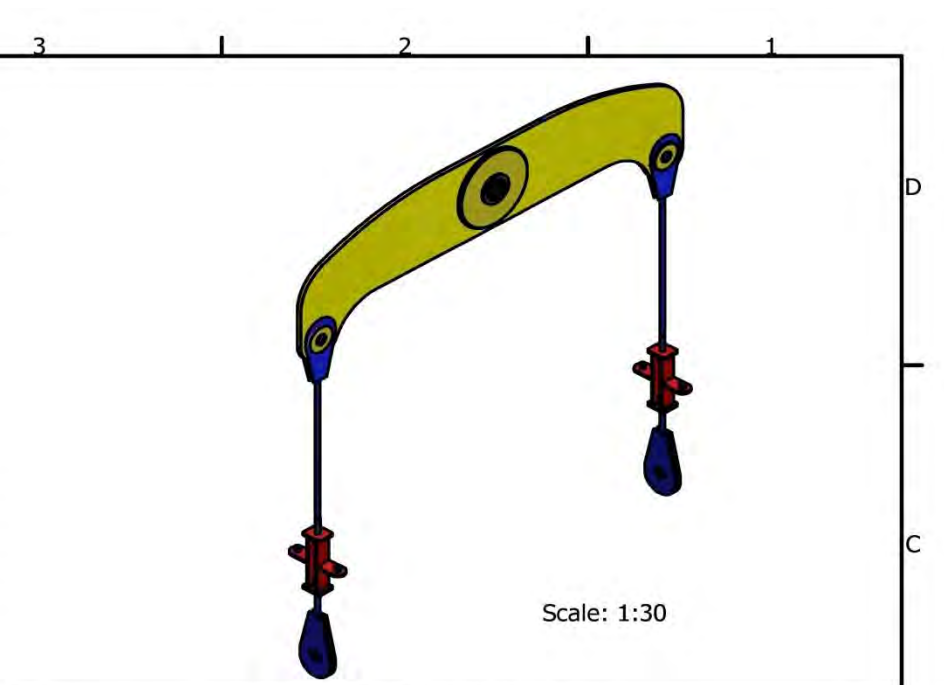
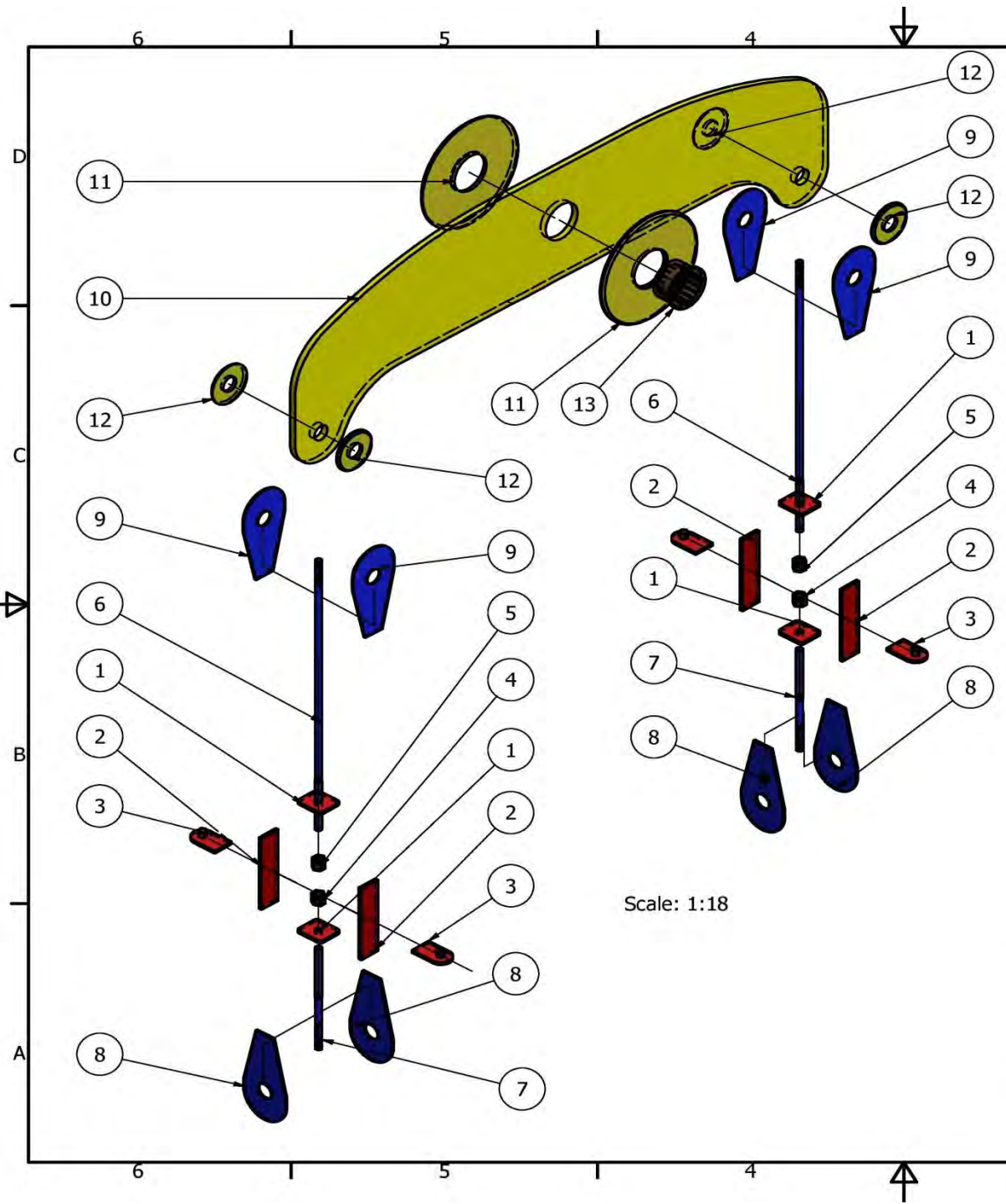
R (1 : 8)



Scale: 1:8



Designed by Brian Hand	Checked by	Approved by	Date 13/02/2014
Design Realisation			Edition
			Sheet 6 / 8



PARTS LIST			
ITEM	QTY	PART NUMBER	DESCRIPTION
1	4	Turnbuckle Top Plate	
2	4	Turnbuckle Side Plate	
3	4	Turnbuckle Torque Plate	
4	2	RH Nut	
5	2	LH NUT	
6	2	Top Shaft	
7	2	Bottom Shaft	
8	4	Bottom Link Plate	
9	4	Top Link Plate	
10	1	Equaliser Beam	
11	2	Centre Bearing Plate	
12	4	Connection Bearing Plate	
13	1	Bushing	

Designed by Brian Hand	Checked by	Approved by	Date	Date 13/02/2014
Design Realisation			Edition	Sheet 7 / 8

S355 Steel Plate for use by LCC

1. Scope of Application and Purpose

Definition of technical delivery and quality requirements for steel plate. This specification applies to EN10029 hot rolled flat plates with a thickness of more than 3 millimeters, with material complying with EN 10025. The intention is to specify in one document the additional requirements for plates for use by Liebherr Container Cranes or it's subcontractors.

2. Applicable Documents

The following documents are applicable:

EN 10025

EN 10029

SLV guideline for the use of material St 52-3 for structural purposes (19-Mar-1984)

SEP 1390 weld bead bend test (July-1996)

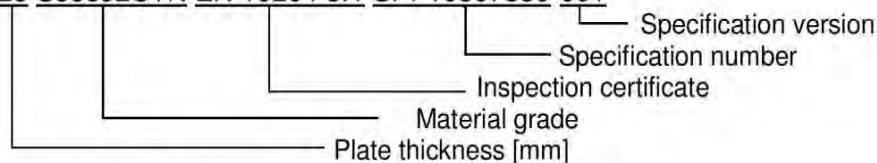
3. Requirements / Description

3.1. Steel grades with additional requirements

Table 1 summarises the steel grades with additional requirements for LCC

3.2. Example of Description

PLATE 25 S355J2C+N EN 10204 3.1 SPF10807330-001



3.3. Delivery Conditions

3.3.1. Standard reference

Products referenced by this specification shall also comply with the technical delivery conditions set by EN 10021, EN 10025-1-4, EN 10163-1+2. Additionally, the standard EN 10164 shall be fulfilled for products with properties in through thickness direction.

3.3.2. Surface Quality

Plates are not ordered in de-scaled quality (except in special cases).

All steel plates shall be suited for shot blasting to assure a surface acc. to ISO 8501-1 grade Sa 2^{1/2}.

Surface flaws and quality variances are accepted according to the standard EN 10163-1+2. Class B, sub assembly 1.

3.3.3. Density

The theoretical weight is the order and acceptance criteria for the steel products. Thus exceeding the nominal weight is not registered.

The calculation of the theoretical weight is based on the density value 7,85 kg/dm³.

3.4. Delivery Requirements

3.4.1. Type of de-oxidation

Products complying with this specification shall be fully killed (FF).

3.4.2. Heat Treatment

The steel shall be supplied in **normalised** condition.

The heat treatment condition shall be stated on the inspection certificate.

3.5. Chemical Analysis (heat analysis in weight percentage)

In addition to the requirements of EN 10025, the chemical composition as stated on the mill certificates shall show compliance with table 2, where required by table 1.

3.6. Tolerances

3.6.1. Thickness tolerances

EN 10029, table 1, class A

3.6.2. Width tolerances

EN 10029, table 2

3.6.3. Length tolerances

EN 10029, table 3

3.6.4. Flatness tolerances

EN 10029, table 4, class N

3.7. Testing and Inspection Certificate

3.7.1. Testing

According to EN 10025 with additional testing defined in table 1.

3.7.2. Inspection certificate

The inspection certificate (acc. to EN 10204) acc. to the order shall be supplied together with the product. The inspection certificates shall be supplied to the purchaser in English language, as original (as a paper form or as a pdf-document) or verified copies (copies of inspection certificates EN 10204 3.2 shall be verified by the Certifying Authority).

Minimum content:

- Identification (material type, dimension, test no., etc.)
- Test results
- Heat treatment condition

3.8. Marking

Each individual plate **of thickness 8mm and above** shall be marked.

Type of marking: Hard stamping of all markings (min. height 6 mm).

The mark shall be located transverse to the rolling direction at a distance of 500 mm from the top or bottom of the plate.

The mark shall be visible surrounded by colour and indicate the following:

- Steel grade
- Heat number
- Specimen number
- Manufacturer's symbol
- Inspector's or surveyor's stamp (for inspection certificate 3.2)

A missing, illegible or incomplete stamping is a reason for a claim.

4. Revisions

Revision 001, documenting current practice as at November 2009

Table 1 - Additional material requirements for LCC

Designation EN 10027-1	Former Designation	Material No. EN 10027-2	Standard	Thickness	Compliance with SLV guideline	Bend test to SEP 1390
S355J2+N	St52-3N	1.0577+N	EN 10025-2	<8mm	-	-
S355J2+N	St52-3N	1.0577+N	EN 10025-2	8-25mm	Required	-
S355J2+N	St52-3N	1.0577+N	EN 10025-2	25-50mm	Required	Required
S355J2+N	St52-3N	1.0577+N	EN 10025-2	>50mm	Required	-
S355J2+N Z35	St52-3N Z35	1.0577+N	EN 10025-2	All	Required	-
S355J2C+N	QSt52-3N		EN 10025-2	All	Required	-

Table 2 - Chemical composition according to SLV guideline

C Max.	Ti Max.	V Max.	Cr Max.	Cu Max.	Nb Max.	S Max.
0.18%	0.02%	0.02%	0.10%	0.10%	0.04%	0.02%

Photoelastic Specifications & Support Rig drawings



PhotoStress® Coatings

Micro-Measurements



PhotoStress Coating Materials and Adhesives



DESCRIPTION

Micro-Measurements manufactures the widest range of PhotoStress coating materials available. All of the materials are produced in an environmentally controlled "clean room" to ensure highest quality.

The selection charts on pages 3 and 4 are arranged to permit easy selection of materials for every application.

The materials are grouped into:

- (1) High-Modulus Materials
- (2) Medium-Modulus Materials
- (3) Low-Modulus Materials

Sheet and liquid plastics for various applications are described on page 3. The adhesives listed on page 4 are recommended for use with these plastics and are similarly grouped to simplify selection and assure proper bonding of the sheet to the part under test.

Sheets for Coating Flat Parts

Pre-manufactured sheets are most economical for testing flat parts. The standard size for all sheet materials is 10 x 10 in [254 x 254 mm]. For the PS-1 type, other standard sizes are 10 x 20 in and 20 x 20 in [254 x 508 mm and 508 x 508 mm, respectively]. Thicknesses of sheets range from 0.010 to 0.120 in [0.25 to 3.05 mm]. All sheets are calibrated for strain sensitivity, are held to very close dimensional tolerances, and are uniform in optical and mechanical properties from sheet to sheet. PS-1 sheets are provided with a reflective backing. All other sheets are clear. All sheets are supplied with a protective paper coating.

Liquids for Coating Complex-Shaped Parts

Liquid plastic materials are used for making coatings for structures with complex contours which cannot be coated satisfactorily with flat sheets. Surface forming, or "contouring", is the method of applying the plastic to the test part.

FEATURES

- High strain-optic sensitivity
- Uniformity in optical and mechanical properties
- Wide variety for coating metals, plastics, concrete, elastomers, wood, composites, and other materials
- Detailed handling and application instructions

The liquid plastics are carefully controlled formulations of resins blended to provide (1) a coating of known photoelastic properties, (2) a controllable and repeatable curing schedule allowing ample time for contouring operations, and (3) repeatable optical and mechanical properties. Sufficient hardener is supplied for complete utilization of the resin.

Adhesive

Selection of the proper adhesive for use with the various photoelastic coatings is important. Micro-Measurements produces a wide variety to match the needs of the test conditions, and the properties of the coating materials to be bonded.

All adhesives listed are of the reflecting type. To obtain a clear adhesive with the same properties, add the letter "C" after the adhesive type (example: PC-1C).

REFERENCE LITERATURE

Tech Note TN-704, How to Select Photoelastic Coatings

Tech Note TN-701, Calibration of Photoelastic Coatings

Tech Note TN-706, Corrections to Photoelastic Coating Fringe-Order Measurements

Tech Note TN-702, Introduction to Stress Analysis by the PhotoStress® Method

Application Note IB-221, Instructions for Casting and Contouring Photoelastic Sheets

Application Note IB-223, Instructions for Bonding Flat and Contoured Photoelastic Sheets to Test-Part Surfaces

Instruction Bulletin IB-238, Calibration of Low-Modulus PhotoStress® Coatings by Imposed Curvature

Instruction Bulletin IB-239, Instructions for Brushing PhotoStress® Coatings on Test-Part Surfaces

Literature available on request from Micro-Measurements.

PhotoStress® Coatings

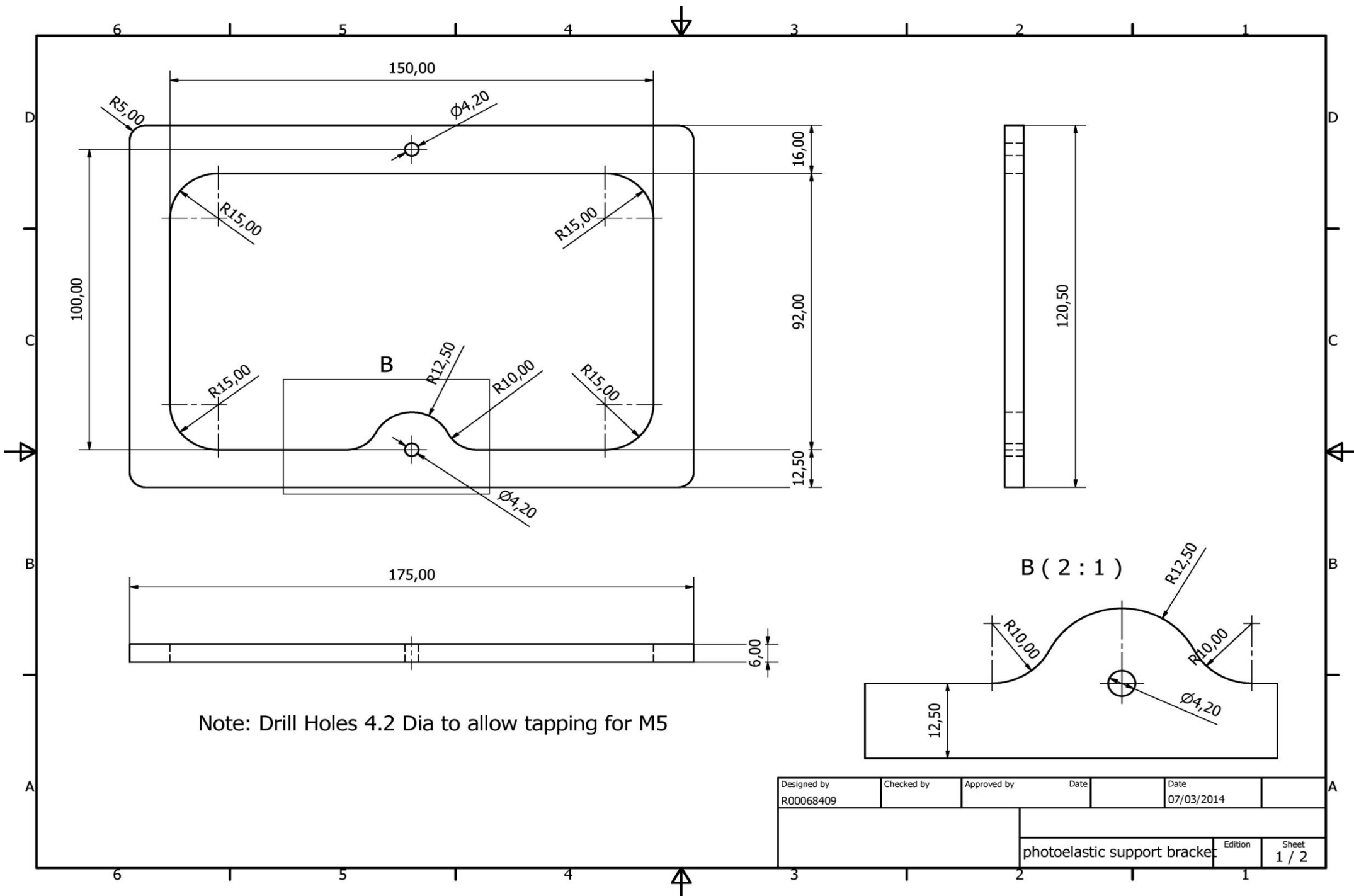
SPECIFICATIONS - HIGH-MODULUS MATERIALS								
Model Number	Strain Optical Coef K	Elongation (%)	Elastic Modulus E 1000 psi [Gpa]	Poisson's Ratio ν	Thickness		Sensitivity Constant to °F [°C]	Max Usable Temperature °F [°C]
					in[mm]	Tolerance		
PS-1 Sheet	0.150	5	360 [2.5]	0.38	0.120 [3.05] 0.080 [2.05] 0.040 [1.00] 0.020 [0.50] 0.010 [0.25]	±0.002 [±0.06]	300 [150]	300 [150]
PS-8 Sheet	0.090	3	450 [3.1]	0.36	0.120 [3.05] 0.080 [2.05] 0.040 [1.00] 0.020 [0.50]	±0.003 [±0.08]	160 [70]	400 [200]
PL-1 Liquid PL-8 Liquid	(PL-1) 0.100 (PL-8) 0.080	3 3	420 [2.9] 420 [2.9]	0.36 0.36	For casting contourable sheets up to 0.125 in [3.2 mm]		180 [80] 160 [70]	450 [230] 400 [200]

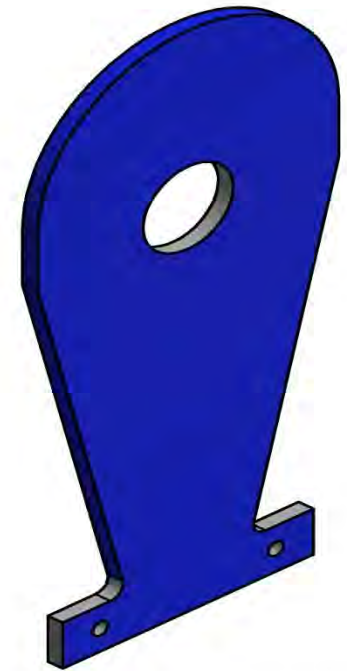
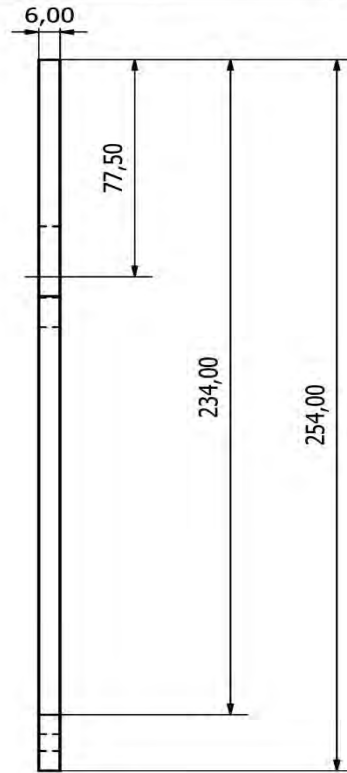
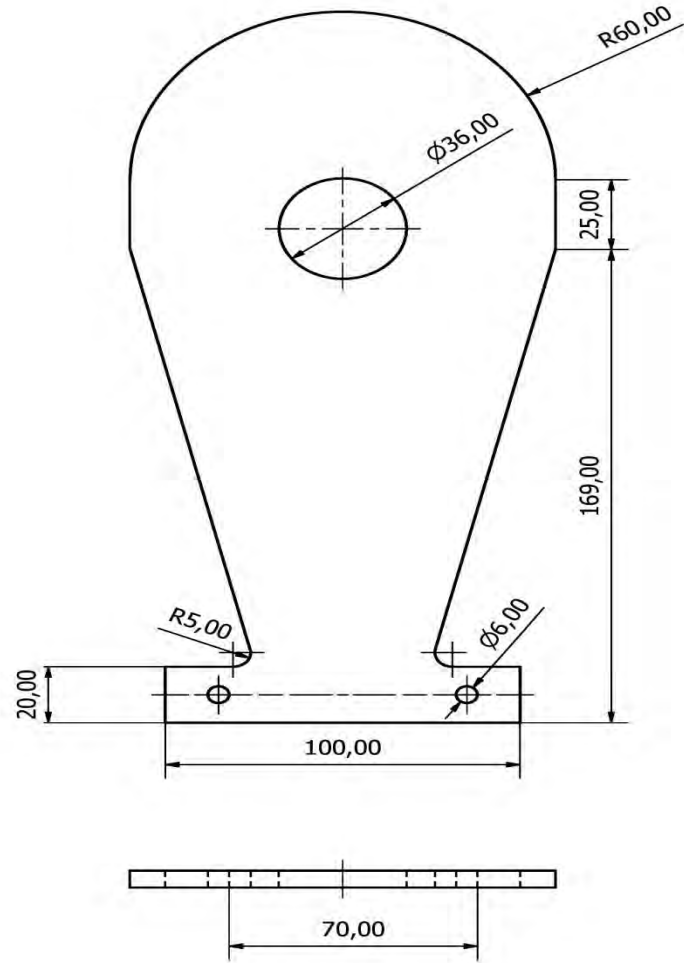
SPECIFICATIONS - MEDIUM-MODULUS MATERIALS								
Model Number	Strain Optical Coef K	Elongation (%)	Elastic Modulus E 1000 psi [Gpa]	Poisson's Ratio ν	Thickness		Sensitivity Constant to °F [°C]	Max Usable Temperature °F [°C]
					in[mm]	Tolerance		
PS-3 Sheet	0.020 (typical)	30	30 [0.21]	0.42	0.120 [3.05] 0.080 [2.05] 0.040 [1.00]	±0.003 [±0.08]	110 [40]	400 [200]
PL-2 Liquid	0.020 (typical)	30	30 [0.21]	0.42	For casting contourable sheets up to 0.125 in [3.2 mm]		110 [40]	400 [200]

SPECIFICATIONS - LOW-MODULUS MATERIALS								
Model Number	Strain Optical Coef K	Elongation (%)	Elastic Modulus E 1000 psi [Gpa]	Poisson's Ratio ν	Thickness		Sensitivity Constant to °F [°C]	Max Usable Temperature °F [°C]
					in[mm]	Tolerance		
PS-4 Sheet	0.009 (typical)	>40	.5 [0.004]	0.500	0.120 [3.05] 0.080 [2.05] 0.040 [1.00] 0.020 [0.50]	±0.003 [±0.08]	350 [175]	350 [175]
PL-3 Liquid	0.002 (typical)	>50	0.2 [0.0014] After 1 min. at constant strain	0.42	For casting contourable sheets up to 0.125 in [3.2 mm]		90 [32]	300 [150]
PS-6 Sheet PL-6 Liquid	0.0006 (typical)	>100	0.1 [0.0007] After 1 min. at constant strain	.500	Sheet: Specify size. Liquid: For casting contourable sheets up to 0.125in [3.2 mm].		90 [32]	300 [150]

All physical and optical properties given are nominal values. NOTES (See below):

- (1) Other than PS-1, all sheets are standard size 10 x 10 in [254 x 254 mm]. Standard packages for liquids are 3 oz [80 gm], 1 pt [0.47 litre], qt [0.950 litre], and gal [3.78 litre].
- (2) For all medium- and low-modulus materials, calibration is required for accurate strain optical coefficient values.





Designed by R00068409	Checked by	Approved by	Date	Date 22/04/2014	
			Photo elastic model		
				Edition	Sheet 1 / 1

Photoelastic Test Piece CNC Code

Operation List POST: Hurco BMC 20

OP 1 DRILL HOLES TOOL 1 FLAT
6MM 2F EC HSS

TOOL DIAMETER 6, HOLE
DIAMETERS 6

FINISH PASS TOOL 1 FLAT
6MM 2F EC HSS

EFFECTIVE DIAMETER 6

FINISH PASS TOOL 1 FLAT
6MM 2F EC HSS

EFFECTIVE DIAMETER 6

Feed Distance: 2631.7 Time for OP
1: 11m 49s

Total Feed Distance 2631.7

Tool Change Time 0m
18s

Total Time 12m 07s

Material: Plastic Roughing

Cut Dry

Recycle swarf

START

'(BRIAN HAND)

%

'(Program Produced - 26 MAR 14)

N10 G90 G71

N20 G40 G80

'(OP 1 DRILL HOLES TOOL 1 FLAT
6MM 2F EC HSS)

'(TOOL DIAMETER 6, HOLE
DIAMETERS 6)

N30 T01 M06

N40 S2500 M03

N50 M08

N60 G90 G0 Z60.

N70 X-35. Y9.75

N80 X-35. Y9.75 Z5.

N90 G81 Z11.5 F60 M08

N100 X35. Y9.75

N110 G80

N120 G90 G0 Z60.

'(OP 1 FINISH PASS TOOL 1 FLAT
6MM 2F EC HSS)

'(EFFECTIVE DIAMETER 6)

N130 X-15. Y176.

N140 Z5.

N150 G1 Z-2.167

N160 G3 X7.497 Y163.008 I0. J176. F250

N170 Y188.992 I0. J176.

N180 X-15. Y176. I0. J176.

N190 G1 Z-4.333 F60

N200 G3 X7.497 Y163.008 I0. J176. F250

N210 Y188.992 I0. J176.

N220 X-15. Y176. I0. J176.

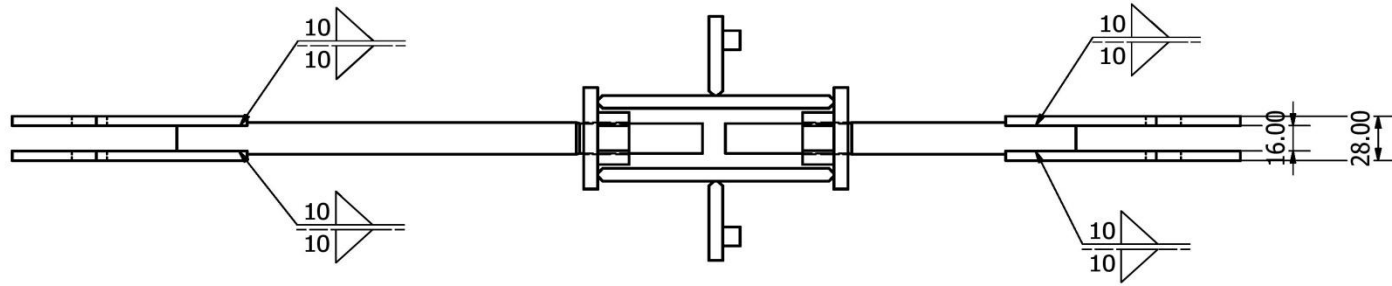
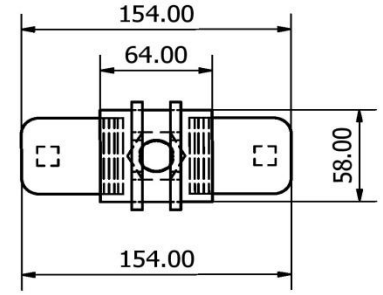
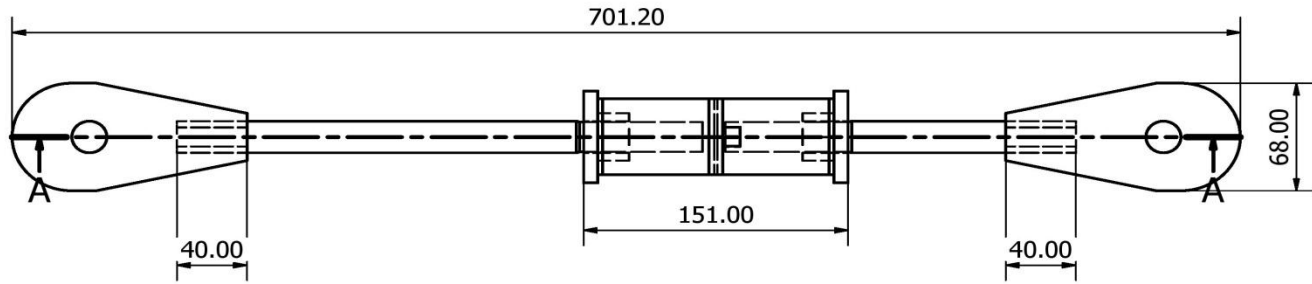
N230 G1 Z-6.5 F60

N240 G3 X7.497 Y163.008 I0. J176. F250

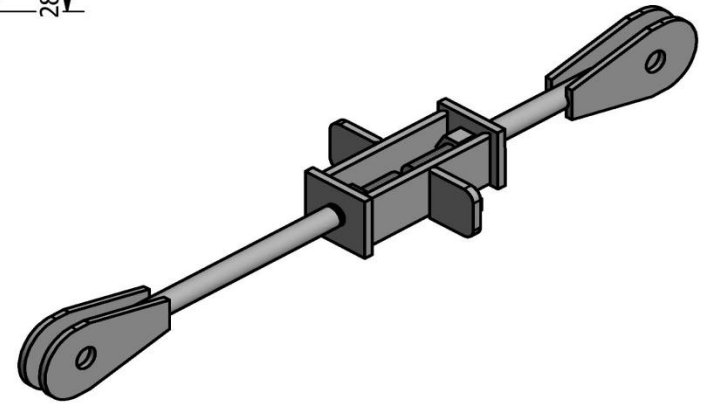
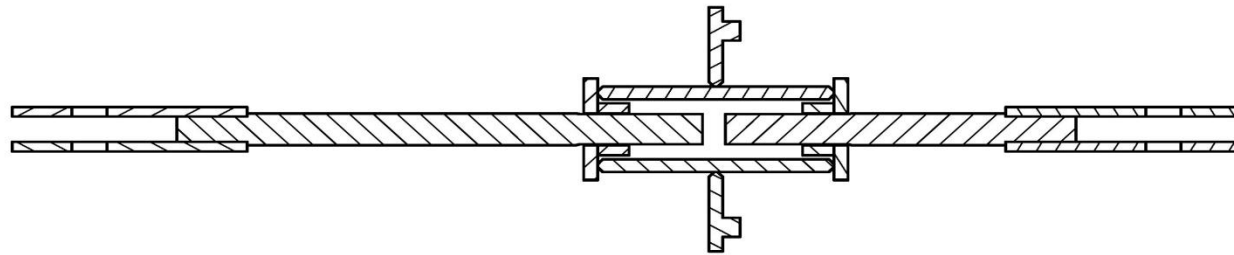
N250 Y188.992 I0. J176.
N260 X-15. Y176. I0. J176.
N270 G0 Z60.
N280 X63. Y194.
N290 Z5.
N300 G1 Z-2.167 F60
N310 Y168.65 F250
N320 X28.94 Y24.627
N330 G3 X30.618 Y22.5 I30.966 J24.5
N340 G1 X53.
N350 Y-3.
N360 X-53.
N370 Y22.5
N380 X-30.621

N390 G3 X-28.954 Y24.748 I-30.969
J24.5
N400 G1 X-63. Y168.65
N410 Y194.
N420 G2 X0. Y257. I0. J194.
N430 X63. Y194. I0. J194.
N440 G1 Z-4.333 F60
N450 Y168.65 F250
N460 X28.94 Y24.627
N470 G3 X30.618 Y22.5 I30.966 J24.5
N480 G1 X53.
N490 Y-3.
N500 X-53.
N510 Y22.5

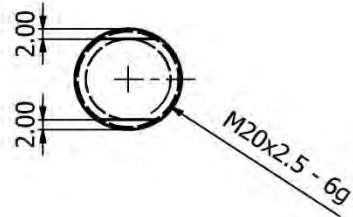
Primary Prototype Manufacture Drawings



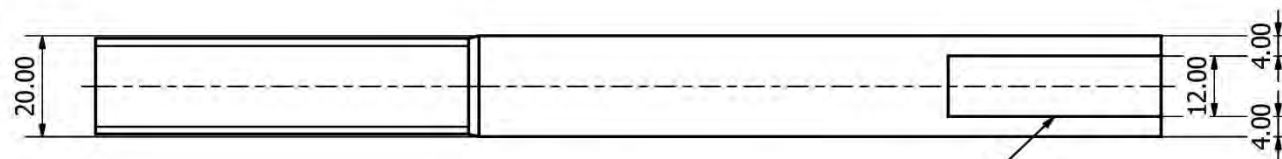
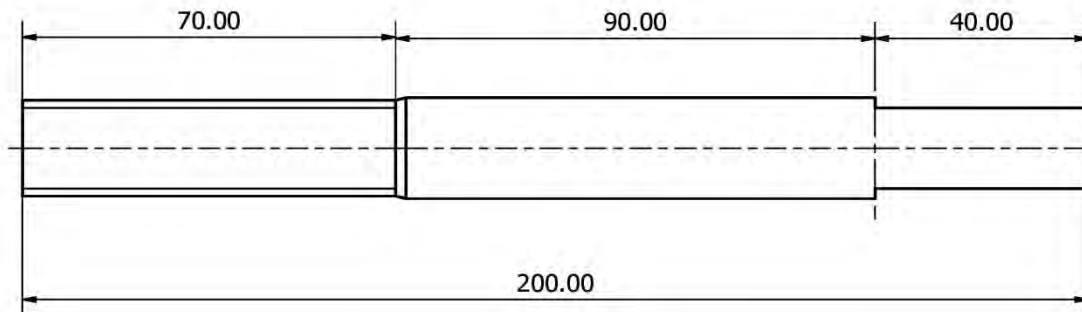
A-A (1 : 3)



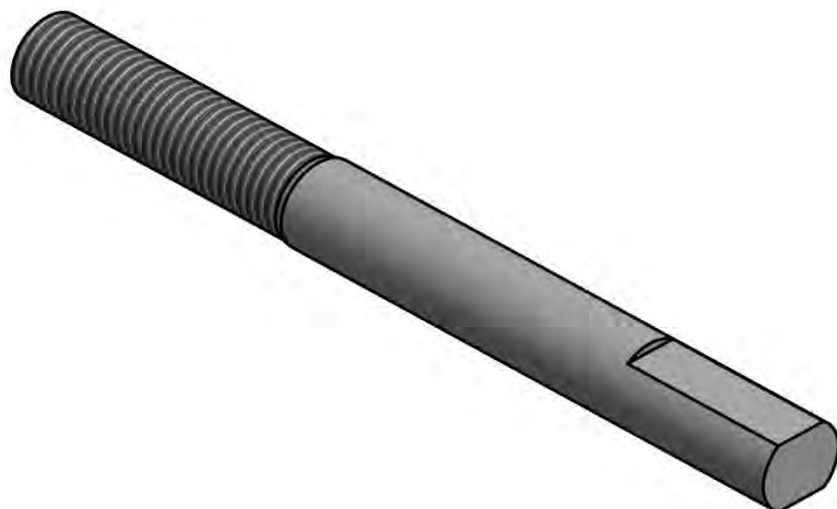
Designed by B Hand	Checked by	Approved by	Date	Date 08/02/2014	
			Assembly		
Assembly				Edition	Sheet 1 / 1



Scale 1:1

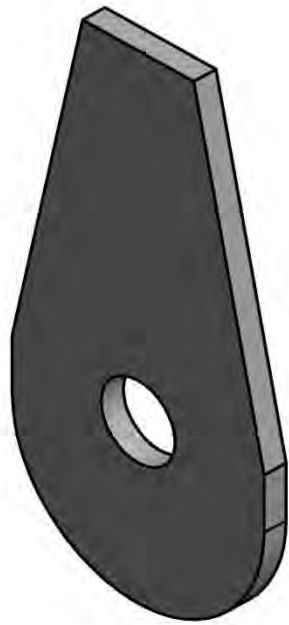


Machine Surfaces Flat

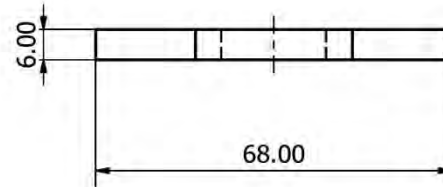
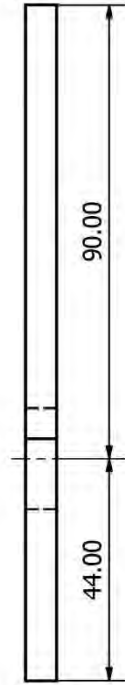
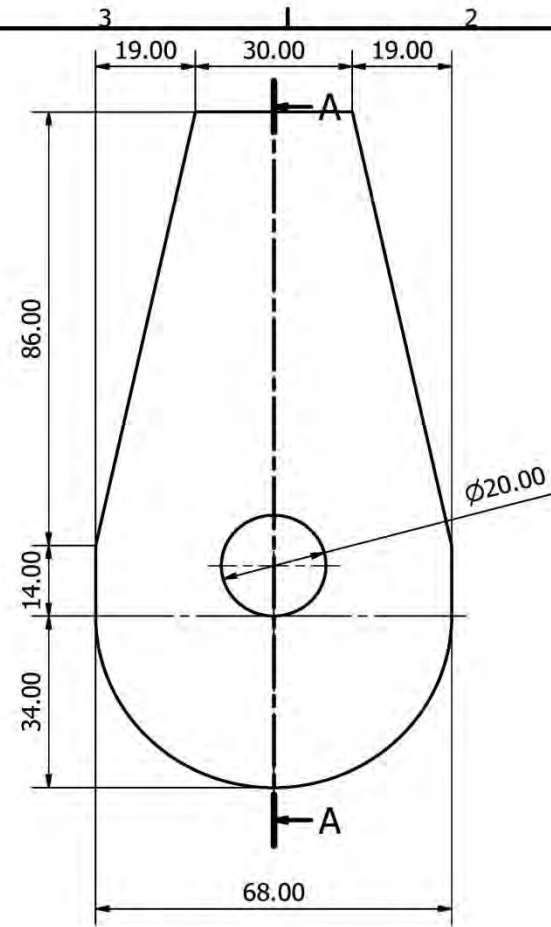


Note:
 Thread is M20
 Pitch is 2.5mm
 Right Hand Thread

Designed by B Hand	Checked by	Approved by	Date	Date 07/02/2014	
Cork Institute of Technology			Bottom Link		
Right hand thread shaft			Edition	Sheet 1 / 1	



A-A (1:1)



Designed by B Hand	Checked by	Approved by	Date	Date 07/02/2014	
			Link Plate		
			Link Plate	Edition	Sheet 1 / 1

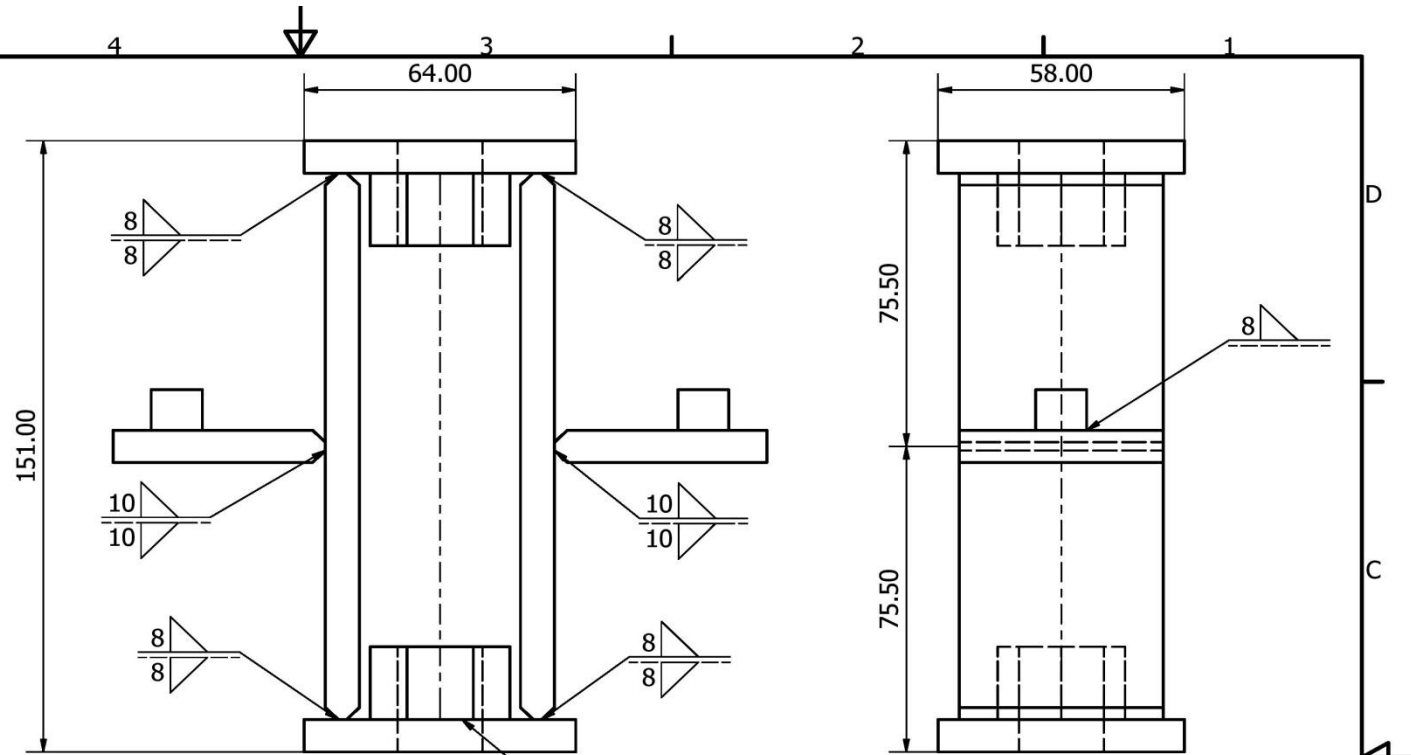
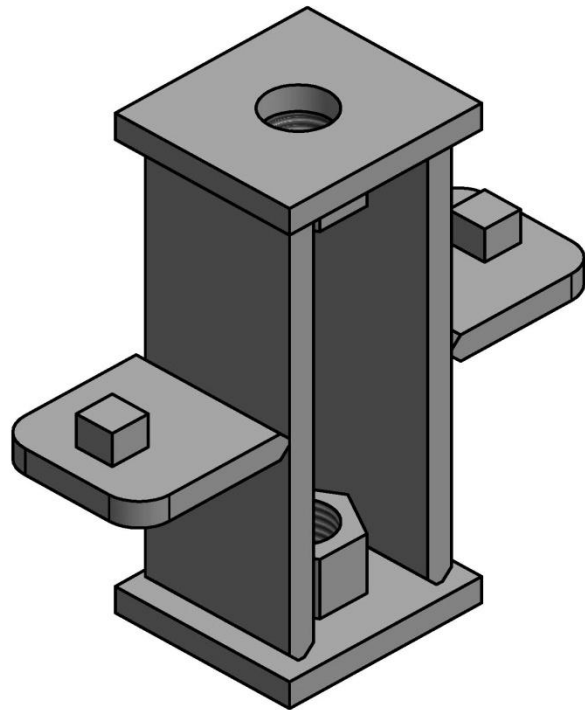
6 5 4 3 2 1

D

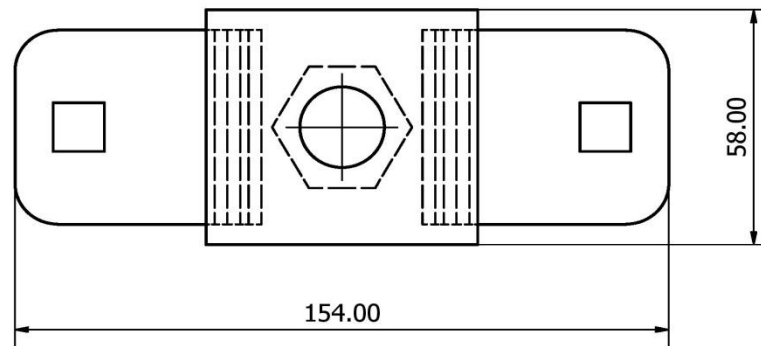
C

B

A



Note: Weld nut to plate before attaching side plate



Scale: 0.8:1

Designed by	Checked by	Approved by	Date	Date	
B Hand				08/02/2014	
			Turnbuckle Weld Assembly		
			turnbuckle weld	Edition	Sheet
					1 / 1

6 5 4 3 2 1

Strain Gauge Specification

FEATURES :

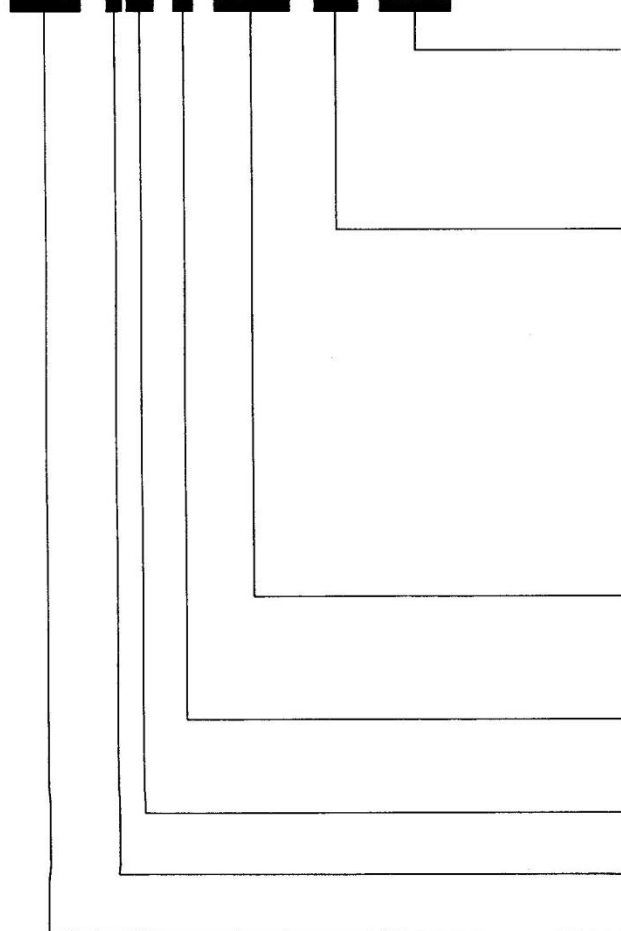
- * Almost no effect on test object.
- * Distant and multi-points measurements are possible.
- * Applicable to both static and dynamic strains.
- * Both surfaces being completely laminated, the gauge grids are entirely protected.
- * The gauges, being fitted with leads, are easy to handle.

STANDARD SPECIFICATIONS :

Gauge Length	0.3 mm. min. to 60 mm. max.
Measurable Strain	2 to 4% maximum. Up to 10% with foil yielding strain gauges.
Temperature Range	FA (Polyester Backing) -30°C to +80°C MA (Polyimide Backing) -30°C to +180°C
Thermal Output (See Fig. 1)	FA: Within $\pm 2\mu\epsilon/^\circ\text{C}$ (At room temperature up to +80°C) MA: Within $\pm 2\mu\epsilon/^\circ\text{C}$ (At room temperature up to +160°C) Within $\pm 5\mu\epsilon/^\circ\text{C}$ (At +160°C up to +180°C)
Gauge Factor Change with Temperature (See Fig. 2)	Within $\pm 0.015\%/^\circ\text{C}$
Gauge Resistance Tolerance	Within $\pm 0.5\%$ of the nominal resistance.
Gauge Factor	2.00 (Nominal)
Gauge Factor Tolerance	Within $\pm 1\%$ of the value indicated on individual gauge packet for gauge lengths of 5 mm. to 60 mm. Within $\pm 2\%$ of the value indicated on individual gauge packet for gauge lengths of 0.3 mm. to 3 mm.
Fatigue Life	More than 10^5 reversals at 1000×10^{-6} strain.

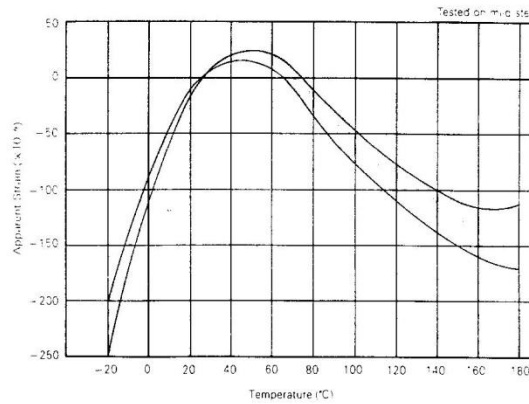
CONFIGURATIONS :

N11-FA-5-350-16-L03

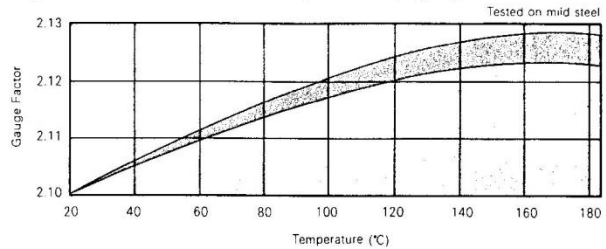


GENERAL PERFORMANCES OF TYPE N11-MA-5-120-11 STRAIN GAUGE

Thermal Output Characteristics (Fig.1)



Gauge Factor variation with temperature (Fig. 2)



- Optional Specifications
03: Length of Leads
L Resin Clad Copper Wire (Up to 0.3m)
W Waterproof Moulded Type* (See page 1)
P Optional Pattern Type
(Subject to special quotations)

- Linear Expansion Factor of Material against which Strain Gauge is self-temperature compensated and its base colour classification

Base Colour	Materials against which strain gauge is self-temperature compensated	Linear expansion factor of materials	Codes
Red	Mild steel	$10.8 \times 10^{-6}/^\circ\text{C}$	11
Orange	Stainless steel	$16.2 \times 10^{-6}/^\circ\text{C}$	16
Blue	Aluminium alloy	$23.4 \times 10^{-6}/^\circ\text{C}$	23

Remarks : Base colour classifications are made in FA Series only. Code of "11" for mild steel can be deleted.

- Gauge Resistance
Expressing strain gauge nominal resistance in the unit of Ω . Can be deleted when nominal resistance is 120Ω .
- Gauge Length
Expressing grid effective length in figures in the unit of mm.
- Foil Material
A: Cu-Ni Alloy
- Base Material
F: Polyester, M: Polyimide
- Basic Pattern and its Combinations

Hazard Analysis Tables

(LO)	Likelihood of Occurrence	(FE)	Frequency of Occurrence	(DPH)	Degree of Possible Harm	(NPR)	Number of Persons at Risk
0	Impossible. Cannot happen.	0.1	Infrequently	0.1	Scratch or bruise	1	1-2 people
0.1	Possible in extreme circumstances	0.2	Annually			3	3-7 people
0.5	Highly unlikely, though conceivable.	1	Monthly	0.5	Laceration or mild ill health effect	4	8-15
1	Unlikely, but could occur	1.5	Weekly			8	16-50 people
2	Possible, but unusual.	2.5	Daily	1	Break a minor bone or minor illness	12	50+ people
5	Even chance. Could happen.	4	Hourly	2	Break a major bone or minor illness		
8	Probable. To be expected.	5	Constantly	8	Loss of limb, eye or serious illness of a temporary nature		
10	Likely, Only to be expected			15	Fatality		
15	Certain. No doubt.						

$$(LO * FE * DPH * NPR) = HRN \text{ (Hazard Rating Number)}$$

LO = Likelihood of Occurrence
 FE = Frequency of Occurrence
 DPH = Degree of Possible Harm
 NPR = Number of Persons at Risk

HRN	0-1	1-5	1-10	10-50	50-100	100-500	500-1000	>1000
RISK	Negligible	Very Low	Low	Significant	High	Very High	Extreme	Unacceptable

Appendix F

Electronic Files

Attached to this report is a CD-ROM containing relevant material associated with this project that the reader may need to refer to. Below are the subsequent folders on the disk and their contents.

Exhibition Material

- Exhibition Posters
- Exhibition Videos

Experimental & Simulation Videos

- Videos of recorded footage during wind tunnel testing on the wind tunnel model including flow visualisation that was carried out.
- CFD simulations created during analysis.

ANSYS Files

- Simulation models belonging to CFD analysis and structural analysis

Excel Files

This folder contains any relevant MS Excel calculations carried out during the course of this project.

Note: In this folder there is a legend that corresponds to each calculation and page numbers in this report.